Universidade de Lisboa

Instituto de Geografia e Ordenamento do Território

Landslide Susceptibility Evaluation and Validation at a Regional Scale

Cristina da Silva Henriques

Doutoramento em Geografia

Geografia Física

2014

Universidade de Lisboa

Instituto de Geografia e Ordenamento do Território

Landslide Susceptibility Evaluation and Validation at a Regional Scale

Cristina da Silva Henriques

Thesis oriented by Professor José Luís Moreira Gonçalves da Silva Zêzere, specially designed for obtaining the Ph.D. degree in Geography, in the specialty of Physical Geography.

Tese orientada pelo Professor Doutor José Luís Gonçalves Moreira da Silva Zêzere, especialmente elaborada para a obtenção do grau de Doutor em Geografia, na especialidade de Geografia Física.

2014

This dissertation was funded by the Portuguese Foundation for Science and Technology through the PhD grant SFRH/BD/46816/2008.

Esta dissertação foi financiada pela Fundação para a Ciência e Tecnologia através da Bolsa de Doutoramento SFRH/BD/46816/2008.

ACKNOWLEDGEMENTS

The results of this dissertation benefits from the contributions of many so I take this opportunity to publicly express my very great appreciation to who directly or indirectly contributed to the work presented in this dissertation.

Thereby, I would like to express my deep gratitude to Prof. Dr. José Luís Zêzere, my adviser, for all his support, knowledge, availability and specially, for his critical evaluation which was crucial for the development of this dissertation.

Special thanks I want to give to Prof. Dr. Rens Van Beek for all the support, time and knowledge transmitted during the traineeship in Utrecht University in Netherlands. I want to thank, especially, his help in doing the meteorological data analysis and for having rewritten the dynamic physically based model (STARWARS + PROBSTAB) as well as other input python scripts for this dissertation.

To Prof. Dr. Theo Van Asch and Prof. Dr. Derek karssenberg I would like to thank for all the support and advices given. Particularly, I would like to thank to Prof. Dr. Derek karssenberg for having offered the PCRaster course which was of crucial help for handle the STARWARS+PROBSTAB script.

My grateful thanks are also extended to Prof. Dr. Fausto Guzzetti, Prof. Dr. Paola Reichenbach, Prof. Dr. Mauro Cardinali and all the research team from Istituto di Ricerca per la Protezione Idrogeologica (IRPI) in Perúgia for having accepted me for the traineeship where I was able to learn and train the techniques of aerial photo interpretation required for the acquisition of the landslide inventories of ancient landslides, the detailed lithological map and the bedding attitude of the lithological features. I am also particularly grateful for the assistance of Prof. Dr. Ivan Marchesini for helping and given me a GIS tool using Python scripting for obtaining the quantitative data of bedding attitude.

I would like to offer also my special thanks to Prof. Dr. Jorge Rocha for all his technical assistance and for his valuable and constructive suggestions during the development of this research work. Your contribution was essential for this dissertation and your company during the field work and especially your friendship much appreciated.

To Prof. Dr. Fernando Marques and Prof. Dr. Isabel Moitinho de Almeida I am particularly grateful for the soil mechanics lessons, for the assistance on the laboratory equipment and for the help during the collection of soil samples.

Special thanks I want to give to Rita Pimenta for helping me to handle the laboratory equipment and for the advices given during the static physically based modeling.

To Sandra Oliveira I am very grateful that you applied your skills to help me and most of all I am very grateful for you friendship and support during all these years.

I am also obliged to Raquel Melo for helping me to understand the procedure that allows obtaining the soil depth theme and for her friendship and company especially during the traineeship in the Netherlands.

To Rui Marques, Teresa Vaz, Clémence Guillard, Sérgio Oliveira, Ricardo Garcia and Aldina Piedade I am very grateful for all the advices, field work, knowledge and friendship.

Institutionally, I would like to thank to the Centre for Geographical Studies (CEG) and to the Institute of Geography and Territory Planning and Management of the University of Lisbon (IGOT UL) for hosting this PhD project. To the Portuguese Foundation for Science and Technology (FCT) I would like to thank for the financial support given by the PhD grant: SFRH/BD/46816/2008. I would also like to extend my great thanks to the Research Institute for Geo-Hydrological Protection (IRPI) from Perúgia and to the Department of Physical Geography of Utrecht University for having received me so nicely during the traineeships and for allow me to deeper the knowledge about slope instability which was crucial to develop this dissertation. To the Faculty of Sciences of the University of Lisbon

(FC UL) I am grateful for letting me use the laboratory equipments which were essential for obtaining the shear strengths parameters.

CONTENTS

LIST OF FIGURES xiii

LIST OF TABLES xxi

ABSTRACT xxix

RESUMO xxxi

ACRONYMS AND ABBREVIATIONS xlv

SYMBOLS xlix

INTRODUCTION 1

CHAPTER 1: PHYSIOGRAPHY OF THE STUDY AREA 9

1.1 Geographical placement 11

1.2 Paleogeographic evolution 14

1.3 Geology and geomorphology 16

1.4 Climate 20

CHAPTER 2: SLOPE DYNAMICS 23

2.1 Susceptibility and hazard 25

2.2 Slope movements: typology 27

2.3 The causes for landslides occurrence: conditioning, preparatory and predisposing factors 33

2.4 Landslide inventories of the study area 35

2.5 Landslides susceptibility assessment 48

2.6 Landslide susceptibility model validation 50

2.6.1 Prediction and Successes rate curves and 50

2.6.2 Area Under Curve 51

CHAPTER 3: RELATIONSHIPS BETWEEN THE LITHOLOGICAL SETTINGS AND THE LANDSLIDES PATTERN AND DISTRIBUTION 53

3.1 Detailed litho-stratigraphic mapping 55

3.1.1 Materials and methods 56

3.1.2 Interpretation and mapping 65

3.1.3 Validation trough field work 75

3.2 Spatial distribution and patterns of landslides according to the lithological data 81

3.3 Comparison between the previous lithological map and the detailed lithological map using the Accountability and Reliability indexes 95

CHAPTER 4: RELATIONSHIPS BETWEEN THE MORPHO-STRUCTURAL SETTINGS AND THE LANDSLIDES PATTERN AND DISTRIBUTION 103

4.1 Bedding attitude qualitative data acquisition: bedding trace mapping 107

4.2 Bedding attitude quantitative data acquisition through Geobed GIS scripting 110

4.2.1 Analysis and correction of probable bedding attitude errors 115

4.2.2 Resulting Morpho-structural map 119

4.2.3 Bedding attitude spatial interpolation: selection of the statistical interpolator through modeling and validation 121

4.2.4 Data validation trough field work 127

4.3 Bedding attitude modeling 131

4.3.1 TOBIA Categorical modeling 133

4.3.2 Analysis of results 137

4.4 Landslides distribution and pattern according to bedding attitude model 138

CHAPTER 5: LANDSLIDE SUSCEPTIBILITY ASSESSMENT USING PHYSICALLY-BASED METHODS..145

5.1 Landslide susceptibility assessment using physically-based methods: Static model VS Dynamic model 147

5.2 Infinite Slope Model 153

5.3 General data 160

5.3.1 Digital Elevation Model 160

5.3.2 Lithology 161

5.3.2.1 Lithological effects on hydrological properties 161

5.3.3 Geotechnical soils characterization 162

5.3.4 Back analysis of landslides for optimizing shear strength parameters 167

5.3.5 Assessment of the soil depth 170

5.3.6 USDA soil classification for further hydrogeological properties establishment 184

5.4 Static modeling of slope hydrology: TOPOG 189

5.4.1 Data 191

5.4.1.1 Contributing upstream area 191

5.4.1.2 Critical rainfall thresholds 192

5.4.1.3 Soil hydrological properties: saturated hydraulic conductivity 194

5.4.2 Static hydrological model implementation 197

5.5 Static modeling of slope stability: applying the Infinite slope equation through raster calculator 200

5.5.1 Analysis and validation of results 204

5.6 Dynamic modeling of slope hydrology: STARWARS 207
5.6.1 Data 220
5.6.1.1 Rainfall 220
5.6.1.2 Evapotranspiration 229
5.6.1.3 Reference Potential Evapotranspiration 230
5.6.1.4 Radiation 231
5.6.1.5 Temperature (T) 233
5.6.1.6 Crop Factor (Kc) 236
5.6.1.7 Soil hydrological properties: hydraulic conductivity and SWRC 241
5.6.2 Calibration 243
5.7 Dynamic modeling of slope stability: applying the Infinite slope equation through PROBSTAB 248
5.7.1 Analysis and validation of results 255
5.8 Comparison between Static and Dynamic models 275

CHAPTER 6: LANDSLIDE SUSCEPTIBILITY ASSESSMENT USING STATISTICALLY-BASED METHODS 281
6.1 Selection and preparation of the landslide predisposing factors 284
6.1.1 DEM derived variables 284
6.1.1.1 Slope angle 285
6.1.1.2 Aspect 286
6.1.1.3 Curvature (cross section profile) 288
6.1.1.4 Inverse of the Wetness Index 290
6.1.2 Lithology 293
6.1.3 Morpho-structure 293
6.1.4 Soil depth 294
6.1.5 Soils 296
6.2 Statistically-based methods 297
6.2.1 Sensitivity analysis of the landslide predisposing factors: Analysis of variable contributions 297
6.2.1.1 Maximum Entropy method (MaxEnt) 299
6.2.1.2 Accountability and Reliability 307
6.2.1.3 Analytical hierarchy process for landslide susceptibility mapping 309
6.2.2 Classification of the landslides susceptibility maps 311
6.2.3 Information Value Method 313
6.3 Analysis and validation of results 322
6.4 Comparison between the statistically-based methods and static physically-based methods 326

CONCLUDING REMARKS 333

REFERENCES 351

APPENDICES 385

1: Calculation form of Accountability and Reliability indexes for each landslide type of each landslide inventory. 387

2: GEOBED GIS SCRIPT. 409

3: Consolidated undrained direct simple shear test of cohesive soils and soil water content determination tests. 421

4: Coefficient of determination (r^2) and slope of the regression line, of each month and for each meteorological station and interpolation of meteorological data (precipitation, temperature, evapotranspiration). 427

5: Convertion of the vegetation types into the global ecosystem types. 460

6: Natural logarithm of capillary pressure (ψ) plotted against the 1- effective saturation. 463

7: Maps used for calibration purposes. 464

8: Pc Raster Script: STARWARS + PROBSTAB. 468

9: annual precipitation, maximum daily precipitation and maximum daily groundwater level observed in each year. 495

CD-ROM

FIGURES

Fig. I.1– Organizational structure of the PhD research project "Models for landslide susceptibility assessment and validation at the regional scale"..... 8

Fig. 1.1 – The study area: East part of the sub-catchments of Arnoia, Tornada and Alfeizerão..... 12

Fig. 1.2 – Geographic placement of the study area..... 13

Fig. 1.3 – Geomorphological placement of the Portuguese Estremadura on the west side of the Candeeiros and Montejunto Mountains. Extracted and adapted from Ferreira (1981)..... 15

Fig. 1.4 – Geological map of the study area..... 17

Fig. 1.5 – Digital Elevation Model (DEM) of the study area..... 18

Fig. 1.6 – Interannual variation and evolutionary trend of the precipitation for Santa Catarina metereological station (1948/49 - 2001/02). Source: Municipally of Caldas da Rainha, 2008..... 20

Fig. 1.7 – Interannual variation of annual maximum daily precipitation for Santa Catarina meteorological station (1948/49 - 2001/02). Source: Municipally of Caldas da Rainha, 2008.. 20

Fig. 2.1 – Types of slides. Extracted from Crosta et al., 2012..... 27

Fig. 2.2 – Shallow rotational shear plan: a) with spoon-shaped; b) approximate to a cylindrical shape. Extracted from Oliveira, 2011..... 29

Fig. 2.3 – Shallow translational slides. Extracted from Oliveira, 2012..... 30

Fig. 2.4 – Responsible factors for the landslides occurrence (adapted from Popescu, 1994 in Zêzere, 2010)..... 34

Fig. 2.5 – Land use map of the study area..... 37

Fig. 2.6 – Depletion zone of each Landslide within LI#1 in the study area. To facilitate visualization landslides depletion areas were magnified..... 39

Fig. 2.7 – Depletion zone of each Landslide within LI#2 in the study area. To facilitate visualization landslides depletion areas were magnified..... 41

Fig. 2.8 – Structural damage types or deformations used to define and delimit the boundaries of landslides: a) Fracture parallel to a road; b) Vertically fractured house; c) Obliquely fractured house; d) Vertically fractured house with translation; e) Fracture parallel to a road; f) Fracture parallel to a road with translation..... 42

Fig. 2.9 – Depletion zone of each Landslide within LI#3 in the study area. To facilitate visualization landslides depletion areas were magnified..... 43

Fig. 2.10 – Rotational landslides within the study area..... 44

Fig. 2.11 – Translational landslides within the study area..... 45

Fig. 2.12 – Non-pure shallow rotational and pure shallow translational slides founded within the study area. To facilitate visualization landslides depletion areas were magnified..... 47

Fig. 2.13 – Graphical definition of a predictive or (success) rate curve..... 50

Fig. 3.1 – Stereoscopic observation system of aerial photographs in digital format for vector drawing. A - Stereoscope; B - LCD monitor; C – Computer……. 57

Fig. 3.2 – Georeferencing: insertion of the aerial photograph corners and its respective measurement between points (227mm in between)……. 58

Fig. 3.3 – Georeferencing: identifying a series of ground control points, known x, y, and z coordinates…… 59

Fig. 3.4 – Georeferencing: error detection after finalizing the linking points. Where Sigma means RMSE…… 61

Fig. 3.5 – Georeferencing: tiepoint omission due to the high RMSE estimated (false active tiepoint inside the blue rectangle)…… 61

Fig. 3.6 – Epipolar Stereo Pair operator…… 62

Fig. 3.7 – Epipolar Stereo Pair operator: insertion of fiducial marks and the TP (through the position of the PP on the georeferenced aerial photograph) on the non-georeferenced aerial photograph…… 63

Fig. 3.8 – Epipolar Stereo Pair operator: stereo pair of aerial photographs ready to be seen by stereoscope…… 63

Fig. 3.9 – Edition of the new lithological detailed boundaries on stereo pair of aerial photographs seen by stereoscope……. 64

Fig. 3.10 – Previous lithological map of the study area……. 66

Fig. 3.11 – Edition of the new alluvium deposits boundaries through the interpretation of orthophotomaps from 2004 (ArcGis 9.3). Overlapping between the previous alluvium boundary and the new interpreted alluvium boundary……. 71

Fig. 3.12 – Detailed litho-stratigraphic map of the study area…… 72

Fig. 3.13– Slope angle map of the study area……. 76

Fig. 3.14 – Sandstones dominated complexes (upper Jurassic), (Estrada N8, Alfeizerão)……. 77

Fig. 3.15 – Shale dominated complexes (upper Jurassic), (Rua Donte dos Carreiros, Painho).. 78

Fig. 3.16 – Overlapping between field validation points and the detailed litho-stratigraphic map…… 79

Fig. 4.1 – Escarpment of the study area. Black lines delineate bedding traces. …… 107

Fig. 4.2 – Bedding plane intersection with topography (Marchesini, et. al., 2012)…… 108

Fig. 4.3 – Bedding trace map……. 109

Fig. 4.4 – a) Bedding trace draped on the DEM; b) bedding trace nodes joining; c) bedding surface (BS) is drawn in green. Extracted from Marchesini et al. (2011)…… 110

Fig. 4.5 – a) BS elevation map (meters a.s.l.); b) BS slope map (degrees); c) BS aspect map (degrees). Extracted from Marchesini et al., (2011). …… 111

Fig. 4.6 – Circular variance: n=3; a=b=c=1.…… 111

Fig. 4.7 – Angular standard deviation: n=3; Δ1=α,Δ2=β,Δ3=γ…… 112

Fig. 4.8 – Geobed scripting output…… 113

Fig. 4.9 – Dip direction angular variance…… 116

Fig. 4.10 – Dip direction angular variance graph: with all BA data (within and outside the study area)..... 117

Fig. 4.11 – Bedding attitude in the study area. BAs can be represented by means of oriented symbols (according to dip direction), and the inclination value. BA probable errors are drawn in red..... 118

Fig. 4.12 – Morpho-structural map: BAs represented by oriented symbols (according to dip direction), and the inclination value..... 120

Fig. 4.13 – Angular interpolation data..... 121

Fig. 4.14 – Dip angle map..... 124

Fig. 4.15 – a) Cosine map of the dip direction. b) Sine map of the dip direction. c) Dip direction resulting map..... 125

Fig. 4.16 – Dip direction reclassified map..... 126

Fig. 4.17 – Slope where rock outcrops and where dip direction (110º) and dip angle (20º) was possible to be properly measured. (Estrada da Navalha e Fraldeu, Óbidos). (Site number 1 in Fig. 4.18)..... 127

Fig. 4.18 – Morpho-structural data collected by field work. The location sites are labeled..... 128

Fig. 4.19 – BA modeling variables: a) slope aspect map; b) topographic slope angle map; c) dip direction map; d) dip angle map..... 131

Fig. 4.20 – Classification of alignment between topography and bedding planes. Orthoclinal orientation is not shown. (Meentemeyer and Moody, 2000)..... 132

Fig. 4.21 – BA map: made through TOBIA categorical model. 136

Fig. 5.1 – Very simplified scheme of the forces acting on a moving landslide. (Extracted from Blasio, 2011)..... 149

Fig. 5.2 – (A) Example of a rainfall-induced shallow landslide of the soil slide type in the study area. (B) Schematic representation of the slope-infinite model showing the coordinate system and variables used in the deterministic and stochastic models. Where: X is the slope parallel coordinate; du is the depth to the top of the capillary fringe; dw is the depth to the water table; dfp is the depth to the sliding plane; δ is the sliding plane; z is the Slope normal coordinate; and Z is the Vertical coordinate, $Z = z/\cos(\delta)$. (modified from Raia et al., 2013)..... 151

Fig. 5.3 – Definition of the infinite slope model for translational slides (extracted from Beek, 2002)..... 156

Fig. 5.4 – Infinite slope failure in cohesive soil with parallel seepage under saturated soil condition (extracted from Sharma, 2002)..... 157

Fig. 5.5 – Soil sample sites..... 163

Fig. 5.6 – PVC samplers for collecting soil samples..... 164

Fig. 5.7 – Laboratory equipment: a) Shear metal box; b) Vacuum pump; c) Shear Stress Test Machine; d) Some of the dried soil samples (after being tested)..... 165

Fig. 5.8 – Direct Shear Test: Measuring instruments of the Shear Stress Test Machine. Acquisition of the shear strength parameters (cohesion and angle of internal friction). The shear stress is imposed on the loading bar in which 30 kg corresponds to a shear stress of 94.3kpa, 70Kg to a 203.3kpa and 100kg to 285.0kpa..... 166

Fig. 5.9 – Back analysis of landslides occurred in Shale dominated Complexes: Relationship between the Safety Factor and the ratio between the thickness of saturated soil and potentially unstable soil thickness (m) arranged in the increasing order of soil thickness (Z)... 169

Fig. 5.10 – Topographic position index performed with 100 surrounding cells of neighborhood size..... 175

Fig. 5.11 – 6 of the 67 sites where was possible to measure the soil depth, i.e., depth to bedrock (drawn as yellow lines)..... 176

Fig. 5.12 – Soil depth measuring sites. 177

Fig. 5.13 – Soil depth contributing factors: a) constant Kc, which is calculated for each lithology from the in situ measurements; b) Profile curvature (Cp index); c) Catenary position within the hillslope profile (P index); d) Slope angle (Sa index)..... 181

Fig. 5.14 – Soil depth map..... 182

Fig. 5.15 – Soil-Texture Triangle, showing the textural terms applied to soils with various fractions of sand, silt and clay. (Extracted from Dingman, 2002)..... 187

Fig. 5.16 – Soil map classified according to Soil Texture Triangle Bulk Density Calculator for each polygon drawn on the map..... 188

Fig. 5.17 – Topographical elements used by the TOPOG program (Montgomery and Dietrich, 1994) defined by the intersection of the contours and limits of the drainage channels. The contribution of the upstream area, (darker blue) is the cumulative drainage area where all topographic elements drain to a particular element, b is the width of the land unit (m), Z is the soil thickness (m), h is the saturated soil thickness or height of the water level and, θ is the slope angle (°). (Extracted from Montgomery and Dietrich, 1994)..... 190

Fig. 5.18 – Contributing area calculated from TOPOG application..... 191

Fig. 5.19 – Framework showing the location and the distance between the study area and Batalha
municipality..... 193

Fig. 5.20 – Parameters needed for transmissivity acquisition: a) saturated hydraulic conductivity of soil (Ksat) (m/d); b) soil depth (Z) (m); c) transmissivity (m2/day)..... 196

Fig. 5.21 – Ratio between saturated soil thickness and the unstable soil thickness (m) using the uncalibrated values of saturated hydraulic conductivity (Ksat) and different effective precipitation: a) 1 day of accumulated rainfall; b) 3 days of accumulated rainfall; c) 5 days of accumulated rainfall; d) 10 days of accumulated rainfall; e) 15 days of accumulated rainfall.. 198

Fig. 5.22 – Ratio between saturated soil thickness and the unstable soil thickness (m) using the calibrated values of saturated hydraulic conductivity (Ksat) and different effective precipitation: a) 1 day of accumulated rainfall; b) 3 days of accumulated rainfall; c) 5 days of accumulated rainfall; d) 10 days of accumulated rainfall; e) 15 days of accumulated rainfall.. 199

Fig. 5.23 – Landslide susceptibility assessed thought the safety factor, assuming saturated soil, i.e., groundwater table located at the topographical surface (m=1): Scenario1: for geotechnical parameters obtained by laboratory measurements and back analysis…….. 201

Fig. 5.24 – Landslide susceptibility assessed thought the safety factor, using the geotechnical parameters obtained by laboratory measurements and back analysis and uncalibrated values of saturated hydraulic conductivity (Ksat): a) Scenario 2: for one day of accumulated rainfall; b) Scenario 3: for three days of accumulated rainfall; c) Scenario 4: for five days of accumulated rainfall; d) Scenario 5: for ten days of accumulated rainfall; e) Scenario 6: for fifteen days of accumulated rainfall…… 202

Fig. 5.25 – Landslide susceptibility assessed thought the safety factor, using the geotechnical parameters obtained by laboratory measurements and back analysis and calibrated values of saturated hydraulic conductivity (Ksat): a) Scenario 7: for one day of accumulated rainfall; b) Scenario 8: for three days of accumulated rainfall; c) Scenario 9: for five days of accumulated rainfall; d) Scenario 10: for ten days of accumulated rainfall; e) Scenario 11: for fifteen days of accumulated rainfall…… 203

Fig. 5.26 – Prediction rate curves…… 205

Fig. 5.27 – Prediction rate curves…… 206

Fig. 5.28 – Model layer Z (extracted from Beek, 2002)…… 210

Fig. 5.29 – Cardinal directions of LDD. To cells without drainage direction, pits, the value 5 is attributed…… 214

Fig. 5.30 – Linear decrease of evapotranspiration from the unsaturated matrix. Maximum evapotranspiration from layer Z is limited by the relative degree of saturation of the overlying layer (extracted from Beek, 2002)…… 220

Fig. 5.31 – Meteorological stations used for interpolation of daily precipitation for the period between 1975/1976 to 2011/2012…… 222

Fig. 5.32 – Actual (blue dots) and estimated (red line) mean daily temperature after adjustment at: a) Cela; b) Óbidos; c) Asseiceira; d) Alcoentre over the period 1980 to 2012… 235

Fig. 5.33 – Global Ecosystem Types according to Olso (1994a, 1994b)…… 238

Fig. 5.34 – Study area incorporating part of Óbidos location and hydrometric stations (discharge stations) used for calibration of the STARWARS model…… 245

Fig. 5.35 – Modeled discharge (here in m3/s). An example of a map from the time step corresponding to the Julian day 365 of 1979)…… 246

Fig. 5.36 – Model structure: input & output. Extracted from Beek (2002)…… 250

Fig. 5.37 – Landslide susceptibility (minimum safety factor over the year) assessed thought the STARWARS+PROBSTAB: a) year 2002; b) year 2003…… 252

Fig. 5.38 – Landslide susceptibility (minimum safety factor over the year) assessed thought the STARWARS+PROBSTAB: a) year 2004; b) year 2005…… 253

Fig. 5.39 – Landslide susceptibility (minimum safety factor over the year) assessed thought the STARWARS+PROBSTAB: a) year 2006; b) year 2007…… 253

Fig. 5.40 – Landslide susceptibility (minimum safety factor over the year) assessed thought the STARWARS+PROBSTAB: a) year 2008; b) year 2009…… 254

Fig. 5.41 – Landslide susceptibility (minimum safety factor over the year) assessed thought the STARWARS+PROBSTAB: a) year 2010; b) year 2011..... 254

Fig. 5.42 – Mean annual precipitation for the years: a) 2002; b) 2003..... 256

Fig. 5.43 – Mean annual precipitation for the years: a) 2004; b) 2005..... 257

Fig. 5.44 – Mean annual precipitation for the years: a) 2006; b) 2007..... 257

Fig. 5.45 – Mean annual precipitation for the years: a) 2008; b) 2009..... 258

Fig. 5.46 – Mean annual precipitation for the years: a) 2010; b) 2011..... 258

Fig. 5.47 – Centroid of each shallow translational landslide showing the instability trends over the period 2002 to 2011..... 269

Fig. 5.48 – Modeled conditions of temporal dynamic maps (map series) at day 30 of november of 2006 (Julian day 334). a) Precipitation; b) Temperature..... 270

Fig. 5.49 – Modeled conditions of temporal dynamic maps (map series) at day 30 of november of 2006 (Julian day 334). a) Potential evapotranspiration; b) Precipitation duration. 271

Fig. 5.50 – Modeled conditions of temporal dynamic maps (map series) at day 30 of november of 2006 (Julian day 334). a) Groundwater level; b) Safety factor..... 271

Fig. 5.51 – Prediction rate curve of the landslide susceptibility maps (minimum safety factor) obtained in 2002, 2003, 2004, 2005 and 2006..... 274

Fig. 5.52 – Prediction rate curve of the landslide susceptibility maps (minimum safety factor) obtained in 2007, 2008, 2009, 2010 and 2011..... 274

Fig. 6.1 – Reclassified slope angle map of the study area..... 285

Fig. 6.2 – Aspect map of the study area..... 287

Fig. 6.3 – Profile Curvature map of the study area..... 289

Fig. 6.4 – IWI map of the study area..... 292

Fig. 6.5 – Soil depth map of the study area..... 295

Fig. 6.6 – Applied sensitivity analysis, from which are extracted the input variables and the model output variables (extracted from Rocha, 2012)..... 298

Fig. 6.7 – Jackknife of regularized training gain for LI#1: a) for Deep-seated rotational slides; b) for shallow rotational slides; c) shallow translational slides..... 306

Fig. 6.8 – Jackknife of regularized training gain for LI#1+LI#2: a) for Deep-seated rotational slides; b) for shallow rotational slides; c) shallow translational slides. 306

Fig. 6.9 – Jackknife of regularized training gain for LI#3: a) for Deep-seated rotational slides; b) for shallow rotational slides; c) shallow translational slides..... 307

Fig. 6.10 – Deep-seated rotational slide susceptibility models assessed thought Information Value method based on: a) LI#1; b) LI#1+LI#2; c) LI#3..... 320

Fig. 6.11 – Shallow rotational slide susceptibility models assessed thought Information Value method based on: a) LI#1; b) LI#1+LI#2; c) LI#3..... 320

Fig. 6.12 – Shallow translational slide susceptibility models assessed thought Information Value method based on: a) LI#1; b) LI#1+LI#2; c) LI#3..... 321

Fig. 6.13 – Prediction rate curves for case A..... 324
Fig. 6.14 – Prediction rate curves for case B..... 324
Fig. 6.15 – Success rate curves for case C..... 325
Fig. 6.16 – Shallow translational slides susceptibility assessed through the statistically-based method (SBM) classified through quartile..... 328
Fig. 6.17 – Shallow translational slides susceptibility assessed through the physically-based method (PBM) classified through quartile..... 329
Fig. 6.18 – Shallow translational slide susceptibility represented by the 24.7% of the study area more susceptible, obtained from: 1) the statistically-based method (SBM); 2) the physically-based method (PBM); 3) and their overlapping. To facilitate visualization landslides depletion boundaries were magnified..... 331

TABLES

Table 1.1 – Municipality area occupied by the study area…… 12

Table 2.1 – Classification of Slides (Dikau et al., 1996; Zêzere, 2000)…….. 28

Table 2.2 – Land use map of the study area…… 37

Table 2.3 – Statistical analysis for the LI#1…….. 40

Table 2.4 – Statistical analysis for the LI#2…….. 40

Table 2.5 – Statistical analysis for the LI#3…….. 44

Table 2.6 – Statistical analysis for the non-pure rotational and pure translational slides founded within LI#3…….. 46

Table 3.1 – Areal distribution of previous litho-stratigraphic classes…….. 67

Table 3.2 – Areal distribution of detailed litho-stratigraphic classes…….. 70

Table 3.3 – Cross-tabulation between previous and detailed litho-stratigraphic maps……. 74

Table 3.4 – Misclassification table: Accuracy of the lithological improvements…….. 80

Table 3.5 – Landslide distribution according to previous lithological classes for LI#1…… 82

Table 3.6 – Cross tabulation area between landslides types and previous lithological classes for LI#1…….. 82

Table 3.7 – Landslide distribution according to detailed lithological classes for LI#1…… 83

Table 3.8 – Cross tabulation area between landslides types and detailed lithological classes for LI#1…….. 84

Table 3.9 – Landslide distribution according to previous lithological classes for LI#2…….. 85

Table 3.10 – Cross tabulation area between landslides types and previous lithological classes for LI#2…….. 86

Table 3.11 – Landslide distribution according to detailed lithological classes for LI#2…… 87

Table 3.12 – Cross tabulation area between landslides types and detailed lithological classes for LI#2…….. 87

Table 3.13 – Landslide distribution according to previous lithological classes for LI#3…… 88

Table 3.14 – Cross tabulation area between landslides types and previous lithological classes for LI#3…….. 89

Table 3.15 – Landslide distribution according to detailed lithological classes for LI#3…… 90

Table 3.16 – Cross tabulation area between landslides types and detailed lithological classes for LI#3…….. 90

Table 3.17 – Landslide distribution according to previous lithological classes for Sum of LIs…. 91

Table 3.18 – Cross tabulation area between landslides types and previous lithological classes for Sum of LIs…… 92

Table 3.19 – Landslide distribution according to detailed lithological classes for Sum of LIs….. 93

Table 3.20 – Cross tabulation area between landslides types and detailed lithological classes for Sum of LIs…… 93

Table 3.21 – Accountability (ACC) and Reliability (RLB) for both previous and detailed lithological maps for deep-seated landslides. The highest mean accountability and Reliability indexes are highlighted in bold…… 96

Table 3.22 – Accountability (ACC) and Reliability (RLB) for both previous and detailed lithological maps for shallow landslides. The highest mean accountability and Reliability indexes are highlighted in bold…… 96

Table 3.23 – Accountability (ACC) and Reliability (RLB) for both previous and detailed lithological maps for the total landslides (shallow and deep-seated landslides). The highest mean accountability and Reliability indexes are highlighted in bold…… 97

Table 3.24 – Calculation form of Accountability and Reliability indexes: Deep seated landslides for LI#1 for the previous lithological map…… 98

Table 3.25 – Calculation form of Accountability and Reliability indexes: Deep seated landslides for LI#1 for the detailed lithological map…… 99

Table 4.1 – Extract of the Geobed script database output…… 114

Table 4.2 – Dip direction cosine uncertainty interpolated by 10 interpolation algorithms……. 123

Table 4.3 – Dip direction sine uncertainty interpolated by 10 interpolation algorithms…… 123

Table 4.4 – Dip angle uncertainty interpolated by 10 interpolation algorithms…… 123

Table 4.5 – Mean of dip direction cosine, dip direction sine and dip angle uncertainty…… 123

Table 4.6 – Confrontation between the acquired BA data on fieldwork and the BA data estimated by the Geobed script…… 130

Table 4.7 – Classification of topography relative to strike and dip of bedding planes (Meentemeyer and Moody 2000) …… 133

Table 4.8 – Areal distribution of the BA classes resulting from the Categorical TOBIA model… 137

Table 4.9 – Landslide distribution according to the TOBIA categorical map classes for LI#1….. 138

Table 4.10 – Cross tabulation area between landslides types and the TOBIA categorical map classes for LI#1…… 138

Table 4.11 – Landslide distribution according to the TOBIA categorical map classes for LI#2… 140

Table 4.12 – Cross tabulation area between landslides types and the TOBIA categorical map classes for LI#2…… 140

Table 4.13 – Landslide distribution according to the TOBIA categorical map classes for LI#3… 141

Table 4.14 – Cross tabulation area between landslides types and the TOBIA categorical map classes for LI#3…… 141

Table 4.15 – Landslide distribution according to the TOBIA categorical map classes for Sum of LIs…… 142

Table 4.16 – Cross tabulation area between landslides types and the TOBIA categorical map classes for Sum of LIs…… 143

Table 4.17 – Cross tabulation area between BA TOBIA categorical classes and slope angle…… 144

Table 5.1 – Relative Slope Stability according to Safety Factor (extracted from Sharma, 2002) …… 150

Table 5.2 – Determination of Geotechnical properties of soil…… 164

Table 5.3 – Summary table with the geotechnical parameters resulted from the tested soil samples for the Shale dominated complexes (upper Jurassic)…… 166

Table 5.4 – Summary table with the geotechnical parameters resulted from the tested soil samples for the Sandstones dominated complexes (upper Jurassic)…… 167

Table 5.5 – Example of a spreadsheet used for back analysis for some of the shallow landslides occurred…… 168

Table 5.6 – Geotechnical parameters, for introduction into the Infinite Slope Equations…… 170

Table 5.7 – Threshold slope angle for triggering mass movement…… 174

Table 5.8 – Soil depth observed by in-situ measurements…… 178

Table 5.9 – Calibration and validation groups of soil depth in-situ measurements…… 180

Table 5.10 – Constant Kc (m) inserted into the model after calibration…… 180

Table 5.11 – Example of a Data base of one polygon…… 185

Table 5.12 – Example of a Data base of one polygon…… 186

Table 5.13 – Example of a Data base of one polygon after the weighted calculation…… 187

Table 5.14 – Ksat values assigned for the study area based on the standard values given by Rawls et al., 1982…… 195

Table 5.15 – Final values of Ksat based on the standard values given by Rawls et al. (1982) and calibration for the study area…… 195

Table 5.16 – 11 Scenarios for verifying the influence of the improvements on Ksat hydrological parameter…… 197

Table 5.17 – AUC of the Scenarios modeled with the geotechnical parameters obtained by laboratory measurements and back analysis and initial values of Ksat…… 205

Table 5.18 – AUC of the Scenarios modeled with the geotechnical parameters obtained by laboratory measurements and back analysis and adjusted values of Ksat…… 205

Table 5.19 – Landslides susceptibility classes, for shallow translational slides obtained through the static physically-based method. Area of each class and landslide area in each class (both in % of the total) 207

Table 5.20 – Elevation (a.s.l.) and caracteristics of the daily precipitation records of each meteorological stations..... 223

Table 5.21 – Monthly rainfall statistics for Alfeizerão (hydrological years 1975/197 - 2011/2012..... 224

Table 5.22 – Monthly rainfall statistics for Cela (hydrological years 1975/1976 – 2011/2012.. 224

Table 5.23 – Monthly rainfall statistics for Salir de Matos (hydrological years 1975/1976 – 2011/2012..... 225

Table 5.24 – Monthly rainfall statistics for Óbidos (hydrological years 1975/1976 – 2011/2012..... 225

Table 5.25 – Monthly rainfall statistics for Asseiceira (hydrological years 1975/1976 – 2011/2012..... 225

Table 5.26 – Monthly rainfall statistics for Alcoentre (hydrological years 1975/1976 – 2011/2012..... 226

Table 5.27 – Monthly rainfall statistics for Alvorninha (hydrological years 1975/1976 – 2011/2012..... 226

Table 5.28 – Monthly rainfall statistics for Santa Catarina (hydrological years 1975/1976 – 2011/2012..... 226

Table 5.29 – Monthly rainfall statistics for Vermelha (hydrological years 1975/1976 – 2011/2012..... 227

Table 5.30 – Monthly rainfall statistics for Vimeiro (hydrological years 1975/1976 – 2011/2012..... 227

Table 5.31 – Monthly rainfall statistics for Turquel (hydrological years 1975/1976 – 2011/2012..... 227

Table 5.32 – Global ecosystem types of Olson (1994a, 1994b)..... 237

Table 5. 33 – Hydrological properties classified by soil texture based on the standard values given by Rawls et al. (1982) necessary for hydrological modeling..... 241

Table 5.34 – RMSE of the discharge values of the hydrometric stations, selected for calibration..... 247

Table 5.35 – Ksat values assigned for the study area after the dynamic calibration..... 247

Table 5.36 – Parameters to constrain the percolation to the deeper bedrock (bc), Beek (2002) 249

Table 5.37 – Model input & output of the coupled hillslope model for hydrology (STARWARS) and slope stability (PROBSTAB). Adopted from Beek, 2002..... 251

Table 5.38 – Landslides susceptibility classes assessing the minimum safety factor, for the years 2002; 2003; 2004; 2005 and 2006. Area of each class and landslide area in each class (both in % of the total) ……. 255

Table 5.39 – Landslides susceptibility classes assessing the minimum safety factor, for the years 2007; 2008; 2009; 2010 and 2011. Area of each class and landslide area in each class (both in % of the total) …….. 256

Table 5.40 – Annual precipitation along the study area for each year (2002; 2003; 2004; 2005; 2006; 2007;2008; 2009; 2010; 2011) …… 259

Table 5.41 – Total duration and period duration (in Julian days) with conditions to instability (SF £ 1), for each shallow translational landslide (ID, from 1 to 33) indentified in the study area, for the years: 2002; 2003; 2004; 2005; 2006…….. 260

Table 5.42 – Total duration and period duration (in Julian days) with conditions to instability (SF £ 1), for each shallow translational landslide (ID, from 34 to 65) indentified in the study area, for the years: 2002; 2003; 2004; 2005; 2006…….. 261

Table 5.43 – Total duration and period duration (in Julian days) with conditions to instability (SF £ 1), for each shallow translational landslide (ID, from 66 to 87) indentified in the study area, for the years: 2002; 2003; 2004; 2005; 2006…….. 262

Table 5.44 – Total duration and period duration (in Julian days) with conditions to instability (SF £ 1), for each shallow translational landslide (ID, from 1 to 33) indentified in the study area, for the years: 2007; 2008; 2009; 2010; 2011…….. 263

Table 5.45 – Total duration and period duration (in Julian days) with conditions to instability (SF £ 1), for each shallow translational landslide (ID, from 34 to 65) indentified in the study area, for the years: 2007; 2008; 2009; 2010; 2011…….. 264

Table 5.46 – Total duration and period duration (in Julian days) with conditions to instability (SF £ 1), for each shallow translational landslide (ID, from 66 to 87) indentified in the study area, for the years: 2007; 2008; 2009; 2010; 2011…….. 265

Table 5.47 – Summary of the conditions to instability (SF≤1) for the period from 2002 to 2011. Analysis performed based on the centroid of the depletion zone of the shallow translational landslides (ID1 to ID33) …….. 266

Table 5.48 – Summary of the conditions to instability (SF≤1) for the period from 2002 to 2011. Analysis performed based on the centroid of the depletion zone of the shallow translational landslides (ID34 to ID65) …… 267

Table 5.49 – Summary of the conditions to instability (SF≤1) for the period from 2002 to 2011. Analysis performed based on the centroid of the depletion zone of the shallow translational landslides (ID66 to ID87) …… 268

Table 5.50 – Modeled conditions at day 30 of november of 2006 (Julian day 334) for the ID41…… 272

Table 5.51 – Daily precipitation on ID41. From first day of maximum annual precipitation (Julian day 320: 16 of November of 2006 until the day of landsliding)…… 273

Table 5.52 – AUC values for the landslide susceptibility maps from 2002 to 2011 assessed through the STARWARS+PROBSTAB…….. 275

Table 6.1 – Reclassified slope angle map of the study area……. 286

Table 6.2 – Reclassified aspect map of the study area…….. 288

Table 6.3 - Reclassified Profile Curvature map of the study area…….. 290

Table 6.4 – Reclassified IWI map of the study area. ……... 293

Table 6.5 - Reclassified soil depth map of the study area. …… 296

Table 6.6 – Reclassified Soil map of the study area……. 296

Table 6.7 – Advantages and disadvantages of the maximum entropy model (Rocha, 2012)…… 302

Table 6.8 – Number of landslides of each landslide inventory according to the typology……. 303

Table 6.9 – Analysis of the predisposing factor contributions to deep-seated rotational slides…… 304

Table 6.10 – Analysis of the predisposing factor contributions to shallow rotational slides……. 304

Table 6. 11 – Analysis of the predisposing factor contributions to shallow translational slides. 304

Table 6.12 – Accountability and reliability of the predisposing factor contributions to deep-seated rotational slides……. 308

Table 6.13 – Accountability and reliability of the predisposing factor contributions to shallow rotational slides…….. 308

Table 6.14 – Accountability and reliability of the predisposing factor contributions to shallow translational slides…… 309

Table 6.15 – Hierarchy of the predisposing factor contributions to deep-seated rotational slides according to the average between PC, ACC and RLB (%)……. 310

Table 6. 16 – Hierarchy of the predisposing factor contributions to shallow rotational slides according to the average between PC, ACC and RLB (%)…… 310

Table 6.17 – Hierarchy of the predisposing factor contributions to shallow translational slides according to the average between PC, ACC and RLB (%)……. 310

Table 6.18 – landslides susceptibility Classes, characterization of the predictive capacity value of each class and form of color representation adopted for the study area…….. 312

Table 6.19 – Information values obtained for each class of each predisposing factor for each landslide type and inventory. Part 1 (aspect, curvature and slope angle themes). Higher IV values are highlighted in bold…….. 315

Table 6.20 – Information values obtained for each class of each predisposing factor for each landslide type and inventory. Part 2 (IWI, detailed lithology and soil depth themes). Higher IV values are highlighted in bold…… 316

Table 6.21 – Information values obtained for each class of each predisposing factor for each landslide type and inventory. Part 3 (soils and morpho-structure themes). Higher IV values are highlighted in bold……. 317

Table 6.22 – Deep-seated rotational slide susceptibility: occupancy of each class……. 320

Table 6.23 – Shallow rotational slide susceptibility models: occupancy of each class…….. 321

Table 6.24 - Shallow translational susceptibility models: occupancy of each class……. 321

Table 6.25 – AUC values for the landslide susceptible models assessed through the Information value method……. 324

Table 6.26 - Landslides susceptibility classes, for shallow translational slides obtained through the static physically-based method for the scenario 11 (see chapter 5)……. 330

Table 6.27 – Comparison between the landslide susceptible maps modeled with physically (PBM) and statistically (SBM) based methods. Total 24.7% of the study area classified with high susceptibility (class below SF < 1, according to scenario 11, see chapter 5)……. 332

ABSTRACT

This dissertation aims to deepen the knowledge about the causes that influence the spatial and temporal occurrence of slope instability at a regional scale. The study area, located 90km north from Lisbon, comprises three sub-catchments, named Arnoia, Tornada and Alfeizerão (275.9 km^2). These sub-catchments were chosen for their geological and geomorphological features and because it is an area prone to slope instability.

Many methods have been proposed worldwide to evaluate landslide hazard. In this dissertation there are presented and performed two approaches that, according to Guzzetti (2002), are the most promising: physically-based methods; and statistically-based methods. Methodologies were applied for acquisition of their input data. In addition, within the physically-based methods was also implemented a temporal dynamic approach, which simulated the hydrology over time and evaluated its effects on slope stability.

Thereby, in order to obtain the overall goal the following 10 specific objectives were stated: 1) Acquisition of multi-temporal landslide inventories; 2) Acquisition and production of new themes based on modeling and field observation (e.g. detailed lithological map, morpho-structural map, DEM, soil depth); 3) Acquisition of soil characteristics according to the hydrogeological and geotechnical properties of soils (through field work, laboratory measurements and back analysis; 4) Landslide susceptibility assessment using the hydrological model coupled to slope stability model under static temporal conditions and its validation through the quantification of the degree of prediction rate; 5) Acquisition, processing and modeling of long term climatic data (e.g., rainfall and temperature); 6) Landslide susceptibility assessment using hydrological model coupled to slope stability model under dynamic temporal conditions and its validation through the quantification of the degree of prediction rate; 7) Comparison between physically base models: static and dynamic approach; 8) Sensitivity analysis and hierarchy of the landslide predisposing factors; 9) Landslide susceptibility assessment using statistically-based method (Information Value Method) and its validation through the quantification of prediction and success rate; 10) Comparison between statistically and physically static models.

Some input data, of extreme importance for every method used in this dissertation, proved to be very difficult to obtain. It is worth mention the case of the geological map, which was only available at a 1:50,000 scale. Thus, being aware that landslides are greatly conditioned by the lithological properties of the terrain, a detailed lithological map at a 10,000 scale was performed through the stereoscopic interpretation of aerial photographs and field work validation.

The quality of the landslide inventory is of crucial importance for any prediction model. Thus, a multi-temporal landslide inventory was achieved through aerial photo-interpretation, orthophotomaps interpretation and field work. Since the models obtained through the Infinite Slope method aim to predict the areas susceptible to shallow translational slides, a validation was made based on the shallow translational slides validated through field work. Further, all the landslides types from each landslide inventory were modeled through a bivariated statistical method (Information Value Method). A comparison, between the shallow translational slides susceptible model obtained from different approaches was also performed.

The main conclusions of the work are the following: 1) The detailed lithological map has a better discriminating power than the original lithological map; 2) Trough a spatial and temporal dynamic physically-based method it is possible to inferred the possible conditions that triggered shallow translational slides; 3) the static physically-based method, presented better skills for predicting the spatial occurrence of shallow translational slides over the study area than the statistically-based method.

Keywords: Landslides; Inventories; Susceptibility; Physically-based methods; Statistically-based methods.

RESUMO

Esta dissertação teve como objetivo geral o desenvolvimento e aplicação de um conjunto de metodologias que permitissem aprofundar o conhecimento sobre as causas que influenciam a ocorrência espacial e temporal da instabilidade de vertentes a uma escala regional.

A área de estudo selecionada para este trabalho compreende três sub-bacias hidrográficas, localizadas 90km a Norte de Lisboa, respectivamente Arnoia, Tornada e Alfeizerão (totalizando 275,9km^2). Estas sub-bacias foram escolhidas devido às suas características geológicas, geomorfológicas e também por se tratar de uma área propensa a instabilidade de vertentes.

Diversos métodos têm sido propostos para avaliar a suscetibilidade à ocorrência deslizamentos. Nesta dissertação são apresentadas e realizadas duas abordagens que, de acordo com Guzzetti (2002), se revelam como as mais promissoras, nomeadamente: os métodos de base física, que se baseiam em leis mecânicas simples de controlo da instabilidade das vertentes; e os métodos de base estatística, que assentam na análise estatística de fatores ambientais (fatores de predisposição) relacionados com a ocorrência de deslizamentos. São também desenvolvidas metodologias para obtenção dos dados de entrada nos modelos. No âmbito dos métodos de base física (Método do Talude Infinito) foi também implementada uma abordagem de dinâmica temporal, que permitiu simular a hidrologia ao longo do tempo e avaliar os seus efeitos sobre a estabilidade das vertentes.

Os inventários de movimentos de vertente são um elemento fundamental na avaliação e validação da susceptibilidade associada à instabilidade de vertentes, fazendo depender da sua qualidade/robustez grande parte da capacidade preditiva dos mapas de susceptibilidade produzidos. Desta forma, a primeira etapa deste trabalho teve como objetivo a criação de um inventário de movimentos de vertente multi-temporal à escala 1:10 000 segmentado em três etapas, i.e.: um inventário de movimentos de vertente antigos, obtido através da interpretação estereoscópica de fotografias aéreas de 1958

(LI#1); um inventário de movimentos de vertente antigos, obtido com base na interpretação estereoscópica de fotografias aéreas de 1982 (LI#2); e um inventário de movimentos de vertente recentes, obtido através da interpretação de ortofotomapas de 2004 e sucessivo trabalho de campo efectuado entre os anos 2006 e 2011 (LI#3).

No que respeita ao inventário de movimentos de vertente recentes (LI#3), é importante mencionar que algumas das rupturas envolvidas nos mecanismos que levaram à ocorrência dos movimentos do tipo deslizamentos rotacionais superficiais, não apresentavam características rotacionais perfeitas, dado o raio de curvatura da superfície de ruptura ser muito elevado. Desta forma, este tipo de deslizamentos, juntamente com os deslizamentos translacionais superficiais puros (do LI#3) foram agrupados de forma a calibrar e validar os modelos de susceptibilidade criados com base no método de base física (Método do Talude Infinito) e para validar o modelo de susceptibilidade a deslizamentos translacionais superficiais do inventário LI#1 + LI#2.

Apesar dos deslizamentos translacionais superficiais não serem predominantes (em área) na área de estudo, são aqueles que ocorrem com mais frequência. Contudo, as suas evidências são mais difíceis de cartografar no campo porque, como a área de estudo é maioritariamente agrícola, as suas evidências são eliminadas constantemente e com relativa facilidade. Desta forma, torna-se crucial obter modelos de susceptibilidade a deslizamentos translacionais superficiais, quer pela sua frequência, quer pelas suas implicações a nível agrícola e económico.

É de salientar a extrema dificuldade na obtenção de alguns parâmetros que serviram como dados de entrada nos modelos, citando o exemplo do mapa geológico, que apenas existia a uma escala 1:50 000. Com o intuito de obter uma correta distribuição e variação das propriedades físicas do solo foi realizado, com base na interpretação de fotografias aéreas de 1958 e cartografia de campo, um levantamento geológico detalhado centrado no carácter litológico e estrutural de cada formação. No mapa lito-estratigráfico construído no decurso deste trabalho, foram corrigidos os limites geológicos entre as formações, as quais foram posicionadas correctamente. Desta forma, é de salientar que a classe litológica previamente dominante na área estudo, de arenitos e argilitos

(*sandstones and claystones complexes*) foi possível separar em: (1) complexos predominantemente areníticos (*sandstone dominated complexes*); (2) complexos predominantemente argilo-siltíticos (*shale dominated complexes*).

Da análise dos resultados, conclui-se que as melhorias aplicadas no mapa litológico de detalhe permitiram compreender que existe um padrão entre ocorrência de deslizamentos e determinadas classes litológicas. A maioria dos deslizamentos (superficiais e profundos) ocorre nos complexos predominantemente argilo-siltíticos de menor resistência. No entanto, alguns deslizamentos profundos foram identificados em rochas mais resistentes (nos complexos predominantemente areníticos). Com base nos índices *Accountability* e *Reliability* foi possível afirmar que existe uma melhoria significativa no mapa litológico de detalhe, i.e., o mapa litológico detalhado possui um maior poder discriminante do que o mapa litológico inicial, produzindo melhores mapas de susceptibilidade à ocorrência de deslizamentos com a separação de classes relevantes.

Para além do mapa litológico de detalhe foi também realizado um modelo morfo-estrutural à escala 1:10 000 para a totalidade da área de estudo. Para a obtenção deste modelo foi necessário efectuar, em primeiro lugar, um mapa lito-estrutural detalhado contento o traçado das camadas litológicas. Com base no traçado das camadas litológicas e com o auxílio do script *Geobed* foi possível obter os dados quantitativos de inclinação e orientação das camadas litológicas. Posteriormente, estes dados quantitativos foram modelados através do método TOBIA permitindo, desta forma, a obtenção do modelo morfo-estrutural. Tal como foi possível verificar no campo, valores elevados de incerteza associados à orientação das camadas litológicas estão mais relacionados com a ocorrência de camadas litológicas sub-horizontais do que com erros de interpretação. Da análise dos resultados é possível afirmar que a elaboração do modelo morfo-estrutural produz um aumento na capacidade preditiva dos modelos de susceptibilidade à ocorrência de deslizamentos. Conclui-se ainda que existe uma maior densidade de deslizamentos nas vertentes cataclinais sobre-inclinadas e nas vertentes anaclinais de inclinação acentuada. Importa referir que o modelo morfo-estrutural foi feito com o intuito de ser usado como variável de entrada no modelo dinâmico de base física (capítulo 5). No entanto, este processo acabou por não ser efectuado uma vez que as inclinações das camadas

litológicas são relativamente baixas na área de estudo (média de 30º). Desta forma, introduzir tal variável apenas aumentaria a redundância do modelo de susceptibilidade final (Philip, 1990). Assim, de acordo com os resultados da análise sensitiva dos factores de predisposição (capítulo 6), conclui-se que a sua obtenção foi deveras importante porque possibilitou o aumento da capacidade preditiva dos modelos de susceptibilidade efectuados com base no método estatístico.

O modelo digital do terreno (MDT) foi também submetido a uma optimização de forma a garantir uma melhoria nos resultados do mapa de susceptibilidade. Para o efeito, foram utilizados três tipos de informação: curvas de nível; pontos cotados; e pontos auxiliares. A informação altimétrica de base é proveniente do Instituto Geográfico Português (IGP), na escala 1:10 000 (curvas de nível com equidistância de 5m e pontos cotados com precisão centesimal). Os pontos cotados auxiliares foram gerados no programa SIG IDRISI, a partir das curvas de nível, com base numa função parabólica, e sujeitos a várias operações automáticas de correcção. A finalidade desta operação residiu na eliminação de superfícies planas incorrectas (como por exemplo interflúvios e fundos de vale) geradas pelos modelos TIN durante os processos de triangulação. O MDT foi posteriormente utilizado para derivar outros mapas, tal como o mapa de declives que, por sua vez, assume um papel relevante no que concerne a ocorrência de deslizamentos.

Entre outras varáveis, o mapa de espessura de solo potencialmente instável é essencial para a modelação da susceptibilidade à ocorrência de deslizamentos translacionais superficiais com base no método do Talude infinito. O método utilizado para a obtenção do mapa de espessura de solo potencialmente instável foi proposto por Catani et. al (2010) e tem por base o MDT, o mapa litológico detalhado e factores geomorfológicos. As principais características e vantagens deste método são: 1) é indicado para a escala da bacia hidrográfica; 2) é possível de implementar em ambiente SIG; 2) é um método bastante acessível e com baixos custos associados; 3) promove uma análise equilibrada dos atributos topográficos em conjunto com os factores geológicos e/ou geomorfológicos. O mapa final de espessura de solo potencialmente instável foi submetido a uma calibração de forma a obter resultados mais robustos. O método utlizado na calibração do modelo foi baseado no valor mínimo do erro médio quadrático

obtido entre os valores modelados (pixéis) e os valores de medição obtidos com base no trabalho de campo (pontos obtidos por GPS com a medição da espessura de solo potencialmente instável) (utilizando 75% dos pontos medidos no campo). Posteriormente este modelo foi submetido a uma validação de forma a garantir a qualidade dos resultados (utilizando a comparação do erro quadrático médio para 25% dos pontos obtidos com base no trabalho de campo).

O mapa final de espessura de solo potencialmente instável reflecte claramente a relação entre os factores que lhe deram origem, nomeadamente: o coeficiente de cultura; a curvatura (perfil transversal das vertentes); a posição catenária ao longo da vertente; e o declive. Tal como esperado, nas áreas concavas (ou de depósito), onde simultaneamente a rocha-mãe é menos resistente á erosão, a espessura do solo é maior; por outro lado, nas áreas de interflúvio, onde simultaneamente a rocha-mãe é menos resistente à erosão, a espessura de solo é menor. A aquisição deste mapa foi crucial para a elaboração dos mapas de susceptibilidade com base no método físico (dinâmico e estático) e também para a integração nos modelos de susceptibilidade com base no método estatístico, como factor de predisposição.

A elaboração do método de base física (estático ou dinâmico) pressupõe a aquisição prévia de dados de base provenientes da análise das condições dos solos (espessura de solo potencialmente instável, propriedades hidrogeológicas e geotécnicas dos solos). Deste modo, a caracterização geotécnica dos materiais foi realizada através de ensaios laboratoriais de 6 amostragens representativas das formações correspondentes aos complexos predominantemente argilo-siltíticos e aos complexos predominantemente areníticos presentes na área de estudo, com a finalidade de obter os parâmetros físicos dos solos de cobertura necessários para aplicação nos modelos de base física. As propriedades geotécnicas obtidas em laboratório foram confrontadas com valores obtidos por retroanálise de rupturas características levantadas no terreno, de modo a obter estimativas fundamentadas das características de resistência operativas nas condições do terreno. Deste processo resultaram os parâmetros geotécnicos das formações relativos às características de resistência ao corte ($c`$ e $\phi`$) coincidentes com as condições de terreno encontradas na altura dos movimentos de vertente. Para as

restantes formações (pouco representativas na área de estudo) os dados geotécnicos foram adquiridos através de referências bibliográficas.

Não havendo possibilidade de obtenção dos parâmetros hidrogeológicos com base em estudos laboratoriais, recorreu-se à recolha dessa informação através de valores estandardizados desenvolvidos por Rawls *et al.* (1982). Deste modo, os parâmetros hidrogeológicos dos solos, necessários para a modelação hidrológica (e.g., condutividade hidráulica saturada, saturação efectiva, porosidade), foram atribuídos com base na textura dos solos (classificados previamente com base nos critérios da USDA). Para as classes de solo que continham deslizamentos foi ainda possível proceder, em ambos os modelos hidrológicos (estático e dinâmico), a uma retroanálise, permitindo desta forma obter valores de condutividade hidráulica saturada mais coerente com a realidade da área de estudo.

Tendo em conta a análise estática, o comportamento hidrológico e o resultante factor de segurança da área de estudo foram calculados com recurso ao método SHALSTAB. Este modelo assenta na premissa de que os deslizamentos translacionais superficiais ocorrem maioritariamente devido a um período intenso e/ou prolongado de precipitação reflectindo o efeito da saturação do solo e consequentemente a diminuição dos valores de resistência ao corte. Para estimar a razão entre o solo saturado e não saturado, o modelo tem em conta a área contributiva a montante, a recarga por precipitação, as propriedades hidrogeológicas das formações (transmissividades) e o declive. Em condições estáticas, o modelo assume apenas um único valor de precipitação para todas as unidades de terreno ao longo da área de estudo (mesmo valor por píxel). Uma vez que não foi possível o cálculo de períodos de retorno e de precipitações criticas, os valores de precipitação efectiva necessária para a introdução do modelo foram adquiridos a partir de um estudo feito para uma área vizinha (concelho de Batalha). Para a avaliação da susceptibilidade foram construídas várias hipóteses que visam ilustrar cenários hipotéticos. Os diferentes cenários obtidos (11) baseiam-se na utilização de 1, 3, 5, 10 e 15 dias de precipitação acumulada e ainda na influência da calibração dos valores de condutividade hidráulica saturada.

Os resultados mostram que os cenários obtidos com base nos valores *standard* prévios de condutividade hidráulica saturada são mais dramáticos e de predição mais fraca, de acordo com a Área Abaixo da Curva (AAC). No entanto, a situação muda quando os mapas de susceptibilidade são modelados com base nos valores calibrados de condutividade hidráulica saturada revelando, regra geral, uma diminuição das áreas de susceptibilidade elevada, acompanhada pelo aumento da capacidade preditiva, quando comparados com os mapas modelados com base nos valores não calibrados de condutividade hidráulica saturada.

O mapa de susceptibilidade modelado com base nos valores calibrados de condutividade hidráulica saturada para um único dia de precipitação apresenta uma boa performance (com uma AAC de 0,81). No entanto, analisando apenas as áreas em que o factor de segurança (FS) é igual ou abaixo de 1, o cenário 11 (correspondente a 15 dias de precipitação acumulada) demonstra ser o modelo com melhor capacidade preditiva, uma vez que incorpora a maioria dos deslizamentos translacionais superficiais da área de estudo. Os melhoramentos obtidos nos parâmetros hidrogeológicos e geotécnicos foram cruciais para a obtenção de mapas de susceptibilidade a deslizamentos translacionais superficiais mais robustos.

O modelo hidrológico do método de base físico dinâmico (STARWARS desenvolvido por Beek, 2002) apresenta consideráveis vantagens em relação ao modelo hidrológico do método físico estático. No caso do modelo hidrológico dinâmico é possível, não só, a obtenção do nível piezométrico diário, como também, do nível dos caudais superficiais. Tal facto possibilita, para além de uma calibração espacial mais rigorosa, uma calibração temporal dos parâmetros hidrogeológicos tornando, desta forma, imprescindível a aquisição de dados climáticos. Em termos globais, existe uma redução média da água de precipitação por evapotranspiração de cerca 62%, variando de acordo com determinados parâmetros (e.g., factor de cultura, índex de área de folha e temperatura). Deste modo, o *input* de precipitação no modelo hidrológico dinâmico deve ser contrabalançado com a perca de água do solo por evapotranspiração efectiva de forma a aferir com maior precisão a quantidade de água disponível, para a infiltração e percolação, que é modelada pelo modelo hidrológico dinâmico. Para o efeito, os dados climáticos adquiridos e

calculados foram: i) precipitação diária; ii) radiação diária; (iii) temperatura diária; (iv) evapotranspiração efectiva diária.

De modo a obter maior detalhe na caracterização do regime pluviométrico na área de estudo foram seleccionadas 11 estações meteorológicas do Sistema Nacional de Informação de Recursos Hídricos (SNIRH), com os respetivos dados de precipitação diária. O período seleccionado para análise inicia-se no ano hidrológico de 1975/1976 até 2011/2012, enquanto o período disponível para calibração (estações hidrométricas com informação sobre os caudais) estende-se entre 1977/1978 e 1989/1990. O período seleccionado para análise corresponde a 37 anos, aproximando-se, deste modo, a um período equivalente a uma normal climatológica (30 anos). Os valores em falta nas séries foram obtidos através da regressão linear múltipla efectuando a correlação entre todas as estações (recorrendo à função PROJ.LIN do Excel), calculando-se os respectivos coeficientes de correlação (r^2) e declives (b). Para garantir maior precisão dos dados, foi elaborada separadamente a correlação mês a mês entre todas as estações. Os mapas contínuos de precipitação foram obtidos através do método de interpolação *Inverse Distance Weighted* (IDW). As maiores diferenças registadas são reflectidas pela variação sazonal.

A radiação solar diária foi também calculada uma vez que se trata de um parâmetro importante para a obtenção da evapotranspiração potencial diária. Este parâmetro foi obtido através do método proposto por Dingman (2002) que visa a integração de parâmetros como a constante solar, a latitude da área de estudo, a velocidade angular e cálculos da radiação extraterrestre, ângulo do dia, correcção da excentricidade, declinação, as horas do nascer e do pôr-do-sol. Como resultado foi possível obter uma mapa contínuo de radiação solar com o mesmo valor espacial para a área de estudo mas com variações temporais (ao longo dos dias ano).

Os dados diários de temperatura, obtidos para quatro estações meteorológicas (SNIRH), foram modelados através do método IDW incorporando o gradiente térmico vertical, ou seja, a taxa de diminuição da temperatura com a altura, de forma a obter os mapas contínuos de temperatura diária.

Uma vez obtidos os mapas de radiação solar e de temperatura diária, foi possível calcular a evapotranspiração potencial diária da área de estudo através do método de Hargreaves. Posteriormente, o cálculo da evapotranspiração real ou efectiva foi obtido através da multiplicação entre a evapotranspiração potencial e o factor de cultura. Com base no mapa de uso do solo (discriminado por tipo de vegetação) foi possível atribuir os valores de índice de área de folha (valores *standard* atribuídos globalmente por Olson, 1994) a partir dos quais foi possível calcular o factor de cultura.

Com base nos factores acima descritos foi possível modelar diariamente o comportamento hidrológico subterrâneo e superficial da área de estudo incluindo os atrasos e as percas da água na zona de percolação do solo não saturado. Acoplando o modelo hidrológico dinâmico (STARWARS) ao modelo de estabilidade de vertentes dinâmico (PROBSTAB) foi possível avaliar o seu efeito na susceptibilidade a deslizamentos translacionais superficiais no tempo e no espaço para a área de estudo, para um período entre 2002 a 2011.

Com base nos mapas de susceptibilidade obtidos, efectuou-se uma análise estatística independente de cada um dos deslizamentos translacionais superficiais de forma a entender quais os anos ou dias mais propensos à ocorrência destes deslizamentos. Esta análise foi efectuada tendo por base o centróide da área de depleção de cada deslizamento translacional superficial. Desta análise conclui-se que, de acordo com as áreas onde o factor de segurança é igual ou inferior a 1 (SF≤ 1), alguns dos locais onde estão inventariados os deslizamentos translacionais superficiais poderiam ter originado instabilidade do mesmo tipo em quase todos os anos. Por outro lado, verifica-se que determinados locais (correspondentes aos locais dos centróide dos deslizamentos translacionais superficiais) possuem uma tendência sazonal para a instabilidade.

Apesar de todas as vantagens do modelo físico dinâmico é de mencionar que existem alguns locais de instabilidade permanente (todos os dias do ano). Este facto não é realista, no entanto, devido à fraca informação sobre as datas de ocorrência dos deslizamentos foi impossível melhor estes resultados através da calibração. No entanto, os resultados deste modelo são promissores, especialmente para os locais

(correspondentes aos centroídes das área de depleção dos deslizamentos translacionais superficiais) que evidenciam uma instabilidade sazonal.

Uma análise mais rigorosa foi efectuada para o centróide correspondente ao deslizamento translacional superficial cuja data de ocorrência é conhecida. Desta análise foi possível verificar que o modelo acertou espacial e temporalmente a ocorrência deste deslizamento e foi também possível reconstituir todas as condições que geraram esta ocorrência para esse dia. Deste modo, é de salientar que, apesar de uma fraca quantidade de precipitação ocorrida nesse dia, o nível piezométrico estava bastante elevado devido a uma ocorrência de precipitação prolongada nos 14 dias anteriores (correspondendo o primeiro dia de precipitação ao máximo diário registado para o ano de 2006) o que, gradualmente, fez aumentar a pressão intersticial dos poros do solo, originando a ocorrência do deslizamento.

Com base numa análise anual foi possível determinar que 2006 foi o ano mais propenso à ocorrência de deslizamentos. Este ano destaca-se pelos máximos atingidos, quer pela precipitação anual quer pelos máximos diários. Através da AAC (0,85) foi possível verificar que o ano 2006 corresponde simultaneamente ao ano com melhor capacidade preditiva espacial. Por outro lado, o ano menos susceptível à ocorrência de deslizamentos translacionais superficiais foi 2008, correspondendo simultaneamente ao ano com menor capacidade preditiva espacial.

Aferir as condições que originaram deslizamentos translacionais superficiais através do método de base físico estático revelou-se uma tarefa complicada uma vez que este modelo não pressupõe a variação temporal dos factores climáticos.

O método de base físico dinâmico (STARWARS + PROBSTAB) parece conseguir ultrapassar estas limitações incorporando sob a forma de séries de mapas diários os dados da precipitação e evapotranspiração. Este facto possibilita aferir as datas (em termos diários) mais propensas à ocorrência dos deslizamentos translacionais superficiais. Apesar de todas as vantagens este modelo, ainda assim, apresenta também limitações, tais como: 1) o tempo de computação (de todos os *outputs* sob a forma de mapas diários) é bastante

elevado (1 ano para apenas 1 *output*, e.g., nível piezométrico = 365 mapas); 2) é necessário aprender linguagem *Python* e *PCRaster*; 3) por vezes torna-se bastante difícil e até mesmo impossível obter todos os parâmetros de entrada no modelo dinâmico. No entanto, apesar de todas estas limitações, este modelo dinâmico e extremamente complexo permite a obtenção de resultados mais realistas, o que justifica a sua utilização em detrimento de métodos estáticos mais simplistas.

Para fins de comparação, bem como para entender a susceptibilidade à ocorrência dos outros tipos de deslizamentos (foto-interpretados e/ou cartografados no campo), foi utilizado um método de base estatística (Valor Informativo). Para este método foram considerados os seguintes factores de predisposição à susceptibilidade: declive; exposição; curvatura (perfil transversal das vertentes); inverso do Wetness Index; litologia; morfo-estrutura; espessura de solo potencialmente instável; e tipos de solo (de acordo com a textura). Cada um destes factores foi reclassificado em variáveis categóricas. De forma a entender o grau de importância relativa de cada variável e a sua hierarquia de acordo com os diferentes tipos de deslizamentos, estes factores foram submetidos a uma análise sensitiva do tipo *leave-one-out*. Destas análises foi possível concluir que todos os temas podem ser incluídos nos modelos de susceptibilidade sem que a sua capacidade preditiva fique comprometida. Posteriormente, com base na percentagem de contribuição e nos índices de *Accountability* e *Realibility* foi possível estabelecer uma hierarquia entre os factores de predisposição sendo a litologia o factor de maior grau de importância relativo independentemente do tipo ou inventário de deslizamento, seguido do declive e da morfo-estrutura. A maioria dos estudos de susceptibilidade a deslizamentos efectuados anteriormente destacam geralmente o declive como o factor de maior grau de importância relativo, uma vez que a litologia utilizada possui geralmente uma escala 1:50 000 e nos melhores dos casos 1:25 000. No entanto, a litologia é destacada neste trabalho com um grau de importância relativo superior, devido a esta se tratar de uma informação bastante mais detalhada (1:10 000), facto pouco investigado até agora.

Os resultados das taxas de predição dos modelos de susceptibilidade a deslizamentos do inventário LI#1 demonstram ser aceitáveis de acordo com os valores estipulados por

Guzzetti (2005), sendo o melhor resultado registado para o modelo dos deslizamentos rotacionais profundos. Os modelos de susceptibilidade a deslizamentos rotacionais e translacionais superficiais não possuem valores tão elevados de predição, no entanto, estes nunca decrescem abaixo do aceitável (0,70). Para o inventário LI#1+LI#2 existem 2 modelos de susceptibilidade, nomeadamente para os deslizamentos rotacionais profundos e os deslizamentos translacionais superficiais, que apresentam uma performance aceitável, de acordo com a AAC (0,78 e 0,75, respectivamente). O modelo de susceptibilidade a deslizamentos rotacionais superficiais possui o valor mais baixo de predição, de acordo com a AAC (0,72). A explicação para estes modelos nunca apresentarem uma predição acima de 0,8 pode estar relacionado com os seguintes factos: 1) os inventários correspondentes aos deslizamentos mais antigos (LI#1 e LI#2) não foram sujeitos a verificação no campo; 2) poderá haver erros associados à georreferenciação e ortorrectificação das fotografias aéreas a partir das quais estes deslizamentos foram foto-interpretados; 3) por vezes torna-se difícil o reconhecimento do tipo de deslizamento que se está a cartografar devido à escala de análise.

Os resultados da validação dos modelos de susceptibilidade do inventário LI#3 devem ser observados com alguma cautela, uma vez que estes não foram validados por meio de uma taxa de predição, como nos casos anteriores, mas sim através de taxas de sucesso, o que implica AAC superiores, independentemente do tipo de deslizamento. Neste caso, todos os modelos apresentam sempre uma boa performance, pois a validação é feita com o mesmo conjunto de deslizamentos utilizados na modelação. O modelo de susceptibiidade a deslizamentos rotacionais superficiais é destacado como o melhor modelo do LI#3 (que com uma AAC de 0,90 o torna um excelente modelo) seguido pelo modelo dos deslizamentos translacionais superficiais (AAC = 0,88) e pelo modelo dos deslizamentos rotacionais profundos (AAC = 0,81).

Posteriormente, procedeu-se a comparação analítica entre os modelos de susceptibilidade a deslizamentos translacionais superficiais de forma a compreender as possíveis vantagens e/ou desvantagens da utilização dos métodos de base física e dos métodos de base estatística. Esta comparação foi feita com base no modelo de base física estático (PBM) e de base estatística (SBM). De acordo com o valor de predição da AAC e

da área com factor de segurança igual ou inferior a 1, o modelo de base física estático (PM) possui uma melhor capacidade preditiva (AAC=0,79) quando comparado com o modelo de base estatística (SM) (AAC=0,75) (modelado com base nos deslizamentos translacionais superficiais do inventario LI#1 + LI#2 e validado pelos mesmos tipos de deslizamentos do inventário LI#3).

As diferenças espaciais tornam-se mais elucidativas quando ambos os mapas são reclassificados pelo método dos quartis (25% do total da área de estudo em cada classe). Deste modo, foi possível observar que o modelo SBM apresenta uma distribuição espacial da susceptibilidade mais difusa, ao passo que, o modelo PBM apresenta uma distribuição mais bem segregada entre as áreas de maior e menor susceptibilidade, estando as primeiras mais concentradas na parte central da área de estudo e as segundas na parte Oeste e Noroeste da área de estudo.

A área correspondente ao factor de segurança igual ou inferior a 1 no modelo PBM (24,7% do total de área mais susceptível da área de estudo) consegue prever espacialmente 72,5% do total da área de deslizamentos translacionais superficiais (do LI#3), ao passo que, no modelo SBM a mesma área (24,7% do total de área mais susceptível da área de estudo) apenas consegue predizer espacialmente 56,1% do total de área de deslizamentos translacionais superficiais (do LI#3). Desta análise é possível concluir que os resultados obtidos com o modelo determinista (de base física estático) são mais robustos do que os resultados apresentados pelo modelo de base estatística.

Considerando a área correspondente ao factor de segurança igual ou abaixo de 1, a sobreposição entre os dois modelos é de 36%. Nesta área de sobreposição, 40,3% do total da área de deslizamentos translacionais superficiais do LI#3 são preditos por ambos os modelos, o que demostra algum grau de concordância entre os dois modelos.

Com base nos resultados desta dissertação é possível concluir que apesar das vantagens evidenciadas pelos métodos de base física, todas as abordagens são validas e até mesmo complementares no que concerne à susceptibilidade aos deslizamentos translacionais superficiais. Do ponto de vista estático temporal, o cruzamento entre os dois modelos

revela-se bastante adequado para a previsão da susceptibilidade a deslizamentos translacionais superficiais.

ACRONYMS AND ABBREVIATIONS

ACC Accountability

API Aerial photographs interpretation

AUC Area under Curve

BA Bedding attitude

BS bedding surface

BT Bedding trace

CA Class area

CEG (*Centro de Estudos Geográficos)* Centre for Geographical Studies

COS (*Carta de Ocupação do Solo) Land cover map*

DEM Digital Elevation Model

DTM Digital Terrain Model

FAO Food and Agriculture Organization

FC Faculty of Sciences

FCT (*Fundação para a Ciência e a Tecnologia)* Portuguese Foundation for Science and Technology

IDW Inverse Distance Weighted

IGOE (*Instituto Geográfico do Exercito)* Army Geographic Institute

IGOT (*Instituto de Geografia e Ordenamento do Território)* Institute of Geography and Spatial Planning

IGP (*Instituto Geográfico Português) Portuguese Geographical Institute*

IRPI (*Istituto di Ricerca per la Protezione Idrogeologica)* Research Institute for Geo-Hydrological Protection

IV Information Value

IWI Inverse Wetness Index

GIS Geographical information system

GPS Global Positioning System

LA Landslide area

LDD Local drainage direction

LFCD Land Facet Corridor Designer

LI Landslide Inventory

MaxEnt Maximum Entropy

OS Operation System

PBM Physically based method

PC Percent contribution

PI Permutation importance

PROBSTAB Slope stability model

RLB Reliability

RMSE Root Mean Square Error

SBM Statistically based method

SF Safety Factor

SHALSTAB Shallow slope stability model

SM Safety Margin

SNIRH (*Sistema Nacional de Informação de Recursos Hídricos)* National Water Resources Information System

STARWARS Slope hydrology model

SWRC Soil water retention curve

TauDEM Terrain Analysis Using Digital Elevation Models

TIN Triangulated Irregular Network

TLU Two-dimensional land-surface units

TOBIA Topographic/Bedding-Plane Intersection Angle Model

TOPOG The Terrain Analysis Hydrologic Model

TPI Topographic position index

TU Terrain unit

UL University of Lisbon

USDA United States Department of Agriculture

UU Utrecht University

SYMBOLS

a Contributing upstream area

A Slope aspect

$\mathbf{A_{sd}}$ Angular standard deviation of the aspect map

β Slope angle

b Land unit width

$_{\mathbf{BC}}$ Regarding the fourth soil layer

c Cohesion

c' Effective cohesion

Δc' Apparent cohesion

C Quantity of water detained on the canopy

$\mathbf{C_a}$ Cell area

$\mathbf{C_p}$ Profile curvature index

$\mathbf{C_{max}}$ Maximum Storage Capacity

D Drainage rate from leaves and stem

D1, D2, D3 Depth of the first, second and third soil layer

Ddt Concentrated routing of water along the stem and branches

DF2 Arbitrary fraction to restrict the depth of the second soil layer to 0.3 m

dfp Depth to the sliding plane

DRA Daily rainfall anomalies

du Depth to the top of the capillary fringe

$\mathbf{D_{unsat}}$ Thickness of the unsaturated zone.

dw Depth to the water table

$\mathbf{E_0}$ Eccentricity correction

$\mathbf{E_i}$ Event

$\mathbf{E_r}$ Evaporation rate

$\mathbf{ET_{act}}$, $\mathbf{ET_0}$, **ETc** Actual, potential and crop evapotranspiration

f_i Growth factor based on temperature

|h| Absolute matric suction

h_A Bubbling pressure (air entry value)

H Entropy

H_{max} Maximum Entropy

H_{min} Minimum Entropy

Ic Gross interception loss of the canopy

J Julian day

Kc Measured soil depth sites

K_c Crop factor

K_{cb}, $K_{cb\ mid}$, $K_{cb\ max}$, $K_{c\ min}$ Basal crop coefficient, during the mid-season, at peak plant size or height and for bare soil

K_e Soil evaporation

$K`_{ET}$ Instantaneous extraterrestrial radiation flux on a horizontal plane

K_{sat} Saturated conductivity of soil

$K_{lateral}$ Saturated lateral hydraulic conductivity

$k(\theta_E)$ Unsaturated hydraulic conductivity

LAI, $LAI_{\ max}$, $LAI_{\ min}$ Leaf area index, leaf area index for the growing season, leaf area index for dormancy season

Limfac Arbitrary fraction to restrict the depth of the third soil layer to 0.95 m

m Ratio between saturated and dried soil

MI Maximum rainfall intensity

p Fraction of not intercepted rainfall (direct throughfall)

P Catenary position within the hillslope profile

Pdt Rainfall intensity

P_{dur} Rainfall duration

Perc Vertical unsaturated matric flow

p_i Probability of an event

ps, pr Soil and rock density

Ps Stemflow

Pt Not intercept flux

P_{tot} Total rain for one day

Q_{sat} Lateral flux over the saturated zone

q Effective precipitation

R Resisting forces

R_a Modulus of the resultant vector of the unitary vectors of each aspect map cell

R_s Incident solar radiation

S Driving forces

S_a Slope angle index

S_d Surface detention

StorMat, StorSat, **StorMax** Unsaturated, saturated and maximum storage

T Temperature

τ Tortuosity

t Shear stress

Δt Time increment

t_f Shearing resistance

T_e Estimated temperature

T_m Transmissivity of soils

Γ Day angle

T_{hr} Solar sunrise

T_{hs} Solar sunset

u Pore pressure

V Circular variance

VMC Volumetric moisture content

WL, $\Sigma D_{sat}(z)$ Groundwater height above the shear surface

γ_d, γ, γ_s, $\gamma`$ Dry, moist, saturated and buoyant bulk densities

γ_w Density of water (γ_w = 9,81 kN/m3)

Z, SDepth, ΣD(z) Soil thickness

σ Sliding plane

Φ Root Mean Square Error

δ Total normal stress

φ Angle of internal friction

δ' Effective normal stress

φ Angle of internal friction

φ' Effective angle of internal friction

∂b/∂t Rate of soil production from bedrock

∂w/∂t Soil lowering rate due to chemical weathering

θ, θ_{sat}, θ_{res} Actual, saturated and residual volumetric moisture content

θ_E Effective saturation or Degree of saturation

Λ Latitude

ω Angular velocity

ϕ Porosity

λ Pore size distribution index

ψ Capillary pressure

INTRODUCTION

INTRODUCTION

Context

Knowledge in the field of slope instability and predisposition of territory for the occurrence of landslides is recognized as an essential condition for a balanced risk management and for an effective spatial planning (Crozier and Glade, 2005; Zêzere, 2007).

Within the context of slope instability, landslides can affect communities and influence their activity. Thus, mapping or delineating areas susceptible to landslides is essential for land-use activities and management decision-making. The methods implemented in this dissertation have the overall objective of developing the understanding on slope instability processes and patterns at a regional scale.

The basis of this study is a PhD research project (SFRH / BD / 46816 / 2008) entitled: "Landslide Susceptibility Evaluation and Validation at a Regional Scale", funded by the Portuguese Foundation for Science and Technology (FCT).

The research was carried out in the Arnoia, Tornada and Alfeizerão sub-catchments located 90km north from Lisbon. This area was chosen due to its abundance of landslides and to its geologic and geomorphologic characteristics.

Problem definition

The causes of landslides, related to geomorphologic instability, are multiple and usually occur at the same time making it difficult to define in any particular case "what is the cause of the landslide" (Zêzere and Trigo 2011).

Landslides are the manifestation of the landscape inertia to adapt to changes in the intrinsic or extrinsic factors that affect slope stability (Crozier, 1986). Intrinsic factors are those that directly influence the stress distribution above the potential slip surface. The extrinsic factors influence the stress distribution indirectly (Crozier, 1986). Most of the times, the intrinsic factors change only gradually over time and can be considered as preparatory factors whereas the extrinsic factors are transient and can regard triggers, i.e., the disturbance that initiates slope instability or failure (Crozier, 1986). Thereby, Glade and Crozier (2005) based on previous work by Crozier (1986) and Popescu (1994), proposed the classification of landslide causes in the following classes: predisposing factors, preparatory factors and triggering factors.

There are two basic methods for landslide susceptibility/hazard zonation: the direct and indirect mapping methods. The direct mapping method is a knowledge-driven geomorphic technique (Schuster 1978). During field surveys, the analyst establishes and evaluates the relationship between landslides and their geologic and geomorphic settings. The indirect mapping technique is an approach which involves the mapping of the parameters considered to be of potential effect to the occurrence of landslides. This is then followed by an analysis of all the factors (predisposing, preparatory and triggering) contributing to the occurrence of landslides (Soeters and van Westen 1996; Suzen and Doyuran 2004). Concerning the indirect mapping technique a variety of approaches have been used in slope instability mapping and can be classified into qualitative factor overlay, statistical models, and geotechnical process (physically-based) models.

In the qualitative approach (heuristic methods), several maps representing the spatial distribution of those environmental parameters (predisposing factors) which may have influence on the occurrence of landslides are combined into a susceptibility map using subjective decision rules, based on the experience of geoscientists involved (Anbalagan, 1992; Pachauri and Pant, 1992; Sarkar et al., 1995).

The physically-based methods allow the quantification of instability through the explanation of the physical mechanisms and responses to the influential factors that lead to the occurrence of the instability and slope rupture and can numerically integrate other

models of hydrogeological and geotechnical nature, whose main objective is mathematically approach reality in order to improve the ability to forecast where and when it will be triggered new landslide events (Beek, 2002).

The statistically-based methods include necessarily steps such as (e.g., Soeters and van Westen, 1996; Guzzetti, 2005): (i) the preparation of landslide inventory, (ii) the identification of a set of predisposition factors that can directly or indirectly relate to the slope instability (iii) the assessment of the statistical relationships between this set of predisposition factors and the distribution of past landslides (iv) the classification of the territory according to the degree of landslide susceptibility (v) the validation of the susceptible models in order to evaluate the predictive ability.

The main difference between the statistically and the physically-based methods is that statistical methods focus only on the predisposition factors, whereas the physically-based methods focus in every predisposing, preparatory and triggering factors.

However, due to the many parameters involved in the landslides phenomena, no single method exists to identify and map landslides, to ascertain landslide susceptibility and hazard, and to evaluate the associated risk (Guzzetti, 2005).

Aims and objectives

The main goal of this study is to contribute to the reduction of the shortcoming knowledge in the causes of landslides, by providing: i) the scientific rationale; ii) several methodologies for input data acquisition; iii) methodologies to derive landslide forecasts, through the implementation of physically and statistically-based methods. In this context, 10 specific objectives were defined, such as:

1) Multi-temporal landslide inventory and classification according to the type of movement and estimated depth in the Arnoia, Tornada and Alfeizerão sub-catchments, since 1958 to the present;

2) Acquisition and production of new themes based on modeling and field observation (e.g. detailed lithological map, morpho-structural map, DEM, soil depth).

3) Acquisition of soil characteristics according to the hydrogeological and geotechnical properties of soils (through field work, laboratory measurements and further back analysis);

4) Landslide susceptibility assessment using a hydrological model coupled to a slope stability model under static temporal conditions. Validation through the quantification of the model prediction rate;

5) Acquisition, processing and modeling of long term climatic data (i.e., rainfall and temperature);

6) Landslide susceptibility assessment using a hydrological model coupled to a slope stability model under dynamic temporal conditions. Validation through the quantification of the model prediction rate;

7) Comparison between physically base models: static and dynamic approach;

8) Sensitivity analysis of the landslide predisposing factors: morphometric data (i.e., elevation, slope, curvature, profile curvature) and nonmorphometric data (i.e., soils, lithology, soil depth);

9) Landslide susceptibility assessment using a statistically-based method (Information Value Method). Validation through the quantification of the model prediction and success rate;

10) Comparison between statistically and physically static models.

In order to answer these objectives, the dissertation was structured in six Chapters.

Chapter 1: gives a physiographic description of the study area contextualized in the Central western Portugal. The boundaries of the hydrographical sub-catchments chosen for this dissertation are defined here.

Chapter 2: is dedicated to the landslide mapping and inventories acquisition. It will be established the criteria for the classification and definition of the landslides morphology, used for this work and it will be presented the methodologies which were used to perform the different landslide inventories of the study area.

Chapter 3: provides a methodology for detailing lithological data and, further, the quantification of the improvement through the relationships between the lithological settings (previous and detailed lithological data) and the landslides pattern and distribution.

Chapter 4: presents a methodology for morpho-structural modeling. Further, it is aimed to determine the relationships between the morpho-structural setting given by the bedding attitude (BA) of the slopes and the distribution and pattern of landslides existing in the study area.

Chapter 5: it is performed landslide susceptibility assessment through the physically-based methods (which couples the slope hydrology with slope stability) using temporal static and temporal dynamic approaches. Methodologies for the acquisition and preparation of the input variables are presented, i.e., soil depth and soil classification for further hydrogeological properties establishment. The acquisitions of geotechnical parameters through field work, laboratory measurements and back analysis are performed. Further, a comparison is made between the models obtained through static and the dynamic approaches. The susceptible models are validated in terms of their spatial predictive capabilities.

Chapter 6: it is performed landslide susceptibility assessment through a statistically-based method (Information Value Method) for each landslide inventory and for each landslide type. It is presented the acquisition and preparation of the predisposition factors, as well

as their sensitivity and hierarchy regarding the landslide susceptibility modeling. Further, a comparison between the results previously obtained for the shallow translational susceptibility model through the static physically-based method (from chapter 5) and the shallow translational susceptibility model obtained statistically is performed.

The figure I.1 summarizes the working flow chart of the present dissertation.

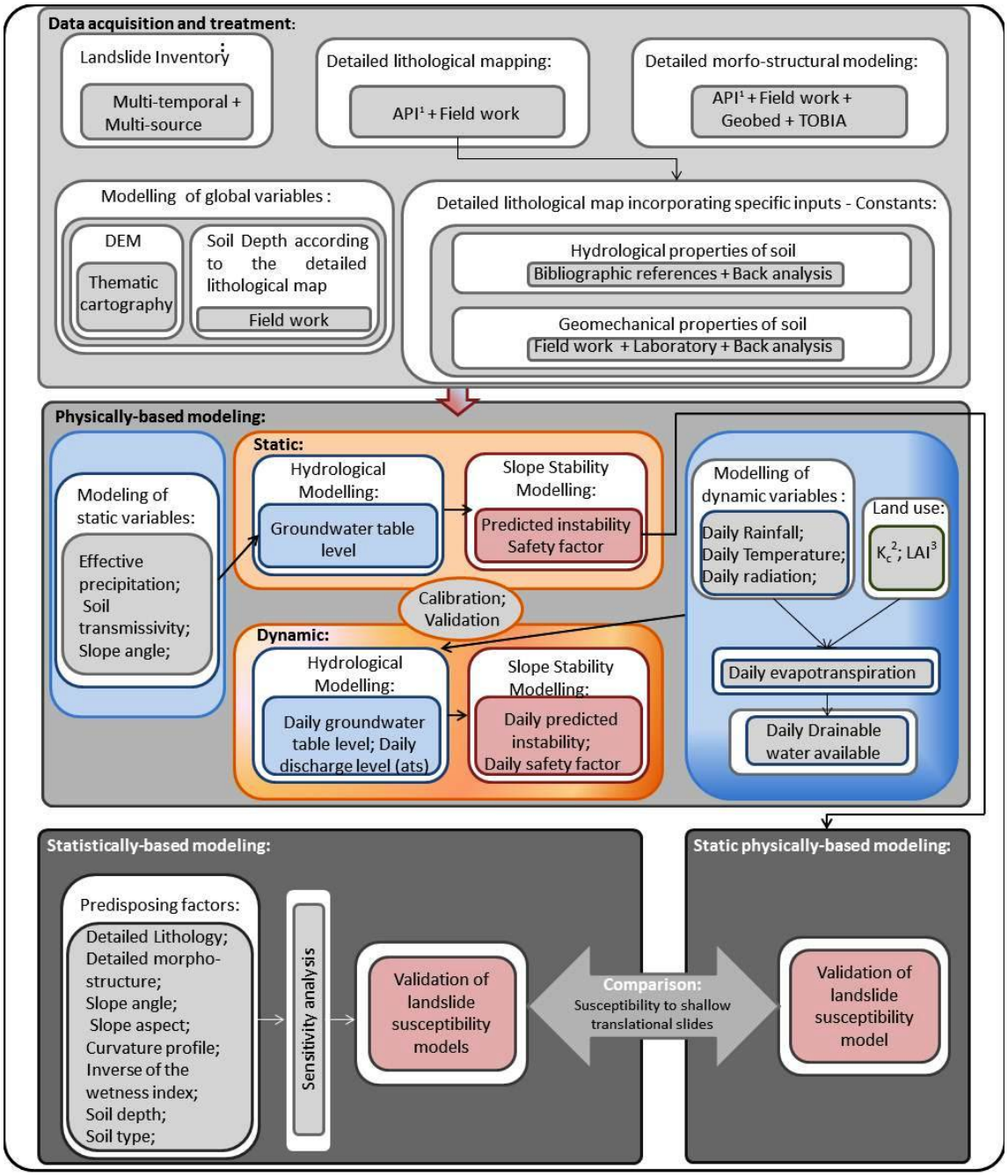

[1] Aerial Photo-Interpretation
[2] Crop Factor
[3] Leaf Area Index

Fig. I.1– Organizational structure of the PhD research project "Models for landslide susceptibility assessment and validation at the regional scale".

CHAPTER 1

PHYSIOGRAPHY OF THE STUDY AREA

1 PHYSIOGRAPHY OF THE STUDY AREA

In this chapter it is made a brief characterization of the study area, contextualized geographically in the Central western Portugal. It will be defined here the boundaries of the hydrographical sub-catchments chosen for this dissertation.

1.1 Geographical placement

This dissertation aims to assess the landslide susceptibility modeled through physically and statistically based models. In what physically based-models concerns it must be noted that most previous studies has been developed for local scales, however, this dissertation aims to assess landslide susceptibility at a regional scale.

Thereby, located 90km north from Lisbon, part of three sub-catchments, named Arnoia (105km^2), Tornada (68.9km^2) and Alfeizerão (102km^2) were selected for this work (Fig. 1.1). Its boundaries were defined by the ridge line, totalizing about 275km^2. These sub-catchments were chosen for its geological and geomorphological features and for the abundance of landslides. It is important to mention that the three sub-catchments are limited on the West side by a fault located on the East side of a geological featured designated diapir of Caldas da Rainha. Thus, only part of these three sub-catchments was selected for this work, leaving apart the west side of the sub-catchments. Such procedure was made in order to avoid the coastal erosion dynamics, which does not match with the aims of this work, and also to avoid introducing a geological feature that, due to its flat character, would overestimate the susceptibility results obtained by the statistical-based methods.

Administratively, the sub-catchments have an inter-municipal covering, distributed among the municipalities of Caldas da Rainha (59.5%), Alcobaça (13.9%), Óbidos (10.8%), Cadaval (10.6%), Bombarral (4.2%), Nazaré (0.9%) and Rio Maior (0.1%) (Table 1.1, Fig. 1.2).

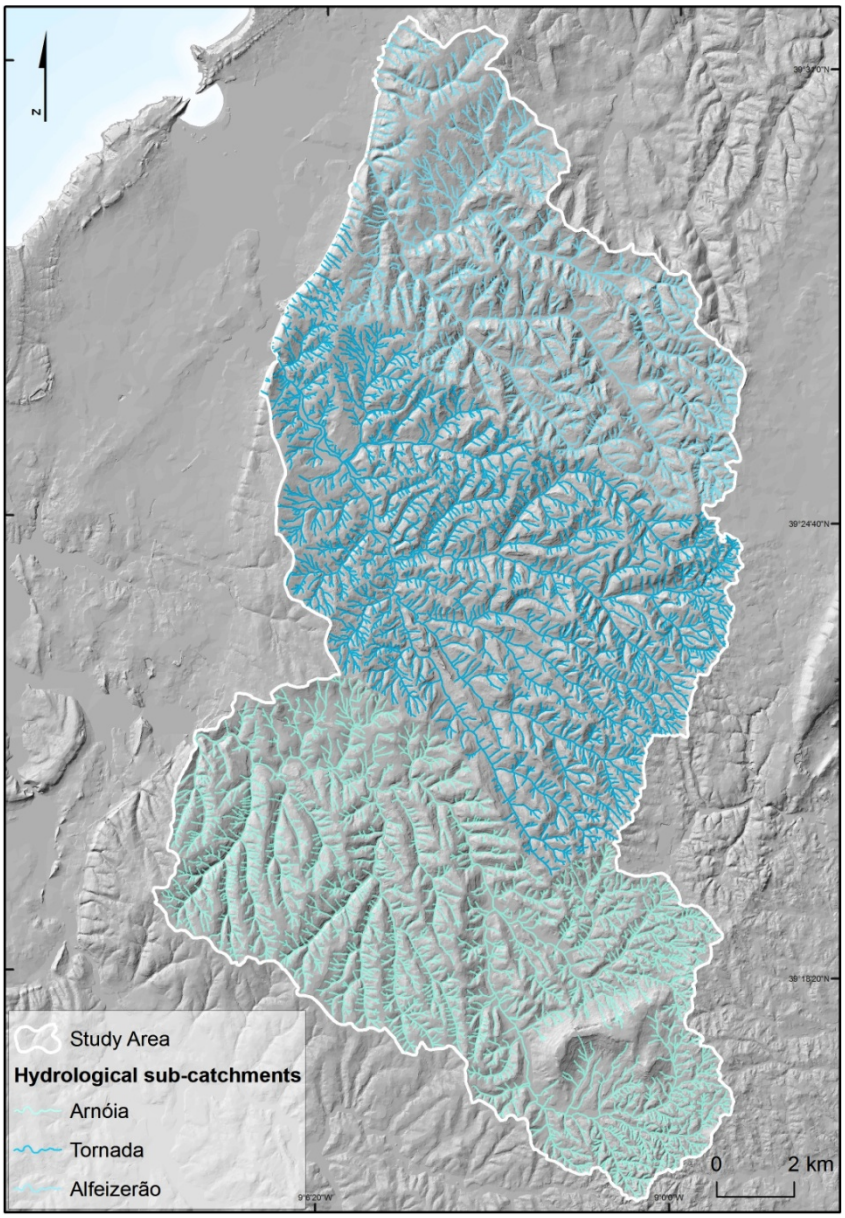

Fig. 1.1 – The study area: East part of the sub-catchments of Arnoia, Tornada and Alfeizerão.

Table 1.1 – Municipality area occupied by the study area.

Municipalities	**km^2**	**%**
Caldas da Rainha	164.1	59.5
Alcobaça	38.3	13.9
Óbidos	29.8	10.8
Cadaval	29.3	10.6
Bombarral	11.6	4.2
Nazaré	2.6	0.9
Rio Maior	0.2	0.1
SUM	275.9	100

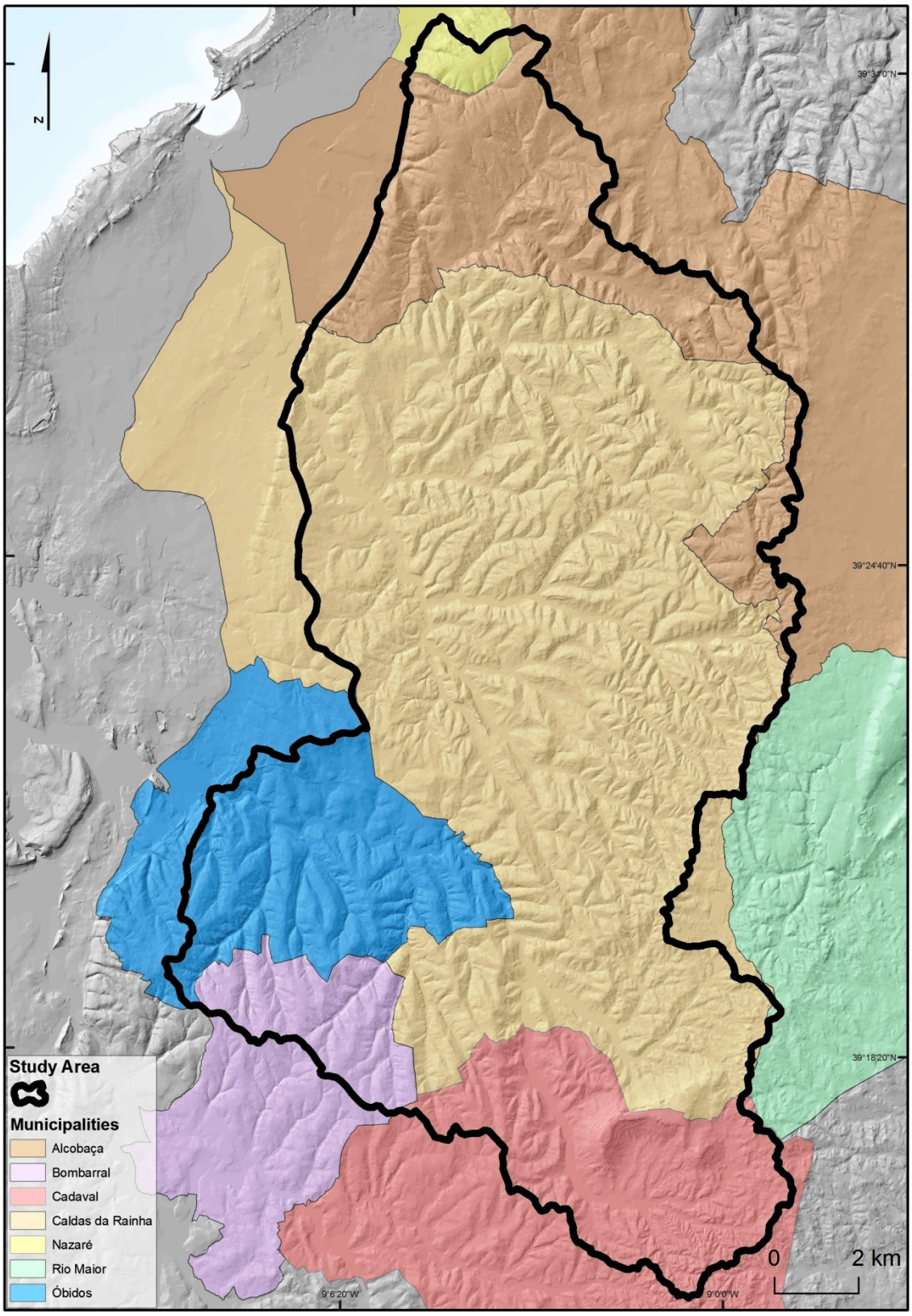

Fig. 1.2 – Geographic placement of the study area.

1.2 Paleogeographic evolution

The western margin of Portugal, where Arnoia, Tornada and Alfeizerão sub-catchments are located, has a strong relationship with the evolution of the North Atlantic Ocean, during the Mesozoic. Such evolution has originated a very rich and varied geological legacy and also an interesting tectonic history, since the Late Triassic. Regarding the Upper Jurassic, several connections can be established between the tectonics and the stratigraphic record in the area surrounding the Caldas da Rainha structure: the basement and salt pillow control on deposition; the beginning of a diapiric and magmatic cycle associated to the onset of sea-floor; the exhumation of both Jurassic deposits and the core of their controlling diapir. The nature of the outcrops and richness in sedimentary environments, related with the different phases of rifting, is a remarkable case for extensional basin studies (Dinis and Bernardes, 2004).

Later, during the Cenozoic, such place was submitted to an intense intraplate compressive deformation which caused lithospheric folding (Cloetingh *et al*., 2002; Tejero *et al*., 2010). Thereby, regarding the geological and the morpho-structural context, which characterize the Portuguese territory, the Arnoia, Tornada and Alfeizerão sub-catchments falls under the Portuguese western Meso-Cenozoic unit (Fig. 1.3). Understanding the tectonic regime is the key for understanding the formation of the geological materials in this region. The Mesozoic Era was marked by episodes of extensional movements, interrupted by short episodes of compressional movements. The compressional phases gave rise to a deep synclinal fold with a NE-SW direction where the study area is located. This deep syncline is laterally limited by anticline folds more or less parallel (Zbyszewski *et al*., 1966). The anticline fold, located on the right side boundary of the study area, is marked by the presence of a compressional fault (Fig. 1.3).

Later, during the Jurassic and the Cretaceous, this region was subjected to contrasting tectonics deformation (subsidence and uplift) originating varied geological materials such as limestone and shale, typical from ocean environment, and sandstones, typical from continental environment (Zêzere 2005a).

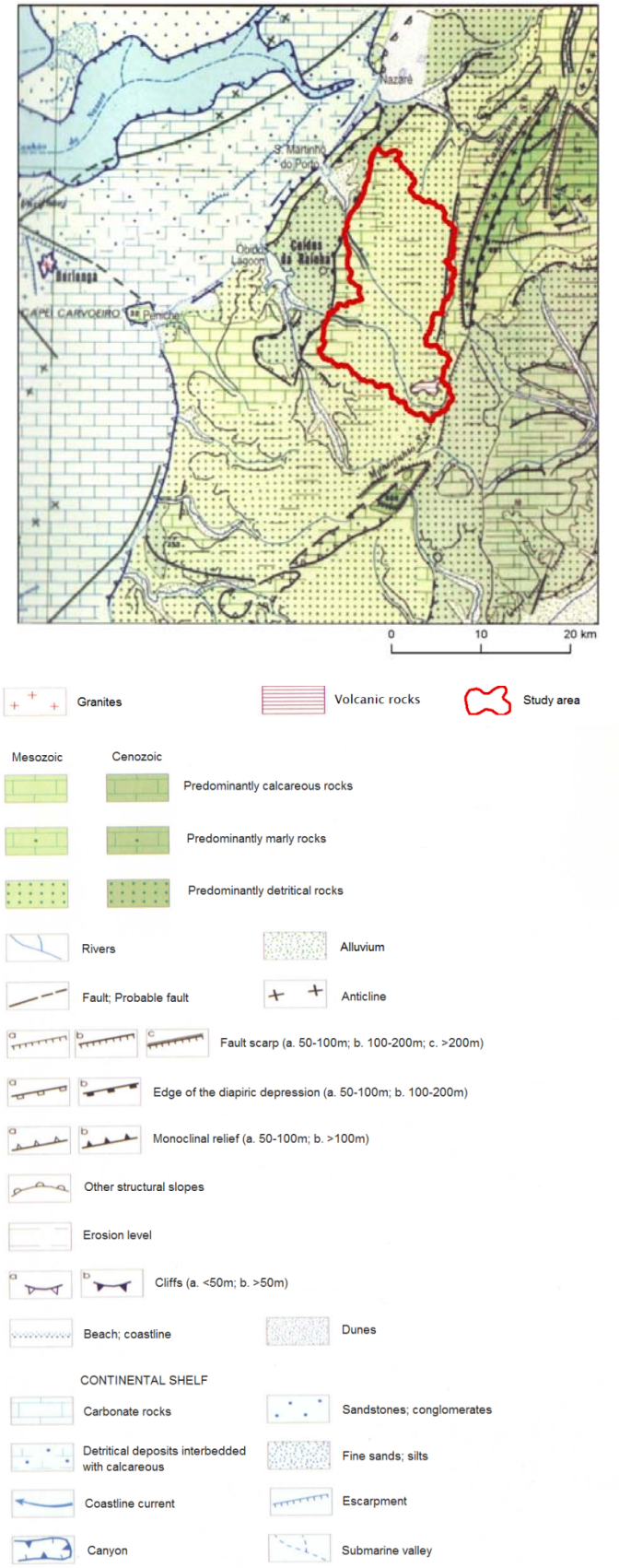

Fig. 1.3 – Geomorphological placement of the Portuguese Estremadura on the west side of the Candeeiros and Montejunto Mountains. Extracted and adapted from Ferreira (1981).

1.3 Geology and geomorphology

From a geomorphologic point of view, the three sub-catchments, of Alfeizerão, Tornada and Arnoia are situated in a dissected old quaternary coastal plateau where the evident syncline structure is located. Here crops out, mainly, upper Jurassic sandstones and claystones (Fig. 1.4).

Due to the poor presentation of the geological map and its implications for future modeling it became imperative to work in its detailing. Thus, the chapter III will be based on detailing the geological map through aerial photo interpretation techniques and there it is possible to have a more detailed description on the lithological materials and how they affect the study area.

Thereby, despite not being explicit in Fig. 1.4, it is possible to understand that the reliefs are controlled primarily by the alternating materials with different erosion resistance, plasticity and permeability, which is responsible for the morphology of the study area, i.e., the degree of conservation dependent on the strength of the different geological materials to differential erosion.

The geological structure and the lithology of the study area explain the morphology and, thus, the elevation variations along the study area. The average elevation is about 114 m (Fig. 1.5). The SE part of the territory, where the higher resistant dolerite rocks crops out, has the predominant higher reliefs. Here it is located the Todo-Mundo Hill (262.4 m).

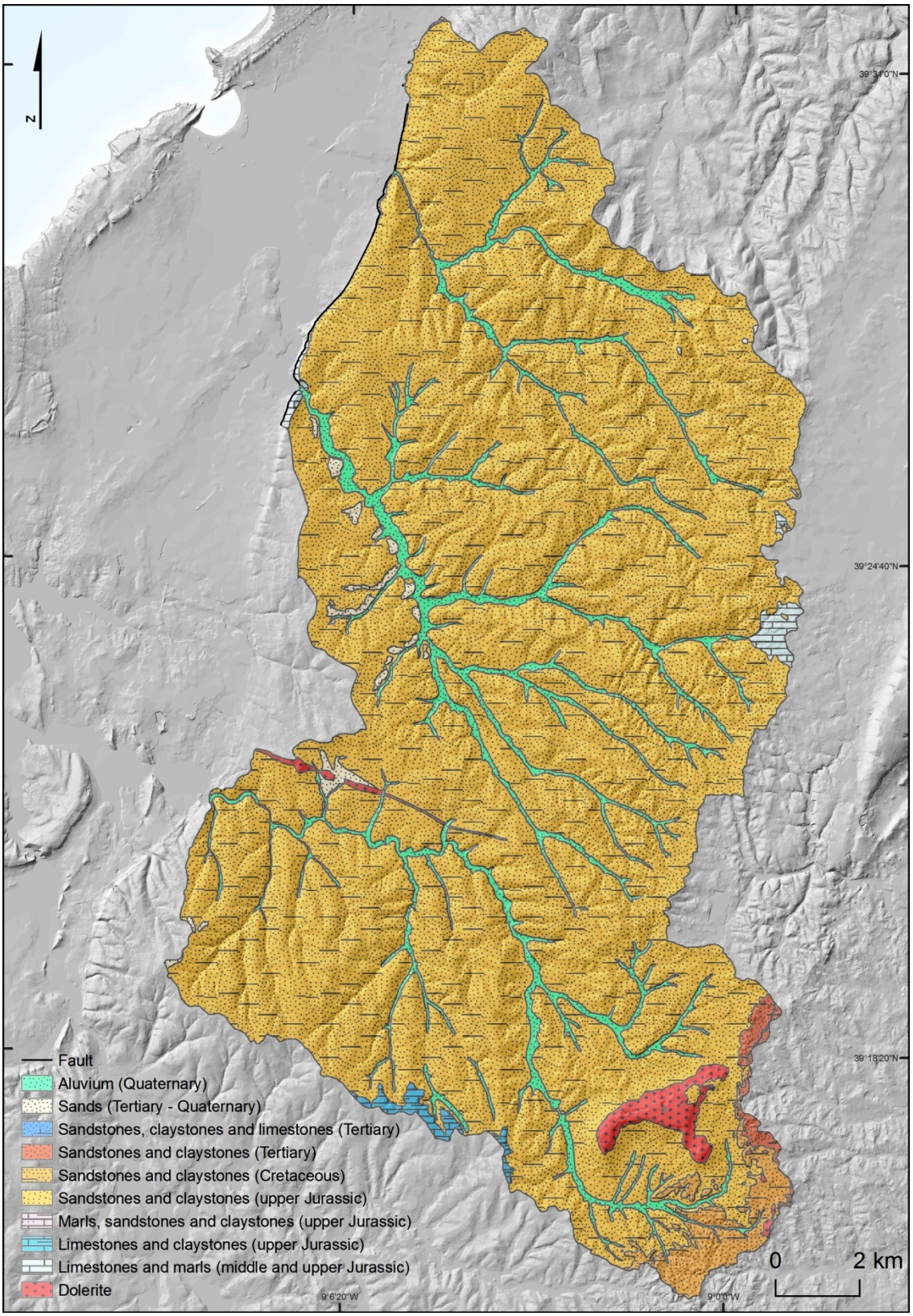

Fig. 1.4 – Geological map of the study area.

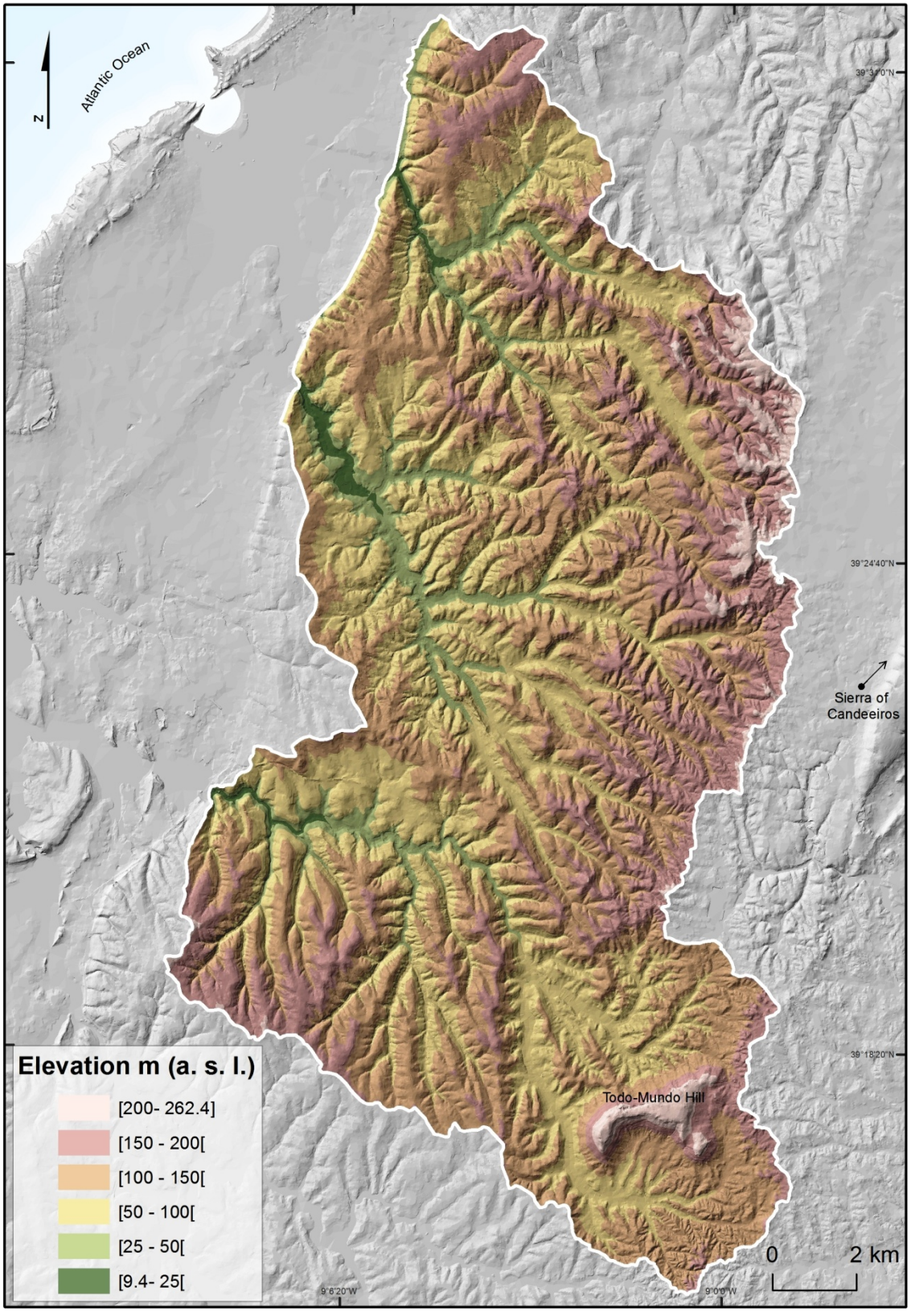

Fig. 1.5 – Digital Elevation Model (DEM) of the study area.

On the NNE-SSW part of the study area a geologic diapir occurs (named Diapir of Caldas-da-Rainha). Although not being located on the geologic diapir it is important to mention

such important geological feature due to its geological impact on the study area. Thereby, places surrounding this geologic feature were clearly affected due to associated diapiric movements affecting the Meso-Cenozoic cover (Dinis and Bernardes, 2004).

The coastal plateau, also known as Aljubarrota coastal plateau, where Arnoia, Tornada and Alfeizerão sub-catchments are located, lies between the diapir, and the western slope of the Candeeiros Mountain (already outside from the boundaries of the study area). According to Henriques (1996), it corresponds to a flattening coastal and it has a shallow ramp form, gently inclined (usually less than 2º), towards the sea.

This coastal plateau is indeed founded greatly eroded by the hydrographic network, which originated a set of elongated hills with flattened tops. It should be noted that the presence of a geological depression, such as the already mentioned diapir, marks a sudden interruption in the coastal plateau(Zêzere 2005a).

The hydrographic network is an important element in the geomorphology description of the study area since this is, in part, responsible for its physiognomy. It can be seen that the main rivers have a dominant NW-SE direction, perpendicular to the major regional structural assemblies as well as the major landforms (Fig. 1.1).

Each of the sub-catchments, selected for this dissertation, is composed by a main river, namely Alfeizerão, Tornada and Arnóia. Regarding the Alfeizerão River, it rises in Ribafria (district of Leiria) and flows towards São Martinho do Porto (Fig. 1.5). The Tornada River rises in the hills of the Candeeiros Mountain and also flows towards São Martinho do Porto. The Arnóia River rises in the hills of the Todo-Mundo Hill and flows towards the Óbidos lagoon. These main rivers have carved the Coast plateau. The valleys have a relatively narrow alluvial bottom and the slopes present a predominantly straight path. The entrance of the rivers into the diapiric depression is marked by a pronounced fitting. The same happens when rivers burst the western edge of the diapir towards the sea. Within the Diapir depression the physiognomy of river valleys is quite contrasted with a flat and wider alluvial bottom, and gentle slope angles (Henriques, 2009).

1.4 Climate

The dominant Atlantic influence determines the climate of the study area. This influence gives rise to summers relatively fresh and mild winters with high monthly values of precipitation (Ribeiro *et al*., 1988). The mean annual precipitation of the study area is about 992 mm, according to the period recorded from 1950/51 to 2001/02 (Henriques, 2009). Combined with a great interannual rainfall variability (rainiest year = 1449mm; driest year = 422 mm), there is also a slight upward trend of the annual precipitation values, which is about 3 mm / year (Fig. 1.6).

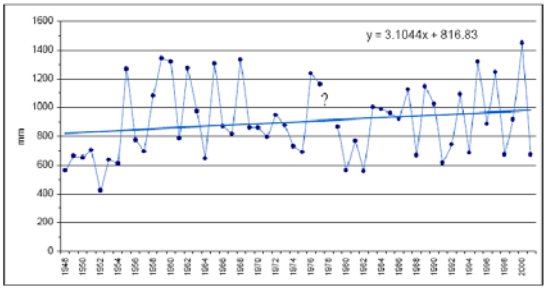

Fig. 1.6 – Interannual variation and evolutionary trend of the precipitation for Santa Catarina metereological station (1948/49 - 2001/02). Source: Municipally of Caldas da Rainha, 2008.

The analysis of the rainfall intensity (maximum annual daily rainfall) shows that there is no clear evolutionary trend in the data series. The highest values occurred in the 60s of the twentieth century (Fig. 1.7). The absolute maximum of daily rainfall value reached 86.3 mm and was recorded in November, 1956.

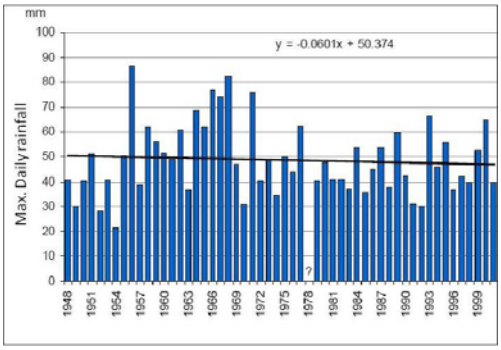

Fig. 1.7 – Interannual variation of annual maximum daily precipitation for Santa Catarina meteorological station (1948/49 - 2001/02). Source: Municipally of Caldas da Rainha, 2008.

The combination of data contained in Fig. 1.6 and 1.7 shows that, in the last half century, there is a tendency for an increased amount of water in the study area (through precipitation) which does not necessarily follow an increased of rainfall intensity (Henriques 2009).

CHAPTER 2

SLOPE DYNAMICS

2 SLOPE DYNAMICS

This chapter aims to establish the criteria for the classification and definition of the landslides morphology, used for this work. Moreover, the methodologies which were used to perform the different landslide inventories of the study area will be presented.

2.1 Susceptibility and hazard

According to Soeters and Van Westen (1996), susceptibility must be understood as the spatial probability of occurrence of a particular phenomenon in a given area, based on the conditioning factors, regardless their period of recurrence. The hazard, on the other hand, takes into account a spatial and also the temporal probability (Guzzetti *et al*., 1999; Van Westen, 1994).

As Varnes (1984) states, "the past and the present are the key to the future". This premise translates the idea that in order to be able to predict the occurrence of a future event and, in turn, to avoid its potential damage, it is important to know precisely the factors that cause or potentiate the occurrence of the phenomenon.

There are two sets of methodologies that allow the evaluation of the susceptibility and the hazard: absolute evaluation methods and the methods of relative evaluation. Absolute evaluation methodologies classify the susceptibility and the hazard with a measurable value (e.g., safety factor (SF) evaluated by deterministic methods). Relative evaluation methodologies are based primarily on the location and distribution of slope movements and factors that influence it. Although there are some differences, all models of relative evaluation are based on common principles, including the identification, analysis and cartography of distribution of the natural phenomenon studied. The methods of evaluation are broken down into direct and indirect mapping methods (Henriques, 2009).

In the methods of direct mapping analysis is performed on the basis of the effects of instability, namely in the distribution of landslides already occurring, allowing a qualitative evaluation of the susceptibility (Zêzere, 2005b). The results of this analysis are of some subjectivity, depending on the experience of the person or persons who made the field survey and selected it, weighed and determined the combinations most relevant factors to define the situations of danger (Zêzere, 2005b).

In the methods of indirect mapping, the analysis is made on the basis of the factors which affect the natural phenomena. This kind of analysis has much less subjectivity than the first kind, allowing the construction of models. This type of evaluation includes two methods subtypes: heuristics, or indexing, which consist in the subjective assignment of "scores" to a number of factors with cartographic representation; and statistical methods, in which the factors which affected the occurrence of a phenomenon present and past are related through a parametric empirical function, enabling quantified prediction of susceptibility, even in areas that have not yet been affected by landslides (Guzzetti, 2005; Zêzere, 2005b; Van Westen 2008).

Varnes (1978) states that "the processes involved in the occurrence of landslide congregate a continuous series of events from the cause to the effect" i.e. until the moment that the slope failure happens there are a group of factors and conditions that leads to slope instability, whether geological, morphological, physical and/or anthropogenic (Varnes, 1978; Popescu, 1994; Cruden and Varnes, 1996).

Terzaghi (1951) cited by Popescu (1994) divided the causes for the landslides occurrence in external causes, resulting from the increase of shear stress and, internal causes, which result from the decrease in shear strength. As external causes it is considered: changes in the slope morphology; erosion at the base of the slope; the slope overload; vibrations of the ground (e.g., by building structures or earthquakes); sudden increase in water level; change of drainage network. As internal causes it is considered: cohesion; pore-water pressure; root strength; seismic acceleration; and external weights.

2.2 Slope movements: typology

In its more common term, landslides are considered as “a mass movement of rock, soil or debris material forming a slope (natural or engineered) towards the lower and external part of the slope"(Terzaghi, 1953; Varnes, 1978; Cruden, 1991). The mass movement only occurs under the effect of gravity, differently from the mass transport, which is when the material is transported by an agent (e.g., water flowing, wind).

There are five types of slope movements (Cruden and Varnes, 1996): i) Falls; ii) Topples; iii) Slides; iv) Spreads; and v) Flows. The slope movement can also be complex by including two or more associated types. However, this dissertation focuses only on slides (Fig. 2.1), since they were the most often landslides founded within the Arnoia, Tornada and Alfeizerão sub-catchments.

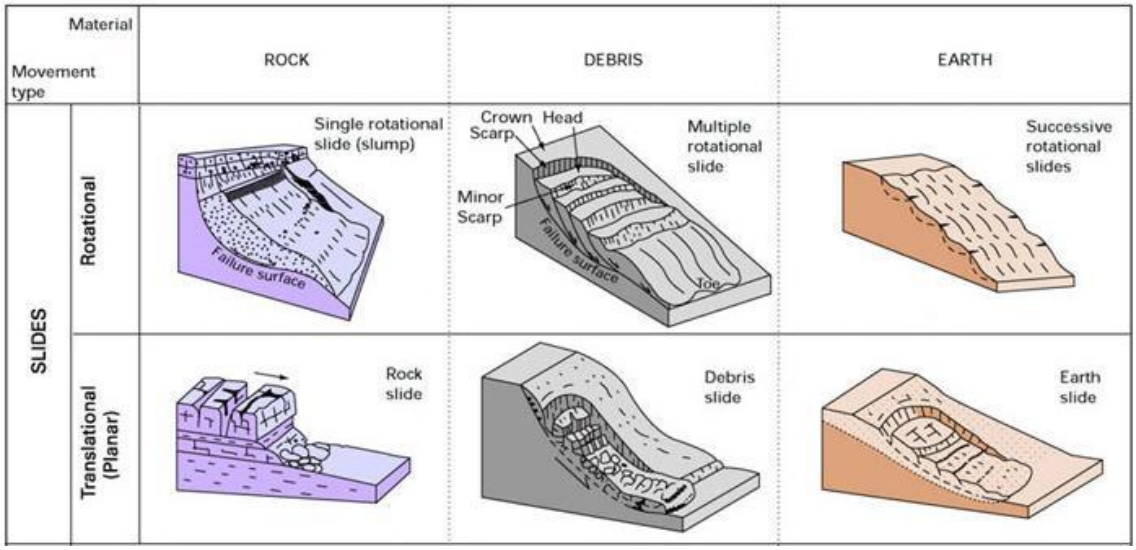

Fig. 2.1 – Types of slides. Extracted from Crosta *et al*., 2012.

Slides are characterized as “a downslope movement of soil or rock mass occurring dominantly on the surface of rupture or on relatively thin zones of intense shear strain" (Cruden and Varnes, 1996). There are two types of slides: i) Rotational slides and ii) Translational slides.

The displacing mass, during the movement, has different degrees of deformation depending on the type of slide, which is characterized according to the type of tangential shear plane and material affected (Table 2.1).

Table 2.1 – Classification of Slides (Dikau *et al.*, 1996; Zêzere, 2000).

		Rock	Debris	Soil
Rotational		Single	Single	Single
		Multiple	Multiple	Multiple
		Successive	Successive	Successive
Translational	Non-rotational	Block slide	Block slide	Slab slide
	Planar	Rock slide	Debris slide	mudslide

Rotational slides (slumps) are described as a slide movement along a surface of rupture that is curved and concave (Cruden and Varnes, 1996). The definition purposed by Cruden and Varnes (1996) means that such type of slide occurs as a rotational movement on a circular, or spoon-shaped, shear surface. They differ in the degree of disintegration in the slide masses and the depositional features in the toe areas. They have a small degree of internal deformation although sometimes soil slump material can liquefy and transforms into a flow at its toe. This type of landslide occurs along curve shear planes in homogeneous and isotropic materials. According to Van Asch (1980) and Hutchinson (1988), regarding the relative position of the shear plane it is possible to distinguish between slope failure, toe failure and base failure. Rotational slides can vary from an area of few square meters to large complexes of several hectares and they can be more or less rotational, regarding the axis parallel to the slope contours, involving shear displacement (sliding) along a concavely upward-curving failure surface, which is visible or may reasonable be inferred (Varnes, 1978).

Soil slides are generally constituted of fine-textured, cohesive materials, like consolidated clays, weathered marls and mudstones. Rotational rock slides often develop in formations of interbedded strong and weaker materials, e.g., marls and limestone or sandstones. Such slide generally produces a disrupted, anomalous drainage pattern.

Normally the rotational slides start with an initial slope failure followed by rotation. During its movement it sometimes disintegrates into several blocks, which tilt backwards while sliding downhill and often flattering or even slope reversal occurs. Sliding along the flanks causes longitudinal and diagonal shear stress. In this way, the lowest part of the slump mass moves over the toe of the failure surface, bulges, curves, overriding and producing transverse tension cracks. The rate velocity of such movement can vary from several orders of magnitude, between a few centimeters a year to several meters per month, while soil slumps can attain velocities up to 3 meters per second. The presence of tilted trees (generally backwards in the head area, forwards in the foot and toe areas) can reveal the presence of rotational slides. The rotational slides are generally triggered by excavation, construction activities and also by an increase of the water table due to periods of rainfall or snowmelt. (Buma and Van Asch, 1996).

The scars of the shallow rotational slides, exposed at the surface, are typically attached to a parabolic shape (concentric in plan and concave in the direction of the displacement) indicating a shear plan in form of "spoon / oval" (Fig. 2.2: a). However, in some cases, the shallow rotational slides can extend perpendicularly to the displacement. According to Varnes (1978), in such cases the shear plane can be assumed as a cylindrical shape, whose axis is parallel to the slope (Fig. 2.2: b).

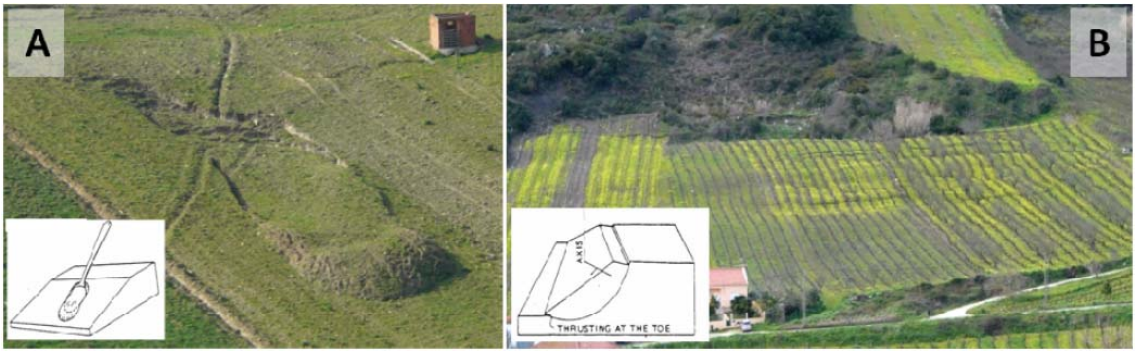

Fig. 2.2 – Shallow rotational shear plan: a) with spoon-shaped; b) approximate to a cylindrical shape. Extracted from Oliveira, 2011.

Translational slides are commonly described as a mass which displaces along a planar or undulating surface of rupture, sliding out over the original ground surface (Cruden and Varnes, 1996). There are two types of translational slides (Table 2.1): translational slides

with composite shear plane (non-rotational) and translational slides occurring along a planar shear plane. The translational slides with non-rotational shear plane normally have two distinct sections. The first section, situated upstream, has a circular or planar shear plane, with strong inclination. The second section, located downstream, has a planar shape, with a reduced slope angle. The displaced mass develops internal stresses, accompanied by differential movements, creating a strong internal distortion of the destabilized materials and the formation of pits and cliffs (Ibsen *et al*., 1996).

The translational slides with planar shear plane are controlled structurally. Translational slides with a planar shear plane are largely controlled by surfaces weakness within the structure of the slope, such as flat stratification, diaclases or the contact between a debris cover and rocky substrate (Varnes, 1978; Zêzere, 2000). The shear plane often determines the displacement of the destabilized material beyond the limits of the shear plane (Fig. 2.3).

Fig. 2.3 – Shallow translational slides. Extracted from Oliveira, 2012.

Landslides can be further subdivided, accordingly to affected material in: rock slides; debris slides and mudslides. Rock slides generally occur in mountainous environments, where the structural discontinuities are in agreement with the slope angle and when the inclination of the bedding planes is slower than the slope angle (Zêzere, 2000). Depending on the slope angle and velocity, slides will either stay as a discrete block on the failure surface or break apart into debris.

A rock slide is a translational movement of rock which occurs along more or less planar or gently undulating surface (Varnes, 1978). It is typical for mountain slopes or rock

exposures where the slope angle is close, or parallel, to the dip of the layers. The movement is controlled by planar structural discontinuities, such as faults, joints and the presence of weaker formations within the rock mass. (Sorriso-Valvo and Gula, 1996; Erismann and Abele, 2001). Rock slides are characterized by well-defined head scarps and flanks, if the rock slides well away from the depletion zone, the scar and flanks may remain visible. There are different mechanisms of movement of rock slides. If the movement is slow (mm to m/day) the whole mass may disaggregate because of differences in velocity along the yields surface. The frequency of events and magnitude of each single may vary (Sorriso-Valvo and Gula, 1996; Erismann and Abele, 2001). In higher velocity slides the mass disaggregates during the movement, transforming it into a rock avalanche or a debris flow. The fundamental cause of a rock slide is the presence of a rock mass which produces such a stress that the resistance of the intact rock or the friction mobilized on existing discontinuities is exceeded. Rock slides have a wide range in volume and velocities and pose considerable hazards to human settlements and lives (Sorriso-Valvo and Gula, 1996); (Erismann and Abele, 2001).

Debris slide, or shallow translational slides, sheet slides or soil slips are failures of unconsolidated material which breaks up into smaller parts as the slide advances downslope. The debris slides are shallow and have their shear plans parallel to the topography surface, often coincident with the contact between a slope deposit and bedrock (Corominas, 1996; Zêzere, 2000). The material involved is mostly colluvium and weathered material of fractured rock masses (i.e. flysch formations, shales and slates). The velocity of sliding and degree of runout tend to increase with slope angle and decrease with clay content (Hutchinson, 1988). Velocities of up to 16m/s have been recorded. Many translational debris slides turn into debris flows. This occurs where water is available, and where the topography favours the convergence of both debris and water into concavities and channels. On very steep slopes, debris slides can reach high velocities. Debris slides are often triggered by intense rainfall or by earthquakes. The probability of a debris slide occurring is greatly increased by the destruction of vegetation cover by fires or logging. Sites most likely to provide failures are first-order basins with hollows where regolith can reach the maximum thickness and high slope angles. Failures are often caused by an increase in pore-water pressure following heavy rains which

reduce the shear strength of the material. After failure, the breakage of the sliding mass allows the water to escape and the debris to stop (Corominas *et al*., 1996).

Mudslide, also known as earthflow, mudflow (redundant usage also climatic and temperate mudflow) or slump-earthflow (complex, lobate mudslide). Mudslides are a form of mass movement in which masses of softened silty or very fine sandy debris slide on discrete boundary shear surfaces in relatively slow-moving lobate or elongate forms. A mudslide is divided into source, track and lobe, and accumulation zone units. The source has a bowl-shaped head. The material in this section is usually soft, weathered debris often with depressions containing water. Mudslide movement rates range from about 1 to 25m/yr and are generally classified as slow mass-movement types. Extreme events range from hundreds of meters per day (Crozier, 1984; Ibsen and Brusden, 1996). The mudslide movements are normally seasonal, as the wetter weather increases the water content to the point where pore water becomes sufficient to generate movement. Mudslides in temperate areas display a pronounced winter-summer cycle. Movements usually start in the late autumn, peak in mid-winter and come to a slow halt by late spring and summer. Heavy rainfall will frequently result in a mudslide surge. The essential planning and engineering implication is that this form of slide requires water. The removal of the source of water influx is critical, as the reduction of pore-water pressure from the mudslide mass. Roads and other linear features are most vulnerable to movement at the lateral shears (Crozier, 1984; Ibsen and Brusden, 1996). As morphological characteristic mudslides includes three distinct sectors: i) shear plane section; ii) channelized transport section; iii) accumulation section. Mudslides has also have a rounded front shape, sinusoidal longitudinal profile (concave upstream and convex downstream) and the lateral edges flanking the affected area (Zêzere, 2005b).

2.3 The causes for landslides occurrence: conditioning, preparatory and predisposing factors

Landslide causes are diverse and have been compiled by several authors (e.g., Terzaghi, 1950; Varnes, 1978; Crozier, 1986; Brunsden, 1993; Cruden and Varnes, 1996; *Pasuto et al*., 1996). The wide variety of landslides typologies reflects the diversity of conditions that can lead to slope instability and, thus, to a variety of triggering processes (Popescu, 2002). The identification of causative factors is the basis of many methods of susceptibility/stability assessment. The factors may be dynamic (e.g., pore water pressure), or static (e.g., lithology) and may also be considered in terms of the roles they perform in destabilizing a slope (Crozier, 1989). From a geotechnical point of view and according to Terzaghi (1950), a distinction must be made between internal changes that induce shear strength reduction, and external causes which give rise to an increase shear stress.

From a geomorphological point of view the identification of the landslide factors, responsible for the instability manifestations, is the basis of the susceptibility assessments (Crozier and Glade, 2005). These factors (Figure 4), dynamic (e.g., pore pressure), or static (e.g., structure) may also be classified according to the role they play in destabilization of slopes, in: 1) predisposing factors; 2) conditioning factors; 3) preparatory factors, which include terrain characteristics (e.g., deforestation); 4) and triggering factors, which are the direct cause of landslides (e.g., rainfall, seismicity) (Crozier and Glade, 2005) (Fig. 2.4). This classification is based on the slope stability stages defined by Crozier (1986), which supports the classification of slopes as stable, potentially unstable (marginal stability) and actively unstable, due to the progressive reduction of the safety margin.

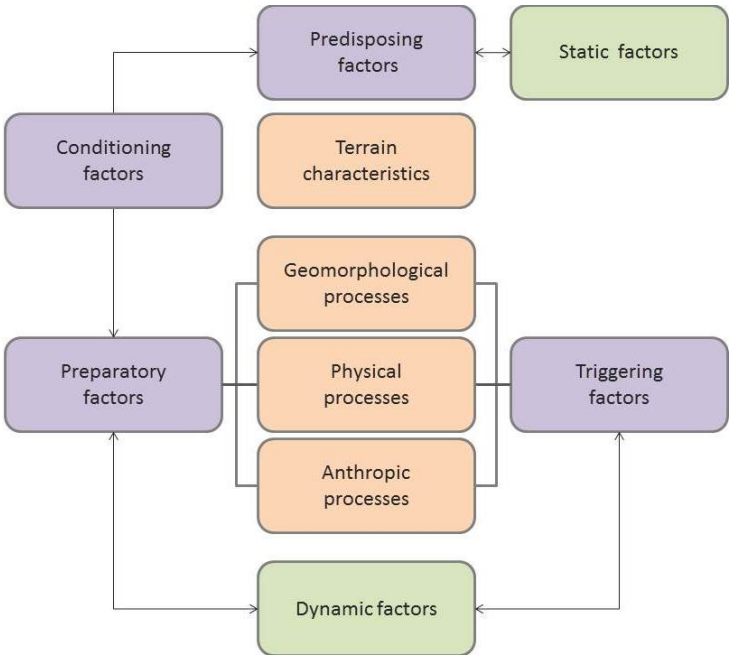

Fig. 2.4 – Responsible factors for the landslides occurrence (adapted from Popescu, 1994 in Zêzere, 2010).

The predisposing factors are static and inherent to the terrain characteristics. Such factors are responsible for conditioning the degree of potential slope instability and for determining the spatial variation of slope susceptibility. These factors, besides influencing the safety margin, act as catalysts, making other destabilizing factors acting more efficiently (Zêzere, 2005b).

The conditioning factors are defined by Popescu (1994), generically, as "preparatory causal factors". They establish the responsible conditions for instability which is based on a complex relationship between the conditions of the terrain and a set of processes (geomorphological, physical and anthropogenic) that act for unstabilizing the slope in a short or long term.

The preparatory factors are dynamic and are capable to reduce the safety margin, however, without initiating the slope movement. Catalyzed by the predisposing factors they become responsible for the change in the equilibrium state of a slope (e.g., changing from a stable state to a marginally stable state). These processes can occur during a long time (e.g., rock alteration), but also at a short-term (e.g., deforestation or changes in the slope system by anthropic actions) (Glade and Crozier, 2005).

The triggering factors are those that provide the actual motion of a landslide. According to the (SF) such factors have the capability to convert a marginally stable state into an actively unstable state. The most common triggers are: rainfall, earthquakes and snow melting. For example, if a critical factor, such as rise in pore water pressure, is successfully correlated with rainfall conditions, it may be possible (with reference to the rainfall record) to determine the probability with which pore water conditions exceed a critical threshold and initiate failure (Glade and Crozier, 2005).

2.4 Landslide inventories of the study area

Recent research has shown that the most important component of any landslide susceptibility or hazard zoning is the preparation of a detailed landslide inventory (LI). Thus, the quality of the LI is of crucial importance, because data-driven models, used for landside susceptibility are based on the spatial correlation between past landslide and a data set of thematic layers representing independent predisposing factors. The acquisition of a robust inventory of the distribution and type of landslides is also of crucial importance for physically-based models validation.

A LI is a spatial distribution of landslides, represented as points or drawn to scale, defining the type of the landslides and other relevant landslide information, when available (e.g., date of occurrence and/or state of activity). The main objective of this chapter therefore, was to produce a multi-temporal LI.

According to Guzzetti (2005), multi-temporal landslide inventories correspond to the most advanced form of landslides inventory. The landslides inventories obtained in this chapter resulted from a systematic interpretation of sets of aerial photographs of different years and orthophotomaps, supplemented by an extensive fieldwork. From this work resulted two inventories of ancient landslides and one inventory of recent landslides at 1:10,000 scale.

For the ancient landslides interpretation two sets of aerial photographs were used, respectively dated from 1958, at a 1:26,000 nominal scale, obtained from *Instituto Geográfico do Exército* (IGEoE), and the aerial photographs, dated from 1982, at a 1:15,000 nominal scale, acquired from *Instituto Geográfico Português* (IGP). The black and white aerial photography interpretation was made through vertical stereoscopic.

Since the landslides inventories were interpreted from different flight scales, the IDRISI software were used for stereoscopic interpretation allowing digital zoom and enabling a balanced output scale among the landslides inventories. In the following chapter (chapter 3), it is explained the procedure of aerial photographs georeferencing, orthorectifying, and stereoscopic photo-interpretation.

From this work two landslide inventories recognizing ancient landslides were obtained (LI#1; LI#2). Through some key information on the stereoscopic aerial photographs such as landforms, tones, shadows and vegetation was possible to identify and draw the ancient landslides. However, it should be mentioned the fact that distinctive landforms created by landsliding are commonly obscured in heavily forested terrain. Neither aerial photos nor photogrammetrically prepared topographic maps accurately depict the ground surface beneath the forest canopy, and this was the main difficulty founded during the inventorying of ancient landslides. As an example it is shown in Fig. 2.5 and Table 2.2 that, according to the land use map obtained from *Centro Nacional de Informação Geográfica* (CNIG) at a 1:25,000 referenced to the year 1990, the forested areas covered the study area in about 26.7% of the total area.

However, in order to test the accuracy of the inventories of the ancient landslides, in chapter 6 it will be made an assessment through a validation technique known as prediction rate curve.

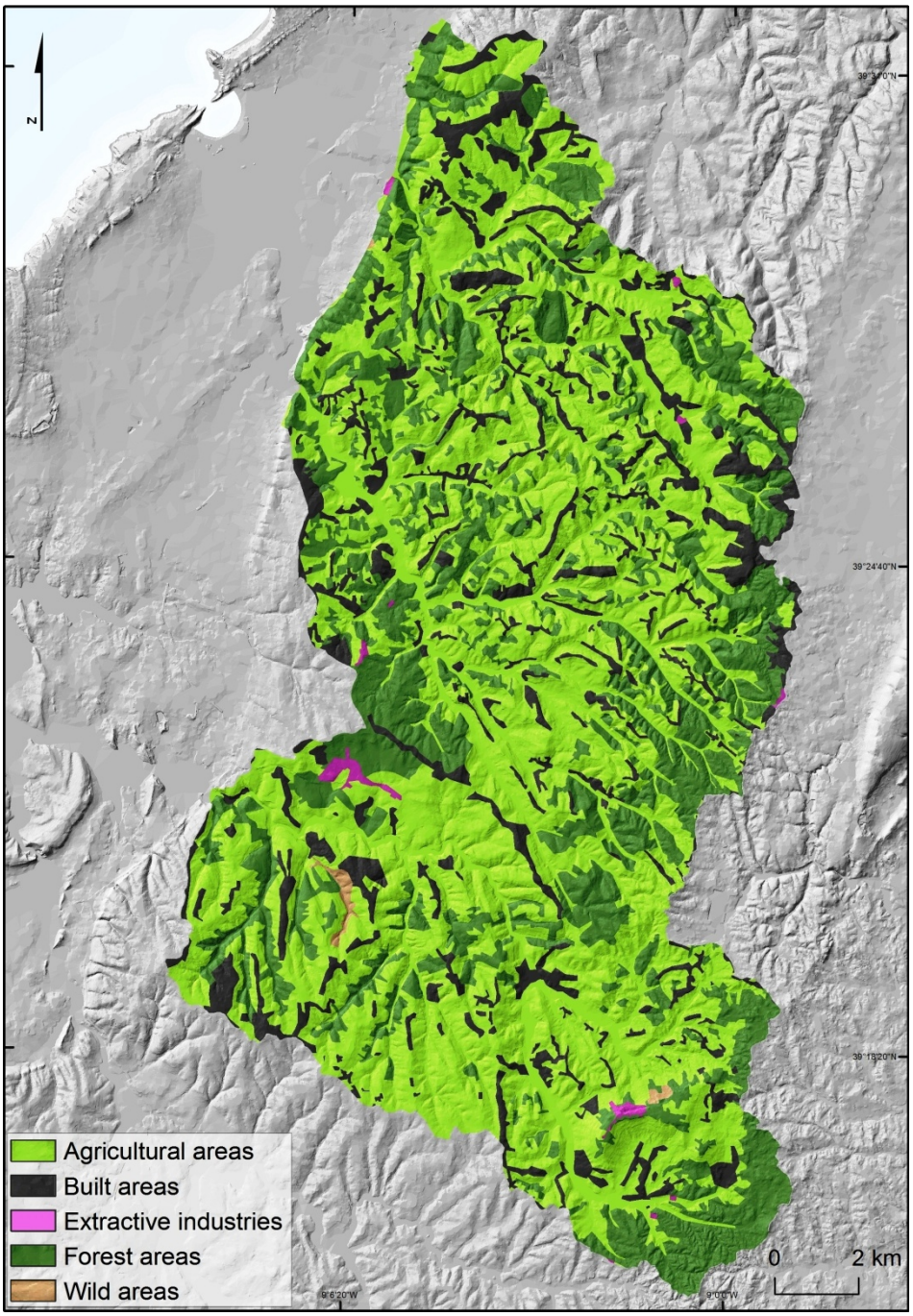

Fig. 2.5 – Land use map of the study area.

Table 2.2 – Land use map of the study area.

Classes	Occupancy area	
	(km^2)	(%)
Agricultural areas	161.6	58.6
Built areas	36.2	13.1
Extractive industries	1.1	0.4
Forest areas	76.2	27.6
Wild areas	0.7	0.3
Total	275.9	100

The third LI (LI#3) is assumed to be more robust than the ancients inventories because it was firstly based on orthophotomaps interpretation and secondly, validated by field work. The orthophotomaps, used for previous interpretation of landslides, are dated from 2004, have a 1:10,000 scale, and with of 0.5 m of pixel size. All the landslides, detected during the interpretation, were then subjected to an intensive field work for validating purposes. The field validation was made during the period between 2007 and 2011, however a landslide dated from 30 of November of 2006 by the Portuguese Civil Protection was included since it was geographically located and well described.

In all inventories the landslides were marked as polygons and classified based on the estimated depth (shallow or deep-seated), and the type of movement (rotational or translational). Thereby from the interpretation of sets of aerial photographs of different dates and orthophotomaps, supplemented by an extensive fieldwork in all the three inventories, landslides are classified into four types: 1) Shallow rotational slides; 2) shallow translational slides; 3) Deep-seated rotational slides; 4) Deep-seated translational slides. It is still important to mention that as the aim of this dissertation is to predict the susceptibility of landslide initiation, it is only relevant to represent the depletion zone of each landslide type.

The ancient landslides, although underused for modeling purposes, were very important for this work because the period of the most recent landslides could be defined in relative terms through a systematic verification of presence/absence of ancient landslides located in the same places of the recent landslides.

The LI#1 resulted in 709 landslides indentified on the aerial photographs of 1958, representing: 1) 584 deep-seated rotational slides; 2) 80 shallow rotational slides; 3) 7 deep-seated translational slides; 4) 38 shallow translational slides (Fig. 2.6 and Table 2.3).

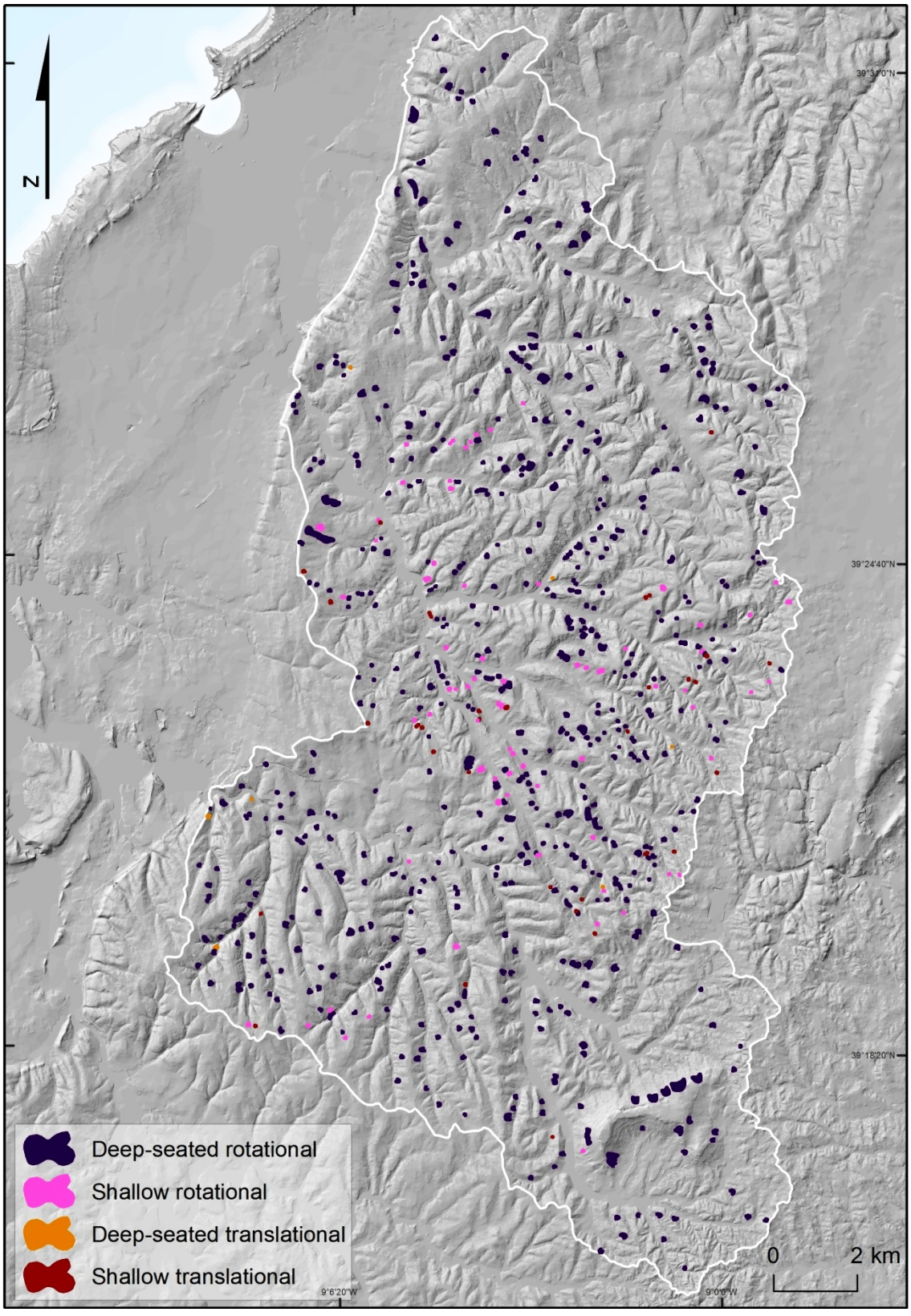

Fig. 2.6 – Depletion zone of each Landslide within LI#1 in the study area. To facilitate visualization landslides depletion areas were magnified.

Table 2.3 – Statistical analysis for the LI#1.

	Landslide types				Total
	Deep-seated rotational	Shallow rotational	Deep-seated translational	Shallow translational	
Nº of landslides	584	80	7	38	709
Landslides density (n/km^2)	2.117	0.290	0.025	0.138	2.570
Total affected area (ha)	234.879	11.985	0.534	2.269	249.666
Unstable (% of the total area)	0.851	0.043	0.002	0.008	0.905
Mean landslide area (ha)	0.402	0.150	0.076	0.060	0.352
Sd landslide area (ha)	0.488	0.145	0.081	0.040	0.459

For the second LI, based on the interpretation of aerial photographs obtained in 1982, has been indentified 535 landslides occurrence, representing: 449 deep-seated rotational slides; 61 shallow rotational slides; 4 deep-seated translational slides; and 21 shallow translational slides (Table 2.4 and Fig. 2.7).

Table 2.4 – Statistical analysis for the LI#2.

	Landslide types				Total
	Deep-seated rotational	Shallow rotational	Deep-seated translational	Shallow translational	
Nº of landslides	449	61	4	21	535
Landslides density (n/km^2)	1.627	0.221	0.014	0.076	1.939
Total affected area (ha)	91.072	5.418	0.333	1.509	98.332
Unstable (% of the total area)	0.330	0.020	0.001	0.005	0.356
Mean landslide area (ha)	0.203	0.089	0.083	0.072	0.184
Sd landslide area (ha)	0.182	0.062	0.028	0.053	0.174

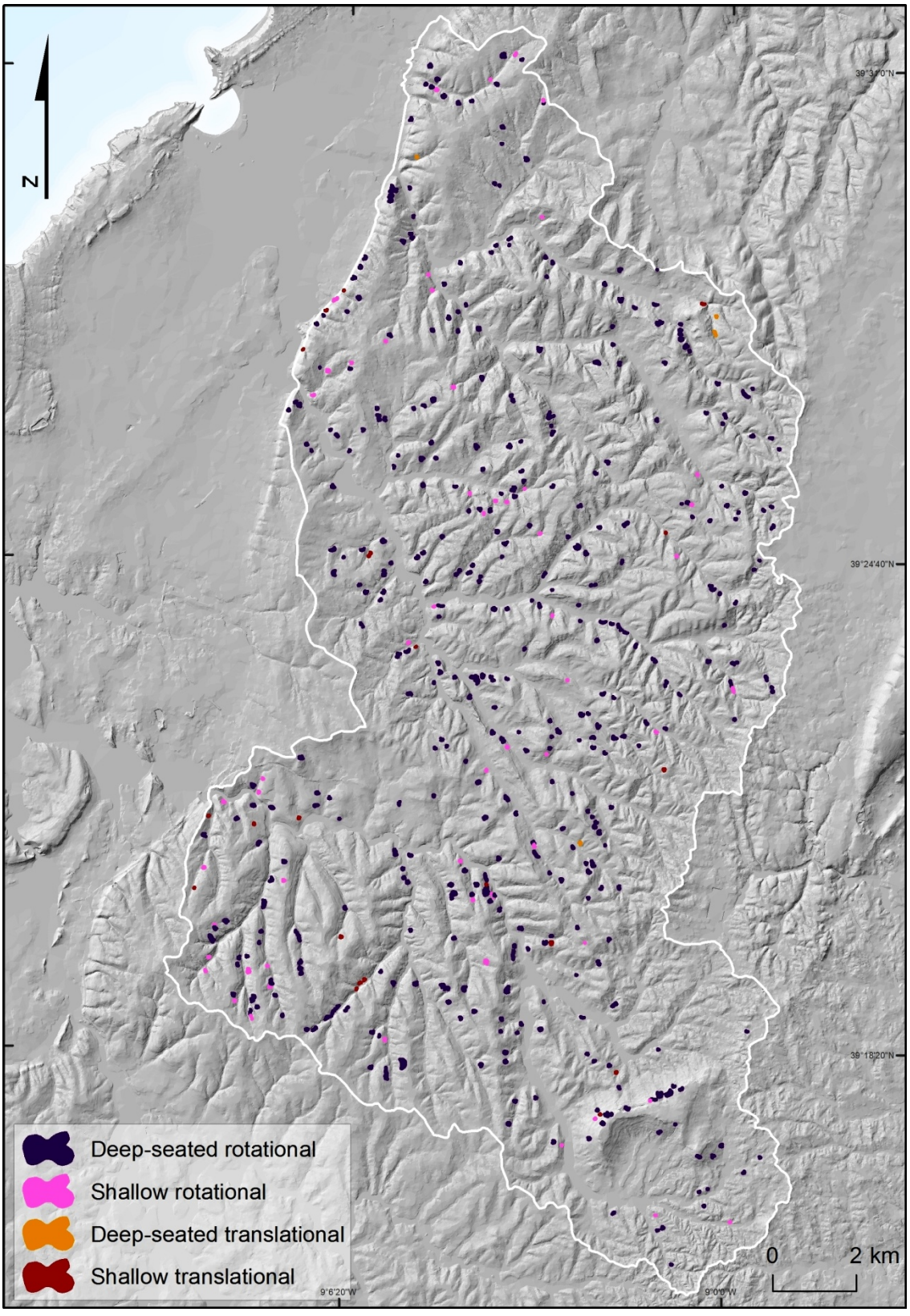

Fig. 2.7 – Depletion zone of each Landslide within LI#2 in the study area. To facilitate visualization landslides depletion areas were magnified.

For the achievement of the LI#3, beyond evident landslide recognition on orthophotomaps and field, also some landslides were inferred from fractures founded in houses, roads and other types of structures. Such instabilities have a key role for the definition of some landslides boundaries. Many landslides, observed in the ancients landslides inventories had no more visible scars on the field. However, it remains inventoried some of the structural damages due to a continuous deformation, which increases every rainy season. The Fig. 2.8 illustrates the deformation/ fracture types that were considered for the determination of the geomorphologic instability.

Fig. 2.8 – Structural damage types or deformations used to define and delimit the boundaries of landslides: a) Fracture parallel to a road; b) Vertically fractured house; c) Obliquely fractured house; d) Vertically fractured house with translation; e) Fracture parallel to a road; f) Fracture parallel to a road with translation.

Thereby for the LI#3 resulted 245 landslides, where 126 were identified as deep-seated rotational slides; 71 as shallow rotational slides; 2 as deep-seated translational slides; and 46 as shallow translational slides (Fig. 2.9 and Table 2.5).

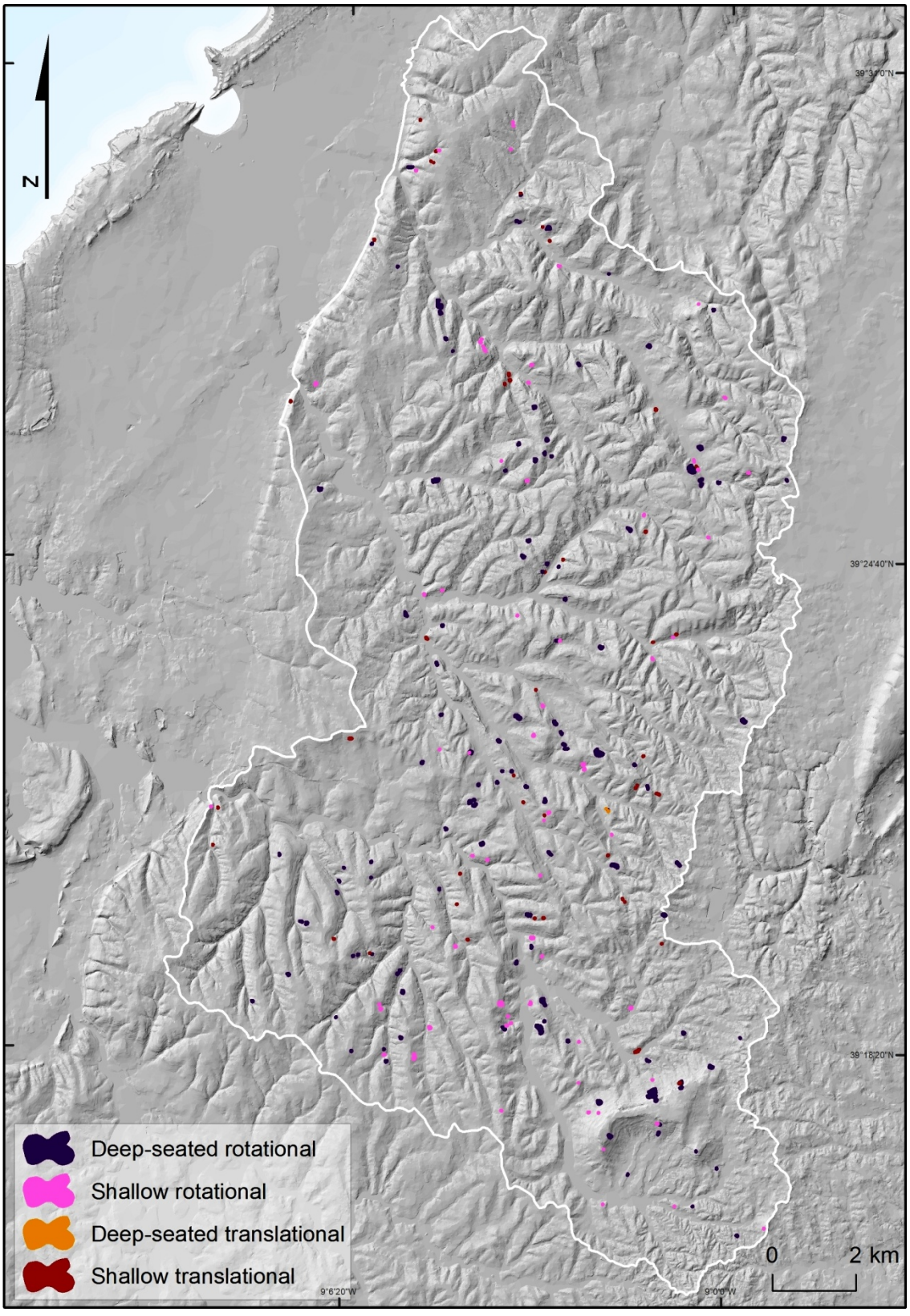

Fig. 2.9 – Depletion zone of each Landslide within LI#3 in the study area. To facilitate visualization landslides depletion areas were magnified.

Table 2.5 – Statistical analysis for the LI#3.

	Landslide types				Total
	Deep-seated rotational	Shallow rotational	Deep-seated translational	Shallow translational	
Nº of landslides	126	71	2	46	245
Landslides density (n/km^2)	0.457	0.257	0.007	0.167	0.888
Total affected area (ha)	28.853	4.296	0.038	1.294	34.481
Unstable (% of the total area)	0.105	0.016	0.000	0.005	0.125
Mean landslide area (ha)	0.229	0.061	0.019	0.028	0.141
Sd landslide area (ha)	0.322	0.079	0.005	0.034	0.253

The Fig. 2.10 and 2.11 shows the main types of landslides founded within the study area.

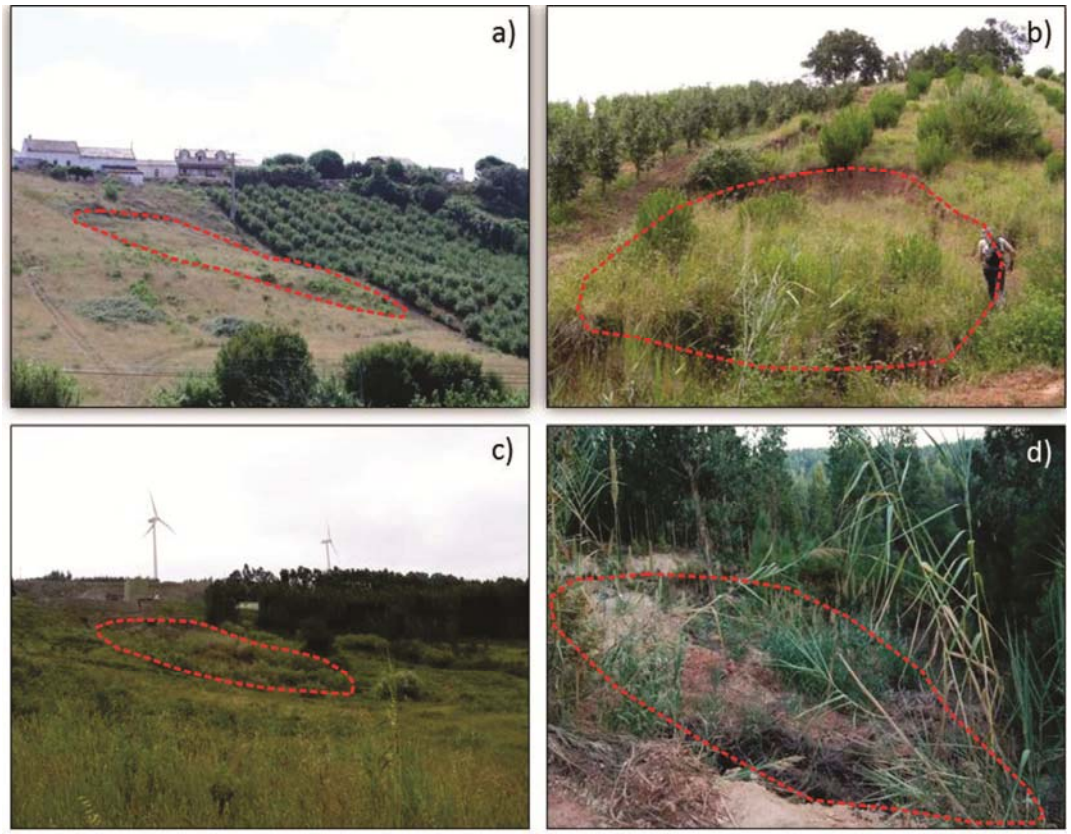

Fig. 2.10 – Rotational landslides within the study area.

Fig. 2.11 – Translational landslides within the study area.

Based on statistical analysis of the LI#1, LI#2 and LI#3 (Tables 2.3, 2.4 and 2.5) some conclusions can be taken. Thereby, it is possible to see that, regardless the inventory, the most common type of landslide founded in the study area are the deep-seated rotational slides followed by the shallow rotational, shallow translational and deep-seated translational slides.

Regarding the average landslides size, it is possible to observe that the deep-seated rotational slides are the larger type of landslides, having about 0.44 ha for LI#1, 0.20 ha for LI#2 and 0.22 ha for LI#3. The shallow rotational slides have about 0.15 ha for LI#1, 0.09 ha for LI#2 and 0.06 ha for LI#3. According to the deep-seated translational slides it is possible to observe an average landslides size of 0.08 ha for the LI#1, 0.08 ha for LI#2 and 0.02 ha for LI#3. Finally, de shallow translational slides have about 0.06 ha for LI#1, 0.07 ha for LI#2 and 0.03 ha for LI#3.

Considering all types of landslides it is possible to view that the mean dimension of the landslides decreases from LI#1 to LI#2 and then from LI#2 to LI#3, which can be explained

by factors such as an increment of landslides triggering factors prior to 1958 than at the years prior to 1982 or 2006 and/or due to the fact that urban areas are smaller on the oldest aerial photographs and thus easier to detect landslides.

Regardless the landslide inventories, the biggest landslides founded in the study area, are the deep-seated rotational slides which are frequently located on the SE part of the study area. Smallest landslides are distributed over the remaining study area, along the slopes.

Deep-seated rotational slides were indeed more often detected on the landslide inventories, however, according to the field experience it was possible to understand that shallow landslides do also often happen though it is more difficult to detect because their evidences are constantly removed by agricultural activity which is intensive in the study area. In 1990 the agricultural areas dominate the study area in about 60% (Table 2.2), a tendency that did not change much until the present days.

During the field work, especially, during the recognition of the shallow rotational slides, for the LI#3, it was possible to infer that 41 of the 71 shallow rotational slides founded in the study area did not presented a pure rotational behavior. Those landslides were classified as having a shear plane with a cylindrical shape whose axis approaches a flat surface, parallel to the surface (Fig. 2.2:b). These types of landslide, which commonly affect the local agricultural activity, were kept separately, together with the pure shallow translational slides, for physically based models validation purposes (Table 2.6 and Fig. 2.12).

Table 2.6 – Statistical analysis for the non-pure rotational and pure translational slides founded within LI#3.

	Non-pure rotational and pure translational slides
Nº of landslides	87
Landslides density (n/km^2)	0.315
Total affected area (ha)	4.269
Unstable (% of the total area)	0.015
Mean landslide area (ha)	0.049
Sd landslide area (ha)	0.075

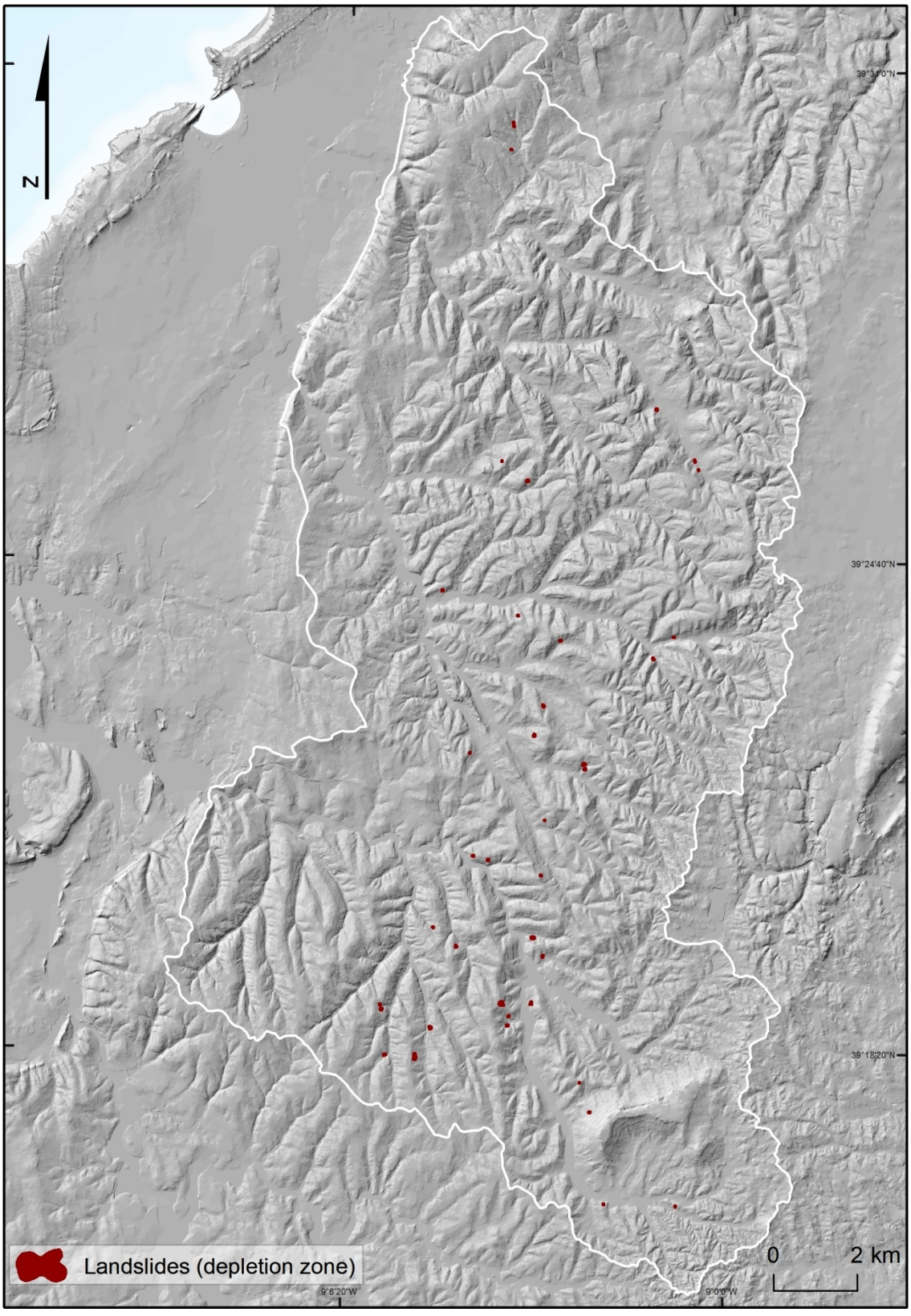

Fig. 2.12 – Non-pure shallow rotational and pure shallow translational slides founded within the study area. To facilitate visualization landslides depletion areas were magnified.

Regarding the preparation of the LI#3, it must be highlighted that in some places it was not possible to map landslides due to the lack of accessibility. The distinctive landforms

created by landsliding were obscured in densely forested terrain and thus impossible to map (Fig. 2.5). There are also some private areas, within the study area, where field work were not allowed, and thus impossible to perform the landslide mapping. These facts are important to be mentioned here because, in case of a statistical assessment of the landslide susceptibility, the results are dependent on the location and distribution of past landslides and, thus, this fact could mask some conditions where, in reality there are susceptibility but, due to the absence of past landsliding, the statistical models cannot precisely predict future instability in those areas.

The sum of all landslide inventories has, thereby, 1489 landslides occurrence (1159 deep-seated rotational slides; 212 shallow rotational slides; 13 deep-seated translational slides; and 105 shallow translational slides).

2.5 Landslides susceptibility assessment

Landslide susceptibility is the likelihood, based on local terrain conditions, of a landslide to occur (Brabb, 1984). It is defined as the degree of probable slope failure, i.e., an estimate of "where" landslides are likely to occur (Guzzetti, 2005). Susceptibility does not consider the temporal probability of failure (i.e., when or how frequently landslides occur), nor the magnitude of landslides, i.e., the size of the new landslides (Guzzetti, 2005).

Landslide susceptibility can be developed through several methods. Those can be statistic, deterministic, or heuristic. Still, all of them are based upon a few, widely accepted assumptions (e.g., Varnes, 1984; Carrara *et al*., 1991; Hutchinson and Chandler, 1991; Hutchinson, 1995; Turner and Schuster, 1996; Guzzetti *et al*., 1999). These are the same assumptions which lay at the base of landslide mapping, namely:

(a) Landslides leave distinct signs that can be recognized, classified and mapped in the field through orbital remote sensing (satellite image) or suborbital remote sensing

(stereoscopic aerial photographs) (e.g., Varnes, 1978; Hutchinson, 1988; Cruden and Varnes, 1996; Dikau *et al*., 1996; Griffiths, 1999).

(b) Slope failures are the result of the interaction of physical processes, and landsliding is controlled by mechanical laws that can be determinated with empiric, statistic or deterministic methods. The conditions that cause landslides (instability factors), directly or indirectly linked to slope failures, can be collected and used to build predictive models of landslide occurrence (e.g., Crozier, 1986; Hutchinson, 1988; Dietrich *et al*., 1995).

(c) For landslides we can adopt the well known principle, which follows from uniformitarianism: "the past and present are keys to the future" (e.g., Varnes, 1984; Carrara *et al*., 1991; Hutchinson, 1995). This principle implies that future landslides will be more likely to occur under the conditions which led to past and present instability. Mapping recent slope failures is important to understand the geographical distribution of past landslides. Thus, the landslide inventory maps are fundamental information to help forecast the future occurrence of landslides. (e.g., Varnes, 1984; Carrara *et al*., 1991, 1995; Hutchinson, 1995; Guzzetti *et al*., 1999).

Moreover, the following assumption also applies:

(d) Landslide occurrence, in space or time, can be inferred through heuristic methods, computed from the analysis of environmental information or inferred from physical models. Therefore, a territory can be zoned into susceptibility (or hazard) classes ranked according to different probabilities (e.g., Carrara *et al.,* 1995; Soeters and van Westen, 1996; Aleotti and Chowdhury, 1999; Guzzetti *et al.*, 1999). Preferably, identification and mapping of landslides should derive from all of these assumptions. Not being able to do so, will limit the applicability of any susceptibility assessment, regardless of the methodology used for the investigation. Unfortunately, satisfactory application of these principles has been proving to be difficult, both operationally and conceptually (e.g., Carrara *et al.,* 1995; Guzzetti *et al.*, 1999; Guzzetti, 2005).

2.6 Landslide susceptibility model validation

2.6.1 Prediction and Successes rate curves and

The validation method selected for this work was the prediction and successes rate curves. Thereby, the evaluation in terms of predictive or success rate curves, (e.g., Chung and Fabbri, 1999, 2003; 2005) is shown graphically in percentage terms, and a scale ranging from 0 to 1, illustrating the x-axis the susceptibility of the study area ranked in a decreasing order and the ordinate axis the cumulative distribution function of the landslide area (Fig. 2.13).

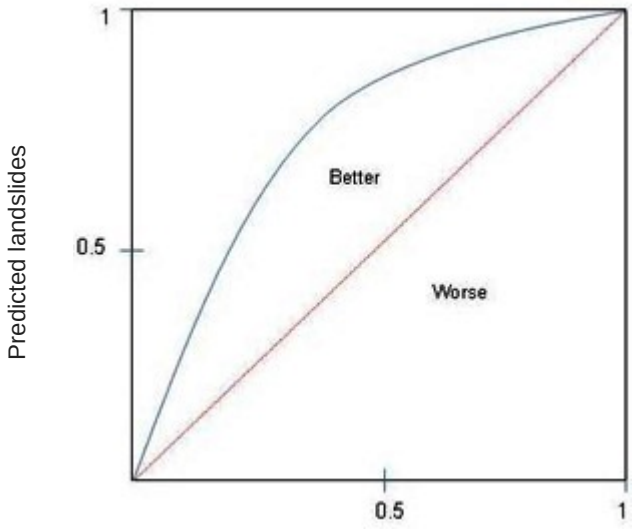

Fig. 2.13 – Graphical definition of a predictive or (success) rate curve.

The straight line, i.e., the diagonal line, starting from the origin of the graph, to the maximum value of the graph, represents a model with a degree of prediction, or success, determined by chance. A "positive" shift of the curve in relation to this diagonal line, indicates a model with a better performance (e.g., Guzzetti, 2005), and a "Negative" deviation to the diagonal line, a model with a very weak performance, clearly unacceptable for determining susceptibility, and must be readily rejected (Oliveira, 2012). Thereby, to validate the static physically based models, a prediction rate curve was performed in order to distinguish the susceptible model that explains better the

distribution of the majority of the shallow translational slides belonging to LI#3 (see chapter 3).

2.6.2 Area Under Curve

The determination of the Area under the Curve (AUC) allows the quantitative evaluation of the overall predictive capability of each susceptibility model (e.g., Bi and Bennett, 2003; Beguería, 2006; Zêzere, 2010) ranging between 0 and 1. A value closer to 1 indicates good predictive ability of the model. A casual predictive ability will be manifest for an AUC value around 0.5, describing a diagonal straight line (as it is possible to observe in Fig. 2.13). AUC value below 0.5 indicates models with a very bad predictive capacity, and should not be considerate (Bi and Bennett, 2003; Beguería, 2006).

The mathematical expression of the AUC is given by Equation 2.1 (e.g., Bennett 2003; Garcia *et al*., 2007; Pereira *et al*., 2012):

$$AUC = \sum_{i=1}^{n} \left[\left(x_{i+1} - x_i \right) \times \frac{y_{i+1} + y_i}{2} \right] \quad (2.1)$$

where x gets the percentage of study area predicted as susceptible by descending order and y the percentage of correctly classified landslide area belonging to the validation group.

According to Guzzetti (2005), The AUC values between 0.75 and 0.8 corresponds to an acceptable model, while AUC values ranging between 0.8 and 0.9 indicates a good susceptibility model. Finally, AUC values > 0.9 typify excellent models.

CHAPTER 3

RELATIONSHIPS BETWEEN THE LITHOLOGICAL SETTINGS AND THE LANDSLIDES PATTERN AND DISTRIBUTION

3 RELATIONSHIPS BETWEEN THE LITHOLOGICAL SETTINGS AND THE LANDSLIDES PATTERN AND DISTRIBUTION

This chapter was developed in order to obtain a more detailed information on the lithology of the study area since, the previous lithological data, due to its scale (1:50,000) was very poor and not suitable to develop the following objectives of the dissertation. Thus, supported by aerial photo interpretation and field work, improvements on the lithological map were performed. These improvements were further analyzed to assess quantitatively the improvements made.

3.1 Detailed litho-stratigraphic mapping

Studies have shown that landslides are greatly conditioned by the lithological properties of the land surface. A more detailed lithological map have greater importance in providing data for susceptibility mapping since different lithological units have different landslide susceptibility values. For this reason, it is essential to group the lithologic properties properly (Carrara *et al*., 1991; Anbalagan 1992; Mejia-Navarro and Wohl 1994; Mejia-Navarro and Garcia 1996; Pachauri *et al*., 1998; Luzi and Pergalani 1999; Dai *et al*., 2001; Duman *et al*., 2006; Yalcin 2008).

In order to improve the lithological data and assess how it can affect the landslide susceptibility, a detailed lithological map was made. Furthermore, a significant refined lithological map may also be the path that leads to a correct distribution and variation of landslides, physical properties of soil, slope and hydrogeological conditions, which improve the predictive capabilities of the susceptibility maps.

According to Varnes (1984) the simplest type of geological map must show conventional geologic formations, with remarks in the map explanation or accompanying tabular text about the relative stability of the geologic units. But in a more purposeful assessment, in order to obtain more refined lithological data, the geological units may be grouped by

lithology, not necessarily preserving stratigraphic order, and ranked according to the observed or inferred slope stability.

Based on pre-existing geological map and according to the lithological and stratigraphic characteristics the map improvements were performed using the interpretation of aerial photographs by stereoscopic analysis. However, especially in lower visibility of outcrops areas and in order to improve the lithological map, a systematic field work confirmation was made.

3.1.1 Materials and methods

The detailed lithological or litho-stratigraphic map, at 1:10,000 scale, was built through the interpretation of stereoscopic aerial photographs dated from 1958 at a 1:26,000 nominal scale. These aerial photographs were chosen because they correspond to the oldest existing aerial photographs covering the total study area. In addition, they exhibit a much less human occupancy and activity allowing a better observation of structural and geological settings.

The interpretation of stereoscopic aerial photographs and the subsequent drawing of the new lithological boundaries were done in an automatic setting system which consists on a LCD monitor connected to a computer and a stereoscope table, as shown in Fig. 3.1 The LCD monitor displays the already georeferenced stereopair aerial photographs which allows the digital interpretation and cartographic drawing.

In order to orthorectify the aerial photographs and draw the new lithological boundaries a GIS software named *ILWIS 3.3* was employed. For the procedure it is first necessary to have the aerial photographs in digital format (raster dataset), the corresponding orthophotomaps (target data) and a digital terrain model of the study area. The orthophotomaps are from 2004 and correspond to the spatially referenced data which will be used to georeference the aerial photographs. The digital terrain model is also

needed to orthorectify, which consists in obtaining the surface elevation for each coordinate pair.

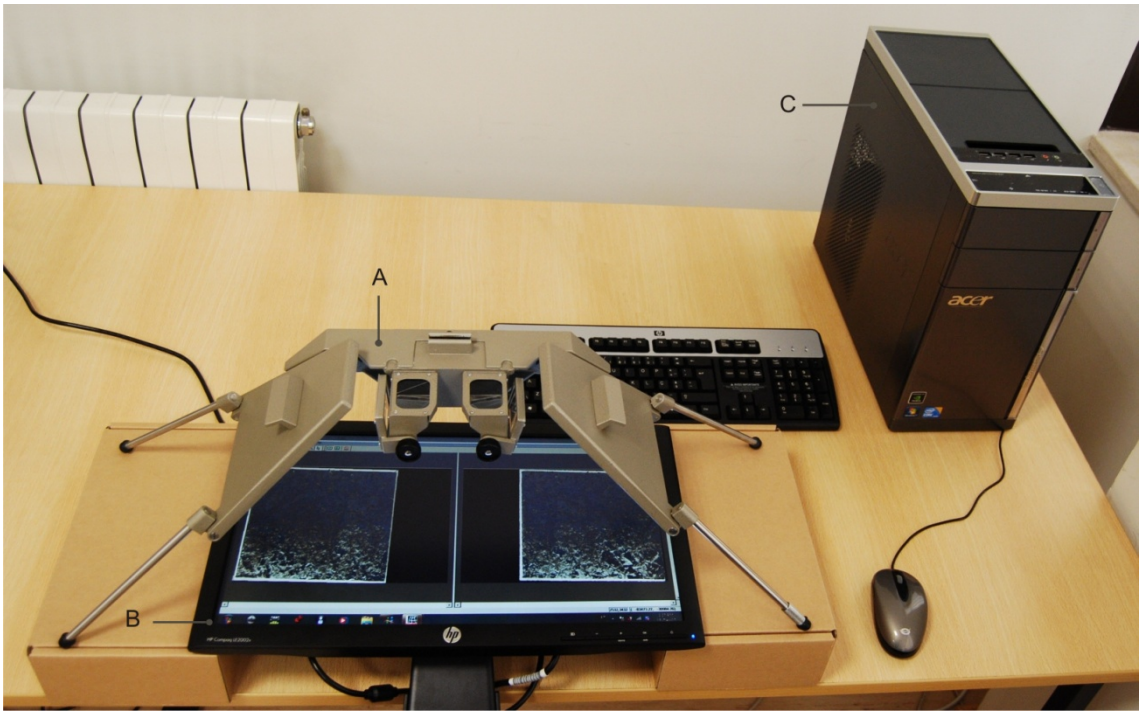

Fig. 3.1 – Stereoscopic observation system of aerial photographs in digital format for vector drawing. A - Stereoscope; B - LCD monitor; C – Computer.

The first step of the procedure aims to establish the type of direct transformation due to the georeferencing process and to obtain the geometric center of the aerial photographs. There are several types of transformations which can be used such as, conformal, affine and polynomial (of several degrees), depending on the geometric errors in the data set (Georgiadou *et al.*, 2001). Linear projections, as conformal or affine, typically require less control points to estimate a global acceptable error. Moreover, a non-linear polynomial transformation requires a huge amount of control points and they need to be very well distributed in order to achieve a reliable global error (Georgiadou *et al.*, 2001). Regarding the age of aerial photographs, establishing consistent control points reveals to be a very hard task because the study area has changed a lot over 50 years. Thus, in order to establish a good quality of control points it was chosen a linear affine transformation. Rather than conformal projection, the affine projection is commonly used in photogrammetry (Stamatopoulos *et al.*, 2011) and it is also quite useable for image orthorectification (Gao, 2009). The affine model is a custom geometric correction model

that allows three modifications to be made to the input image as, scaling (change in image size), offset (lateral shift in image origin), and rotation (change in image orientation). Through offset an image is moved laterally by a user-specified number of pixels in both the easting and northing directions preserving the affine properties of embedded objects such as parallelism (Gao, 2009; Worboys *et al.*, 2004). The great advantage of using an affine transformation is that it does not involve any change in image geometry (e.g., shape) which is extremely important for the lithological improvements that aerial photographs interpretation can provide.

For the geometric center of each aerial photograph is created a georeference system file within each are marked the four corners of the photographs (or, if it exists, the fiducial marks) linked the four corresponding coordinates and inserted the measurement distance between points in millimeters (Fig. 3.2).

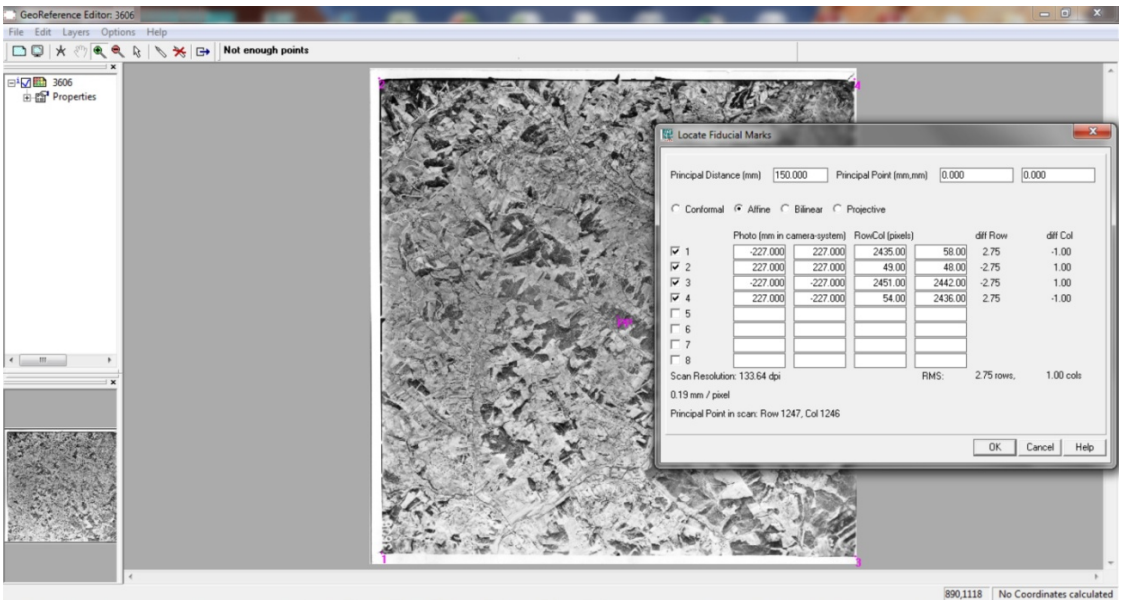

Fig. 3.2 – Georeferencing: insertion of the aerial photograph corners and its respective measurement between points (227mm in between).

The second step consists on identifying a series of ground control points, known x, y, and z coordinates, that link locations on the aerial photographs with locations in the orthophotomaps (target data). If possible, is preferable to spread out the control points over the entire aerial photograph rather than concentrating them in one area (ESRI, 2008).

The number of control points needed depends on the complexity of the transformation we are planning to use. In this case, once it is used an affine transformation, the minimum number of control points needed are three, but usually is preferable to use at least one more than the minimum (Georgiadou *et al*., 2001), so we can access the error attached to the process. However, adding an indiscriminate quantity of control points will not necessarily yield a better registration because they will have a increasable error-prone (ESRI, 2008).

Typically, having at least one control point near each corner of the raster dataset and a few ones throughout the interior produces the best results (ESRI, 2008). Once established the links, the z coordinate can be automatically added for each coordinates pair through the digital terrain model allowing, in this way, the orthorectification of the aerial photographs (Fig. 3.3).

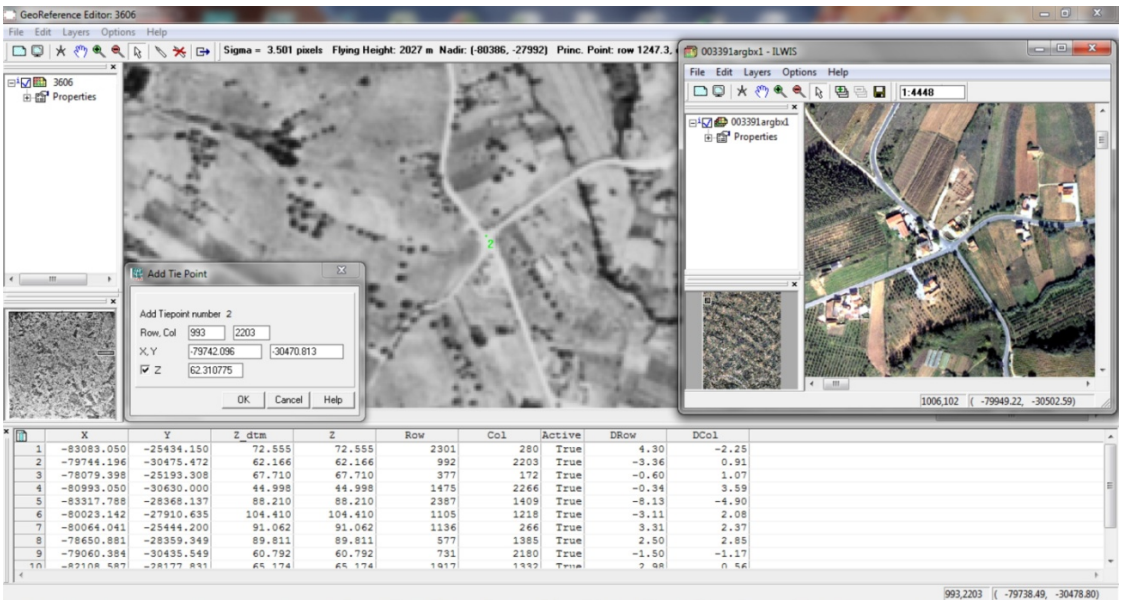

Fig. 3.3 – Georeferencing: identifying a series of ground control points, known x, y, and z coordinates.

There are many different types of elements that can be used as identifiable locations. It may be considered physical elements, such as stream intersections, the mouth of a stream, rock outcrops, the end of a jetty of land, and/or anthropic elements such as corners of houses, road intersections and street corners. In this case, since it is used very old aerial photographs, it was chosen not to georeference based on physical elements but

on anthropic elements such as corners of houses and road intersections which remained unchangeable over time and are still identifiable on the target data.

The overall accuracy of the transformation is indicated by the average of the errors in the reference points, known as Root Mean Square Error (RMSE). According to some literature the RMSE should be less than or equal to 1/2 of the side of the image cell (Dimitriou, 2005; Erdas, 2009). Regarding the purposes of the study which aims to prepare a 1:10,000 scale map with a 5 meters resolution it is admitted a RMSE less than or equal to 2.5 meters.

There should be a sufficient number of control points in order to estimate the error (at least four control points). According to the individual RMSE it was considered 11 or 12 control points (tiepoints) in most of the cases (Fig. 3.4). Sometimes more than 12 control points are established but some were disregarded due to their high RMSE. Thus, in software ILWIS, it is possible to exclude a tiepoint from the transformation computation by putting True or False respectively in the column Active (Fig. 3.5). Considering or excluding tiepoints depends on:

A tiepoint is considered well positioned if:

$$\left(\mathrm{DRow}^2 + \mathrm{DCol}^2\right) <= \left(1.2 * \mathrm{RMSE}\right) \tag{3.1}$$

A tiepoint is considered to have a medium error if:

$$\left(1.2 * \mathrm{RMSE}\right) < \sqrt{\left(\mathrm{DRow}^2 + \mathrm{DCol}^2\right)} <= \left(2 * \mathrm{RMSE}\right) \tag{3.2}$$

A tiepoint is considered to have a large error if:

$$\left(\mathrm{DRow}^2 + \mathrm{DCol}^2\right) > \left(2 * \mathrm{RMSE}\right) \tag{3.3}$$

where “Drow” represents Row deviation, and “Dcol” represents Colum deviation (Fig. 3.4). By excluding control points with large error, it becomes possible to evaluate the performance of the transformation due to the RMSE value. If RMSE value decreases the performance of the transformation can be considered reliable (ITC, 2007). In this software

it is possible to see, in the Customize Georeference Tiepoints editor dialog box, the errors of control points shown by colors. Green control points are considered well positioned, yellow control points are considered with a medium error, red control points are considered with a large error and passive (excluded) control points are shown in blue (Fig. 3.5). It is preferable to ensure that the error never exceeds 2.5m in each control point because, only in this way, is possible to guarantee high accuracy (low RMSE) and reliable stereoscope visualization.

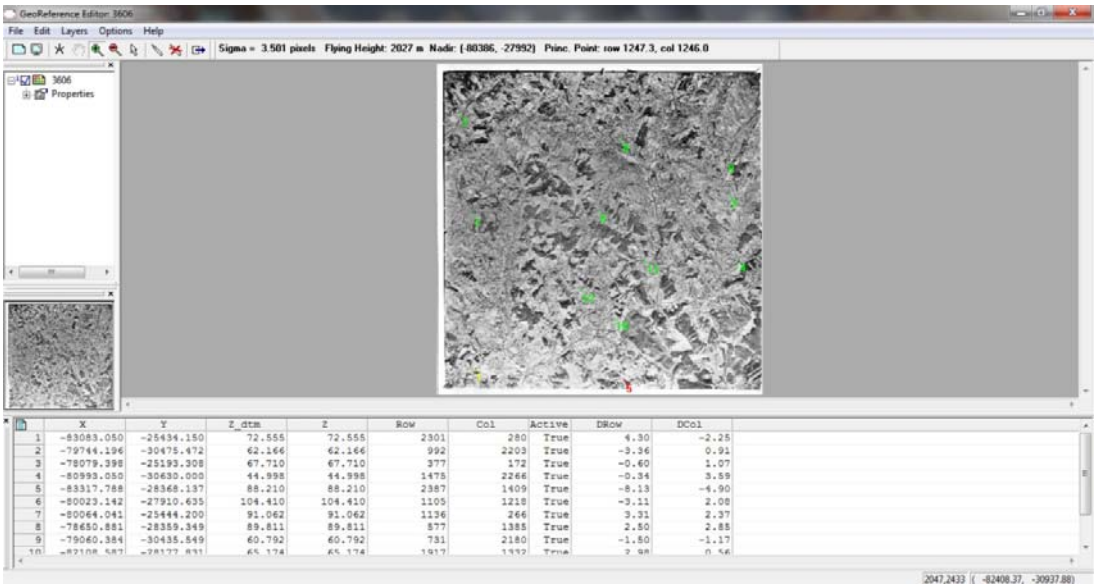

Fig. 3.4 – Georeferencing: error detection after finalizing the linking points. Where Sigma means RMSE.

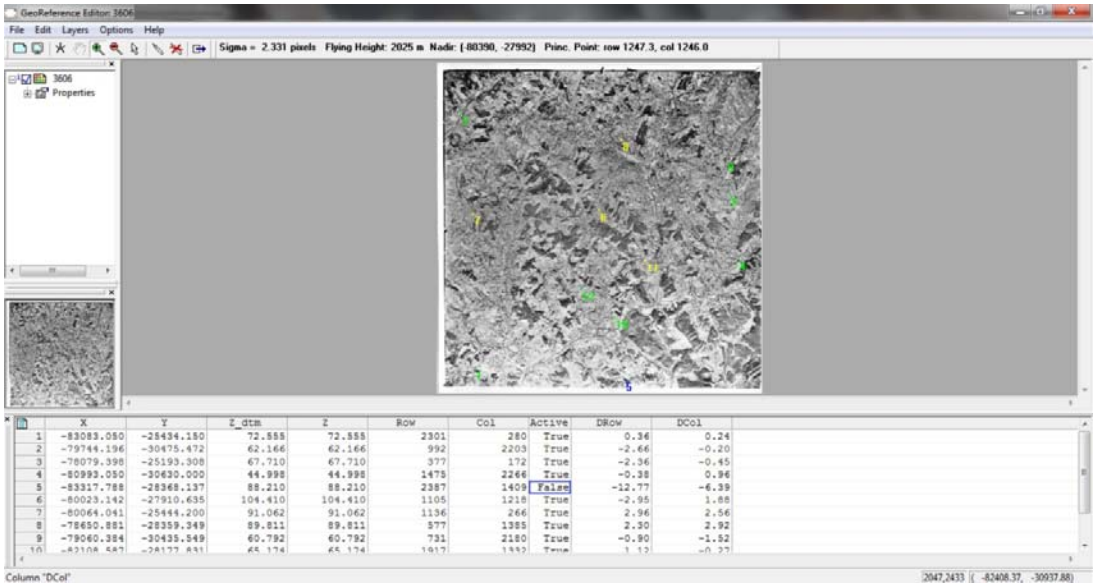

Fig. 3.5 – Georeferencing: tiepoint omission due to the high RMSE estimated (false active tiepoint inside the blue rectangle).

In order to view a calculated stereo pair of aerial photographs by a stereoscope it is necessary to create a stereo pair view through a pair of photographs with overlap (ITC, 2007). In software ILWIS, this third step, is done with the Epipolar Stereo Pair operation. To create an epipolar stereo pair it is necessary to have two overlapping (about 60%) sequential images where one of them must be georeferenced (Fig. 3.6).

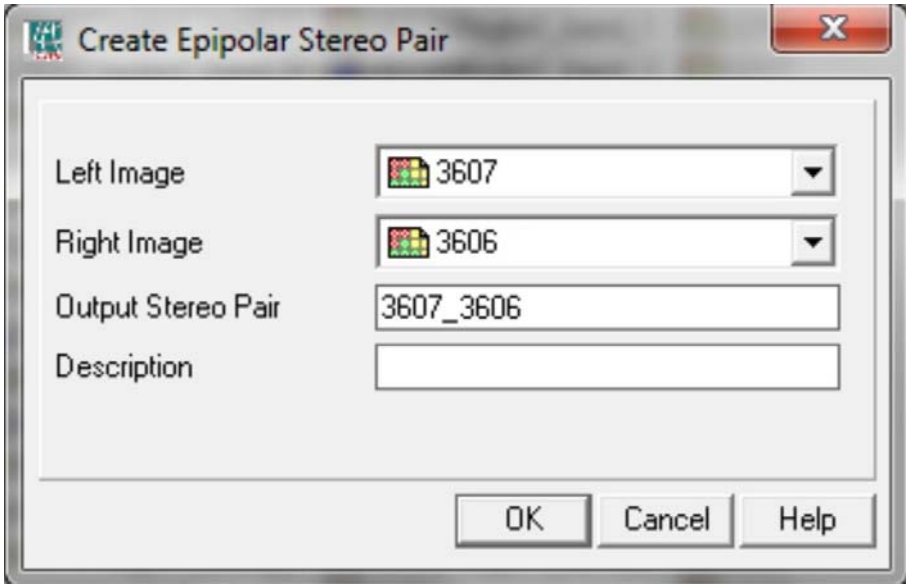

Fig. 3.6 – Epipolar Stereo Pair operator.

The object definition file (Fig. 3.7) contains the corners positions of the aerial photograph (fiducial marks), principal points (PP), transferred points (TP) and the optional scaling points. In each photograph (input raster map), the principal point (PP) of the photograph (geometric center) is calculated from the intersection of the two lines linking opposite fiducial marks. The transferred point corresponds to the principal point of the orthorectified aerial photograph. The photograph will be rotated around this point. How much each photograph should be rotated is determined from the position of the principal point of the other aerial photograph that has been transferred to the current photograph (Fig. 3.7 and 3.8). To correct possible scaling differences between the input photographs the positions of the optional scaling points can be used (ITC, 2007).

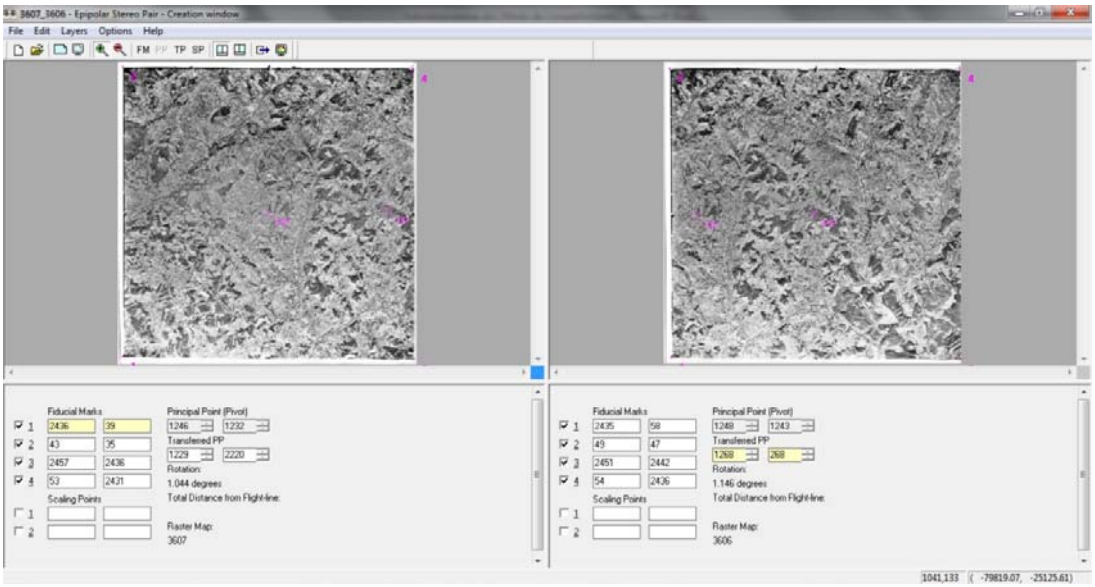

Fig. 3.7 – Epipolar Stereo Pair operator: insertion of fiducial marks and the TP (through the position of the PP on the georeferenced aerial photograph) on the non-georeferenced aerial photograph.

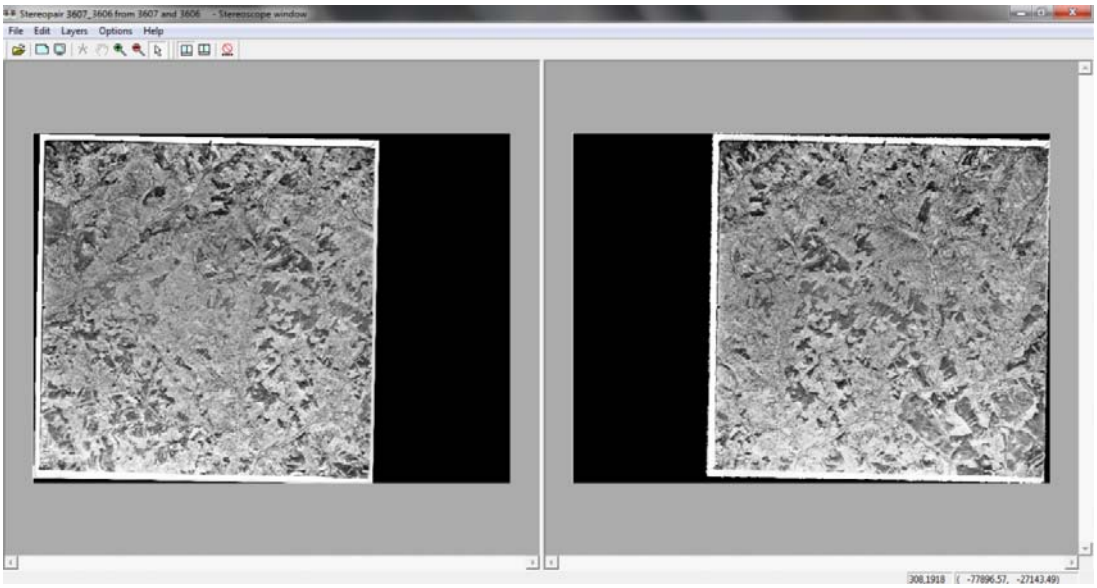

Fig. 3.8 – Epipolar Stereo Pair operator: stereo pair of aerial photographs ready to be seen by stereoscope.

The output raster maps of an epipolar stereo pair will have two very important georeference files. The first one, named georef Scale_Rotate, ensures that the columns in the two output raster maps are perpendicular to each other allowing, in this way, the stereo view of the overlapping area between the two photographs. The second file, named georef StereoMate, is created from the DTM which defines the angle at which the area is looked at from above by a stereoscope.

It is important to refer that one of the properties/advantages of using this software is due to the link between files. The stereo pair stores the names of the input raster maps and other parameters allowing the output stereo pair and its output raster maps to be always recalculated if needed (ITC, 2007).

The output stereo pair can be editable and within this file is also possible to create a new vector map and start georeferenced screen vectorization for the new lithological detailed boundaries over the stereo pair aerial photographs. This on screen vectorization must be done on the georeferenced aerial photograph side of the screen view, in order to ensure a georeferenced vector map (Fig. 3.9).

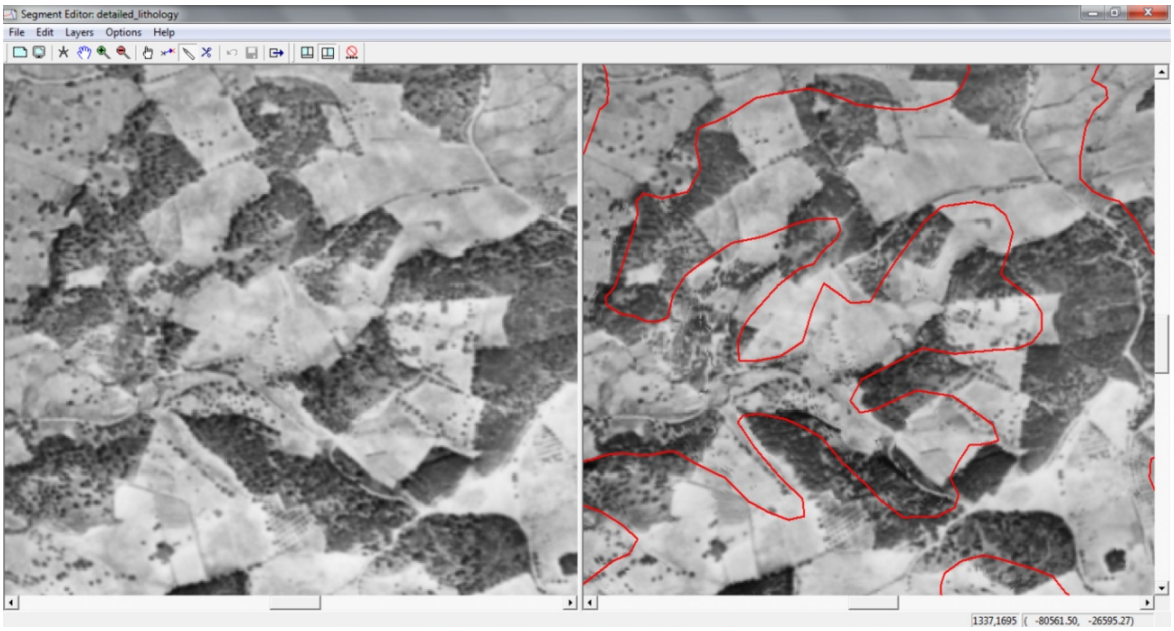

Fig. 3.9 – Edition of the new lithological detailed boundaries on stereo pair of aerial photographs seen by stereoscope.

Using GIS software in the vectorization process enables digital zooms which improves the aerial photographs details without losing stereoscopy. This procedure becomes very advantageous because it involves less positional errors compared with manual methods of stereoscopic interpretation and drawing.

Due to the camera focal length and the aircraft altitude during the images acquisition all photographs has angular errors. These angular errors decrease toward the center and

increase towards the edges of aerial photographs, and to prevent it, is necessary to have a reasonable amount of aerial photographs covering the entire study area. This was achieved with 41 aerial photographs (which 18 were submitted to the process above described). This is a reasonable coverage, guaranteeing that these angular tilts were minimized.

3.1.2 Interpretation and mapping

By means of bibliographic references (Zbyszewski and Almeida, 1960; França and Zbyszewski, 1963; Zbyszewski et. al., 1966; Ribeiro, 1984; Cabral, 1993; Henriques, 1996; Henriques et. al., 2002; Zêzere, 2005a; CM Caldas da Rainha, 2008), existing geological map from the sheets 26D, 26B and 30 B published at the 1:50,000 scale (respectively: Zbyszewski and Matos, 1959; Zbyszewski, França and Ferreira, 1961; Zbyszewski, França and Ferreira, 1965), field work and aerial photo interpretation, it was possible to build a detailed litho-stratigraphic map with 1:10,000 scale.

For the lithological or litho-stratigraphic mapping, was chosen to keep grouped stratigraphically the different geological formations, detailing within each one of them the present lithologies. When it was not possible to detail or rectify the geological boundaries it was chosen to maintain the representation of the pre-existing geological map. The pre-existing data was obtained through the digital vectorization of the geological map from INETI, Department of geology (Fig. 3.10).

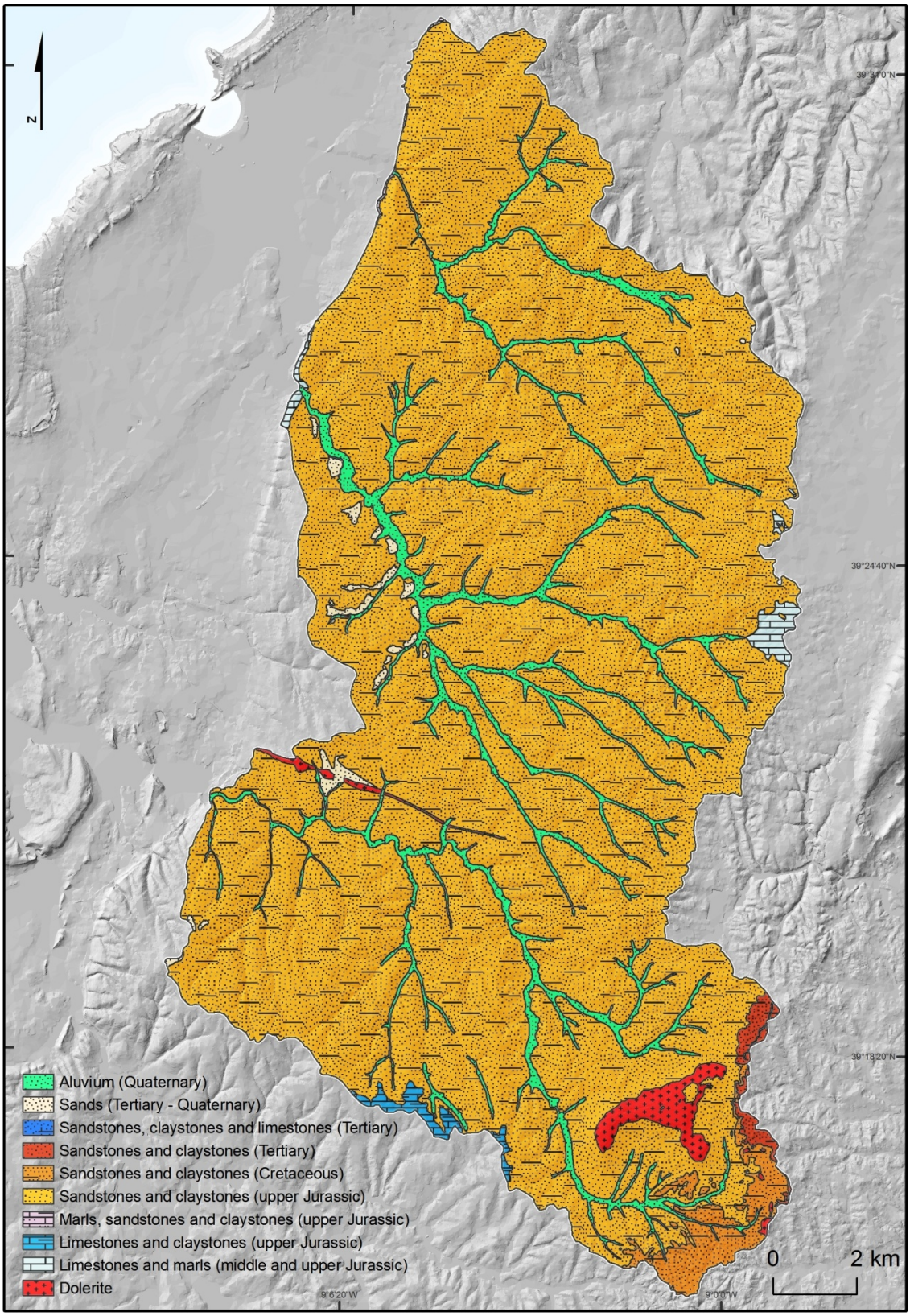

Fig. 3.10 – Previous lithological map of the study area.

The previous lithological map shows materials dating from Middle and upper Jurassic to Quaternary and it was already divided into ten lithological complexes (Table 3.1).

Table 3.1 **–** Areal distribution of previous litho-stratigraphic classes.

Classes	Epoch	Period	km^2	%
Aluvium	Holocene	Quaternary	19.38	7.02
Sands	Pliocene	Tertiary - Quaternary	1.83	0.66
Sandstones, claystones and limestones	Miocene	Tertiary	0.04	0.02
Sandstones and claystones	lower and middle Miocene	Tertiary	1.35	0.49
Sandstones and claystones	Albian - Aptian	Cretaceous	4.91	1.78
Sandstones and claystones	Upper Kimmeridgian	Upper Jurassic	242.47	87.88
Marls, sandstones and claystones	lower Kimmeridgian	Upper Jurassic	0.12	0.04
Limestones and claystones	Tithonian	Upper Jurassic	1.14	0.41
Limestones and marls	Oxfordian	Middle and upper Jurassic	1.47	0.53
Dolerite			3.18	1.15
Sum			**275.89**	**100**

The oldest materials, dated from middle to upper Jurassic, are located on both west and east flanks of the territory and correspond to Limestones and Marls, which together occupy 0.53% of the total study area. Located on the northwest site of the study area are the Marls, sandstones and claystones complexes dated from upper Jurassic and occupying a small area of 0.04 % of the total.

Moreover the most recent geological materials are alluvium deposits, sand deposits and sandstones, claystones and limestones complexes. Sandstones, claystones and limestones complexes are the oldest of the latest geological materials and have the smallest

occupancy on the study area (0.02% of the total). Sand deposits are mostly located alongside the alluvium deposits and correspond to 0.66% of the total area.

Magmatic rocks, essentially dolerite, outcrop as a vein form in a WNW-ESE direction and as a chimney form located on the southern part of the study area, specifically on Todo-Mundo Hill and together represent a sum of 1.15% of the total study area. Where Dolerite rocks crop out, slope is regular, long and rectilinear, with a relative high relief that locally exceeds two hundred meters.

Noteworthy that the study area is mostly dominated by sandstones and claystones complexes (respectively dated from Upper Jurassic, Cretaceous and Tertiary) which correspond to 90.15% of the total area (Table 3.1 and Fig. 3.10). This fact was the main problem/stimulus for trying to get a better detailed data for such significant portion of the study area through the interpretation of aerial photographs.

The central part of the lithological map, located between the oldest lithological complexes of the study area (between the diapir and sierra of Candeeiros), is occupied by the A-dos-Francos Syncline and the upper Jurassic sandstones, and claystones form here a large outcrop area (87.88% of the total) (Zbyszewski et. al., 1959). Sandstones and claystones complexes from cretaceous and tertiary are located respectively on the south and southeast part of territory corresponding to 2.27% of the total study area. Beyond sandstones and claystones complexes, the previous alluvium deposit (7.02% of the total area) was also subjected to a significant improvement based on the interpretation and drawing on orthophotomaps from 2004.

The sandstones and claystones complexes, despite its homogeneous appearance (Fig. 3.10) reveals considerable heterogeneity from a detailing lithological point of view comprising different rock types varying in strength from hard to weak and soft rocks. Hard rocks correspond to sandstones and weak rocks correspond to claystones. On the aerial photographs stereopairs it was possible to identify and detailed this heterogeneous sandstones and claystones complexes through some key information on the aerial photographs such as tones, shadows, vegetation and relief. The study area shows

frequently the existence of hummocky terrain, revealing undulating topography on the basis of the predominant slope angles, which helped to the lithological interpretation because this undulating topography corresponded frequently to layers with greater and lower resistance respectively that could influence the slope stability and change hydrogeological conditions.

Thus, from the sandstones and claystones complexes proposed by Zbyszewski and Matos (1959) were obtained new complexes, through the detailing and improvement of the lithological data, namely: sandstones dominated complexes and shale dominated complexes (Matula, 1981), where sandstones dominated complexes correspond to hard rocks and shale dominated complexes correspond to weak and soft rocks. From the previous three sandstones and claystones complexes were obtained six new complexes, namely: 1) Upper Jurassic sandstone dominated complexes (28.75% of the total area); 2) Upper Jurassic shale dominated complexes (59.30% of the total area); 3) Cretaceous sandstone dominated complexes (0.53 % of the total area); 4) Cretaceous shale dominated complexes (1.25 of the total area); 5) Tertiary sandstone dominated complexes (0.25% of the total area); and 6) Tertiary shale dominated complexes (0.24% of the total area) (Table 3.2).

Comparing with the previous lithological data, the alluvium deposits have now a lower percentage of occupancy. This fact is not due to a decrease in sediment deposition but to an overvalued mapping of this alluvium deposits derived from the previous lithological map scale (1:50,000) and implied generalization (Fig. 3.11).

Table 3.2 – Areal distribution of detailed litho-stratigraphic classes.

Previous Lithology classes	Detailed Lithology classes	Epoch	Period	km^2	%
Aluvium	Alluvium (Holocene)	Holocene	Quaternary	18.79	6.81
Sands	Sands (Pliocene)	Pliocene	Tertiary - Quaternary	1.96	0.71
Sandstones, claystones and limestones	Sandstones, claystones and limestones (Miocene)	Miocene	Tertiary	0.04	0.02
Sandstones and claystones	Sandstone dominated complexes (lower and middle Miocene)	lower and middle Miocene	Tertiary	0.68	0.25
	Shale dominated complexes (lower and middle Miocene)			0.67	0.24
Sandstones and claystones	Sandstone dominated complexes (Cretaceous)	Albian - Aptian	Cretaceous	1.47	0.53
	Shale dominated complexes (Cretaceous)			3.44	1.25
Sandstones and claystones	Sandstone dominated complexes (upper Jurassic)	Upper Kimmeridgian	Upper Jurassic	79.31	28.75
	Shale dominated complexes (upper Jurassic)			163.61	59.30
Marls, sandstones and claystones	Marls, sandstones and claystones (upper Jurassic)	lower Kimmeridgian	Upper Jurassic	0.12	0.04
Limestones and claystones	Limestones and claystones (upper Jurassic)	Tithonian	Upper Jurassic	1.14	0.41
Limestones and marls	Limestones and marls (middle and upper Jurassic)	Oxfordian	Middle and upper Jurassic	1.47	0.53
Dolerite	Dolerite			3.19	1.16
	Sum			275.89	100

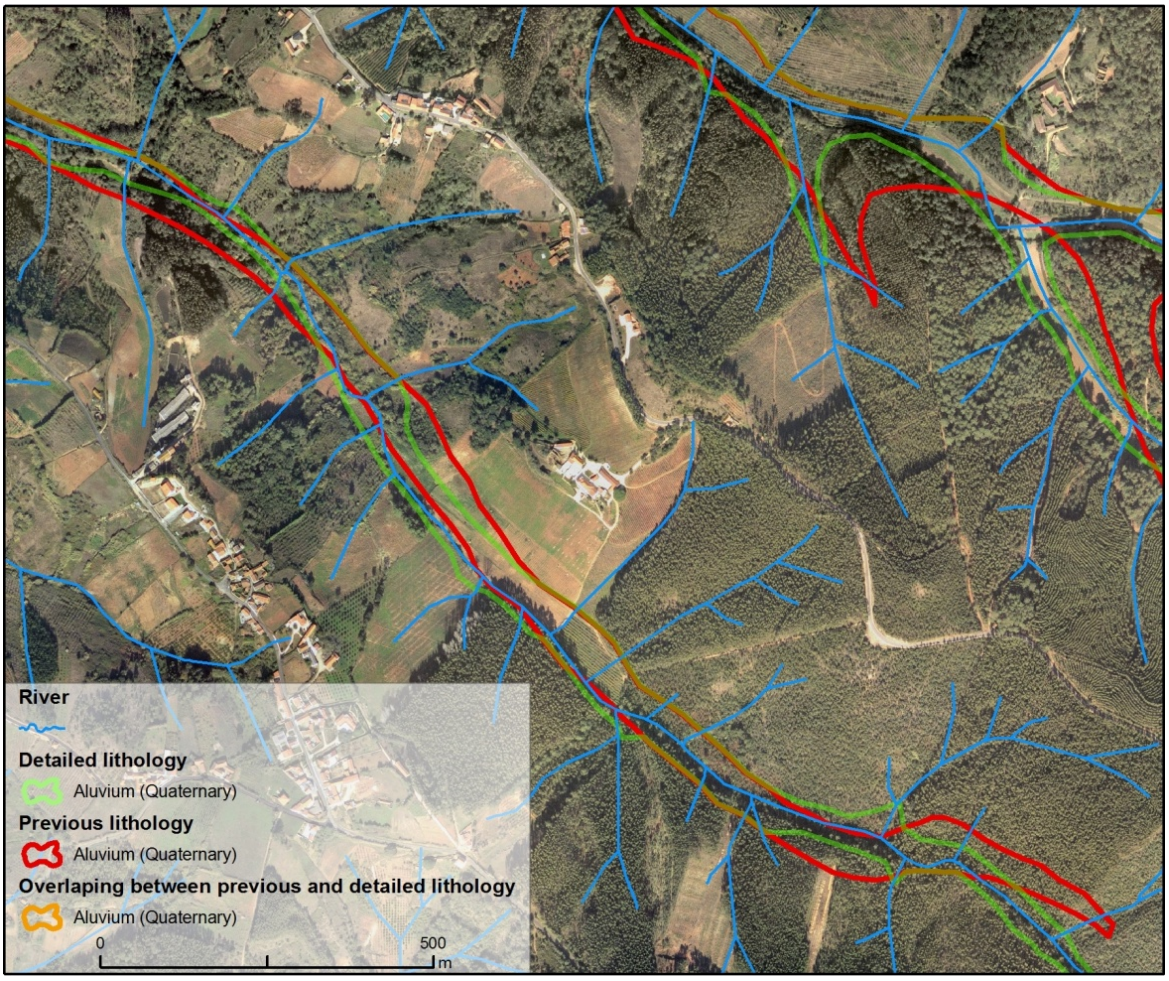

Fig. 3.11 – Edition of the new alluvium deposits boundaries through the interpretation of orthophotomaps from 2004 (ArcGis 9.3). Overlapping between the previous alluvium boundary and the new interpreted alluvium boundary.

After improving the boundaries specifically on alluvium deposits and within the sandstones and claystones complexes the final detailed lithological map was achieved (Fig. 3.12).

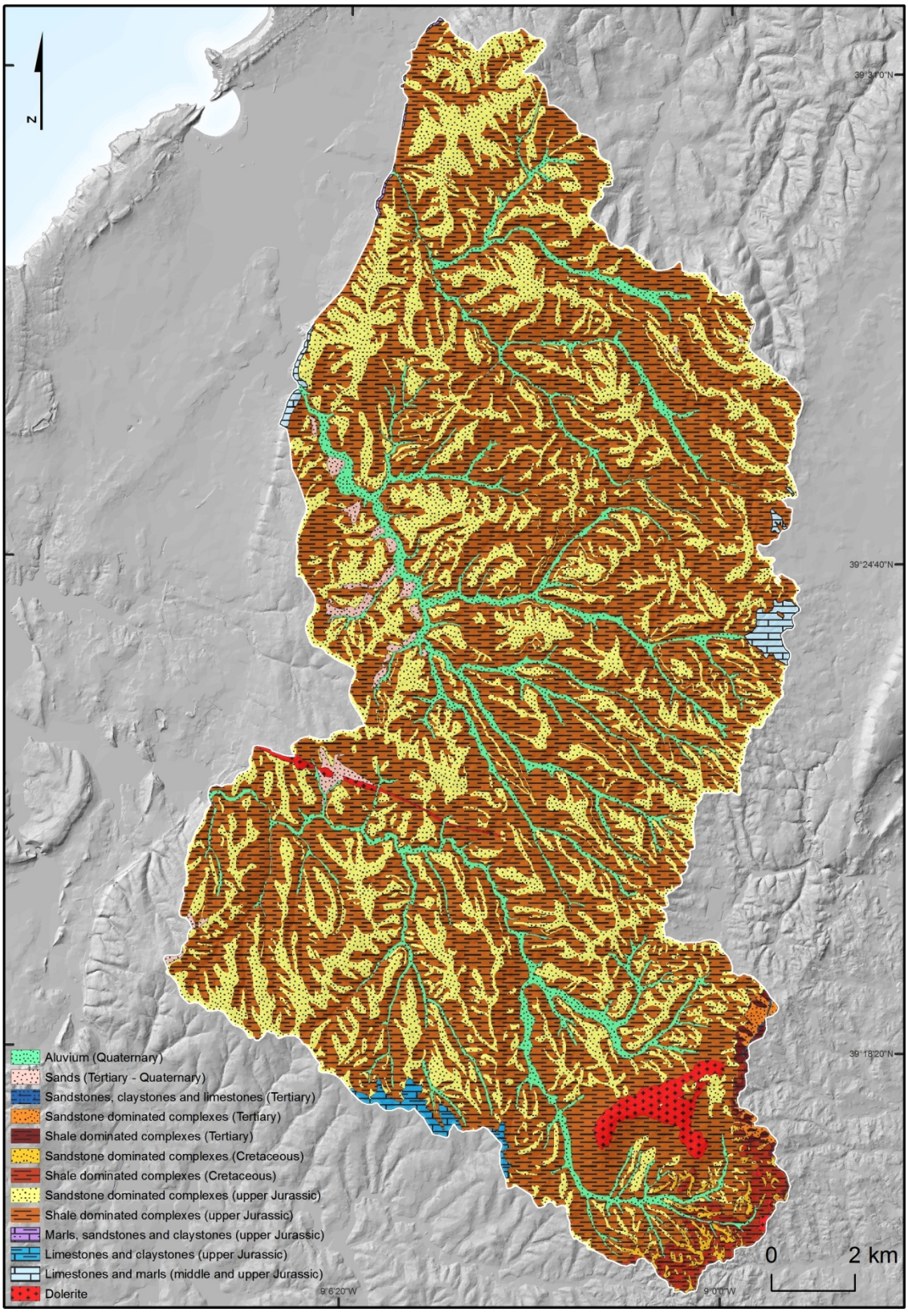

Fig. 3.12 – Detailed litho-stratigraphic map of the study area.

Inevitably, it is necessary to consider that, unlike the sandstones and claystones complexes, which lithological improvements are done within the boundaries (without changing the previous outside boundaries), the improvements on alluvium deposits boundaries will necessarily change the boundaries and/or the percentage of occupancy of other lithological material where it spends, such as: sands (Tertiary - Quaternary) now with 0.71% of the total study area ; sandstone dominated complexes (upper Jurassic) and shale dominated complexes (upper Jurassic) together with a new total occupancy of 88.05% and dolerite now with 1.16% of the total study area (Table 3.2).

From Table 3.3 it is possible to understand how these transitions were made. As it can be seen, a reduction of the alluvium deposits area is due to its transition to sands deposits (0.66% of the alluvium deposits) to Sandstone dominated complexes (upper Jurassic) (1.69% of the alluvium deposits), to Shale dominated complexes (upper Jurassic) (25.70% of the alluvium deposits) and to dolerite (0.04% of the alluvium deposits). Moreover, an increase on the alluvium deposits area comes from the transition of previous sandstones and claystones (upper Jurassic) (2%) and dolerite (0.21%) to alluvium deposits. As it can be seen in the Table 3.3, the others lithological materials did not suffer any modification/transition (and correspond to 100%).

Table 3.3 – Cross-tabulation between previous and detailed litho-stratigraphic maps.

		Previous Lithology									
		AL*	SD*	SCL*	SC-T*	SC-C*	SC-UP*	MSC*	LC*	LM*	D*
		(%)									
Detailed Lithology	Alluvium (Quaternary)	71.9	0	0	0	0	2	0	0	0	0.2
	Sands (Tertiary - Quaternary)	0.7	100	0	0	0	0	0	0	0	0
	Sandstones, claystones and limestones (Tertiary)	0	0	100	0	0	0	0	0	0	0
	Sandstone dominated complexes (Tertiary)	0	0	0	50.5	0	0	0	0	0	0
	Shale dominated complexes (Tertiary)	0	0	0	49.5	0	0	0	0	0	0
	Sandstone dominated complexes (Cretaceous)	0	0	0	0	29.9	0	0	0	0	0
	Shale dominated complexes (Cretaceous)	0	0	0	0	70.1	0	0	0	0	0
	Sandstone dominated complexes (upper Jurassic)	1.7	0	0	0	0	32.6	0	0	0	0
	Shale dominated complexes (upper Jurassic)	25.7	0	0	0	0	65.4	0	0	0	0
	Marls, sandstones and claystones (upper Jurassic)	0	0	0	0	0	0	100	0	0	0
	Limestones and claystones (upper Jurassic)	0	0	0	0	0	0	0	100	0	0
	Limestones and marls (middle and upper Jurassic)	0	0	0	0	0	0	0	0	100	0
	Dolerite	0.04	0	0	0	0	0	0	0	0	99.8

AL* = Alluvium (Quaternary)

SD* = Sands (Tertiary - Quaternary)

SCL* = Sandstones, claystones and limestones (Tertiary)

SC-T* = Sandstones and claystones (Tertiary)

SC-C* = Sandstones and claystones (Cretaceous)

SC-UP* = Sandstones and claystones (upper Jurassic)

MSC* = Marls, sandstones and claystones (upper Jurassic)

LC* = Limestones and claystones (upper Jurassic)

LM* = Limestones and marls (middle and upper Jurassic)

D* = Dolerite

3.1.3 Validation trough field work

The study area is mostly agricultural and for this reason sometimes becomes very difficult to identify some lithological materials through the interpretation of aerial photographs. This difficulty is exacerbated by the fact that this region is occupied and modified by other types of anthropogenic activity and also because sometimes the most resistant rocks (sandstones dominated complexes) are removed for exploitation of soils for agriculture. For all these reasons and in order to fulfill some gaps, fieldwork has become a crucial element for the final validation of the lithology vector layer.

The sandstones dominated complexes correspond mostly to the top of the slopes which have a quite variable lateral continuity. However it is possible to observe some lenticular character throughout the area.

The thickness of these complexes varies a lot across the area from south to north. Thicker layers are located on the north and south part of the study area (50m to 70m, respectively). The thinner layers are located on the central west and central part of the study area, near A-dos-Francos measuring from 5m to 6m. Through field work it was possible to observe that the thickness of these complexes are mostly expressed by morphological evidences through the hill slopes of the general slope area (Fig. 3.13). Further, the slope map (Fig. 3.13) evidences the hummocky topography characteristic already identified through the stereoscope interpretation of the aerial photographs. Thus it is possible to observe an undulating terrain consisting on a series of adjacent slump blocks forms and depressions more or less concentrically aligned.

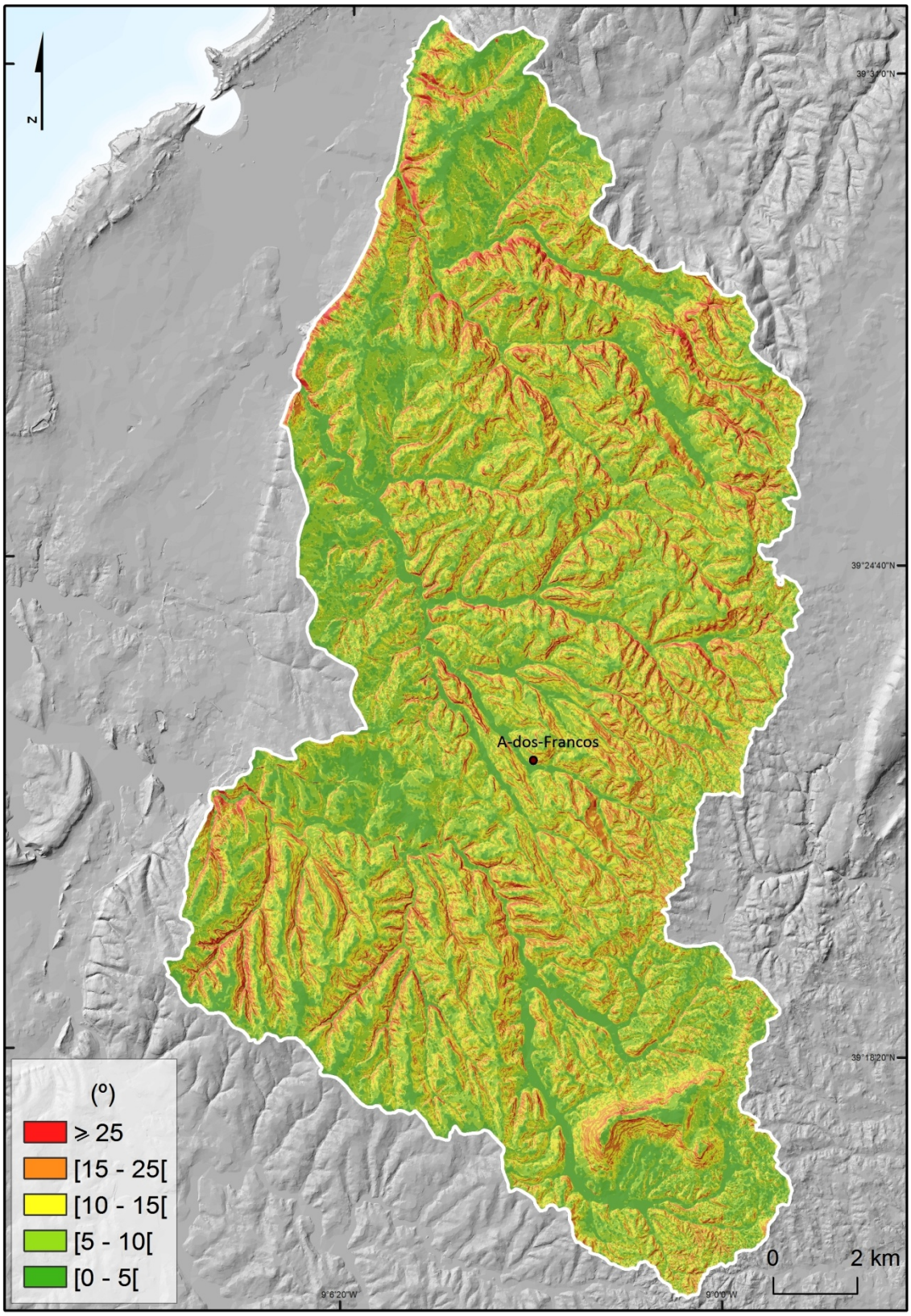

Fig. 3.13– Slope angle map of the study area.

In some locals it was possible to observe that the sandstones dominated complexes were altered and are not as resistant as the current sandstones dominated complexes observed in the study area. The sandstones dominated complexes were found to be permeable, presenting many often fractures through which the water drainage is done. Being incapable to identify any spatial pattern regarding the color of these complexes, it can be said that the color varies between white, yellow and light brownish (presenting many times a mix between all these colors) (Fig. 3.14).

Fig. 3.14 – Sandstones dominated complexes (upper Jurassic), (Estrada N8, Alfeizerão).

The shale dominated complexes varies in color throughout the study area, it can be red, green or grayish, corresponding to a spatial variation of the type of mineral and organic material that they are constituted, however it seemed to be mostly red (Fig. 3.15). These complexes seemed to be completely structureless, thicker than the sandstones dominated complexes, impermeable and with low porosity.

Fig. 3.15 – Shale dominated complexes (upper Jurassic), (Rua Donte dos Carreiros, Painho).

Generally it is quite difficult to validate the presence of alluvium deposits mapped on orthophotomaps along the sides of narrow watercourses due to the surrounding and heavy woods. Moreover, on some wider watercourses and rivers with easier access was possible to observe the presence of minerals deposits made by rivers and validate it through the collection of their precise location via GPS.

After clarifying all the lithological identification doubts through field work and finalized the detailed lithological map the next step consisted in collecting some georeferenced samples in order to validate and estimate the accuracy of the final detailed litho-stratigraphic map. For this process was collected a stratified sample of 72 random validation points, distributed as: 8 validated points correspond to alluvium deposits; 16 to sandstones dominated complexes; and 48 to shale dominated complexes (Fig. 3.16).

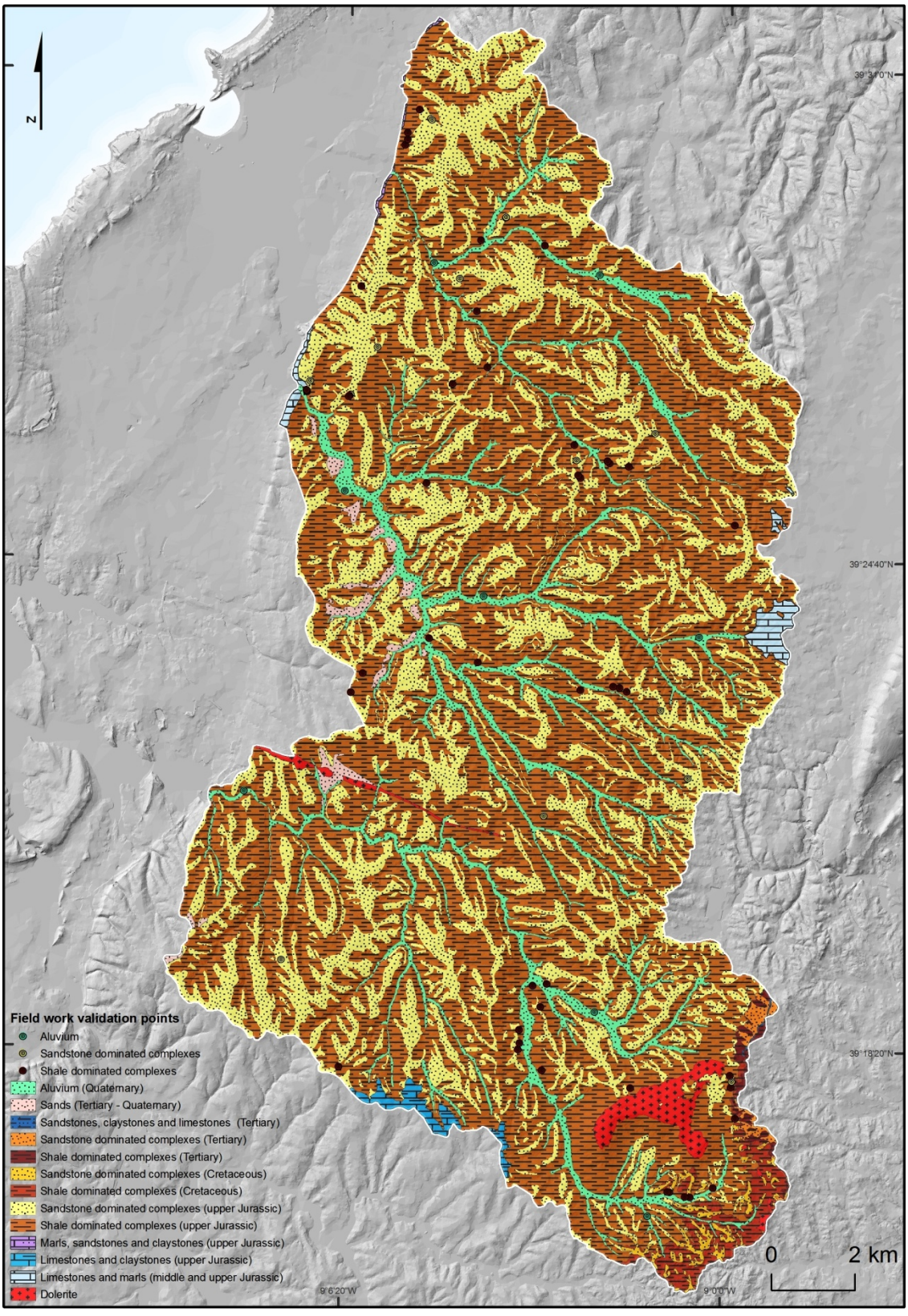

Fig. 3.16 – Overlapping between field validation points and the detailed litho-stratigraphic map.

This field work validated points were only collected on lithological materials subjected to improvements (respectively: sandstone dominated complexes; shale dominated complexes; and alluvium deposits) (Table 3.4). The rest of the lithological data remained unchanged and unvalidated throughout the process.

Table 3.4 – Misclassification table: Accuracy of the lithological improvements.

		Foto-interpretation				
		Alluvium	Sandstone dominated complexes	Shale dominated complexes	Sum	Accuracy (%)
Field work	Alluvium	8			8	100
	Sandstone dominated complexes		14	2	16	87.5
	Shale dominated complexes		2	46	48	95.8
	Sum	**8**	**16**	**48**	**72**	**94.4**

It can be said that the improvements made on the lithological map reveal themselves fairly consistent taking into account the 94.4% of global accuracy (Table 3.4). All items identified as alluvium deposits, on the field, correspond to alluvium deposits mapped on the final detailed lithological map, presenting an accuracy of 100% (Table 3.4). The 16 field work validation points marked as sandstones dominated complexes, on the field, only 2 seemed to be incorrect when compared with sandstones dominated complexes mapped on the final map, presenting an accuracy of 87.5%. The 48 field work validation points identified as shale dominated complexes on the field only 2 seemed incorrect when compared to the shale dominated complexes mapped on the final detailed lithological map, presenting an accuracy of 95.8%. It has to be noted that initially were obtained more field work points, however through a random partition of this points, half were used to improve the boundaries of the final detailed lithological map. Thus, the accuracy and validation would be more consistent using more field work validation points but, due to the lack of outcrops, was not possible to obtain more. Identifying the lithological substrate was only possible on relief where substrate rocks outcrop and where was perfectly identifiable the type of existing lithological material. Many often was very hard to access the narrow watercourses in order to collect some georeferenced alluvium deposits validation points thus only eight well distributed points were obtainable for validation.

3.2 Spatial distribution and patterns of landslides according to the lithological data

According to Wu *et al*. (2009), the factors affecting the development of landslides can be classified into two types: exterior and interior factors. Exterior factors include rainfall, earthquakes and made-man factors and correspond to the triggering factors which are occasional and spasmodic. The interior factors include lithology, slope angle, slope aspect, slope profile and correspond to the predisposing factors which are static and inherent to the terrain (Zêzere, 2005b).

Studying the relationship between a predisposing factor as lithology and the distribution and pattern of landslides provides the basis for obtaining the weight of each lithological class taking into account the type of landslide. Four landslides inventories were analyzed. Two oldest landslides LI#1 and LI#2, obtained through the interpretation of aerial photographs and a recent LI LI#3, obtained through the interpretation of orthophotomaps from 2004 and subsequently field work validation and a fourth LI corresponding to the sum of all landslides inventories Sum LI (chapter 2). Only the area of the landslide depletion zone was considered because only in this way it is possible to estimate the weight of each lithological class to assess susceptibility to landslide initiation.

Furthermore, the present study aims to evaluate quantitatively the relevance of the lithological improvements in each landslide typology for each LI. It is noted that, in all landslides inventories, the most abundant landslide type in the study area correspond to deep-seated rotational landslide followed by shallow rotational landslide, shallow translational landslides and deep-seated translational landslides (chapter 2).

Regarding the LI of 1958 is possible to observe that in the previous lithological data some landslides, especially shallow rotational landslides (2.65%) and shallow translational landslides (1.76%) seemed to occur on the alluvium deposits causing a landslide density of 0.05% in this lithological class (Table 3.5 and 3.6). However, this fact does not correspond to reality, because after a significant improvement on alluvial deposits

boundaries it is possible to verify that in 1958 there is indeed no landslide occurrences in this class (Table 3.7 and 3.8).

Table 3.5 – Landslide distribution according to previous lithological classes for LI#1.

		Landslide area					
	Area	Deep-seated rotational	Shallow rotational	Shallow translational	Deep-seated translational	Sum	Total density
			(m^2)				(%)
Alluvium (Quaternary)	19376169	5700	3175	400	0	9275	0.05
Sands (Tertiary - Quaternary)	1832444	1250	0	1500	0	2750	0.15
Sandstones, claystones and limestones (Tertiary)	43777	0	0	0	0	0	0.00
Sandstones and claystones (Tertiary)	1353233	825	0	0	0	825	0.06
Sandstones and claystones (Cretaceous)	4906541	5950	0	0	0	5950	0.12
Sandstones and claystones (upper Jurassic)	242459903	2193175	113600	20875	5300	2332950	0.96
Marls, sandstones and claystones (upper Jurassic)	122573	0	0	0	0	0	0.00
Limestones and claystones (upper Jurassic)	1142319	0	0	0	0	0	0.00
Limestones and marls (middle and upper Jurassic)	1467536	4950	3050	0	0	8000	0.55
Dolerite	3187888	136050	0	0	0	136050	4.27
Sum	275892386	2347900	119825	22775	5300	2495800	

Table 3.6 – Cross tabulation area between landslides types and previous lithological classes for LI#1.

	Landslide area (%)				
	Deep-seated rotational	Shallow rotational	Shallow translational	Deep-seated translational	All types
Alluvium (Quaternary)	0.24	2.65	1.76	0.00	0.37
Sands (Tertiary - Quaternary)	0.05	0.00	6.59	0.00	0.11
Sandstones, claystones and limestones (Tertiary)	0.00	0.00	0.00	0.00	0.00
Sandstones and claystones (Tertiary)	0.04	0.00	0.00	0.00	0.03
Sandstones and claystones (Cretaceous)	0.25	0.00	0.00	0.00	0.24
Sandstones and claystones (upper Jurassic)	93.41	94.80	91.66	100.00	93.48
Marls, sandstones and claystones (upper Jurassic)	0.00	0.00	0.00	0.00	0.00
Limestones and claystones (upper Jurassic)	0.00	0.00	0.00	0.00	0.00
Limestones and marls (middle and upper Jurassic)	0.21	2.55	0.00	0.00	0.32
Dolerite	5.79	0.00	0.00	0.00	5.45
Sum	100	100	100	100	100

The sand deposits seem to be quite the same comparing the previous lithological data with the detailed lithological data. However there is a slight difference related to shallow translational landslides (about 0.65%) due to the improvements on the alluvium deposits boundaries which, collaterally, altered the occupancy percentage of the landslides occurrence but without altering the landslide density in this lithological class (Tables 3.5, 3.6, 3.7 and 3.8).

The same collateral effects due to the improvement on alluvium deposits boundaries seemed to occur on dolerite complex. It is possible to observe an increase of the dolerite complex area resulting from a decrease on alluvium deposits boundaries. However, it is so small that the landslide density remains unchanged on this lithological class (Tables 3.5, 3.6, 3.7 and 3.8).

Table 3.7 – Landslide distribution according to detailed lithological classes for LI#1.

	Area	Landslide area					
		Deep-seated rotational	Shallow rotational	Shallow translational	Deep-seated translational	Sum	Total density
		(m^2)					(%)
Alluvium (Quaternary)	18786915	0	0	0	0	0	0.00
Sands (Tertiary - Quaternary)	1960623	1250	0	1650	0	2900	0.15
Sandstones, claystones and limestones (Tertiary)	43777	0	0	0	0	0	0.00
Sandstone dominated complexes (Tertiary)	683297	0	0	0	0	0	0.00
Shale dominated complexes (Tertiary)	669936	825	0	0	0	825	0.12
Sandstone dominated complexes (Cretaceous)	1465098	750	0	0	0	750	0.05
Shale dominated complexes (Cretaceous)	3441443	5200	0	0	0	5200	0.15
Sandstone dominated complexes (upper Jurassic)	79310722	71525	0	0	0	71525	0.09
Shale dominated complexes (upper Jurassic)	163608615	2127350	116775	21125	5300	2270550	1.39
Marls, sandstones and claystones (upper Jurassic)	122573	0	0	0	0	0	0.00
Limestones and claystones (upper Jurassic)	1142319	0	0	0	0	0	0.00
Limestones and marls (middle and upper Jurassic)	1467536	4950	3050	0	0	8000	0.55
Dolerite	3189527	136050	0	0	0	136050	4.27
Sum	275892386	2347900	119825	22775	5300	2495800	

Table 3.8 – Cross tabulation area between landslides types and detailed lithological classes for LI#1.

	Landslide area (%)				
	Deep-seated rotational	Shallow rotational	Shallow translational	Deep-seated translational	All types
Alluvium (Quaternary)	0.00	0.00	0.00	0.00	0.00
Sands (Tertiary - Quaternary)	0.05	0.00	7.24	0.00	0.12
Sandstones, claystones and limestones (Tertiary)	0.00	0.00	0.00	0.00	0.00
Sandstone dominated complexes (Tertiary)	0.00	0.00	0.00	0.00	0.00
Shale dominated complexes (Tertiary)	0.04	0.00	0.00	0.00	0.03
Sandstone dominated complexes (Cretaceous)	0.03	0.00	0.00	0.00	0.03
Shale dominated complexes (Cretaceous)	0.22	0.00	0.00	0.00	0.21
Sandstone dominated complexes (upper Jurassic)	3.05	0.00	0.00	0.00	2.87
Shale dominated complexes (upper Jurassic)	90.61	97.45	92.76	100.00	90.97
Marls, sandstones and claystones (upper Jurassic)	0.00	0.00	0.00	0.00	0.00
Limestones and claystones (upper Jurassic)	0.00	0.00	0.00	0.00	0.00
Limestones and marls (middle and upper Jurassic)	0.21	2.55	0.00	0.00	0.32
Dolerite	5.79	0.00	0.00	0.00	5.45
Sum	100	100	100	100	100

The major differences lie on the sandstones and claystones complexes (from upper Jurassic, Cretaceous and Tertiary). Once these complexes comprises different rock types varying in strength, from hard to weak and soft rocks, there was the need to make the properly identification and separation in different complexes (sandstones dominated complexes and shale dominated complexes). It was possible to realize that landslide abundance and pattern vary largely within the new lithological complexes obtained on the detailed lithological map and this is also due to the distinctive hydrogeological properties which characterize differently these two new complexes. Thereby this lithological separation comes out to be very important because otherwise it would be considered a false landslide density regarding the previous lithological data (Table 3.5 and 3.6). Generally landslides are more abundant where weak rocks crop out regardless the type of landslide. Landslides are less frequent in the sandstones dominated complexes, only a few deep-seated rotational landslides seemed to occur there (3.05%). The majority of shallow landslides and all deep seated translational landslides occur on the shale dominated complexes (Table 3.7 and 3.8).

The following lithological classes: sandstones, limestones and claystones (Tertiary); marls, claystones and sandstones (upper Jurassic); limestones and claystones (upper Jurassic);

and limestones and marls (middle and upper Jurassic), were not subject to any change or improvement thus the landslides occupation or susceptibility remained unchanged between the previous lithological data and the detailed lithological data (Table 3.7 and 3.8).

According to the LI of 1982 is possible to observe that, in the previous lithological data, some landslides as the deep-seated rotational landslides (1.29%), shallow translational landslides (0.82%) and deep-seated translational landslides (0.79%) seemed to occur on the alluvium deposits causing a landslide density of 0.06% (Table 3.9 and 3.10). But, after the lithological data improvements it is possible to see that in reality there are no landslide occurrences on alluvium deposits in this period (Table 3.11 and 3.12).

Table 3.9 – Landslide distribution according to previous lithological classes for LI#2.

		Landslide area					
	Area	**Deep-seated rotational**	**Shallow rotational**	**Shallow translational**	**Deep-seated translational**	**Sum**	**Total density (%)**
			(m^2)				
Alluvium (Quaternary)	19376169	11775	0	125	25	11925	0.06
Sands (Tertiary - Quaternary)	1832444	3925	750	0	0	4675	0.26
Sandstones, claystones and limestones (Tertiary)	43777	0	0	0	0	0	0.00
Sandstones and claystones (Tertiary)	1353233	675	0	0	0	675	0.05
Sandstones and claystones (Cretaceous)	4906541	3975	575	0	0	4550	0.09
Sandstones and claystones (upper Jurassic)	242459903	844275	52875	15000	3125	915275	0.38
Marls, sandstones and claystones (upper Jurassic)	122573	0	0	0	0	0	0.00
Limestones and claystones (upper Jurassic)	1142319	0	0	0	0	0	0.00
Limestones and marls (middle and upper Jurassic)	1467536	2975	0	150	0	3125	0.21
Dolerite	3187888	42325	400	0	0	42725	1.34
Sum	275892386	909925	54600	15275	3150	982950	

Table 3.10 – Cross tabulation area between landslides types and previous lithological classes for LI#2.

	Landslide area (%)				
	Deep-seated rotational	Shallow rotational	Shallow translational	Deep-seated translational	All types
Alluvium (Quaternary)	1.29	0.00	0.82	0.79	1.21
Sands (Tertiary - Quaternary)	0.43	1.37	0.00	0.00	0.48
Sandstones, claystones and limestones (Tertiary)	0.00	0.00	0.00	0.00	0.00
Sandstones and claystones (Tertiary)	0.07	0.00	0.00	0.00	0.07
Sandstones and claystones (Cretaceous)	0.44	1.05	0.00	0.00	0.46
Sandstones and claystones (upper Jurassic)	92.79	96.84	98.20	99.21	93.12
Marls, sandstones and claystones (upper Jurassic)	0.00	0.00	0.00	0.00	0.00
Limestones and claystones (upper Jurassic)	0.00	0.00	0.00	0.00	0.00
Limestones and marls (middle and upper Jurassic)	0.33	0.00	0.98	0.00	0.32
Dolerite	4.65	0.73	0.00	0.00	4.35
Sum	100	100	100	100	100

The sand deposits class in the new detailed lithological data seemed to have enlarged a little bit its area when compared with the previous lithological data. However, there is no difference related to landslides occupancy which urges a landslide density decrease of 0.02% (Table 3.9, 3.10, 3.11 and 3.12).

On what dolerite complex concerns there are no landslide occurrence variation comparing the previous and detailed lithological data. In addition, the variation of the area of this lithological class seemed to be not enough to cause a landslide density variation (Table 3.9, 3.10, 3.11 and 3.12).

As for sandstones and claystones complexes, previously inside only one class, with the separation made on the new detailed lithological data is now possible to understand that also in this period was registered an abundance of landslide occurrence on the shale dominated complexes. Like in 1958, all types of landslide seemed to occur mostly within this lithological class. Only a few percentages of deep-seated rotational landslides seemed to occur on sandstones dominated complexes (6.47% of the total deep-seated rotational landslides) (Table 3.9, 3.10, 3.11 and 3.12).

Table 3.11 – Landslide distribution according to detailed lithological classes for LI#2.

		Landslide area					
	Area	Deep-seated rotational	Shallow rotational	Shallow translational	Deep-seated translational	Sum	Total density
			(m^2)				(%)
Alluvium (Quaternary)	18786915	0	0	0	0	0	0.00
Sands (Tertiary - Quaternary)	1960623	3925	750	0	0	4675	0.24
Sandstones, claystones and limestones (Tertiary)	43777	0	0	0	0	0	0.00
Sandstone dominated complexes (Tertiary)	683297	0	0	0	0	0	0.00
Shale dominated complexes (Tertiary)	669936	675	0	0	0	675	0.10
Sandstone dominated complexes (Cretaceous)	1465098	150	0	0	0	150	0.01
Shale dominated complexes (Cretaceous)	3441443	3825	575	0	0	4400	0.13
Sandstone dominated complexes (upper Jurassic)	79310722	58675	0	0	0	58675	0.07
Shale dominated complexes (upper Jurassic)	163608615	797375	52875	15125	3150	868525	0.53
Marls, sandstones and claystones (upper Jurassic)	122573	0	0	0	0	0	0.00
Limestones and claystones (upper Jurassic)	1142319	0	0	0	0	0	0.00
Limestones and marls (middle and upper Jurassic)	1467536	2975	0	150	0	3125	0.21
Dolerite	3189527	42325	400	0	0	42725	1.34
Sum	275892386	909925	54600	15275	3150	982950	0.36

Table 3.12 – Cross tabulation area between landslides types and detailed lithological classes for LI#2.

	Landslide area (%)				
	Deep-seated rotational	Shallow rotational	Shallow translational	Deep-seated translational	All types
Alluvium (Quaternary)	0.00	0.00	0.00	0.00	0.00
Sands (Tertiary - Quaternary)	0.43	1.37	0.00	0.00	0.48
Sandstones, claystones and limestones (Tertiary)	0.00	0.00	0.00	0.00	0.00
Sandstone dominated complexes (Tertiary)	0.00	0.00	0.00	0.00	0.00
Shale dominated complexes (Tertiary)	0.07	0.00	0.00	0.00	0.07
Sandstone dominated complexes (Cretaceous)	0.02	0.00	0.00	0.00	0.02
Shale dominated complexes (Cretaceous)	0.42	1.05	0.00	0.00	0.45
Sandstone dominated complexes (upper Jurassic)	6.45	0.00	0.00	0.00	5.97
Shale dominated complexes (upper Jurassic)	87.63	96.84	99.02	100.00	88.36
Marls, sandstones and claystones (upper Jurassic)	0.00	0.00	0.00	0.00	0.00
Limestones and claystones (upper Jurassic)	0.00	0.00	0.00	0.00	0.00
Limestones and marls (middle and upper Jurassic)	0.33	0.00	0.98	0.00	0.32
Dolerite	4.65	0.73	0.00	0.00	4.35
Sum	100	100	100	100	100

Also in this period the lithological classes corresponding to: sandstones, limestones and claystones (Tertiary); marls, claystones and sandstones (upper Jurassic); limestones and claystones (upper Jurassic); and limestones and marls (middle and upper Jurassic), remained unchangeable, in what landslide occurrence concerns, when comparing the previous lithological data with the detailed lithological data (Table 3.9, 3.10, 3.11 and 3.12).

According to the field work validated LI (LI#3) is possible to observe that a large percentage of shallow translational landslides (14.9% of the total) is registered on alluvium deposits on the previous lithological data (Table 3.13 and 3.14), however according to the detailed lithological data it is possible to observe no landslides occurrence and therefore no landslide density on alluvium deposits (Table 3.13, 3.14, 3.15 and 3.16).

Table 3.13 – Landslide distribution according to previous lithological classes for LI#3.

		Landslide area					
	Area	Deep-seated rotational	Shallow rotational	Shallow translational	Deep-seated translational	Sum	Total density
			(m^2)				(%)
Alluvium (Quaternary)	19376169	2500	1500	1825	0	5825	0.03
Sands (Tertiary - Quaternary)	1832444	0	0	0	0	0	0.00
Sandstones, claystones and limestones (Tertiary)	43777	0	0	0	0	0	0.00
Sandstones and claystones (Tertiary)	1353233	275	0	0	0	275	0.02
Sandstones and claystones (Cretaceous)	4906541	950	200	0	0	1150	0.02
Sandstones and claystones (upper Jurassic)	242459903	248300	41525	9275	400	299500	0.12
Marls, sandstones and claystones (upper Jurassic)	122573	0	0	0	0	0	0.00
Limestones and claystones (upper Jurassic)	1142319	0	0	0	0	0	0.00
Limestones and marls (middle and upper Jurassic)	1467536	0	0	375	0	375	0.03
Dolerite	3187888	36725	475	775	0	37975	1.19
Sum	275892386	288750	43700	12250	400	345100	

Table 3.14 – Cross tabulation area between landslides types and previous lithological classes for LI#3.

	Landslide area (%)				
	Deep-seated rotational	**Shallow rotational**	**Shallow translational**	**Deep-seated translational**	**All types**
Alluvium (Quaternary)	0.87	3.43	14.90	0.00	1.69
Sands (Tertiary - Quaternary)	0.00	0.00	0.00	0.00	0.00
Sandstones, claystones and limestones (Tertiary)	0.00	0.00	0.00	0.00	0.00
Sandstones and claystones (Tertiary)	0.10	0.00	0.00	0.00	0.08
Sandstones and claystones (Cretaceous)	0.33	0.46	0.00	0.00	0.33
Sandstones and claystones (upper Jurassic)	85.99	95.02	75.71	100.00	86.79
Marls, sandstones and claystones (upper Jurassic)	0.00	0.00	0.00	0.00	0.00
Limestones and claystones (upper Jurassic)	0.00	0.00	0.00	0.00	0.00
Limestones and marls (middle and upper Jurassic)	0.00	0.00	3.06	0.00	0.11
Dolerite	12.72	1.09	6.33	0.00	11.00
Sum	100	100	100	100	100

There are no landslide occurrence variation on dolerite complexes comparing the previous and the detailed lithological data and also no landslide density variation (Table 3.13, 3.14, 3.15 and 3.16). As in all the landslide periods, also in this LI all types of landslide seem to occur mostly within the shale dominated complexes. Only a few percentages of deep-seated rotational landslides seem to occur on sandstones dominated complexes (6.12% of the total deep-seated rotational landslides) (Tables 3.15 and 3.16).

In this period the lithological classes corresponding to: sands deposits (Tertiary - Quaternary); sandstones, limestones and claystones (Tertiary); marls, claystones and sandstones (upper Jurassic); limestones and claystones (upper Jurassic); and limestones and marls (middle and upper Jurassic), remained unchangeable in what landslide occurrence concerns when comparing the previous and the detailed lithological data (Table 3.13, 3.14, 3.15 and 3.16).

Table 3.15 – Landslide distribution according to detailed lithological classes for LI#3.

		Landslide area					
	Area	Deep-seated rotational	Shallow rotational	Shallow translational	Deep-seated translational	Sum	Total density (%)
			(m^2)				
Alluvium (Quaternary)	18786915	0	0	0	0	0	0.00
Sands (Tertiary - Quaternary)	1960623	0	0	0	0	0	0.00
Sandstones, claystones and limestones (Tertiary)	43777	0	0	0	0	0	0.00
Sandstone dominated complexes (Tertiary)	683297	0	0	0	0	0	0.00
Shale dominated complexes (Tertiary)	669936	275	0	0	0	275	0.04
Sandstone dominated complexes (Cretaceous)	1465098	0	0	0	0	0	0.00
Shale dominated complexes (Cretaceous)	3441443	950	200	0	0	1150	0.03
Sandstone dominated complexes (upper Jurassic)	79310722	17675	0	0	0	17675	0.02
Shale dominated complexes (upper Jurassic)	163608615	233125	43025	11100	400	287650	0.18
Marls, sandstones and claystones (upper Jurassic)	122573	0	0	0	0	0	0.00
Limestones and claystones (upper Jurassic)	1142319	0	0	0	0	0	0.00
Limestones and marls (middle and upper Jurassic)	1467536	0	0	375	0	375	0.03
Dolerite	3189527	36725	475	775	0	37975	1.19
Sum	275892386	288750	43700	12250	400	345100	

Table 3.16 – Cross tabulation area between landslides types and detailed lithological classes for LI#3.

	Landslide area (%)				
	Deep-seated rotational	Shallow rotational	Shallow translational	Deep-seated translational	All types
Alluvium (Quaternary)	0.00	0.00	0.00	0.00	0.00
Sands (Tertiary - Quaternary)	0.00	0.00	0.00	0.00	0.00
Sandstones, claystones and limestones (Tertiary)	0.00	0.00	0.00	0.00	0.00
Sandstone dominated complexes (Tertiary)	0.00	0.00	0.00	0.00	0.00
Shale dominated complexes (Tertiary)	0.10	0.00	0.00	0.00	0.08
Sandstone dominated complexes (Cretaceous)	0.00	0.00	0.00	0.00	0.00
Shale dominated complexes (Cretaceous)	0.33	0.46	0.00	0.00	0.33
Sandstone dominated complexes (upper Jurassic)	6.12	0.00	0.00	0.00	5.12
Shale dominated complexes (upper Jurassic)	80.74	98.46	90.61	100.00	83.35
Marls, sandstones and claystones (upper Jurassic)	0.00	0.00	0.00	0.00	0.00
Limestones and claystones (upper Jurassic)	0.00	0.00	0.00	0.00	0.00
Limestones and marls (middle and upper Jurassic)	0.00	0.00	3.06	0.00	0.11
Dolerite	12.72	1.09	6.33	0.00	11.00
Sum	100	100	100	100	100

Considering all the LIs together is possible to observe that in the previous lithological data some landslide occurrence is registered on the alluvium deposits (0.71% of the total landslides). Shallow translational landslides seemed to occur more frequently (4.97% of the total shallow translational landslides) which causes a landslide density of 0.14% registered on the previous lithological data (Table 3.17 and 3.18). However, after the lithological improvement on alluvium deposits boundaries it is possible to realize that there are no landslide occurrences in this class regardless the period of landslides (Table 3.19 and 3.20).

Table 3.17 – Landslide distribution according to previous lithological classes for Sum of LIs.

		Landslide area					
	Area	**Deep-seated rotational**	**Shallow rotational**	**Shallow translational**	**Deep-seated translational**	**Sum**	**Total density**
			(m^2)				**(%)**
Alluvium (Quaternary)	19376169	19800	4450	2450	0	26700	0.14
Sands (Tertiary - Quaternary)	1832444	5200	800	1475	0	7475	0.41
Sandstones, claystones and limestones (Tertiary)	43777	0	0	0	0	0	0.00
Sandstones and claystones (Tertiary)	1353233	1800	0	0	0	1800	0.13
Sandstones and claystones (Cretaceous)	4906541	10950	675	0	0	11625	0.24
Sandstones and claystones (upper Jurassic)	242459903	3244025	205950	44900	8400	3503275	1.44
Marls, sandstones and claystones (upper Jurassic)	122573	0	0	0	0	0	0.00
Limestones and claystones (upper Jurassic)	1142319	0	0	0	0	0	0.00
Limestones and marls (middle and upper Jurassic)	1467536	8050	3025	500	0	11575	0.79
Dolerite	3187888	198300	850	0	0	199150	6.24
Sum	275892386	3488125	215750	49325	8400	3761600	

Table 3.18 – Cross tabulation area between landslides types and previous lithological classes for Sum of LIs.

	Landslide area (%)				
	Deep-seated rotational	Shallow rotational	Shallow translational	Deep-seated translational	All types
Alluvium (Quaternary)	0.57	2.06	4.97	0.00	0.71
Sands (Tertiary - Quaternary)	0.15	0.37	2.99	0.00	0.20
Sandstones, claystones and limestones (Tertiary)	0.00	0.00	0.00	0.00	0.00
Sandstones and claystones (Tertiary)	0.05	0.00	0.00	0.00	0.05
Sandstones and claystones (Cretaceous)	0.31	0.31	0.00	0.00	0.31
Sandstones and claystones (upper Jurassic)	93.00	95.46	91.03	100.00	93.13
Marls, sandstones and claystones (upper Jurassic)	0.00	0.00	0.00	0.00	0.00
Limestones and claystones (upper Jurassic)	0.00	0.00	0.00	0.00	0.00
Limestones and marls (middle and upper Jurassic)	0.23	1.40	1.01	0.00	0.31
Dolerite	5.69	0.39	0.00	0.00	5.29
Sum	100	100	100	100	100

The sand deposits seem to have some slight differences comparing the two lithological settings. Beyond the increase of this deposits area (due to the improvements on the alluvium deposits boundaries) it is observed that the shallow translational landslides increased its percentage of occupancy from 2.99% to 3.29% (of the total shallow translational landslides) with the lithological improvements (Tables 3.17, 3.18, 3.19 and 3.20).

Table 3.19 – Landslide distribution according to detailed lithological classes for Sum of LIs.

		Landslide area					
	Area	Deep-seated rotational	Shallow rotational	Shallow translational	Deep-seated translational	Sum	Total density
			(m^2)				(%)
Alluvium (Quaternary)	18786915	0	0	0	0	0	0.00
Sands (Tertiary - Quaternary)	1960623	5200	800	1625	0	7625	0.39
Sandstones, claystones and limestones (Tertiary)	43777	0	0	0	0	0	0.00
Sandstone dominated complexes (Tertiary)	683297	0	0	0	0	0	0.00
Shale dominated complexes (Tertiary)	669936	1800	0	0	0	1800	0.27
Sandstone dominated complexes (Cretaceous)	1465098	925	0	0	0	925	0.06
Shale dominated complexes (Cretaceous)	3441443	10025	675	0	0	10700	0.31
Sandstone dominated complexes (upper Jurassic)	79310722	147200	0	0	0	147200	0.19
Shale dominated complexes (upper Jurassic)	163608615	3116625	210400	47200	8400	3382625	2.07
Marls, sandstones and claystones (upper Jurassic)	122573	0	0	0	0	0	0.00
Limestones and claystones (upper Jurassic)	1142319	0	0	0	0	0	0.00
Limestones and marls (middle and upper Jurassic)	1467536	8050	3025	500	0	11575	0.79
Dolerite	3189527	198300	850	0	0	199150	6.24
Sum	275892386	3488125	215750	49325	8400	3761600	

Table 3.20 – Cross tabulation area between landslides types and detailed lithological classes for Sum of LIs.

	Landslide area (%)				
	Deep-seated rotational	Shallow rotational	Shallow translational	Deep-seated translational	All types
Alluvium (Quaternary)	0.00	0.00	0.00	0.00	0.00
Sands (Tertiary - Quaternary)	0.15	0.37	3.29	0.00	0.20
Sandstones, claystones and limestones (Tertiary)	0.00	0.00	0.00	0.00	0.00
Sandstone dominated complexes (Tertiary)	0.00	0.00	0.00	0.00	0.00
Shale dominated complexes (Tertiary)	0.05	0.00	0.00	0.00	0.05
Sandstone dominated complexes (Cretaceous)	0.03	0.00	0.00	0.00	0.02
Shale dominated complexes (Cretaceous)	0.29	0.31	0.00	0.00	0.28
Sandstone dominated complexes (upper Jurassic)	4.22	0.00	0.00	0.00	3.91
Shale dominated complexes (upper Jurassic)	89.35	97.52	95.69	100.00	89.93
Marls, sandstones and claystones (upper Jurassic)	0.00	0.00	0.00	0.00	0.00
Limestones and claystones (upper Jurassic)	0.00	0.00	0.00	0.00	0.00
Limestones and marls (middle and upper Jurassic)	0.23	1.40	1.01	0.00	0.31
Dolerite	5.69	0.39	0.00	0.00	5.29
Sum	100	100	100	100	100

On the dolerite complex, although a slight difference on the area of this lithological class among the two lithological settings, it is still observed the same percentage of landslide density (Tables 3.17, 3.18, 3.19 and 3.20).

As already seen in all cases, landslides are more abundant on shale dominated complexes regardless the type of landslide. Although, there are some deep-seated rotational landslides (4.25% of the total deep-seated rotational landslides) occurring on sandstones dominated complexes. The majority of deep seated translational landslides and all shallow landslides occur on the shale dominated complexes (Table 3.19 and 3.20). Regardless the period, it was noted that landslides that occurred on alluvium deposits on the previous lithological data ended mostly on the shale dominated complexes on the detailed lithological data.

The following lithological classes: sandstones, limestones and claystones (Tertiary); marls, claystones and sandstones (upper Jurassic); limestones and claystones (upper Jurassic); and limestones and marls (middle and upper Jurassic), remained unchanged between the previous and the detailed lithological data (Tables 3.19 and 3.20).

Regarding the landslide density given for the previous and detailed lithological maps (Tables 3.5, 3.7, 3.9, 3.11, 3.13, 3.15, 3.17, 3.19), two lithological classes on the previous lithological map were evidenced since they had higher landslide density such as dolerite and sandstones and claystones complexes when comparing with the remaining lithological classes, however, through the lithological improvements, by discriminating the sandstones and claystones complexes into resistant and weak/soft rocks were possible to settle that the shale dominated complexes is much more important in what landslide density concerns than the sandstone dominated complexes.

3.3 Comparison between the previous lithological map and the detailed lithological map using the Accountability and Reliability indexes

The final goal of this chapter aims to evaluate quantitatively the relevance of the lithological improvements through the landslide assessment analysis of shallow landslides and deep-seated landslides for each LI period. The analysis was chosen to be carried out in this way because the lithological classes seemed to be more related with depth of the slope failure than with landslides typology (Tables 3.5 to 3.20).

Thus, the two lithological maps were individually cross-tabulated (in ArcGis 9.3 software) with the four landslides inventories (LI#1; LI#2; LI#3; Sum LI) in order to calculate the densities of landslides in all classes of both lithological maps. For the analysis of the different lithological maps contributing to landslides predisposition, two estimators named accountability and Reliability were employed. They were introduced by Greenbaum *et al*. (1995a,b) and used by Abella (2008) as simple indicators of the importance of particular classes of factor maps for a preliminary susceptibility analysis and selection of an appropriate combination of the factor maps for detailed analysis (Blahut *et al*., 2010).

The accountability is calculated as the sum of landslide cells in the classes of the lithological maps with a landslide density greater than the average density in the whole area, divided by the sum of landslide cells over the whole area and multiplied by 100 (Blahut *et al*., 2010):

$$Accountability = \frac{\Sigma(\mathrm{Npixsld1})}{\Sigma(\mathrm{Npixsld})} \times 100 \qquad (3.4)$$

Where *Npixsld1* are the landslide cells in the classes of the lithological maps with a landslide density greater than the average density in the whole area, and *Npixsld* are the landslide pixels over the entire study area.

The Reliability is calculated as the sum of landslide cells in those classes of lithological maps with density values greater than the average density in the whole area, divided by the pixels area of those classes and multiplied by 100 (Abella, 2008):

$$\mathrm{Re}\,liability = \frac{\Sigma(\mathrm{Npixsld1})}{\Sigma(\mathrm{Npixcls})} \times 100 \tag{3.5}$$

Where *Npixcls* are the landslide and non-landslide cells in the classes of the lithological maps with a landslide density greater than the average density in the whole area.

The Accountability index explains how the classes of the lithological maps that are relevant for the analysis (with densities higher than regional average) contain landslide cells/area. The Reliability index gives an idea of the average landslide density in the classes of lithological maps that are relevant for landslide occurrence (with values higher than 1) (Blahut *et al*., 2010). The Accountability (ACC) and Reliability (RLB) indexes were calculated individually for the deep-seated landslides, shallow landslides and for whole landslides (sum of shallow and deep-seated landslides) for the previous and detailed lithological maps (Table 3.21, 3.22 and 3.23, respectively).

Table 3.21 – Accountability (ACC) and Reliability (RLB) for both previous and detailed lithological maps for deep-seated landslides. The highest mean accountability and Reliability indexes are highlighted in bold.

Lithological settings	LI#1		LI#2		LI#3		Sum LIs		Mean	
	ACC	*RLB*	*ACC*	*RLB*	*ACC*	*RLB*	*ACC*	*RLB*	*ACC*	*RLB*
Previous lithology	99.21	0.95	97.44	0.36	12.64	1.15	96.82	1.51	76.53	0.99
Detailed lithology	96.41	1.36	92.26	0.50	93.38	0.16	95.05	1.99	**94.23**	**1.00**

Table 3.22 – Accountability (ACC) and Reliability (RLB) for both previous and detailed lithological maps for shallow landslides. The highest mean accountability and Reliability indexes are highlighted in bold.

Lithological settings	LI#1		LI#2		LI#3		Sum LIs		Mean	
	ACC	*RLB*	*ACC*	*RLB*	*ACC*	*RLB*	*ACC*	*RLB*	*ACC*	*RLB*
Previous lithology	96.41	0.06	98.24	0.03	93.66	0.02	96.58	0.11	96.22	0.06
Detailed lithology	100.00	0.09	98.46	0.04	99.69	0.03	99.14	0.16	**99.32**	**0.08**

Table 3.23 – Accountability (ACC) and Reliability (RLB) for both previous and detailed lithological maps for the total landslides (shallow and deep-seated landslides). The highest mean accountability and Reliability indexes are highlighted in bold.

Lithological settings	LI#1		LI#2		LI#3		Sum LIs		Mean	
	ACC	*RLB*	*ACC*	*RLB*	*ACC*	*RLB*	*ACC*	*RLB*	*ACC*	*RLB*
Previous lithology	98.93	1.01	97.46	0.39	11.00	1.19	98.45	1.53	76.46	1.03
Detailed lithology	96.43	1.44	92.71	0.55	94.36	0.20	95.28	2.18	**94.70**	**1.09**

The accountability scores for the previous lithological map seemed to be a little bit higher than those for the detailed lithological map observing the whole (Table 3.23) and deep-seated landslides (Table 3.21). This is due to two facts. First, because the deep-seated landslides are the most representative landslides observed in the study area (92.76% of the total landslide area considering all inventories periods) and are distributed on both hard and weak rocks (sandstone dominated complexes and shale dominated complexes). Second, having more lithological classes (on the detailed lithological map) the average area of these new classes will therefore decrease in relation to previous lithological map, so it is more likely that the landslide area on the lithological classes above-average area are smaller, resulting in a lower accountability value.

Obviously the values of accountability would always be greater for the previous lithological map since the deep-seated landslides exist on both hard and soft rocks of the previous sandstones and claystones dominated complexes and therefore after a lithological detailing it is obvious that, even if the shale dominated complexes have the majority of landslides occurrence and distribution than the sandstones dominated complexes, when calculating the accountability index, those values would be smaller for the detailed lithological map. This becomes easier to understand when observing the accountability calculation method shown for the previous and detailed lithological map (Table 3.24 and 3.25).

Table 3.24 – Calculation form of Accountability and Reliability indexes: Deep seated landslides for LI#1 for the previous lithological map.

	A	B	C	D	E	F	G
1	Previous Lithology classes	Area (m2)	Deep seated landslides area (m2)	"C"/"D"	"C" values to be used	ACC	RLB
2	Aluvium and sand dunes (Holocene)	19376170	5700	0.000			
3	Sands (Pliocene)	1832444	1250	0.001			
4	Sandstones, claystones and limestones (Miocene)	43777	0	0.000			
5	Sandstones and claystones (lower and middle Miocene)	1353234	825	0.001			
6	Sandstones and claystones (Cretaceous)	4906542	5950	0.001			
7	Sandstones and claystones (upper Jurassic)	242466538	2198475	0.009*	2198475		
8	Marls, sandstones and claystones (upper Jurassic)	122573	0	0.000			
9	Limestones and claystones (upper Jurassic)	1142319	0	0.000			
10	Limestones and marls (middle and upper Jurassic)	1467536	4950	0.003			
11	Dolerite	3181253	136050	0.043*	136050		
12	**SUM**	275892387	2353200		2334525		
13				"C12"/"B12"= **0.009**		"E12"/"C12" *100= 99.21	"E12"/("B7" +"B11") *100= 0.95

* Green values are the values that are greater or equal than the value on E13 cell. Those values indicate whose values on C and B column will be inserted for Accountability and Reliability scores.

Table 3.25 – Calculation form of Accountability and Reliability indexes: Deep seated landslides for LI#1 for the detailed lithological map.

	A	B	C	D	E	F	G
1	Detailed Lithology classes	Area (m2)	Deep seated landslides area (m2)	"C"/"D"	"C" values to be used	ACC	RLB
2	Alluvium and sand dunes (Holocene)	18786916	0	0.000			
3	Sands (Pliocene)	1960624	1250	0.001			
4	Sandstones, claystones and limestones (Miocene)	43777	0	0.000			
5	Sandstone dominated complexes (lower and middle Miocene)	683297	0	0.000			
6	Shale dominated complexes (lower and middle Miocene)	669937	825	0.001			
7	Sandstone dominated complexes (Cretaceous)	1465099	750	0.001			
8	Shale dominated complexes (Cretaceous)	3441443	5200	0.002			
9	Sandstone dominated complexes (upper Jurassic)	79310723	71525	0.001			
10	Shale dominated complexes (upper Jurassic)	163608615	2132650	0.013*	2132650		
11	Marls, sandstones and claystones (upper Jurassic)	122573	0	0.000			
12	Limestones and claystones (upper Jurassic)	1142319	0	0.000			
13	Limestones and marls (middle and upper Jurassic)	1467536	4950	0.003			
14	Dolerite	3189527	136050	0.043*	136050		
15	**SUM**	275892387	2353200		2268700		
16				C12/B12= **0.009**		"E15"/"C15" *100= 96.41	"E15"/("B10" +"B14") *100= 1.36

* Green values are the values that are greater or equal than the value on E16 cell. Those values indicate whose values on C and B column will be inserted for Accountability and Reliability scores.

Having a landslide distribution of 2198475m^2 on the sandstones and claystones dominated complexes and 136050m2 on the dolerite for the previous lithological map the accountability value will correspond to 99.21% (Table 3.24). However, after a lithological detailing it is possible to settle that only the soft rocks part of the sandstones and claystones dominated complexes will be important for the accountability scores of the detailed lithological map (Table 3.25). Since there is some deep-seated landslide occurrence on the detailed sandstones dominated complexes class, the accountability score will obviously decrease (96.41%).

Through this analysis is still possible to assume that the previous lithological map would be error-prone when assessing landslide susceptibility because, according to the

calculating method of accountability index, the sandstones and claystones dominated complexes will have a great importance weight for accountability scores (Tables 3.24 and Tables 1 and 3 in appendix), however this fact does not correspond to reality because according with the accountability scores calculated for the detailed lithological map only the soft rock part of the sandstones and claystones dominated complexes (shale dominated complexes) along with dolerite will have a great importance weights (Tables 26 and Tables 4 and 6 in appendix).

When analyzing together the two landslides types (the sum between shallow and deep-seated landslides) the situation is similar to the deep-seated landslides, since the landslides on the study area are mostly deep-seated landslide type (Tables 15, 16, 17, 18, 19, 20, 21 and 22 in appendix).

The Reliability scores, in almost every cases, seemed to be higher for the detailed lithological map than for the previous lithological map, which ensures quality to the detailed lithological map. However, it should be noted that the LI#3 has less landslides occurrence than the other landslides inventories and with a little difference of landslides distribution among the lithological classes which can explain the differences observed on the LI#3 for the deep-seated and whole landslides comparing with other landslides inventories for the same type of landslides. Reliability scores seemed to be lower on the detailed lithological map but, on the other hand, accountability scores seemed to be much higher on the detailed lithological map than on the previous lithological map (Table 3.22 and 3.23). Regarding the other LIs the classes that seemed to be important according with the accountability and Reliability calculating methods were dolerite and sandstones and claystones dominated complexes for the previous lithological map (Tables 3.24 and Tables A1.1, A1.3, A1.15, A1.16 and A1.18 in Appendix 1) and dolerite and shale dominated complexes for the detailed lithological map for both deep-seated and whole landslides (Tables 3.25 and Table A1.4, A1.6, A1.19, A1.20 and A1.22 in Appendix 1), however, on the LI#3, according to the previous lithological map, only one lithological class (dolerite) seemed to be important regarding the accountability and Reliability calculating methods (Tables A1.2 and A1.17 in Appendix 1) but, when detailing the lithological map, beyond the dolerite lithological class, another lithological class (shale

dominated complexes) seemed to be also important, although with a lower importance weight comparing with other LIs (Tables A1.5 and A1.21 in Appendix 1). This fact explains the increase of the accountability scores and the decrease of the Reliability scores for the detailed lithological map, which means that despite having a lower average of landslides density occurrence on the detailed lithological classes than on the previous lithological classes, the detailed lithological map has a better discriminating power, i.e. is more capable of separating relevant classes for landslide occurrence than the previous lithological map for the LI#3.

Regarding the shallow landslides (Table 3.22) it is possible to see that the detailed lithological map is much more consistent regardless the period of landslides. This is because there are no shallow landslide occurrences on the resistance sandstones dominated complexes. As it is shown on Table 3.22, in all cases the accountability and Reliability scores are always higher for the detailed lithological map than for previous lithological map.

Generally, the lithological map with the highest accountability and Reliability mean values over the four landslides inventories seemed to be always the detailed lithological map, which means that regardless the landslide period and typology, the detailed lithological map seemed to have much relevant classes for the landslide susceptibility analysis than the previous lithological map (Tables 3.21, 3.22 and 3.23).

CHAPTER 4

RELATIONSHIPS BETWEEN THE MORPHO-STRUCTURAL SETTINGS AND THE LANDSLIDES PATTERN AND DISTRIBUTION

4 RELATIONSHIPS BETWEEN THE MORPHO-STRUCTURAL SETTINGS AND THE LANDSLIDES PATTERN AND DISTRIBUTION

This chapter aims to acquire more detailed geomorphological data for the study area. Thereby, it is presented here, a methodology for morpho-structural modeling. Further, it is aimed to determine the relationships between the morpho-structural setting given by the bedding attitude (BA) of the slopes and the distribution and pattern of landslides existing in the study area.

In geomorphologic applications it is known that the BA information is useful to define such structural and also geological setting of an area and, thereby, to determine landslide susceptibility (Guzzetti *et. al*., 2006). BA can be defined as the spatial arrangement of the bedding planes, and is commonly expressed by dip direction and dip angle (inclination) values (Marchesini *et al*., 2011).

Different methods for quantitative spatial interpolation of BA data have been proposed (e.g., de Kemp, 1998; Meentemeyer *et al*., 2000; Günther 2003; Grelle *et al*., 2011) in order to assess the conformity between topographic and geological surfaces, producing spatially distributed fields of geometric alignment between topography and the orientation of geologic bedding planes (topographic/bedding-plane intersection angle) (Meentemeyer *et al*., 2000). BA measurements can be obtained during structural surveys through field work, or through the interpretation of aerial photographs (API). The first method provides quantitative local (point) measures of BA that may not be representative of the regional structural setting. The second method provides semi-quantitative BA information, representative of a general geological and structural arrangement, suitable for medium to small scale assessments (Marchesini *et al*., 2011).
Due to the already investigated relationships between morpho-structural data, hydrological conditions and landslide spatial distribution (Santangelo *et al*., 2012), it becomes important to understand those relationships within the study area in order to assess how it can affect the landslide susceptibility.

As in Chapter 3, this work reveals to be important in order to enable more detailed and reliable data versus the previous lithological data already existing (at a 1:50,000 scale) which proved to be very homogeneous and constant throughout the study area producing low quality results when assessing landslide susceptibility.

Typically, the relationship of the topographic/bedding and plane intersection angle is known only at point locations where strike and dip have been determined by GIS means or in the field. Although this relationship has been mapped (e.g., Eaton, 1986), it has proven so monotonous to do so that studies requiring such data are limited to specific slopes or theoretical scenarios (e.g., Freeze and Cherry, 1979; Selby, 1993). The availability of GIS scripting (in order to produce BA quantitative data through qualitative data), digital elevation models (DEMs) and methods for digital terrain analysis creates an opportunity to characterize these relationships over much larger areas using geologic structure data in combination with DEMs in a spatially distributed framework. DEMs have been used alone (e.g., Chorowicz *et al*., 1991; Ichoku *et al*., 1994) and in combination with satellite imagery (e.g., Morris, 1991; Chorowicz *et al*., 1995) to estimate the strike and dip of bedding planes. However, few work exists, on producing spatially distributed fields that represent the degree of conformity between topographic and geological surfaces (Meentemeyer *et al*., 2000). Thus, in this chapter will be purposed and described all the necessary steps for qualitative and quantitative BA data acquisition and a method for producing BA model in order to obtain spatially distributed fields of geometric alignment between topography and the orientation of geologic bedding planes.

Beyond landslides pattern and distribution, the geometric relationships between topography and geologic structure can influence sub-surface drainage (Freeze and Cherry, 1979; Selby, 1993). This is particularly evident where geologic structure is characterized by penetrative discontinuities, such as sedimentary bedding or schistosity (Sander, 1970; Cruden, 1989). As such, the degree of conformity between topographic slope and aspect relative to the strike and dip of bedding planes is often measured in these contexts (e.g. Cruden and Hu, 1996).

Thereby, estimating the morpho-structural settings through the purposed methods in this charter is of most importance because it provides an efficient means for estimating topographic/bedding plane intersection angles over large areas. Resulting surfaces are useful not only for prediction of landslides patterns and distribution, but also for a variety of landscape-scale modeling applications, such as the prediction of potential hillslope failure, hydrologic flow paths, and vegetation patterns (Meentemeyer et. al., 2000).

4.1 Bedding attitude qualitative data acquisition: bedding trace mapping

In order to obtain BA data, which result from the conformity between topographic and geological surfaces, a detailed morpho-structural map, designed by bedding traces (BTs) at 1:10,000 scale was prepared through aerial photographs interpretation (API) dated from 1958 with an acquisition scale of 1:26,000. As on chapter 3, these old aerial photographs were chosen because they correspond to the oldest existing aerial photographs for the complete study area. Therefore they exhibit a much less human occupancy and activity, allowing a better observation of structural and geological settings. BTs are the intersection line between a bedding plane and topography (Fig. 4.1).

Fig. 4.1 – Escarpment of the study area. Black lines delineate bedding traces.

With the BTs data is possible to infer the bedding surface, i.e. the flat surface that locally approximates the bedding plane (green plane in Fig. 4.2). The estimation of the BA is expressed by a dip direction and a dip angle value (black symbol in Fig. 4.2).

The API was initiated in the Research Institute for Hydrogeological Protection in Italy (IRPI- CNR). The stereoscope used in this institute has two zooms (1.5x e 3x), and the great advantage of allowing two persons to observe the elements at the same time, which is very important for teach and learn this technique. After this first experience and due to the unavailability of a two zooms stereoscope (1.5x e 3x), another technique was adopted in order to conclude the BTs map. The technique adopted was carried out using ILWIS 3.3, a GIS software that allows aerial photographs stereoscopy.

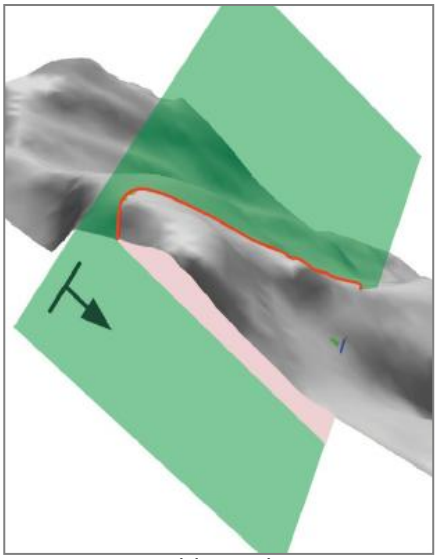

Fig. 4.2 – Bedding plane intersection with topography (Marchesini, et. al., 2012).

As already described in the previous chapter, this technique enables any digital zoom on the aerial photographs without ever losing stereoscopy. Subsequently, with a one zoom stereoscope above the screen monitor it was possible to determine and draw with precision the BTs position on the aerial photographs. BTs can be identified by photographic and morphological elements such as: sub-parallel bands having different color tones in unvegetated areas; the presence of sub-parallel vegetation bands; the repetitive variations in terrain gradient along a slope (hummocky topography); and geomorphological considerations on the asymmetry of a relief (Marchesini *et al.*, 2011).

The frequent existence of hummocky topography along the study area, evidenced by the typical exaggeration of stereoscopic view, reveals a very undulating terrain varying on a series of adjacent slump blocks forms and depressions more or less concentrically aligned in many places of the study area which were also determinant for the BTs drawing. It should be noted that the interpretation of the lithological data for a detailed lithological map (made on the previous charter) and the identification of the morphological structure

used the same key information and in this way both settings seemed to be interrelated. Thereby on the following map (Fig. 4.3) it is possible to observe that the BT position were found to be connected to the transition between hard rocks (sandstone dominated complexes) and weak or soft rocks (shale dominated complexes) (Fig. 3.12 from Chapter 3).

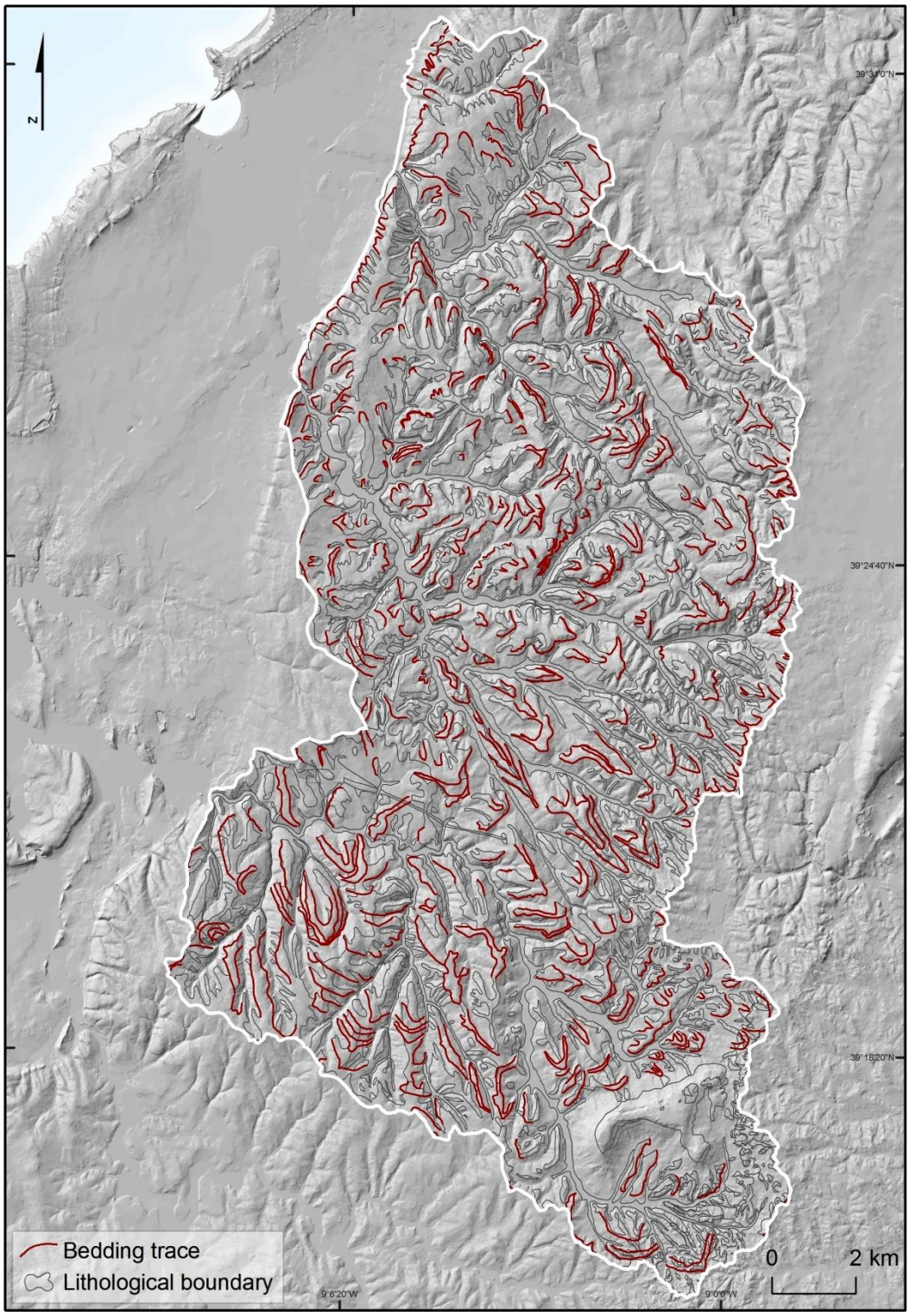

Fig. 4.3 – Bedding trace map.

4.2 Bedding attitude quantitative data acquisition through Geobed GIS scripting

Through API only BA qualitative data are commonly collected. Thus, in order to obtain BA quantitative data a GIS tool using Python scripting (Geobed scripting by Ivan Marchesini (2011) showed in Appendix 2 in *GRASS* GIS environment and *GNU-Linux OS*[4] was used. The requested inputs are a BT layer (BA qualitative data) and a digital elevation model (DEM). At the end of the process the script returns a vector layer of points whose attributes contain information on dip angle, dip direction and associated uncertainty (Marchesini *et al*., 2011). The method was performed using 662 BTs (Fig. 4.3) and a 5 meters resolution DEM (Fig. 1.4, Chapter 1).

The *Geobed GIS* script (Appendix 2) is processed by five steps, which are replicated for each BT. First, the bedding trace is draped on the DEM, becoming a 3D line (Fig. 4.4 a). Second, a three-dimensional segment, joining the two end nodes of the bedding trace, is created forming a 3D polygon (Fig. 4.4 b). Third, the 3D polygon boundary is sampled to obtain a sequence of regularly spaced points. Point spacing depends on the resolution of the DEM. Finally, a three-dimensional delaunay triangulation[5] is performed. The result is a nearly flat surface corresponding to the bedding surface (BS) (Fig.4.4 c and Fig. 4.5 a).

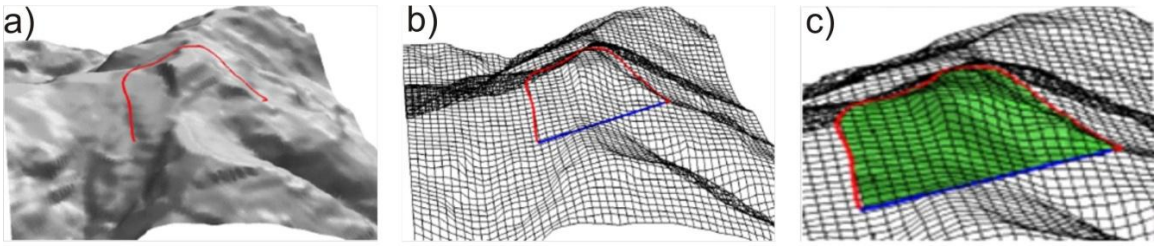

Fig. 4.4 – a) Bedding trace draped on the DEM; b) bedding trace nodes joining; c) bedding surface (BS) is drawn in green. Extracted from Marchesini *et al*. (2011).

The fourth step consists in calculating the BS slope (Fig. 4.5:b) and aspect raster maps (Fig. 4.5:c).

[4] Operation system.

[5] Delaunay triangulation for a set number of points (P) in a plane is a triangulation DT(P) which requires that no point in P is inside the circumcircle of any triangle in DT(P). Delaunay triangulations maximize the minimum angle of all the angles of the triangles in the triangulation; they tend to avoid skinny triangles (Berg *et al*., 2008).

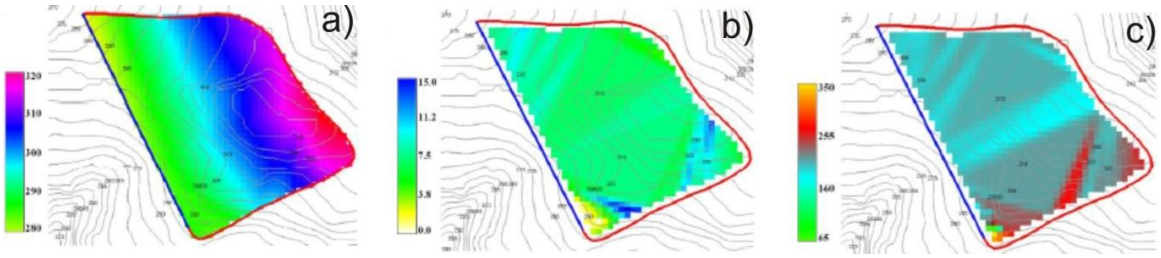

Fig. 4.5 – a) BS elevation map (meters a.s.l.); b) BS slope map (degrees); c) BS aspect map (degrees). Extracted from Marchesini *et al*., (2011).

Finally, in the fifth step are estimated the mean values for the dip angle and the dip direction of the BS. The average BS inclination is the median of the slope map values. Then, the standard deviation (a measure of uncertainty) of the slope map is calculated (Marchesini *et al*., 2011).

Average BS dip direction is calculated following the method proposed by Davis (1973). Sine and cosine of the aspect map are calculated. Then, the average aspect (dip direction) of the BS is determined using mean sine and cosine values. The statistical spread of the dip direction is calculated with two methods. In the first method, circular variance (V) is calculated as:

$$V = 1 - \frac{R_a}{n} \tag{6.1}$$

where n is the number of cells of the BS aspect map, and R_a is the modulus of the resultant vector of the unitary vectors of each aspect map cell. V can take values in the ranging from 0 to 1. Low V values indicate a nearly flat surface, and higher values indicate a steep surface (Davis, 1973; Nichols, 2009) (Fig. 4.6) (Marchesini *et al*., 2011).

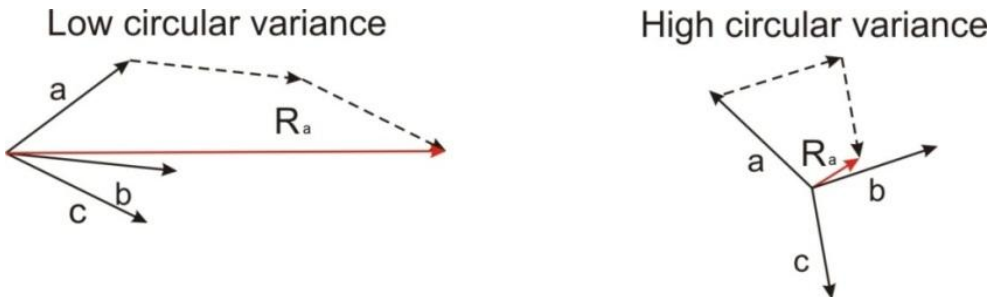

Fig. 4.6 – Circular variance: $\boldsymbol{n = 3}$; $|\boldsymbol{a}| = |\boldsymbol{b}| = |\boldsymbol{c}| = \boldsymbol{1}$.

The second method estimates the angular standard deviation of the aspect map as (Butler, 1992):

$$A_{sd} = \frac{1}{(n-1)} \sum_{i=1}^{n} \Delta_i^2 \tag{6.2}$$

where, Δ_i is the angle between the aspect of the *i*-th cell and the average aspect, and n is the number of the aspect map cells.

All the values (i.e. median slope, slope standard deviation, average aspect, circular variance, angular standard deviation) are assigned to a BA point-vector layer. Each point in the layer is the centroid of the bounding box of the corresponding BT (Marchesini *et al.*, 2011) (Fig. 4.7).

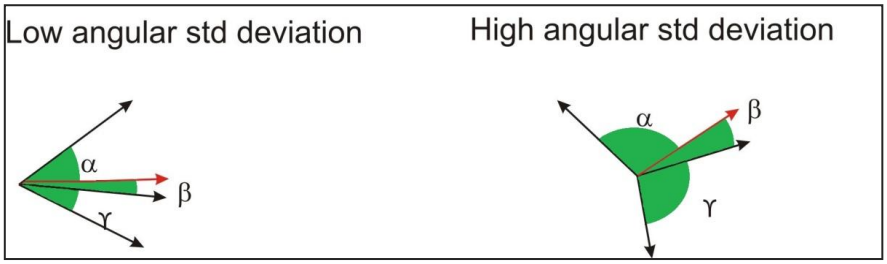

Fig. 4.7 – Angular standard deviation: $\boldsymbol{n = 3}$; $\Delta_1 = \boldsymbol{\alpha}, \Delta_2 = \boldsymbol{\beta}, \Delta_3 = \boldsymbol{\gamma}$.

Through the process above described a point vector data with 662 BA points was created, corresponding to the centroid of each bedding surface, containing important bedding attitude data such as dip angle, dip direction, and associated uncertainty. Once the Geobed script is run, performing an interpolation, it is necessary to make a buffer containing bedding trace data around the study area in order to avoid no data values. However, the figures below only show the results within the study area (Fig. 4.8 and Table 4.1).

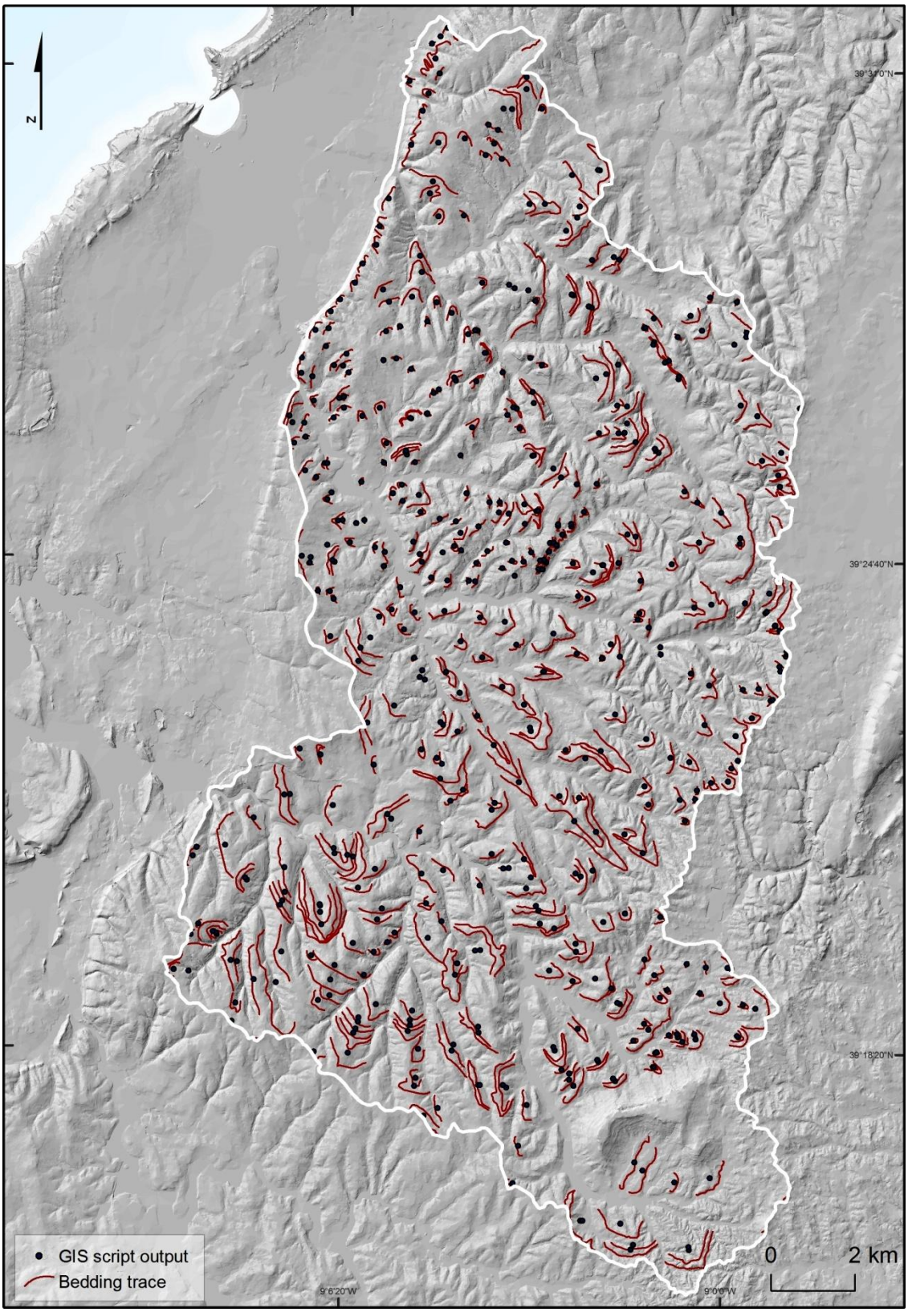

Fig. 4.8 – Geobed scripting output.

By running the Geobed script several times it was possible to understand that shorter BTs improve the results. In this sense and in order to avoid interpolation errors it was decided to shorten the BTs that were initially too high.

As it is shown in Table 1 for each vector point a bedding attitude data is associated. The Geobed script returns a database contemplated by some field values such as, "cat", "value", "slopestdev", "slope50", "invslope50", "aspect", "azimuth", "angstddev" and "circvar". The "cat" field value is the identify BT value which is unique for each point/row. The "value" field is always assigned with value one for every point/row, because it means the BT presence. The "slope50" corresponds to the dip angle data and "azimuth" corresponds to the dip direction data. The "invslope50" field value corresponds to the calculation of: "90" – "slope50"; and it is the median of *i*-th distribution of the slope cells that represents the plain passing through the bedding trace. The "aspect" field value is the common aspect data derived only from the DEM which displays the cardinal direction of the terrain slope surface .

The "slopestdev" field value is the slope standard deviation which consists on the uncertainly data calculated for dip angle. The "angstddev" field value is the angular standard deviation uncertainty and "circvar" is the circular variance uncertainty data on the Geobed script database output (Table 4.1).

Table 4.1 – Extract of the Geobed script database output.

cat	value	slopestdev	slope50	invslope50	aspect	circvar	angstddev
674	1.00	1.63	4.00	86.00	197.00	0.13	30.32
676	1.00	2.69	3.00	87.00	131.00	0.30	49.11
677	1.00	2.87	17.00	73.00	351.00	0.01	9.69
678	1.00	2.71	21.00	69.00	347.00	0.02	10.18
…	…	…	…	…	…	…	…

4.2.1 Analysis and correction of probable bedding attitude errors

According to the angular standard deviation field value given by the Geobed script database output ("angstddev" shown on the Table 4.1) it is possible to assess the uncertainty of dip direction associated with each BA point. For better observation the BA points were converted to BA symbols as shown on the Fig. 4.9 The orientation of BA symbols is accorded to the dip direction.

The BA symbols were classified according to low (0º to 16º), medium (16º to 30º) and high (30º to 96º) dip direction uncertainty. Therefore, it resulted on 208 BA symbols (31.4% of the total BA symbols) with low dip direction uncertainty (green BA symbols shown on the map), 147 BA symbols (22.2% of the total BA symbols) with medium uncertainty (yellow BA symbols shown on the map) and 307 BA symbols (46.4% of the total BA symbols) with high dip direction uncertainty.

High values of angular standard deviation can be related to: sub-horizontal strata; the positioning errors when transferring BTs from the aerial photographs to the GIS dataset; identification errors (it wasn't a bedding trace); and/or to presence of folds errors. However, It is important to underline that, high values of uncertainty of angular standard deviation are frequently related to sub-horizontal strata (low inclination angle) once it is obvious that dip direction is particularly uncertain for sub-horizontal strata (Marchesini *et al.*, 2011).

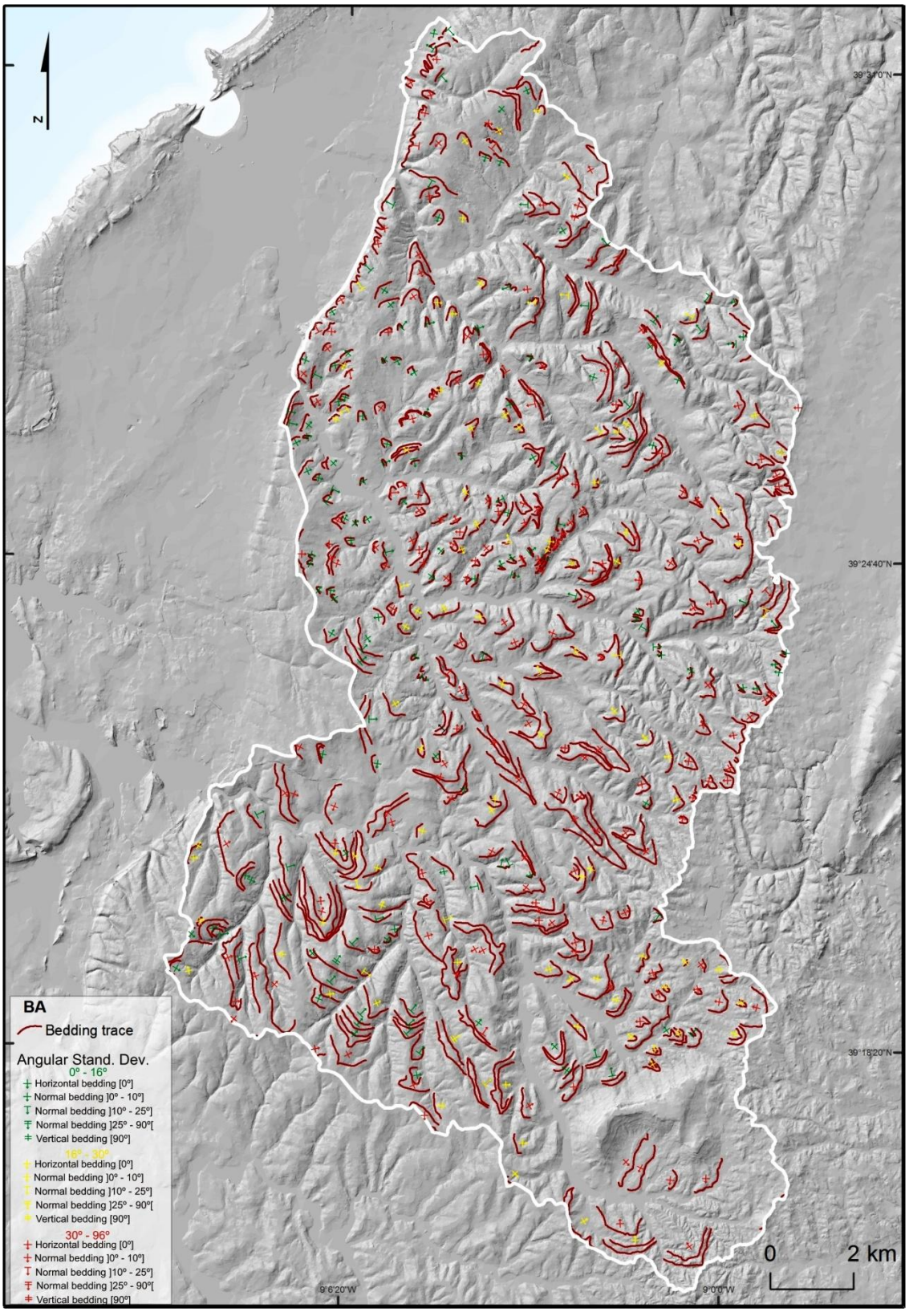

Fig. 4.9 – Dip direction angular variance.

Based on extensive field observation it can be considered that, in the study area, most of the high values of angular standard deviation are more related to the occurrence of sub-horizontal strata than with interpolator errors. It is possible to reinforce this affirmation according to the Fig. 4.10.

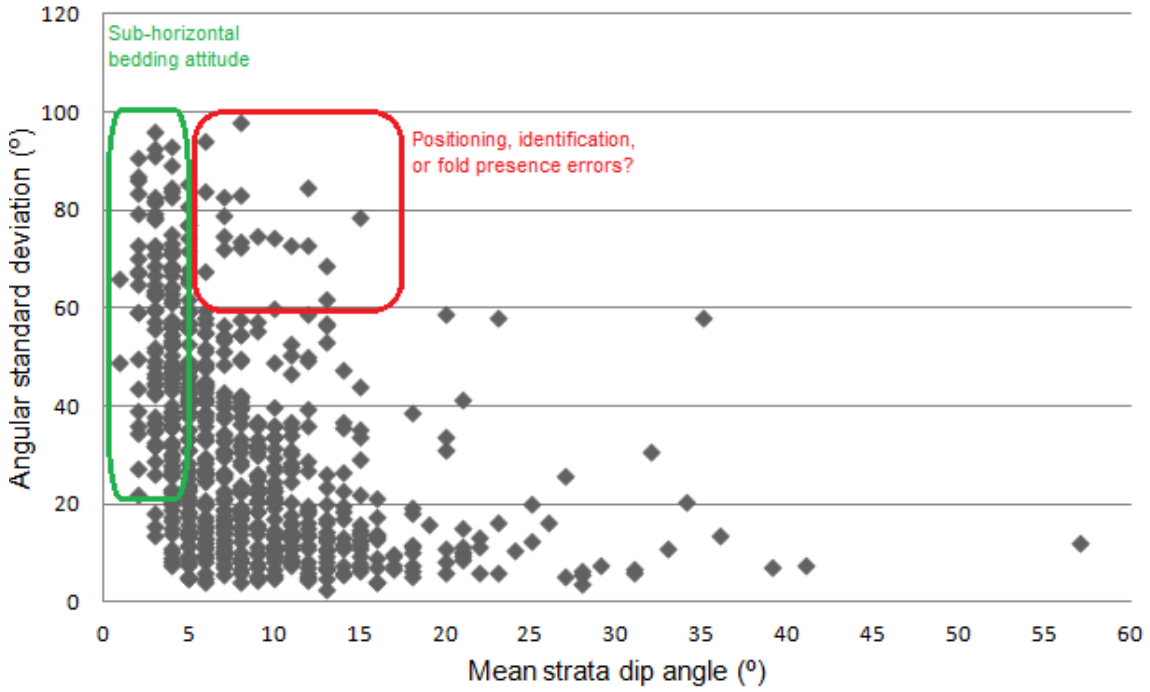

Fig. 4.10 – Dip direction angular variance graph: with all BA data (within and outside the study area).

As shown in Fig. 4.10, most of the high values of angular standard deviation are more related to the occurrence of sub-horizontal strata (low dip angle values) and just 19 BA points are related to the positioning, identification and/or presence of folds errors. The value of 19 BA points is achieved through the natural break shown in Fig. 4.10. Those BA errors were excluded, i.e., all BA points where strata is not relatively flat (> 6) and with high values of angular standard deviation (dip direction uncertainty) (>60) which correspond to probable errors already mentioned above were, therefore, not considered for further BA analysis and modeling (Fig. 4.11).

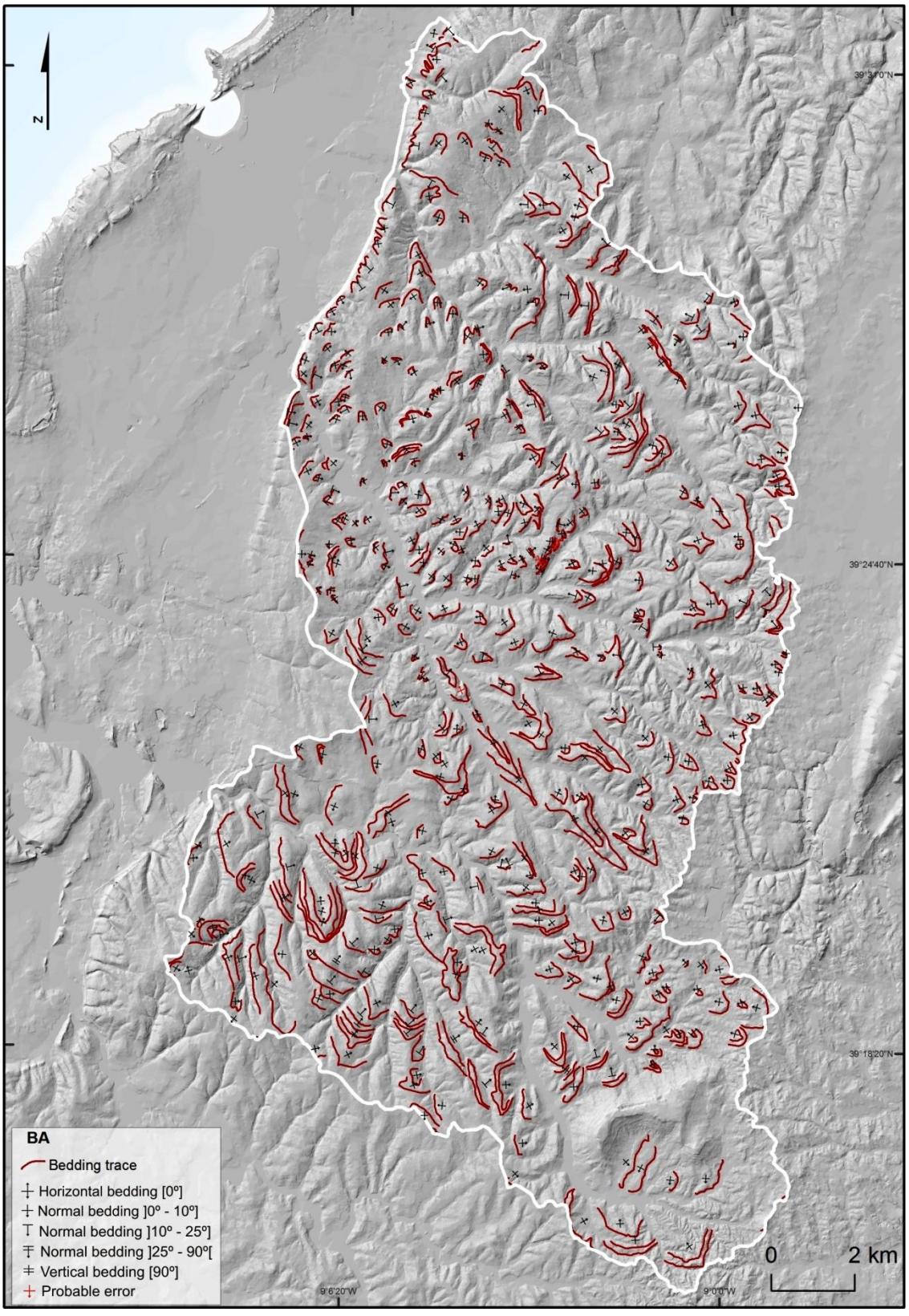

Fig. 4.11 – Bedding attitude in the study area. BAs can be represented by means of oriented symbols (according to dip direction), and the inclination value. BA probable errors are drawn in red.

Noteworthy that Fig. 4.11 only shows the respective data within the study area, i.e. some points corresponding to probable errors were located outside the study area (the already mentioned buffer of BA data which surrounded the study area avoiding no data on the study area bordering) and therefore are not visible on the map of Fig. 4.11. Further all BA points that lied on the condition above described, which corresponded to the probable errors, were removed.

4.2.2 Resulting Morpho-structural map

Through the acquisition of BTs and BA quantitative data was possible to build a morpho-structural map (Fig. 4.12). Based on stereoscopic interpretation of aerial photographs and the results from Geobed script it was further possible to identify syncline and anticline areas and also probable faults (Fig. 4.12).

As it is shown in the Fig. 4.12 the compressive deformation produced an anticline evidence on the NW part of the study area and another on the central West part of the study area, both corresponding to two prominent reliefs. A syncline evidence, associated with thrusts, is also identifiable on the SW sector part of the study area. Some faults were likewise inferred on the study area. In some localities along the higher reliefs was possible to identified triangular facets through API, this geomorphic feature characteristic highlights the existence of probable normal fault activity (e.g., Ganas et. al, 2005; Menges, 1990; Leeder and Jackson, 1993; Jackson and Leeder, 1994). Other geomorphic evidences identified on aerial photographs such as range-front escarpments, large slope angle values, V-shaped valleys, were also crucial for inferred some faults on the study area.

A more detailed analysis shows that some inferred faults, when compared with the detailed lithological data of the study area, were found to be controlled by the relative position of sedimentary and tectonic discontinuities, by the relative abundance of hard versus weak or soft rocks, and by the attitude of permeable and impermeable layers.

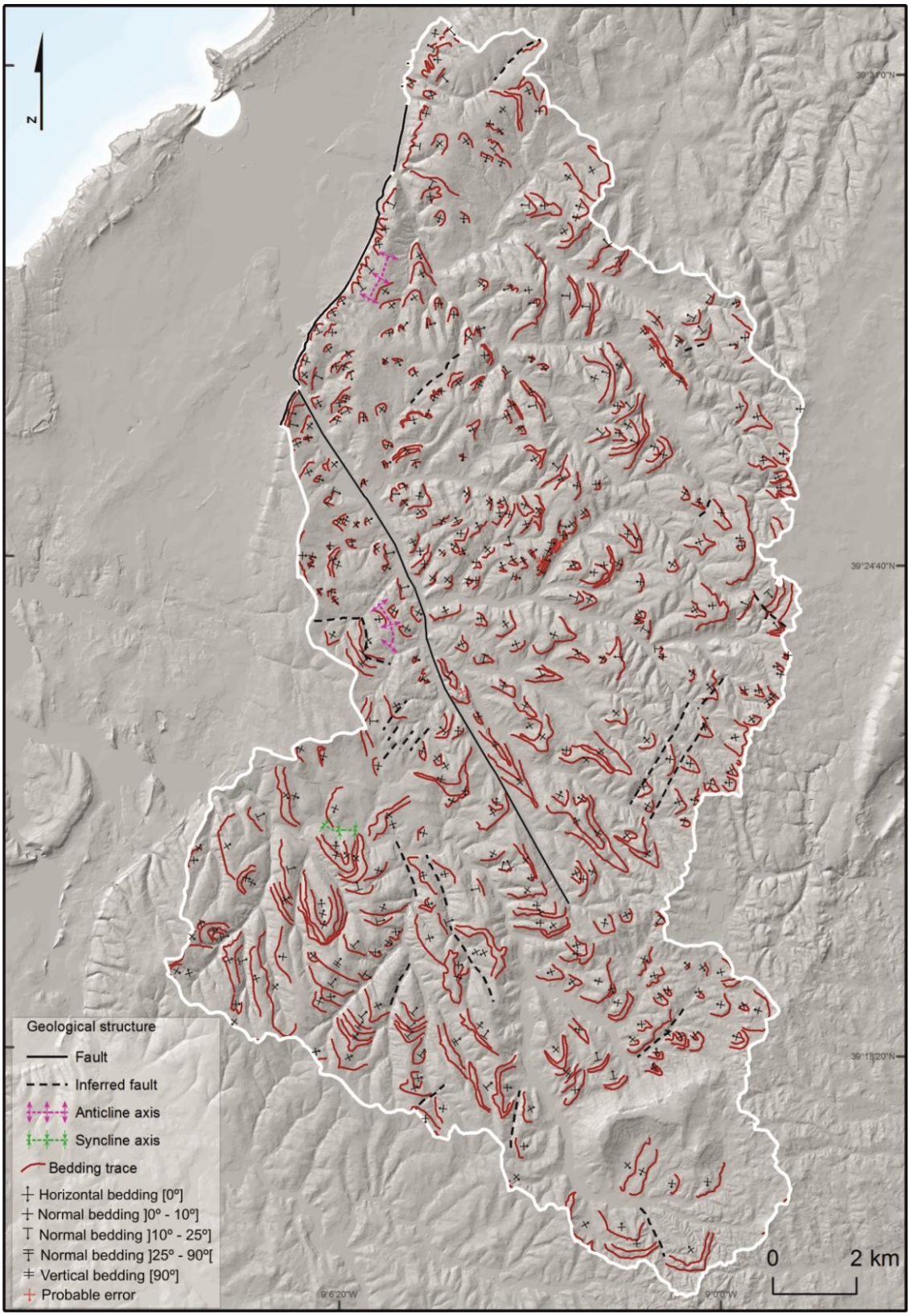

Fig. 4.12 – Morpho-structural map: BAs represented by oriented symbols (according to dip direction), and the inclination value.

4.2.3 Bedding attitude spatial interpolation: selection of the statistical interpolator through modeling and validation

Once having the BA quantitative data it is possible to build the respective models of dip direction and dip angle through statistical interpolators.

According to some authors (e.g., Meentemeyer and Moody 2000, Bonham-Carter, 1994; Burrough and McDonnell, 1998; Isaaks and Srivastava, 1989), Kriging is frequently used to spatially interpolate point measurements in numerous Earth system science applications. However, in this case, to interpolate spatially continuous fields of dip direction and dip angle from point measurements of strike and dip, many interpolation algorithms such as Inverse Distance Weighted (IDW), regularized Spline, Spline with tension, Ordinary Kriging and Universal Kriging have been tested in order to compare the accuracy of different interpolation methods and to select the one that best fits the purpose of each BA data (dip direction and dip angle).

Unlike the dip angle, interpolating dip direction data revealed to be problematic because the interpolation algorithms do not consider the circumferential distribution of the given angular dip direction distribution, and in this sense it interpolates data in a totally wrong manner (Fig. 4.13). Thus, values between 350º and 10º will always be inadequately interpolated (Fig. 4.13).

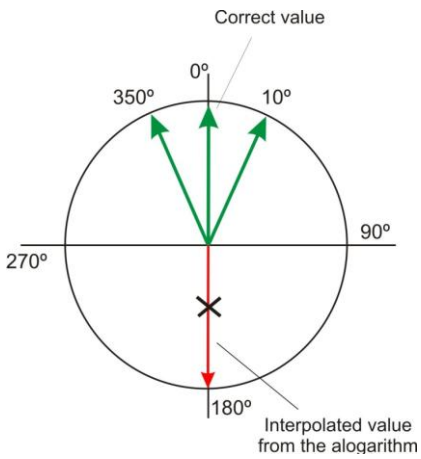

Fig. 4.13 – Angular interpolation data.

The interpolation problem of spatial dip direction data has been investigated in previous studies (e.g. Meentmeyer and Moody, 2000; de Kemp, 1998). However, according to de Kemp (1998), there are a way to overcome this problem without taking the risk of being wrongly interpolated. The method consists in convert angular values of dip direction data into sine and cosine values.

The conversation process of angular dip direction values to sine and cosine dip direction values were carried out using Raster Calculator tools from ArcGis software. It is noteworthy that this software only calculates radians values, so in order to convert properly, the angular values were first converted to radian values (multiplying by 0.0174532925) and then converted into sine and cosine values.

Once the aim, in this phase of the study, is to select the interpolation algorithm that best fits dip direction and dip angle data, was performed a random separation of the BA points into two groups. One group containing 75% of the total BA points, to modulate dip direction (resulting a continuous sine and cosine raster maps) and dip angle raster maps, and a second one, containing 25% of the total BA points, for validating the results (sine, cosine and dip angle raster maps). This random separation was performed on the STATISTICA software and the further interpolation methods were made through *Spatial analyst* tools from ArcGis software.

Regarding the dip angle map it is important to note that the minimum value founded on the BA data ("slope50" field value on the Table 4.1) is 1º, and the maximum value is 57º. Sometimes the interpolation algorithms surpassed the value 57º as well as bellowed the value 1º. In order to avoid such situation a condition was implement in Raster Calculator tools of ArcGis software, given value 1º to the interpolated values below 1º and 57º to the interpolated values above 57º.

Once achieved the sine, cosine and dip angle maps the next step consisted in obtaining the root mean square deviation (RMSE) associated to each interpolation algorithm for the three BA maps, which was obtained through the differences registered between the raster maps and the BA points selected for validation (those 25% of the total BA points).

To accomplish this procedure was used the *Spatial Analyst* tools from *ArcGis* software, where was possible to extract the values from the raster sine, cosine and dip angle maps into the validating BA points database.

Among all the interpolation algorithms tested, the one that best fitted the dip direction cosine, dip direction sine and dip angle maps was the Gaussian ordinary kriging (Table 4.2, 4.3, 4.4 and 4.5).

Table 4.2 – Dip direction cosine uncertainty interpolated by 10 interpolation algorithms.

Cos (dip direction)										
	IDW	**Regularized Spline**	**Spline with tension**	**spherical Ordinary Kriging**	**Circular Ordinary Kriging**	**Exponential Ordinary Kriging**	**Gaussian Ordinary Kriging**	**Linear Ordinary Kriging**	**Linear Universal kriging**	**Quadratic Universal kriging**
mean	0.51	0.70	0.54	0.52	0.52	0.52	0.52	0.52	0.52	0.51
standard deviation	0.34	0.55	0.42	0.34	0.34	0.34	0.34	0.34	0.36	0.38

Table 4.3 – Dip direction sine uncertainty interpolated by 10 interpolation algorithms.

Sin (dip direction)										
	IDW	**Regularized Spline**	**Spline with tension**	**spherical Ordinary Kriging**	**Circular Ordinary Kriging**	**Exponential Ordinary Kriging**	**Gaussian Ordinary Kriging**	**Linear Ordinary Kriging**	**Linear Universal kriging**	**Quadratic Universal kriging**
mean	0.50	0.56	0.48	0.50	0.50	0.49	0.50	0.50	0.52	0.51
standard deviation	0.37	0.50	0.44	0.37	0.37	0.36	0.37	0.36	0.39	0.49

Table 4.4 – Dip angle uncertainty interpolated by 10 interpolation algorithms.

Dip angle										
	IDW	**Regularized Spline**	**Spline with tension**	**spherical Ordinary Kriging**	**Circular Ordinary Kriging**	**Exponential Ordinary Kriging**	**Gaussian Ordinary Kriging**	**Linear Ordinary Kriging**	**Linear Universal kriging**	**Quadratic Universal kriging**
mean	4.05	6.00	5.27	3.99	4.00	3.98	3.78	4.01	4.09	4.15
standard deviation	3.71	6.21	5.87	3.67	3.67	3.66	3.49	3.68	3.87	4.04

Table 4.5 – Mean of dip direction cosine, dip direction sine and dip angle uncertainty.

	IDW	**Regularized Spline**	**Spline with tension**	**spherical Ordinary Kriging**	**Circular Ordinary Kriging**	**Exponential Ordinary Kriging**	**Gaussian Ordina-ry Kriging**	**Linear Ordinary Kriging**	**Linear Universal kriging**	**Quadratic Universal kriging**
General mean of mean	1.69	2.42	2.10	1.67	1.67	1.66	**1.60**	1.67	1.71	1.73

According to the Tables 4.2, 4.3 and 4.4 the results given by the Gaussian ordinary kriging for dip direction cosine and dip angle have always the lowest uncertainty (lower mean values) and lowest standard deviation values when comparing to others interpolation algorithms. Dip direction sine data seemed to be performed a little bit better when using the exponential Ordinary Kriging method, however, it does not make much sense using different Ordinary Kriging methods for the same data type, so through the general mean of the mean (Table 4.5) of each BA data was possible to establish that the best interpolation algorithm for this specific data and for the study area, is the Gaussian Ordinary Kriging. After knowing that the Gaussian Ordinary Kriging is the best interpolation algorithm, the dip angle and the cosine and sine maps were again calculated using the 100% of the total BA points in order to increase the quality of the final dip angle and the cosine and sine maps.

According to the resulting dip angle raster map, the lithological strata are generally slightly inclined, however, it is possible to notice some tenuous variation across the study area (Fig. 4.14).

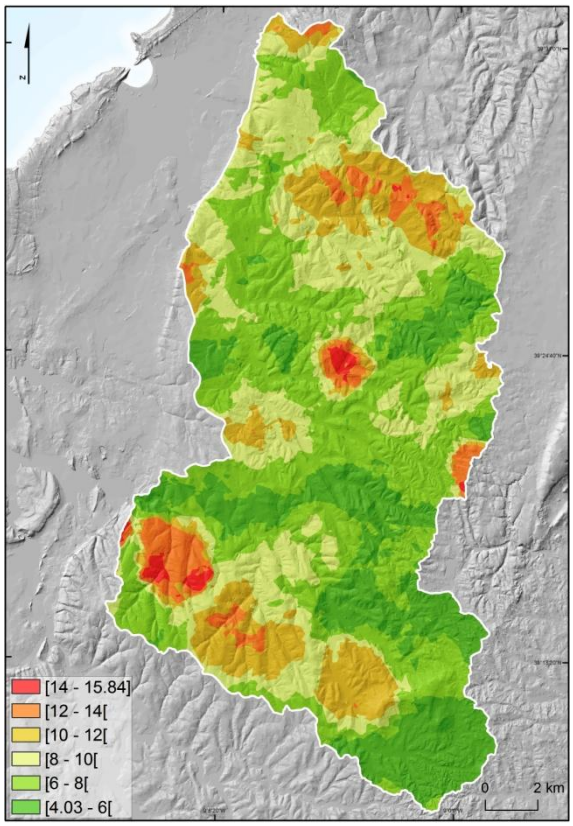

Fig. 4.14 – Dip angle map.

The dip direction map was obtained from the cosine and sine map according to a condition implemented on Raster Calculator tools from ArcGis software. Thus, the rules to achieve the final dip direction map (Fig. 4.15) were: 1) For the sine and cosine of the dip direction higher than zero was given the value 90º subtracting by the inverse of the cosine of the dip direction; 2) For the sine of the dip direction higher than zero and the cosine lower than zero was given the inverse of the cosine of the dip direction; 3) For the sine of the dip direction lower than zero and cosine of the dip direction lower than zero was given the value 90º subtracting by the inverse of the cosine of the dip direction; 4) For the sine of the dip direction lower than zero and cosine of the dip direction higher than zero was given the value 360º subtracting by the inverse of the cosine of the dip direction.

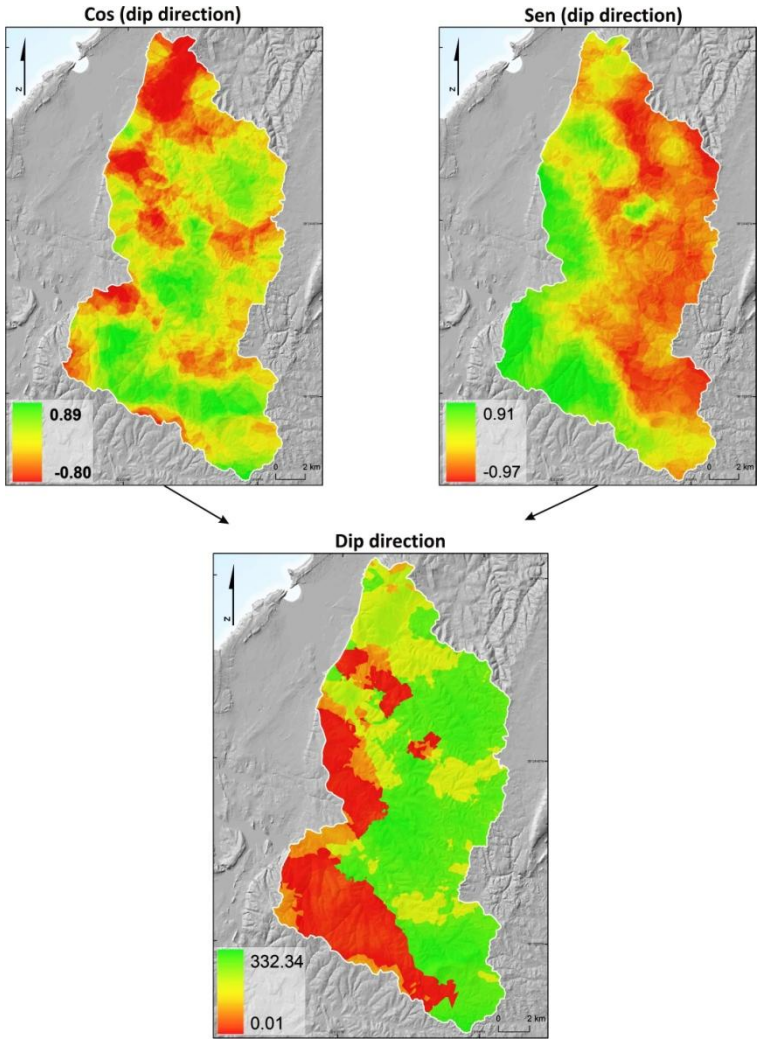

Fig. 4.15 – a) Cosine map of the dip direction. b) Sine map of the dip direction. c) Dip direction resulting map.

In order to get a better visualization of the dip direction tendency along the study area, the dip direction layer (Fig. 4.15:c) was reclassified into 8 aspect classes (North, Northeast, East, Southeast, South, Southwest, West and Northwest) as it is shown on Fig. 4.16.

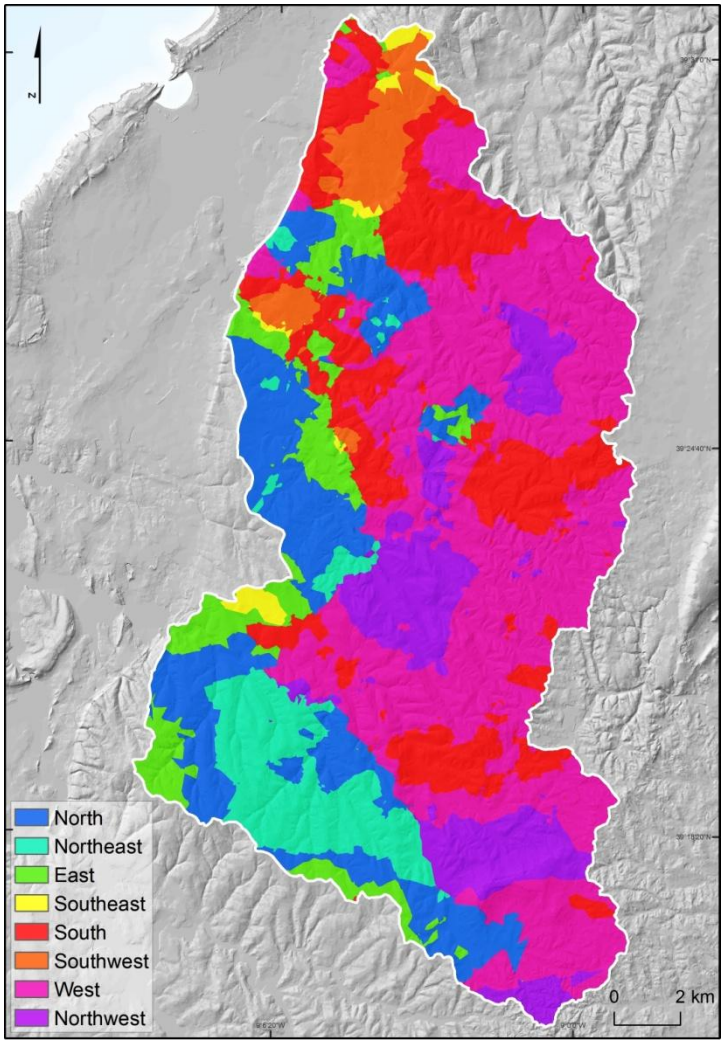

Fig. 4.16 – Dip direction reclassified map.

According to the dip direction map (Fig. 4.16) it is clear that generally the East part of the study area are mostly directed to West and the West part of the study area are mostly directed to North, Northeast and East, establishing two main dip direction blocks. Furthermore these two main blocks evidence the *A-dos-Francos* Syncline already mentioned in the chapter 3.

The conversion of the sine and cosine map into dip direction map on this stage of the study is only for allowing a general visualization of the dip azimuth tendency of the bedding surface and for validating the field work data. However, for further BA modeling the sine and cosine map will be again used.

4.2.4 Data validation trough field work

Obtaining BA validated data through field work revealed to be a very hard task because it is necessary the existence of slopes where the rock crops out and allowing its visualization from many perspectives in order to ensure a proper dip angle and dip direction measurements.

An exhaustive search of locals with those conditions was made through orthophotomaps and field survey, however, few sites were find (Fig. 4.17).

Fig. 4.17 – Slope where rock outcrops and where dip direction (110º) and dip angle (20º) was possible to be properly measured. (Estrada da Navalha e Fraldeu, Óbidos). (Site number 1 in Fig. 4.18).

Due to the difficulty to find places with such conditions, only 15 validated points were possible to obtain. Dip direction was obtained using a compass and dip angle using a compass clinometer. For each point measure the respective coordinates were assign using a *GPS* in order to transpose afterwards all information on GIS environment (Fig. 4.18).

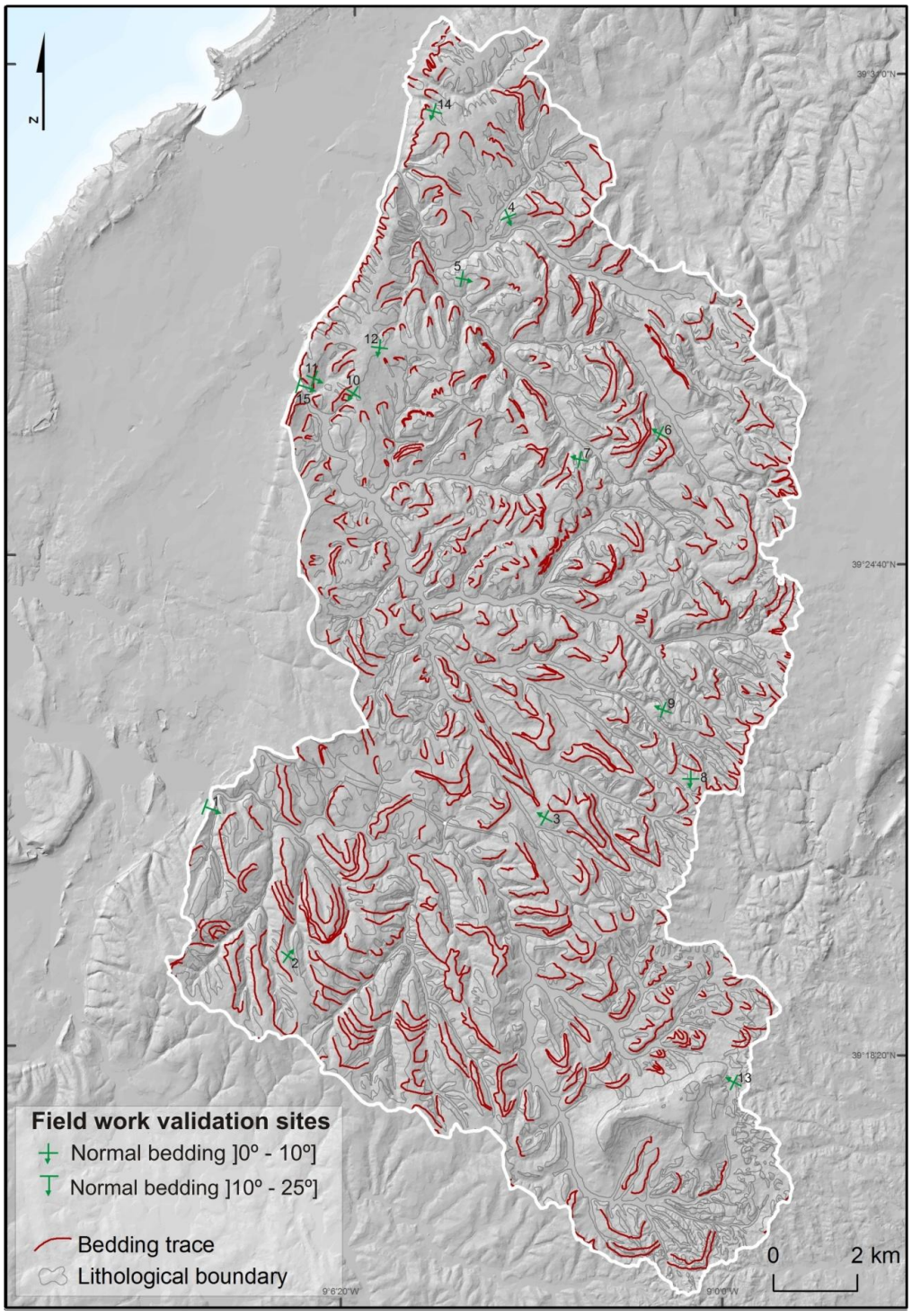

Fig. 4.18 – Morpho-structural data collected by field work. The location sites are labeled.

Despite realizing that only 15 BA points validated through field work are not enough to achieve a consistent validation of the dip direction and the dip angle, an attempt was made in order to understand some of the uncertainty associated to the final dip direction and dip angle map.

Thus, to calculate uncertainty (RMSE) associated to each BA point, first there was the need to extract the BA value from each Raster maps (dip angle and dip direction). This procedure was, again, made through the *Spatial Analyst* tools from *ArcGis* software where it was possible to extract the values from the raster maps and, based on the BA fieldwork values, were possible to calculate the RMSE and the standard deviation.

As it is shown in Table 4.6 the uncertainty associated to dip angle values seemed to be low according to the RMSE value (2.87º) and standard deviation (3.60º). However it has to be noted that there are two BA points validated by fieldwork where the dip angle of strata seemed to be higher than those calculated by Geobed scripting causing an uncertainty discrepancy of 13.81º in one case and 9.16º in another (Table 4.6).

Although with a few BA points obtained by field work it is possible to confirm that in almost every cases, the strata is mostly sub-horizontal as it was already known by the BA quantitative data obtained by Geobed script. The most steepest beddings found on the field were both located on the West part of the study area (sites number 1 and 15 in Fig. 4.18).

Through field work it was possible to realize that, many often, it is quite hard to estimate the azimuth of the soft dip angle beddings, in some cases it was take into account the dip direction from the previous geological map. A pre-conceited idea was already made before going to the field.

Table 4.6 – Confrontation between the acquired BA data on fieldwork and the BA data estimated by the Geobed script.

	Field work		GEOBED model output			
ID*	**Dip angle (º)**	**Dip direction (º)**	**Dip angle (º)**	**Dip direction (º)**	**Dip angle difference (º)**	**Dip direction difference (º)**
1	20	110	6.19	90.66	13.81	19.34
2	10	20	10.16	34.02	0.16	14.02
3	5	300	6.38	297.98	1.38	2.02
4	10	200	8.83	202.74	1.17	2.74
5	10	100	10.10	101.31	0.10	1.31
6	10	300	8.57	295.66	1.43	4.34
7	5	300	8.41	281.54	3.41	18.46
8	5	290	6.42	180.40	1.42	109.60
9	10	290	7.76	289.55	2.24	0.45
10	10	200	9.24	212.09	0.76	12.09
11	10	110	8.84	111.75	1.16	1.75
12	10	200	6.75	187.20	3.25	12.80
13	5	320	6.41	297.65	1.41	22.35
14	10	200	7.85	194.78	2.15	5.22
15	20	110	10.84	107.12	9.16	2.88
			RMSE		2.87º	15.29º
			Standard deviation		3.60º	26.20º

*Field work validation sites can be found on the previous map (Fig. 4.18).

Regarding dip direction data, the estimated uncertainty is 15.29º and the standard deviation is 26.20º. According to the discrepancy between the BA points validated by fieldwork and those calculated by Geobed scripting ("dip direction sub" field value on Table 4.6) is possible to settle that in general the values seemed to be consistent. There is only one value where the uncertainty seemed to be very high (site 8 on Table 4.6 and Fig. 4.18) which contributes for a higher general RMSE value and a higher standard deviation.

While seeing the results from Table 4.6 it must not be forgotten that the BA validated points by field work are a correct measurement of the precise local while the values obtain from the raster maps (of dip direction and dip angle) are obtained through the

mean average of the bedding surface which arises from each bedding trace. According to this fact it can be assumed that both the BA data obtained qualitatively from API and BA data obtained quantitatively from the Geobed script and then spatially interpolated by Gaussian Ordinary Kriging appears to have an acceptable accuracy when validated by BA values obtained by fieldwork.

4.3 Bedding attitude modeling

Once having the dip direction and dip angle continuous maps was now possible to build the BA model. There are different ways of modeling BA data (Meentemeyer and Moody, 2000; Santangelo *et al*., 2012).

In this work it will be presented a computational technique of producing spatially distributed fields of geometric alignment between topography and the orientation of geologic bedding planes (topographic/bedding-plane intersection angle). The computation and digital mapping of the topographic/bedding-plane intersection angle requires the derivation of four spatially distributed variables: slope aspect, topographic slope, dip direction, and dip angle (Fig. 4.19).

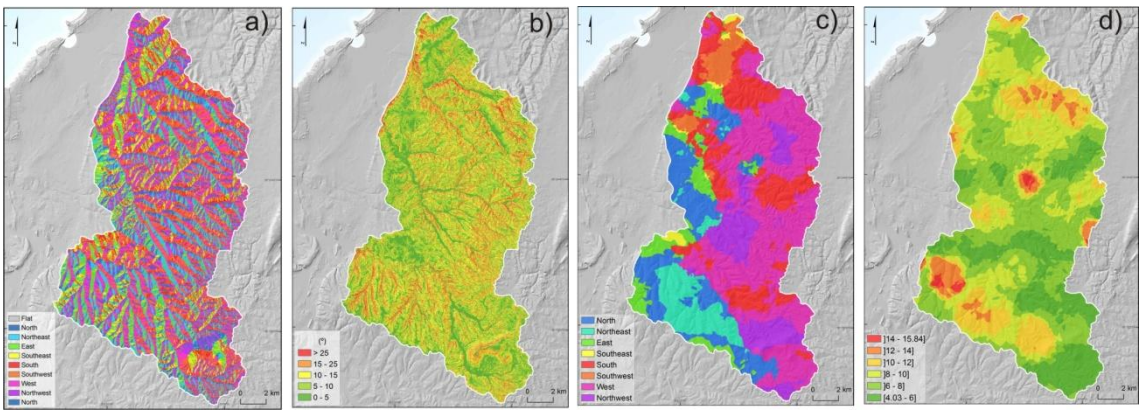

Fig. 4.19 – BA modeling variables: a) slope aspect map; b) topographic slope angle map; c) dip direction map; d) dip angle map.

As the dip direction and dip angle, the topographic slope angle and slope aspect surfaces are derived from the very high resolution (5 m) digital elevation model.

The method used to modeling the BA is called TOBIA[6] categorical model. This model was originally proposed by Meentemeyer and Moody (2000) and it requires two steps. First, slopes are classified into three functional types based on the alignment between the dip direction and slope aspect. Slopes are then partitioned based on the alignment between slope angle and dip angle. The method provide an efficient mean for estimating topographic/bedding plane intersection angles over large areas.

When a rock mass contains a distinct bedding plane the BA models are categorized into three basic classes (Fig. 4.20) (Cruden, Hu, 1996; Cruden, 1988, 1989; Powell, 1875). If the bedding plane dips in the same direction as the slope, the slope is classified as cataclinal. If the bed dips in the direction opposite to the slope, then the slope is classified as anaclinal. When the azimuth of the dip direction is perpendicular to the azimuth of the slope direction the slopes are classified as orthoclinal (not shown in Fig. 4.20).

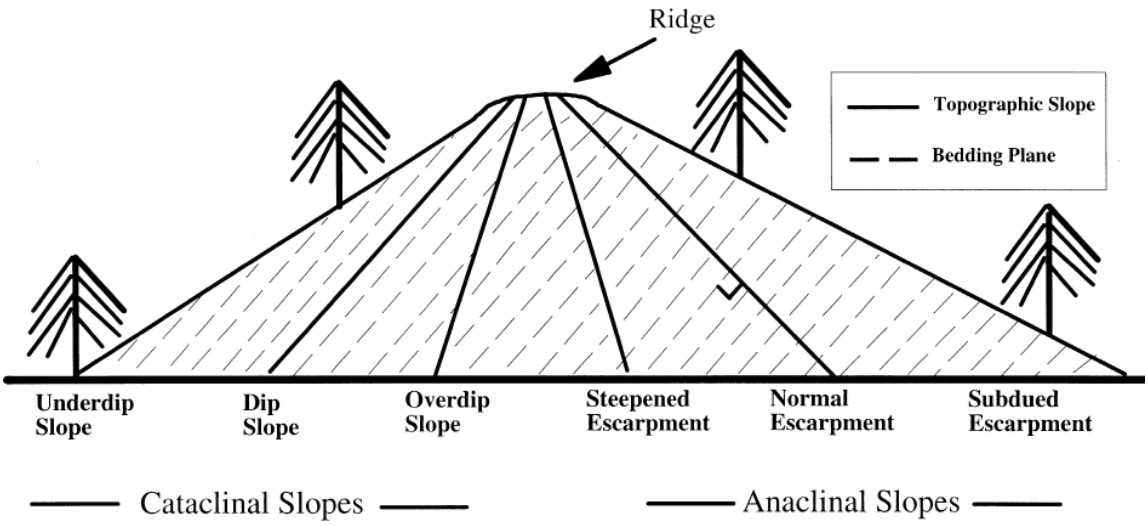

Fig. 4.20 – Classification of alignment between topography and bedding planes. Orthoclinal orientation is not shown. (Meentemeyer and Moody, 2000).

Cataclinal and anaclinal slopes may be further divided based on the alignment between the dip of the bedding plane and topographic slope. Cataclinal slopes that are steeper than the dip of the bedding plane are overdip slopes. Cataclinal slopes that are less steep than the dip of the bedding plane are underdip slopes. Cataclinal slopes that follow the bedding plane are dip slopes. Anaclinal slope divisions include normal escarpments which

[6] Topographic/Bedding-Plane Intersection Angle Model.

are perpendicular to the dip of the bedding plane, steepened escarpments which are steeper than the bedding plane, and subdued escarpments which are less steep than the bedding plane (Meentemeyer and Moody 2000).

4.3.1 TOBIA Categorical modeling

Using variables such as slope angle, slope aspect, dip angle and dip direction, the landscape can be stratified into the slope types discussed above (Table 4.7).

Table 4.7 – Classification of topography relative to strike and dip of bedding planes (Meentemeyer and Moody 2000).

Division	Slope Type	Abbreviation	Orientation
Cataclinal	Overdip	D_o	S> θ
Cataclinal	Underdip	D_u	S< θ
Cataclinal	Dip	D	S= θ
Anaclinal	Steepened escarpment	E_{st}	S> θ
Anaclinal	Subdued escarpment	E_{su}	S< θ
Anaclinal	Normal escarpment	E_n	S= θ

Slopes are classified into cataclinal, anaclinal, and orthoclinal types based on the conformity between dip direction (α) and slope aspect (A). Cataclinal slopes are classified where the difference between α and A is 0 ± 45. Anaclinal slopes occur if the difference between α and A is 180 ± 45, and orthoclinal slopes occur if the difference is 90 ± 45 or 270 ± 45. In order to determine these differences, the chord length subtended by the angle between α and A on the unit circle was computed. The chord describes a continuous function between zero and two on the unit circle. The chord length is:

$$L = \sqrt{(\cos\alpha - \cos A)^2 + (\sin\alpha - \sin A)^2} \quad (6.3)$$

Beyond the sine dip direction map (sin α) and cosine dip direction map (cos α) now there was the need to convert also the slope aspect map into sine slope aspect map (sin A) and cosine aspect map (cos A) in order to build the previous chord length map (L) (Meentemeyer and Moody, 2000).

Each slope type is then classified based on the chord length ranges corresponding to the four categories above. These are expressed as:

$$if\ 0 \leq L \leq\ 0.7654\ \text{then}\ a_c\ (0^{\circ}\ \pm\ 45^{\circ}) \tag{6.4}$$

$$if\ 0.7654\ < L \leq\ 1.8478\ \text{then}\ a_o\ (90^{\circ}\ \pm\ 45^{\circ}\ \text{or}\ 270^{\circ}\ \pm\ 45^{\circ}) \tag{6.5}$$

$$if\ 1.8478\ < L\ \leq 2\ \text{then}\ \text{a}_\text{a}\ (180^{\circ}\ \pm\ 45^{\circ}) \tag{6.6}$$

where a_c is cataclinal slope, a_a is anaclinal slope, and a_o is orthoclinal slope (Meentemeyer and Moody 2000).

Cruden and Hu (1996) noted that slope types are conventionally categorized using a 20º range. However, the range and number of categories can be adapted to different applications. For example, using such narrow range could be required for hillslope stability applications at a slope-level scale. However, for landscape-scale applications, such as mapping relationships between the output of the model TOBIA and potential hillslope stability, substrate conditions, or vegetation patterns, a larger range is probably more appropriate given the scale and the potential error associated with spatial data previously obtained (Meentemeyer and Moody 2000).

Cataclinal and anaclinal slopes are additionally partitioned based on the conformity between slope angle and dip angle. Orthoclinal slopes are not further partitioned (Meentemeyer and Moody, 2000). The following logic is used for cataclinal slopes:

$$if\ -5^{\circ} \leq \theta - S \leq 5^{\circ}\ then\ a_c = D\ (dip\ slope) \tag{6.7}$$

$$if\ \theta - S > 5^{\circ}\ then\ a_c = D_u\ (underdip\ slope) \tag{6.8}$$

$$if\ \theta - S < -5°\ then\ a_c = D_o\ (overdip\ slope) \quad (6.9)$$

For anaclinal slopes:

$$if\ -5° \leq \theta - S \leq 5°\ then\ a_a = E_n\ (normal\ escarpment) \quad (6.10)$$

$$if \theta - S > 5°\ then\ a_a = E_{su}\ (subdued\ escarpment) \quad (6.11)$$

$$if \theta - S < -5°\ then\ a_a = E_{st}\ (steepened\ escarpment) \quad (6.12)$$

All the statements above described were calculate through *Raster Calculator* tools from *ArcGis* software. The chord length was achieved by implementing the equation 4.11.

Then, in order to build the final TOBIA categorical map a condition, where were included the equations from 4.11 to 4.20, was performed. For an accurate BA model it should be noted that there are some lithological elements for whom cannot be applied BA data such as the geological recent alluvium deposits and some volcanic rocks (as the dolerites). Thus, it was made a raster map containing this two lithological classes for the study area. Where alluvium deposits and dolerite exists it was given the value 0 (not applied) and for the remaining data the value 1. Further, this new binary mask raster map was multiplied with the BA model on *Raster Calculator* tool (from ArcGis software) and the final and accurate BA model was achieved (Fig. 4.21).

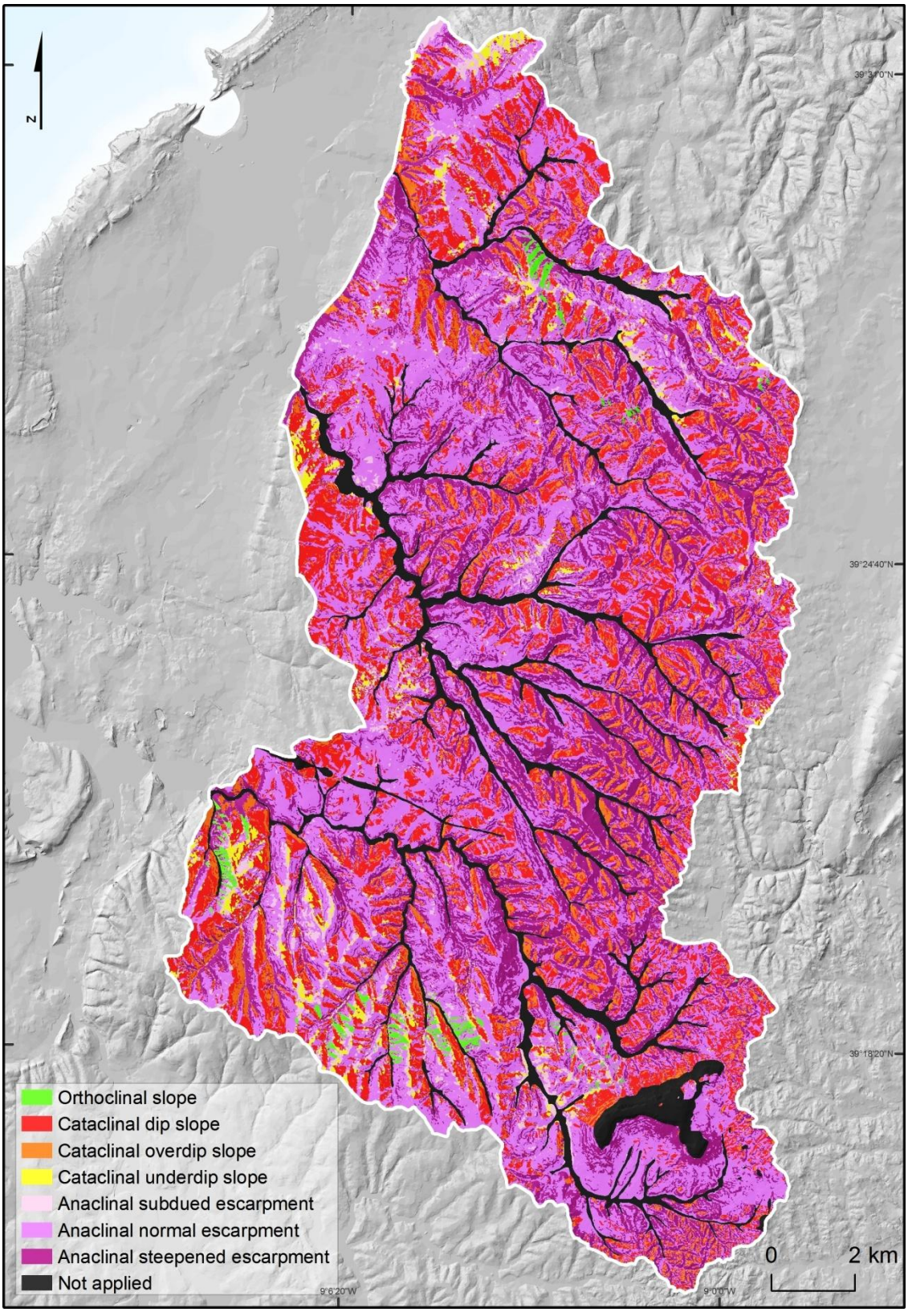

Fig. 4.21 – BA map: made through TOBIA categorical model.

4.3.2 Analysis of results

According to the BA modeling map (Fig. 4.21 and Table 4.8) the study area is mostly dominated by anaclinal normal escarpment slopes (38.97% of the total study area) followed by anaclinal steepened escarpment (22.09% of the total study area) and cataclinal dip slope (17.74% of the total study area).

Table 4.8 – Areal distribution of the BA classes resulting from the Categorical TOBIA model.

BA classes	Area	
	(m^2)	(%)
Orthoclinal slope	1896850	0.69
Cataclinal dip slope	48946825	17.74
Cataclinal underdip slope	5685350	2.06
Cataclinal overdip slope	18715925	6.78
Anaclinal normal escarpment	107498625	38.97
Anaclinal subdued escarpment	10209550	3.70
Anaclinal steepened escarpment	60936625	22.09
Not applied	21977100	7.97

It is now clear that the range chosen by Meentemeyer and Moody (2000) is such that the final BA modeling map contain a very few percentage of orthoclinal slopes (0.69% of the total study area).

Cataclinal dip slope have a higher percentage of occupancy (17.74% of the total study area) than other cataclinal slopes. This is an important fact to be noticed because theoretically the cataclinal dip slopes are more susceptible to deep-seated translational landslides occurrence than other BA classes but only if it matches with steep slope angles.

4.4 Landslides distribution and pattern according to bedding attitude model

Regarding the LI#1 it is possible to observe that, in the map generated through TOBIA categorical approach, most of the landslides, regardless the type, seemed to occur mostly on anaclinal normal escarpment and anaclinal steepened escarpment (respectively, 32.31% and 34.28% of the total landslides occurrence on Table 4.9 and 4.10).

Table 4.9 – Landslide distribution according to the TOBIA categorical map classes for LI#1.

		Landslide area					
	Area	Deep-seated rotational	Shallow rotational	Shallow translational	Deep-seated translational	Sum	Total density
			(m^2)				(%)
Orthoclinal slope	1896850	12225	300	0	0	12525	0.66
Cataclinal dip slope	48946825	331225	17075	4150	0	352450	0.72
Cataclinal underdip slope	5685350	6625	125	300	0	7050	0.12
Cataclinal overdip slope	18715925	283850	8625	3750	5375	301600	1.61
Anaclinal normal escarpment	107498625	757000	40925	8500	0	806425	0.75
Anaclinal subdued escarpment	10209550	22875	1475	25	0	24375	0.24
Anaclinal steepened escarpment	60936625	798525	51200	5900	0	855625	1.40
Not applied	21977100	136200	0	0	0	136200	0.62

Table 4.10 – Cross tabulation area between landslides types and the TOBIA categorical map classes for LI#1.

	Landslide area (%)				
	Deep-seated rotational	Shallow rotational	Shallow translational	Deep-seated translational	All types
Orthoclinal slope	0.52	0.25	0.00	0.00	0.50
Cataclinal dip slope	14.10	14.26	18.34	0.00	14.12
Cataclinal underdip slope	0.28	0.10	1.33	0.00	0.28
Cataclinal overdip slope	12.09	7.20	16.57	100.00	12.08
Anaclinal normal escarpment	32.23	34.18	37.57	0.00	32.31
Anaclinal subdued escarpment	0.97	1.23	0.11	0.00	0.98
Anaclinal steepened escarpment	34.00	42.76	26.08	0.00	34.28
Not applied	5.80	0.00	0.00	0.00	5.46

Although the anaclinal normal escarpment and anaclinal steepened escarpment present higher landslides occurrences the one who have the highest landslide density is the cataclinal overdip slopes (1.61%, Table 4.9).

The deep-seated rotational landslides occur more often on anaclinal steepened escarpment (34% of the total deep-seated rotational landslide of the study area) and on anaclinal normal escarpment (32.23% of the total deep-seated rotational landslide of the study area) (Table 4.10).

Despite shallow landslides occurrence are less interconnected with the geometric alignment between topography and the orientation of geologic bedding planes (topographic/bedding-plane intersection angle) it can be observed that shallow rotational landslides occur mostly on the anaclinal steepened escarpment (42.76% of the total shallow rotational landslide of the study area) and that the shallow translational landslides occur mostly on the anaclinal normal escarpment (37.57% of the total shallow translational landslide of the study area) (Table 4.10), which, can be related to the fact that the anaclinal normal escarpment and the anaclinal steepened escarpment are the most frequent geometric alignment between topography and the orientation of geologic bedding planes in the study area (respectively, 38.97% and 22.09 of the total BA slopes on Table 4.8). It is observed that deep-seated translational landslides only occur within the cataclinal overdip slopes (100% of the total translational landslides of the study area) (Table 4.10).

Regarding the LI#2 (Table 4.11) it is possible to observe that, most of the landslides, regardless the type, seemed to occur mostly on the anaclinal steepened escarpment and anaclinal normal escarpment slopes (respectively, 49.51% and 24.62% of the total landslides occurrence (Table 4.12).

Table 4.11 – Landslide distribution according to the TOBIA categorical map classes for LI#2.

	Area	Landslide area					
		Deep-seated rotational	Shallow rotational	Shallow translational	Deep-seated translational	Sum	Total density
			(m^2)				(%)
Orthoclinal slope	1896850	6900	0	0	0	6900	0.36
Cataclinal dip slope	48946825	77825	4800	1525	0	84150	0.17
Cataclinal underdip slope	5685350	2250	0	100	0	2350	0.04
Cataclinal overdip slope	18715925	103200	5400	2500	3250	114350	0.61
Anaclinal normal escarpment	107498625	227300	11700	3125	0	242125	0.23
Anaclinal subdued escarpment	10209550	4000	150	150	0	4300	0.04
Anaclinal steepened escarpment	60936625	447050	32175	7650	0	486875	0.80
Not applied	21977100	42000	425	0	0	42425	0.19

Table 4.12 – Cross tabulation area between landslides types and the TOBIA categorical map classes for LI#2.

	Landslide area (%)				
	Deep-seated rotational	Shallow rotational	Shallow translational	Deep-seated translational	All types
Orthoclinal slope	0.76	0.00	0.00	0.00	0.70
Cataclinal dip slope	8.55	8.78	10.13	0.00	8.56
Cataclinal underdip slope	0.25	0.00	0.66	0.00	0.24
Cataclinal overdip slope	11.33	9.88	16.61	100.00	11.63
Anaclinal normal escarpment	24.96	21.41	20.76	0.00	24.62
Anaclinal subdued escarpment	0.44	0.27	1.00	0.00	0.44
Anaclinal steepened escarpment	49.10	58.87	50.83	0.00	49.51
Not applied	4.61	0.78	0.00	0.00	4.31

According to the landslide density it is clear that the anaclinal steepened escarpment and the cataclinal overdip slopes have the highest landslide density (0.80% and 0.61%, respectively) (Table 4.11). As in the LI#1, in LI#2 the deep-seated rotational landslides occur more often on anaclinal steepened escarpment (49.10% of the total deep-seated rotational landslide of the study area) and on anaclinal normal escarpment (24.96% of the total deep-seated rotational landslide of the study area) (Table 4.12). It is observed that the shallow rotational and translational landslides occur mostly on the anaclinal steepened escarpment (respectively, 58.87% and 50.83% of the total shallow rotational and translational landslides of the study area Table 4.12).

As in the LI#1 it is observed that deep-seated translational landslides only occur within the cataclinal overdip slopes (100% of the total translational landslides of the study area) (Table 4.12).

According to the LI#3, it is possible to observe that, as in the previous landslide inventories (LI#1 and LI#2), most of the landslides seemed to occur on anaclinal steepened escarpment (42.80% of the total deep-seated rotational landslide of the study area) and on anaclinal normal escarpment (26.94% of the total deep-seated rotational landslide of the study area) (Table 4.13 and 4.14). The excessive landslide occurrence on the anaclinal steepened escarpment leaded to an also high landslide density (0.24%) (Table 4.13).

Table 4.13 – Landslide distribution according to the TOBIA categorical map classes for LI#3.

	Area	Landslide area					
		Deep-seated rotational	Shallow rotational	Shallow translational	Deep-seated translational	Sum	Total density
			(m^2)				(%)
Orthoclinal slope	1896850	925	1925	125	0	2975	0.16
Cataclinal dip slope	48946825	30750	4475	275	225	35725	0.07
Cataclinal underdip slope	5685350	75	50	0	0	125	0.00
Cataclinal overdip slope	18715925	19225	6225	175	125	25750	0.14
Anaclinal normal escarpment	107498625	80125	10900	1950	0	92975	0.09
Anaclinal subdued escarpment	10209550	1375	175	350	0	1900	0.02
Anaclinal steepened escarpment	60936625	119000	19875	8825	0	147700	0.24
Not applied	21977100	36750	425	775	0	37950	0.17

Table 4.14 – Cross tabulation area between landslides types and the TOBIA categorical map classes for LI#3.

	Landslide area (%)				
	Deep-seated rotational	Shallow rotational	Shallow translational	Deep-seated translational	All types
Orthoclinal slope	0.32	4.37	1.00	0.00	0.86
Cataclinal dip slope	10.67	10.16	2.20	64.29	10.35
Cataclinal underdip slope	0.03	0.11	0.00	0.00	0.04
Cataclinal overdip slope	6.67	14.13	1.40	35.71	7.46
Anaclinal normal escarpment	27.80	24.74	15.63	0.00	26.94
Anaclinal subdued escarpment	0.48	0.40	2.81	0.00	0.55
Anaclinal steepened escarpment	41.29	45.12	70.74	0.00	42.80
Not applied	12.75	0.96	6.21	0.00	11.00

As in the LI#1 and LI#2 the deep-seated rotational landslides occur more often on anaclinal steepened escarpment (41.29% of the total deep-seated rotational landslide of the study area) and on anaclinal normal escarpment (27.80% of the total deep-seated rotational landslide of the study area) (Table 4.14).

Like in the LI#2, it is observed that the shallow rotational and translational landslides occur mostly on the anaclinal steepened escarpment (respectively, 45.12% and 70.74 of the total shallow rotational and translational landslides of the study area Table 4.14). The 2 deep-seated translational landslides only occur within the cataclinal overdip slopes (100% of the total translational landslides of the study area on Table 4.14), an event also recorded in the previous landslides inventories (LI#1 and LI#2).

Considering all the landslide inventories together (Sum of LIs) is possible to strengthen the notion that most of the landslides, regardless type and period, seemed to occur on anaclinal steepened escarpment (38.87% of the total deep-seated rotational landslide of the study area) and on anaclinal normal escarpment (30.07% of the total deep-seated rotational landslide of the study area) (Table 4.15 and 4.16). However, landslide density is higher for the classes anaclinal steepened escarpment and cataclinal overdip slopes (respectively, 2.40% and 2.35%) (Table 4.15).

Table 4.15 – Landslide distribution according to the TOBIA categorical map classes for Sum of LIs.

		Landslide area					
	Area	Deep-seated rotational	Shallow rotational	Shallow translational	Deep-seated translational	Sum	Total density
			(m^2)				(%)
Orthoclinal slope	1896850	20050	2225	125	0	22400	1.18
Cataclinal dip slope	48946825	435900	26350	5950	225	468425	0.96
Cataclinal underdip slope	5685350	8800	175	400	0	9375	0.16
Cataclinal overdip slope	18715925	404650	20250	6425	8425	439750	2.35
Anaclinal normal escarpment	107498625	1054375	63325	13575	0	1131275	1.05
Anaclinal subdued escarpment	10209550	27150	1800	525	0	29475	0.29
Anaclinal steepened escarpment	60936625	1338775	101525	22225	0	1462525	2.40
Not applied	21977100	198275	850	0	0	199125	0.91

Table 4.16 – Cross tabulation area between landslides types and the TOBIA categorical map classes for Sum of LIs.

	Landslide area (%)				
	Deep-seated rotational	**Shallow rotational**	**Shallow translational**	**Deep-seated translational**	**All types**
Orthoclinal slope	0.57	1.03	0.25	0.00	0.60
Cataclinal dip slope	12.50	12.17	12.09	2.60	12.45
Cataclinal underdip slope	0.25	0.08	0.81	0.00	0.25
Cataclinal overdip slope	11.60	9.35	13.05	97.40	11.69
Anaclinal normal escarpment	30.23	29.25	27.58	0.00	30.07
Anaclinal subdued escarpment	0.78	0.83	1.07	0.00	0.78
Anaclinal steepened escarpment	38.38	46.89	45.15	0.00	38.87
Not applied	5.68	0.39	0.00	0.00	5.29

The deep-seated rotational landslides occur more often on anaclinal steepened escarpment (38.38% of the total deep-seated rotational landslide of the study area) and on anaclinal normal escarpment (30.23% of the total deep-seated rotational landslide of the study area) (Table 4.16).

The shallow rotational and translational landslides occur mostly on the anaclinal steepened escarpment (respectively, 46.89% and 45.15% of the total shallow rotational and translational landslides of the study area Table 4.16). Finally, as registered in all landslide inventories the deep-seated translational landslides only occur within the cataclinal overdip slopes (100% of the total translational landslides of the study area) (Table 4.16).

Theoretically it would be expected that cataclinal dip slopes would be more deep-seated translational landslides prone than the cataclinal overdip slopes, however this does not occur due to the fact that when cataclinal dip slopes occur the slope angle is generally lower (Table 4.17). Moreover, cataclinal overdip slopes occur mostly when the slope angle is higher (Table 4.17).

Table 4.17 – Cross tabulation area between BA TOBIA categorical classes and slope angle.

Slope	Orthoclinal slope	Cataclinal dip slope	Cataclinal underdip slope	Cataclinal overdip slope	Anaclinal normal escarpment	Anaclinal subdued escarpment	Anaclinal steepened escarpment	Not applied	sum
(°)	(%)								
0 – 5	10.94	15.25	69.67	0.00	16.54	74.30	0.00	53.81	17.70
5 -10.	25.19	56.33	30.32	0.12	52.87	25.66	0.18	30.42	34.82
10 – 15	32.56	26.83	0.00	39.48	28.81	0.04	35.66	9.18	27.50
15 – 20	15.77	1.59	0.00	36.92	1.77	0.00	37.18	3.71	12.10
20 – 25	7.98	0.00	0.00	13.81	0.00	0.00	15.32	1.61	4.50
25 – 30	3.90	0.00	0.00	5.49	0.00	0.00	6.41	0.69	1.87
30 – 35	1.92	0.00	0.00	2.31	0.00	0.00	2.80	0.28	0.81
35 - 40	0.94	0.00	0.00	0.96	0.00	0.00	1.27	0.14	0.36
> 40	0.79	0.00	0.00	0.91	0.00	0.00	1.18	0.16	0.34
Sum	100	100	100	100	100	100	100	100	100

CHAPTER 5

LANDSLIDE SUSCEPTIBILITY ASSESSMENT USING PHYSICALLY-BASED METHODS

5 LANDSLIDE SUSCEPTIBILITY ASSESSMENT USING PHYSICALLY-BASED METHODS

This chapter aims to assess landslide susceptibility through the physically-based methods (which couples the slope hydrology with slope stability) using temporal static and temporal dynamic approaches. Methodologies for the acquisition and preparation of the input variables are presented, i.e., soil depth and soil classification according to USDA for further hydrogeological properties establishment. The acquisitions of geotechnical parameters through field work, laboratory measurements and back analysis are performed. Further, a described comparison is made between the models obtained through static and the dynamic approaches. The susceptible models are validated in terms of their spatial predictive capabilities.

5.1 Landslide susceptibility assessment using physically-based methods: Static model VS Dynamic model

Landslides, and everything from the Universe to the human psychology, embodies a physical system (Blasio, 2011). Understanding landslides and their behaviour requires in principle a few basic laws of mechanics (Blasio, 2011). Thus, in this chapter, the landslide susceptibility is assessed through physically-based methods.

Guzzetti (2005) states that the physically-based methods tend to be more stringent and should have good results. In fact, at a regional scale due to a lack of data, this could be not always the case, making sense to use the statistical based methods instead. However, for the present study, an effort was made in order to obtain all the possible and necessary data for landslide susceptibility assessment, using physically-based methods, at a regional scale. The physically-based methods allow the quantification of instability through the explanation of the physical mechanisms and responses to the influential factors that lead to slope failure. Such models may numerically integrate other mathematical models of

hydrogeological and geotechnical nature, whose main objective is to improve the ability to forecast where and when new instability events will be triggered.

Landslides considered as part of a complex dynamic system in space and time are triggered by factors such as prolonged rainfall, earthquakes and snow melting. However, according to many authors (e.g., Sidle *et al*., 1985; Crozier, 1986; Brabb and Harrod, 1989); the main factor triggering landslides in most physiographical environments is the rainfall. Many often, an episode of intense rainfall triggers the downslope movement of material that was already in its slope failure threshold (Van Asch *et al*. 2007, Zêzere *et al*., 2008).

Beek (2002) assumed that landslides and soil erosion, considered as the main component in erosion processes, are closely linked through the hydrologic system and that landslides triggered by rainfall episodes are considered the most important due to the geomorphological work they perform. Hence, increasing knowledge about the main variables and their elementary mechanisms that trigger slope failures by implementing physically-based models became crucial.

Literature reveals that the deterministic or physically-based models are preferred to forecast the spatial and the temporal occurrence of shallow landslides triggered by rainfall events over a given area (Raia *et al*., 2013). The shallow landslides are often associated with the occurrence of debris flows, corresponding to places where soil rupture occurs. This loose material, when in contact with a certain amount of water, may evolve into debris flows causing damage of catastrophic proportions (Reginatto *et al*., 2012).

The physically-based methods are favoured by the capability of predicting alterations in the hydrological behaviour by means of the constituent equations (Grayson *et al*., 1992). The applicability of such models for future scenarios is, however, limited. Practical limitations are the related problems of spatial and temporal resolution, numerical stability and computation time. Even if all model parameters can be acquired, it remains

doubtful whether the changes in the model output are discernible against the ensuing uncertainty (Nandakumar and Mein, 1997).

Many physically-based models link the triggering groundwater level or matric suction in a deterministic manner to a static stability model or an observed stability threshold (e.g., Montgomery and Dietrich, 1994; Beek, 2002). Thus, according to these characteristics, the prediction of the groundwater level or matric suction, as a measure of the pore pressure at the potential shear plane, gives the exceedance of the critical condition. The subsequent changes after failure in the hydrological and mechanical behaviour of the system are not considered and feedback mechanisms that influence the occurrence of landslides are ignored. All in all, the model outcome gives an idea of the system response in terms of landslide susceptibility to the changing environmental conditions remaining constant all the other factors. The variability within the catchment and induced changes in the spatial and temporal distribution of landslide activity are most times neglected altogether (Beek, 2002).

These models (using a static or a dynamic approach) for the assessment of landslide susceptibility rely upon the understanding of the physical laws controlling slope instability. Their apparently complex and unpredictable behavior is due more to lack of knowledge on the physical conditions and materials characteristics, rather than to a lack of knowledge for the basic laws (Blasio, 2011). The motion of landslides may consequently be described in terms of well-known laws of friction, cohesion, and gravity (Blasio, 2011) (Fig. 5.1).

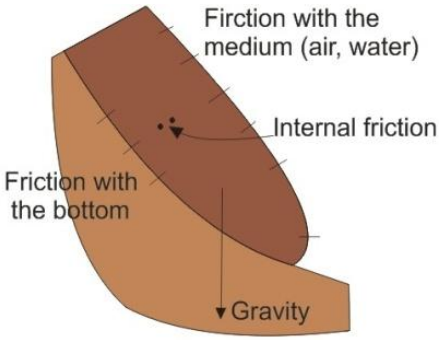

Fig. 5.1 – Very simplified scheme of the forces acting on a moving landslide. (Extracted from Blasio, 2011).

In the geotechnical engineering field, the simplified slope stability models are widely adopted, (e.g., Taylor, 1948; Wu and Sidle, 1995; Wyllie and Mah, 2004). The stability of a slope is calculated using parameters such as normal stress, angle of internal friction, cohesion, pore-water pressure, root strength and seismic acceleration. Computation results in the safety factor (SF), an index expressing the ratio between the local resisting (R) and driving forces (*S*):

$$SF = \frac{R}{S} \tag{5.1}$$

Index value smaller than 1, corresponds to $R < S$ and denotes instability, on a cell-by-cell basis, according to the adopted model (Table 5.1).

Table 5.1 – Relative Slope Stability according to Safety Factor (extracted from Sharma, 2002).

Safety Factor (SF)	Slope Stability
SF ≤ 1	Unstable (rupture)
1 <SF< 1.25	Unstable (likely rupture)
1.25 <SF< 1.5	Marginally Unstable
1.5 <SF< 2	Marginally Stable
SF> 2	Stable

In order to calculate the resisting and the driving forces, the geometry of the sliding mass must be defined, including the geometry of the topographic surface and the location of the (hypothetical) slip surface. Most commonly, an infinite-slope approximation is adopted (Taylor, 1948; Wu and Sidle, 1995; Beek, 2002; Baum *et al*., 2002, 2008). Within the infinite-slope approximation, in each cell, the slip surface is assumed to be of infinite extent, planar, at a fixed depth, and parallel to the topographic surface. Forces acting on the sides of the sliding mass are neglected (Raia, 2013).

Modeling shallow planar landslides (Fig. 5.2), triggered by rainfall, adopting the infinite slope approach requires time-invariant and time-dependent information. Time-invariant information includes the mechanical and hydrological properties of the slope material

(e.g. unit weight, cohesion, angle of internal friction, saturated hydraulic conductivity), and the geometrical characteristics of the sliding mass (e.g. gradient of the slope and of the sliding plane and depth of the sliding plane). The fact that these parameters are constant in time is an assumption of these models.

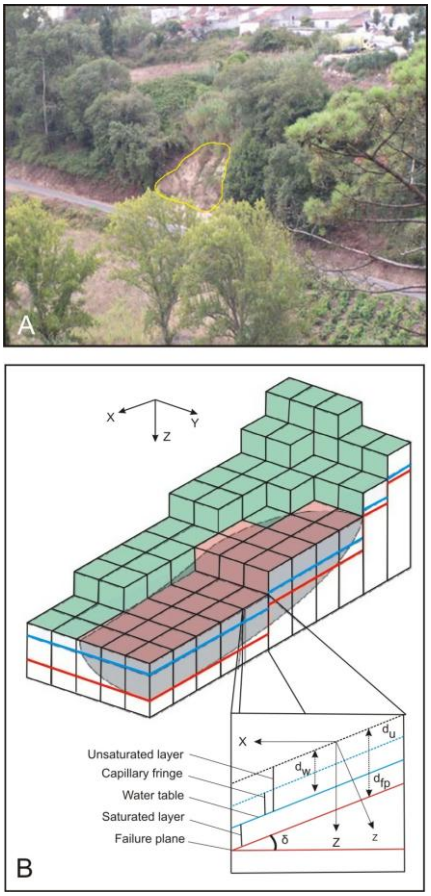

Fig. 5.2 – (A) Example of a rainfall-induced shallow landslide of the soil slide type in the study area. (B) Schematic representation of the slope-infinite model showing the coordinate system and variables used in the deterministic and stochastic models. Where: X is the slope parallel coordinate; du is the depth to the top of the capillary fringe; dw is the depth to the water table; dfp is the depth to the sliding plane; δ is the sliding plane; z is the Slope normal coordinate; and Z is the Vertical coordinate, Z = z/cos(δ). (modified from Raia *et al*., 2013).

Time-dependent information consists on the pressure head, i.e. the pressure exerted by water in soil material, a function of the amount (depth, dw) of water in the terrain (Freeze and Cherry, 1979). Determining the soil pore pressure, and its spatial and temporal variations, requires understanding on how rainfall infiltrates and how the water moves into the ground. This is described with some differences according to: simplified hydrological models in static conditions (e.g., Montgomery and Dietrich, 1994; Dietrich *et*

al., 1995) and complex hydrological models under dynamic interaction between precipitation, infiltration, runoff and piezometric level variation over time linked to rainfall events (e.g, Iverson, 2000; Beek, 2002).

Simplest physically-based models, as the infinite slope model, have often been used. However, these methods usually do not address influences of temporally varying precipitation and vegetation dynamics. Outputs from these methods are limited to only a snapshot of spatial prediction of landslide susceptibility and cannot account for dynamic processes (Gorsevski *et al*., 2006). Prediction of landslide susceptibility based on static environmental factors and/or the existence of steadystate conditions appears to be insufficient for a temporal landslide susceptibility analysis (Wu and Sidle, 1995; Gorsevski *et al*., 2003, Gorsevski *et al*., 2006). Relatively static environmental factors (i.e., elevation, slope, aspect, and topographic curvatures) exhibit negligible changes in their state through time, and differ from dynamic factors such as climatic or human activities, which tend to alter landslide susceptibility through time. To predict the spatial and temporal patterns of areas susceptible to landslides, a distributed approach is needed that incorporates, for instance, varying precipitation intensity and vegetation.

This chapter aims to carry out landslide susceptibility assessment using two different approaches of hydrogeological models, a static and a dynamic, coupled to the slope stability model (infinite slope model). Subsequently, those models will be compared, in order to understand the possible advantages of using a dynamic approach. Both models allow the integration of both hydrogeological and geotechnical parameters, whose main objective is a mathematical approximation of reality in order to improve the ability to forecast where and when new events of geomorphologic instability will occur.

5.2 Infinite Slope Model

The soil above a potential shear plane located in a slope is subject to a driving force (S), that includes the downslope component of the own weight of the soil and any additional loads acting on it. At the same time, the movement is resisted by the reaction force of the mobilized shear strength. The mobilized shearing resistance is finite and can be considered as the capacity of the soil to resist failure (R). Failure occurs as soon as the demand exceeds the capacity to resist. This principle is the basis for the limiting equilibrium approach, which forms the basis for the slope stability assessment in the coupled hillslope model; the maximum shearing resistance that can be mobilized is equal to the disturbing forces at imminent failure (hence the name limiting equilibrium) (Beek, 2002).

With the limiting equilibrium method, the stability can be expressed as the ratio or the difference between the capacity of the soil to resist failure (R) and the demand of the driving force (S). As already mentioned, this measure is known as the safety factor, SF (see Equation 5.1).

Thus, the infinite slope model fits the stability analysis through the limiting equilibrium method which calculates the safety factor. Along a potential shear plane it is calculated the ratio between the destabilizing forces, resulting from the own weight of the slice of the potentially unstable soil and the effects of water on land, including the effects of percolation, and the capacity of the soil to resist failure along that surface. Thus, for the same terrain conditions a constant safety factor is observed over an entire shear plane surface (IGME, 1987; Sharma, 2002, Vallejo *et al*.,2002).

This model assumes that the slope extends for a relatively long distance and has a consistent subsoil profile enabling to be analyzed as an infinite slope. The failure plane for this case is parallel to the surface of the slope and the limit equilibrium method can be applied readily (Sharma, 2002).

At F= 1, failure is imminent and the situation is critical. When F< 1, the slope should theoretically had failed. The difference between shear strength and shear stress is known as the safety margin, SM,

$$SM = R - S \tag{5.2}$$

The safety factor is dimensionless whereas the safety margin has the units of the driving forces and capacity to resist failure forces. It is most convenient to define the conditions at the potential shear plane as forces, the average of the inter-particle forces over an elementary area, i.e., f= ΣF/A.

The limiting equilibrium method takes into account the plastic failure approach. The maximum shearing resistance can then be described by the Mohr-Coulomb failure criterion:

$$t_f = c + \delta \tan(\varphi) = \boldsymbol{R} \tag{5.3}$$

Where t_f is the shearing resistance at failure (SF=1), c is the cohesion, δ is the total normal stress and φ is the angle of internal friction. The expression φ is defined as an angle, while the other variables have units of stress or forces ($N.m^{-2}$ or kPa). The contribution of cohesion is considered constant and consists on: 1) the inter-particle bonds due to the presence of cement which promotes the bonding process between grains; 2) a potential molecular or colloidal attraction; 3) the effect of capillary pressure in the interstitial soil (Blasio, 2011).

The variation of the friction component of the shearing resistance depends on the average inter-particle stress normal to the potential shear plane, σ. If the weight of the soil, W is the only load acting on the potential shear plane, the total normal stress for an area of unit width and length is given by:

$$\delta = W \times cos^2(\beta) \tag{5.4}$$

where β is the slope angle and W is the weight of the soil which depends on Z.γ (m^2), respectively, the soil depth (m) and the bulk density of the soil ($KN.m^{-3}$). Under the same assumptions, the disturbance is given by the shear stress, t:

$$t = W \times sin\beta cos\beta = \boldsymbol{S} \tag{5.5}$$

The friction component of the shear resistance depends on the effective normal stress, δ', when a part of the load is carried by the water that is present in the pores. This is given by the normal total stress reduced from the pore pressure, u:

$$\delta` = \delta - u \tag{5.6}$$

The primed symbols are used for indicate the effective conditions, as the normal stress and the shear strength parameters, c' and ϕ'. Under the assumption that the groundwater levels that occur are unconfined, the effective stress is affected by the fluctuation of the particles below the groundwater level, so:

$$\delta` = [(Z - WL) \times \gamma + WL \times \gamma`]cos^2\beta \tag{5.7}$$

Where WL represents the groundwater height above the shear surface and respectively, γ and γ`are the moist and buoyant bulk unit weight ($KN \cdot m^{-3}$). The weight is determined by the depth of the potential shear plane acting upon. The potential shear plane may correspond to a structural weakness as bedding planes or horizons in the soil profile, like lower boundary of the root zone or the lower zone of the weathering profile (Beek, 2002).

When the depth of the landslides is defined by structural weaknesses, its shape can be described as planar or translational, and its length is much greater than its depth (Crozier, 1973). This approaches a situation in which the soil mantle has an infinite length which is the major premise of the infinite slope model. Under this assumption, it can be said that considering a homogeneous soil, all the forces that act on the ascending part of an

element are balanced by descendent forces that are also great, but opposite in sign (Nash, 1987).

The infinite slope model is based on the slope stability, which is governed by the values of demand of the driving force and the capacity of the soil to resist failure. Such values are primarily influenced by the self weight of the soil above the potential shear plane (Equation 5.3 and 5.5). The stability is assessed in terms of effective stress, with the frictional component of the shear strength set to (σ - u) tan ϕ'. In the infinitive slope model it is assumed that the water flow is parallel to the shear plane and the topographic surface. Under this assumption, the pore pressure is determined. As an alternative to Equation 5.7, the pore pressure which is necessary for calculating the effective normal stress is given by:

$$u = \gamma_w WL \times cos^2 \beta \tag{5.8}$$

Where WL represents the groundwater height above shear surface, γ_w is the density of water (KN·m^3) and β is the slope angle (Beek, 2002) (Fig. 5.3).

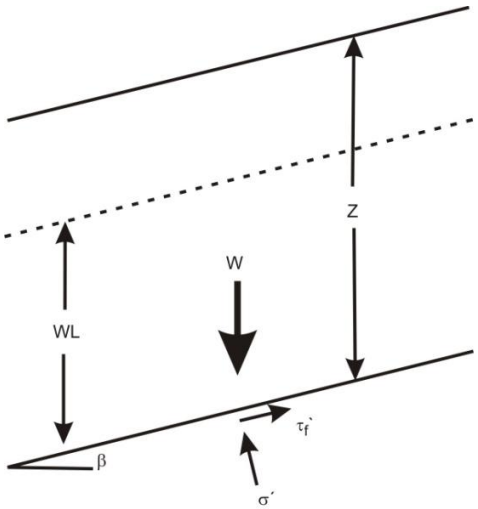

Fig. 5.3 – Definition of the infinite slope model for translational slides (extracted from Beek, 2002).

There are many variations of this method, but this seems to be the most complete formulations allowing its use in cohesive materials, such as on the materials present in the study area (Fig. 5.4).

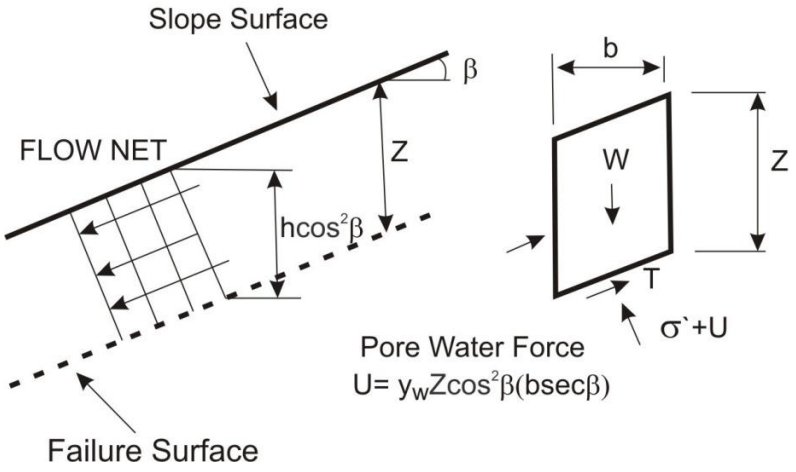

Fig. 5.4 – Infinite slope failure in cohesive soil with parallel seepage under saturated soil condition (extracted from Sharma, 2002).

One of the advantages of using the dynamic model, instead of the static one, is that it can be added the matric suction as an additional interstitial force. This force is added to the shear strength when no groundwater is present. According to the model of Fredlund (Fredlund, 1987), this force is additional to the frictional shear strength and not an intrinsic part of it. This parameter is dynamically given by the hydrological model (STARWARS) over a unit area. It can be represented as an apparent cohesion term Δc':

$$\Delta c' = |h| \tan\varphi^b \tag{5.9}$$

which is positive and consists on the absolute matric suction, |h| (kPa), and ϕ^b, the friction angle that describes the increase in shear strength at higher values of suction (Beek, 2002). In the static approach it is not possible to acquire the matric suction as an output from the hydrological model since it is a dynamic parameter and depends on the net rainfall amount.

Despite using the same infinite slope model, the static and dynamic approaches differ somewhat in their equation, due to their nature. Thus, it is shown bellow two different manners to calculate slope stability using the infinite slope model.

According to Sharma (2002), through an articulation between a hydrological (Montgomery and Dietrich, 1994: SHALSTAB) and a geotechnical model, the safety factor, for a given area can be calculated. In this equation it is assumed that the water level is located at a dw height above the shear plane. The water level is thus, dependent on the relation between the water height and the soil depth, more precisely, it is dependent on the ratio between the saturated soil thickness and the total soil thickness of the potential unstable soil. Thereby, the general expression of the safety factor (Equations 5.10 and 5.11) given by Sharma (2002) is:

$$SF = \frac{c` + Z + \cos^2\beta\left[\left(1-m\right)\times\gamma + m\times\gamma`\right]tan\varphi`}{h\sin\beta\cos\beta\left[\left(1-m\right)\times\gamma + m\times\gamma_s\right]} \quad (5.10)$$

$$m = \frac{dw}{Z} \quad (5.11)$$

The equation of the infinite slope model, for the dynamic approach, appears slightly different from the previous one. In this case, the model has the capability to simulate the pore pressure conditions adequately over time in order to assess the activity of rainfall-induced landslides, through a dynamic and distributed hydrological model (Beek, 2002: STARWARS) coupled with the probabilistic slope stability model (Beek, 2002: PROBSTAB). Awareness of the possible impact of changing environmental conditions, such as land use and climate, on the controlling pore pressures and the absence of long term observational records has lead to the importance of using dynamic physically-based hydrological models to evaluate the consequences of future landslide activity. Thereby, in a dynamic approach the two parameters of the apparent cohesion equation can be included in the equation of the infinite slope model. Thus, the hydrologic input consists of the absolute matric suction, |h|, and the groundwater height, WL, which stem from the hydrological model component, STARWARS. With stability expressed by the safety factor,

SF, this equation is derived by substituting Equations 5.3, 5.5, 5.6 and 5.9 into Equation 5.1. This results in:

$$SF = \frac{c` + \Delta c` + \left[\left(Z - WL \right) \times \gamma + WL \times \gamma` \right] cos^2 \beta tan\varphi`}{\left[\left(Z - WL \right) \times \gamma + WL \times \gamma_s \right] sin\beta cos\beta} \quad (5.12)$$

where c' and Δc' are respectively the true and the apparent cohesion, ϕ' is the angle of internal friction, Z is the depth to the potential shear plane, β is the slope angle, WL is the water level above the shear plane and y, y_s and y' are respectively the moist, saturated and buoyant bulk densities.

In both, static and dynamic approaches, the slope stability assessment is deterministic and requires the input of the soil depth, Z, and other parameters. The soil depth was obtained through an altered simplified Geomorphological Indexed Soil Thickness model (sGIST) developed by Catani *et al.*, 2010 (section 5.3.5). These two manners, for calculating slope stability, should be applied carefully and their results interpreted with scrutiny. After all, no model can predict nor assess changes beyond its original scope and cannot escape from a certain amount of empirism (Beek, 2002).

It must be mentioned that, after several attempts, it was noted that the dynamic hydrological model worked better with a 25m pixel size, especially for the discharge data, which is one of the important outputs of the model, for calibration purposes (which will be explained later). Thus, in order to be consistent all the hydrological models (static and dynamic) were developed with a 25m pixel size. Then, these models were resampled to a 5m pixel size in order to perform the remaining safety factor equation for both static and dynamic approaches. In the case of the soil depth map (Z), it must be mentioned, that, since it enters in both, hydrological, and safety factor equations, the acquisition of such map was made, previously, with a 5m pixel size, then, in order to be input within the hydrological models, it was resampled to a 25m of pixel size.

The remaining parameters of the safety factor equation were developed with a 5m pixel size, because, according to Frattini *et al*. (2010), using a high resolution terrain unit, such as a cell of 5 x 5 m, enables the identification of potential unstable areas with a large spatial precision.

5.3 General data

Despite the difficulty on data acquisition an effort was carried out for trying to get all the data needed for the physically-based modeling. There are physical variables that fall within both static and dynamic approaches and thus will be following described.

5.3.1 Digital Elevation Model

Digital Elevation Model (DEM) with high quality (accurate) provides also higher quality of its derivatives and models that come into account with DEM. In order to carry out a more detailed geomorphologic analysis a DEM, with a 5 m pixel size, of the study area was constructed (see Fig 1.5, Chapter 1). This model was generated from three types of data: contours, quoted points and quoted auxiliary points. The altimetric data derived from the Portuguese Geographic Institute (IGP), at 1:10,000 scale (contours with 5m of interval contour and quoted points with centesimal precision). The quoted auxiliary points were generated by IDRISI GIS *software*, through contours, based on a parabolic function, and subjected to several operations for automatic correction. The purpose of this operations aims to remove incorrect flat surfaces (such as interfluves and valley bottoms) generated by TIN models during the process of triangulation. However, for the development of such process it is necessary to have a very wide knowledge of the study area, in order to avoid the elimination of really plans valley bottoms or interfluves.

Subsequently the optimized DEM was used to derive variables such as slope angle which is one of the most important variables controlling variables (see Fig.3.13, Chapter 3).

5.3.2 Lithology

For a correct distribution and variation of the physical properties of soil, slope and hydrogeological conditions, a detailed litho-structural map was previously built (see Chapter 3) in order to improve the predictive capabilities of the landslide susceptibility maps.

This detailed lithological map was made through the stereoscopic analysis of aerial photographs which was kept faithful to the pre-existing lithological map when it was not possible to map the lithological boundaries (see Fig 3.12, Chapter 3).

5.3.2.1 Lithological effects on hydrological properties

The soil hydrology behave differently depending on the underlying lithology. These differences can be understood by subdividing the regional lithology into two main groups. On the first group, containing the shale dominated complexes, the water percolation tends to be very low due to the low lithological permeability and to a low permeability of the dominant clay loam covering soil. Heavy rainfall events in the low permeability materials favors the increase of the water table leading to saturation and hence to runoff (Montgomery and Dietrich, 1994; Iverson, 2000).

On the second group, containing the sandstones dominated complexes, the water percolation takes place through the existing fractures which can be, eventually, retained on the low permeable clay loam covering soil. During a field campaign it was actually possible to observe water resurgence in some places. This phenomenon is often responsible for erosion leading to slope instability. The differences registered in the lithological resistance strongly influence the slope morphology. The resistant sandstones dominated complexes located on the upper sections of the topography present steep slopes. Moreover, the underlying shale dominated complexes presenting concave slopes denounce less resistance to erosion.

5.3.3 Geotechnical soils characterization

Through field observation and landslide inventory it was possible to note that most landslides occur on shale dominated complexes, regardless the landslide type. This occurrence is naturally promoted by deficient geotechnical characteristics, high slope angles and significant changes in the hydrological conditions. However, it is worth mention the presence of large deep landslides occurring on sandstones dominated complexes. These two are the dominant lithologies in the study area, where the shale dominated complexes correspond to 60.79% and sandstones dominated complexes correspond to 29.53% of the total study area (Chapter 3).

In order to understand the role of the two dominant lithologies for landslide occurrence there was the necessity of knowing the physical properties of these lithologies and the local hydrological conditions. Initially there was no information on the geotechnical parameters for the study area and for this reason, based on the detailed lithological map (Chapter 3) six collections of soil samples were made for further laboratory analysis (Fig. 5.5). These collections were only made on the two dominant lithologies by removing, in situ, the covering soil, i.e.: 1) four samples from de shale dominated complexes; 2) and two samples from the sandstones dominated complexes.

The samples were collected on undeformed areas in order to preserve the natural strength and saturated conditions and in a sufficient quantity for the direct shear stress laboratory tests.

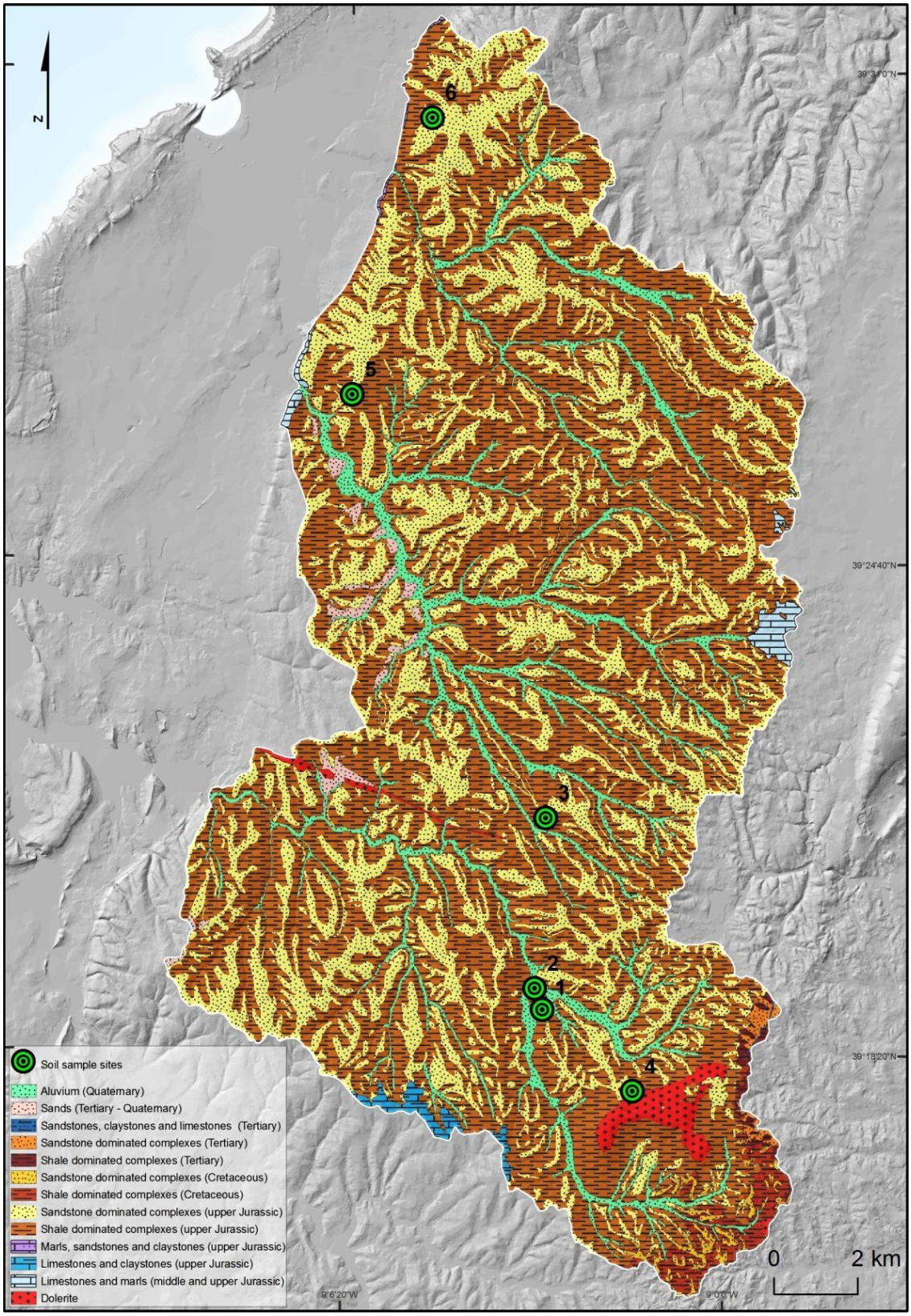

Fig. 5.5 – Soil sample sites.

The covering soil samples, used for the laboratory tests, were collected in cylindrical samplers built from PVC (1) Shear Tests: 7 cm height and 11 cm radius; 2) Weights

Densities: 11 cm height and 4.5 cm radius) and covered with cling film in order to avoid the loss of the natural humidity (Fig. 5.6). The consolidated undrained direct simple shear testing and water content determination for the acquisition of the geotechnical properties of soil needed for the infinite slope equation were made according to methods described in Table 5.2.

Fig. 5.6 – PVC samplers for collecting soil samples.

Table 5.2 – Determination of Geotechnical properties of soil.

Test Performed	Methodology	Parameters
Consolidated Undrained Direct Simple Shear Testing of Cohesive Soils	D6528 – 00 (ASTM, 2004)	C, Φ
Soil Water Content Determination	NP – 84 (LNEC, 1965)	γ, γ_s, $\gamma`$ e, n

The Direct Shear Test was made in order to determine the shear strength of the cohesive soil samples. The test equipment consists of a metal shear box (Fig. 5.7:a) in which the soil sample is placed. Many times the soil samples did not contain complete water saturation in the field. Thereby, to provide an accurate soil water content determination the soil samples were submitted to laboratory saturation with the aid of a vacuum pump. To insure a complete saturation of the samples a period of a week, inside the vacuum pump, was needed for each soil sample (Fig. 5.7:b). After this period, the metal shear box was inserted in the Shear Test machine (Fig. 5.7: c). The Consolidated Undrained Direct Simple Shear Test is split horizontally into two halves: Vertically force (normal stress) is applied through a metal platen; Shear force is applied by moving one half of the box relative to the other to cause failure in the soil sample (Fig 5.8). After being tested each soil sample is then dried naturally for further test completion (Fig. 5.7:d).

The complete results obtained from laboratory tests for each soil sample are showed in Fig A3.1, A3.2 and Tables A3.1, A3.2, A3.3 and A3.4 in Appendix 3. The final resulting parameters of the soil water determination for each soil sample were obtained through the median function between each different imposed shear stress (Table 5.3 and 5.4). The median function between the samples of both lithological type (shale dominated complexes and sandstones dominated complexes) was adopted because, when compared to the mean, the median function has the advantage of not being influenced by individual erratic or not significant values, which is important, in case of any anomaly on laboratory tests (Pimenta, 2011) (Table 5.3). Though, for the sandstones dominated complexes adopting the mean or the median function is irrelevant since there were only two soil samples.

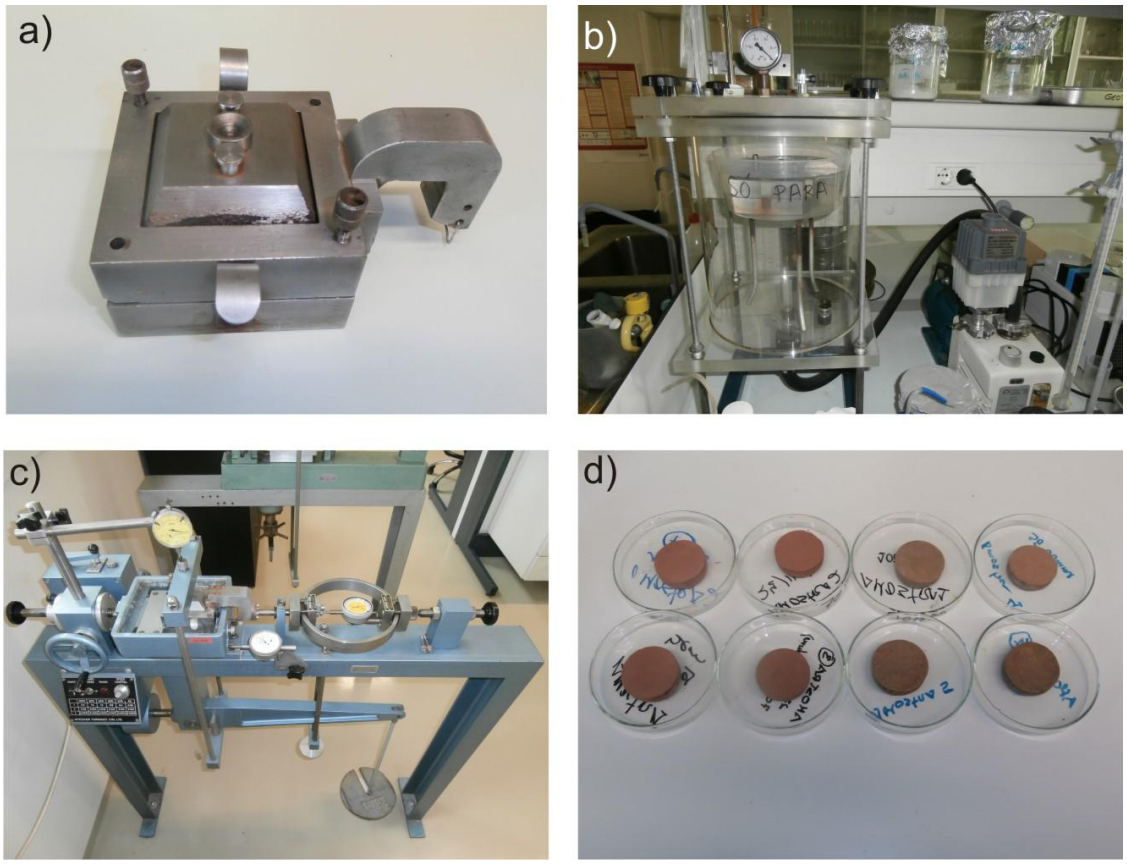

Fig. 5.7 – Laboratory equipment: a) Shear metal box; b) Vacuum pump; c) Shear Stress Test Machine; d) Some of the dried soil samples (after being tested).

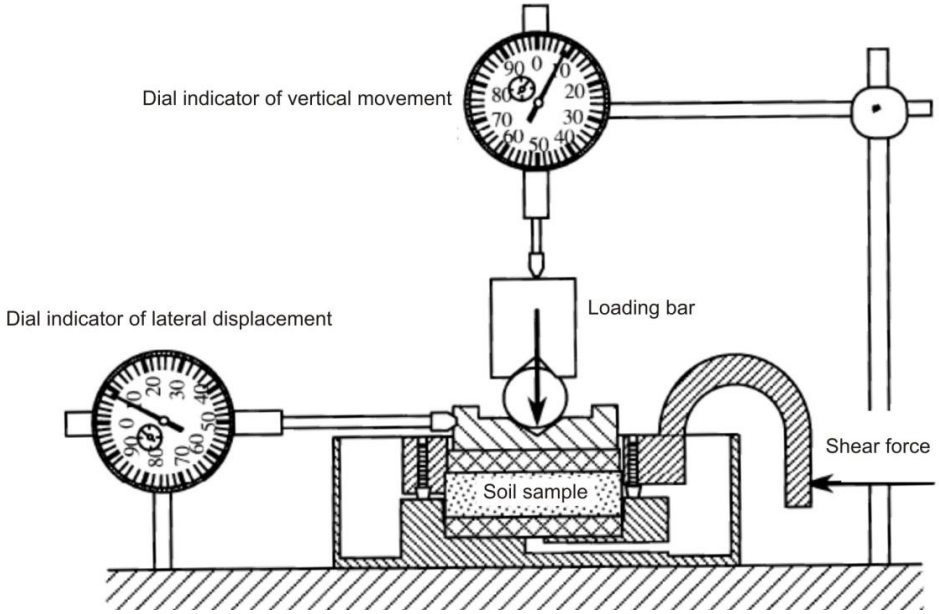

Fig. 5.8 – Direct Shear Test: Measuring instruments of the Shear Stress Test Machine. Acquisition of the shear strength parameters (cohesion and angle of internal friction). The shear stress is imposed on the loading bar in which 30 kg corresponds to a shear stress of 94.3kpa, 70Kg to a 203.3kpa and 100kg to 285.0kpa.

Table 5.3 – Summary table with the geotechnical parameters resulted from the tested soil samples for the Shale dominated complexes (upper Jurassic).

Sample sites	**γ (KN/m^3)**	**γ` (KN/m^3)**	**γ_s (KN/m^3)**	**Void ratio (e) (KN/m^3)**	**Porosity (n) (%)**	**c` (Kpa)**	**ϕ` (º)**
1	18.54	10.42	20.23	0.23	19.02	6.70	21.00
2	18.58	10.19	20.00	0.12	10.66	4.80	28.00
3	18.94	10.94	20.75	0.19	15.63	10.40	27.00
4	18.90	11.22	21.03	0.13	11.50	0.40	28.00
Median	18.7	10.7	20.5	5.6	26	18.7	10.7

Table 5.4 – Summary table with the geotechnical parameters resulted from the tested soil samples for the Sandstones dominated complexes (upper Jurassic).

Sample sites	γ (KN/m^3)	$\gamma`$ (KN/m^3)	γ_s (KN/m^3)	Void ratio (e) (KN/m^3)	Porosity (n) (%)	c` (Kpa)	$\phi`$ (º)
5	19.41	12.04	21.85	0.00	0.33	0.80	34.00
6	17.76	10.97	20.78	0.13	11.44	17.80	25.00
Median	18.6	11.5	21.3	9.3	29.5	18.6	11.5

When completely saturated, the covering soil of the shale dominated complexes seems to have lower cohesion and lower internal friction when compared to the values obtained for the sandstones dominated complexes. Actually, as it was showed in the previous chapters, th proportion of landslides is higher in shale dominated complexes when compared with sandstones dominated complexes, i.e., the covering soil located on shale dominant complexes are less resistant and then, more prone to slope failure.

To improve the geotechnical parameters, a systematic back analysis of landslide was performed (as it can be seen on the following section). This method was applied in order to adjust the geotechnical parameters according to the behavior of the covering soils present on the study area.

5.3.4 Back analysis of landslides for optimizing shear strength parameters

Despite the majority of shallow and deep-seated rotational slides observed in the study area, it is important to mention that most of the shallow rotational slides have not a perfect rotational characteristics, since the curvature radius of the shear plane is very high. Taking into account this fact, some of the primarily identified shallow rotational slides, could actually be assumed as planar slides and integrated in the infinite slope model for further calibration and validation purposes.

Thereby, using the infinite slope equation coupled with the static hydrological approach (Equations 5.10 and 5.11) developed by Sharma (2002) and assuming that the slope failure occurs when the safety factor is equal to 1, it can be reconstituted the snapshot conditions of the shear strength parameters (cohesion and angle of internal friction) when the slope failure occurred.

Through the landslide inventory, validated by field work, and the detailed litho-stratigraphic map (Chapter 3) was collected the landslide data needed for the back analyses, whose goal was the calibration of the shear strength values, of the affected material. For each lithological unit several typical landslides were selected and the mean slope of each landslide was calculated (b). In a spreadsheet, the information regarding the lithological unit in order to calculate the Safety Factor ≈ 1 was introduced (Table 5.5).

Within each lithological unit the values of cohesion and internal friction angle were changed, separately, until a convergence of Safety Factor ≈ 1. The Table 5.5 shows an example of how the back analysis was performed for the typical landslides within each lithological unit in the study area.

Table 5.5 – Example of a spreadsheet used for back analysis for some of the shallow landslides occurred.

ID	Type	Position along the hillslope profile	b (º)	Lithology	c'	ϕ'	z	d_w	γ	γ`	γ_s	b	m	sen β	cos β	tg ϕ'	FS
44	Translacional shallow	Middle	22.8	Shale dominated comlexes	5.0	26.0	0.4	1.4	18.7	10.7	20.5	22.8	3.5	0.4	0.9	0.5	1.00
41	Translacional shallow	Toe	6.0	Shale dominated comlexes	5.0	26.0	0.4	1.9	18.7	10.7	20.5	6.0	4.8	0.1	1.0	0.5	1.00
65	Translacional shallow	Middle	23.7	Shale dominated comlexes	5.0	26.0	0.4	1.4	18.7	10.7	20.5	23.7	3.1	0.4	0.9	0.5	1.00
86	Translacional shallow	Toe	13.8	Shale dominated comlexes	5.0	26.0	0.4	1.7	18.7	10.7	20.5	13.8	3.8	0.2	1.0	0.5	1.00
57	Translacional shallow	Middle	26.4	Shale dominated comlexes	5.0	26.0	0.4	1.3	18.7	10.7	20.5	26.4	2.9	0.4	0.9	0.5	1.00
...	...	...	...	...	...	...	...	...	...	...	...	...	...	...	...	...	...

With this procedure, it was possible to obtain an improvement on the shear strength parameters (c` and ϕ`) coinciding with the conditions at the time when the mass movement occurred for each lithological unit containing landslides.

The potential unstable soil thickness was estimated through the landslide main scraps (Z), observed during the field work. The thickness of the saturated soil (dw) were estimated through back analyses taking into account the slope position (middle, toe or top position along the hillslope profile) of each landslide.

The calibrated geotechnical properties are given in Table 5.6. The Fig. 5.9 shows the variation between the safety factor (SF) plotted against the ratio between the groundwater and total soil thickness (m=dw/Z). This calibration was made through the typical landslides located on the shale dominated complexes (which is where the majority of the landslides are mostly located).

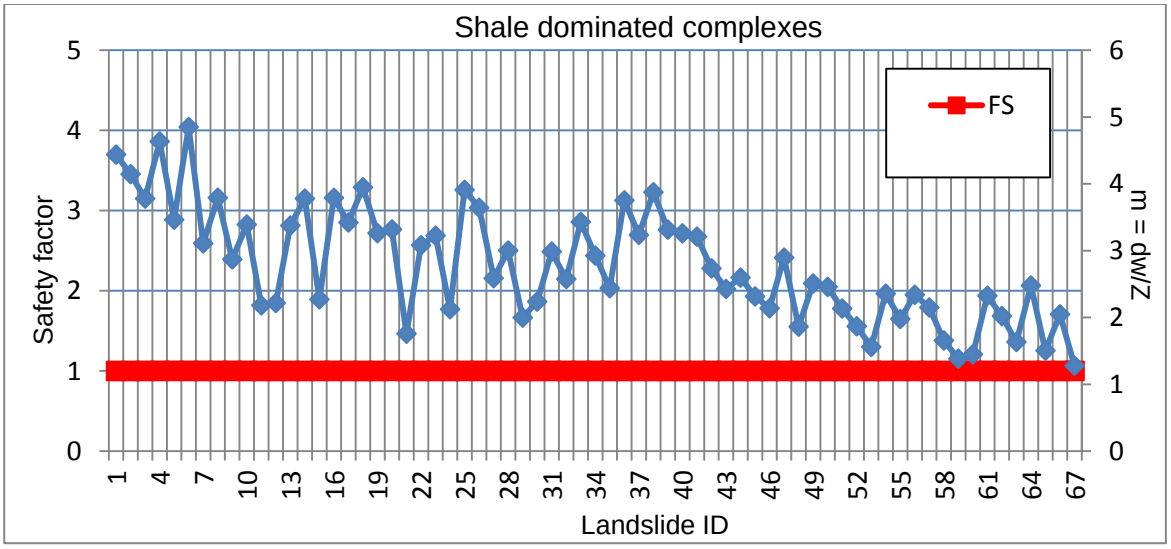

Fig. 5.9 – Back analysis of landslides occurred in Shale dominated Complexes: Relationship between the Safety Factor and the ratio between the thickness of saturated soil and potentially unstable soil thickness (m) arranged in the increasing order of soil thickness (Z).

Only the shear strength values of the shale dominated complexes were possible to be improved, since they have a sufficient amount of slope movements. The other lithological units remained with the initial values, due to impossibility to performed back analysis when few or no landslide occurs.

For the lithologies sands and sandstones, claystones and limestones (representing 0.73% of the total study area) due to the fact that it was not possible to obtained consistent soil samples and due to the similarities observed in the field, it was decided to assign the same values of the sandstones dominated complexes. For the alluvium and dolerite standard values were adopted from Fernandes, 1994, Cernica, 1995; Jeremias, 2000; Vallejo *et al*., 2002; and Baptista, 2004. For the limestones and claystones, limestones and marls, marls, sandstones and claystones the geotechnical parameters obtained through laboratory tests made by Pimenta, 2011 were adopted. Although it is not the same study area, the lithologies are very similar enabling the assignment of the Pimenta 2011 values to these lithologies, which represent only 0.98% of the total study area (Table 5.6).

Table 5.6 – Geotechnical parameters, for introduction into the Infinite Slope Equations.

Lithology	γ (kN/m3)	γ' (kN/m3)	γ_s (kN/m3)	c' (kPa)	ϕ' (º)	Data source
Aluvium	16.0	8.2	18.0	3	19	References
Dolerite	28.0	18.2	28.0	2000	45	References
Limestones and claystones	25.0	17.2	27.0	11	24	References
Limestones and marls	25.0	17.2	27.0	11	24	References
Marls, sandstones and claystones	24.7	16.9	26.7	7	12	References
Sands (Pliocene)	18.6	11.5	21.3	9.3	29.5	Laboratory
Sandstones, claystones and limestones	18.6	11.5	21.3	9.3	29.5	Laboratory
Sandstones dominated complexes	18.6	11.5	21.3	9.3	29.5	Laboratory
Shale dominated complexes	18.7	10.7	20.5	5	26	Laboratory and back analysis

5.3.5 Assessment of the soil depth

Soil thickness, (Z), perceived as depth to bedrock, or depth to the first marked change in hydrological properties, is widely recognized as a controlling factor in numerous surface and subsurface processes, e.g., landscape evolution, sediment budgets and landsliding (Catani *et al*., 2010). However, this is one of the least understood and difficult to obtain physical variable. This is the reason why, traditional soil mapping usually does not include continuous information on spatially variable soil properties and direct measurement of Z.

It is only possible to obtain this kind of data for small and well monitored test sites (Catani *et al*., 2010).

Some attempts have been made world wide in order to obtain this physical variable. One that can be mentioned is based on a linear correlation between soil thickness and elevation or slope gradient (e.g., Saulnier *et al*., 1997). However, the performance of such models is usually poor due to the lack of consideration of fundamental parameters such as slope curvature, lithology and relative position within the soil sequence or catena. Better results, although usually site specific, were described by Boer *et al*. (1996) and Tsai *et al*. (2001) using multivariate statistical models that correlate soil depth with a combination of independent variables assumed to influence the spatial distribution of soil depth (Catani *et al*., 2010).

Over time, the soil thickness prediction has been studied and improved by many authors (Heimsath *et al*., 1999, 2000, 2001a, 2001b; Mudd and Furbish, 2004, 2006; Saco *et al*., 2006; Park *et al*., 2001; Catani *et al*., 2010). Significant statistical correlations between Z and a number of terrains attributes have led to the incorporation of factors such as surface curvature, topographic wetness index and upslope contributing area. Deterministic methods, based on these factors, have been developed. However, at regional scale, such methods are less suitable for soil thickness prediction (Heimsath *et al*., 2001b; Catani *et al*., 2010).

All these previous attempts were crucial to raise the knowledge about the weight importance of the variables controlling soil thickness and for the development of a continuous soil depth model. Thus, in 2010 Catani and co-authors developed a model, called GIST (Geomorphological Indexed Soil Thickness) and sGIST (simplified Geomorphological Indexed Soil Thickness), which allows calculating the thickness of soil (Z) of a particular area, with a given resolution, discarding the hypothesis of variation and evolution of soil thickness through time.

The GIST and sGIST models are based on topographic Digital Terrain Model (DEM) data, digital geological maps and general information on the land-surface units. The main goal

of the model, is the prediction of the depth of the colluvial and residual layers with an accuracy compatible with the requirements of slope stability and rainfall-runoff models. The main characteristics and advantages of using these models are the following: 1) they are performed for catchment-scale analysis; 2) it is possible the implementation within a geographic information system (GIS) environment; 3) they have a wide availability and low cost of the required parameters; 4) and have more balanced consideration of topographic attributes in conjunction with geological and/or geomorphological factors (Catani *et al*., 2010).

The models proposed by Catani *et al*. (2010) are based on the equations of conservation of mass for the soil column proposed by Heimsath *et al*. (1997, 1999) and Minasny and McBratney (1999, 2001). This equation is expressed as:

$$ps\frac{\partial Z}{\partial t} = -pr\frac{\partial b}{\partial t} - ps\frac{\partial w}{\partial t} - \nabla.(psqs) \tag{5.13}$$

where ps and pr are soil and rock density, qs is the soil flux, Z is surface layer thickness, b and w are the elevation of bedrock and ground surface with respect to an arbitrary elevation reference, ∂b/∂t is the rate of soil production from bedrock and ∂w/∂t is the soil lowering rate due to chemical weathering.

However, in models proposed by Catani *et al*. (2010) the previous equation was subject to the following modifications: 1) the rate of soil production from bedrock ∂b/∂t and that of soil chemical dissolution ∂w/∂t are replaced with implicit constant coefficients within boundary conditions that depend locally on lithology and geological history; 2) for simple creep, depth-dependent creep and overland flow erosion, which expresses soil loss for sediment transport (right side of the equation), the authors showed that soil transfer by diffusion depends mainly on slope, linking the soil losses to hillslope laplacian curvature, since it was already proven, by many other authors, that local soil depth is inversely correlated with slope curvature (Heimsath *et al*., 1999, 2001a; Braun *et al*., 2001; Park *et al*., 2001). Other parameters, such as slope length or upslope contributing area, ignored by many previous work about soil depth are considered also by the methodology

developed by Catani *et al*., 2010, i.e., the soil thickness distribution will be taken into account by linking them to position along the hillslope profile; 3) According to Roering *et al*. (2001); Montgomery and Brandon (2002), and Catani *et al*. (2010), the net contribution, of soil losses and gains, due to mass movements, can be linked to threshold processes associated to slope gradient that in some cases decouple relief from soil losses. The sediment loss by intermittent landsliding in the upper portions of the hillslope is taken into account by defining appropriate, lithology-dependent thresholds for the triggering of mass transport.

For the GIST model, it is also considered the position of a point along the hillslope profile. For this the following two steps are required: 1) calculation of the catenary position (P) within the hillslope profile; 2) convertion of P into an index varying from 0 to 1. Using a raster DEM, P can be determined by a simple algorithm that calculates the shortest upslope hydrologic distance to the hilltop and the shortest downslope path to the channel network, following the method proposed by Tucker *et al*. (2001).

Catani *et al*. (2010), spatially partitioned the study area into two-dimensional land-surface units (TLU) which were based on similar relationships between topography, active geomorphic processes and soil thickness. TLUs were delineated from digital geological and geomorphological maps, field surveys and DEM data. However, to estimate soil thickness with this model it is not necessary to perform a complete analysis and classification of the soil toposequences present within an area. A simpler approach that identifies large land-surface units according to the "nine-unit" model of Conacher and Dalrymple (1977) through detailed field surveys and in which, the TLUs are not differentiated on a geomorphological basis, can be achieved through the implementation of a simplified Geomorphological Indexed Soil Thickness (sGIST).

For the present work, the sGIST model was performed, although with some modifications. Thus, for lithology-dependent thresholds, instead of using the threshold processes associated to slope gradient, a simpler approach, using the slope angle, was performed (S_a). It was processed in this manner due to a lack of landslides in some lithologies and

due to the fact that, the dominant lithologies, contain substantially, the same triggering slope gradient (Table 5.7).

Table 5.7 – Threshold slope angle for triggering mass movement.

Lithology	Prevalent Threshold Slope Angle (º)
Dolerite	20
Limestones and marls	25
Sandstones dominated complexes	15
Shale dominated complexes	15

In S_a nondimensional index, it is assumed that higher the slope angle lower the soil depth and vice versa. This soil depth contributing factor must then range between 0 and 1, by means of linear normalization, where 0 corresponds to soil depth minimum value and 1 to soil depth maximum value.

Then, based on the assumption that on the concave lower sections soil depth is higher and on the convex sections soil depth is thinner (Heimsath *et al*., 1999, 2001a; Braun *et al*., 2001; Park *et al*., 2001), the nondimensional index C_p (regarding the calculation of the profile curvature) was also calculated, ranging between 0 and 1. This index expresses the expected soil depth of each pixel with respect to slope curvature.

The P factor is referred to the relative soil depth value, by means of the catenary position within the hillslope profile. While the other two factors were simply obtained from ArcGis *software*, through Spatial Analyst tools, the P factor was obtained using the Land Facet Corridor Designer (LFCD) tool, an extension for ArcGIS *software*. The LFCD performs topographic analysis using the topographic position index (TPI), which is the difference between each pixel's elevation and the average elevation of the surrounding pixels. TPI was calculated from a DEM producing a new raster of TPI values (Fig. 5.10).

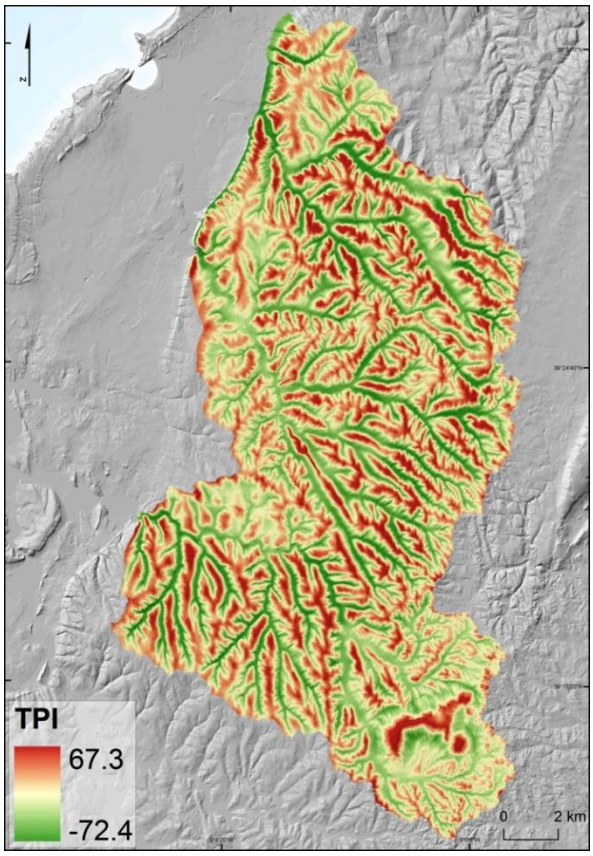

Fig. 5.10 – Topographic position index performed with 100 surrounding cells of neighborhood size.

A negative TPI value indicates that the pixel is at a lower elevation than the surrounding cells (e.g., in a valley), while a positive TPI indicates that the surrounding cells are lower (e.g., on a ridge). A TPI value near zero indicates a hillside slope or a flat area, and these can be distinguished by using the slope angle at that point (i.e., a slope angle near zero suggests a flat area, while higher slope angles indicates a hillside slope). By varying the TPI neighborhood size (the number of surrounding cells) it is possible to control the scale-or resolution-of the modeled topographic position. A large TPI neighborhood tends to minimize smaller features and capture larger ones. A small TPI neighborhood emphasizes finer-scale features. The user can tailor the scale according to the goal of the study (Jenness *et al*., 2011). Due to the scale of this work and after several calibration attempts 100 surrounding cells were selected for TPI performing. Subsequently, for modeling purposes, the TPI was converted into the P index represented by the adimensional scale factor Z (where $0 \leq Z \leq 1$). Assuming that Z increases linearly from the minimum value (Z = 0) in the interfluves (p = 0) to the maximum (Z = 1) in the toeslope (p = 1).

Through a combination of soil depth contributing factors which are delineated from digital lithological map, field surveys and DEM data, was possible to obtain a continuous soil depth model (altered sGIST model):

$$sGIST = Kc \times C \times P \times S \tag{5.14}$$

All the factors in the formula (in the form of pure numbers ranging from 0 to 1) express the propensity of a point to accumulate soil cover, while the constant Kc, which is calculated for each lithology from the in situ measurements, calibrates the formula and transforms the pure number to a metric value (in m) (Fig. 5.12). Direct measurements of soil depth, for Kc achievement, were made from preexisting or newly excavated soil profiles (Fig. 5.11 and 5.12).

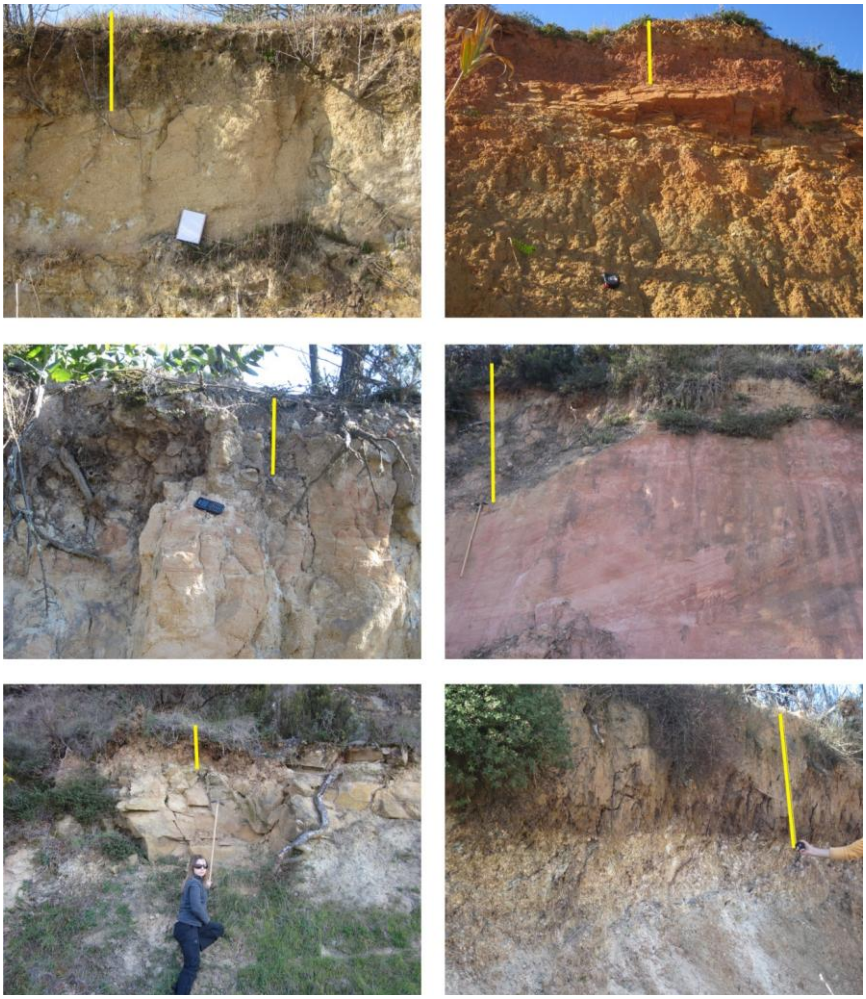

Fig. 5.11 – 6 of the 67 sites where was possible to measure the soil depth, i.e., depth to bedrock (drawn as yellow lines).

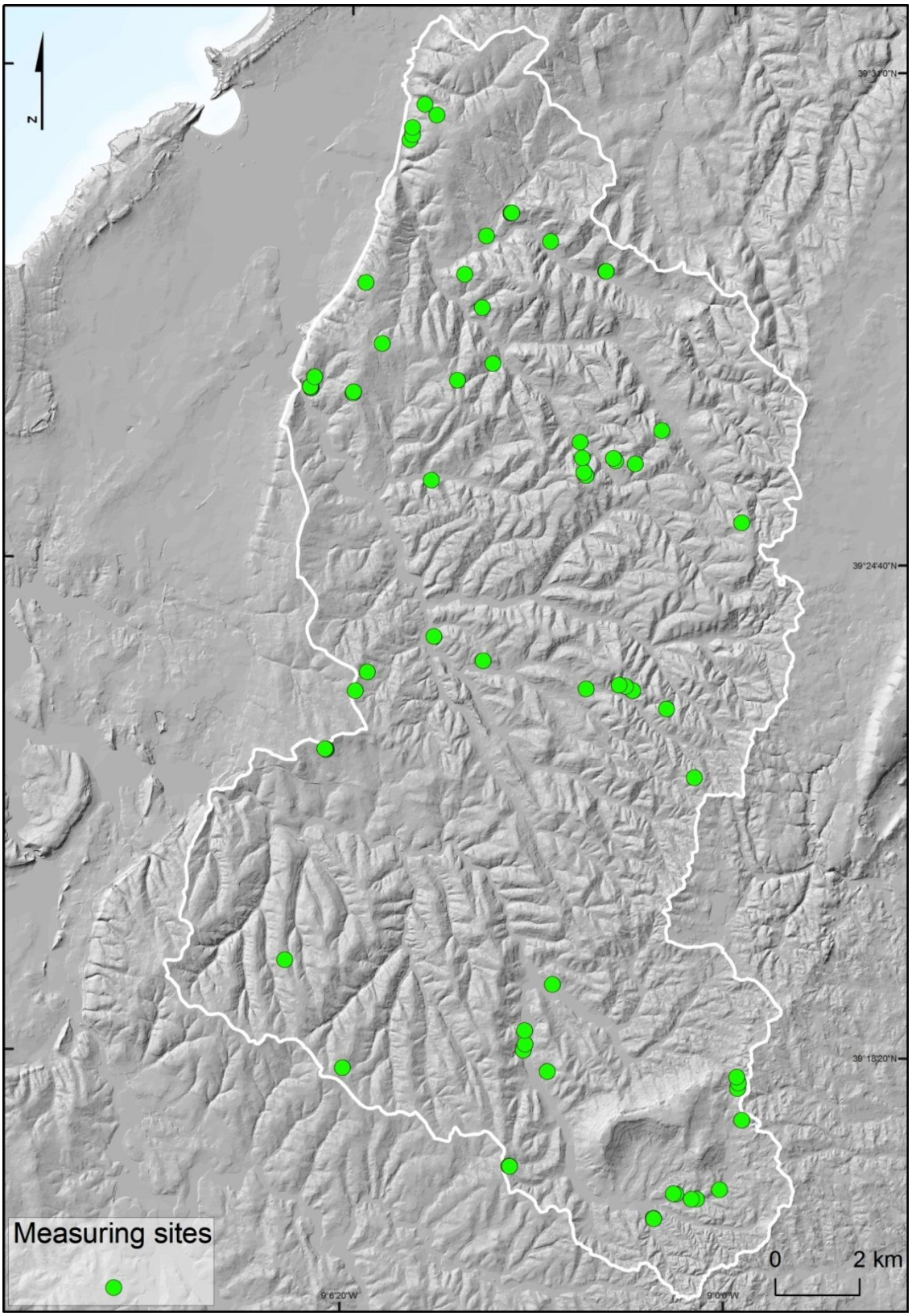

Fig. 5.12 – Soil depth measuring sites.

The measures were made taking into account the local detailed lithology grouped into nine units, mainly according to bedrock lithology, respectively: Shale dominated

complexes; Sandstone dominated complexes; Sand; Limestones and claystones; Alluvium; Marls, sandstones and claystones; Limestones and marls; Sandstones, claystones and limestones; and Dolerite. However it was not possible to acquired measurements in every lithological units. Only for Shale dominated complexes; Sandstone dominated complexes; Sands; Limestones and claystones; and Alluvium was possible to obtain measurements. As it can be seen in Table 5.8 the values range from 0.1 to 1.82 m and are evidently correlated with the lithology resistance.

Table 5.8 – Soil depth observed by in-situ measurements.

Lithology	Minimum Measured Depth (m)	Maximum Measured Depth (m)	Nº of Measuring sites	Occupancy area (% of the total study area)
Shale dominated complexes	0.11	1.82	45	60.8
Sandstone dominated complexes	0.1	0.3	13	29.5
Sands	0.3	0.3	3	0.7
Limestones and claystones	0.25	0.25	2	0.4
Alluvium	0.85	1	4	6.8

For the four units (Marls, sandstones and claystones; Limestones and marls; Sandstones, claystones and limestones and Dolerite), together occupying 1.8% of the total study area, it was not possible to obtain a single soil thickness measure.

For the kc factor it would be preferable measurements in all lithological units, in order to assign a constant that could best fits the measurements through field work. However, it was not possible to do so, due to the lack of exposed soil profiles matching the location of the remaining unmeasured lithological units. Beyond this fact, it must be said that more measurements would be preferable, even for the measured units. One manner to overcome this disability relies upon geophysical measurements, though, in order to achieve the remaining objectives of this work, it was not possible to perform. It must be noteworthy that higher quality on this data would require more time and dedication and

could lead itself to a dissertation. However, in order to circumvent this issue it were assigned values to the unmeasured lithological units based on its similarity with the measured lithologies. Thereby, for the Marls, sandstones and claystones was assigned the same constant value as the Shale dominated complexes, for the Limestones and marls was assigned the same constant value as Limestones and claystones, for the Sandstones, claystones and limestones was assigned the same constant value as the Sandstone dominated complexes. For the dolerite, since it is a volcanic rock and has a different nature comparing with the other lithologies, it was assigned the mean value of the most resistant and thinner soil depth registered for two measured lithologies, i.e. Limestones and claystones; and Sandstone dominated complexes.

Therefore, the constant Kc, which is calculated for each lithology from the in situ measurements, was obtained through means of calibration (by trial and error until it returns the lowest RMSE possible). This is a crucial step, as it summarizes the effects of the curvature, slope angle and catenary position for every cell.

For calibration were used 75% of the total measured points on Shale dominated complexes, 75% of the total measured points on Sandstones dominated complexes, 75% of the total measured points on Sands, 50% of the total measured points on Limestones and Claystones and 75% of the total measured points on Alluvium, which were randomly partitioned (Table 5.9).

Table 5.9 – Calibration and validation groups of soil depth in-situ measurements.

Lithology	Calibration Group		Validation Group		
	% of the measured sites used for calibration	Nº of Measured sites for calibration	% of the measured sites used for validation	Nº of Measured sites for validation	Occupancy area (% of the total study area)
Shale dominated complexes	75	34	25	11	60.8
Sandstone dominated complexes	75	10	25	3	29.5
Sands	75	2	25	1	0.7
Limestones and claystones	50	1	50	1	0.4
Alluviums	75	3	25	1	6.8
SUM	-	50	-	17	98.2

Global RMSE	0.23	0.27
STD	0.24	0.31

Some lithological units do not have a desirable amount of soil thickness measurements, though it is worth noting that they occupy a very small percentage of the total study area which causes a non dramatic insufficiency. After several tests and due to the lowest global RMSE value founded (0.23 meters) it was given the soil depth values according to Table 5.10.

Table 5.10 – Constant Kc (m) inserted into the model after calibration.

Lithology	Kc (m)	Attributions according to:
Aluvium	2.5	Lowest RMSE
Limestones and claystones	1.15	Lowest RMSE
Sands	1.3	Lowest RMSE
Sandstone dominated complexes	0.85	Lowest RMSE
Shale dominated complexes	2.4	Lowest RMSE
Marls, sandstones and claystones	2.4	Same as shale dominated complexes
Limestones and marls	1.15	Same as Limestones and claystones
Sandstones, claystones and limestones	0.85	Same as Sandstones dominated complexes
Dolerite	1.1	Mean between Limestones and claystones; and Sandstone dominated complexes

Further, to perform a validation were used the remaining 25% of the total measured points on Shale dominated complexes, 25% of the total measured points on Sandstones dominated complexes, 25% of the total measured points on Sands, 50% of the total measured points on Limestones and Claystones and 25% of the total measured points on Alluvium. After RMSE assessment it is possible to assume that the model have an acceptable error of 0.27 meters (Table 5.9).

Finally, after obtaining the calibrated Kc constant and the remaining soil depth contributing factors (Fig. 5.13) it was possible to implement the altered sGIST equation (Equation 5.14) and to obtain the soil depth model (Fig. 5.14).

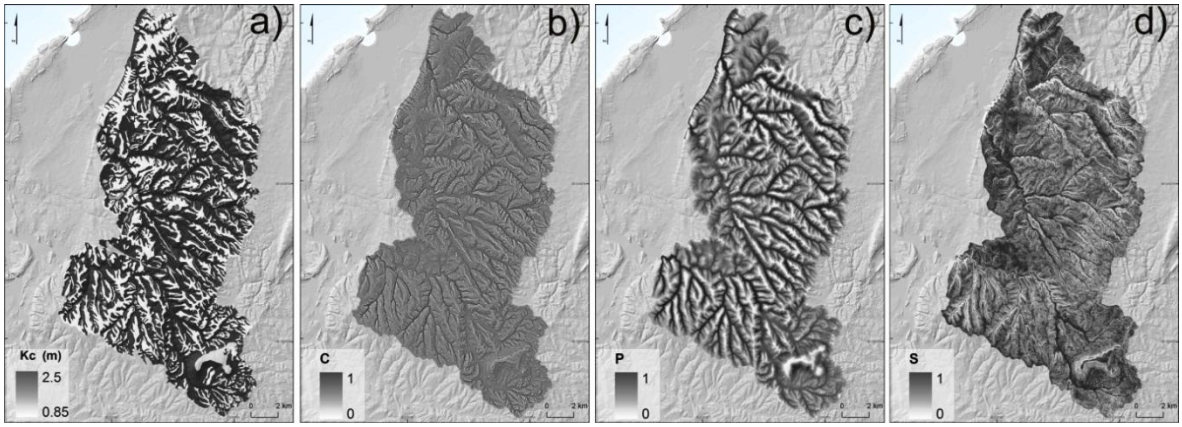

Fig. 5.13 – Soil depth contributing factors: a) constant Kc, which is calculated for each lithology from the in situ measurements; b) Profile curvature (Cp index); c) Catenary position within the hillslope profile (P index); d) Slope angle (Sa index).

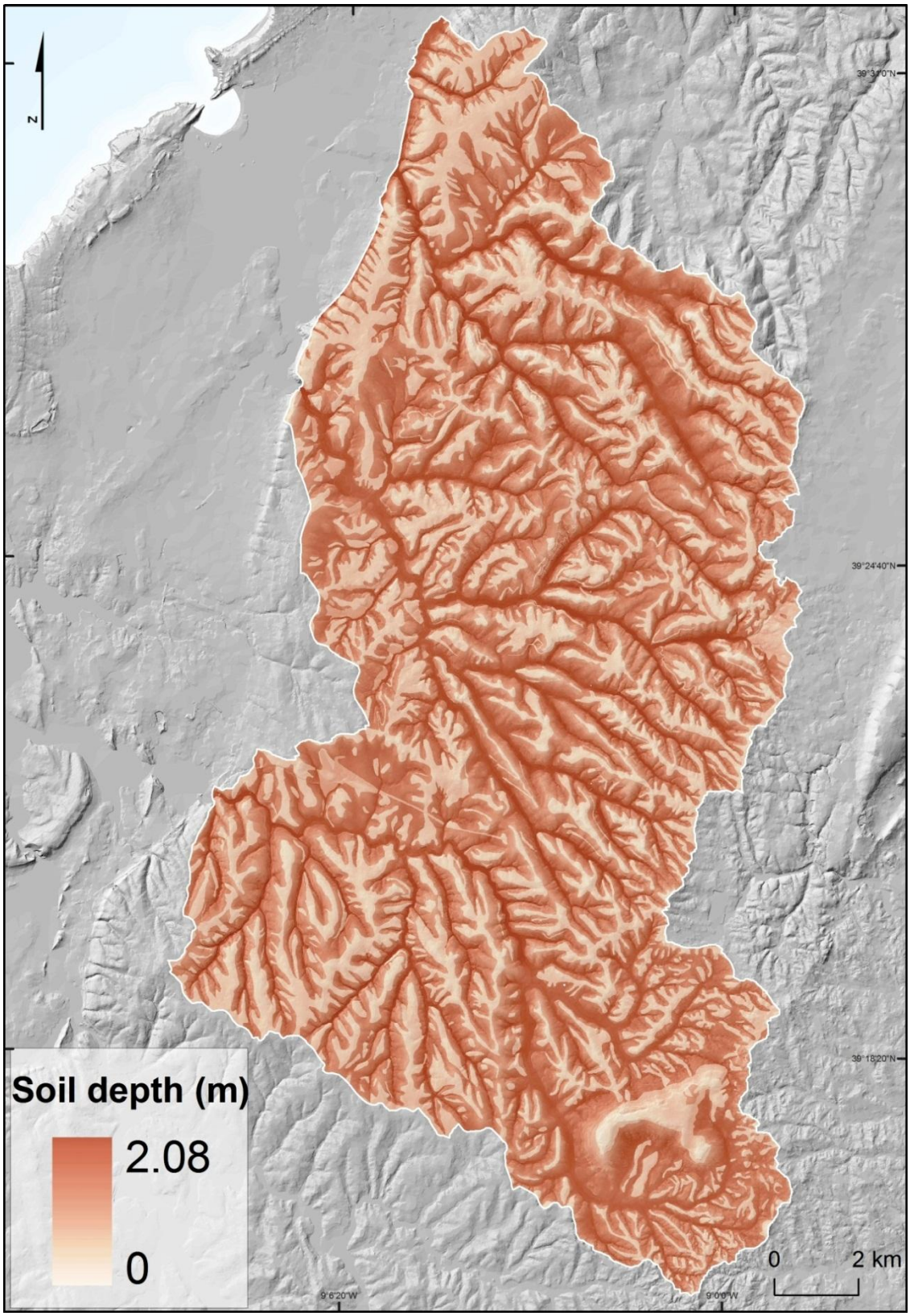

Fig. 5.14 – Soil depth map.

The final soil depth map reflects the commitment between the four soil depth contributing factors. As expected, on the colluvial areas, where simultaneously the

bedrock is less resistant to erosion, the soil thickness is higher. Controversy, on interfluves areas, where the bedrock is simultaneously more resistant to erosion, the soil thickness is thinner.

Although the altered sGIST may not be the optimal method for soil depth data achievement it appears to be a very interesting one when resources are scarce (e.g., lack of geoelectrical equipment for measurements in the field). It must be remember that, despite some constraints regarding the constant kc, the altered sGIST model seems to be a consistent method since it takes into account morphometric variables so far neglected by other methods, such as the linear correlation between soil thickness and elevation or slope gradient, so commonly used by several authors (Saulnier *et al*., 1997; Bourennane *et al*., 2000).

The soil depth map achieved through the altered sGIST model appears especially promising for rainfall-runoff predictions, where subsurface flow is prominent and small-scale soil depth variability may strongly influence water transfer behavior and thus the hydrological and geomechanical behavior of the slopes in the area. However, it should be mentioned that the simulated soil depth provides no more than an approximation of the actual soil depth in the study area.

Soil depth is a very important parameter for the simulation of the hydrological and geomechanical behavior. However, the way this variable is applied depends on the model nature, i.e., if it a static or a dynamic approach. The static model relies on the concept that typically the boundary between the soil and the underlying variably weathered bedrock is abrupt. In line with this, the soil depth variable achieved is directly inserted into the static model without any division into soil horizons. However, for the dynamic model, the soil profile is subdivided into three layers that can be interpreted as the A, B and C horizons. As the study area is dominated, in many places, by shallow depths, some operations were needed to be performed. Thus, for thin soil layers, the depth of the first soil layer were stick to 0.2 m and the second soil layer were stick to 0.3 m. Whenever the soil were deeper those values were proportionally scaled (Beek, 2002). These operations were performed in the dynamic model according to the following equations:

$$D1 = min\left(SDepth, DF1\right); \tag{5.15}$$

$$D2 = min(DF2, SDepth - D1); \tag{5.16}$$

$$D3 = max(SDepth - (D1 + D2), 0); \tag{5.17}$$

$$D3 = if\,(D3 < (1 - Limfac) \times SDepth, 0, D3); \tag{5.18}$$

$$D2 = max(SDepth - (D1 + D3), 0); \tag{5.19}$$

Where “D1”, “D2” and “D3” are, respectively, the depth of the first, second and third soil layer (m). “SDepth” is the soil depth map (m). “DF1” is an arbitrary fraction to restrict the depth of the first soil layer to 0.2 m whenever the soil layers were thin. “DF2” is an arbitrary fraction to restrict the depth of the second soil layer to 0.3 m whenever the soil layers were thin. “Limfac” is an arbitrary fraction to restrict the depth of the third soil layer to 0.95 m whenever the soil layers were thin (Beek, 2002).

5.3.6 USDA soil classification for further hydrogeological properties establishment

Due to the nonexistence of previous work related to the hydrological properties of soil, carried out in the study area, and due to an impossibility to perform flow discharges tests, a standard approach developed by Rawls *et al*. (1982) was used.

Being awarded that field and laboratory measurement for hydrological soil properties acquisition is very difficult, laborious and costly to obtain, the authors developed a study based on 1323 soils with 5350 horizons, which allowed to obtain standard values of several hydrological parameters which includes the saturated hydraulic conductivity, bubbling pressure, total porosity and pore size distribution which are necessary parameters for further hydrological modeling purposes. In their work, a comprehensive compilation of soil-water and hydraulic properties have been assembled and statistically studied. Relationships for predicting water retention volume for particular tensions and saturated hydraulic conductivities based on soil properties, were presented along with a set of a mean hydraulic soil properties for the 12 United States Department of Agriculture

soil texture classes (Rawls, *et al*., 1982). This study, according to Rawls *et al*. (1982), may be used by hydrologists and soil scientist for: 1) the study of theoretical models by comparison with a large set of experimental data; 2) to check the reliability of empirical formula; 3) and to model soil water flow problems for a wide range of soils.

Unfortunately it was not possible to perform a textural analysis of the soil samples collected in the field and, therefore, assign the hydrogeological parameters for each lithological unit. However, the soil map, from Instituto de Desenvolvimento Rural e Hidráulica (IDRHa), contains a very detailed textural data of soils in the study area. For this reason the soil map with a scale of 1:25,000 was used for this work.

For the soil classification, the taxonomy from the United States Department of Agriculture (USDA) was adopted, This taxonomy comprises 12 soil texture classes as follows: sand, loamy sand, sandy loam, sandy clay loam, loam, silt loam, silt, silty clay loam, clay, clay loam, sandy clay and silty clay. In order to ensure a correct soil classification according to the 12 USDA soil texture classes it is necessary to know the soil constituents in relation to its content of sand, silt, clay and organic matter, as well as information on the permeability and structure. Normally the Portuguese soil maps associates several types of soils to a same polygon (may be two or three), with a certain percentage of occupancy according to its contents on sand, silt, clay and organic matter. Thus, in order to ensure a correct classification of each soil polygon on the study area, the calculation of a weighted average was performed taking into account the percentages of occupancy of its contents for each soil type in each polygon. On Table 5.11 it can be seen three types of soil associated to a single polygon.

Table 5.11 – Example of a Data base of one polygon.

Polygon ID	Soil types according to SROA classification			Occupancy (%)		
1	Pato	Vato	Vt	50	30	20

And for each soil type the following constituents are shown on Table 5.12.

Table 5.12 – Example of a Data base of one polygon.

Occupancy (%)	SROA* Classification	USDA Classification	Clay (%)	Silt (%)	Sand (%)	OM (%)
50	Pato	Loam	9.7	44.6	45.7	2.3
30	Vato	Clay loam	31.0	44.4	24.6	1.2
20	Vt	Loam	6.8	44.3	49.0	0.7

* Portuguese Service Recognition and agricultural planning.

In order to assign a single value of clay, silt, sand and organic matter, for further soil classification, the calculation of a weighted average was performed as followed:

For clay:

$$\frac{(9.7\times 50)+(31.0\times 30)+(6.8\times 20)}{100}=15.5 \tag{5.20}$$

For silt:

$$\frac{(44.6\times 50)+(44.4\times 30)+(44.3\times 20)}{100}=44.4 \tag{5.21}$$

For sand:

$$\frac{(45.7\times 50)+(24.6\times 30)+(49.0\times 20)}{100}=40.0 \tag{5.22}$$

For Organic matter:

$$\frac{(2.3\times 50)+(1.2\times 30)+(0.7\times 20)}{100}=1.7 \tag{5.23}$$

After this calculation it was possible to achieve a single value of clay, silt, sand and organic matter and thus a final soil classification (Table 5.13).

Table 5.13 – Example of a Data base of one polygon after the weighted calculation.

Polygon ID	Clay	Silt	Sand	OM
1	15.5	44.4	40.0	1.7

According to these values and using the USDA Soil Texture Triangle Bulk Density was possible to classify this soil within this polygon as Loam (Fig. 5.15). This procedure was then repeated through ArcGIS software for the remaining 880 polygons, existing in the soil map of the study area with the aid of Raster calculator tool (Fig. 5.16).

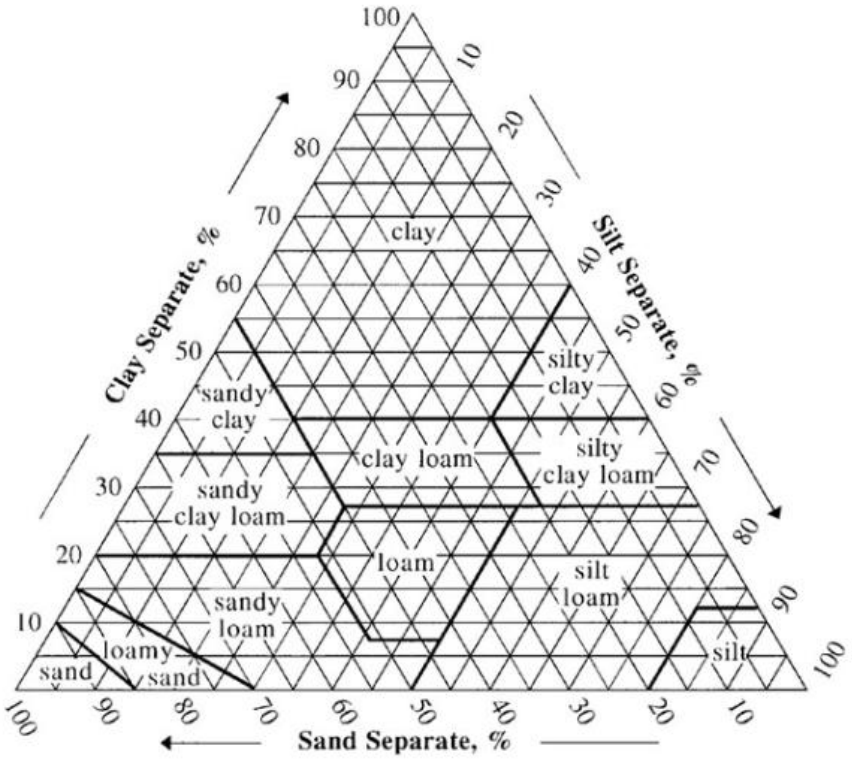

Fig. 5.15 – Soil-Texture Triangle, showing the textural terms applied to soils with various fractions of sand, silt and clay. (Extracted from Dingman, 2002).

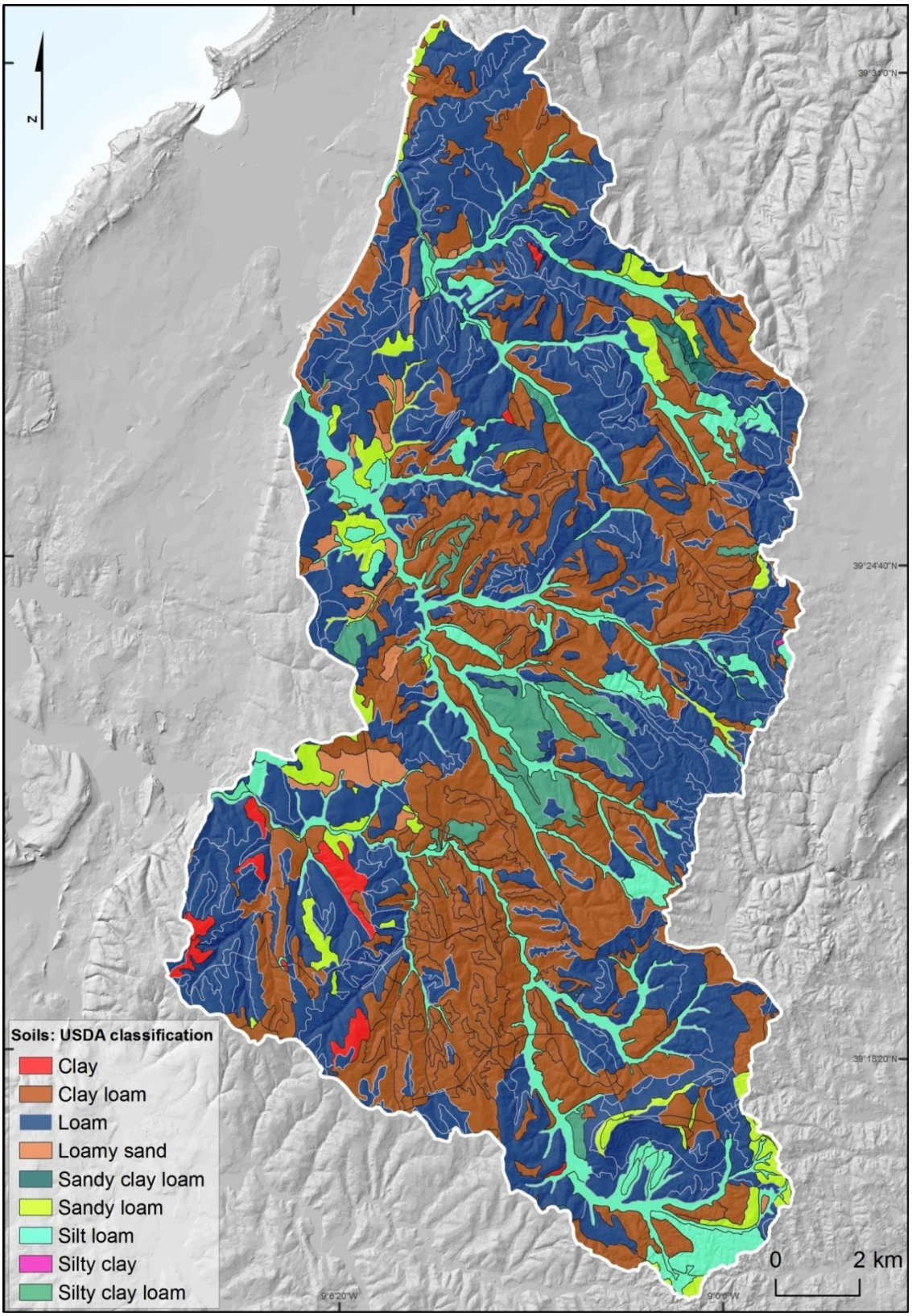

Fig. 5.16 – Soil map classified according to Soil Texture Triangle Bulk Density Calculator for each polygon drawn on the map.

5.4 Static modeling of slope hydrology: TOPOG

O'Loughlin (1986) developed a hydrological model under static conditions that predicts the degree of soil saturation in response to a steady state rainfall for topographic elements defined by the intersection of contours and flow tube boundaries. This model is then coupled to a slope stability model in order to assess the response of the slopes to a critical threshold of a constant rainfall needed for slope failure occurrence. Assuming that landslides occur mostly due to an intense and/or prolonged rainfall event, the resulting hydrological model, performed through the implementation of TOPOG, reflects the effect of soil saturation in loss of effective shear strength.

According to Dietrich and Montgomery (1998) the concentration of superficial runoff and the slope angle are the topographical factors that most influence the stability of slopes. The spatial distribution of shallow slides is also influenced by other factors such as the soil thickness, hydraulic conductivity, shear strength parameters, the duration and intensity of precipitation, the flow direction of the groundwater, the water percolation in fractured rock underlying the covering soil and the resistance of roots of plants and trees.

It is assumed that, while the local properties affect the activity, size and behavior of a shallow slide, the predominant control of where landslides take place is more due to the local topography, since it defines the location where slope failure occurs and water flow (surface and groundwater) converge. The model allows the identification of similar topographic control areas where shallow slides may be triggered (Montgomery and Dietrich, 1995).

As already mentioned, the SHALSTAB model (Dietrich and Montgomery, 1998) is based on the TOPOG hydrogeological model developed by O'Loughlin (1986), which uses constant values of precipitation and maps of soil saturation in equilibrium based on analysis of contributive areas, soil transmissivity and local slope angle (Fig. 5.17). This model divides the basin into topographic elements (Land Units: in this case pixels) defined by the intersection of the topographic contours lines and the limits of the flow channels, orthogonal to the topographic contour lines. When the runoff goes from laminar to

turbulent, the groundwater flow, near surface, runs through the preferred flow channels, allowing the calculation of local flow in each topographic element (Dietrich and Montgomery, 1998).

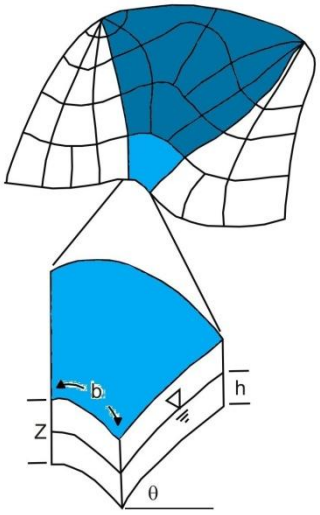

Fig. 5.17 – Topographical elements used by the TOPOG program (Montgomery and Dietrich, 1994) defined by the intersection of the contours and limits of the drainage channels. The contribution of the upstream area, (darker blue) is the cumulative drainage area where all topographic elements drain to a particular element, b is the width of the land unit (m), Z is the soil thickness (m), h is the saturated soil thickness or height of the water level and, θ is the slope angle (°). (Extracted from Montgomery and Dietrich, 1994).

To estimate the ratio between saturated and dried soil (m) (see Equation 5.11), the model takes into account the contribution of the upstream area (a in m) per land unit width (b in m), the effective precipitation (q in m/day), the transmissivity of the soils (T_m in m^2/day) and the slope angle (β^o).

Thus, the ratio between saturated and dry soil (m) being dw the relative position of the piezometric level within the soil thickness (Z) is calculated according to the following equation:

$$m = \frac{dw}{Z} = \frac{q}{T_m} \times \frac{a}{b \times sin\beta} \tag{5.24}$$

The expected result is the value of the parameter m varying spatially throughout the area.

5.4.1 Data

5.4.1.1 Contributing upstream area

The contributing area (a), for each land unit (pixel), was estimated using the SHALSTAB application (Montgomery and Dietrich, 1998) (Fig. 5.18).

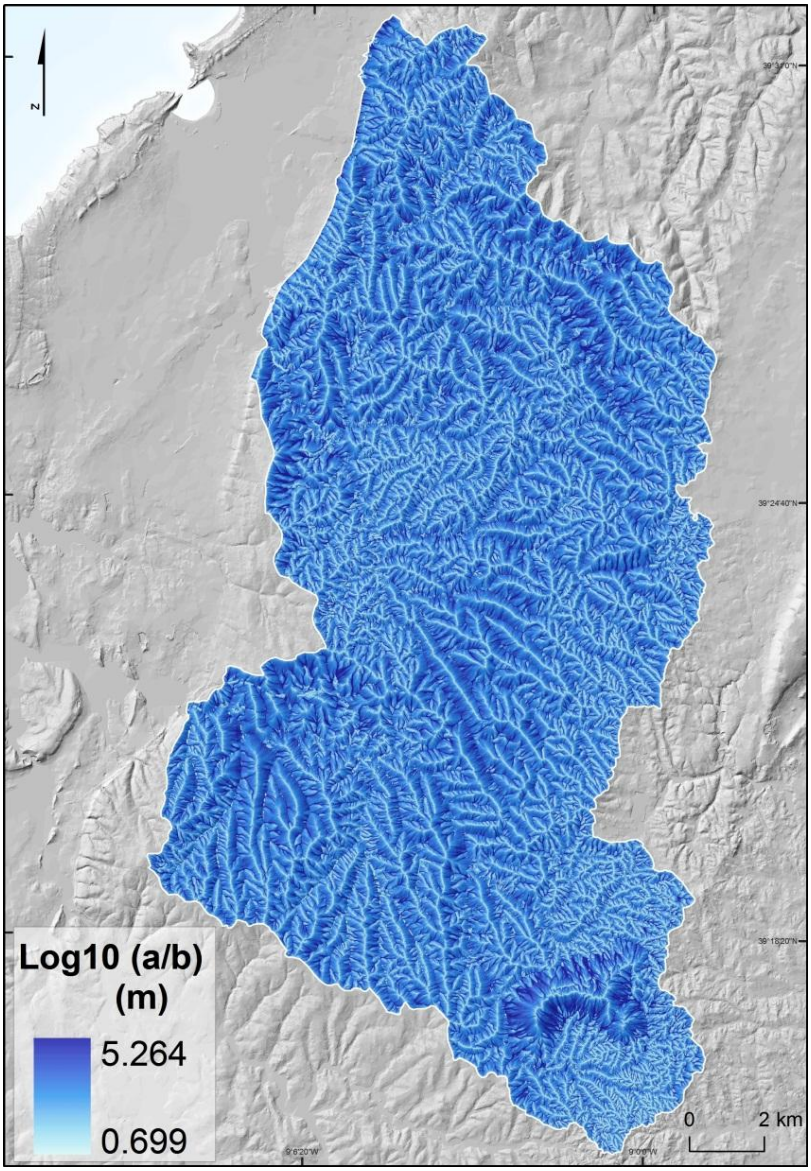

Fig. 5.18 – Contributing area calculated from TOPOG application.

By analyzing the Fig. 5.18 it is found that longer slopes produce higher contributing area downstream. Thus, higher hydraulic loads are applied along the water courses and flows, and lower hydraulic loads are applied on ridges areas.

5.4.1.2 Critical rainfall thresholds

The effective precipitation (q) (m/d) referred in Equation 5.24, is given by a threshold which is defined according to White *et al*. (1996), as a minimum or a maximum quantity needed to occur a given process or to change a state. A minimum threshold defines the lowest level below which a process does not occur. A maximum threshold represents the level, above which a process always occurs, i.e., there is 100% chance of occurrence whenever the threshold is exceeded (Crozier 1996 cited by Reichenbach 1998).

According to Reichenbach *et al*. (1998), for rainfall-induced slope failures, a threshold may represent the minimum intensity or duration of rain, the minimum level of pore water pressure, the slope angle, the reduction of shear strength or the displacement required for a landslide to take place.

For the hydrological model under static conditions, only a single value of precipitation is taken into account and in this sense there is the need to obtain a critical threshold of minimum rainfall capable to trigger landslides in the study area.

The empirical rainfall thresholds are based on the statistical and probabilistic analysis of the relationship between rainfall and the occurrence of mass movements for a certain period of time in a certain area (Reichenbach *et al*. 1998; Zêzere and Rodrigues, 2002; Pereira, 2010). This type of analysis requires accurate rainfall data as well as detailed information on the dates of occurrence of slope failures (Reichenbach *et al*., 1998).

Unfortunately, for this work, it was not possible to obtain dates of occurrences for a reasonable amount of landslides and, in this sense, hypothetic scenarios were used based on work carried out in a neighboring area.

To calculate the effective precipitation and perform the static hydrological model (Montgomery and Dietrich, 1998) it is first necessary to estimate, under static conditions, the critical scene of landslides occurrence under critical rainfall thresholds which can trigger shallow landslides.

For this step 7 different scenarios were used. First, a scenario where the soil is under a complete saturated condition (m=1). Second, a scenario where the soil is completely dry (m=0) and additional five different scenarios where the soil moisture varies spatially according to effective precipitation. For these five scenarios were used the critical rainfall threshold obtained by Ascenso (2011) for the Batalha municipality located, approximately, 26 km Northeast from the study area (Fig. 5.19):

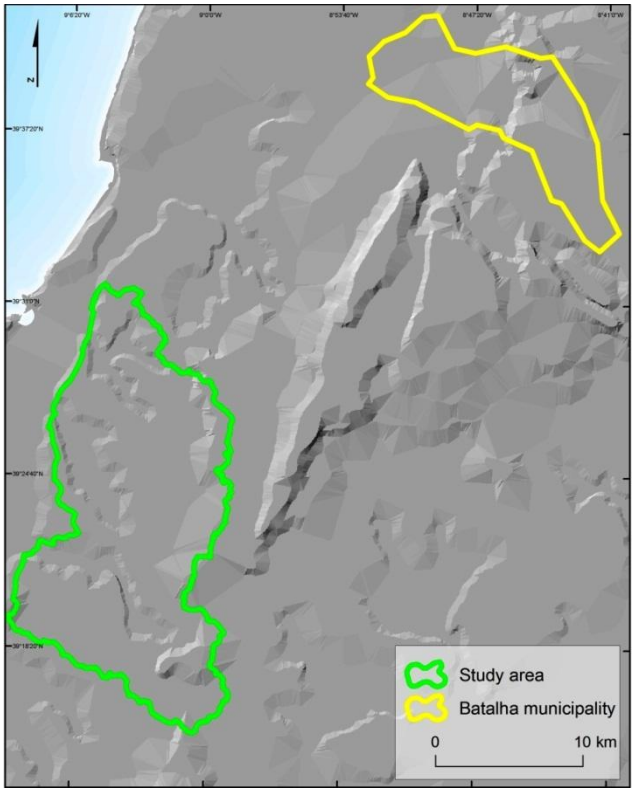

Fig. 5.19 – Framework showing the location and the distance between the study area and Batalha municipality.

In a very succinct description, the critical rainfall threshold is calculated from the return period which is achieved through the Gumbel law. Then, by identifying the highest return period obtained for each event it is possible to obtain the critical rainfall threshold by means of regression analysis (Ascenso, 2011). For the Batalha municipality 30 landslide and flood events occurred from 1980 to 2010 were taken into account. Based on the rainfall over the same period at the Batalha meteorological station, the critical rainfall threshold for flood and landslide occurrence in the following (Ascenso, 2011):

$$Cr = 6.68D + 86.7 \quad (5.25)$$

Where Cr is the Critical rainfall threshold and D is the number of cumulate antecedent rainfall days. The Critical rainfall threshold (Cr) is the effective precipitation (q) parameter of the SHALSTAB model.

According to Zêzere and Trigo (2011), shallow translational soil slips are most commonly triggered by intense precipitation, falling within the 1 to 15 days long range. Thus, the five different scenarios, mentioned above, will vary according to the number of accumulated rainfall days, specifically for 1, 3, 5, 10 and 15 days. It is important to mention that this work should have been done taking into account the return periods and the critical thresholds computed for rainfall registered data in meteorological stations within the study area. However, due to lack of knowledge of the occurrence dates of landslides it was impossible to achieve the precise critical rainfall threshold for each meteorological station. Thus, it is important to emphasize that the scenarios proposed here should be analyzed carefully and with some restriction since it does not reflect the reality of the diverse geomorphological territory but it is only an approximation of what could happen if the critical thresholds of the meteorological station Batalha fitted within the heterogeneous study area.

5.4.1.3 Soil hydrological properties: saturated hydraulic conductivity

As it can be seen on Equation 5.24 to perform the static hydrological model the hydrological parameter transmissivity is required. The transmissivity (m^2/d) takes into account the saturated hydraulic conductivity of soil (K_{sat}) (m/d) and the soil thickness (Z) (m) (Custodio and Llamas, 1976; Lencastre and Franco, 2006).

$$T_m = K_{sat} \times Z \tag{5.26}$$

The K_{sat} values were initially assigned according to the standard values published by Rawls *et al.*, (1982) (Table 5.14).

Table 5.14 – K_{sat} values assigned for the study area based on the standard values given by Rawls *et al*., 1982.

Soils	K_{sat} (m/d)
Clay	0.0144
Clay loam	0.0552
Loam	0.3168
Loamy sand	1.4664
Sandy clay loam	0.1032
Sandy loam	0.6216
Silt loam	0.1632
Silty clay	0.0216
Silty clay loam	0.036

However, as it will be possible to observe later on this chapter, such K_{sat} values resulted in hydrological models presenting the piezometric level located above the topographic surface, regardless the input of rainfall. In terms of susceptibility this situation causes a large area of the study area classified as unstable (SF≤1), which is not realistic for the study area.

Thus, in order to calibrate the k_{sat} values, an iterative process was implemented, which consistently tested the values of k_{sat} for the soil types where landslides occur (clay loam; silt loam; loam), against the results of the prediction rate curve (in terms of AUC value) for 40% of the shallow translational areas. The k_{sat} values were progressively increased maintaining the relative proportions between the different soil types. The calibrated K_{sat} was achieved when k_{sat} values reached its maximum without compromising the model performance. The maximum was achieved with a multiplier factor of 4.8 (Table 5.15).

Table 5.15 – Final values of K_{sat} based on the standard values given by Rawls *et al*. (1982) and calibration for the study area.

Soils	K_{sat} (m/d)	Data source	Occupancy (%)
Clay	0.0144	References	1.00
Clay loam	0.26496	References and back analysis	34.42
Loam	1.52064	References and back analysis	45.54
Loamy sand	1.4664	References	1.52
Sandy clay loam	0.1032	References	0.27
Sandy loam	0.6216	References	3.46
Silt loam	0.78336	References and back analysis	10.58
Silty clay	0.0216	References	0.01
Silty clay loam	0.036	References	3.21

The multiplication between the two statements given on Equation 5.26, i.e., between the K_{sat} map and the soil thickness map were performed on Raster calculator tool from ArcGis software (Fig. 5.20).

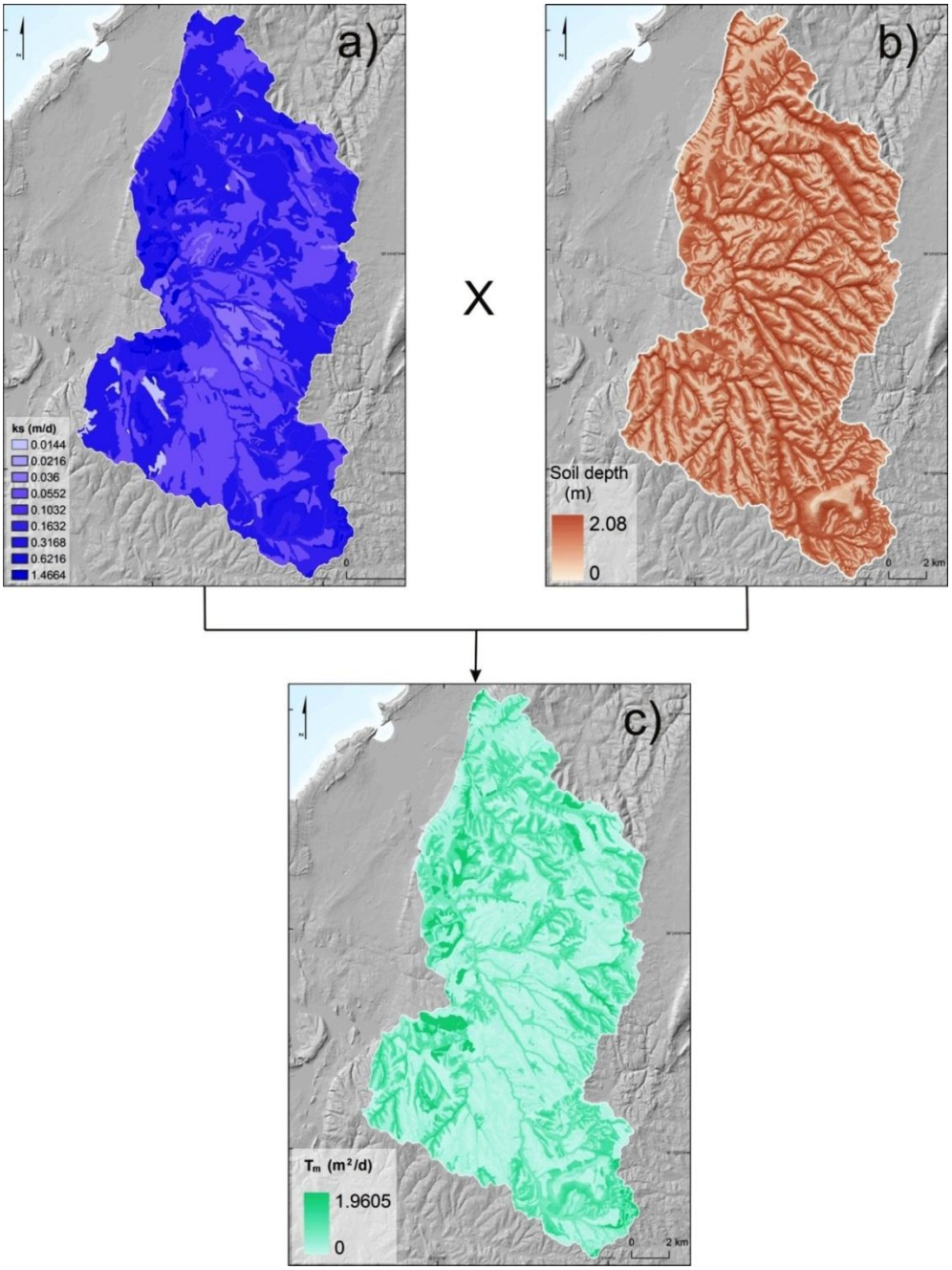

Fig. 5.20 – Parameters needed for transmissivity acquisition: a) saturated hydraulic conductivity of soil (Ksat) (m/d); b) soil depth (Z) (m); c) transmissivity (m^2/day).

The hydraulic transmissivity seems to be lower on the central part of the study area where clay loam is mostly located. However, this lower hydraulic transmissivity area is interrupted by areas of higher hydraulic transmissivity due to the existence of alluvium, or

more specifically, to silt loam. Moreover, on the West and East part of the study area, there are some places where hydraulic transmissivity is very high registering the highest values of the study area due to the influence of Loam and Loamy sand here located. Due to the calibration of the K_{sat} and the critical rainfall scenarios it is possible to define 11 different scenarios which will be used for further SHALSTAB and slope stability modeling (Table 5.16).

Table 5.16 – 11 Scenarios for verifying the influence of the improvements on K_{sat} hydrological parameter.

	Scenarios	**Hydrological soil condition**	**Ratio between saturated and dried soil (m)**
With Back analysis on the geotechnical parameters	Scenario 1	Saturated	1

By varying spatiality the hydrological soil conditions:				
		Rainfall accumulated days	Effective Precipitation (q) (mm/d)	Effective Precipitation (q) (m/d)
With back analysis on the geotechnical parameters	Scenario 2	1	93.37	0.09337
	Scenario 3	3	106.73	0. 10673
	Scenario 4	5	120.09	0.12009
	Scenario 5	10	153.48	0.15348
	Scenario 6	15	186.87	0.18687
With back analysis and on the geotechnical and hydrological parameters	Scenario 7	1	93.37	0.09337
	Scenario 8	3	106.73	0. 10673
	Scenario 9	5	120.09	0.12009
	Scenario 10	10	153.48	0.15348
	Scenario 11	15	186.87	0.18687

5.4.2 Static hydrological model implementation

Gathering all the necessary variables (effective precipitation, transmissivity, contributing upstream area and slope angle) it was possible to perform the hydrological static model, varying according to the different scenarios, i.e., according to the effective precipitation input and the K_{sat} data (Fig. 5.21 and 5.22). The following Fig. 5.21 shows the ratio

between saturated soil thickness and the unstable soil thickness (m) using different effective precipitation and the standard values of K_{sat} without any adjustment.

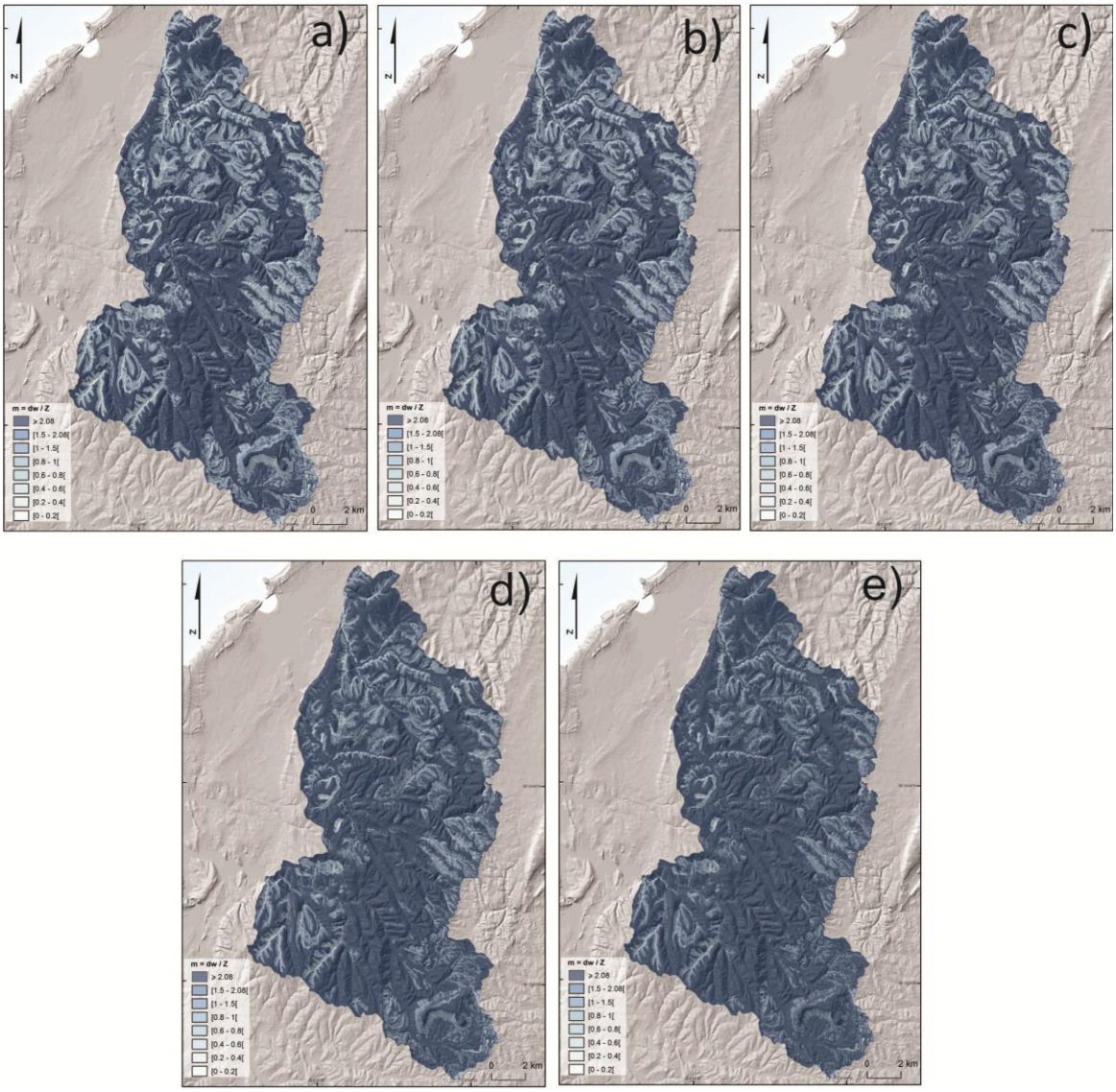

Fig. 5.21 – Ratio between saturated soil thickness and the unstable soil thickness (m) using the uncalibrated values of saturated hydraulic conductivity (Ksat) and different effective precipitation: a) 1 day of accumulated rainfall; b) 3 days of accumulated rainfall; c) 5 days of accumulated rainfall; d) 10 days of accumulated rainfall; e) 15 days of accumulated rainfall.

From Fig. 5.21:a to Fig. 5.21:e there is an accumulation of rainfall days according to the different scenarios given by the Table 5.16. Regardless the soil type, the maps given by Fig. 5.21 are influenced by the very low values of saturated hydraulic conductivity. In most part of the territory, such K_{sat} values results in hydrological models presenting the piezometric level located above the topographic surface, regardless the accumulated rainfall. Since the K_{sat} values were not obtained by field and/or laboratory measurements

and due to these unrealistic scenarios, unconfirmed by field observations, there was the need to calibrate the values of K_{sat}. Thus, in order to make it more realistic the values of K_{sat} were increased, for the soil types where landslide occurred. The following Fig. 5.22 shows the ratio between saturated soil thickness and the unstable soil thickness (m) using the different effective precipitation and calibrated K_{sat} values.

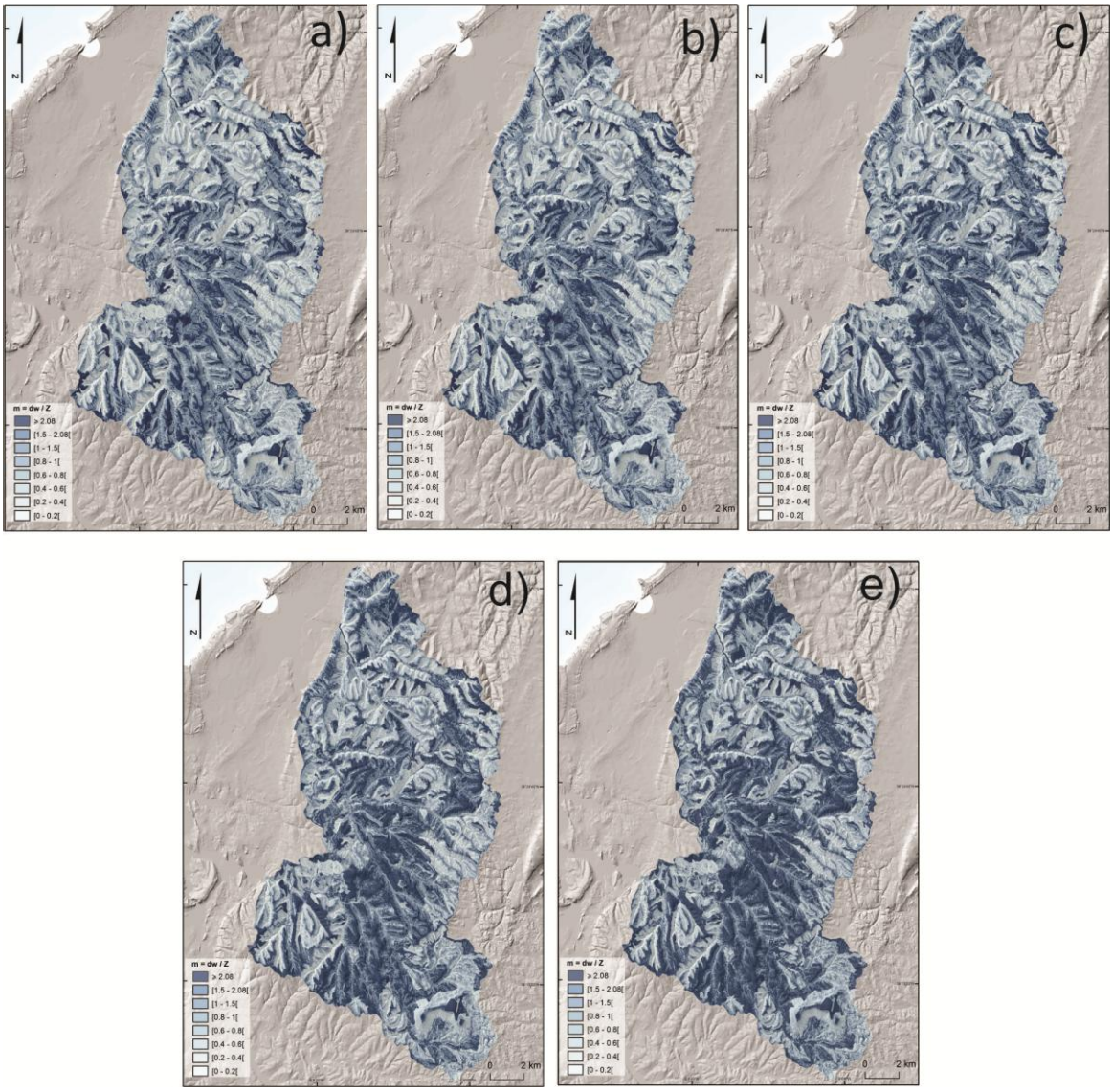

Fig. 5.22 – Ratio between saturated soil thickness and the unstable soil thickness (m) using the calibrated values of saturated hydraulic conductivity (Ksat) and different effective precipitation: a) 1 day of accumulated rainfall; b) 3 days of accumulated rainfall; c) 5 days of accumulated rainfall; d) 10 days of accumulated rainfall; e) 15 days of accumulated rainfall.

Based on Fig. 5.22 from a) to e) it is possible to observe that, soils with higher permeability along with higher slope angles present lower groundwater level compared to the also higher permeable soils but in conjunction with lower slope angles. In lower

permeable soils, such as the clay (1% of the total study area), silty clay (0.01% of the total study area), silty clay loam (3.21% of the total study area) and the dominant clay loam (34.42% of the total study area) (Fig. 5.16, Table 5.15) along with topographically flat areas, it is possible to observe that the piezometric level is positioned at a higher elevation or even above the surface topography. From Fig. 5.22:a to Fig. 5.22:e it is possible to observe that the increase of rainfall increases the groundwater table in the unsaturated layers, and the increase of piezometric level located above the surface topography.

5.5 Static modeling of slope stability: applying the Infinite slope equation through raster calculator

In a raster GIS, such as ArcGis in which the coupled static hillslope model is embedded, calculations take place on the level of the individual cells. The hydrological modeling were made using a pixel size of 25m. However, for the slope stability model a resize were made in order to perform all the following calculations in a 5m pixel size.

By implementing the Equation 5.10, on the Raster calculator tool of the ArcGis software, it was possible to obtain 11 scenarios of safety factor, which correspond to the variation of effective precipitation and uncalibrated and calibrated values of saturated hydraulic conductivity (Fig. 5.23, 5.24 and 5.25).

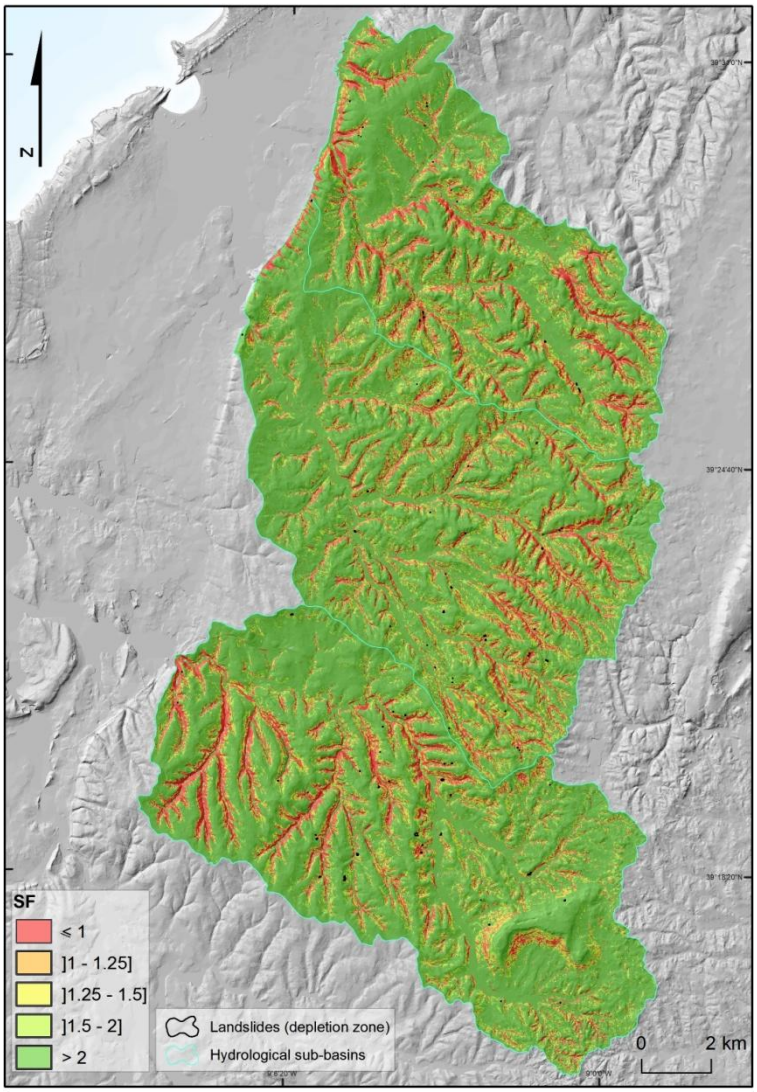

Fig. 5.23 – Landslide susceptibility assessed thought the safety factor, assuming saturated soil, i.e., groundwater table located at the topographical surface (m=1): Scenario1: for geotechnical parameters obtained by laboratory measurements and back analysis.

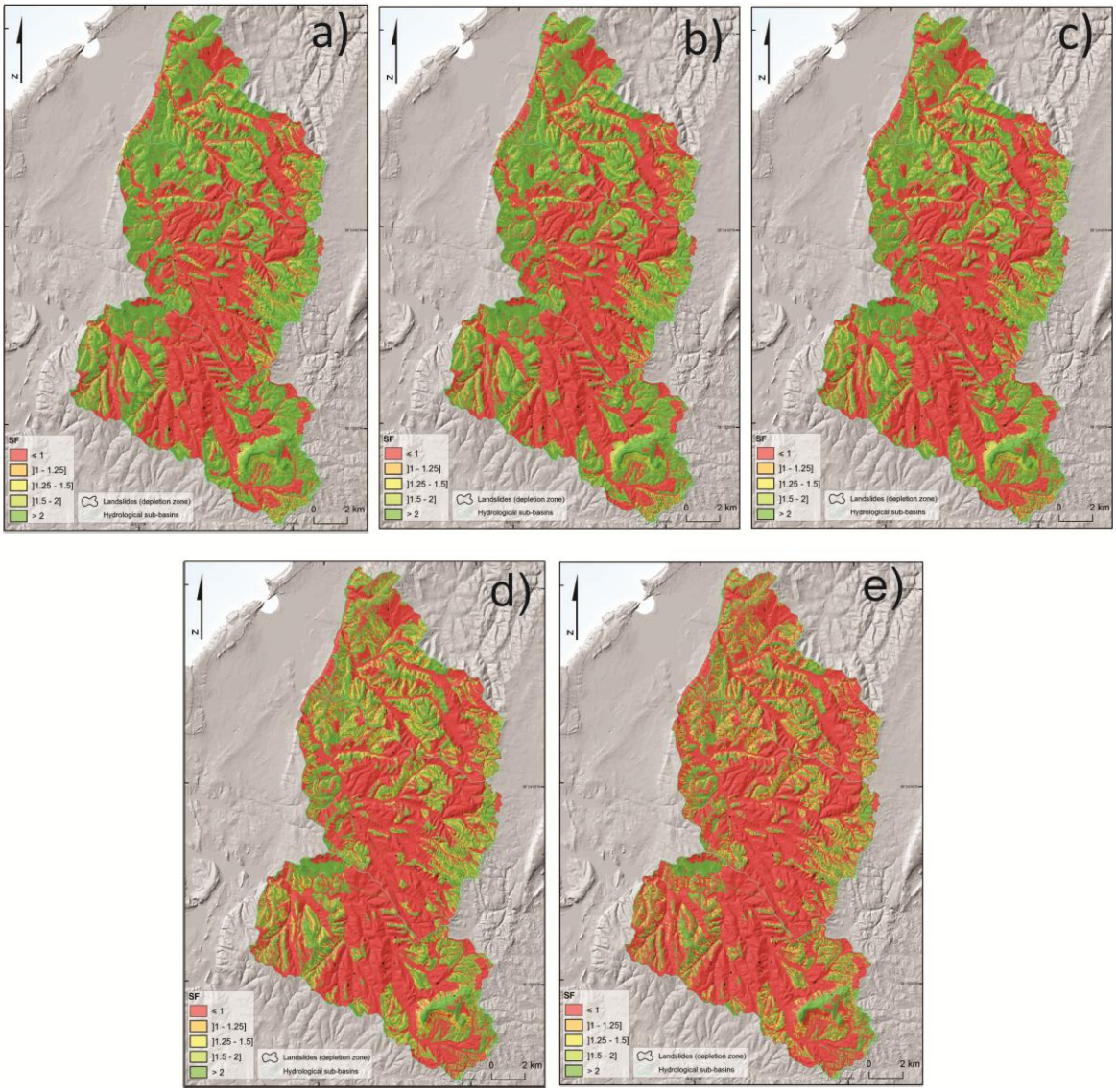

Fig. 5.24 – Landslide susceptibility assessed thought the safety factor, using the geotechnical parameters obtained by laboratory measurements and back analysis and uncalibrated values of saturated hydraulic conductivity (Ksat): a) Scenario 2: for one day of accumulated rainfall; b) Scenario 3: for three days of accumulated rainfall; c) Scenario 4: for five days of accumulated rainfall; d) Scenario 5: for ten days of accumulated rainfall; e) Scenario 6: for fifteen days of accumulated rainfall.

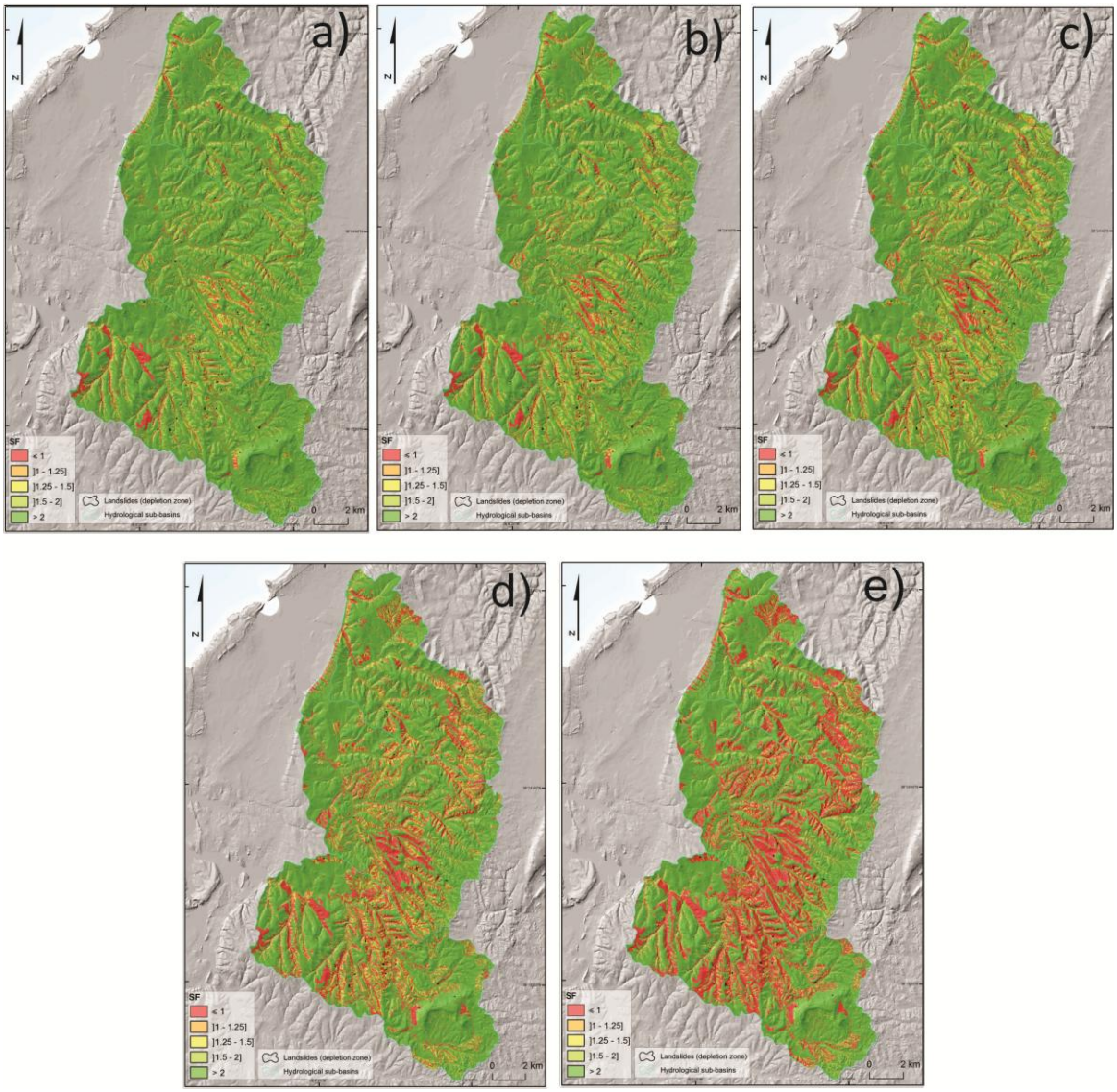

Fig. 5.25 – Landslide susceptibility assessed thought the safety factor, using the geotechnical parameters obtained by laboratory measurements and back analysis and calibrated values of saturated hydraulic conductivity (Ksat): a) Scenario 7: for one day of accumulated rainfall; b) Scenario 8: for three days of accumulated rainfall; c) Scenario 9: for five days of accumulated rainfall; d) Scenario 10: for ten days of accumulated rainfall; e) Scenario 11: for fifteen days of accumulated rainfall.

5.5.1 Analysis and validation of results

Comparing the previous maps of safety factor (SF), it can be denoted major differences between the maps modeled with the uncalibrated (Fig. 5.24) and calibrated values of saturated hydraulic conductivity (Fig. 5.25). The Fig. 5.24 presents much more dramatic scenarios due to the uncalibrated low values of saturated hydraulic conductivity. Regardless the accumulated rainfall, those maps present a very large area classified as unstable (SF≤1). Those unstable areas increase in about more 10% as the rainfall accumulates to 15 consecutive days. The situation changes drastically when the modeling is based on the calibrated values of saturated hydraulic conductivity which results in a very low percent of the total occupancy of the study area classified as unstable (SF≤1).

When the piezometric level is located at the topographical surface (Fig. 5.23), the unstable areas presents a very similar situation when compared with the maps modeled through the calibrated values of saturated hydraulic conductivity, for one day of critical precipitation (Fig. 5.25:a). However, it can be observed that, for the calibrated values of saturated hydraulic conductivity, the SW part of the study area presents a much more critical situation for Fig. 5.25 then for Fig 5.23. This can be explained by the low values of saturated hydraulic conductivity founded for this region, which encourages the piezometric level to exceed the topographical surface with only one day accumulated rainfall, and thereby, decreasing the safety factor for this part of the study area.

In order to understand if this reduction of the unstable area corresponds to an improvement of the performance of the model it will be carried out a validation using the prediction rate curves and the Area Under Curve (AUC) technique. It should be noted that, for this work, instead of using all the landslide areas, it was only used the depletion area of the landslides. Such procedure provides the prediction of the future disruption areas due to shallow translational slides in the study area.

There are major differences between the scenarios using the uncalibrated and calibrated values of saturated hydraulic conductivity (Table 5.17, corresponding to scenario 1 to 6, compared to the Table 5.18 for the scenario 7 to 11). Through calibration, improvements

were achieved which can be proved through highest AUC values (Table 5.17, 5.18 and Fig. 5.26 and 5.27).

Table 5.17 – AUC of the Scenarios modeled with the geotechnical parameters obtained by laboratory measurements and back analysis and initial values of K_{sat}.

	Rainfall accumulated days	Effective Precipitation (q) (mm/d)	Effective Precipitation (q) (m/d)	AUC (All landslides)
Scenario 1			M=1	0.746
Scenario 2	1	93.37	0.09337	0.662
Scenario 3	3	106.73	0. 10673	0.647
Scenario 4	5	120.09	0.12009	0.635
Scenario 5	10	153.48	0.15348	0.611
Scenario 6	15	186.87	0.18687	0.586

Table 5.18 – AUC of the Scenarios modeled with the geotechnical parameters obtained by laboratory measurements and back analysis and adjusted values of K_{sat}.

	Rainfall accumulated days	Effective Precipitation (q) (mm/d)	Effective Precipitation (q) (m/d)	AUC (All landslides)
Scenario 7	1	93.37	0.09337	0.806
Scenario 8	3	106.73	0. 10673	0.801
Scenario 9	5	120.09	0.12009	0.792
Scenario 10	10	153.48	0.15348	0.791
Scenario 11	15	186.87	0.18687	0.786

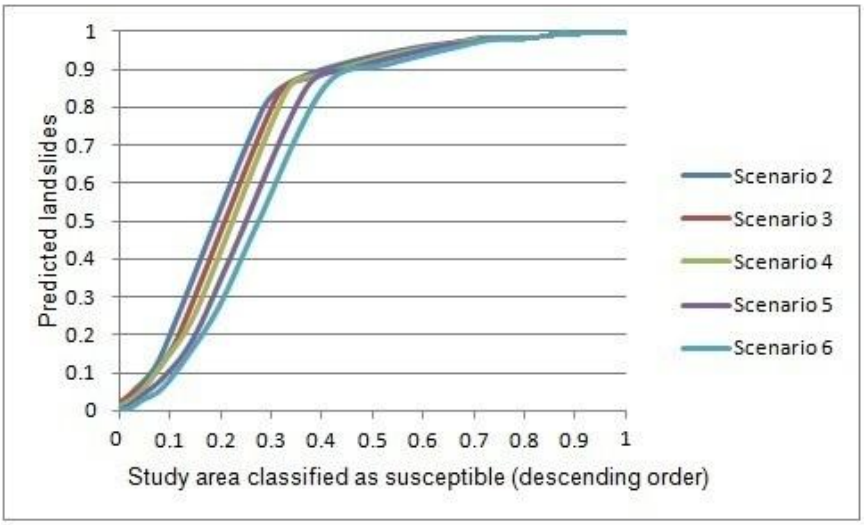

Fig. 5.26 – Prediction rate curves.

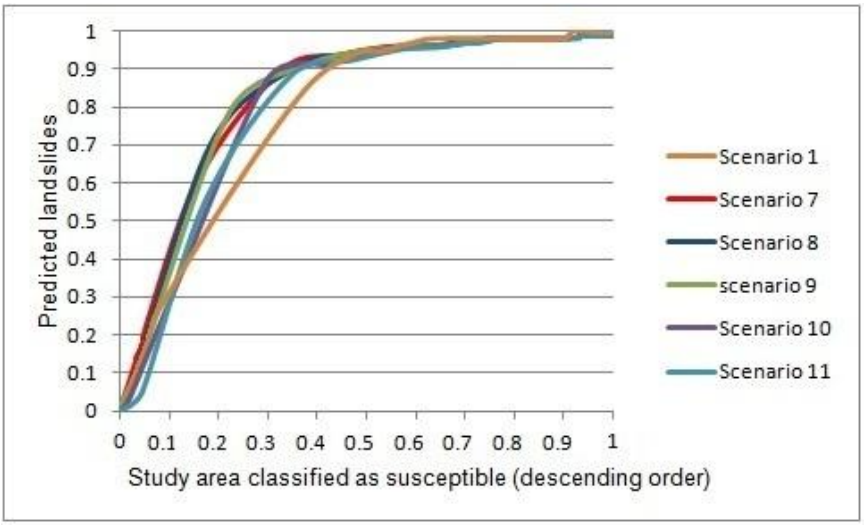

Fig. 5.27 – Prediction rate curves.

Globally, it is possible to conclude that the calibration of the saturated hydraulic conductivity parameters is very important for this kind of analysis. When analyzing the AUC values, the models based on the calibrated values of Ksat reveal a better performance. The AUC values are, indeed, good indicators for comparing model performances. However, to be considered a good model the physically-based models must not only take into account the AUC values but also the ability of the modeled unstable areas to predict landslides. Thus, considering only the susceptibility model based on the groundwater table located at the topographical surface (scenario 1) and the calibrated models (scenario 7 to 11) it is possible to observe, in Table 5.19, that the scenario 11 seems to be the susceptible model with better predictive ability.

Although with better AUC value the scenario 7, with only one day of accumulated rainfall (93.37 mm), is not enough to predict most of the shallow translational slides, i.e., the highest susceptible 5.9% of the total study area is not enough to predict the majority of the total shallow translational slides occurrences. Whereas, the unstable (rupture) area of the scenario 11, which corresponds to the highest susceptible 24.7% of the total study area, is enough to predict 72.5% of the total shallow translational slides area.

Table 5.19 – Landslides susceptibility classes, for shallow translational slides obtained through the static physically-based method. Area of each class and landslide area in each class (both in % of the total).

Safety Factor (SF)	Slope Stability	Scenario 1		Scenario 7		Scenario 8		Scenario 9		Scenario 10		Scenario 11	
		CA	LA	CA	LA	CA	LA	CA	LA	CA	LA	CA	LA
SF ≤ 1	Unstable (rupture)	11.8	26.4	5.9	6.4	7.6	12.4	9.7	18.7	16.6	42.9	24.7	72.5
1 <SF< 1.25	Unstable (likely rupture)	4.6	13.8	3.1	12.7	3.7	15.6	4.2	18.5	6.4	28.3	5.4	10.1
1.25 <SF< 1.5	Marginally Unstable	4.8	6.3	4.1	18.1	4.6	18.4	5.4	24.5	5.7	10.6	3.7	4.4
1.5 <SF< 2	Marginally Stable	9.3	17.6	9.9	36.1	10.8	33.2	11.1	22.8	7.7	6.7	6.1	2.5
SF> 2	Stable	69.5	36.0	77.0	26.8	73.3	20.4	69.7	15.5	63.7	11.4	60.1	10.5
TOTAL		100	100	100	100	100	100	100	100	100	100	100	100

CA Class area
LA Landslide area

Noteworthy that these results, despite seeing promising, depict only hypothetical scenarios. It is actually possible to equip these models with greater analytical ability when using the dynamic approach, which it is showed in the following sections.

5.6 Dynamic modeling of slope hydrology: STARWARS

Mathematical methods are already capable to reproduce the change of water level taking into account the dynamics of precipitation, infiltration and temporally varying flow, under dynamic conditions (e.g. Iverson, 2000; Amaral, 2009, 2010, Baum, 2010).

Unlike the model proposed by Montgomery and Dietrich (1994), these models allow to address influences of temporally varying precipitation and vegetation dynamics. The prediction of landslides based on static environmental factors and/or the existence of steady state conditions appears to be insufficient for this kind of analysis (Wu and Sidle, 1995; Gorsevski, 2002; Gorsevski *et al.*, 2003, Gorsevski *et al.*, 2006). Relatively static

environmental factors (i.e., elevation, slope, aspect, and topographic curvatures) exhibit negligible changes in their state through time, and differ from dynamic factors such as climatic factors or human activities, which tend to alter landslide susceptibility through time.

Frequently, information on the piezometric level is hard to obtain. With limited equipment it is also hard to obtain such data via field measurements. Due to such conditions, simulating the groundwater level is crucial.

As previously mentioned, rainfall is the main triggering factor of landslides. However, in this section we intend to go further in this matter by evaluating and incorporating, in the dynamic hydrological model, specific parameters, such as the contribution of the vegetation for the evaporation, over time, which can influence the water available for percolation and, subsequently, the matric suction (i.e. the additional interstitial force within the soils). This procedure derives from the fact that the antecedent moisture condition of soil revealed to be also a factor of utmost importance, especially when the rainfall distribution becomes more erratic in time, as in the case of Mediterranean areas. Percolation through the unsaturated zone can actually attenuate the response of the groundwater level to a large rainfall event (Iverson, 2000; Beek, 2002).

The dynamic hydrological model, STARWARS, developed by Beek (2002), is here implemented with the aim of simulating the spatial and temporal groundwater level. This phase of the work was carried out at the University of Utrecht, in Netherlands, under the supervision of Dr. Rens Van Beek, author of the scripts of slope hydrology and stability (Starwars + Probstab: Script A8.1 in Appendix 8).The model takes into account the soil water infiltration and percolation including the delay and loss of percolation in the unsaturated zone which influences the critical pore pressures over time. The model describes the saturated and the unsaturated transient flow in the vertical and lateral directions. It is worth mention that, in the model, the saturated and unsaturated zones are taken as freely draining describing only unconfined groundwater levels.

This model, based on a constant groundwater level or generated over semi-impervious lithological boundary, restricts the direct loss of soil moisture into deeper strata. The transient saturated and unsaturated flow is described, in the hydrological component, as a function of the elevation potential only, neglecting the matric potential for the flow in the unsaturated zone. Thus, the percolation is limited to gravitational vertical flow only. Whereas, in the saturated zone, it is the piezometric level which defines the lateral flow (Beek, 2002).

The matric potential in the unsaturated zone is here neglected because, even if the lateral unsaturated flux is substantial, the large vertical gradient directs it effectively towards the saturated zone (Jackson, 1992; Van Asch *et al*., 2001; Beek, 2002). Thereby, the resulting fluxes under the gradient of the matric potential are small when compared to those of the vertical and lateral gravitational flows (Beek, 2002).

In some specific cases the lateral flow is influenced by the bedding inclination, however according to Philip (1990), for a planar slope, the lateral flux is negligible for all inclinations below 30°. Originally, it was thought to introduce information about the bedding attitude into the dynamic hydrologic model. However, this has not been done since the study area is dominated by low slope angles (below 30º) as it was demonstrated in chapter 4. Therefore, adding such data would only increase the redundancy.

For modelling purposes, the soil profile is subdivided into three layers that can be interpreted as the A, B and C soil horizons. These subdivisions simulate the resulting fluxes over the differentiated soil profile above the semi-impervious lithic contact (Fig. 5.28).

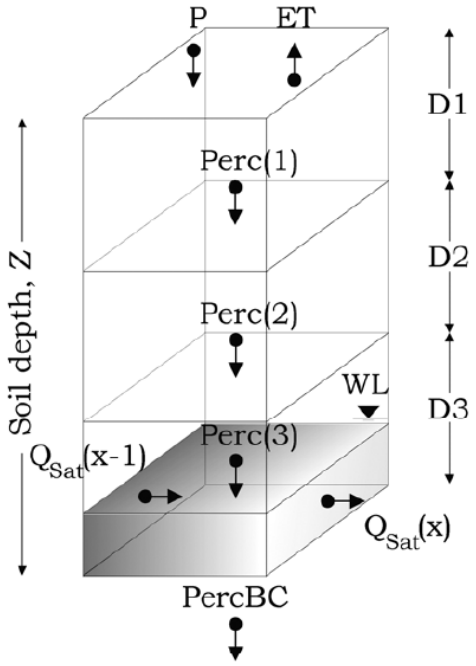

Fig. 5.28 – Model layer Z (extracted from Beek, 2002).

Although assuming three layers, in the third (deeper) layer it is considered a fourth infinite layer whenever the substratum is not considered impervious. In such cases some water will be lost to bedrock. The influence that this layer causes in the modelling results will be further discussed.

For each layer the fluxes and water storage are given in units of waterslice. This approach has the advantage of facilitating the computation of the relative degree of saturation which is achieved through the maximum storage. Subsequently, based on the relative degree of saturation it is possible to calculate the percolation in the unsaturated zone. By definition, the relative degree of saturation, θ_E, is given by:

$$\theta_E = \frac{\theta - \theta_{res}}{\theta_{sat} - \theta_{res}} \tag{5.27}$$

Where, θ is the volumetric moisture content, θ_{sat} is the saturated moisture content and θ_{res} is the residual moisture content, all in units of $m^3.m^{-3}$

The porosity and the residual moisture content are the parameters needed for obtaining the saturated moisture content which is usually set to a fraction of this maximum. The relative degree of saturation varies by definition between zero and one when the soil is respectively at its residual and its saturated moisture content (Beek, 2002). The numerator, of the previous equation, corresponds to the actual amount of drainable pore water, while the denominator represents the maximum amount of drainable pore water. Thereby, the effective degree of saturation is achieve in units of waterslice by multiplying by the thickness of the unsaturated zone above the groundwater table, which is given by:

$$\theta_E = \frac{D_{unsat} \times \theta - \theta_{res}}{D_{unsat} \times \theta_{sat} - \theta_{res}} = \frac{StorMat}{D_{unsat}\ (\theta_{sat} - \theta_{res})} \tag{5.28}$$

where D_{unsat} is the thickness in (m) of the unsaturated zone and StorMat is the actual storage ($m \cdot m^3 \cdot m^{-3}$) of the unsaturated zone.

The vertical unsaturated matric flow, *Perc,* for each model layer Z, is based on the unsaturated hydraulic conductivity, $k(\theta_E)$. This parameter is obtained through the soil grain size and degree of saturation which can be calculated from the soil water retention curve (SWRC) using the mathematical formulation of Farrel and Larson (1972) and the saturated hydraulic conductivity, k_{sat} (obtained through the soil grain size). Both, the saturated and the unsaturated hydraulic conductivity, are defined in units of ($m \cdot d^{-1}$). The model for the SWRC is empirical and it is based on analogies in thermo-dynamics. The original model was defined in terms of θ/θsat. Rewritten in terms of θ_E, it is given by:

$$|h| = h_A\, exp[\alpha(1-\theta_E)] \tag{5.29}$$

where |h| is the absolute value of matric suction in (m), h_A is the absolute matric suction which corresponds to the air entry value in (m) and α is the dimensionless slope of the log-linear relationship between ln(|h|) and $(1-\theta_E)$ (Beek, 2002).

The unsaturated hydraulic conductivity is obtained thought the calculation of the capillary of Millington and Quirk (1959, 1961).These authors stated that the relative unsaturated hydraulic conductivity ($K_r(\theta_E)$ is an analogous function of filled capillaries representing the filled pores at different suction levels. Thus, the relative unsaturated hydraulic conductivity, based on the SWRC, is achieved by:

$$k_r = \theta_E^t \frac{[\exp(2\alpha\theta_E) - 2\alpha\theta_E - 1]}{[\exp(2\alpha) - 2\alpha - 1]} \quad (5.30)$$

Where the parameter of the tortuosity, τ, is set to 4/3 (-). The $kr(\theta_E)$ ranges from zero at the residual moisture content to 1 at complete saturation and is dimensionless. The absolute unsaturated hydraulic conductivity, $k(\theta_E)$, is subsequently obtained by multiplying the relative unsaturated hydraulic conductivity with K_{sat} ($m \cdot d^{-1}$).

In the model, the travel time of the water percolation is defined by the ration between the depth of the unsaturated zone, D_{unsat}, over the absolute unsaturated hydraulic conductivity ($m \bullet m^{-1} \bullet d=d$) for each model layer Z. The percolation is then set to the proportional loss of the unsaturated storage for layer Z, StorMat, over the time increment Δt:

$$Perc = StorMat \times \frac{k(\theta_E) \times \Delta t}{D_{unsat}} \quad (5.31)$$

An increasing of the groundwater table will shorten the thickness of the unsaturated zone (D_{unsat}) and the travel time for percolation soil moisture will be then reduced (Beek, 2002).

The iterative hydrological model applied must be understood dynamically, i.e., the model calculates and stipulates the variations on the groundwater level over time through timesteps. For the present purposes, was established that one timestep should correspond to one day. In this sense, according to the loss of water percolation to the groundwater table over the lowest semi-impervious layer, the degree of saturation (θ_E),

of the following timestep (next day), can be deducted directly from the drainable storage in the unsaturated zone and used to recalculate the resulting θ_E. From the degree of saturation the model can project the saturated hydraulic conductivity at the end of the timestep. If the expected θ_E=0, it is set to an arbitrary value. The new unsaturated hydraulic conductivity is then used to calculate the average for the current timestep as the geometric mean, i.e. $k(\theta_E)=\sqrt{k(\theta_E)'\cdot k(\theta_E)''}$. This average of the unsaturated hydraulic conductivity is then reused in Equation 5.31.

As it was already mentioned, the model includes three layers, representing different strata over the depth of the soil mantle. The lateral flux is determined by the piezometric head and the effective K_{sat} and the condition must be satisfied that the flux density for a cell does not exceed the cell length over the timestep. It must be noted that the fluxes in the present timestep are calculated from the state variables obtained at the end of the previous one.

In order to simulate the bypass flow through macrospores or fissures in the regolith an option is included to transfer a fraction of the rainfall excess directly to the lithic contact within one timestep. If the substratum is considered impervious, no water is lost and the groundwater table will form instantaneously. If this is not the case, an alternative boundary condition must be applied: at the lithic contact, water is lost into an infinite fourth layer, i.e., the bedrock. In order to simulate the effect of the hydrostatic pressure over the contact of this fourth layer, the height of the water level, $WL=\Sigma D_{sat}(z)$, is divided by the total soil depth, $Z=\Sigma D(z)$, and the geometric mean is used to obtain the bulk K_{sat} of the horizontal layers (Kutílek and Nielsen, 1994):

$$Perc_{BC} = \sqrt{k(\theta_{E\,BC}) \times \mathrm{K}_{\mathrm{sat}\,BC} \times \mathrm{WL}/\mathrm{Z})} \times \Delta t \tag{5.32}$$

Where $Perc_{BC}$ is represented in meters, $k(\theta_{Ebc})$ is the absolute unsaturated hydraulic conductivity of the fourth layer, and $\mathrm{K}_{\mathrm{sat}bc}$, is the saturated hydraulic conductivity of the fourth layer (Fig. 5.28).

According to this statement, if no groundwater table exists, the vertical loss into the fourth infinite store is only dependent on $k(\theta_{E\ BC})$. In order to generate groundwater the percolation from the basal layer must exceed this water loss. Thus, the fourth layer determines the response of the hydrological system. This is the reason why the antecedent moisture conditions are crucial for the triggering of landslides.

The matric suction $|h|_{BC}$ in (m) of this fourth layer as a fixed value. This parameter is preferred since the matric suction is continuous over space whereas the relative degree of saturation depends on the local conditions of the SWRC. Thereby, $|h|_{BC}$ has to be defined after which the $\theta_{E\ BC}$ and $k(\theta_{E\ BC})$ are calculated with incorporation of any spatially varying attributes of the SWRC and the saturated hydraulic conductivity assessment (Beek, 2002).

Over the saturated zone (Q_{sat}), the lateral outflow is given by the piezometric gradient which is defined by the absolute elevation of the phreatic surface. This absolute elevation is obtained by summing the elevation of the lithic contact in the cell with the height of the water level, WL (both in m). Over a window of 3x3 cells (Fig. 3.3), the maximum slope of the phreatic surface, tan(α), is obtained for each timestep (Beek, 2002).

The flow direction (already obtained for the static model) or local drainage direction map (LDD) indicates in which the lateral outflow is directed. Thereby, the flow can be drained in one of the eight cardinal directions, i.e. the cell that coincides with this maximum slope is designed as the drainage direction for the saturated lateral outflow from the central cell. The piezometric gradient, i, for the central cell under consideration is given by the difference in elevation over the slope parallel distance (Fig. 5.29) (Beek, 2002).

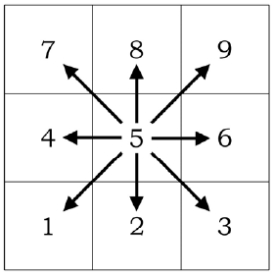

Fig. 5.29 – Cardinal directions of LDD. To cells without drainage direction, pits, the value 5 is attributed.

When the lateral outflow, Q_{sat}, passes the common height of the saturated zone it begins to travel from the central cell to downward cell, along the LDD, with the apparent velocity of the saturated lateral conductivity, $k_{lateral}$. The Q_{sat} and the $k_{lateral}$ are defined as the arithmetic average between the central cell x and the downstream cell x+1. The bulk saturated hydraulic conductivity is used for obtaining the lateral saturated hydraulic conductivity, $K_{lateral}$, over the entire table over the lithic contact, i.e.:

$$k_{sat} = \frac{\sum D_{sat} \times k_{sat}}{WL} \tag{5.33}$$

The average saturated lateral conductivity in the downstream direction in $m.d^{-1}$, is then:

$$k_{lateral} = \frac{1}{2} \times (k_{sat}(x) + k_{sat}(x+1)) \tag{5.34}$$

Likewise, the height of the common saturated zone is averaged over the water levels. The resulting lateral flux over the saturated zone is given by:

$$Q_{sat} = k_{lateral} \times i \times \frac{1}{2}(WL(x) + WL(x+1)) \tag{5.35}$$

Which has units of ($m^{-2}.d^{-1}$). The use of the lateral saturated hydraulic conductivity makes the necessity that all models layers are of equal depth, superfluous. In each cell the storage of the saturated zone is balanced by the outgoing and incoming fluxes. Regarding the lateral flow, the change in storage (in m) is obtained by multiplying the net lateral flow with the time increment and dividing it over the cell length in the direction of the flow. Thereby, within a timestep, the water is added to the saturated storage by percolation from the unsaturated zone and from bypass flow, if any occurred. The saturated storage is diminished by the loss over the semi-impervious lithic contact and by evapotranspiration. However, this loss by evapotranspiration is only substantial when the groundwater table is close to the surface (Beek, 2002).

Whenever the next timestep starts, it starts with the water that is storage in the saturated zone (groundwater level) in the end of the previous one. The inherent convergence of the LDD leads to a concentration of Q_{sat} in the downstream direction at the junctions of the LDD. The losses are summed and compared to the available storage after the incoming percolation and the bypass flow have been added. Those fluxes are reduced to match the available budget when the total loss exceeds the storage. Finally, after the local changes are balanced, the saturated lateral flow Q_{sat} is directed over the LDD to obtain the water level for the following timestep.

When a saturated storage is in excess of the maximum storage of the soil, the remaining water is removed as exfiltration. This exfiltration is directed over the LDD of the topographical surface. In the nearest downstream cell it is treated as surface detention in the next timestep and available for evaporation (Beek, 2002).

Beyond percolation, the STARWARS model also includes infiltration and evapotranspiration. These inputs are given as daily totals. The infiltration capacity is defined as a ratio, k_0, of the saturated hydraulic conductivity of the top layer. Infiltration excess occurs if the rain that reaches the surface exceeds the infiltration capacity (Beek, 2002).

Differently from the previous hydrological model (SHALSTAB), in the STARWARS model the amount of rainfall that is available for infiltration is limited by the evapotranspiration and by interception. All rainfall is subject to interception by the vegetation, which is included in the model as a canopy store of finite capacity.

Before reaching the topographical surface the net precipitation is subjected to evapotranspiration and interception by the vegetation, which is also included in the model. The interception is defined as the amount of water that is detained by the canopy and lost to evaporation. This loss is proportional to the gross precipitation rate, P, over a certain time period. The amount of water that is not intercepted by the canopy is passed to the surface. Whereas, the amount of water that is intercepted by the vegetation and litter, that cover the soil, become not available for infiltration (Beek, 2002).

In the hydrological component of the model, the evaporation loss of the interception at the surface is accommodated by the actual evapotranspiration. For the canopy, the precipitation balance is:

$$C = (1-p)\int P - \int D - \int E_r \tag{5.36}$$

where p is the fraction of not intercepted rainfall, P is the rainfall intensity, D is the drainage rate from leaves and stem, E_r is the rate of evaporation and C is the quantity of water detained on the canopy (Aston, 1979 cited by Beek, 2002). All rates are in units of waterslice over time and defined over a unit area of the projected canopy.

The amount of water that reaches the surface is defined by the first two terms of Equation 5.36. The direct transfer, conditioned by the proportion p, and the drip of the foliage are not separated in the model. Thus, both fluxes are aggregated into one quantity, the throughfall (Pt). The concentrated routing of water along the stem and branches, the stemflow (Ps), is defined by D. Summarizing the gross interception loss of the canopy (Ic) can be achieve through:

$$\sum I_c = \sum P - \sum P_t - \sum P_s \tag{5.37}$$

Thus, the net rainfall, ΣPn, that is available for infiltration equals ΣP-ΣIc = ΣPt+ΣPs. The effective rainfall intensity, including the loss due to evaporation, determines the moment at which saturation is reached.

It must be mentioned that the parameter D only become fully operative when saturation of canopy is reached (maximum storage capacity (C_{max})) (Rutter *et al*., 1971 cited by Beek, 2002). For this reason, it is stipulated that most interception equations have the general appearance of a curvilinear relation that is bounded by C_{max} (Beek, 2002). Thus, a simple conceptual model developed by Merriam (1960) which defines the detained water at a

given time, as an exponential function of the maximum storage capacity and the accumulated rainfall:

$$C = C_{max}\left[1-\exp(-(1-p)\sum P / C_{max})\right] \quad (5.38)$$

Where "1-p" is replaced by coefficient k, increasing the number of parameters to two. Because the fraction "p" specifies the amount of direct throughfall, it is also referred to as the free throughfall coefficient. However, this parameter can be estimated from measurements of the leaf area index, the ratio of the leaf surface over the projected canopy area (LAI, $m^2.m^{-2}$) (Beek, 2002).

Once the interception has been deducted, the remaining net rainfall achieves the ground surface and it is stored as surface detention. Thereby, after all water reductions, by interception and/or evapotranspiration, the remaining water namely surface detention, becomes available for infiltration and further, for percolation or if it exceeds the field capacity, available for surface water runoff along the flow direction as exfiltration.

It is noteworthy that both, interception as well as the surface detention, are subjected to evaporation. The evapotranspiration that is used as an input for the model is the reference potential evapotranspiration, ET_0, which was obtained thought Hargreaves equation (Hargreaves and Samani, 1985; Wu, 1997), which is treated in detail in section 5.6.1.3.

The rate of evaporation is strongly reduced when the temperatures are low and the relative humidity is high, however being conscious of the importance of evapotranspiration for the study area a detailed module to simulate the loss to evapotranspiration has been incorporated in the STARWARS model as a timeseries. The model is building in such way that any interception can be lost directly to the potential reference evapotranspiration over the current timestep (Beek, 2002).

The actual evapotranspiration, ET_{Act}, is achieved through the incorporation of dimensionless scaling factors or crop factors, kc, for specific vegetation covers, on the potential evapotranspiration, $ET_{0.}$

The actual evapotranspiration, ET_{Act}, decreases with the decreasing water storage in the soil and this is simulated by the model by scaling the remainder of the potential evapotranspiration with the ratio between actual and the maximum storage of an element (Beek, 2002):

$$ET_{Act} = K_c \times ET_0 \times \frac{(\sum StorMat + \sum StorSat)}{\sum StorMax} \tag{5.39}$$

where StorMat, StorSat and StorMax represent respectively the unsaturated, saturated and the maximum storage in units of waterslice (m).

The actual loss by evapotranspiration, in each layer, is proportional to the available storage. The calculation of the rate of evapotranspiration is made through the gradient, i.e., through the slope of evapotranspiration over the depth of the unsaturated zone (Fig. 5.30). The evapotranspiration of each unsaturated layer is limited by the difference in the relative degree of saturation between the layer under consideration, Z, and the overlying layer, Z-1.n. To be certain that the soil moisture content deeper in the soil cannot decrease below that of the top layer due to evapotranspiration, as in nature, a condition is imposed that the relative degree of saturation is a substitute for the continuity of matric suction in the unsaturated zone (Beek, 2002).

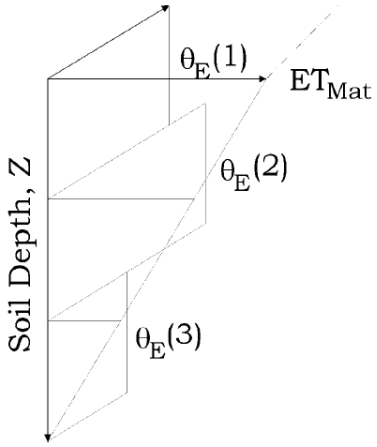

Fig. 5.30 – Linear decrease of evapotranspiration from the unsaturated matrix. Maximum evapotranspiration from layer Z is limited by the relative degree of saturation of the overlying layer (extracted from Beek, 2002).

Many input variables necessary for STARWARS implementation have already been obtained and described previously (e.g., soil depth, LDD map) for the static modeling implementation. However, there are still some variables not used for the static modeling which will be further described, namely, daily precipitation, daily radiation, daily temperature, land use (for daily evapotranspiration acquisition), among others.

5.6.1 Data

5.6.1.1 Rainfall

There is an increasing need of knowledge on the behavior of precipitation over time since, according to many authors (e.g., Sidle *et al*. 1985, Crozier, 1986 and Beek, 2002), it is the main factor triggering landslides. This net input is defined by the climatic variables of precipitation and evapotranspiration.

For landsliding, depending on the geometry and strength of the slope materials, a single rainfall event can be enough to trigger a critical pore pressures in some occasions. However, most landslides require a more substantial period of rainfall (Iverson, 2000; Beek, 2002; Crosta and Frattini, 2003). Under those circumstances, evapotranspiration becomes more important because it uses the available soil moisture storage and thus

attenuates the response of following new rainfall events. On a seasonal and interannual scale both, precipitation and evapotranspiration, exhibit a temporal variability. The evapotranspiration is the steadiest process and less susceptible to extreme events, differently from the precipitation which is defined by its extreme events. These extreme events are more prone to trigger landslides (Beek, 2002).

According to Wolman and Miller (1960) the high geomorphic power of the most extreme events is compensated by their rare occurrence, whereas the relative work done by events of intermediate frequency (return periods of extreme events: once every 5 to 100 years) is the most important. For the present study it was not possible to obtain all the necessary data to calculate the return periods of extreme events. Thus, the landslide susceptibility will be assessed based on the modeled actual annual events and their influences on the observed landslides over the same time-frame. It is intended that the temporal variability of the precipitation and evapotranspiration, at a regional scale, explains the activity of rainfall-induced landslides for the heterogeneous spatial patterns of the study area. The causes of the spatio-temporal variation must be understood in order to reduce the uncertainty in the interpolated climatic input.

Precipitation data are available as 24 hours totals from the Sistema Nacional de Informação de Recursos Hídricos (SNIRH) for eleven meteorological stations, namely, Alfeizerão, Cela, Salir de Matos, Óbidos, Asseiceira, Alcoentre, Alvorninha, Santa Catarina, Vermelha, Vimeiro and Turquel, which are within or near the study area (Fig. 5.31). A considerable time length, from 1975/1976 to 2011/2012, was choosen because: i) the available real discharge data, which will be used for further calibration of the spatio-temporal hydrological model (STARWARS), has a time length from 1977/1978 to 1989/1990; ii) the shallow translational slides, included in LI#3, were inventoried from 2006 to 2011. The length of the record is thus 37 years, which is close to the conventional 30 years used in climatic research.

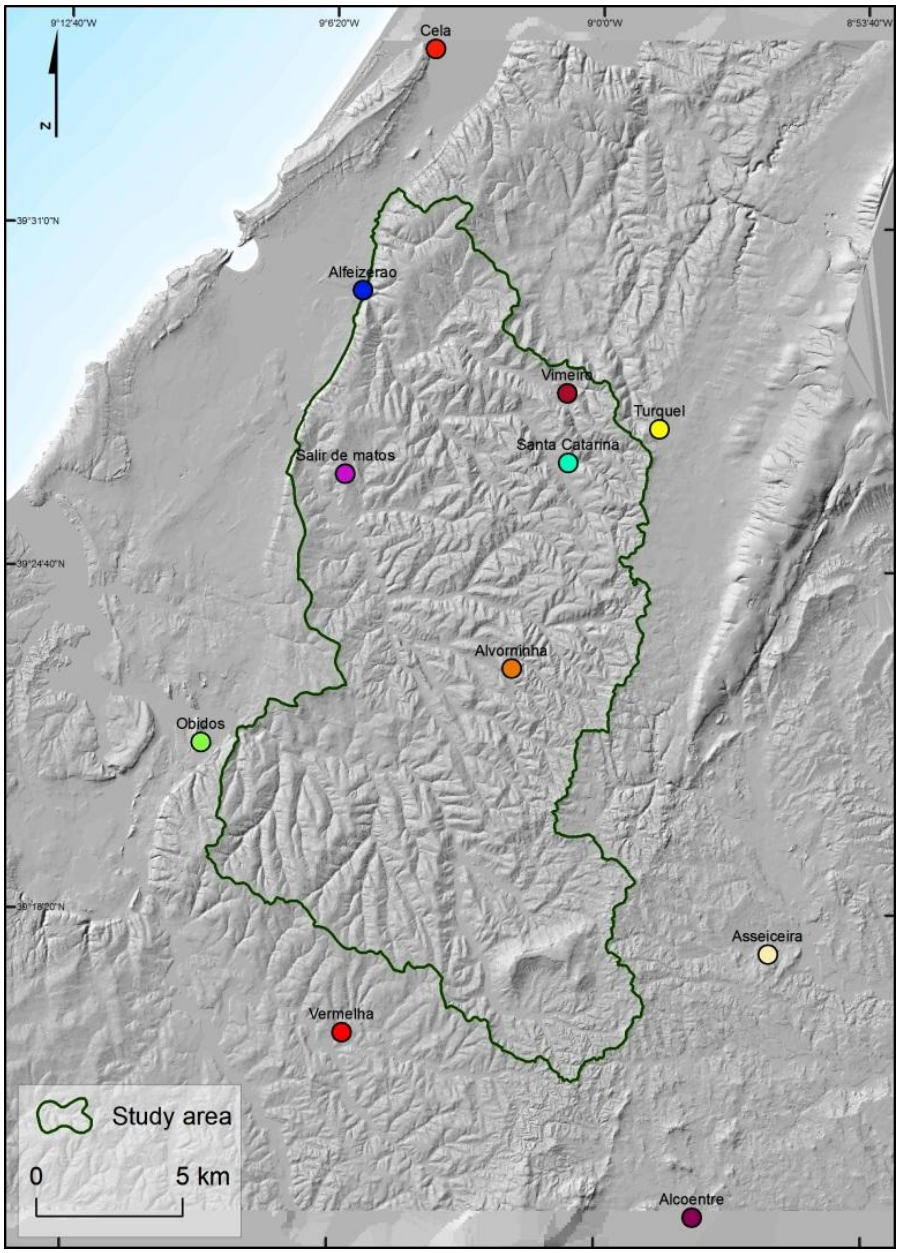

Fig. 5.31 – Meteorological stations used for interpolation of daily precipitation for the period between 1975/1976 to 2011/2012.

Due to the vast extension of the study area (275km^2) more meteorological station would be preferable for interpolation, although, those were the only available, for the study area, with observational records of considerable length.

The Table 5.20 contains the characteristics of the daily precipitation records of each meteorological stations. Some of the meteorological stations contained several gaps and to avoid the presence of missing values, a multiple linear regression (using the PROJ.LIN function of Excel) was performed.

Table 5.20 – Elevation (a.s.l.) and caracteristics of the daily precipitation records of each meteorological stations.

Meteorological stations	Elevation (a.s.l.)	Daily precipitation records		
		N.º of values	Beginning	Ending
Alfeizerão	13	22021	6/2/1948	25/03/2009
Cela	2	13258	1/1/1938	12/8/2013
Salir de Matos	91	10932	1/10/1979	30/12/2009
Óbidos	53	9474	1/10/1979	10/3/2010
Asseiceira	82	9433	1/10/1979	22/09/2005
Alcoentre	69	10497	1/10/1979	23/07/2008
Alvorninha	117	10829	1/10/1979	30/12/2009
Santa Catarina	84	15940	8/2/1948	30/09/2002
Vermelha	50	9691	1/10/1980	8/4/2009
Vimeiro	90	20863	1/9/1951	11/2/2010
Turquel	213	7036	1/10/1990	5/4/2011

Rainfall distribution shows striking difference along the study area, for this reason it was chosen to calculate the monthly rainfall anomalies first. The choice of using the monthly rainfall anomalies is preferable since it reduces the uncertainties in the calculated missing values. The daily rainfall anomalies of each month (DRA) are given by:

$$DRA = \frac{P}{\overline{P}} \tag{5.40}$$

Where P is the precipitation observed for the analyzed day, and $\overline{P}$, is the mean daily precipitation of each month of the observed records. This calculation is done for each day of the period under analysis (1975/1976 to 2011/2012) but only when rainfall data exists. Once having the rainfall anomalies for each day of the considered period, the correlation between each pair of meteorological station was determined. From this analysis was achieved the coefficient of determination (r^2) and the slope of the regression line, of each month and for each meteorological station, which allowed to fill the missing records with a acceptable accuracy (Tables A4.1 to A4.24 in Appendix 4). The multiple regression equation has the following form:

$$Y = a + b1x1 + b2x2 + \ldots + bkxk \tag{5.41}$$

where a is the interception on y axis; b is the slope and k is the number of independent variables.

Based on the coefficient of determination and the slope of the regression equation was possible to fill the missing data automatically, with the aid of a script built in python informatics language (Script A4.1 in Appendix 4), allowing to complete the series of daily precipitation for the considered period.

The large differences between the individual hydrological years are reflected by the seasonal variability. The mean monthly precipitation (calculated from the daily totals, of each month, over the period 1975/1976 to 2011/2012) exhibits a large range over the period of 37 years in every meteorological stations (Tables 5.21 to 5.31).

Table 5.21 – Monthly rainfall statistics for Alfeizerão (hydrological years 1975/1976 – 2011/2012.

	Oct	Nov	Dec	Jan	Feb	Mar	Apr	May	Jun	Jul	Aug	Sep	Tot.
	Rainfall totals (mm)												
Mean	103.5	109.5	114.1	93.1	83.9	68.0	74.9	53.5	21.6	9.9	10.9	35.4	778.4
St. Dev.	73.5	75.3	86.5	65.2	56.8	86.8	39.0	41.1	22.1	11.5	11.6	31.4	600.8
	Rainfall occurrence (days)												
Mean	13.8	15.2	17.3	16.4	14.8	13.0	14.0	10.7	6.2	5.1	5.2	8.4	140.1
St. Dev.	7.2	7.5	6.6	7.9	6.5	8.2	5.3	5.2	5.0	4.4	4.5	6.2	74.5

Table 5.22 – Monthly rainfall statistics for Cela (hydrological years 1975/1976 – 2011/2012.

	Oct	Nov	Dec	Jan	Feb	Mar	Apr	May	Jun	Jul	Aug	Sep	Tot.
	Rainfall totals (mm)												
Mean	104.0	106.3	121.2	92.3	88.7	67.6	74.3	53.8	23.3	8.8	13.8	35.5	789.8
St. Dev.	74.3	72.4	100.9	64.0	65.4	70.5	41.4	41.6	25.6	10.0	18.6	36.0	620.7
	Rainfall occurrence (days)												
Mean	15.2	16.3	18.0	16.7	15.0	13.1	14.5	11.0	6.4	5.3	5.0	8.7	145.3
St. Dev.	6.6	7.9	7.2	7.8	6.7	7.7	5.7	5.2	4.8	4.5	4.1	5.9	74.0

Table 5.23 – Monthly rainfall statistics for Salir de Matos (hydrological years 1975/1976 – 2011/2012.

	Oct	Nov	Dec	Jan	Feb	Mar	Apr	May	Jun	Jul	Aug	Sep	Tot.
	Rainfall totals (mm)												
Mean	104.2	113.6	115.9	97.3	89.9	66.7	78.9	56.3	20.6	10.8	12.5	37.7	804.3
St. Dev.	71.3	74.1	88.7	71.8	63.1	59.2	50.6	43.5	20.8	15.3	14.6	35.3	608.4
	Rainfall occurrence (days)												
Mean	13.4	14.9	16.5	15.5	14.3	12.3	13.1	10.8	6.1	4.8	4.7	7.9	134.2
St. Dev.	6.7	7.3	6.3	7.5	6.3	7.6	5.4	5.6	5.3	4.2	4.4	5.7	72.4

Table 5.24 – Monthly rainfall statistics for Óbidos (hydrological years 1975/1976 – 2011/2012.

	Oct	Nov	Dec	Jan	Feb	Mar	Apr	May	Jun	Jul	Aug	Sep	Tot.
	Rainfall totals (mm)												
Mean	79.2	88.8	98.4	82.4	67.7	54.6	57.6	43.9	19.6	6.1	6.9	29.3	634.5
St. Dev.	60.6	68.2	82.4	62.5	45.9	42.7	35.8	37.3	22.7	9.6	10.3	32.2	510.2
	Rainfall occurrence (days)												
Mean	14.2	14.6	17.1	15.9	15.4	13.4	13.4	10.6	6.1	4.2	4.3	8.6	137.6
St. Dev.	7.0	7.6	7.0	7.5	7.3	8.0	5.9	5.3	5.1	3.7	4.0	6.2	74.5

Table 5.25 – Monthly rainfall statistics for Asseiceira (hydrological years 1975/1976 – 2011/2012.

	Oct	Nov	Dec	Jan	Feb	Mar	Apr	May	Jun	Jul	Aug	Sep	Tot.
	Rainfall totals (mm)												
Mean	92.6	103.3	111.2	87.4	80.2	63.8	68.8	50.9	20.8	6.8	7.8	33.3	727.0
St. Dev.	64.6	77.3	104.6	68.8	55.3	60.5	43.2	41.8	25.3	10.6	10.1	31.8	594.0
	Rainfall occurrence (days)												
Mean	14.5	14.9	17.4	14.1	13.1	12.2	12.8	10.2	5.7	3.7	3.8	7.9	130.3
St. Dev.	7.5	8.2	7.9	7.0	6.8	8.5	5.1	5.4	5.3	3.9	3.9	5.7	75.4

Table 5.26 – Monthly rainfall statistics for Alcoentre (hydrological years 1975/1976 – 2011/2012.

	Oct	Nov	Dec	Jan	Feb	Mar	Apr	May	Jun	Jul	Aug	Sep	Tot.
	Rainfall totals (mm)												
Mean	98.7	106.9	118.1	93.7	87.7	67.0	71.2	50.4	18.8	5.9	6.1	33.8	758.3
St. Dev.	73.9	87.0	110.9	74.9	64.0	63.6	45.1	42.7	23.0	8.4	7.4	34.0	634.9
	Rainfall occurrence (days)												
Mean	14.5	16.0	18.3	15.2	15.2	12.2	13.7	10.3	5.5	3.3	3.6	7.4	135.2
St. Dev.	7.9	8.7	7.6	7.2	7.3	7.8	5.4	5.1	4.8	3.4	3.7	5.1	74.0

Table 5.27 – Monthly rainfall statistics for Alvorninha (hydrological years 1975/1976 – 2011/2012.

	Oct	Nov	Dec	Jan	Feb	Mar	Apr	May	Jun	Jul	Aug	Sep	Tot.
	Rainfall totals (mm)												
Mean	101.6	103.0	108.6	95.7	88.2	65.1	70.3	55.1	22.1	7.6	8.4	37.0	762.5
St. Dev.	80.5	76.4	90.8	77.1	58.4	57.3	40.0	43.7	25.5	9.5	9.5	35.0	603.6
	Rainfall occurrence (days)												
Mean	13.6	14.8	16.6	14.3	13.2	12.1	13.5	11.3	6.3	4.6	4.3	8.4	133.0
St. Dev.	7.0	7.4	6.7	6.8	6.4	7.7	5.1	5.6	5.0	4.1	3.9	5.9	71.6

Table 5.28 – Monthly rainfall statistics for Santa Catarina (hydrological years 1975/1976 – 2011/2012.

	Oct	Nov	Dec	Jan	Feb	Mar	Apr	May	Jun	Jul	Aug	Sep	Tot.
	Rainfall totals (mm)												
Mean	96.2	108.8	112.2	94.6	88.0	61.1	75.3	55.7	20.7	7.5	8.9	38.6	767.7
St. Dev.	67.8	76.5	94.4	84.1	65.4	52.6	45.1	49.6	26.1	10.5	10.1	37.6	619.8
	Rainfall occurrence (days)												
Mean	14.2	15.1	16.4	14.0	14.8	11.9	13.1	10.1	6.1	4.6	4.0	7.9	132.1
St. Dev.	7.6	8.2	8.0	7.2	7.2	7.5	5.5	5.7	5.2	4.7	4.3	5.5	76.6

Table 5.29 – Monthly rainfall statistics for Vermelha (hydrological years 1975/1976 – 2011/2012.

	Oct	Nov	Dec	Jan	Feb	Mar	Apr	May	Jun	Jul	Aug	Sep	Tot.
	Rainfall totals (mm)												
Mean	91.4	97.2	108.5	81.4	75.7	59.2	71.3	48.8	18.1	6.5	8.9	28.2	695.4
St. Dev.	64.6	68.5	93.3	70.3	54.1	57.9	43.4	37.8	22.9	9.2	9.6	29.8	561.5
	Rainfall occurrence (days)												
Mean	13.9	14.8	16.8	14.5	13.1	11.5	12.5	9.8	5.6	3.1	3.7	6.9	126.2
St. Dev.	7.8	8.2	8.1	8.0	7.8	8.1	5.9	5.7	4.9	3.6	4.4	4.9	77.3

Table 5.30 – Monthly rainfall statistics for Vimeiro (hydrological years 1975/1976 – 2011/2012.

	Oct	Nov	Dec	Jan	Feb	Mar	Apr	May	Jun	Jul	Aug	Sep	Tot.
	Rainfall totals (mm)												
Mean	105.7	122.1	130.0	103.6	96.3	67.4	79.9	57.7	23.6	9.2	12.4	40.4	848.2
St. Dev.	73.9	77.3	102.7	74.6	67.9	57.5	46.6	45.0	26.1	12.1	14.2	35.2	632.9
	Rainfall occurrence (days)												
Mean	13.9	15.2	17.1	16.8	15.5	12.6	13.6	11.2	6.4	4.8	4.4	7.9	139.4
St. Dev.	7.3	7.6	7.2	7.8	7.3	8.0	5.0	5.3	5.3	4.9	4.5	5.7	75.8

Table 5.31 – Monthly rainfall statistics for Turquel (hydrological years 1975/1976 – 2011/2012.

	Oct	Nov	Dec	Jan	Feb	Mar	Apr	May	Jun	Jul	Aug	Sep	Tot.
	Rainfall totals (mm)												
Mean	97.4	110.9	115.3	95.7	86.8	63.2	64.7	51.6	18.4	7.6	10.6	32.9	755.3
St. Dev.	74.0	80.6	96.8	72.2	57.8	54.8	43.0	45.6	21.5	9.3	12.2	29.5	597.2
	Rainfall occurrence (days)												
Mean	14.3	14.6	16.1	15.3	14.5	12.6	13.7	11.6	6.5	5.2	4.7	8.0	137.1
St. Dev.	6.5	7.3	6.8	7.0	6.6	7.6	5.1	5.5	5.2	4.7	4.3	6.2	72.8

According to the previous Tables 5.21 to 5.31, it is possible to realize that Salir de Matos and Vimeiro are the most extreme locations, regarding its mean annual precipitation. For those sites it is recorded the higher mean annual precipitation, along the considering time

period (between 1975/1976 – 2011/2012), respectively, 804.3mm and 848.2mm. On the other hand, the Obidos and Vermelha sites yield the lowest amounts of mean annual precipitation (634.5mm and 695.4 mm).

Cela and Alfeizerão are highlighted here as the places where there was a greater number of rainy days for the same period, which corresponds to an amount of, respectively, 145 and 140 average days with precipitation. Contrary, Vermelha and Asseiceira are the locals where in average it was registered less rainy days (respectively, 126 and 130 days). For the Asseiceira site it is registered a mean annual precipitation of 727.0mm, while in Vermelha is registered, as already mentioned, one of the lowest quantity of mean annual precipitation.

The bulk of rainfall, in all places, is delivered in the period between October and March. In contrast, dry spells last for most of the summer from July to August (Tables 5.21 to 5.31). For such kind of study the calculation of the extreme rainfall events in each meteorological station as well as it return period would be important. However, as already explained when describing the static methodology, only one event was registered within the study area which disabled a more profound study about the probability distribution of extreme values. This only one dated event, registered within the study area, occurred in Santa Catarina in November, 30, 2006.

Beyond the total daily rainfall another important parameter to be considered is the duration of rainfall in each day. This parameter is especially important for temporal calibration and validation purposes since it allows obtaining the discharge in m^3 of the surface runoff, dynamically over time. The surface runoff will occurs when the soil is infiltrated to its full capacity. Thus, this excess of water, will then start to flow over the land according to the flow direction. The parameters for the precipitation duration function are obtained by the following equations (Morgan, 2005):

$$P_{dur} = a \times P_{tot}^{\ b} \tag{5.42}$$

and:

$$MI = \frac{2 \times P_{tot}}{P_{dur}} \tag{5.43}$$

Where P_{tot} (mm) is the total rain for one day, P_{dur} is the duration (fraction of day, where 1=1day) and MI is the maximum intensity (mm/h), a is the rainfall duration constant, which equals 0.052704628, and b is the rainfall duration power, which equals 0.5. According to Morgan (2005) and Carvalho *et al*. (2010) it is considered a maximum intensity of 30 mm/hour and a mean of 15 mm/hour due to the rainfall Intensity-Duration-Frequency (IDF) Curve performed for a Mediterranean environment. Thus, for the given example, the duration approaches one day if P_{tot}= 360 mm (which derived from 15mm/h X 24h).

To produce the continuous spatial daily rainfall maps (total and duration) an interpolator, named, Inverse Distance weight (IDW), was used. Such procedure allowed to use the known actual and estimated values of daily precipitation (of each meteorological stations) to estimate values at other unknown locations. Producing a map per day, for 37 years, has revealed to be time consuming. In this sense, in order to facilitate this task, a script was developed, in python language, which allows calculating, in an expeditious manner, the maps of daily rainfall for each year (Script A4.2 in Appendix 4).

5.6.1.2 Evapotranspiration

Globally, about 62% of the precipitation that falls on the continents is evapotranspirated (Dingman, 1994). In this sense, the input of net precipitation has to be balanced against the loss of the soil moisture by evapotranspiration in order to quantify the available water for infiltration and further percolation in the hydrological cycle (Beek, 2002).

5.6.1.3 Reference Potential Evapotranspiration

The reference potential evapotranspiration is a rate reflecting the maximum amount of water that can be evaporated from a large area completely and uniformly covered with growing vegetation or water surface when the water supply is not a limiting factor, and without advection or heat storage effects (Doorenbos and Pruitt, 1977; Brutsaert, 1982; Dingman, 2002). Being aware that land use has a strong influence on evapotranspiration and soil moisture availability, it becomes crucial to assess quantitatively the influence of such parameter.

The water loss by evapotranspiration is defined through the presence of limiting factors such as stomata closure and advection. The relation between the local evapotranspiration of a soil covered by vegetation and the reference potential evaporation is represented by simple empirical constants, which are commonly known as crop factors (K_c) (Beek, 2002). The reference potential evapotranspiration (ET_0), which depends only on the atmospheric conditions, is defined as the rate of evapotranspiration from an extensive surface of 8 to 15cm tall green grass cover with uniform height, actively growing and completely shading the ground in conjunction with an available sufficient water source (Doorenbos and Pruitt, 1977). The specifics loss, ET_c in mm.d-1, by disease-free crop is then given by:

$$ET_c = K_c \times ET_0 \tag{5.44}$$

The crop evapotranspiration (ET_c) differs distinctly from the reference potential evapotranspiration (ET_0) because the ground cover, canopy properties and aerodynamic resistance of the crop are different from grass. The effects of characteristics that distinguish field crops from grass are integrated into the crop coefficient (K_c).

The reference potential evapotranspiration can be calculated by the physically-based model of the Penman equation (Penman, 1948). However, due to the lack of standard agro-climatic weather parameters (such as relative air humidity and wind velocity) a simple approach, named Hargreaves equation (Hargreaves and Samani, 1985), was

performed in this study in order to obtain the mean daily ET_0. The Hargreaves model is a simpler model that requires only two climatic parameters, which is incident radiation and temperature. The Hargreaves equation is expressed as:

$$ET_0 = 0.0135(T + 17.78) R_s \left(\frac{238.8}{595.5 - 0.55T} \right) \quad (5.45)$$

where ET_0 is the potential daily evapotranspiration (mm/day), T is the daily temperature (°C) and R_s is the incident solar radiation expressed as (MJ/m^2/day).

5.6.1.4 Radiation

The energy of the sun, referred as solar radiation or shortwave radiation, is usually an important contributor to the energy balance at the Earth`s surface and hence is an important input parameter to assess evapotranspiration (Dingman, 2002). Due to the difficulty in obtaining measured shortwave radiation, in this section, it will be estimated the radiation based on the latitude of the study area, for each Julian day.

For calculating the incoming shortwave radiation we use the approach, given by Dingman, (2002). This methodology includes the solar constant, the latitude of the study area (39.36 º S), the angular velocity and several calculations such as extraterrestrial radiation, day angle, eccentricity correction, declination, solar sunrise and solar sunset, which will be described below. For further calculation purposes, the angular parameters, such as latitude and angular velocity, were converted in radians.

The extraterrestrial radiation, which is intent to develop in this section, consists on a set of astronomical relations which gives the daily radiation incident at the top atmosphere directly above an arbitrary point (Dingman, 2002).

The solar constant (I_{sc}=1367 W m^{-2}) is the average radiation flux on a plane perpendicular to the solar beam at the surface of the atmosphere. The angular velocity (15º hr^{-1}) is defined as the rate of change of angular displacement which specifies the angular speed (rotational speed) of the earth and its axis about which the earth is rotating (Dingman, 2002).

The extraterrestrial radiation flux incident on a plane tangent to the earth`s surface is a function of the radiation flux on a plane perpendicular to the solar beam and the angle of the tangent plane relative to beam. The position of the earth in its orbit is given by the day angle (Dingman, 2002):

$$\Gamma = \frac{2 \times \pi \times (J - 1)}{365} \tag{5.46}$$

Where Γ is the day angle and J is the Julian day.

The relative earth-sun distance changes regularly during the year. Because radiative flux follows the inverse-square law, this is most usefully expressed as the eccentricity correction, E_0, which is the square of the ratio of the average distance, r_0, to the distance at any time, r (Dingman, 2002). E_0 can be calculated for any day of the year as:

$$E0 = (r_0 / r)^2 = 1.000110 + 0.034221 \times \cos(\Gamma) + 0.001280 \times \sin(\Gamma) + 0.000719 \times \cos(2 \times \Gamma) + 0.000077 \times \sin(2 \times \Gamma) \tag{5.47}$$

The angle between a horizontal (tangent) plane and the solar beam is determined by the latitude, Λ, of the plane and declination of the sun, σ. The sun`s declination is the latitude at which the sun is directly overhead at noon; due to the 23.5º tilt of the earth`s rotational axis, this latitude changes regularly between +23.5º and -23.5º as the earth revolves around the sun. The declination is given by:

$$\sigma = (180 / \pi) \times \left[\begin{array}{l} 0.006918 - 0.39912 \times \cos(\Gamma) + 0.070257 \times \sin(\Gamma) - 0.006758 \times \cos(2 \times \Gamma) + \\ 0.000907 \times \sin(2 \times \Gamma) - 0.002697 \times \cos(3 \times \Gamma) + 0.00148 \times \sin(3 \times \Gamma) \end{array} \right] \tag{5.48}$$

The solar sunrise (T_{hr}) and sunset (T_{hs}) which are also needed for shortwave radiation calculation is given by:

$$T_{hr} = -\frac{cos^{-1}\left[-\tan(\sigma)\times\tan(\Lambda)\right]}{\omega} \quad (5.49)$$

and

$$T_{hr} = +\frac{cos^{-1}\left[-\tan(\sigma)\times\tan(\Lambda)\right]}{\omega} \quad (5.50)$$

Where Λ is the latitude and ω is the angular velocity.

The instantaneous extraterrestrial radiation flux on a horizontal plane, $K`_{ET}$, can be finally calculated as:

$$K`_{ET} = 2\times I_{sc}\times E_0\times[cos(\sigma)\times cos(\Lambda)\times sin(\omega\times Thr)/\omega + sin(\sigma)\times sin(\Lambda)\times Thr] \quad (5.51)$$

In order to perform all this calculations automatically, for each day in a year, a python script has been written (script A4.2 in Appendix 4), which allowed to obtain the incoming shortwave radiation, for the study area, per Julian day (in W/m^2).

5.6.1.5 Temperature (T)

In order to calculate the evapotranspiration, the temperature data for the considered period (1975/1976 to 2011/2012) was needed. For the study area only four of the eleven meteorological stations have the daily temperature records, namely: Cela; Óbidos; Asseiceira and Alcoentre. Beside the reduced number of meteorological stations with temperature data it also presents additionally two problems: missing values along the records; the oldest records only start at 1980.

To estimate the missing values along the records, for each meteorological station, the following equation was implemented (Dingman, 2002):

$$T_e = T_0 + \Delta t \cdot sin\left(\frac{d}{365} - d_0\right)2\pi \tag{5.52}$$

Where T_e is the estimated daily temperature, T_0 is the mean annual temperature; t is the amplitude (between the maximum and minimum) of actual temperature registered and divided by two; d_0 is the displacement in time, which correspond to the Julian day where first appears the value correspondent to the mean annual temperature (T_0). After obtaining the estimated temperature was calculated its Root Mean squared error (RMSE):

$$RMSE = \left(\frac{T_e}{T}\right)^2 \tag{5.53}$$

Where T is the daily temperature registered by the meteorological stations.

After obtaining the daily RMSE between the actual and the estimated temperature data was possible to calculate the mean Root Mean squared error (MRMSE). In order to reduce the MRMSE between the actual and estimated temperature data were applied the Solver function (in Excel software). This function allows reducing the MRMSE while adjusting the other parameters (T_0, t and d_0) (Fig. A4.1 in Appendix 4). Therefore the estimated temperature is also adjusted reducing the uncertainty between the actual and the estimated values (Fig. 5.32).

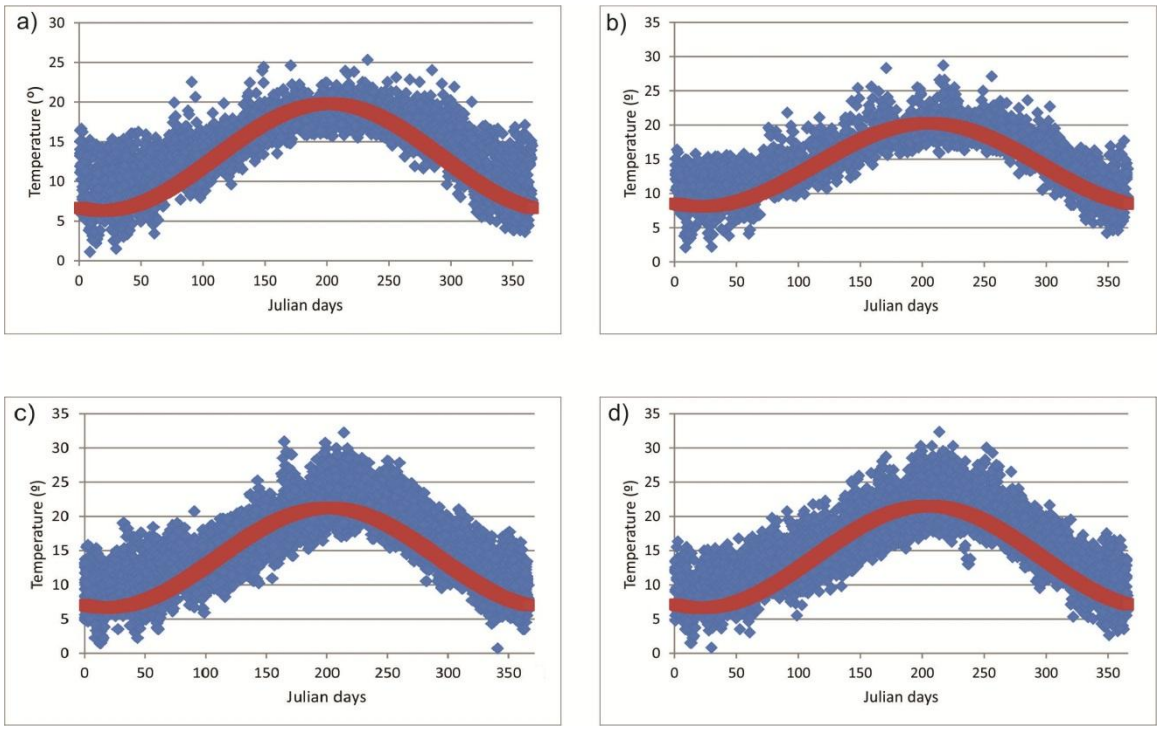

Fig. 5.32 – Actual (blue dots) and estimated (red line) mean daily temperature after adjustment at: a) Cela; b) Óbidos; c) Asseiceira; d) Alcoentre over the period 1980 to 2012.

According to the Fig. 5.32 it is possible to observe that Asseiceira and Alcoentre have hotter summer days, according to the actual mean daily temperature than in Cela and Óbidos, over the period 1980 to 2012. This is explained by the fact that Asseiceira and Alcoentre are more distant from the ocean than Cela and Óbidos.

To estimate the values before 1980, once it is considering the hydrologic years from 1975/1976 to 2011/2012, correlations were done with the Lisbon meteorological station for which temperature records are avaiable for the considering period. The differences between the actual and the estimated data (temperature anomalies) were calculated for all the meteorological stations in order to perform a linear regression between the additive temperature anomalies at Lisbon and at the others four meteorological stations. From this method it was possible to obtain the coefficient of determination and the slope of the regression equation, which were used to calculate the estimated temperature for Cela, Óbidos, Asseiceira and Alcoentre from 1975 to 1980.

Once having the daily temperature data of each year and for each meteorological station (Cela, Óbidos, Asseiceira and Alcoentre) an *IDW* interpolating method was performed

which incorporates the Lapse rate, i.e., the rate of decrease with height for temperature. This rate is commonly used in hydrology and terrestrial models for interpolate near-surface air temperature measurements from meteorological stations to locations at different elevations where measurements do not exist (Running *et al*., 1987; Régnière, 1996; Thornton *et al*., 1997; Martinec and Rango, 1998). This so commonly used average environmental lapse rate of 0.65°C $(100\ m)^{-1}$ (Barry and Chorely, 1987) is a spatially global and temporally climatic average (or standard) which was used for interpolating the continuous daily temperature data for the study area.

5.6.1.6 Crop factor (K_c)

The crop factor K_c serves as an aggregation of the physical and physiological differences between crops combining all the effects of the vegetation on the evapotranspiration including those of ground cover and surface roughness (Allen *et al*., 1998; Beek, 2002). For the acquisition of the K_c parameter, which intends to predict the effects of specific wetting events on the value for the crop coefficient, the K_c must be divided into two separate coefficients, one for crop transpiration, i.e., the basal crop coefficient (K_{cb}), and one for soil evaporation (K_e):

$$K_c = K_{cb} + K_e \tag{5.54}$$

The transpiration component (K_{cb}) must represent the changes in K_{cb} over the course of the growing season, depending on changes in vegetation cover and physiology. Definitions for three K_{cb} values ($K_{cb\ min}$, $K_{cb\ mid}$ and $K_{cb\ max}$) are required to associate definitions for growth stage periods and relative ground cover over the seasons. This procedure is conducted on a daily basis and is intended for applications using computers (Allen *et al*., 1998).

During the initial period, shortly after planting of annuals or prior to the initiation of new leaves for perennials, the value of K_{cb} is often small (stipulated as the minimum K_c for

bare soil ($K_{cb\ min} \approx 0.15$ - 0.20) (Allen *et al.*, 1998). The basal $K_{cb\ max}$ correspond to the peak plant size or height. The $K_{cb\ mid}$ is the estimated basal K_{cb} during the mid-season, when plant density and/or leaf area are lower than for full cover conditions. As the K_c has not been derived by ET measurement, it is here estimated from a fraction of ground cover or leaf area index (LAI) (Allen, 2003; Olson, 1994a, 1994b; Hagemann, 2002).

To obtain the parameters needed for calculating the transpiration component (K_{cb}), the Land use, derived from *Centro Nacional de Informação Geográfica* (CNIG) at a 1:25,000 scale, was used. Such kind of data discriminates the types of vegetation, which is crucial for converting into the global ecosystem types (according to Olson, 1994a, 1994b) (Table A5.1 in Appendix 5). The global ecosystem types of Olson (presented in Hagemann, 2002) present a global dataset of land surface parameters (LSP) needed for K_{cb} estimation (e.g., leaf area index: LAI) and it is provided for the use in global and regional climate modeling (Table 5.32 and Fig. 5.33).

Table 5.32 – Global ecosystem types of Olson (1994a, 1994b).

Global Ecosystem Type	Classes	**LAI $_{min}$**	**LAI $_{max}$**	**h (m)**	$K_{cb\ max}$ *
Urban	1	0.00	0.00	0	0
Low Sparse Grassland	2	0.12	1.75	0.03	1.003
Coniferous Forest	3	9.00	9.20	1	1.2
Deciduous Broadleaf Forest	4	0.10	5.20	1	1.2
Evergreen Broadleaf Forests	5	9.50	9.90	0.68	1.2
Irrigated Grassland	6	0.00	4.50	0.03	1.003
Cool Mixed Forest	7	0.10	4.20	1	1.2
Mixed Forest	8	1.00	7.00	0.68	1.2
Crops and Town	9	1.10	4.50	0.1	1.01
Rice Paddy and Field	10	0.00	4.60	0.06	1.006
Hot Irrigated Cropland	11	1.30	4.40	0.05	1.005
Cool Irrigated Cropland	12	0.00	3.00	0.05	1.005
Mediterranean Scrub	13	2.50	4.30	0.46	1.2
Dry Evergreen Woods	14	1.70	1.80	0.04	1.004
Sand Desert	15	0.00	0.00	0.05	1.005
Forest and Field	16	2.20	6.10	0.17	1.017
Crops, Grass, Shrubs	17	0.80	2.70	0.1	1.01

*It is estimated from h (m) parameter, according to Allen *et al.*, 1998.

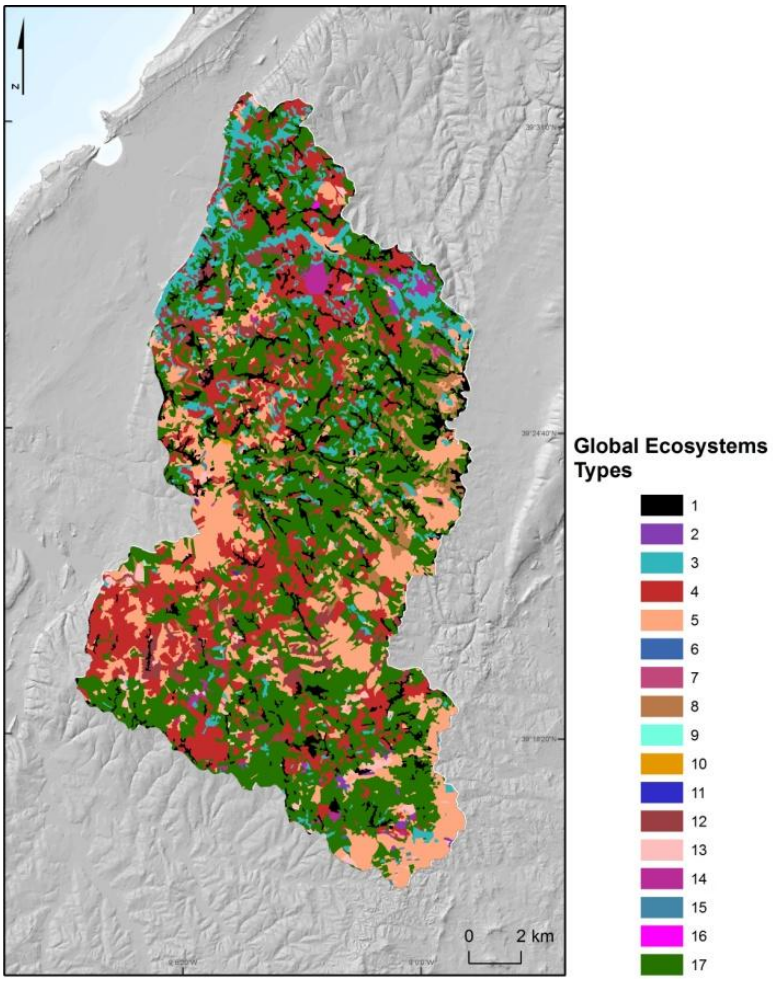

Fig. 5.33 – Global Ecosystem Types according to Olso (1994a, 1994b).

The $K_{cb\ max}$ is estimated through the mean maximum plant height (h) (Table 33) using the Allen *et al*. (1998) approach:

$$K_{cb\,max} = 1.0 + 0.1\ h \text{ for } h \leq 2\ m \tag{5.55}$$

where Kcb max is limited to 1.20 when h > 2 m. The value of 1.2 represents a general upper limit on Kcb for tall vegetation having full ground cover and LAI > 3 under the sub-humid and calm wind conditions (Allen *et al*., 1998).

In latitudes such, as the study area, the growth of the vegetation is mainly limited by temperature. According to Hagemann (2002) this limiting parameter is defined by f_i:

$$f_i = 1 - \left(\frac{T_{max} - T_i}{T_{max} - T_{min}} \right)^2 \quad (5.56)$$

Where T_i is the daily temperature of day $_i$. T_{min} and T_{max} are, respectively the minimum and maximum annual temperature.

Using the growth factor f_i based on Equation 5.56, the daily LAI_i (analogous for the vegetation ratio) can be parameterized and computed as:

$$LAI_i = LAI_{min} + f_i \times (LAI_{max} - LAI_{\min}) \quad (5.57)$$

Where LAI_{max} is the leaf area index for the growing season and LAI_{min} is the leaf area index for dormancy season.

Natural vegetation typically has less leaf area or fraction of ground cover than does the agricultural vegetation that has been developed for full ground cover and for soil water conditions favoring vigorous growth. The value for $K_{cb\ mid}$ for natural or non-pristine vegetation should be reduced when plant density and/or leaf area are lower than for full cover conditions (generally defined as when LAI ≥ 3). Where LAI can be measured or approximated, a peak $K_{cb\ mid}$ for natural, non-typical or non-pristine agricultural vegetation can be approximated similar to a procedure used by Ritchie (1998). In this sense, the Crop factor can be now calculated using the following equation (Allen *et al.*, 1998):

$$K_{cb\ mid} = K_{cb\ min} + (K_{cb\ max} - K_{cb\ min})(1 - exp[-0.7\,LAI]) \quad (5.58)$$

Where $K_{cb\ mid}$ is the estimated basal K_{cb} during the mid-season, when plant density and/or leaf area are lower than for full cover conditions. $K_{cb\ max}$ is the estimated basal K_{cb} during the mid-season (at peak plant size or height) for vegetation having full ground cover or LAI > 3. $K_{c\ min}$ is the minimum K_c for bare soil ($K_{c\ min}$ ≈ 0.15 - 0.20). LAI is the actual leaf area

index, defined as the one-sided green leaf area per unit of ground surface area (m^2 m^{-2}) (Allen *et al*., 1998).

The potential rate of soil evaporation (K_e) is then calculated using the leaf area index, LAI. When LAI is less than 1,

$$K_e = E_0 \times (1 - 0.43 \times LAI) \quad (5.59)$$

and when LAI is greater than 1,

$$K_e = E_r \times EXP(-0.4 \times LAI) \quad (5.60)$$

Where E_0 is the potential evaporation and E_r is the evaporation rate. These final parameters are automatically calculated in STARWARS model.

It must be mentioned that, since it is a dynamic approach, a major number of land use maps with different dates would be important for modeling the variations of the Kc parameter, over certain years (in this case, from 1975 to 2012). However, only the previous land use map (named COS 90) from 1990 was possible to obtain. There are more land use maps for the study area for different years, although, only the map from 1990 has all the detailing needed for subsequent acquisition of the Kc parameter.

This fact is here reported as an additional limitation in the landslide susceptibility assessment based on the dynamic approach. A way of overcoming this problem could be achieved by working on satellite images, in order to detail the land use information and get it for several years. However, this work requires new methodologies, care and time and thus, unfortunately, it was not possible to carry out for the present study.

5.6.1.7 Soil hydrological properties: hydraulic conductivity and SWRC

Since the hydrological properties of soils are determinant for the movement of water in the unsaturated zone, from the soil surface into the soil (infiltration), and the subsequent movement of infiltrated water in the unsaturated zone (percolation) (Dingman, 1998), it is important to considered parameters such as the saturated hydraulic conductivity in m/d (K_{sat}), effective saturation (θ_e), bubbling pressure (air entry) in m (h_A), total porosity in m3/m3 (ϕ), pore size distribution index (λ) and capillary pressure in m (ψ), for further hydrological modeling.

The soil properties, determined by the proportions of clay, silt, and sand, was already obtained in section 5.3.6. Using the USDA classification was possible to assigned the hydrological parameters. The K_{sat}, ϕ, ψ and h_A were directly obtained from Rawls *et al*. (1982). The $h_{A\ min}$ (or ψ_s) is obtained from h_A and it is the minimal matric suction that is required to start drainage from fully saturated pores. The α is the dimensionless slope of the loglinear relationship between ln(|h|) and (1- θ_e) for minimal matric suction. The |h| is obtain through a relationship so called, soil water retention curve (SWRC) (Table 5.33).

Table 5. 33 – Hydrological properties classified by soil texture based on the standard values given by Rawls *et al*. (1982) necessary for hydrological modeling.

USDA classification	ID	K_{sat} (m/d)	ϕ (m^3/m^3)	λ	h_A (m)	ψ (m)	$h_{A\ min}$ (m)	α
Clay	9	1.4664	0.475	0.131	0.373	0.373	0.361	8.681
Clay loam	1	0.0144	0.464	0.194	0.259	0.2589	0.234	6.52
Loam	2	0.0216	0.463	0.22	0.112	0.1115	0.090	6.411
Loamy sand	8	0.6216	0.437	0.474	0.087	0.0869	0.06	4.143
Sandy clay loam	5	0.1032	0.398	0.25	0.281	0.3256	0.250	5.322
Sandy loam	7	0.3168	0.453	0.322	0.147	0.1466	0.112	4.878
Silt loam	3	0.036	0.501	0.211	0.208	0.2076	0.18	6.265
Silty clay	4	0.0552	0.479	0.127	0.342	0.3419	0.328	8.995
Silty clay loam	6	0.1632	0.471	0.151	0.326	0.3256	0.309	7.791

This SWRC is primarily used to predict the soil water storage, i.e., the water supply to the plants (field capacity) and soil aggregate stability. According to the amount of water in the pores, different wetting and drying curves may be distinguished. The soil is close to

saturation when potentials or capillary pressure are close to zero. Moreover, the water is hell in the soil by capillary forces. When θ decreases, the binding of the water becomes stronger, and at small potentials (more negative, approaching wilting point) water is strongly bound in the smallest pores (Dingman, 2002).

According to the different types of soil, the hydrological behave will act differently, e.g., sandy soils will involve mainly capillary binding, and will therefore release most of the water at higher potentials, while clayey soils, with adhesive and osmotic binding, will release water at lower (more negative) potentials (Dingman, 2002).

To establish the relationship between the water content, θ, and the soil water potentials, ψ, it is first necessary to calculate the retain water content which is expressed as the volumetric moisture content (VMC). Since this measure is dependent on the absolute porosity, it is commonly transformed into the relative degree of saturation, θ_e (Nielsen, *et al.*, 1986):

$$\theta_E = \left(\frac{h_A}{\psi} \right)^{\lambda} = \frac{\theta - \theta_{res}}{\theta_{sat} - \theta_{res}} \tag{5.61}$$

Where θ_e is the effective saturation or degree of saturation; θ is the actual volumetric soil water content (m^3/m^3); θ_{res} is the residual volumetric moisture content (m^3/m^3); and θ_{sat} is the saturated volumetric moisture content (m^3/m^3). The residual moisture content, i.e., the amount of water bounded to the soil particles, which cannot be released by suction, has been set to a constant fraction of 5% of the porosity (Beek, 2002).

A model for the SWRC can be fitted to these standard data to obtain the relative degree of saturation for a given matric suction and vice versa. Here, the SWRC of Farrel and Larson (1972) has been used. This function describes the SWRC as an exponential relationship:

$$|h| = h_{A\,min} exp[\alpha(1-\theta_E)] \tag{5.62}$$

where α is the shape factor describing exponential relationship and $h_{A\ min}$ is the air entry value, interpreted here as the minimal matric suction. By definition, matric suction is taken as positive. At suction smaller than the air entry value, the soil remains saturated and will behave accordingly. The shape factor α can be interpreted as a measure for the pore size distribution. High values of α are associated with heterogeneous porous media that experience a more gradual loss of pore water as the matric suction increases (Beek, 2002). This is shown by the SWRCs (Fig. A6.1 in Appendix 6) where it is plotted the logarithm of the matric suction ($\ln(|h|)$) against $1-\theta e$. The SWRCs have been performed and fitted for all type of soils present in the study area.

It is important to mention that, ideally, the acquisition of the hydrological properties of soils, would be preferable to be obtained from field work and subsequent laboratory measurement, however, it was very laborious and costly to do so, and thus, impossible to obtain for the present work.

All the input parameters of the STARWARS model where generated according to all the procedures, already described, in an automatically manner, by implementing the Script A4.2 in Appendix 4.

5.6.2 Calibration

In order to reduce the discrepancy, between the observed and simulated hydrological response, a calibration was performed. This step provides a great advantage when compared to the static hydrological model, where only a static calibration of the K_{sat} values was possible to be made.

Calibration is a very important step because, indirectly, it enhances the performance of the coupled hillslope model. Under this assumption, it is expected that the calibrated hydrological model have predictive power for the unknown hydrological conditions under which landslides are triggered. This requires that the physically-based model describes the relevant processes and that these processes are continuous in time and space (Beek, 2002).

The parameter available for calibration was the actual water discharges. Such data was obtained from *Sistema Nacional de Informação de Recursos Hídricos* (*SNIRH*). In this sense, based on the input parameters, an equation, which calculates the simulated water discharge, was included in STARWARS model, as following (Beek, 2002):

$$D_{sch} = \frac{S_d \times c_a}{\mathrm{P_{dur}} \times 24 \times 3600} \tag{5.63}$$

Where D_{sch} is the simulated water discharge in m^3/s. S_d (in m), is the surface detention, i.e., it is the water that is removed as exfiltration when any saturated storage is in excess of the maximum storage of the soil. C_a is the cell area in m^2. The numerator expression is then divided by the precipitation duration (P_{dur} in days) times 24 hours, times 3600 (in order to obtain the precipitation duration in seconds per fraction of day).

Unfortunately, the actual water discharges are only available for three sites, which are geographically close and two are located outside the study area. Thus, for calibrating purposes, a small area of a location called Óbidos, was considered as shown in Fig. 5.34 (Fig. A7.1 to Fig. A7.4 in Appendix 7). However, it is important to mention that, for further comparisons with other resulting models, only the previous study area was considered.

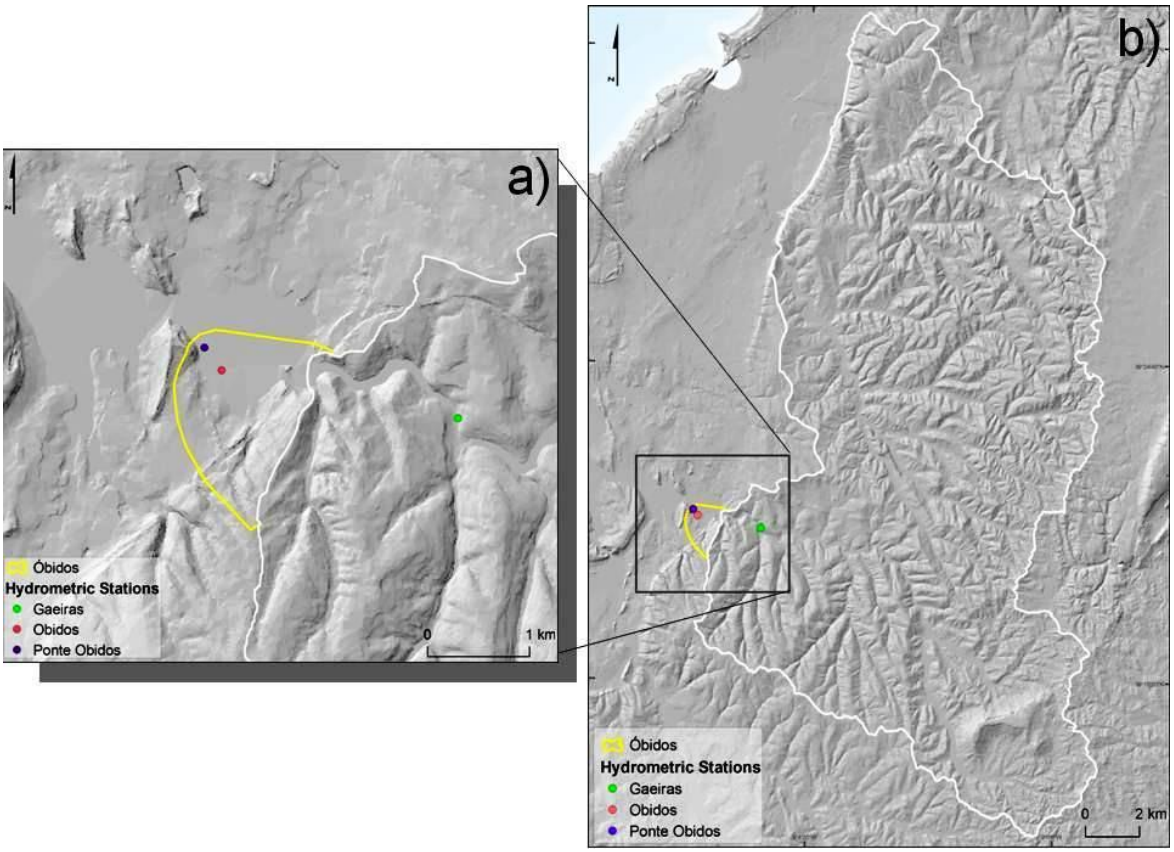

Fig. 5.34 – Study area incorporating part of Óbidos location and hydrometric stations (discharge stations) used for calibration of the STARWARS model.

The three sites, corresponding to hydrometric stations, are located in Gaeiras, Óbidos and Ponte de Óbidos. The actual water discharges are available for Óbidos since October 1977 to September 1980, for Gaeiras since October 1981 to September 1983, and for Ponte de Óbidos since October 1982 to September 1990.

Considering the observed and simulated time steps (day by day) of water discharges, the calibration was based on equal intervals of discharge and volume of water as proposed by Westerberg *et al*. (2011). The model, however, requires initial conditions that are equally important for its performance. Hence, the hydrological model must start being simulated, at least, two years before the calibration period (Beek, 2002). In the present case it was chosen to start modeling since October, 1975. To avoid inconsistencies as a result of the differences in soil depth and water height, the comparison between the simulated and observed water discharge was made with reference to the topographical surface.

For the calibration of the model was used a function (Φ) which is defined as the squared sum of the deviations between the generated model output (Fig. 5.35) and the actual observations, i.e:

$$\Phi = \sum (b_0 - \beta_0)^2 \tag{5.64}$$

Where b and β stand for the simulated and actual value of the observation (0). If the square root of the objective function divided by the number of observation were taken, it will be obtained the root mean square error (RMSE).

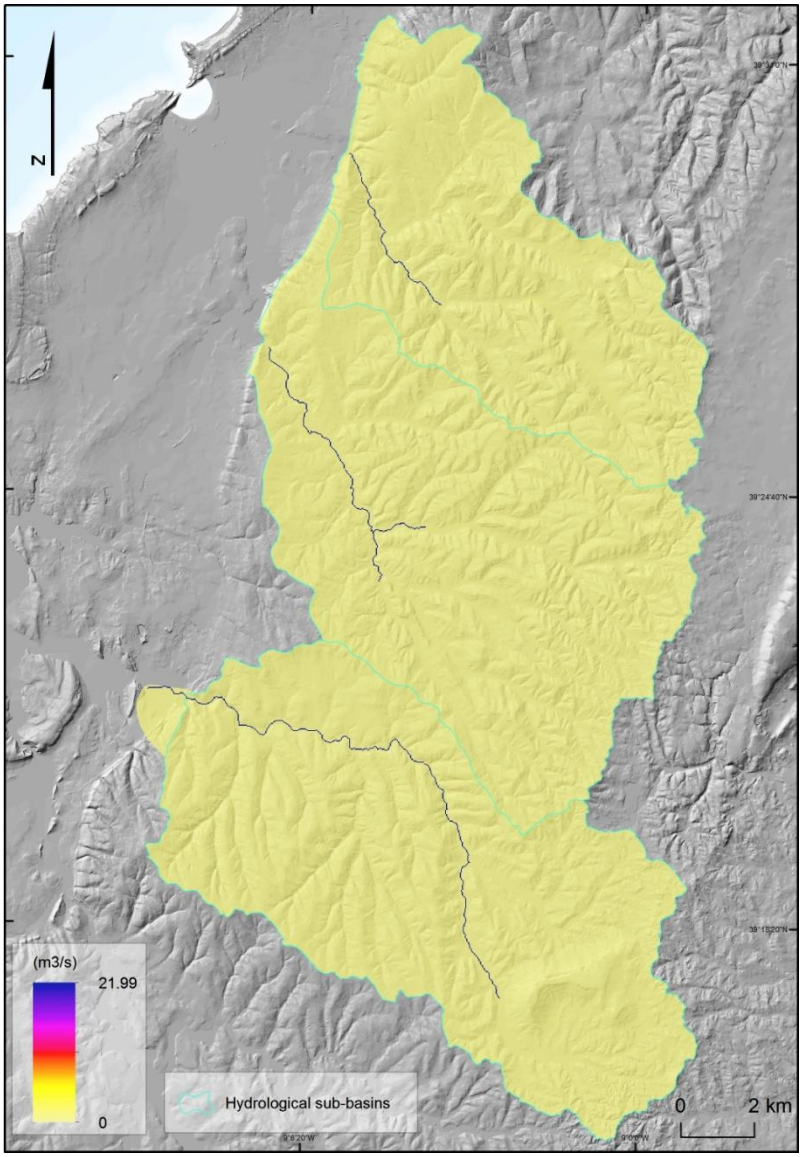

Fig. 5.35 – Modeled discharge (here in m3/s). An example of a map from the time step corresponding to the Julian day 365 of 1979).

The hydrological model is then improved by changing the input data. Due to the source of errors and uncertainties associated to the input data it was decided to calibrate only the K_{sat} values since it is the most influent variable in both, dynamic and static models. The calibration has stopped when the minimal RMSE was achieved (Table 5.34). As in the static hydrological model, it was used a multiplier factor which allowed to test the values of Ksat iteratively. However here a multiplier factor of 2.1 proved to be sufficient to provide lower results of RMSE.Above this multiplier value, RMSE become stable or even increase.

In Table 5.34 it is possible to observe that using the K_{sat} values from Table 14 (initial values) the results of RMSE are higher than those provided by a multiplier factor of 3.1 to the soil types where landslides occur (clay loam; silt loam; loam).

Table 5.34 – RMSE of the discharge values of the hydrometric stations, selected for calibration.

	Gaeiras	Óbidos	Ponte de Óbidos
	(m^3/s)	(m^3/s)	(m^3/s)
Initial values	5.7	4.0	4.1
Final values	3.4	2.6	2. 9

From this operation new values of K_{sat} have emerged (Table 5.35).

Table 5.35 – K_{sat} values assigned for the study area after the dynamic calibration.

USDA classification	K_{sat} (m/d)	Data source
Clay	0.0144	References
Clay loam	0.17112	References and back analysis
Loam	0.98208	References and back analysis
Loamy sand	1.4664	References
Sandy clay loam	0.1032	References
Sandy loam	0.6216	References
Silt loam	0.50592	References and back analysis
Silty clay	0.0216	References
Silty clay loam	0.036	References

Good hydrological performance in terms of water discharge does not necessarily provide a good reproduction of the observed landslides. For this reason a calibration of the cohesion was again performed.

Slope stability models have the limitation that they often overestimate the potentially unstable area. So, in order to avoid that, it is important to select the run that after calibration: 1) gives good water discharge (minimize RMSE); 2) encloses all landslide locations but; 3) is conservative in its estimation of landslide occurrence (smallest area with SF≤1).

The only lithological class incorporating shallow translational slides was the shale dominated complexes, thus, the calibration was only possible in such lithological class. After some calibrating tests (by rerunning the model) it was observed that the cohesion value that best fitted the statements above was 3 kPa. This value enables the model prediction of the initial instability conditions that may have triggered the dated landslide (from 30 of november of 2006). Values above 3kpa did not predict the dated landslide (i.e. the SF was >1).

´

5.7 Dynamic modeling of slope stability: applying the Infinite slope equation through PROBSTAB

Beyond the already described, geotechnical parameters of soil, as cohesion and angle of internal friction, the PROBSTAB model also includes parameters in order to determine the lower boundary conditions, i.e., the conditions of, the already described, fourth layer (bed rock) which is crucial for determining the response of the hydrological system. These parameters were used in accordance with the values given by Beek (2002) (Table 5.36).

Table 5.36 – Parameters to constrain the percolation to the deeper bedrock (bc), Beek (2002).

Lithology	θ_{satbc}	θ_{resbc}	k_{satb}
Alluvium	0.23	0	2.5
Dolerite	0.04	0	0.1
Limestones and claystones	0.05	0	1
Limestones and marls	0.05	0	1
Marls, sandstones and claystones	0.05	0	0.1
Sands (Pliocene)	0.04	0	1
Sandstones, claystones and limestones	0.04	0	1
Sandstones dominated complexes	0.04	0	1
Shale dominated complexes	0.05	0	0.01

The θ_{satbc} and the θ_{resbc} are, respectively, the saturated and residual moisture content for the bedrock material. k_{satbc} it is the saturated hydraulic conductivity for the bedrock material. The θ_{satbc} and the θ_{resbc} describe the groundwater recession and k_{satbc} is also used to constrain the percolation to the deeper bedrock.

The landslide inventory validated by field work (LI#3) incorporate relative recent occurrences. Therefore, it was decided to run the model for a time series of the latest 10 years (from 2002 to 2011), in order to further validate the spatial distribution of these landslides (shallow translational slides from LI#3) over the period 2002-2011. Later, it is also inferred, what would be the days, within these years, most susceptible to the occurrence of those landslides (according to the SF results).

Thereby, having all the parameters and the calibrated values of K_{sat} of soil, for the period 1977 to 1990, was possible to run the model until 2011. All the parameters and calculations needed for the safety factor evaluation were performed by the PROBSTAB model (Fig. 5.36 and Table 5.37).

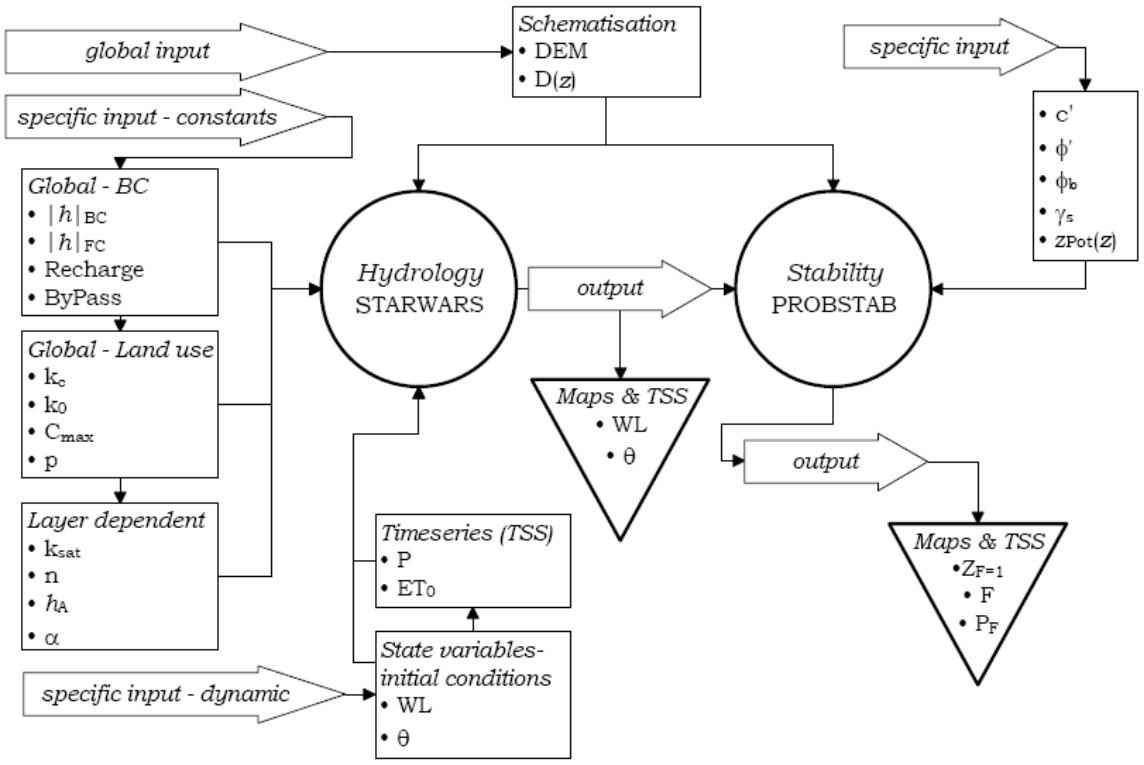

Fig. 5.36 – Model structure: input & output. Extracted from Beek (2002).

The parameters required from PROBSTAB are entered as constant, tables or maps, which relate the parameter value to a spatial attribute. The PROBSTAB returned, respectively, the daily safety factor and the minimum safety factor over the year for each location (pixel).

It is important to remind that the hydrological model (STARWARS) was performed with a 25m pixel size, while the remaining data, which served as inputs for the equation of the safety factor, was used a 5m pixel size, in order to take into account the smallest shallow translational slide. Thus, the outputs from the STARWARS model (i.e., groundwater level and volumetric soil moisture content), which serves as input into the PROBSTAB model, were resampled to a 5 m resolution (Table 5.37).

Table 5.37 – Model input & output of the coupled hillslope model for hydrology (STARWARS) and slope stability (PROBSTAB). Adopted from Beek, 2002.

Model component:	Hydrology – STARWARS		Stability – PROBSTAB	
Model Input				
Schematisation	High resolution DEM (m) Layer depth D(z) (m)			
Constant parameter values	Global boundary conditions		Layer-dependent	
	Matric suction for lower boundary condition	$\|h\|_{BC}$ (m)	Cohesion	c' (kPa)
	Matric suction at field capacity, 1st layer	$\|h\|_{FC}$ (m)	Internal friction angle	ϕ' (°)
	Residence* of surface detention	Recharge (-)	Bulk units weight of the soil	γ_s (kN·m^{-3}) γ` (kN·m^{-3}) γ (kN·m^{-3})
	Soil depth	Z (m)		
	Fraction of bypass flow	ByPass (-)	Soil depth	Z (m)
	Global – land use dependent Evapotranspiration		All parameters can be considered as layer and land use dependent	
	Crop factor	k_c (-)		
	Infiltration			
	Infiltration constant	K_0 (-)		
	Max. storage capacity	C_{max} (m)		
	Direct throughfall ratio	p (-)		
	Layer-dependent*			
	Saturated hydraulic conductivity*	K_{sat} (m·d^{-1})		
	Porosity	n (m^3·m^{-3})		
	Air entry value*	h_A (m)		
	SWRC slope*	α (-)		
	All parameters of the top layer can be considered as land use dependent			
Dynamic input – All timesteps	Reference potential evapotranspiration	ET_0 (m·d^{-1})	Groundwater level	WL (m)
	Precipitation	P (m·d^{-1})	Volumetric soil moisture content	θ (m^3·m^{-3})
	Precipitation duration	P_{dur} (fraction of day)		
Initial conditions – state variables	Groundwater level	WL (m)		
	Volumetric soil moisture content	θ (m^3·m^{-3})		
Model Output				
Maps and Timeseries	Groundwater level	WL (m)	Safety Factor	SF (-)
	Volumetric soil moisture content	θ (m^3·m^{-3})		
	Water discharge	D_{sch} (m^3·d^{-1})	Critical depth	ZF =1 (m)

*: also required for lower boundary condition.

The spatial and temporal components of simulated safety factor were reported from the model in the form of daily maps (map series). Since the temporal information of the landslide inventory is poor, it was choosen to present only the minimum safety factor obtained over each year, which, obviously, does not occur on the same day in every pixel. Thereby, through the Script A8.1 in Appendix 8, and all the provided parameters (Table 5.37) were possible to obtain the following maps for each year (from 2002 to 2011) (Figs. 5.37, 5.38, 5.39, 5.40, 5.41).

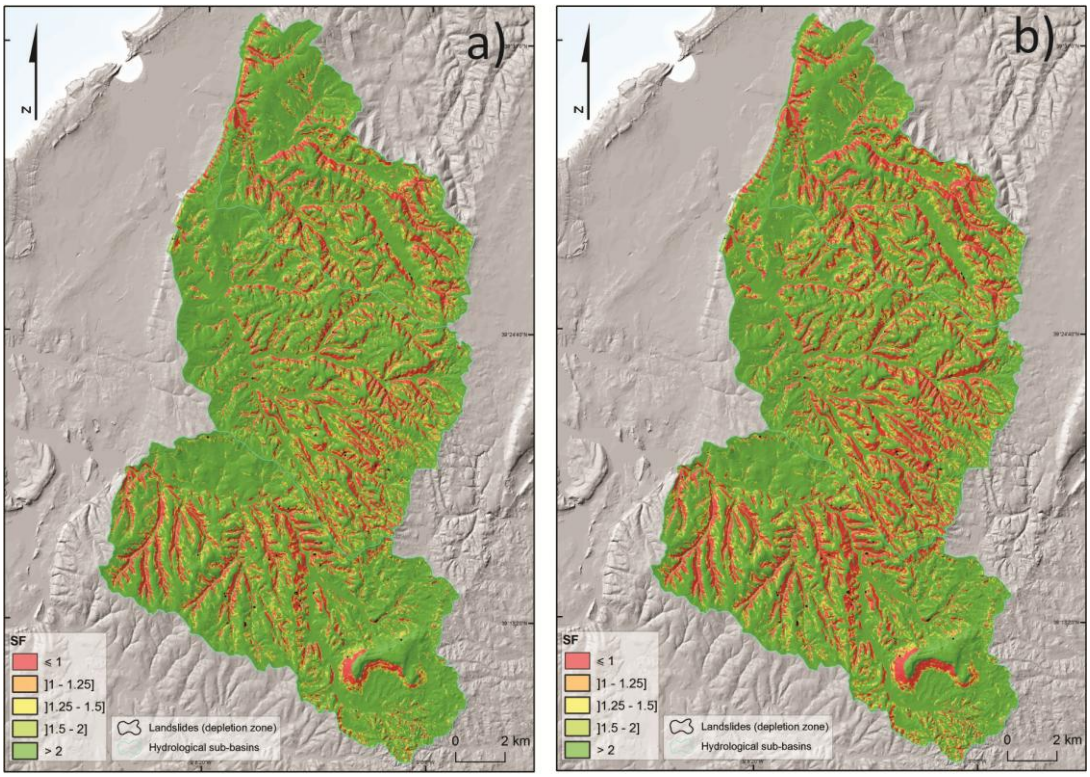

Fig. 5.37 – Landslide susceptibility (minimum safety factor over the year) assessed thought the STARWARS+PROBSTAB: a) year 2002; b) year 2003.

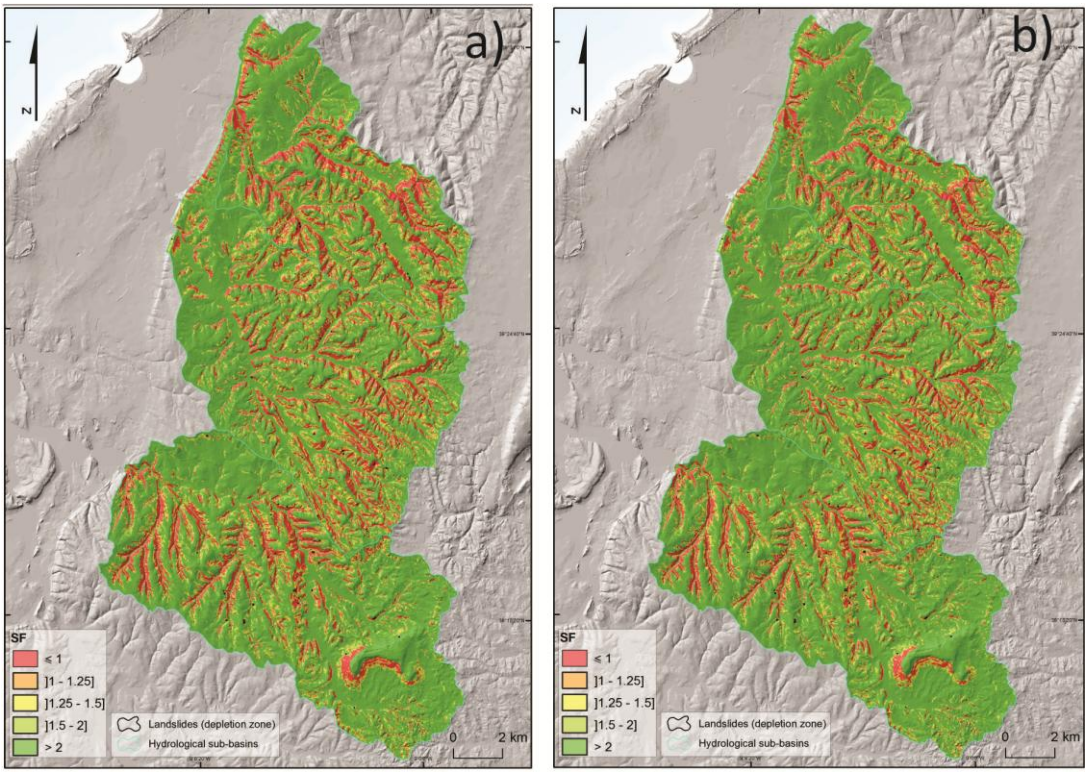

Fig. 5.38 – Landslide susceptibility (minimum safety factor over the year) assessed thought the STARWARS+PROBSTAB: a) year 2004; b) year 2005.

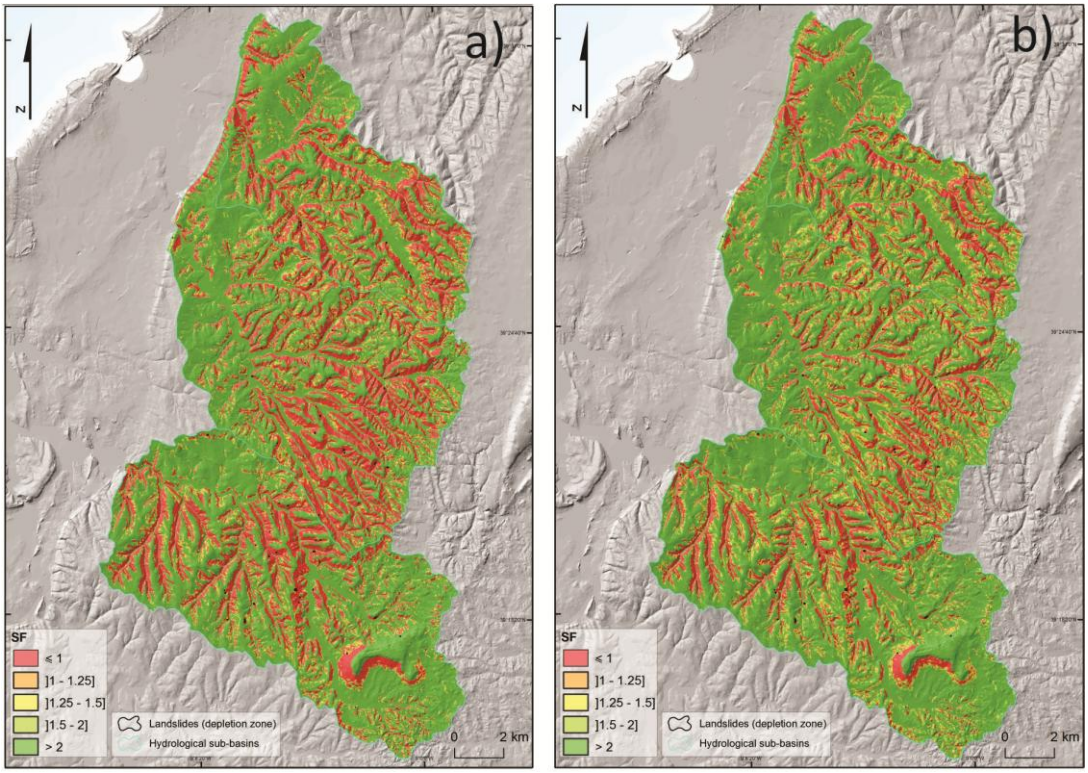

Fig. 5.39 – Landslide susceptibility (minimum safety factor over the year) assessed thought the STARWARS+PROBSTAB: a) year 2006; b) year 2007.

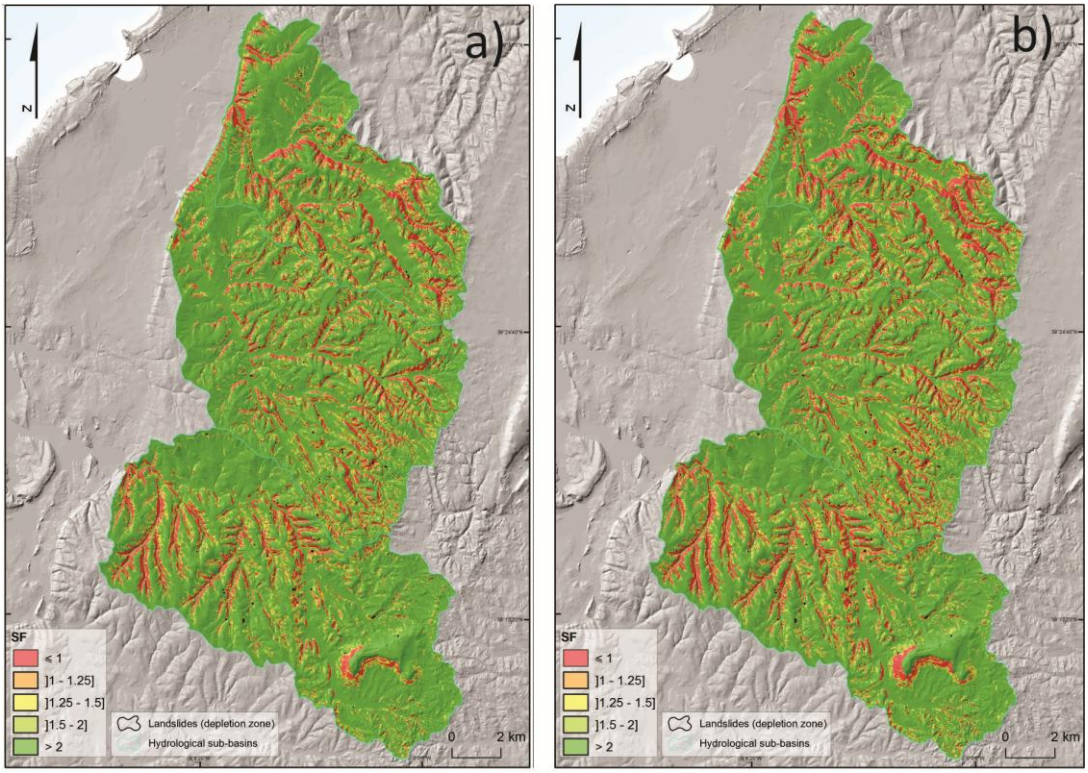

Fig. 5.40 – Landslide susceptibility (minimum safety factor over the year) assessed thought the STARWARS+PROBSTAB: a) year 2008; b) year 2009.

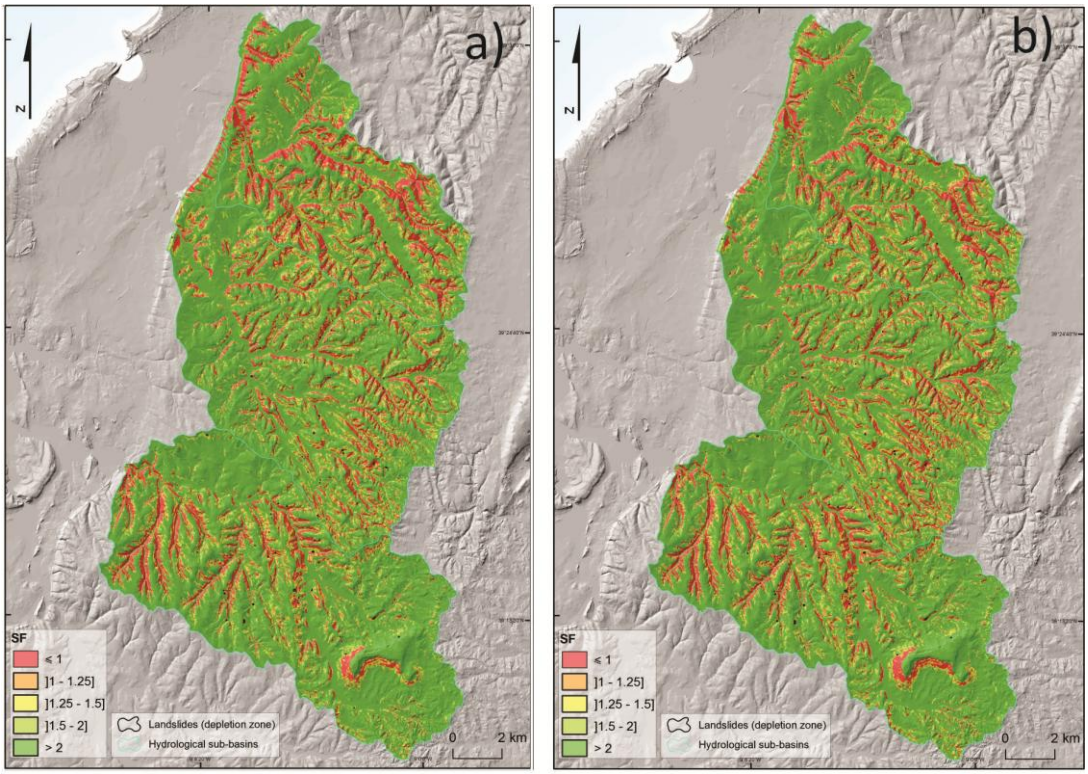

Fig. 5.41 – Landslide susceptibility (minimum safety factor over the year) assessed thought the STARWARS+PROBSTAB: a) year 2010; b) year 2011.

5.7.1 Analysis and validation of results

Globaly, it is possible to verify that, among all the years, and in accordance with the minimum safety factor, the year 2006 was the most unstable year (higher instability class occupying 25.8% of the total study area). Conversely, it is noted that the year 2008 was the lowest unstable year (higher instability class occupying only 9.8% of the total study area) (Table 5.38 and 5.39).

Through a spatial assessment of the shallow translational slides distribution is possible to verify that 2006 was the year with higher predictive ability (79% of the total shallow translational slides). Whereas 2008 was the year with lower predictive ability (37.1% of the total shallow translational slides).

Table 5.38 – Landslides susceptibility classes assessing the minimum safety factor, for the years 2002; 2003; 2004; 2005 and 2006. Area of each class and landslide area in each class (both in % of the total).

Safety Factor (FS)	Slope Stability	Years									
		2002		2003		2004		2005		2006	
		CA	LA	CA	LA	CA	LA	CA	LA	CA	LA
FS ≤ 1	Instable (rupture)	13.0	53.2	17.7	67.7	13.9	53.2	11.8	43.5	25.8	79.0
1 <FS< 1.25	Instable (likely rupture)	5.7	12.9	6.4	19.4	6.0	12.9	5.5	12.9	5.8	12.9
1.25 <FS< 1.5	Marginally Unstable	5.7	22.6	5.9	6.5	5.9	21.0	5.6	19.4	5.1	1.6
1.5 <FS< 2	Marginally Stable	10.3	4.8	10.0	0	10.5	6.5	10.4	17.7	8.2	0
FS> 2	Stable	65.3	6.5	60.0	6.5	63.7	6.5	66.6	6.5	55.1	6.5
	TOTAL	100	100	100	100	100	100	100	100	100	100

CA Class area
LA Landslide area

Table 5.39 – Landslides susceptibility classes assessing the minimum safety factor, for the years 2007; 2008; 2009; 2010 and 2011. Area of each class and landslide area in each class (both in % of the total).

Safety Factor (FS)	Slope Stability	Years									
		2007		2008		2009		2010		2011	
		CA	LA	CA	LA	CA	LA	CA	LA	CA	LA
FS ≤ 1	Instable (rupture)	17.1	67.7	9.8	37.1	12.2	46.8	12.7	40.3	12.2	50.0
1 <FS< 1.25	Instable (likely rupture)	6.3	19.4	5.0	11.3	5.6	12.9	5.6	16.1	5.6	11.3
1.25 <FS< 1.5	Marginally Unstable	6.0	6.5	5.3	14.5	5.7	22.6	5.7	12.9	5.7	21.0
1.5 <FS< 2	Marginally Stable	10.2	0	10.4	29.0	10.5	11.3	10.6	24.2	10.5	11.3
FS> 2	Stable	60.5	6.5	69.5	8.1	66.0	6.5	65.4	6.5	66.0	6.5
	TOTAL	100	100	100	100	100	100	100	100	100	100

CA Class area
LA Landslide area

However, regarding the mean annual precipitation (Fig. 5.42 to 5.46 and Table 5.40), it is possible to observe that 2008 was not the driest year, but the year before (2007).

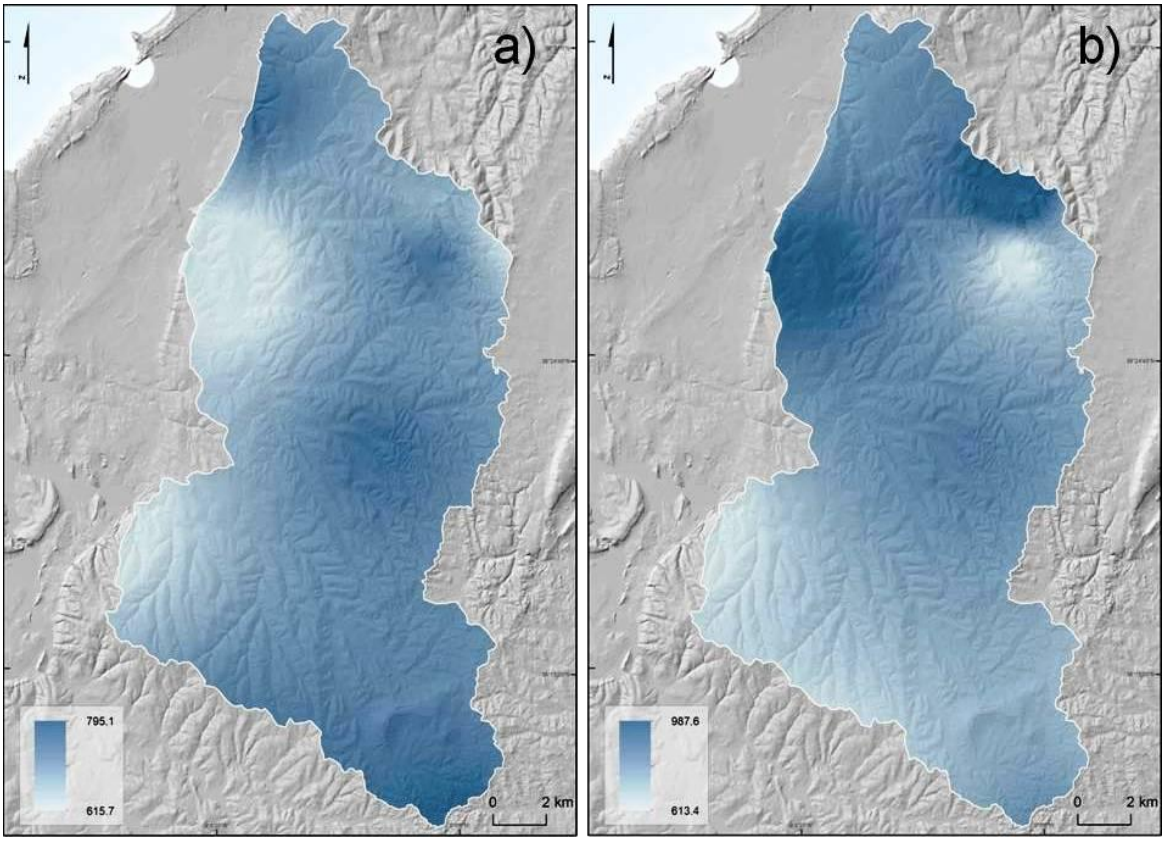

Fig. 5.42 – Mean annual precipitation for the years: a) 2002; b) 2003.

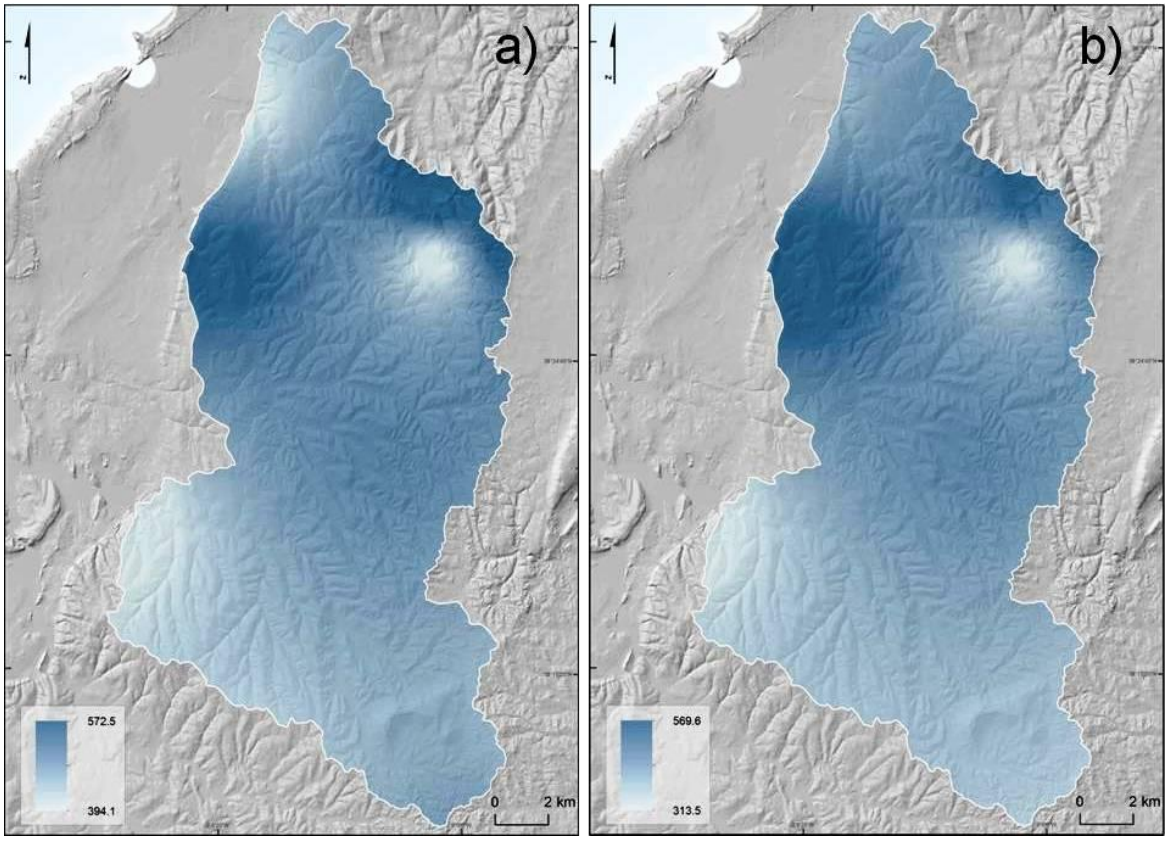

Fig. 5.43 – Mean annual precipitation for the years: a) 2004; b) 2005.

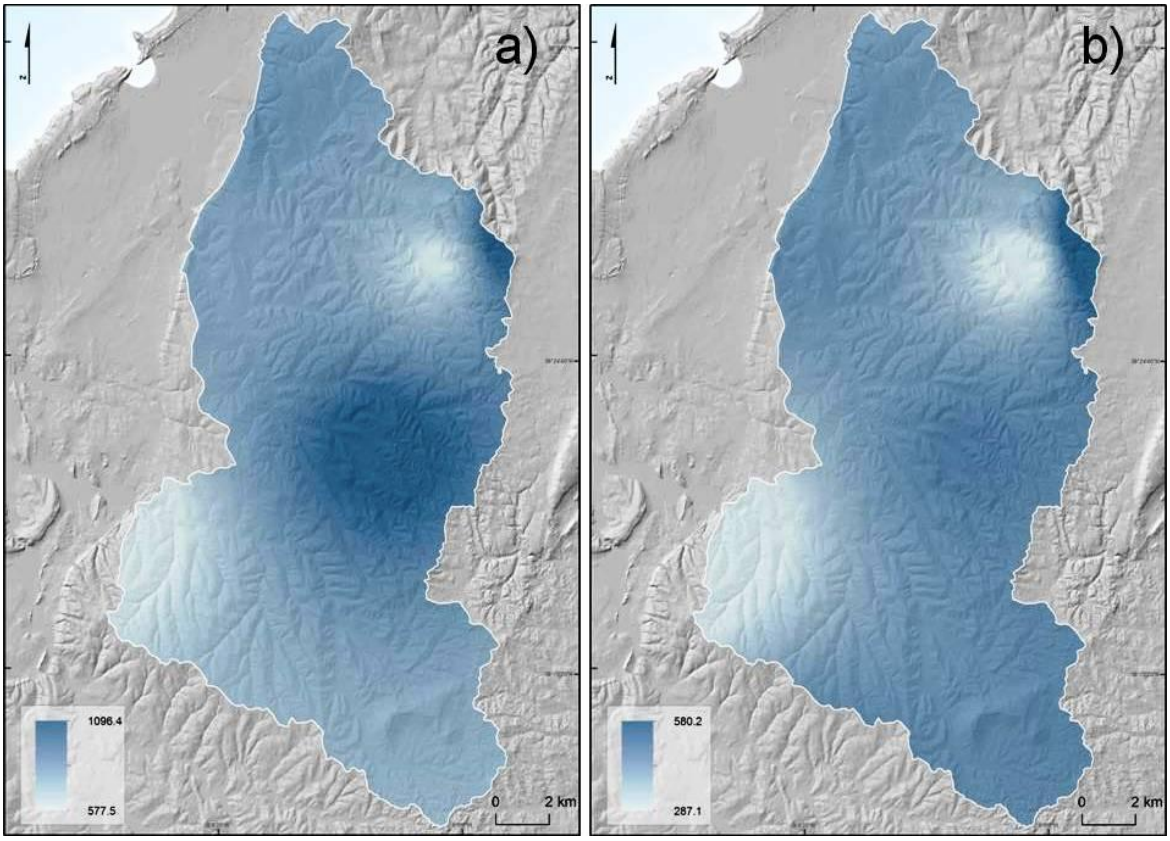

Fig. 5.44 – Mean annual precipitation for the years: a) 2006; b) 2007.

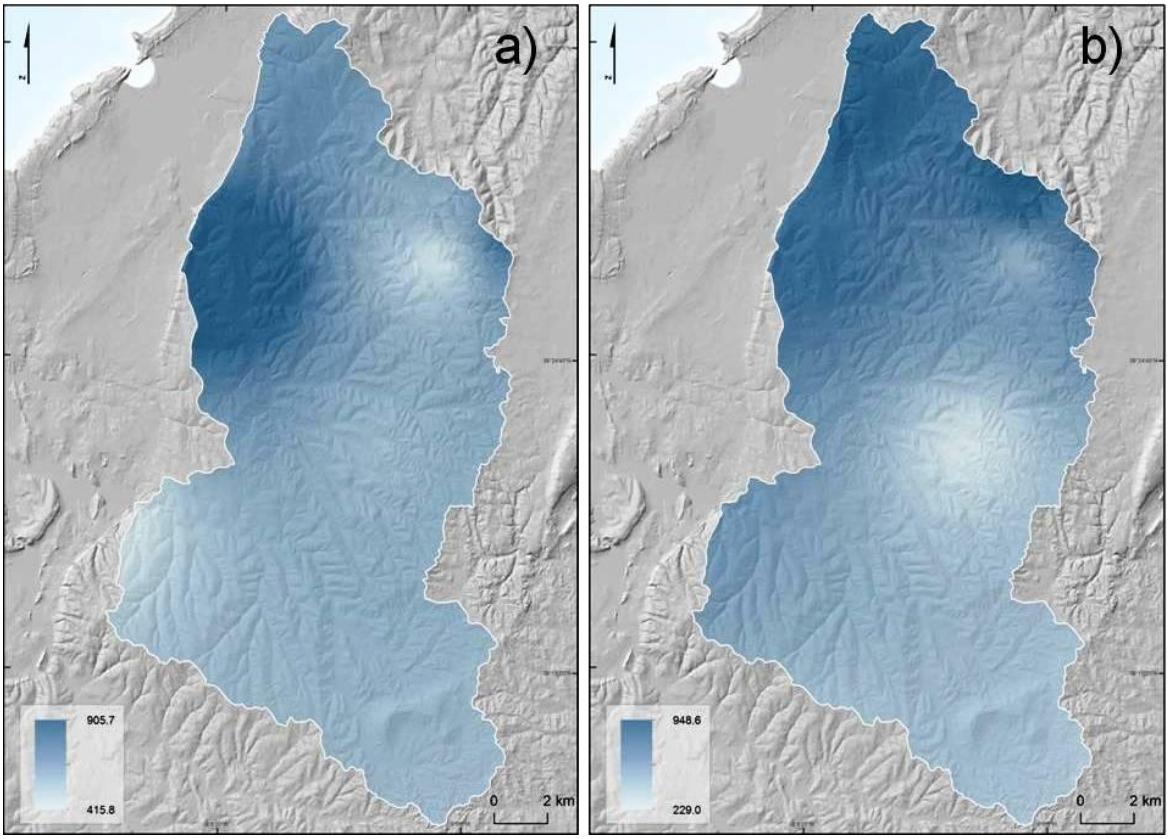

Fig. 5.45 – Mean annual precipitation for the years: a) 2008; b) 2009.

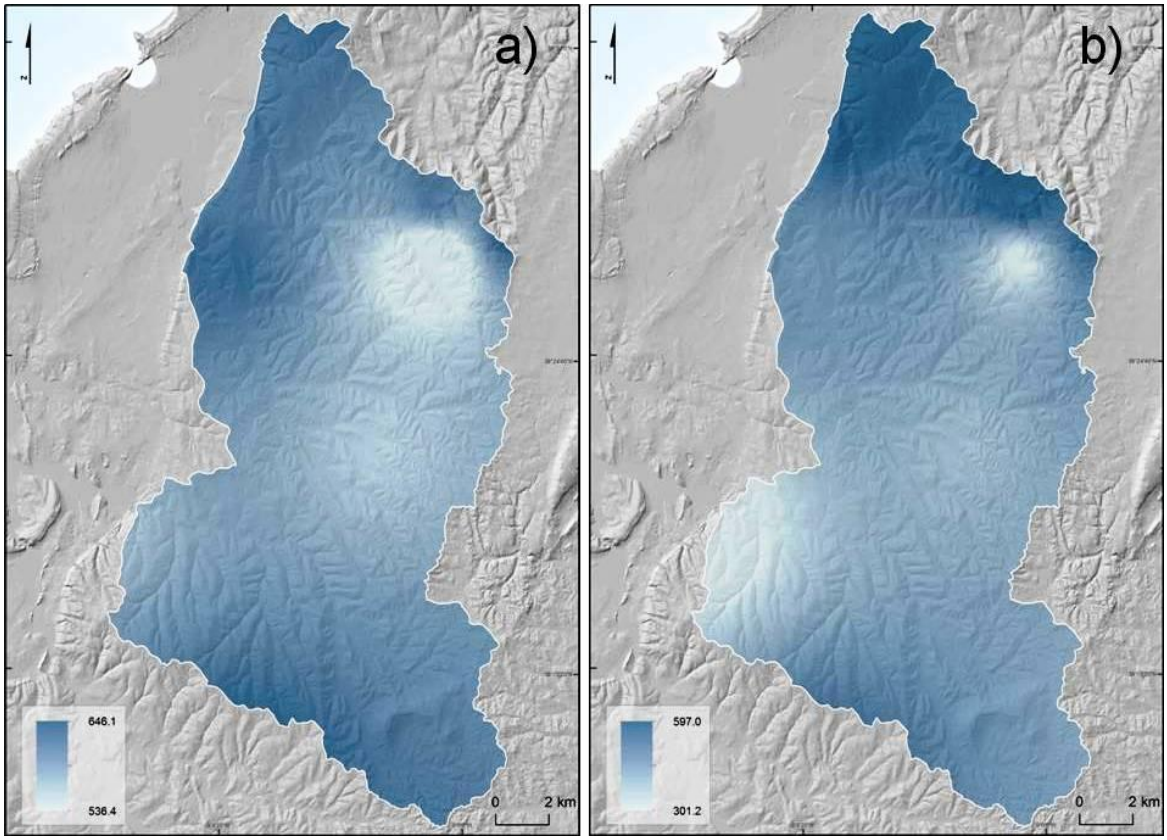

Fig. 5.46 – Mean annual precipitation for the years: a) 2010; b) 2011.

Table 5.40 – Annual precipitation along the study area for each year (2002; 2003; 2004; 2005; 2006; 2007;2008; 2009; 2010; 2011).

Year	Min (mm)	Max (mm)	Mean (mm)
2002	615.7	795.0	718.3
2003	613.4	987.6	757.5
2004	394.1	572.5	476.9
2005	313.5	569.6	424.6
2006	577.47	1096.4	827.4
2007	287.1	580.2	404.2
2008	415.8	905.7	563.9
2009	229.0	948.6	558.1
2010	536.4	646.1	612.8
2011	301.2	597.0	463.4

The previous observations allows saying that, the response between precipitation and increased groundwater table, may not be done instantaneously. Thus, considering only the precipitation for such studies, may not be as precise as intended, since the pore pressure in the soil, which increases with the increasing presence of water, is the responsible factor for slope instability. On the other hand, the differences registered between 2007 and 2008, may be due to the fact that although being a driest year, 2007 could have a day or more where the precipitation has been intense originating, thus, higher susceptibility.

Each of the observed landslides (centroid of the depletion zone) was analyzed in order to estimate the differences between the total annual precipitation, maximum daily precipitation and the maximum daily groundwater level observed in each year (Tables from A9.1 to A9.15 in Appendix 9). This observation noticed that, many times, the maximum level of groundwater table is reached within a few days after a maximum rainfall (with reduced rainfall during this period).

Once it was implemented a dynamic approach it became possible to dynamically assess the instability along time. Thereby, it was proceeded an analysis of each landslide, independently, in order to understand which could have been the years or, more precisely, the exact days or periods more prone to the occurrence of instability. This statistical analysis was performed based on the centroid of the depletion zone of each shallow translational slide (Tables from 5.41 to 5.46).

Table 5.41 – Total duration and period duration (in Julian days) with conditions to instability (SF $\leq$ 1), for each shallow translational landslide (ID, from 1 to 33) indentified in the study area, for the years: 2002; 2003; 2004; 2005; 2006.

ID	Year									
	2002		2003		2004		2005		2006	
	Total Duration	Period Duration	Total Duration	Period Duration	Total Duration	Period Duration	Total Duration	Period Duration	Total Duration	Period Duration
1	365	f	365	f	366	f	365	f	365	f
2	0	0	0	0	0	0	0	0	0	0
3	356	1-308; 318-365;	365	1-365;	362	1-278; 282-366;	277	1-216; 222-225; 303-365;	365	f
4	0	0	0	0	0	0	0	0	0	0
5	171	1-135; 137; 331-365;	198	1-170; 338-365;	155	1-125; 336-366;	50	1-30; 346-365;	198	1-135; 303-365;
6	5	361-365;	96	1-93; 363-365;	5	1-5;	0	0	38	328-365;
7	365	f	365	1-365;	366	f	365	f	365	f
8	365	f	365	f	366	f	365	f	365	f
9	365	f	365	f	366	f	365	f	365	f
10	365	f	365	f	366	f	365	f	365	f
11	0	0	71	9-79;	0	0	0	0	55	311-365;
12	365	f	365	f	366	f	365	f	365	
13	5	361-365;	133	1-109; 342-365;	105	1-105;	23	343-365;	116	1-70; 320-365;
14	365	f	365	f	366	f	365		365	
15	1	365	54	1-54;	0	0	0	0	33	333-365;
16	365	1-365;	365	f	366	f	365	f	365	
17	239	1-194; 261; 322-365	288	1-229; 243-245;	229	1-171; 308-366;	154	1-111; 114; 324-365;	268	1-200;298-365;
18	365	f	365	f	366	f	365	f	365	f
19	0	0	0	0	0	0	0	0	4	346-349;
20	0	0	0	0	0	0	0	0	22	332-353;
21	365	f	365	f	366	f	365	0	365	f
22	9	357-365	92	1-78; 352-365;	5	1-5;	0	0	61	305-365;
23	0	0	32	10-41;	0	0	0	0	38	328-365;
24	365	f	365	f	366	f	365	f	365	
25	0	0	0	0	0	0	0	0	22	334-355;
26	365	f	365	f	366	f	365	f	365	f
27	0	0	41	25-54; 355-365;	14	1-14;	0	0	28	338-365
28	165	1-118; 128-129;	238	1-205; 243-244; 335-365;	182	1-182;	35	331-365;	186	1-123; 167; 304-365;
29	26	340-365;	126	1-107; 347-365;	61	1-61;	0	0	49	317-365;
30	0	0	0	0	0	0	0	0	0	0
31	0	0	0	0	0	0	0	0	0	0
32	0	0	0	0	0	0	0	0	0	0
33	0	0	0	0	0	0	0	0	0	0

f*; full year (1-365; or 1-366)

Table 5.42 – Total duration and period duration (in Julian days) with conditions to instability (SF $\leq$ 1), for each shallow translational landslide (ID, from 34 to 65) indentified in the study area, for the years: 2002; 2003; 2004; 2005; 2006.

ID	Year									
	2002		2003		2004		2005		2006	
	Total Duration	Period Duration	Total Duration	Period Duration	Total Duration	Period Duration	Total Duration	Period Duration	Total Duration	Period Duration
34	0	0	0	0	0	0	0	0	14	344-357;
35	365	f	365	f	366	f	365	f	365	f
36	0	0	0	0	0	0	0	0	0	0
37	189	1-148; 325-365;	238	1-198; 326-365;	189	1-139; 142-143;	109	1-71; 85;87; 330-365;	240	1-173; 299-365;
38	97	59-68; 72-132;	185	1-165; 346-365;	114	1-114;	0	0	152	37-139; 317-365;
39	0	0	0	0	0	0	0	0	0	0
40	0	0	0	0	0	0	0	0	0	0
41	121	1-7; 52-139; 340-365;	140	1-120; 346-365;	91	1-89; 92-93;	0	0	36	330-365;
42	0	0	0	0	0	0	0	0	0	0
43	169	1-123; 128-135; 328-365;	176	1-141; 331-365;	155	1-125; 336-366;	87	1-47; 53-63; 337-365;	209	1-137; 142-143; 166-169; 300-365;
44	0	0	23	27-32; 349-365;	0	0	0	0	33	333-365;
45	0	0	0	0	0	0	0	0	0	0
46	365	f	365	f	366	f	365	f	365	f
47	0	0	0	0	0	0	0	0	0	0
48	365	f	365	f	366	f	365	f	365	f
49	365	f	365	f	366	f	365	f	365	f
50	0	0	0	0	0	0	0	0	0	0
51	365	f	365	f	366	f	365	f	365	f
52	365	f	365	f	366	f	365	f	365	f
53	365	f	365	f	366	f	365	f	365	f
54	365	f	365	f	366	f	365	f	365	f
55	0	0	0	0	0	0	0	0	0	0
56	365	f	365	f	366	f	365	f	365	f
57	365	f	365	f	366	f	365	f	365	f
58	365	f	365	f	366	f	365	f	365	f
59	7	23-24; 361-365;	150	1-123; 339-365;	131	1-131;	21	345-365;	130	1-86; 309; 320-365;
60	365	f	365	f	366	f	365	f	365	f
61	0	0	55	7-56; 58; 60-63;	0	0	0	0	38	328-365
62	0	0	0	0	0	0	0	0	0	0
63	0	0	0	0	0	0	0	0	0	0
64	365	f	365	f	366	f	365	f	365	f
65	0	0	0	0	0	0	0	0	0	0

f*; full year (1-365; or 1-366).

Table 5.43 – Total duration and period duration (in Julian days) with conditions to instability (SF $\leq$ 1), for each shallow translational landslide (ID, from 66 to 87) indentified in the study area, for the years: 2002; 2003; 2004; 2005; 2006.

ID	Year									
	2002		2003		2004		2005		2006	
	Total Duration	Period Duration	Total Duration	Period Duration	Total Duration	Period Duration	Total Duration	Period Duration	Total Duration	Period Duration
66	365	f	365	f	366	f	365	f	365	f
67	0	0	0	0	0	0	0	0	19	335; 337-354;
68	0	0	0	0	0	0	0	0	0	0
69	365	f	365	f	366	f	365	f	365	f
70	365	f	365	f	366	f	365	f	365	f
71	365	f	365	f	366	f	365	f	365	f
72	365	f	365	f	366	f	365	f	365	f
73	365	f	365	f	366	f	365	f	365	f
74	0	0	0	0	0	0	0	0	0	0
75	0	0	36	4-39;	0	0	0	0	37	329-365;
76	0	0	0	0	0	0	0	0	0	0
77	33	3; 334-365;	158	1-135; 343-365;	102	1-102;	21	345-365;	190	1-128; 304-365;
78	365	f	365	f	366	f	365	f	365	f
79	365	f	365	f	366	f	365	f	365	f
80	365	f	365	f	366	f	365	0	365	f
81	72	1-32; 34-39; 332-365;	152	1-127; 341-365;	95	1-95;	30	336-365;	148	1-85; 300-365;
82	0	0	73	7-61; 348-365;	7	1-7;	0	0	38	328-365;
83	365	f	365	f	366	f	365	0	365	f
84	0	0	64	23-86;	0	0	0	0	20	346-365;
85	182	1-144; 328-365;	223	1-188; 331-365;	177	1-148; 337-366;	54	1-24; 336-365;	226	1-157; 166-169; 301-365;
86	0	0	0	0	0	0	0	0	17	344-360;
87	0	0	0	0	0	0	0	0	0	0

f*; full year (1-365; or 1-366).

Table 5.44 – Total duration and period duration (in Julian days) with conditions to instability (SF $\leq$ 1), for each shallow translational landslide (ID, from 1 to 33) indentified in the study area, for the years: 2007; 2008; 2009; 2010; 2011.

ID	Year									
	2007		2008		2009		2010		2011	
	Total Duration	Period Duration	Total Duration	Period Duration	Total Duration	Period Duration	Total Duration	Period Duration	Total Duration	Period Duration
1	365	f	366	f	365	f	365	f	365	f
2	0	0	0	0	0	0	0	0	0	0
3	295	1-287; 324-330; 354;	0	0	340	2-339; 341;365	365	f	365	f
4	0	0	0	0	0	0	0	0	0	0
5	135	1-135;	0		106	32-137;	39	126-164;	149	5-153;
6	34	1-34;	0	0	0	0	0	0	0	0
7	365	f	366	f	365	f	365	f	365	f
8	365	f	366	f	365	f	365	f	365	f
9	365	f	366	f	365	f	365	f	365	f
10	365	f	366	f	365	f	365	f	365	f
11	28	1-28;	0	0	0	0	0	0	0	0
12	365		366		365		365		365	
13	96	1-96;	0	0	24	64;67-68; 70;73; 347-365	91	1-91;	92	19-110;
14	365	f	366	f	365	f	365	f	365	f
15	14	1-14;	0	0	0	0	0	0	0	0
16	365	f	366	f	365	f	365	f	365	f
17	178	1-178;	0	0	176	4-176; 179-181;	210	46-232; 282-284; 346-365;	220	1-220;
18	365	f	366	f	365	f	365	f	365	f
19	0	0	0	0	0	0	0	0	0	0
20	0	0	0	0	0	0	0	0	0	0
21	365	f	366	f	365	f	365	f	365	f
22	18	1-18;	0	0	0	0	0	0	0	0
23	5	1-5;	0	0	0	0	0	0	0	0
24	365	f	366	f	365	f	365	f	365	f
25	0	0	0	0	0	0	0	0	0	0
26	365	f	366	f	365	f	365	f	365	f
27	28	1-28;	0	0	0	0	0	0	0	0
28	176	1-176;	0	0	195	22-171; 179-181; 324-365;	262	1-234; 282-286; 343-365;	210	1-191; 347-365;
29	72	1-34; 53-90;	0	0	45	38-82;	0	0	73	15-87;
30	0	0	0	0	0	0	0	0	0	0
31	0	0	0	0	0	0	0	0	0	0
32	0	0	0	0	0	0	0	0	0	0
33	0	0	0	0	0	0	0	0	0	0

f*; full year (1-365; or 1-366).

Table 5.45 – Total duration and period duration (in Julian days) with conditions to instability (SF $\leq$ 1), for each shallow translational landslide (ID, from 34 to 65) indentified in the study area, for the years: 2007; 2008; 2009; 2010; 2011.

ID	Year									
	2007		2008		2009		2010		2011	
	Total Duration	Period Duration	Total Duration	Period Duration	Total Duration	Period Duration	Total Duration	Period Duration	Total Duration	Period Duration
34	0	0	0	0	0	0	0	0	0	0
35	365	f	366	f	365	f	365	f	365	f
36	0	0	0	0	0	0	0	0	0	0
37	152	1-152;	0	0	108	32-139;	133	56-186; 362-365;	162	1-162;
38	127	1-127;	0	0	78	38-115;	0	0	132	15-146;
39	0	0	0	0	0	0	0	0	0	0
40	0	0	0	0	0	0	0	0	0	0
41	75	1-75;	0	0	28	338-365	71	1-71;	90	12-101;
42	0	0	0	0	0		0	0	0	0
43	131	1-130; 146;	0	0	87	41-124; 131-133;	0	0	131	4-132; 137-138;
44	8	1-8;	0	0	0	0	0	0	0	0
45	0	0	0	0	0	0	0	0	0	0
46	365	f	366	f	365	f	365	f	365	f
47	0	0	0	0	0	0	0	0	0	0
48	365	f	366	f	365	f	365	f	365	f
49	365	f	366	f	365	f	365	f	365	f
50	0	0	0	0	0	0	0	0	0	0
51	365	f	366	f	365	f	365	f	365	f
52	365	f	366	f	365	f	365	f	365	f
53	365	f	366	f	365	f	365	f	365	f
54	365	f	366	f	365	f	365	f	365	f
55	0	0	0	0	0	0	0	0	0	0
56	365	f	366	f	365	f	365	f	365	f
57	365	f	366	f	365	f	365	f	365	f
58	365	f	366	f	365	f	365	f	365	f
59	108	1-106; 122-123;	0	0	127	41-127; 130-134; 333-365;	118	1-117; 129;	121	6-126;
60	365	f	366	f	365	f	365	f	365	f
61	9		0	0	32	46-54; 343-365;	48	1-48;	0	
62	0	0	0	0	0	0	0	0	0	0
63	0	0	0	0	0	0	0	0	0	0
64	365	f	366	f	365	f	365	f	365	f
65	0	0	0	0	0	0	0	0	0	0

f*; full year (1-365; or 1-366).

Table 5.46 – Total duration and period duration (in Julian days) with conditions to instability (SF ≤ 1), for each shallow translational landslide (ID, from 66 to 87) indentified in the study area, for the years: 2007; 2008; 2009; 2010; 2011.

ID	Year									
	2007		2008		2009		2010		2011	
	Total Duration	Period Duration	Total Duration	Period Duration	Total Duration	Period Duration	Total Duration	Period Duration	Total Duration	Period Duration
66	365	f	366	f	365	f	365	f	365	f
67	0	0	0	0	0	0	0	0	0	0
68	0	0	0	0	0	0	0	0	0	0
69	365	f	366	f	365	f	365	f	365	f
70	365	f	366	f	365	f	365	f	365	f
71	365	f	366	f	365	f	365	f	365	f
72	365	f	366	f	365	f	365	f	365	f
73	365	f	366	f	365	f	365	f	365	f
74	0	0	0	0	0	0	0	0	0	0
75	2	1-2;	0	0	0	0	0	0	0	0
76	0	0	0	0	0	0	0	0	0	0
77	123	1-123;	0	0	50	49-98;	0	0	107	14-118; 121-122;
78	365	f	366	f	365	f	365	f	365	f
79	365	f	366	f	365	f	365	f	365	f
80	365	f	366	f	365	f	365	f	365	f
81	122	1-118; 121-124;	41	325-366;	19	1-19;	0	0	71	29-94; 110-114;
82	28	1-28;	0	0	2	347-348;	0	0	0	0
83	365	f	366	f	365	f	365	f	365	f
84	28	1-28;	0	0	0	0	74	1-74;	0	0
85	151	1-151;	0	0	113	34-146;	187	5-191;	148	6-153;
86	0	0	0	0	0	0	0	0	0	0
87	0	0	0	0	0	0	0	0	0	0

f*; full year (1-365; or 1-366).

Based on Tables from 5.41 to 5.46, it became possible to understand that there are some landslides which, according to the modeled high instability (SF≤1), could have occurred in almost every year, while some, according to the total duration and period, have an occasional or seasonal trend. Nevertheless, it should be noted that the model was calibrated with only one event, i.e. one dated landslide. This lack of data lead to an overestimation of the total duration of instability (sf<=1), and therefore, to unrealistic situations of 365 days of instability. Considering this, the important results to take into account are the ones where occasional or seasonal instability takes place. In order to better understand these trends, a summary for each landslide was carried out (Tables 4.47, 4.48 and 4.49).

Table 5.47 – Summary of the conditions to instability (SF≤1) for the period from 2002 to 2011. Analysis performed based on the centroid of the depletion zone of the shallow translational landslides (ID1 to ID33).

ID	Years with continued SF≤1	Years with seasonality for SF≤1	Years without SF≤1
1	10	0	0
2	0	0	10
3	4 (2003;2006;2010;2011)	5 (2002; 2004; 2005; 2007; 2009)	1 (2008)
4	0	0	10
5	0	9 (2002;2003;2004;2005;2006; 2007;2009;2010;2011)	1 (2008)
6	0	5 (2002;2003;2004;2006;2007)	5 (2005;2008;2009;2010;2011)
7	10	0	0
8	10	0	0
9	10	0	0
10	10	0	0
11	0	3 (2003;2006;2007)	7 (2002;2004;2005;2008;2009;2010;2011)
12	10	0	0
13	0	9 (2002;2003;2004;2005;2006;2007;2009;2010;2011)	1 (2008)
14	10	0	0
15	0	4 (2002;2003;2006;2007)	6 (2004;2005;2008;2009;2010;2011)
16	10	0	0
17	0	9 (2002;2003;2004;2005;2006;2007;2009;2010;2011)	1 (2008)
18	10	0	0
19	0	1 (2006)	9 (2002;2003;2004;2005;2007;2008;2009;2010;2011)
20	0	1 (2006)	9 (2002;2003;2004;2005;2007;2008;2009;2010;2011)
21	10	0	0
22	0	5 (2002;2003;2004;2006;2007)	5 (2005;2008;2009;2010;2011)
23	0	3 (2003;2006;2007)	7 (2002;2004;2005;2008;2009;2010;2011)
24	10	0	0
25	0	1 (2006)	9 (2002;2003;2004;2005;2007;2008;2009;2010;2011)
26	10	0	0
27	0	4 (2003;2004;2006;2007)	6 (2002;2005;2008;2009;2010;2011)
28	0	9 (2002;2003;2004;2005;2006;2007;2009;2010;2011)	1 (2008)
29	0	7 (2002;2003;2004;2006;2007;2009;2011)	3 (2005;2008;2010)
30	0	0	10
31	0	0	10
32	0	0	10
33	0	0	10

Table 5.48 – Summary of the conditions to instability (SF≤1) for the period from 2002 to 2011. Analysis performed based on the centroid of the depletion zone of the shallow translational landslides (ID34 to ID65).

ID	Years with continued SF≤1	Years with seasonality for SF≤1	Years without SF≤1
34	0	1 (2006)	9 (2002;2003;2004;2005;2007;2008;2009;2010;2011)
35	10	0	0
36	0	0	10
37	0	9 (2002;2003;2004;2005;2006;2007;2009;2010;2011)	1 (2008)
38	0	7 (2002;2003;2004;2006;2007;2009;2011)	3 (2005;2008;2010)
39	0	0	10
40	0	0	10
41	0	8 (2002;2003;2004;2006;2007;2009;2010;2011)	2 (2005;2008)
42	0	0	10
43	0	8 (2002;2003;2004;2005;2006;2007;2009;2011)	2 (2008;2010)
44	0	3 (2003;2006;2007)	7 (2002;2004;2005;2008;2009;2010;2011)
45	0	0	10
46	10	0	0
47	0	0	10
48	10	0	0
49	10	0	0
50	0	0	10
51	10	0	0
52	10	0	0
53	10	0	0
54	10	0	0
55	0	0	10
56	10	0	0
57	10	0	0
58	10	0	0
59	0	9 (2002;2003;2004;2005;2006;2007;2009;2010;2011)	1 (2008)
60	10	0	0
61	0	5 (2003;2006;2007;2009;2010)	5 (2002;2004;2005;2008;2011)
62	0	0	10
63	0	0	10
64	10	0	0
65	0	0	10

Table 5.49 – Summary of the conditions to instability (SF≤1) for the period from 2002 to 2011. Analysis performed based on the centroid of the depletion zone of the shallow translational landslides (ID66 to ID87).

ID	Years with continued SF≤1	Years with seasonality for SF≤1	Years without SF≤1
66	10	0	0
67	0	1 (2006)	9 (2002;2003;2004;2005;2007;2008;2009;2010;2011)
68	0	0	10
69	10	0	0
70	10	0	0
71	10	0	0
72	10	0	0
73	10	0	0
74	0	0	10
75	0	3 (2003;2006;2007)	7 (2002;2004;2005;2008;2009;2010;2011)
76	0	0	10
77	0	8 (2002;2003;2004;2005;2006;2007;2009;2011)	2 (2008;2010)
78	10	0	0
79	10	0	0
80	10	0	0
81	0	9 (2002;2003;2004;2005;2006;2007;2008;2009;2011)	1 (2010)
82	0	5 (2003;2004;2006;2007;2009)	0
83	10	0	0
84	0	4 (2003;2006;2007;2010)	6 (2002;2004;2005;2008;2009;2011)
85	0	9 (2002;2003;2004;2005;2006;2007;2009;2010;2011)	1 (2008)
86	0	1 (2006)	9 (2002;2003;2004;2005;2007;2008;2009;2010;2011)
87	0	0	10
SUM	35	31	21

The Fig.5.47 shows the precise location of each centroid of the depletion zone of each shallow translational slides. In this map it is also possible to be recognized, according to its ID, where are located the occasional and permanent places of higher instability.

There are some landslides lying in a permanent area of SF≤1, and others are subject to occasional or seasonal SF≤1. There are also some landslides, generally located on the south part of the study area, that are not explained by this model. (green dots in Fig.5.47).

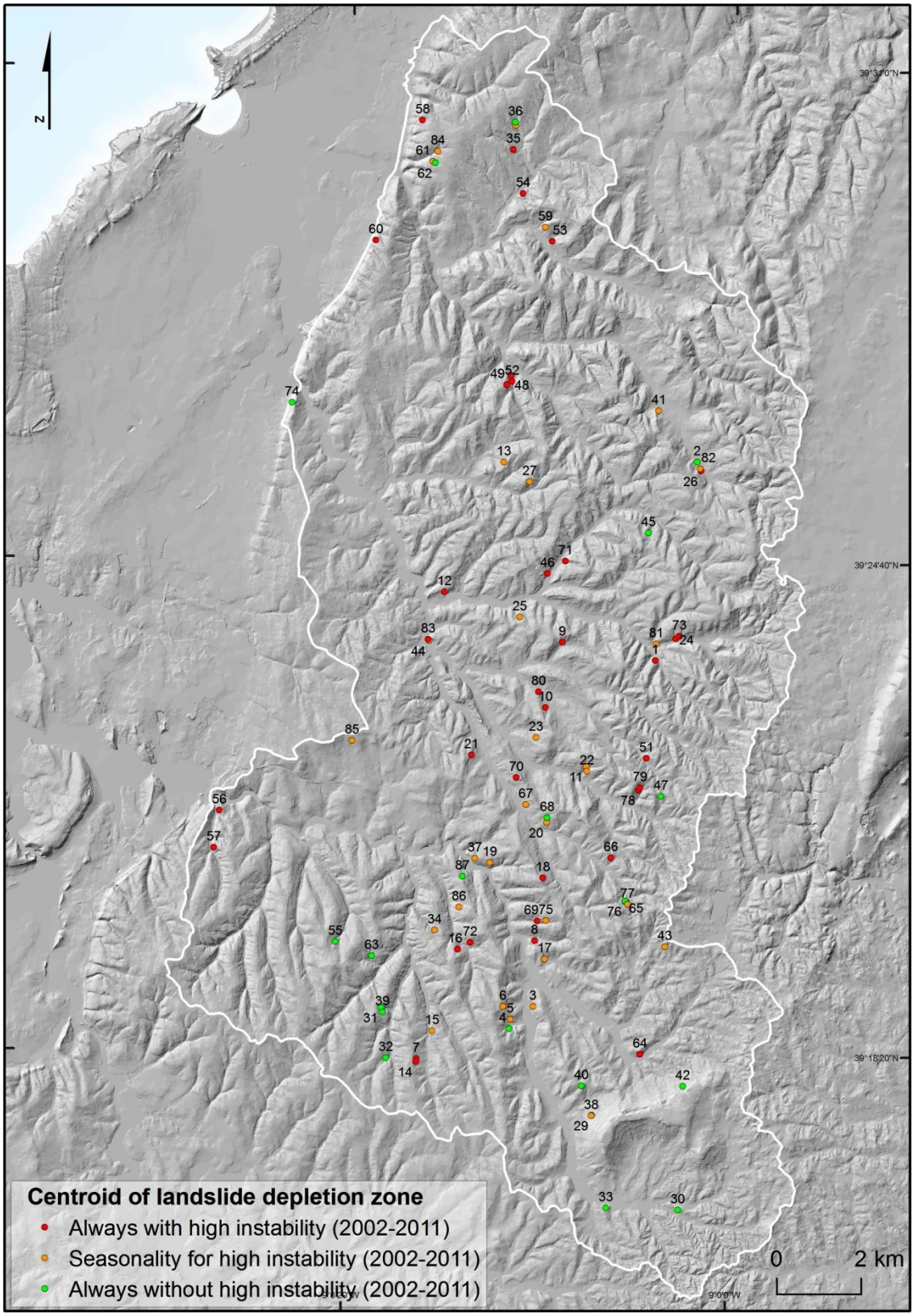

Fig. 5.47 – Centroid of each shallow translational landslide showing the instability trends over the period 2002 to 2011.

Unfortunately, this landslide inventory has no precise dates of occurrences. The only exception is a landslide occurred in the municipality of Caldas da Rainha, respectively in Santa Catarina (ID41), dating 30 of november of 2006 (Julian day: 334). This date matches with the days of higher instability predicted by the model, which predicts that, this area, should have been very instable (SF ≤ 1) from julian day 330 (26 November of 2006) until the end of the year (2006). According to the model this same area was instabilized occasionally in other years (2002, 2003, 2004, 2007, 2009, 2010, 2011), however, in different Julian days. For the years 2005 and 2008 this area was always stable.

From the inputs and outputs of the STARWARS + PROBSTAB model it is also possible to gather all the conditions that have occurred in the landsliding day (or in any other day if wanted) (Fig. 5.48 to 5.50 and Table 5.50).

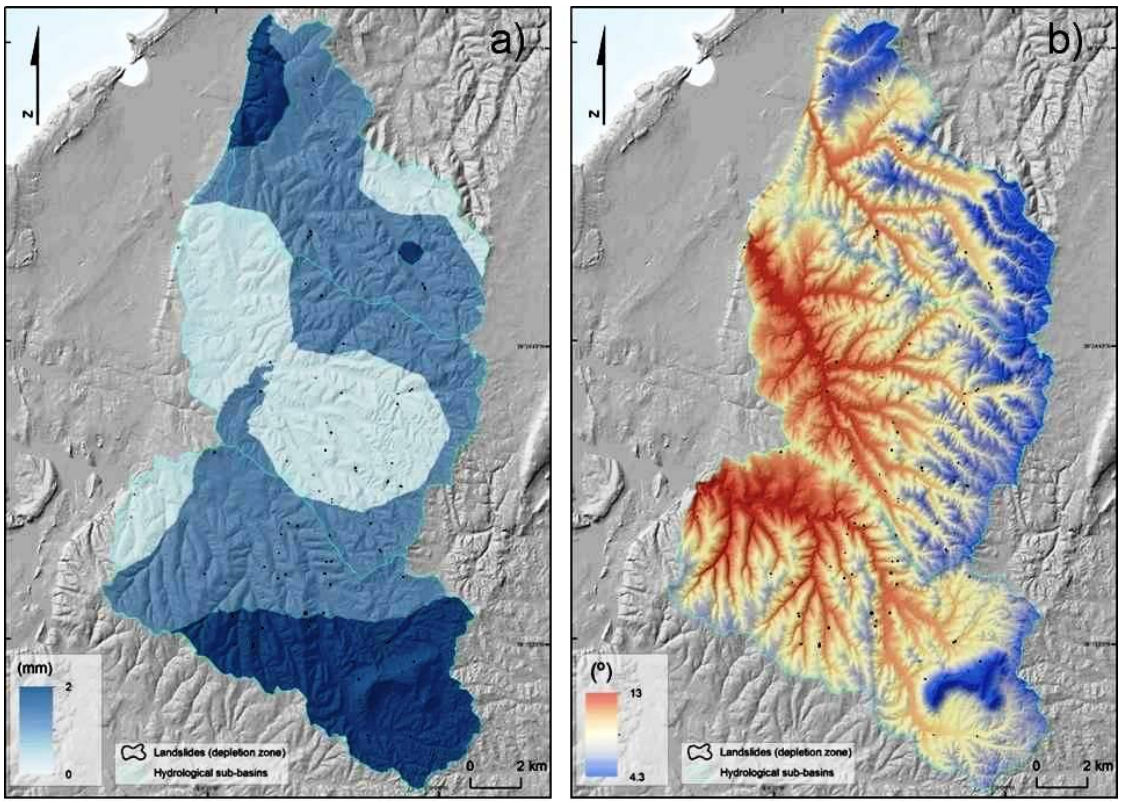

Fig. 5.48 – Modeled conditions of temporal dynamic maps (map series) at day 30 of november of 2006 (Julian day 334). a) Precipitation; b) Temperature.

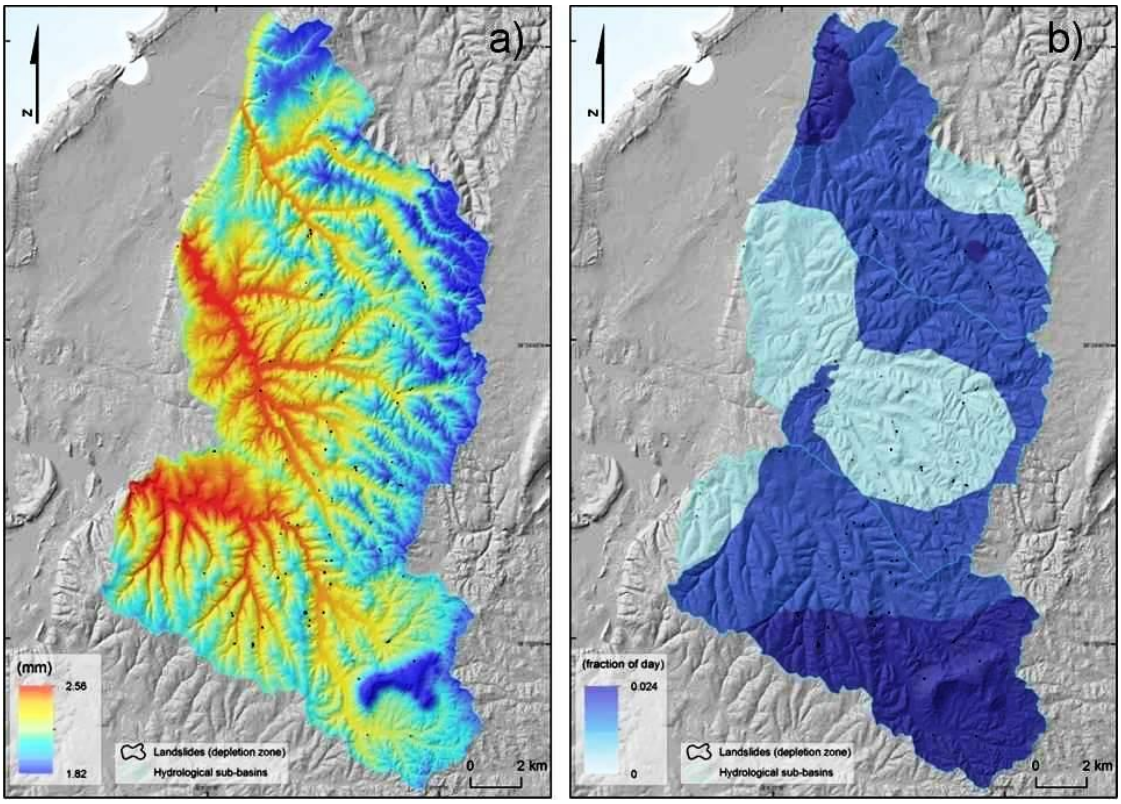

Fig. 5.49 – Modeled conditions of temporal dynamic maps (map series) at day 30 of november of 2006 (Julian day 334). a) Potential evapotranspiration; b) Precipitation duration.

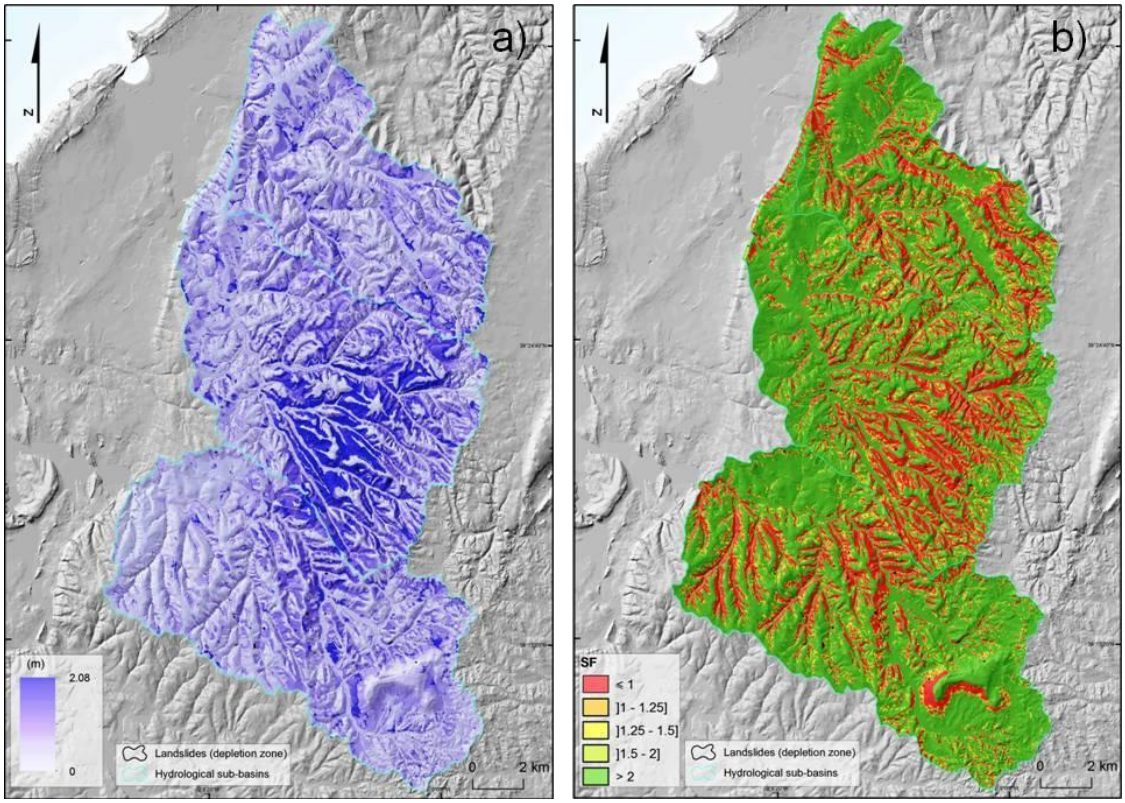

Fig. 5.50 – Modeled conditions of temporal dynamic maps (map series) at day 30 of november of 2006 (Julian day 334). a) Groundwater level; b) Safety factor.

Table 5.50 – Modeled conditions at day 30 of november of 2006 (Julian day 334) for the ID41.

TU condictions	Role in the Model	PCRaster Map type	Value
DEM (m, asl)	Input	Map	88
Slope angle (°)	Input	Map	14
soil depth (m)	Input	Map	0.77
Precipitation (mm/day)	Input	Map series*	1
Temperature (°)	Input	Map series*	9.2
Potential Evapotranspiration (mm/day)	Input	Map series*	2.232
Pdur (fraction of day, (1day=1))	Input	Map series*	0.016667
Groundwater level (m)	Output	Map series*	0.54
Safety factor	Output	Map series*	0.9

Map series: specifically for time step 334 (year 2006).

On the Julian day 334 (30 of November of 2006) when the event ID41 happened, there was a greatly reduced amount of precipitation on that day, however, this occurrence can be explained by the groundwater table which had acquired a very high level (0.54m), considering the soil thickness at that location (0.77m) (Table 5.50).

Despite only occuring 1 mm of precipitation on that day, it must be considered the precipitation occurred on previous days, which explains the rise in groundwater table (Table 5.51).

Table 5.51 – Daily precipitation on ID41. From first day of maximum annual precipitation (Julian day 320: 16 of November of 2006 until the day of landsliding).

JD	Accumulation days	Rainfall (mm/day)	Groundwater level (m)
320	1	36.3	0.36
321	2	1.3	0.37
322	3	10.9	0.37
323	4	3.3	0.37
324	5	0.3	0.38
325	6	0.5	0.38
326	7	0.5	0.39
327	8	2.3	0.39
328	9	33.6	0.4
329	10	15.7	0.41
330	11	2.4	0.42
331	12	2.3	0.43
332	13	22.3	0.46
333	14	0	0.49
334	15	1	0.54
SUM		132.7 mm	

*JD: Julian Day.

It is noted that the maximum daily precipitation, for the year 2006, occurred at the ID41 location 14 days before the landsliding, reaching an annual maximum amount of 36.3mm of precipitation (Julian day 320). Subsequently on this same place another day with a significant amount of rainfall (33.6 mm of precipitation at Julian day 328) occurred which, combined with a continuous rainfall (although lower) gave the rise to an increase of the groundwater table level, which increased the pore pressure and thus leaded to landsliding.

The spatial and temporal components of simulated safety factor were reported from the model in the form of daily maps. The observed landslide activity provides the necessary parameter for model validation. Thus, the predicted instability, regarding the minimum safety factor obtained over each year, has been compared with the landslide inventory in order to assess the spatial performance of the model for each year. The temporal information of the landslide inventory is poor and consequently, the possibilities to compare the temporal component of landslide activity in the validation is limited. Thus, for such operation prediction rate curves were preformed in order to assess the performance of previous models through the AUC (Fig. 5.51 and 5.52).

Since the hydrologic component of the model was already temporally calibrated, it is assumed that the landslides occurred whenever the safety factor was lower or equal to 1. As it was already possible to verify, 2006 was the year more susceptible to landslides. This is the year where the values of mean annual precipitation and also the daily maximum precipitation (among all the other years) were higher. It is, at the same time, the year with higher SF≤1 area predicting 79% of the total shallow translational slides. Throught the prediction rate it was possible to verify that 2006 was also the year with best predictive ability (AUC value of 0.85) (Fig. 5.51 and Table 5.52).

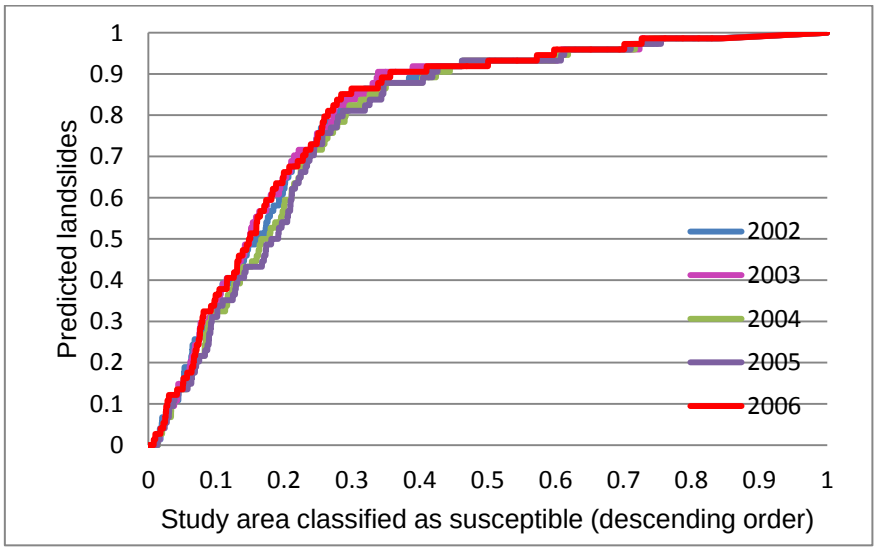

Fig. 5.51 – Prediction rate curve of the landslide susceptibility maps (minimum safety factor) obtained in 2002, 2003, 2004, 2005 and 2006.

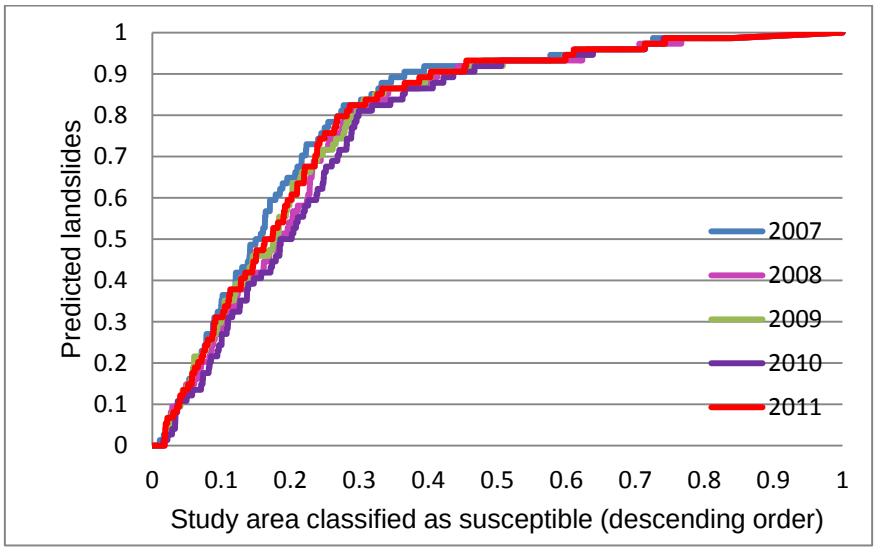

Fig. 5.52 – Prediction rate curve of the landslide susceptibility maps (minimum safety factor) obtained in 2007, 2008, 2009, 2010 and 2011.

Table 5.52 – AUC values for the landslide susceptibility maps from 2002 to 2011 assessed through the STARWARS+PROBSTAB.

Years	AUC
2002	0.83
2003	0.84
2004	0.82
2005	0.82
2006	0.85
2007	0.84
2008	0.81
2009	0.82
2010	0.81
2011	0.83

Moreover, 2008 was the year less susceptible to landslides, although not being the year with the lowest mean annual precipitation, or with the lowest maximum daily precipitation (Table A9.1 to A9.6 in Appendix 9). The minimum SF of 2008 (SF≤1) predicts only 37.1% of the total shallow translational slides. By comparing the AUC values (Fig. 5.52 and Table 5.52) with other years it is possible to note that the year 2008 was also the year with the lowest predictive ability.

5.8 Comparison between Static and Dynamic models

The study area is characterized by the unpredictable distribution of high intensity rainfall events and the existence of a soil moisture deficit over summer. In such environment, water is the most important agent in the process of landsliding. Thus, the development of mathematical models to evaluate effects of rainfall infiltration on landslide occurrence reveals to be crucial. In line with this, the present section provides a described comparison between the static and dynamic models of slope hydrology and slope stability, implemented in the previous sections. Only a described comparison will be performed because comparing a spatio-temporal model (dynamic model) with a spatial model (static model) becomes incongruent.

Based on the results obtained from the physically-based models, which couples the slope hydrology with stability, it is possible to mention that, the acquisition of geotechnical and

hydrological parameters through field work, laboratory measurements and further back analysis reveals to be crucial for increasing the robustness of the predicting models. Unfortunately, the acquisition of the hydrological parameters, such as K_{sat}, was not possible to obtain in this manner. However, from the standard values of K_{sat}, calibrations were carried out in both cases in order to improve predictive ability of the models.

The static approach was performed through the SHALSTAB modeling, developed by Montgomery and Dietrich (1994). The model relies on the concept that typically the boundary between the soil and the underlying variably weathered bedrock is abrupt and that, soil mantle, is a highly conductive layer of colluviums which varies in thickness in a relatively systematic way across the landscape (Montgomery and Dietrich, 1994). Globally, it has the capability to assess that, flat areas are stable, and that ridges (with divergent subsurface flow) may be steep enough to fail, depending on the rainfall event. In such model steep unchanneled valley requires the smallest concentration of rainfall to fail (due to the convergent subsurface flow) being, therefore, more susceptible to landslide occurrence. There are some advantages in using a more simplest approach as SHALSTAB, respectively: 1) it is fast to compute; 2) it can be applied in diverse environments without costly attempts of parameterization; 3) it takes little special training to use the model; and 4) it becomes an hypothesis that could be rejectable, i.e., the model can fail, rather than just be tuned until it work. As a simplest approach, it can effectively indicate processes and parameters not included in the model that could be important for landslide susceptibility, or, from another point of view, it can be simply an inappropriate approximation of the superficial mechanics controlling slope stability due to the lack of knowledge on dynamic temporally influences. SHALSTAB is more indicated for identifying the safety factor over long time-periods, rather than predicting the onset of safety factor at particular time period (Dietrich and Montgomery, 1998).

Due to the black box existing in such simplest models it becomes very difficult to reconstitute the previous conditions of precipitation and/or water storage that triggered landslides. These simplest approaches do not address influences of temporally varying precipitation, vegetation dynamics, uncertainty associated with input parameters, as well as various scenarios that may be implemented through an extended management period.

The input precipitation of the static approach is based on the return periods obtained for a neighboring location (Batalha), since it was not possible to calculate it, for the study area, due to the lack of data (dated landslides). Considering only one day of effective precipitation the model can be assumed as having a good performance (with an AUC of 0.81), however, when analyzing the SF≤1 area the model with best predictive ability is considered to be the susceptible model corresponding to scenario 11 (15 days of accumulated rainfall). These differences are due to the fact that the model assumes the same value of effective precipitation for all the terrain units (pixels) of the study area. Such fact creates unrealistic situations in some locals of the study area where, due to morphological characteristics and/or distance from the sea, those values may be never verified. Being a hypothetical scenario of rainfall such result must be understood merely as a hypothesis. The lack of knowledge on the precise date of landslide occurrences is a limiting factor for getting better and more accurate input variables. Without such data it is not possible to calculate, for instance, the return period and critical precipitation that triggered landslides within the study area.

Globally, despite the calibrated landslide susceptible models based on a static approach, seeing promising, due to the high values of AUC, such models do not take into account important parameters such as the antecedent moisture conditions, which can obscure the relation between the triggering rainfall events and landslide occurrence. Thereby, in order to overcome this handicap, a dynamic approach, which also couples the hydrology with stability, has been implemented. Such model is much more stringent and time consuming when compared with a simplest approach as SHALSTAB, however, when it is pretended to be more thorough, on the triggering landslide assessment, such implementation is justified.

The SHALSTAB model has the problem of increasing the piezometric level sometimes above the topographical surface with the continuous input of rainfall, without any restriction. Whereas, in STARWARS model this situation is overcome because this excess of water, above the topographical surface, is treated as exfiltration which subsequently flows over the LDD at the topographical surface. This behavior is indeed a great advantage of the STARWARS model because it allows the calculation of the water

discharge, which serves as a temporal and spatial calibration parameter of the for the soil hydrological properties (K_{sat}).

For the period modeled dynamically (from 2002 to 2011) there was no need to have high inputs of rainfall to be observed areas with SF≤1. This situation turns out to be not realistic. However, not having the precise date of the landslide occurrence, an accurate procedure of temporal calibration and validation of the geotechnical parameters becomes impossible to be performed.

By using a dynamic approach, it is possible to simulate the hydrology over time and evaluate its effects on the slope stability. As it was already mentioned, the main factor triggering landslides is rainfall, however, this study went further in this matter, by evaluating and incorporating the dynamic parameters over time (precipitation, evapotranspiration and matric suction), which contribute for the water available for percolation, giving thus, more realism to the subsequent landslide susceptibility assessment. Another great advantage, when compared to the static approach, is the possibility to calibrate the model not only spatially but also temporally by comparing the modeled discharge data to the actual discharge data obtained from the available hydrometric stations.

Besides all the advantages already described, the dynamic model has also the ability to assess the key dates, which could have lead to landsliding. Such procedure is based on a spatial comparison between landslides (already occurred) and the modeled safety factor (map series: day by day). This is also considered an important contribution to the evaluation of past landslides on which, it was not possible to obtain the date of occurrence. However, such model is not free from limitations and it can be actually enumerated some of them, e.g.: 1) It is very time computing consuming; 2) it is necessary to learn python and pc raster programming, at least, to a level that allows handling the program (the models and its inputs); 3) Many times it is difficult and very time consuming to obtained all the parameters needed for modeling. Despite these limitations implementing such dynamic and complex model allows the acquisition of much more

realistic and consistent results, which justify its use in preference to static and simplest models.

In a raster based GIS environment, both models allow the coupling between the output of the hydrological model (TOPOG or STARWARS) and the slope stability model (Infinite slope model). The disadvantage of using stringent models such as the STARWARS for coupling to the slope stability model is the transfer of data and calculations applicants in which, at a regional scale, become very heavy. Otherwise such model provides much more realism than the static approach (SHALSTAB).

Despite using simplest and/or complex models it is noteworthy that all are simplifications of the real world, and thus, probable other variables were neglected. However, in both cases they were compensated by the calibration of the parameters that are included in the models. For this reason no model will be right in an absolute manner (Konikow and Bredehoeft, 1992), but represents rather a possible realization of the actual system (Beven, 1989).

CHAPTER 6

LANDSLIDE SUSCEPTIBILITY ASSESSMENT USING STATISTICALLY-BASED METHODS

6 LANDSLIDE SUSCEPTIBILITY ASSESSMENT USING STATISTICALLY-BASED METHODS

In this chapter it will be performed landslide susceptibility models through the statistically-based method. Thereby, from each landslide inventory (LI#1, LI#2 and LI#3 from chapter 2) nine landslide susceptible models will be elaborated, for three types of landslides: 1) shallow rotational slides; 2) shallow translational slides; and 3) deep-seated rotational slides. The deep-seated translational slides were not taken into account since they have a very low representation in the study area.

Due to the, highly proven, good performance of the statistical models, it reveals also to be interesting to perform, in this chapter, a comparison between the results already obtained for the shallow translational susceptibility model through the static physically-based method and the shallow translational susceptibility model obtained statistically. The results from the dynamic physically-based method were not considered for comparisons since it take into account different kind of nature of inputs (dynamic inputs).
The statistical method used to perform the landslide susceptibility evaluation is the Information Value. This statistical bivariate method has been widely used due to the good results produced (e.g., Zêzere, 1997; Henriques, 2009; Pereira, 2009; Garcia, 2012; Oliveira, 2012).

The choice for the set of predisposing factors, which generate slope instability, is an important task for landslide susceptibility assessed statistically. Accordingly, it is expected a discriminatory capacity from these factors, in order to rebuild the conditions that generated the slope instability in the past. These predisposing factors, inherent to the terrain, are often static, influence the potential level of slopes instability and determine the spatial variation of the terrain to landslide susceptibility (Zêzere, 2005). In this context, the specific objectives of this chapter are: (1) Defining the predisposition factors which will be used for landslide susceptibility assessment at a regional scale; (2) Establishing the criteria for the classification of each predisposing factors; 3) Establishing their relationship with the different types of landslide and inventories and the

determination of their sensitivity and hierarchy; 4) Comparison between the results obtained through the statistically-based and the static physically-based methods for the susceptibility assessment to shallow translational slide occurrence.

6.1 Selection and preparation of the landslide predisposing factors

The landslide predisposing factors are those that, due to their static characteristics and terrain representativeness, are more often used for landslide susceptibility, assessed through statistically-based models. Such factors are described as a data of layers that are expected to have control on the occurrence of landslides, and can be used as causal factors in the prediction of future landslides (van Westen *et al*., 2008).

There are a wide set of thematic data, with a wide spatial variation, type of data and scales, that represent the predisposing factors (Van Westen, 2008). Thereby, in this section, it is presented and characterized the seven variables that were considered as predisposing factors for modeling the landslide susceptibility in the study area. These static data sets are related to lithology, soil types and morphography. Further it will be performed a sensitive analysis in order to identify the variables that most contribute for landsliding.

To acquire the landslide predisposing factors a pixel of 5X5 m was used. As already described, in chapter 5, such resolution allows the identification of potential unstable areas with a large spatial precision (Frattini *et al*., 2010).

6.1.1 DEM derived variables

Digital Elevation Model (DEM) with high quality (accuracy) provides also higher quality of its derivatives and thus, more reliable landslide susceptibility models.
The local topographic features derived from the DEM (e.g. slope, aspect) play a crucial role in a number of morphological, ecological, and hydrological processes and, thus, for

landslide occurrence. Thereby the optimized DEM, described in chapter 5, was used to derive variables such as: 1) slope angle; 2) aspect; 3) profile curvature; 4) and inverse wetness index.

6.1.1.1 Slope angle

Slope angle is defined as the angle between the horizontal and the slope topographic surface. For classification purposes it was considered the limits already adopted by many authors for many regions in Portugal mainland (Garcia, 2002; Reis *et al.*, 2003; Zêzere *et al.*, 2004;; Lopes, 2008; Guillard, 2009; Piedade, 2009;; Henriques, 2009; Oliveira 2012; Garcia 2012). For this dissertation it was decided to classify the map in 9 classes (Fig. 6.1).

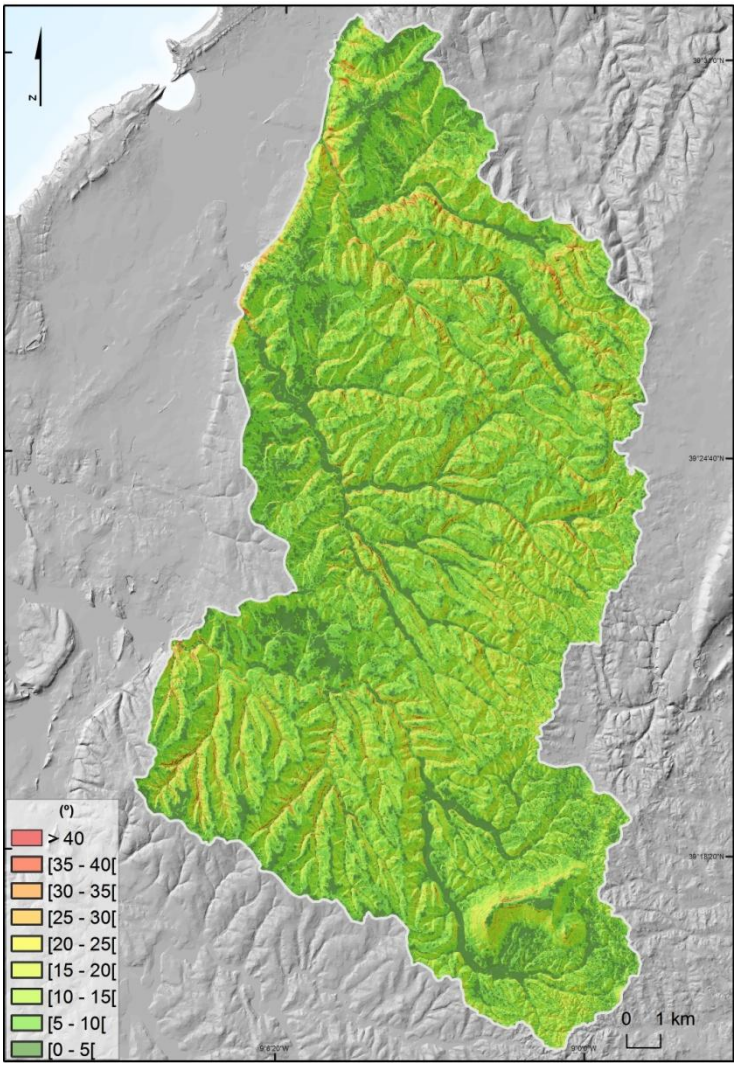

Fig. 6.1 – Reclassified slope angle map of the study area.

There is a strong relationship between slope angle and landslide occurrence (Guzzetti, 2005). Thus, higher values of slope angle, at least, up to a certain value, tend to be related to an increase of landslide occurrence.

According to Table 6.1 it is possible to verify that 80% of the study area is dominated by slope angles below 15º and that only 1.5% of the study area has slope angles above 30º.

Table 6.1 – Reclassified slope angle map of the study area.

Classes (º)	Occupancy area (km^2)	(%)
0 - 5	48.8	17.7
5 - 10	96.1	34.8
10 - 15	75.9	27.5
15 - 20	33.4	12.1
20 - 25	12.4	4.5
25 - 30	5.2	1.9
30 - 35	2.2	0.8
35 - 40	1.0	0.4
> 40	0.9	0.3
	275.9	100

6.1.1.2 Aspect

Aspect is defined by a plane tangent to a topographic surface. It identifies the downslope direction of the maximum rate of change in value from each cell to its neighbors. Thus, aspect can be thought of as the slope direction. Aspect is measured clockwise in degrees from 0 (due north) to 360 (again due north), coming full circle. The value of each cell in an aspect dataset indicates the direction of the cell's slope faces. Flat areas having no downslope direction are given a value of -1 (Burrough, 1986).

Long recognized as an important topographic variable, aspect affects the amount and daily cycle of solar radiation received at different times of the year and has a strong influence on the microclimate, especially air temperature, humidity, and soil moisture (Rosenberg *et al.*, 1983). All this environmental influences must be considered. Thus, incorporating the aspect as a predisposing factor for landslide susceptibility assessment through the statistically-based model makes much sense.

The slopes, within the study area, are mostly exposed to Southwest and West, as it is possible to observe in Fig. 6.2 and Table 6.2.

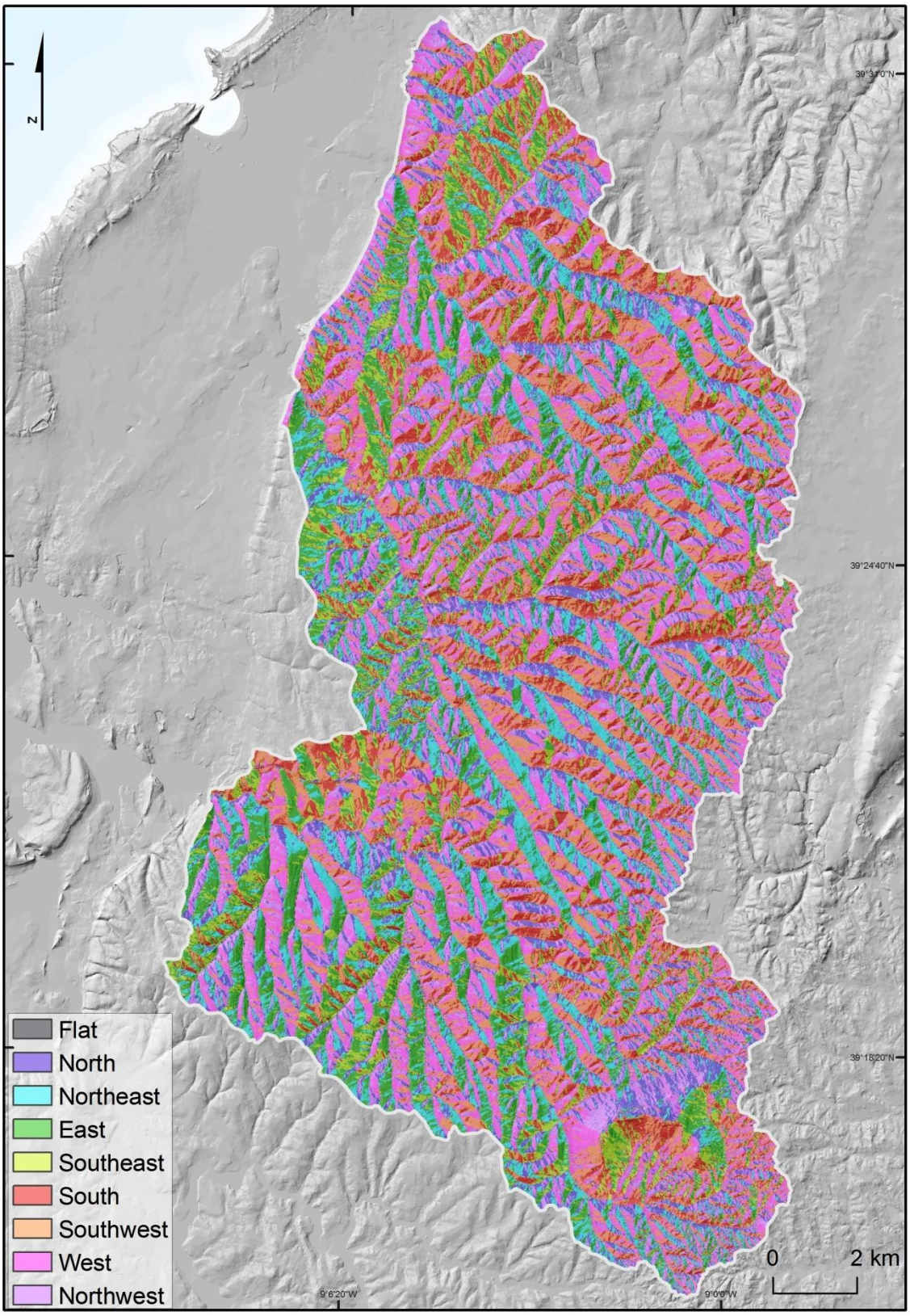

Fig. 6.2 – Aspect map of the study area.

Table 6.2 – Reclassified aspect map of the study area.

Classes	Occupancy area	
	(km^2)	(%)
Flat	0.7	0.2
North	27.7	10.1
Northeast	37.1	13.4
East	33.9	12.3
Southeast	25.0	9.1
South	31.0	11.2
Southwest	45.2	16.4
West	44.7	16.2
Northwest	30.6	11.1
SUM	275.9	100.0

6.1.1.3 Curvature (cross section profile)

The curvature of the slopes is the inverse of the radius of a circle tangent to the soil surface and it can be measured in three ways: 1) in a longitudinally profile; 2) in a transversally (cross sectional) profile; 3) or in a tangentially profile (Clerici *et al.*; 2010). The relationship between the curvature and slope instability is difficult to compare due to different and often unspecified types of curvature used. Overall, the concave slopes are those that are most susceptible, because it is associated with the concentration of surface and subsurface runoff (Zêzere *et al.*, 2004).

In the present work it was decided to use the cross-sectional profile, since this allows defining the preferred areas for convergence of water flows at the surface. The profile curvature was obtained by fitting a fourth order polynomial function for each group of 3 x 3 neighboring cells with 25m pixel size. Differently from the other predisposing factors the choice for such pixel size was because, after several attempts, this pixel dimension was the one that best visual fitted with the DEM.

The profile curvature map was classified into three classes and it expresses the variation between positive (concavities) and negative values (convexities) (Fig.6.3 and Table 6.3). Thus, the class that correspond the rectilinear slopes and flat areas is defined by positive and negative values near zero. The other classes (representing concavities and convexities are defined by the limits -0.05 and 0.05.

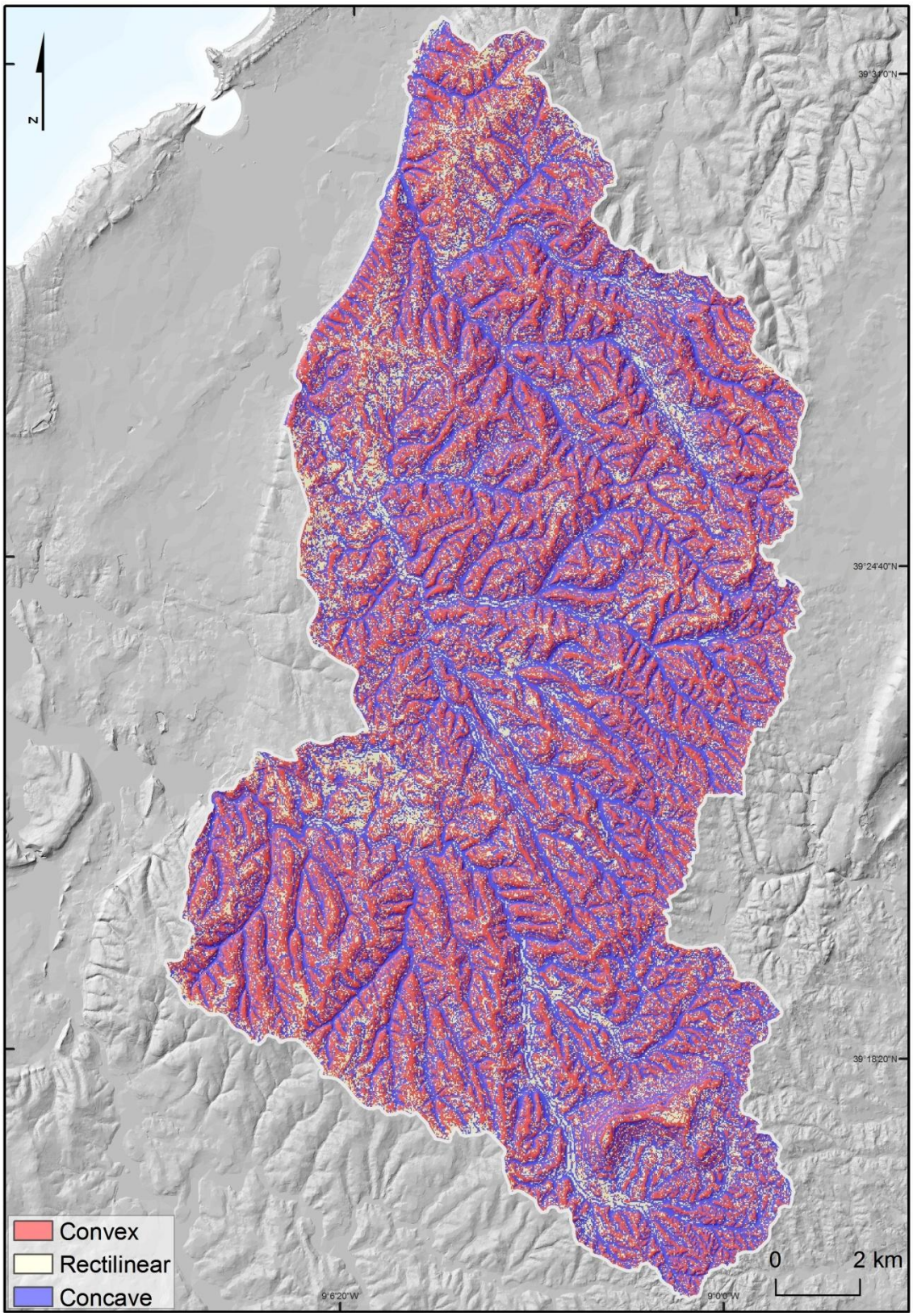

Fig. 6.3 – Curvature (cross section profile) of the study area.

Table 6.3 - Reclassified Profile Curvature map of the study area.

Classes	Occupancy area	
	(Km^2)	(%)
Convex	114.9	41.6
Rectilinear	50.3	18.2
Concave	110.7	40.1
SUM	275.9	100

6.1.1.4 Inverse of the Wetness Index

The Topographic Wetness Index (WI) is frequently used to simulate the soil moisture conditions in a watershed quantitatively, and it is the most commonly used indicator for static soil moisture content as well. Thus, it plays an important role in the research of soil erosion and distributed hydrological model in watersheds (Sørensen *et al.*, 2005).

While concave areas, with low gradient, have a predisposition to gather water (low WI values), steep and convex areas are more prone to shed water (high WI values). The WI uses Flow Direction and Flow Accumulation rasters as inputs. The Flow direction derived from DEM and, from this model, it is possible to obtain the flow accumulation. Typically the WI values range from less than 1 (dry cells) to greater than 20 (wet cells). Threshold values are applied to the output raster, via classification, based on local knowledge, field characteristics, and observations of the local terrain's response to heavy precipitation and overland flow. Specifically, the WI relates drainage areas with slope variations within a catchment and it can be expressed by the following Equation 6.1, defined by Beven and Kirkby (1993):

$$WI = ln\left(\frac{\mathrm{a}}{Tan\ (\beta)}\right) \tag{6.1}$$

Where a is contributing upstream area (m^2) from flow accumulation raster, and β is the local slope angle (degrees). It is important to mention that for it calculations it is important to convert degrees to radians.

The application of the Inverse Wetness Index (equation 4.3) avoids the errors arising where cell division matches with β = 0, since a, correspond to the denominator value (Oliveira, 2012).

$$IWI = \frac{\beta}{a} \tag{6.2}$$

There are two algorithms for determining the flow direction: D8 and D∞. For this work was selected the algorithm D∞. Such algorithm enables the determination of multiple flow directions, providing thus, better results when compared to algorithms that only assume 8 possible directions of flow (as the case of D8 algorithm) for determining the contribution area or other related hydrological parameters (e.g., Sorensen *et al*., 2005; Erskine, 2006).

The procedure was developed using the application TauDEM (Terrain Analysis Using Digital Elevation Models) for ArcGIS software, which presupposes the existence of a DEM free of artificial sinks. Then, the flow direction model was derived from DEM. The IWI map was classified into seven classes, which revealed better discrimination. For this purpose were applied a range of classes based on a logarithmic progression of base 10. The Table 6.4 discriminates the frequency of IWI classes and the Fig. 6.4 shows the IWI spatial distribution along the study area. The first IWI class represents the places where β = 0. Such areas are mostly concentrated in the valley bottoms. However, it may also arise from interfluves areas, as it can be seen in Fig. 6.4. Therefore, these areas should not be related only to the maximum potential of water accumulation. Instead, it should be kept independently in the classification. The IWI class]0.001 - 0.01] covers most of the study area, summarizing 64.8% of the total study area (Tornada, Arnoia and Alfeizerão catchments).

Regarding the spatial distribution, of the potential for water accumulation, it can be observe, that, generally, it increases due to the proximity to the hydrographical network (IWI classes]0 - 0.00001] and]0.00001 - 0.0001]) being, the permanent or temporary watercourses, the places where water accumulates. The steepest slope areas are

associated to the IWI classes]0.0001 - 0.001] and]0.001 - 0.01], and the interfluves areas are dominated by the IWI classes]0.01 - 0.1] and > 0.1.

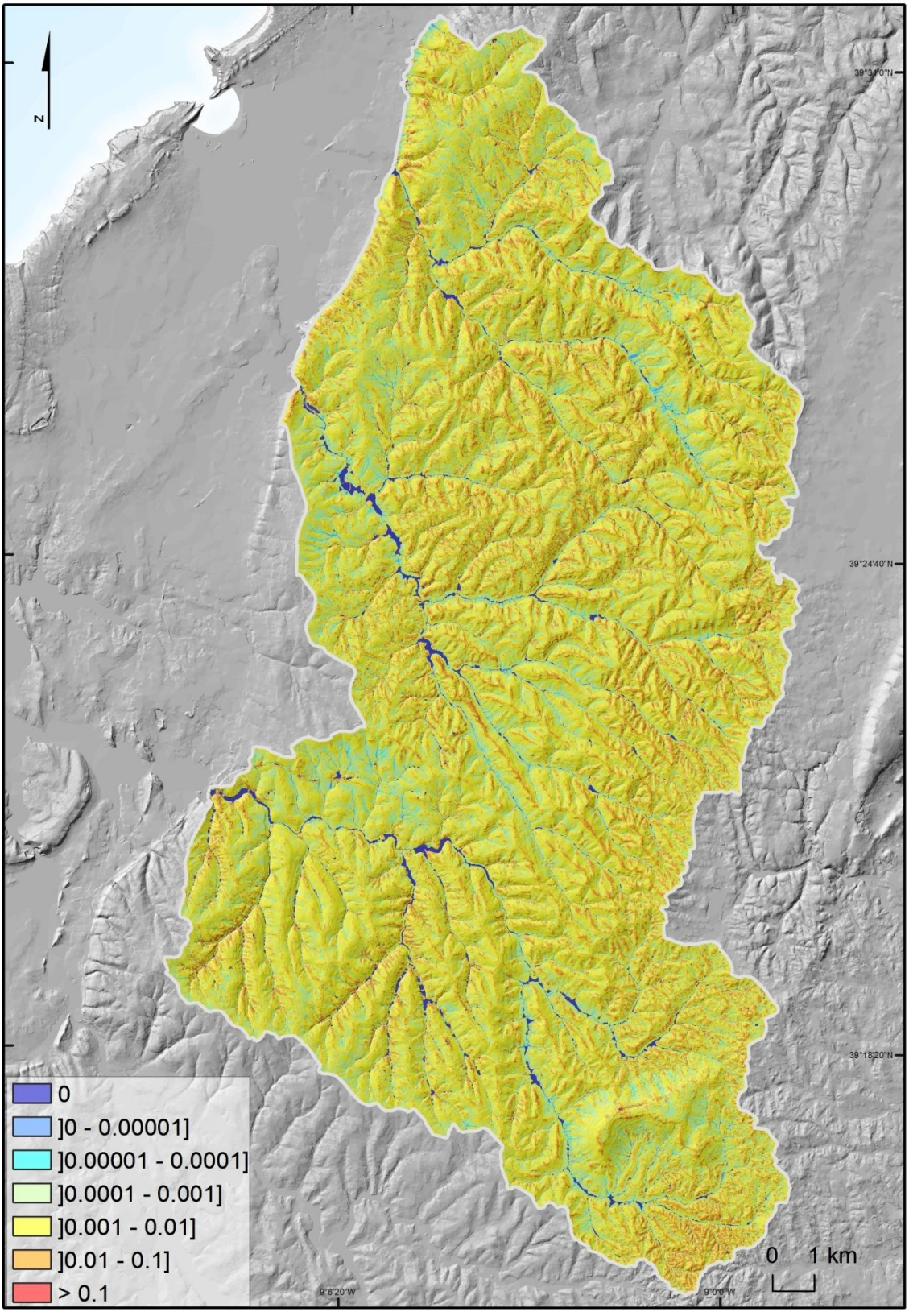

Fig. 6.4 – IWI map of the study area.

Table 6.4 – Reclassified IWI map of the study area.

Classes	Occupancy area (Km^2)	(%)
0	4.0	1.4
]0 - 0.00001]	2.7	1.0
]0.00001 - 0.0001]	5.7	2.1
]0.0001 - 0.001]	41.5	15.0
]0.001 - 0.01]	178.2	64.8
]0.01 - 0.1]	43.7	15.8
> 0.1	0.1	0
SUM	275.9	100

6.1.2 Lithology

Many studies worldwide have shown that landslides are greatly conditioned by the lithological properties of the land surface (e.g., Carrara *et al*., 1991; Mejia-Navarro and Wohl 1994; Mejia-Navarro and Garcia 1996; Pachauri *et al*., 1998; Luzi and Pergalani 1999; Dai *et al*., 2001; Yalcin 2005; Duman *et al*., 2006). For this reason, the lithology corresponds to one of the most important predisposing factors and it is frequently used to assess landslide susceptibility (e.g., Chacon *et al*., 2006; Clerici *et al*., 2010).

A more detailed lithological map has greater importance in providing data for susceptibility mapping, since different lithological unit correlates spatiality different according to the landslide typology. Thus, a detailed lithological map (obtain in Chapter 3) was included as a predisposing factor for landslide susceptibility assessment. This lithological map was classified according to the Fig. 3.12 from chapter 3 and its spatial distribution is shown in Table 3.2 from chapter 3.

6.1.3 Morpho-structure

The landslide distribution and pattern is mostly related to the natural conditions, which exhibit some regionally differentiations. Although the geologic, geomorphologic, climatic and tectonic conditions are different at every region, the natural conditions may not show

a homogeneous structure even at small areas bounded by physiographic, lithological and climatologic conditions. In line with this, and despite the considerable morpho-structural heterogeneity founded in the study area, similarities between landslides types and patterns were identified (Chapter 4). Thus, it was decided to include this variable as a predisposing factor in the landslide susceptibility assessment through a statistically-based method.

The morpho-structure model was classified according to the Fig. 4.23 from Chapter 4 and its distribution over the study area can be observed in Table 4.8 from Chapter 4.

6.1.4 Soil depth

Soil depth is widely recognized as a controlling factor in numerous surface and subsurface processes, e.g., landscape evolution, sediment budgets and landsliding (Catani et. al., 2010). Thereby, incorporating such variable (obtained in chapter 5) as a predisposing factor, for landslide susceptibility assessment, through statistically-based model, makes total sense. This data was classified into 4 classes, as it can be seen in Fig. 6.5.

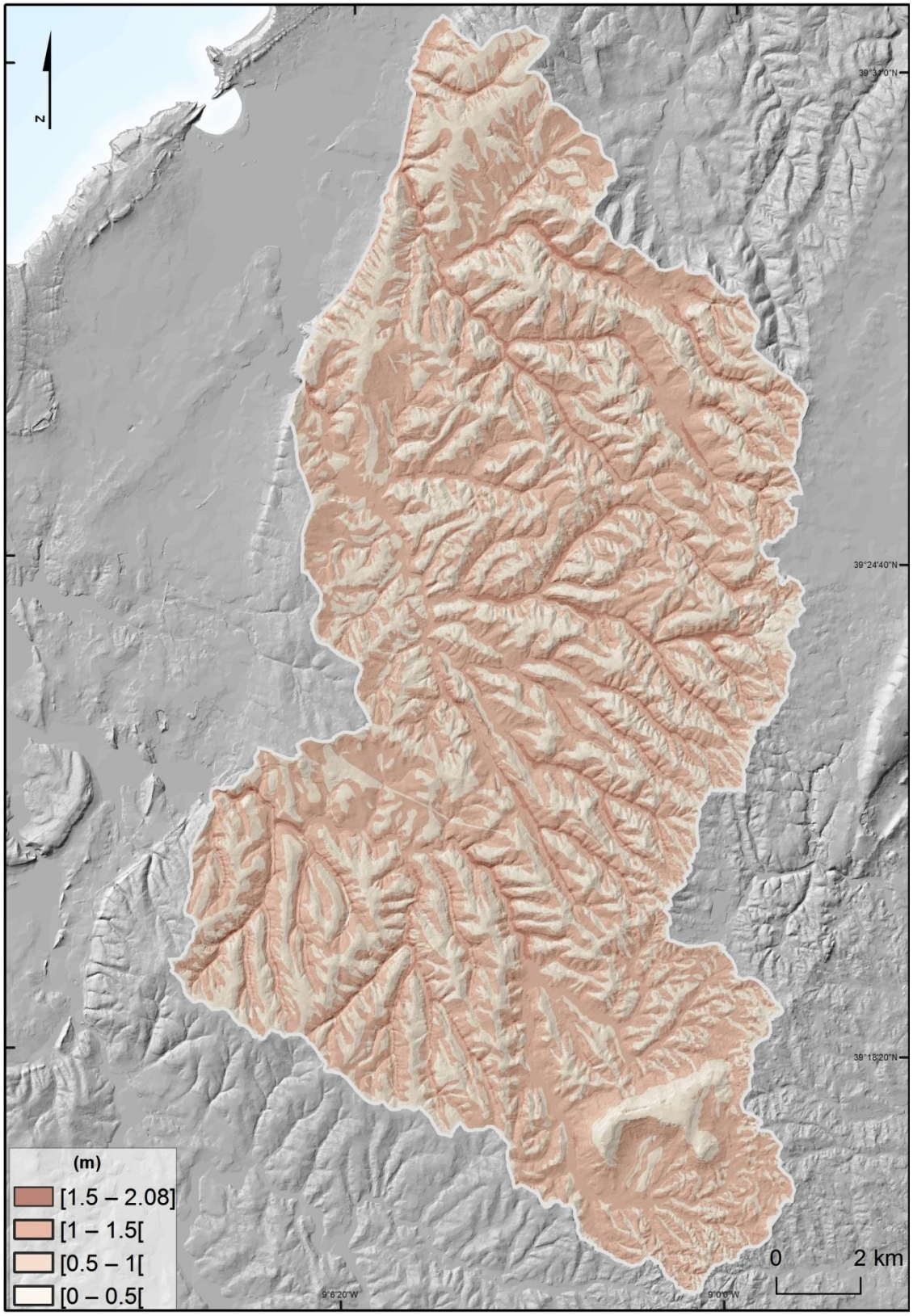

Fig. 6.5 – Soil depth map of the study area.

Regarding the spatial distribution (Fig. 6.5), it can be observed that, the classes "0 – 0.5" and "0.5 – 1" which correspond to thinner soils, dominate the study area, respectively in 40.3% and 54.9% (Table 6.5).

Table 6.5 - Reclassified soil depth map of the study area.

Classes	Occupancy area	
	(Km^2)	(%)
0 – 0.5	109.8	40.3
0.5 – 1	152.3	54.9
1 – 1.5	10.9	3.9
1.5 – 2.08	3.0	0.9
	275.9	100

6.1.5 Soils

The different soils types, detected in the study area (chapter 5), with their different characteristics and resistances may influence the propensity of slopes to landslide activity. Thus, it is important to consider such variable for landslide susceptibility assessment through the statistically-based-methods.

The compatibility with the USDA classification resulted in 9 classes of soil types as it is possible to observe in Fig 5.16 in Chapter 5. According to Table 6.6, it is possible to observe that the study area is mostly dominated by clay loam and loam soils which, together, summarize 79.96 % of the total study area.

Table 6.6 – Reclassified Soil map of the study area.

Classes	Occupancy area	
	(Km^2)	(%)
Clay loam	95.1	34.5
Loam	125.5	45.5
Silt loam	29.2	10.6
Silty clay	0.03	0.01
Silty clay loam	8.9	3.2
Sandy loam	9.5	3.5
Loamy sand	4.1	1.5
Clay	2.8	1.0
Sandy clay loam	0.7	0.3
SUM	275.9	100.0

6.2 Statistically-based methods

In recent decades, several statistical methods have been proposed to evaluate the landslide susceptibility (e.g., Carrara, 1983; Aleotti and Chowdhury, 1999; Carrara *et al*., 2003; Guzzetti *et al*., 2005; Chacón *et al*., 2006). These methods introduce objectivity in the process of landslide susceptibility evaluation and allow the validation of the results, through the determination of the respective rates of prediction and success (Fabbri *et al*., 2002; Chung and Fabbri, 2003; Guzzetti *et al*., 2006).

Statistical methods are applied to cartographic units defined *a priori*, as raster units, units of unique-condition, geological-geomorphological units, morpho-hydrographical units, or administrative units (Guzzetti, 2005). As it was already mentioned, raster (matrix) units with 5 m pixel are used in the present work.

The statistical methods are bivariated or multivariated. On bivariated statistical analysis each conditioning factor is combined individually with the landslide distribution map, assigning the respective weighting, based on the density of slop movements observed in each class of each variable. On the other hand, in multivariated statistical analysis, the award of the degree of importance, for each class of each variable, also considers other variables that go into the process analysis (Suzen and Doyuran 2004). In this study, a bivariated statistical method is used, respectively the Informational Value, to model landslide susceptibility. In addition, a multivariated method, the Maximum Entropy (MaxEnt), is used to perform an expeditious sensitivity analysis of each variable used as predisposing factor.

6.2.1 Sensitivity analysis of the landslide predisposing factors: Analysis of variable contributions

The sensitivity analysis of the set of predisposing factors is a very important task to be performed because this technique allows assessing which predisposing factors have the higher contribution to increase the landslide susceptibility models performance. The

global aim of this technique is to check the stability of the model (or its predictive capability), by analyzing the variation on results when inserting or removing some input variable or variables. The results from the sensitivity analysis indicate which variables should continue in the modeling process, to achieve better results (Rocha, 2012).

The sensitivity analysis, in theory, should determine the following statements:

1) The factors that contribute to the results. It is required a test of several hypotheses in order to reduce the uncertainty of the modeling results. Such procedure contributes to the knowledge about the factors that are not significant for the explanation and thus, could be eliminated (Rocha, 2012);

2) If there is a group of factors with high correlation. In the final phase, it can be said that this type of analysis helps to improve the models because it provides knowledge about the sensibility before modifying certain parameters. The Fig. 6.6 presents, in a very simplified way, the process to follow in this type of analysis. Firstly, it is necessary to remove a number of samples of the input factors, secondly the model runs a significant number of times, and thirdly it is made an analysis to the modeling results (Rocha, 2012).

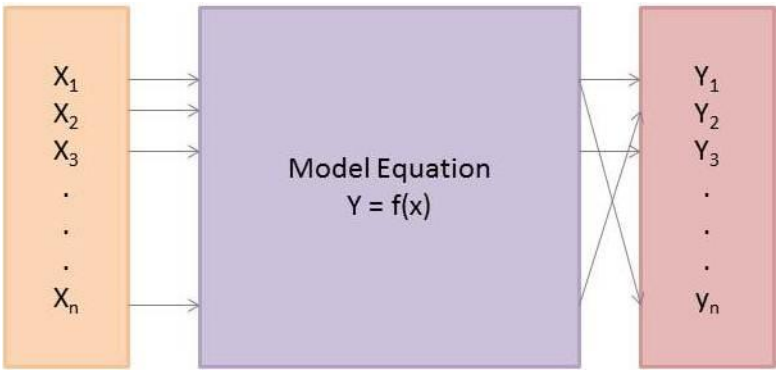

Fig. 6.6 – Applied sensitivity analysis, from which are extracted the input variables and the model output variables (extracted from Rocha, 2012).

6.2.1.1 Maximum Entropy method (*MaxEnt*)

The origin of the entropy concept goes back to Ludwig Boltzmann (1877). The entropy formula expresses the expected information content or uncertainty of a probability distribution. Let E_i stand for an event (e.g. landslide) and p_i for the probability of event E_i to occur. Let there be n events E_1, …, E_n with probabilities P_1,…, P_n adding up to 1. Since the occurrence of events with smaller probability yields more information (since these are least expected), a measure of information h should be a decreasing function of P_i. Shannon (1948) proposed a logarithmic function to express information h(P_i):

$$h(p_i) = \ln\left(\frac{1}{p_i}\right) \tag{6.3}$$

which decreases from infinity to 0 for P_i ranging from 0 to 1. The function reflects the idea that the lower the probability of an event to occur, the higher the amount of information of a message stating that the event occurred.

From the *n* number of information values $h(P_i)$, the expected information content of a probability distribution, called entropy, is derived by weighing the information values $h(P_i)$ by their respective probabilities:

$$H = \sum_{i=1}^{n} p_i \ln\left(\frac{1}{p_i}\right) \tag{6.4}$$

Where *H* stands for entropy and if *Pi*=0 usually is considered *Pi* ln(1/*Pi*)=0, which is in accordance to the limit value of the left term for P_i approaching zero (Theil, 1972). The entropy value *H* is non-negative (ranges from 0 to 1). The minimum possible entropy value is zero when a event has unit probability:

$$H_{\min} = 1 \cdot \ln\left(\frac{1}{1}\right) = 0 \tag{6.5}$$

When all states are equally probable ($p_i = \frac{1}{n}$), the entropy value is maximum (Theil, 1972):

$$H_{\max} = \sum_{i=1}^{x} \frac{1}{x} \ln(x) = x \frac{1}{x} \ln(x) = \ln(x) \quad (6.6)$$

The Maximum entropy model was initially proposed by Jaynes (1957) and recently turned in a standalone GIS aplications called MaxEnt (Philips *et al*., 2004). The MaxEnt weights each variable with a constant. The probability distribution is the weighted sum of each variable divided by a scaling constant to ensure that the scale of probability values ranges between 0 and 1. The model starts with a uniform distribution of the probability and iteratively changes the weight at each time, to maximize the probability to achieve the best probability distribution. The algorithm is always convergent and hence the outputs are deterministic.

Thereby, entropy can be considered as a measure of uncertainty. Theil (1972) remarks that the entropy concept in this regard is similar to the variance of a random variable. The main difference is that entropy applies to qualitative rather than quantitative values, and, as such, depends exclusively on the probabilities of possible events.

Since the traditional implementation of the maximum entropy is prone to over-adjustment, the MaxEnt uses a relaxivity[7]. Does not constrict the estimated distribution to the exact empirical average but within the limits of the empirical error of the mean value for a given predictor data. This smoothing procedure is called regularization. The user has the option of changing the parameters of this procedure to potentially compensate small sample sizes. The predictions of the MaxEnt for each cell in analysis are cumulative values represented as a percentage of the mean value of the probability for cell under analysis, and all the remaining with equal values or lower probability.

[7] It is a measure of the ability to increase the relaxation rates. The term relaxation describes the process by which a model set in a non-equilibrium state return to the equilibrium. In other words, relaxation describes how fast MaxEnt "forget" the direction in which is oriented, i.e., over adjustment, and come back to proper adjustment.

Summarizing, this model attempts after a set of iterations, to find the probability distribution of maximum entropy based on the limitations imposed by the data distribution and the conditions of the entire study area. One of the features provided by this algorithm is related to the possibility to incorporate a non-absence data for the dependent variable, which are obtained through the generation of pseudo-random absences. Other features presented by this model are that the final information display continuous values, allowing great flexibility in choosing their limits, and submitting a concise mathematical definition, being expressed from the following equation:

$$H(\hat{\pi}) = -\sum_{X \in X} \hat{\pi}(x) ln\, \pi(x) \tag{6.7}$$

Where π corresponds to the unknown probability distribution, lying on a finite set of data designated as X, corresponding to individual elements such as dots. The distribution π assumes a non-negative probability $(\ )\ \pi$ x for each point x, and the sum of all probabilities equals 1. The approximation of π is in the same sense, a probability distribution, being represented by $\hat{\pi}$ (Philips *et al*., 2004).

In the landslide context, maximum entropy characterises the distributions of a random occurrence of landslides with an equal probability to be present in any set of predisposing factors. When behaving in a non-random way, e.g. when landslides occur on specific conjugations of predisposing factors, the resulting distribution is skewed and entropy is lower (Prigogine and Stengers, 1984). MaxEnt automatically invert the values, converting 0 (no entropy) to 1 (maximum probability of landslide occurrence). The advantages and disadvantages of applying this model can be found in Table 6.7.

Table 6.7 – Advantages and disadvantages of the maximum entropy model (Rocha, 2012).

Advantages	Disadvantages
The probability distribution is defined mathematically and therefore the formulation of the model.	Does not have a selection procedure of variables.
Is relatively transparent.	Extremely computationally intensive.
Consider interactions between variables.	Possible weaknesses in dealing with samples biased.
Provides the possibility of considering polynomial transforms of the predictors.	
It has the potential to evaluate the influence of each predictor in the final distribution.	
Relatively easy to run, independent application (standalone).	
Works well with relatively small samples.	

A sensitivity analysis of the model was performed using the method based on multiple sub-samples called jackknife, proposed by Lachenbruch (1967). The jackknife method is a statistical technique consensual in the sensitivity analysis and it is particularly useful in models involving small sample sizes. In this method all observations can be used for estimating of the model parameters (Neophytou *et al*., 2000).

The method is based on the principle leave-one-out and consists on: i) separate a variable from an original input set; ii) estimate the coefficients of the model based on the remaining variables $(n - 1)$; iii) classify the dependent variable using the new equation. The procedure is repeated for all the input independent variables (n times) so that, all variables are sorted by models whose parameters were estimated based on the independent variables.

For the present work, three types of landslides from the three landslide inventories (LI#1, LI#2 and LI#3 from Chapter 2) were modeled (Table 6.8), which resulted in nine landslide susceptible models: 1) three landslide susceptibility models for deep-seated rotational

slides, respectively, from LI#1, LI#2 and LI#3; 2) three landslide susceptibility models for shallow rotational slides from LI#1, LI#2 and LI#3; 3) three more landslide susceptibility models for shallow translational slides from LI#1, LI#2 and LI#3.

Table 6.8 – Number of landslides of each landslide inventory according to the typology.

Landslide inventory	Deep-seated rotational	Shallow rotational	Shallow translational
LI#1	584	80	38
LI#2	449	61	21
LI#3	126	71	46

It is important to mention that, for the shallow translational susceptible model from LI#3, the same landslides selected for validating the physically-based models were used, which took into account not only the pure shallow translational slides, but also some that were firstly identified as shallow rotational but, due to the large curvature radius of its shear plane surface, were selected to incorporate the susceptibility assessment to shallow translational landslides. Thus, for LI#3 the landslide susceptibility model of the shallow rotational slides was done taking into account 30 pure shallow rotational slides and the landslide susceptibility model of the shallow translational slides was performed taking into account 46 pure shallow translational plus 41 non-pure shallow rotational slides.

In order to assess the variables contribution, the maximum entropy method, described above, was used. This method was selected due to its expeditious behavior on sensitivity analysis. Differently from the bivariated Information value, in this method, was chosen to enter the landslides as points, which were the centroid of each depletion zone of each landslide. This method is usually stated in a deceptively simple way: from among all the probability distributions compatible with empirical data, it chose the one with the highest information-theoretic entropy (Philips *et al.*, 2004).

The following tables (from Table 6.9 to 6.11) give estimates of relative contributions of the predisposing factors for each model. To determine the first estimate, in each iteration

of the training algorithm, the increase in regularized gain is added to the contribution of the corresponding variable, or subtracted from it if the change to the absolute value of lambda (λ) is negative. For the second estimate, for each environmental variable in turn, the values of that variable on training presence and background data are randomly permuted. The model is reevaluated on the permuted data, and the resulting drop in training AUC is shown in the table, normalized to percentages (Rocha, 2012).

Table 6.9 – Analysis of the predisposing factor contributions to deep-seated rotational slides.

Theme	LI#1		LI#1 + LI#2		LI#3	
	PC*	PI*	PC*	PI*	PC*	PI*
Lithology	**74.2**	**68.3**	**58.6**	**29.5**	**58.3**	**52.7**
Slope angle	9.6	**14.5**	13.2	17	**20.3**	**25.1**
Morpho-structure	0.3	0.1	3	0.5	4.2	0.2
Soil depth	**11.9**	9.1	5.4	5.5	0.7	1.1
IWI	1.7	6.2	**17.9**	**45.3**	12.1	12.2
Curvature	0.9	0.8	0.2	0.2	0.4	0
Soils	0.4	0.6	0.6	1.3	1.2	3.9
Aspect	1	0.5	1.2	0.7	2.8	4.9

PC* - Percent contribution
PI* - Permutation importance

Table 6.10 – Analysis of the predisposing factor contributions to shallow rotational slides.

Theme	LI#1		LI#1 + LI#2		LI#3	
	PC*	PI*	PC*	PI*	PC*	PI*
Lithology	**72.2**	**80.2**	**70.5**	**82.9**	**39.8**	**40.5**
Slope angle	6.3	3.2	4.3	3.7	15.6	20.1
Morpho-structure	**7.2**	2.6	**14.8**	**4.6**	4.9	0.5
Soil depth	1.8	1.4	1.7	0.8	0.1	0.6
IWI	1.4	1.8	2.2	2.6	0.1	0.6
Curvature	1.3	1.5	0.5	0.7	7.4	6.4
Soils	6.2	**6.3**	2.4	0.6	**28.7**	**28.8**
Aspect	3.5	3	3.5	4	3.5	2.5

PC* - Percent contribution
PI* - Permutation importance

Table 6. 11 – Analysis of the predisposing factor contributions to shallow translational slides.

Theme	LI#1		LI#1 + LI#2		LI#3	
	PC*	PI*	PC*	PI*	PC*	PI*
Lithology	**74.7**	**74.6**	**75.9**	**84.4**	**43.7**	**66**
Slope angle	8.4	6.5	**8.9**	**5.5**	5.8	2.8
Morpho-structure	6.7	3.8	6	1.9	**30.9**	**15.2**
Soil depth	0.9	0.9	1.2	1.9	4.2	1.9
IWI	0	0	0.1	0.2	3.2	0.1
Curvature	2.1	3.6	0.7	1.4	8.4	11.7
Soils	0.8	3.5	2.2	2	2.2	1
Aspect	**6.4**	**7.1**	5.1	2.8	1.7	1.4

PC* - Percent contribution
PI* - Permutation importance

These percent contribution values are only heuristically defined: they depend on the particular path that the MaxEnt uses to get to the optimal solution, and a different algorithm could get to the same solution via a different path, resulting in different percent contribution values.

For each landslide group modeling, the right-hand column in the table shows a second measure of variable contributions, called permutation importance. This measure depends only on the final MaxEnt model, not the path used to obtain it. The contribution for each variable is determined by randomly permuting the values of that variable among the training points (both presence and background) and measuring the resulting decrease in training AUC. A large decrease indicates that the model depends heavily on that variable. Values are normalized to give percentages.

The Fig. 6.7, 6.8 and 6.9 show the results of the weigh importance variables of each landslide inventory through the jackknife test (performed through MaxEnt software), for each landslide type. The variable with the highest gain for every landslide inventory and type seem to be always the detailed lithology, which appears to have - by itself - the most useful information that is not present in the other variables. This is incredible strong when considering the inventories associated to ancient landslides (Fig. 6.7 and 6.8). Moreover, the variable that most reduces the gain when omitted is, again, the detailed lithology which seems to have the much relevant information which is not present in the other variables.

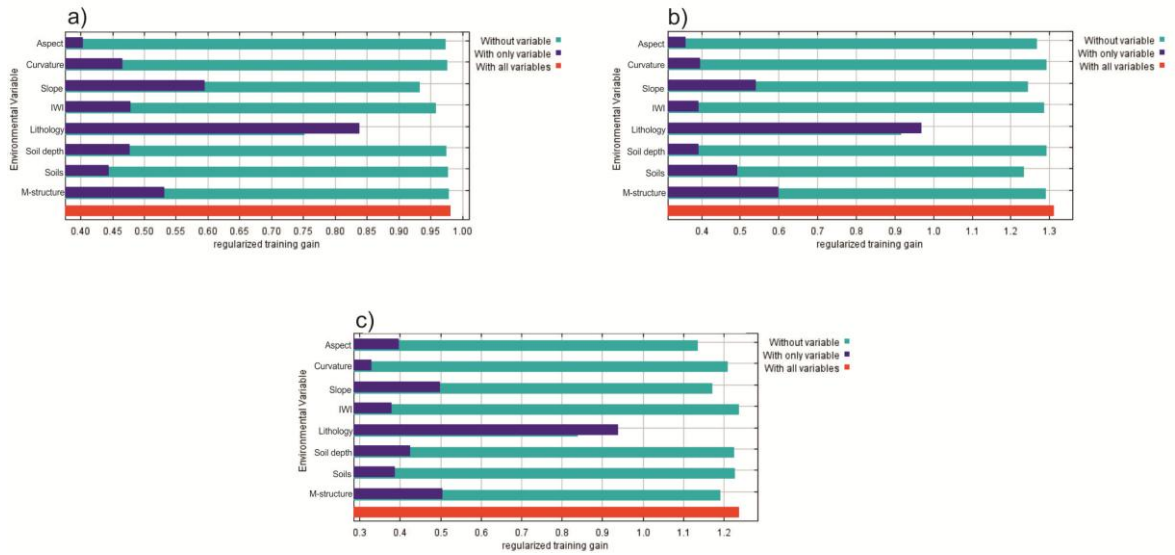

Fig. 6.7 – Jackknife of regularized training gain for LI#1: a) for Deep-seated rotational slides; b) for shallow rotational slides; c) shallow translational slides.

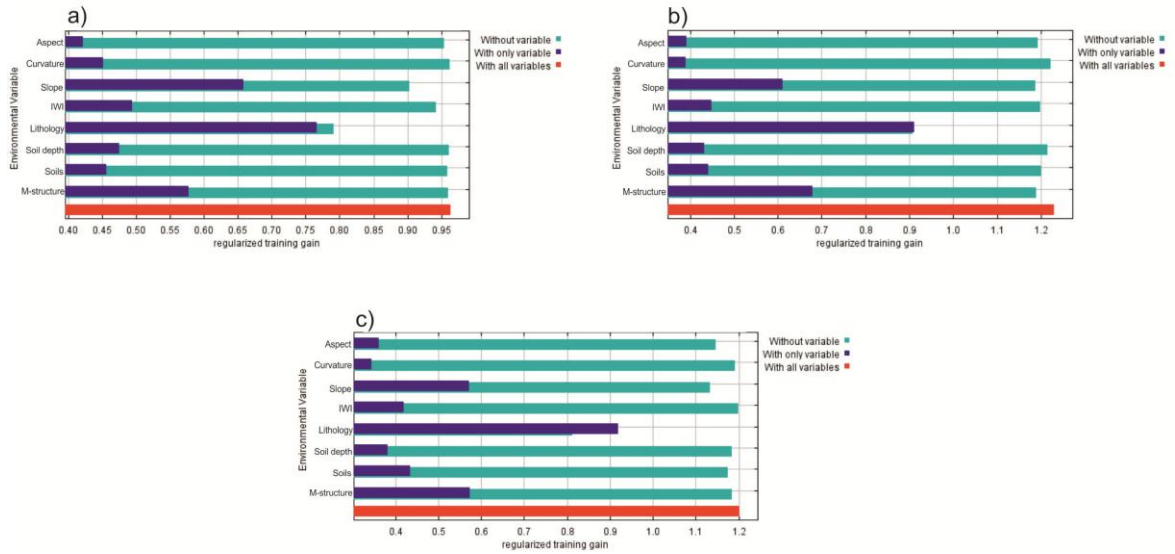

Fig. 6.8 – Jackknife of regularized training gain for LI#1+LI#2: a) for Deep-seated rotational slides; b) for shallow rotational slides; c) shallow translational slides.

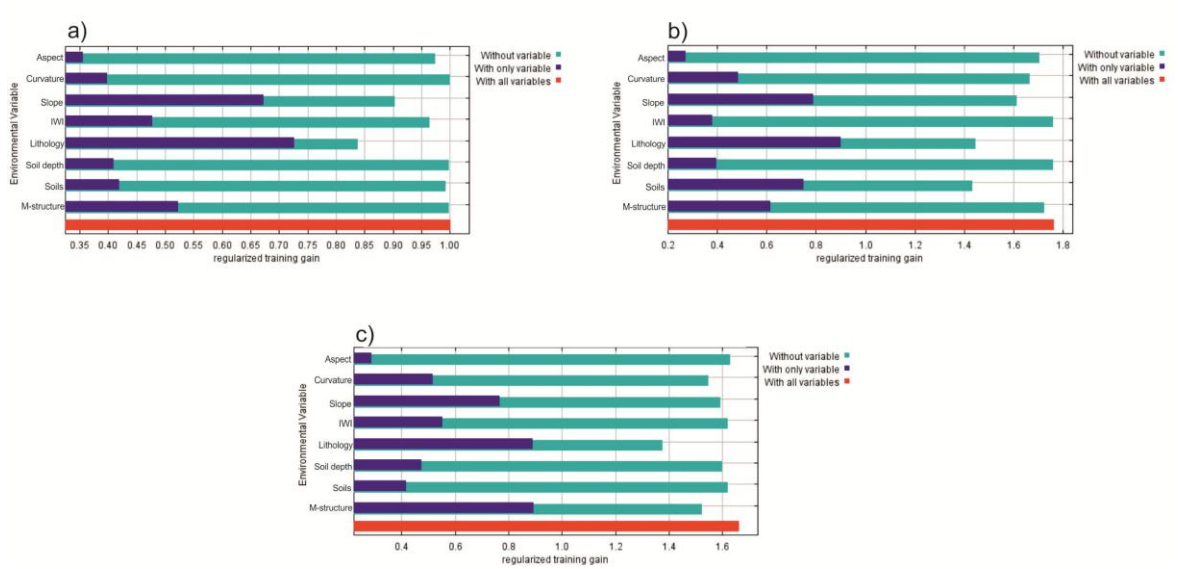

Fig. 6.9 – Jackknife of regularized training gain for LI#3: a) for Deep-seated rotational slides; b) for shallow rotational slides; c) shallow translational slides.

Through the interpretation of Fig. 6.7, 6.8 and 6.9 it is possible to conclude that, generally, and within the study area context, the increment of a number of predisposing factors, translates into an increase of quality of the susceptibility models to most types of landslides, regardless the inventory period. When this is not the case, the increment of predisposing factors, above the strictly necessary, does not cause entropy that justifies a need to exclude them. Generally, the aspect variable seemed to be always the less important predisposing factor, regardless the type and age of the landslide. However, even on a reduced way, all variables, selected as inputs, contribute to increase the predictive ability of landslides present in the study area. Thus, all variables will be used for future modeling.

6.2.1.2 Accountability and Reliability

Beyond the maximum entropy method we also used the Accountability and Reliability methods (e.g., Greenbaum *et al*., 1995a,b; Abella, 2008; Blahut *et al*., 2010) in order to conduct an independent analysis of each variable of each predisposing factor. These methods allow determining the relative importance of each variable according to landslide events based on the typology of each LI.

Thereby, the eight themes were individually cross-tabulated (in ArcGis 9.3 software) with the three landslides types (deep-seated rotational slides; shallow rotational slides and shallow translational slides) of each LI (LI#1; LI#1+LI#2; and LI#3) in order to calculate the densities of landslides in all classes or variables of the eight themes (Tables 6.12, 6.13 and 6.14).

The accountability index explains how the classes of the themes that are relevant for the analysis (with densities higher than regional average) contain landslide cells/area. The reliability index gives an idea of the average landslide density in the classes of the themes that are relevant for landslide occurrence (with values higher than 1) (Blahut *et al.*, 2010), i.e., the accountability index only takes into account the total area of landslides present in a certain class while the reliability index takes into account the area of the class (i.e. the ratio between landslides area and class area).

Table 6.12 – Accountability and reliability of the predisposing factor contributions to deep-seated rotational slides.

Theme	LI#1		LI#1 + LI#2		LI#3	
	ACC*	RLB*	ACC*	RLB*	ACC*	RLB*
Lithology	**96.4**	**1.357**	**95.2**	1.838	**93.4**	0.162
Slope angle	74.3	1.332	**77.2**	**1.898**	**80.4**	**0.183**
Morpho-structure	46.1	**1.359**	52.6	**2.021**	54	**0.189**
Soil depth	61.4	0.884	45.1	1.202	51.1	0.135
IWI	87.1	0.932	71.7	1.295	75.4	0.122
Curvature	46.9	0.995	45	1.310	48.9	0.127
Soils	**94.9**	0.919	49.4	1.391	60.1	0.153
Aspect	57.7	0.942	42.9	1.398	50.5	0.153

ACC*- Accountability
RLB* - Reliability

Table 6.13 – Accountability and reliability of the predisposing factor contributions to shallow rotational slides.

Theme	LI#1		LI#1 + LI#2		LI#3	
	ACC*	RLB*	ACC*	RLB*	ACC*	RLB*
Lithology	**100**	0.073	**99**	**0.104**	**100**	0.008
Slope angle	62.8	0.057	71.1	0.095	81.1	0.008
Morpho-structure	50	**0.075**	55.9	**0.122**	61.8	**0.010**
Soil depth	58	0.046	6.2	0.102	61.8	0.005
IWI	**89.2**	0.049	**88**	0.070	23.3	0.007
Curvature	69.3	0.052	60.8	0.066	59.2	0.007
Soils	68.2	**0.079**	61.9	0.103	**89.1**	**0.009**
Aspect	49	0.055	62.1	0.076	64	0.006

ACC*- Accountability
RLB* - Reliability

Table 6.14 – Accountability and reliability of the predisposing factor contributions to shallow translational slides.

Theme	LI#1		LI#1 + LI#2		LI#3	
	ACC*	RLB*	ACC*	RLB*	ACC*	RLB*
Lithology	**100**	**0.014**	**99.6**	**0.023**	**99.5**	0.026
Slope angle	**88.1**	0.009	70.2	0.020	**88.1**	0.030
Morpho-structure	61	0.011	52.6	**0.025**	67.4	**0.036**
Soil depth	62	0.009	**98.1**	0.014	54.3	0.020
IWI	77.5	0.010	74	0.016	73.2	0.018
Curvature	28.3	**0.013**	62.2	0.014	50.3	0.020
Soils	49	0.011	97.8	0.016	84.1	**0.035**
Aspect	72.7	0.013	77.9	0.016	51.5	0.025

ACC*- Accountability
RLB* - Reliability

According to Table 6.12, 6.13 and 6.14 it can be conclude that higher values of accountability mean classes of themes with higher discriminant power (classes more prone to landsliding regardless the class area), while high values of reliability means classes with high proportion of landslides (mainly due to a reduced class area). Although being both important, it is possible to observe that high values of accountability does not necessary implies high values of reliability, thus, it became crucial to simplify this analysis by establish a hierarchy among the predisposing factors (themes) for each type of landslide and for each LI.

6.2.1.3 Analytical hierarchy process for landslide susceptibility mapping

The Accountability and Reliability values were scaled from 0 to 100, based on the sum of all factors, in order to be comparable with the Percent contribution values from the *MaxEnt*. Afterwards we proceeded to an average between the three parameters (PC, ACC and RLB) in order to establish a hierarchy of the predisposing factors for each landslide type within each LI. The obtained results are summarized in Tables 14, 15 and 16.

Table 6.15 – Hierarchy of the predisposing factor contributions to deep-seated rotational slides according to the average between PC, ACC and RLB (%).

LI#1	LI#1 + LI#2	LI#3
Lithology (35.6)	**Lithology (31.1)**	**Lithology (29.9)**
Slope angle (12.7)	**Slope angle (14.9)**	**Slope angle (17.0)**
Soil depth (11.0)	IWI (14.4)	IWI (12.2)
IWI (9.3)	Morpho-structure (10.1)	Morpho-structure (10.1)
Soils (9.2)	Soil depth (8.2)	Soils (8.5)
Morpho-structure (8.0)	Soils (7.4)	Aspect (8.4)
Aspect (7.3)	Aspect (7.2)	Soil depth (7.2)
Curvature (6.9)	Curvature (6.7)	Curvature (6.8)

Table 6. 16 – Hierarchy of the predisposing factor contributions to shallow rotational slides according to the average between PC, ACC and RLB (%).

LI#1	LI#1 + LI#2	LI#3
Lithology (35.2)	**Lithology (34.7)**	**Lithology (23.9)**
Soils (11.6)	**Morpho-structure (14.1)**	**Soils (20.1)**
Morpho-structure (10.6)	Slope angle (10.4)	Slope angle (14.6)
Slope angle (9.8)	IWI (9.7)	Morpho-structure (11.0)
IWI (9.3)	Soils (9.5)	Curvature (10.0)
Curvature (8.2)	Aspect (8.7)	Aspect (8.4)
Aspect (7.9)	Curvature (7.2)	Soil depth (6.6)
Soil depth (7.3)	Soil depth (5.6)	IWI (5.4)

Table 6.17 – Hierarchy of the predisposing factor contributions to shallow translational slides according to the average between PC, ACC and RLB (%).

LI#1	LI#1 + LI#2	LI#3
Lithology (36.3)	**Lithology (35.9)**	**Lithology (24.5)**
Slope angle (12.1)	**Slope angle (11. 3)**	**Morpho-structure (20.0)**
Morpho-structure (10.9)	Morpho-structure (10.6)	Slope angle (11.9)
Aspect (10.1)	Soils (9.6)	Soils (11.2)
IWI (8.5)	Aspect (9.5)	Curvature (8.9)
Soil depth (7.5)	Soil depth (8.8)	IWI (8.2)
Soils (7.4)	IWI (7.6)	Soil depth (7.8)
Curvature (7.3)	Curvature (6.8)	Aspect (7.6)

The themes more important for deep-seated rotational slide activity are lithology and slope angle, whereas the importance of slope curvature and aspect is very low (Table 6.15). Concerning the shallow rotational slides, the highest weight is observed for lithology and soils (for LI#1 and LI#3) and for lithology and morpho-structure (for LI#1+LI#2).Soil depth (for LI#1 and LI#1+LI#2) and IWI (for LI#3) appears to be the less important themes (Table 6.16).

Finally, the themes with highest weight for shallow translational slides are the lithology and slope angle for LI#1 and LI#1+LI#2, whereas for LI#3 are the lithology and morpho-structure. As for the deep seated rotational slides, slope curvature and aspect are the less important themes to justify landslide distribution (Table 6.17).

It is noted that, regardless the landslide type and the landslide inventory, the theme with the highest gain (which appears to have the most useful information), is the detailed lithology (at 1:10,000 scale). This is due to the lithological detailing performed in Chapter 3, which shows that the shale dominated complexes class from upper Jurassic, corresponding to 59.3% of the total study area, contains, in many cases, about 90% of landslide occurrence regardless the typology and LI.

6.2.2 Classification of the landslides susceptibility maps

The classification process of the landslide susceptibility models is a very sensitive component in the final definition of landslide susceptibility (Oliveira, 2012). At the regional scale, the landslides susceptibility maps are the first step to achieve a risk assessment, which can contribute for the security of the communities where these potentially hazardous phenomena occur (e.g., Guzzetti *et al*., 1999; Glade *et al*., 2005; Sterlacchini *et al*., 2011). However, different classification methods may cause significant differences, although using the same susceptible model (e.g., Garcia, 2002; Garcia *et al*., 2007).

The inherent subjectivity in the process of classification and their influence on the final cartographic results were demonstrated by Garcia (2002) and by Garcia *et al.* (2007), making it clear that the performance of different classification methods, all statistically correct, may lead to very different visual results.

One of the most common and appropriate classification methods is performed by using the natural breaks classification based on accumulative weight and score of the prediction or success rate curve (e.g., Garcia, 2002; Henriques, 2009; Zêzere, 2010). Thus, for each susceptibility map the classification is based on the interpretation and segmentation of the prediction or success rate curve using the following criteria: i) very high susceptibility class, containing 70% of the total unstable area; ii) The class of high susceptibility containing 15% of the total unstable area; iii) the class of moderate susceptibility containing 10% of the total unstable area; and iv) low susceptibility class contain 5% of the total unstable area. In Table 6.18, the limits of the classes are expressed into four susceptibility classes adopted in this work, its predictive ability and form of color representation. The designation is in accordance with some proposals expressed in literature (e.g., Baeza and Corominas, 2001).

Table 6.18 – landslides susceptibility Classes, characterization of the predictive capacity value of each class and form of color representation adopted for the study area.

Designation	Accumulated landslide area (%)	Predictive capacity of the class (%)	Color
Very high	0 - 70	70	
High	70 – 85	15	
Moderate	85 – 95	10	
Low	95 - 100	5	

6.2.3 Information Value Method

The assessment of susceptibility was made separately for each type of landslide (deep-seated rotational, shallow rotational and shallow translational slides) and for each landslide inventory. The method chosen to evaluate the landslide susceptibility in the study area is, the already mentioned, Information Value and its principle is as follows: Once the landslides of the study area are located, physical characteristics of hillslope affected by landslides are studied and mapped. These characteristics are the predisposing factors that serve as thematic maps for assessing the susceptibility (slope angle, aspect and curvature, inverse wetness index, lithology, morpho-structure, soil depth, soil type). Each variable is divided into different classes (as described above).

The Information Value (IV) Method was used to assess quantitatively the landslide susceptibility independently for each type of landslide. Accordingly, the weighting of each class within each variable is given by (Yin and Yan 1988):

$$IV_i = log \frac{S_i / N_i}{S / N} \tag{6.8}$$

where S_i is the number of pixels with landslides belonging to modeling group and the presence of variable X_i. N_i is the number of pixels with variable X_i. The S is the total number of pixels with landslides belonging to the modeling group. N is the total number of pixels. The S/N is the a priori probability. It is the probability for each pixel to have a landslide without considering predisposing factors. The Si/Ni is the conditional probability. It is the probability to have a landslide given the presence of variable Xi.

Negative values of IV_i means that the presence of the variable is favorable to slope stability. Positive IV_i indicates a relevant relationship between the presence of the variable and landslide distribution; the higher the score, the stronger the relationship (Yin and Yan, 1988). IV_i equal zero means no clear relationship between variable and landslide occurrence. The classes of each variable not containing any landslide have a conditioned

probability equal to zero. In this case, IV_i cannot be obtained because of log transformation, and therefore the IV_i was forced to be equal to the lowest value of IV_i, within the variable (brown in Tables 6.19, 6.20 and 6.21).

The final susceptibility is then determined for each cell by the sum of the Information values obtained for each theme used as a predisposing factor (Equation 6.9).

$$IV_j = \sum_{i=1}^{m} X_{ij}\, IV_i \qquad (6.9)$$

where m is the number of variables and Xji is either 0 if the variable is not present in the pixel j, or 1 if the variable is present.

This method allows the quantification of the susceptibility via a score for the terrain unit (TU) even for areas that are not unstable yet (Zêzere, 2002). The higher Information values, reveals greater predisposition for landslide occurrence for a certain TU (Yin and Yan, 1988).

It should be noted that, as for the physically-based methods, also in this chapter, the depletion of the landslides were used for modeling and validating purposes, in order to predict the future disruption areas in the study area.

Nine susceptibility models were built using the Information Value method, one for each type of landslide for each landslide inventory. The obtained results are summarized in Tables 6.19, 6.20 and 6.21.

Table 6.19 – Information values obtained for each class of each predisposing factor for each landslide type and inventory. Part 1 (aspect, curvature and slope angle themes). Higher IV values are highlighted in bold.

Classes of Predisposing Factors	Occupancy area (%)	Dee-seated rotational			Shallow rotational			Shallow translational		
		LI#1	LI#1 + LI#2	LI#3	LI#1	LI#1 + LI#2	LI#3	LI#1	LI#1 + LI#2	LI#3
Aspect:										
Flat	0.2	-0.66	-0.73	-1.72	-0.66	-0.88	0.44	-0.78	-0.19	-0.74
North	10.1	0.05	0.05	0.44	-0.22	-0.42	0.25	-1.62	0.09	-0.20
Northeast	13.4	0.01	0.17	**0.46**	**0.38**	**0.31**	0.23	**0.62**	0.39	-0.01
East	12.3	**0.23**	**0.28**	-0.12	-0.37	0.12	-0.18	-0.13	0.00	**0.75**
Southeast	9.1	-0.01	-0.04	-0.83	0.15	0.09	**0.59**	-0.85	-0.49	0.04
South	11.2	-0.23	-0.31	-0.39	-0.58	-0.72	-0.12	-0.51	-1.02	0.36
Southwest	16.4	0.09	-0.04	-0.06	0.06	-0.04	-0.25	0.34	0.02	-0.81
West	16.2	-0.05	-0.08	-0.34	0.15	0.20	0.08	0.41	0.11	-0.31
Northwest	11.1	-0.22	-0.16	0.20	-0.05	-0.10	-1.31	-1.08	0.10	-0.37
Curvature:										
- <-0.05	41.6	-0.09	-0.03	-0.14	-0.30	-0.06	**0.35**	-0.24	0.03	-0.15
(-0.05) - 0.05	18.2	-0.20	-0.22	-0.19	0.16	0.03	-0.75	**0.44**	0.06	-0.28
0.05 - >	40.1	**0.16**	**0.12**	**0.20**	**0.18**	**0.04**	-0.23	-0.03	-0.06	**0.23**
Slope angle:										
0-5	17.7	-1.81	-1.99	-3.02	-1.08	-1.40	-2.25	-0.75	-1.17	-2.39
5. – 10	34.8	-0.42	-0.54	-0.68	-0.11	-0.35	-0.71	0.01	-0.36	-1.22
10. -15	27.5	0.32	0.28	0.44	0.00	0.13	0.25	0.09	0.10	0.37
15-20	12.1	0.52	0.60	0.68	0.59	0.63	0.34	0.46	0.65	0.90
20-25	4.5	0.71	0.85	**0.78**	0.56	0.67	1.30	-0.34	0.45	0.90
25-30	1.9	0.73	**0.91**	0.71	0.44	0.81	1.34	0.12	0.74	0.87
30-35	0.8	0.63	0.84	-0.13	0.52	0.85	0.61	**0.78**	0.90	0.30
35-40	0.4	0.69	0.80	-0.64	0.40	**1.21**	1.42	-3.51	**1.88**	0.80
>40	0.3	**0.77**	0.83	-0.45	**0.76**	1.10	**1.89**	-0.03	1.26	**1.12**

Table 6.20 – Information values obtained for each class of each predisposing factor for each landslide type and inventory. Part 2 (IWI, detailed lithology and soil depth themes). Higher IV values are highlighted in bold.

Classes of Predisposing Factors	Occupancy area (%)	Dee-seated rotational			Shallow rotational			Shallow translational		
		LI#1	LI#1 + LI#2	LI#3	LI#1	LI#1 + LI#2	LI#3	LI#1	LI#1 + LI#2	LI#3
IWI:										
0	1.4	-4.32	-3.86	-4.74	-3.17	-3.49	-2.32	-3.51	-2.08	-3.51
0.00001	1.0	-1.97	-2.12	-4.74	-3.17	-3.14	-2.32	-3.51	-2.01	-3.51
0.0001	2.1	-0.42	-0.51	-0.99	-0.49	-0.66	-0.32	**0.26**	-0.25	-0.68
0.001	15.0	0.07	-0.05	-0.20	**0.41**	0.20	-0.06	-0.02	-0.45	-0.14
0.01	64.8	**0.10**	**0.10**	**0.15**	0.03	0.08	-0.06	0.15	0.13	0.12
0.1	15.8	-0.32	-0.22	-0.31	-0.51	-0.37	0.37	-0.69	-0.06	-0.22
> 0.1	0.04	-0.21	0.09	-1.41	-0.53	**1.17**	**2.76**	-3.51	**0.62**	**1.87**
Detailed Lithology:										
Sandstone dominated complexes (upper Jurassic)	28.75	-2.25	-1.97	-1.53	-3.17	-3.49	-2.32	-3.51	-2.08	-3.51
Shale dominated complexes (upper Jurassic)	59.30	0.42	0.42	0.31	0.50	0.49	0.48	0.47	0.49	**0.49**
Limestones and marls (middle and upper Jurassic)	0.53	-0.91	-0.74	-4.74	**1.55**	**1.17**	-2.32	-3.51	-0.29	**0.49**
Sands (Pliocene)	0.71	-2.46	-1.44	-4.74	-3.17	-0.41	-2.32	**2.28**	**1.77**	-3.51
Dolerite	1.16	**1.62**	**1.53**	**2.41**	-3.17	-1.62	**1.12**	-3.51	-2.08	0.40
Aluvium (Holocene)	6.81	-4.32	-3.86	-4.74	-3.17	-3.49	-2.32	-3.51	-2.08	-3.51
Sandstone dominated complexes (Cretaceous)	0.53	-2.75	-2.86	-4.74	-3.17	-3.49	-2.32	-3.51	-2.08	-3.51
Sandstone dominated complexes (lower and middle Miocene)	0.25	-4.32	-3.86	-4.74	-3.17	-3.49	-2.32	-3.51	-2.08	-3.51
Limestones and claystones (upper Jurassic)	0.41	-4.32	-3.86	-4.74	-3.17	-3.49	-2.32	-3.51	-2.08	-3.51
Marls, sandstones and claystones (upper Jurassic)	0.04	-4.32	-3.86	-4.74	-3.17	-3.49	-2.32	-3.51	-2.08	-3.51
Sandstones, claystones and limestones (Miocene)	0.02	-4.32	-3.86	-4.74	-3.17	-3.49	-2.32	-3.51	-2.08	-3.51
Shale dominated complexes (Cretaceous)	1.25	-1.73	-1.49	-1.41	-3.17	-1.42	-2.32	-3.51	-2.08	-0.99
Shale dominated complexes (lower and middle Miocene)	0.24	-1.85	-1.60	-1.03	-3.17	-3.49	-2.32	-3.51	-2.08	-3.51
Soil depth:										
0 – 0.5	40.3	-0.03	0.03	**0.25**	-0.01	-0.01	-0.07	-0.09	**0.03**	0.21
0.5 – 1	54.9	0.03	-0.01	-0.15	**0.05**	-0.02	**0.10**	**0.09**	-0.01	-0.19
1 – 1.5	3.9	0.11	0.03	-1.00	-0.42	**0.47**	-2.32	-1.75	-0.72	**0.32**
1.5 – 2.08	0.9	**0.77**	**0.46**	-4.74	-3.17	-3.49	-2.32	-3.51	-2.08	-3.51

Table 6.21 – Information values obtained for each class of each predisposing factor for each landslide type and inventory. Part 3 (soils and morpho-structure themes). Higher IV values are highlighted in bold.

Classes of Predisposing Factors	Occupancy area (%)	Dee-seated rotational			Shallow rotational			Shallow translational		
		LI#1	LI#1 + LI#2	LI#3	LI#1	LI#1 + LI#2	LI#3	LI#1	LI#1 + LI#2	LI#3
Soils:										
Clay loam	34.5	0.06	0.13	0.20	0.42	0.38	-2.00	0.19	0.09	**0.81**
Loam	45.5	0.05	-0.01	-0.16	-0.45	-0.32	**0.66**	0.01	0.13	-1.27
Silt loam	10.6	-1.05	-1.17	-2.51	-2.13	-1.37	-0.54	-1.04	-1.55	-1.22
Silty clay	0.01	-4.32	-3.86	-4.74	-3.17	-3.49	-2.32	-3.51	-2.08	-3.51
Silty clay loam	3.2	0.26	0.32	**1.35**	**1.61**	**1.25**	-2.32	**0.95**	**0.44**	0.70
Sandy loam	3.5	0.24	0.27	0.52	-1.18	-0.54	-2.32	-0.45	0.34	-3.51
Loamy sand	1.5	-0.05	-0.10	-4.74	-3.17	-3.49	-2.32	-3.51	-2.08	-3.51
Clay	1.0	0.17	-0.05	-1.80	-0.50	-0.88	-2.32	-3.51	-2.08	-3.51
Sandy clay loam	0.3	**1.43**	**1.62**	-4.74	-3.17	-3.49	-2.32	-3.51	-2.08	-3.51
Morpho-structure:										
Orthoclinal slope	0.69	-0.28	-0.15	-0.76	-1.01	-1.39	-2.32	-3.51	-2.08	**1.95**
Cataclinal dip slope	17.74	-0.23	-0.34	-0.51	-0.22	-0.35	-1.02	0.03	-0.16	-0.67
Cataclinal underdip slope	2.06	-1.99	-2.03	-4.37	-2.98	-3.36	-1.71	-0.44	-0.66	-3.51
Cataclinal overdip slope	6.78	**0.58**	**0.57**	-0.02	0.06	0.17	**0.97**	**0.89**	**0.89**	0.34
Anaclinal normal escarpment	38.97	-0.19	-0.25	-0.34	-0.13	-0.26	-0.35	-0.04	-0.23	-0.63
Anaclinal subdued escarpment	3.70	-1.33	-1.53	-2.05	-1.10	-1.38	-1.37	-3.51	-2.08	-1.33
Anaclinal steepened escarpment	22.09	0.43	0.54	**0.63**	**0.66**	**0.77**	0.69	0.17	0.49	0.88
Not applied	7.97	-0.32	-0.40	0.47	-3.17	-3.49	-0.92	-3.51	-2.08	-1.53

Regarding the detailed lithology, for every landslide inventory, the dolerite followed by shale dominated complexes (upper Jurassic) are the lithological classes more prone to deep-seated rotational slides. The shale dominated complexes (upper Jurassic) seemed to be always the most unstable lithological class, since it includes the majority of landslide occurrences. However, the Information Value is not higher than dolerite because the study area is dominated by this lithological class (59.3%). According to the Information Value, the dolerite is very prone to deep-seated rotational sliding because it only occupies 1.16% of the total study area, and thus the proportion of landslides increases the Information Value. The limestones and marls (middle and upper Jurassic) and also the shale dominated complexes (upper Jurassic) are more prone to the occurrence of shallow rotational slides for LI#1 and for LI#1 + LI#2 (Table 6.20). However, for LI#3 beyond shale dominated complexes (upper Jurassic) also the dolerite seemed to be prone to shallow rotational sliding. Regarding the shallow translational slides, it can be seen that for LI#1 the class more susceptible to landslides is the shale dominated complexes (upper Jurassic), for LI#1 + LI#2 beyond the shale dominated complexes, also the sands (Pliocene) seemed to be prone to shallow translational sliding. However, for the LI#3 three classes are distinguished as more susceptible to shallow translational slides, respectively, shale dominated complexes (upper Jurassic), limestones and marls (middle and upper Jurassic) and dolerite. Similar to the dolerites, the high Information values assigned to limestones and marls (middle and upper Jurassic) and Sands (Pliocene), for the shallow rotational and shallow translational slides are due to the fact that these classes are very poorly represented in the study area (respectively, 0.53% and 0.71%), and therefore a small area containing landslide is enough to classify these areas as very susceptible due to its proportion of landslides.

Regarding the Information Value of slope angle, there are some discrepancies among the landslide inventories. Thereby, for LI#1, the slopes above 40º are more prone to deep-seated rotational slide. However, for LI#1 + LI#2, to the highest IV is found for the slope angle class 25º to 30º. For LI#3 the class more prone to deep-seated rotational landslide occurrence is 20º to 25º (Table 6.19). Slope angles above 40º are more prone to shallow rotational landsliding considering the LI#1. For LI#1 + LI#2 the class more prone to shallow rotational landsliding correspond to 35º to 40º and in LI#3 this situation changes to the

class 30º to 35º (Table 6.19). Regarding the shallow translational slides the class 30º to 35º seemed to be more susceptible. For LI#1 + LI#2 the higher susceptibility class is from 35º to 40 º and for LI#3 is above 40º. Generally, we can conclude that the landslide occurrence, in the study area, is more related to slope angles above 20º, being the more significant the classes ranging between 30º to 40º.

According the morpho-structure the classes cataclinal overdip slope and anaclinal steepened escarpment seemed to be more prone to deep-seated rotational landsliding for IV#1 and IV#1 + IV#2. For the IV#3 only the anaclinal steepened escarpment seem to be more prone to deep-seated landsliding. The cataclinal overdip slope and anaclinal steepened escarpment seem to be always the classes more prone to shallow rotational landsliding, regardless the inventory. The same happens for shallow translational landslides. Thereby, it is concluded that any of the two morpho-structural classes (Cataclinal overdip slope, Anaclinal steepened escarpment) are very susceptible to landslides regardless the type and inventory.

Once calculated, the Information values were assigned to the respective class of its respective variable in order to be, subsequently, summed through the *Raster Calculator* tool of the *ArcGIS* software. From this procedure resulted nine maps of landslides susceptibility, respectively, three deep-seated landslide susceptibility map for LI#1, LI#1 + LI#2 and LI#3, three shallow rotational slide susceptibility maps for LI#1, LI#1 + LI#2 and LI#3 and three shallow translational slide susceptibility maps for LI#1, LI#1 + LI#2 and LI#3. All these maps were reclassified into the four classes described in the previous section (Fig. 6.10, 6.11, 6.12 and Tables 6.22, 6.23, 6.24).

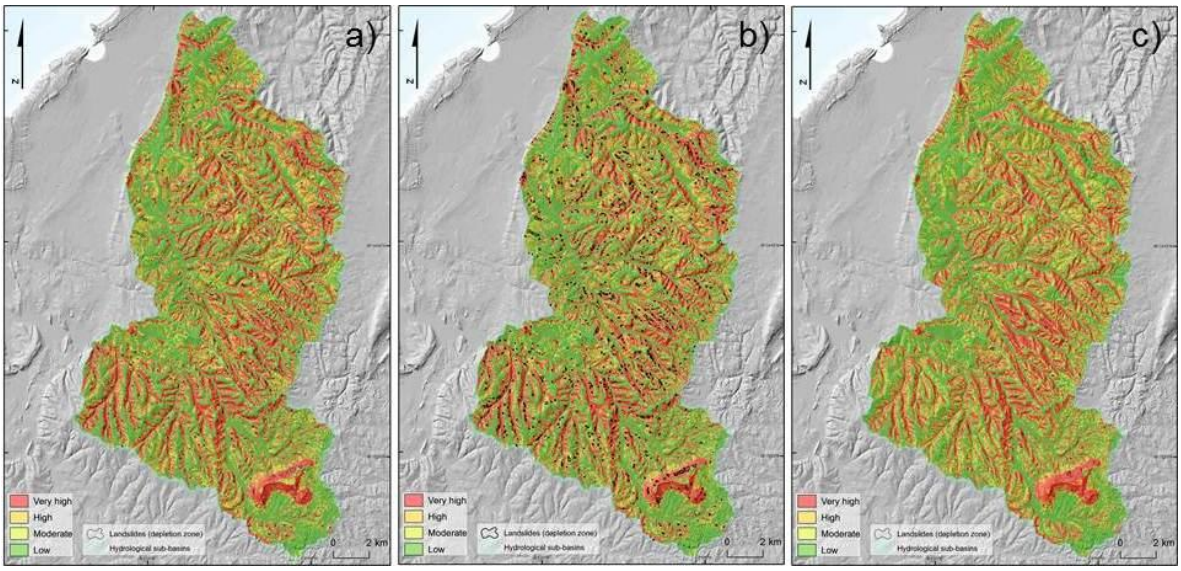

Fig. 6.10 – Deep-seated rotational slide susceptibility models assessed thought Information Value method based on: a) LI#1; b) LI#1+LI#2; c) LI#3.

Table 6.22 – Deep-seated rotational slide susceptibility: occupancy of each class.

	LI#1		**LI#1+LI#2**		**LI#3**	
	(Km^2)	(%)	(Km^2)	(%)	(Km^2)	(%)
Very high	79.5	28.8	79.9	29.0	73	26.5
High	39.6	14.4	36.7	13.3	42.8	15.5
Moderate	34.1	12.4	35.5	12.9	44.4	16.1
Low	122.7	44.5	123.8	44.9	115.7	41.9
SUM	275.9	100	275.9	100	275.9	100

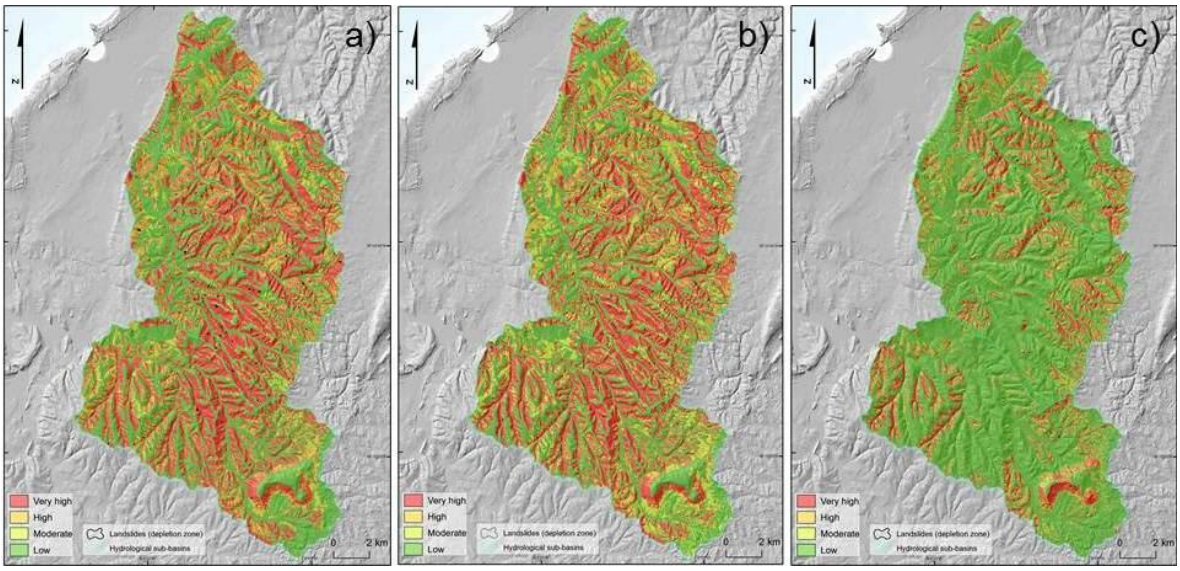

Fig. 6.11 – Shallow rotational slide susceptibility models assessed thought Information Value method based on: a) LI#1; b) LI#1+LI#2; c) LI#3.

Table 6.23 – Shallow rotational slide susceptibility models: occupancy of each class.

	LI#1		**LI#1+LI#2**		**LI#3**	
	(Km^2)	(%)	(Km^2)	(%)	(Km^2)	(%)
Very high	95.3	34.5	97.4	35.3	35.7	12.9
High	34.1	12.4	23.9	8.7	19.6	7.1
Moderate	23.3	8.4	46.5	16.9	20.8	7.5
Low	123.2	44.7	108.1	39.2	199.8	72.4
SUM	275.9	100	275.9	100.0	275.9	100

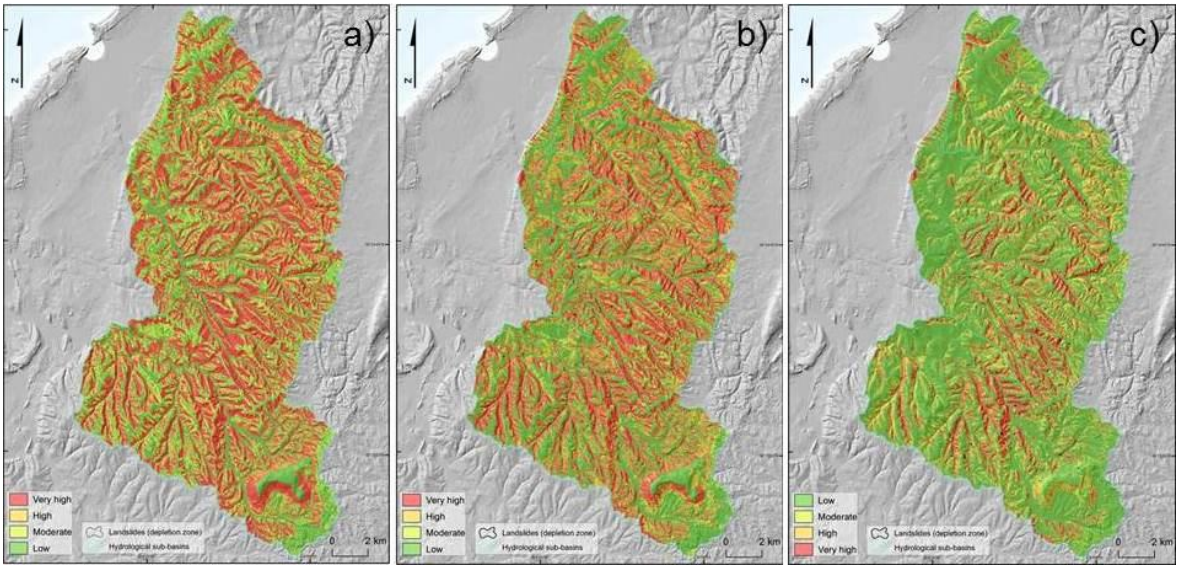

Fig. 6.12 – Shallow translational slide susceptibility models assessed thought Information Value method based on: a) LI#1; b) LI#1+LI#2; c) LI#3.

Table 6.24 - Shallow translational susceptibility models: occupancy of each class.

	LI#1		**LI#1+LI#2**		**LI#3**	
	(Km^2)	(%)	(Km^2)	(%)	(Km^2)	(%)
Very high	111.6	40.4	88.5	32.1	32.3	11.7
High	26.9	9.7	39.4	14.3	33.4	12.1
Moderate	65.3	23.7	40.8	14.8	47.5	17.2
Low	72.1	26.1	107.2	38.9	162.7	59.0
SUM	275.9	100	275.9	100	275.9	100.0

When analyzing the landslide susceptibility maps, in a joint perspective, it is possible to conclude that there are two distinct parts in the study area. Generally, the Fig. 6.10, 6.11 and 6.12 identifies, the Western part of the study area as less susceptible to landslides, whereas, the center and East parts, of the study area are more susceptible to landslides. However, for the specific case of shallow rotational slides from the LI#3, the result does not follow the generality. This is probably due to the fact that in this LI the non-pure shallow rotational slides were kept apart for further built the shallow translational slide susceptibility model. Probably there are also non-pure rotational slides in LI#1 and in

LI#1+LI#2, however those ancient landslides were not possible to be validated through field work and thus, not possible to assure its degree of rotationally. Regardless the LI, the Todo-Mundo hill (where dolerite outcrops) together with the slopes of the main valleys (Arnoia, Tornada and Alfeizerão), are the places more susceptible to deep-seated rotational sliding.

The slopes of the main valleys (Arnoia, Tornada and Alfeizerão) are the most susceptible places for shallow landslides. The Todo-Mundo hill together with the Western part of the study area is less susceptible to shallow landslides (rotational and translational). The soil depth of the Todo-Mundo hill is very thin and therefore the shallow landslides will rarely occur in these places. However, the deep-seated rotational slides, which can occur independently of the soil thickness, will occur more easily on these locations than the shallow landslides.

For the landslide susceptibility models based on the LI#3, it can be observed a distinction between the location of the susceptibility areas to shallow rotational and shallow translational slides. The latest, are mostly located on the Center/Northern part of the study area, whereas, the same place is identified as the least susceptible to shallow rotational slides (Fig. 6.12:b).

6.3 Analysis and validation of results

As for the static physically-based model, also the statistically-based model were submitted to a validation through the prediction and, in this case, success rate curves. In order to determine the success rate, the susceptibility map should be crossed with the same landslide inventory that was used to build the susceptibility model. This procedure allows defining the degree of adjustment of the model to the input data (e.g., Zêzere, 2010) i.e., the success rate curve is obtained by varying the decision threshold and plotting the respective sensitivities against the total proportions of the data set classified as landslide. For the predictive rate, the validation process requires that the susceptibility maps should be crossed with a group of landslides independent from those that were

used to generate the respective susceptibility model, i.e., prediction rate curves are the same as success rate curves, except that they are computed for landslide distribution patterns (possibly in the training area) for a posterior time than the training data sets temporal domain. This means that the landslide inventories must be divided into two separate groups (Chung and Fabbri, 2003). This partition was not done for the physically-based models since it does not take into account the location of past landslides for modeling purposes.

For this work six predictive rate curve were made in order to define the predictive capacity of the susceptible models, of deep-seated rotational, shallow rotational and shallow translational landslides from LI#1 and LI#1 + LI#2. Therefore, the susceptible model to deep-seated rotational slides based on LI#1 was validated using the deep-seated rotational slides from LI#2+LI#3. The susceptible model to shallow rotational slides based on LI#1 was validated using the shallow rotational slides from LI#2+LI#3. The susceptible model to shallow translational landslide based on LI#1 was validated using the shallow translational slides from LI#2 + LI#3.

On the other hand, the susceptible model to deep-seated rotational slides based on LI#1+LI#2 was validated using the deep-seated rotational slides from LI#3. The susceptible model to shallow rotational slides based on LI#1+LI#2 was validated using the shallow rotational slides from LI#3 and the susceptible model to shallow translational slides based on LI#1+LI#2 was validated using the shallow translational slides from LI#3 (Table 6.25). The susceptible models based on the landslides from LI#3 were validated through a success rate curve with the same set of landslides from the same LI, regarding to the landslide typology. As it was already mentioned, the landslides used for validating, through a predictive rate curve, for the LI#1 and LI#1 + LI#2, were the landslides that occurred in a posterior time (Table 6.25 and Fig. 6.13 and 6.14). For the LI#3, since there are no posterior landslides, the same set of landslides used for modeling were also used for validating (Table 6.25 and Fig. 6.15).

Table 6.25 – AUC values for the landslide susceptible models assessed through the Information value method.

Case	Modeling group	Validation group	Landslide typology and depth			Validation type
			Deep-seated rotational	Shallow rotational	Shallow translational	
A	LI#1	LI#2 + LI#3	0.78	0.74	0.70	Prediction curve
B	LI#1 + LI#2	LI#3	0.78	0.72	0.75	Prediction curve
C	LI#3	LI#3	0.81	0.90	0.88	Success curve

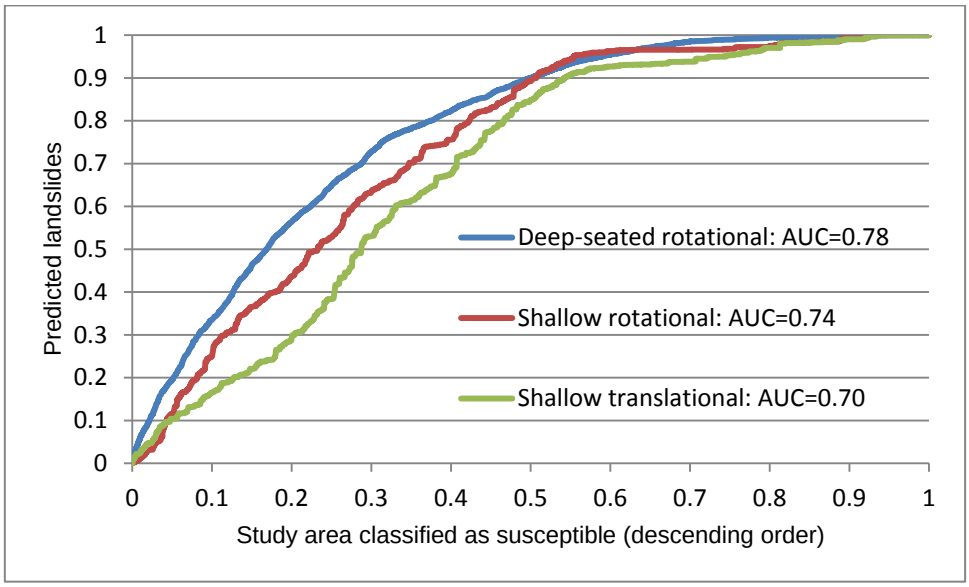

Fig. 6.13 – Prediction rate curves for case A.

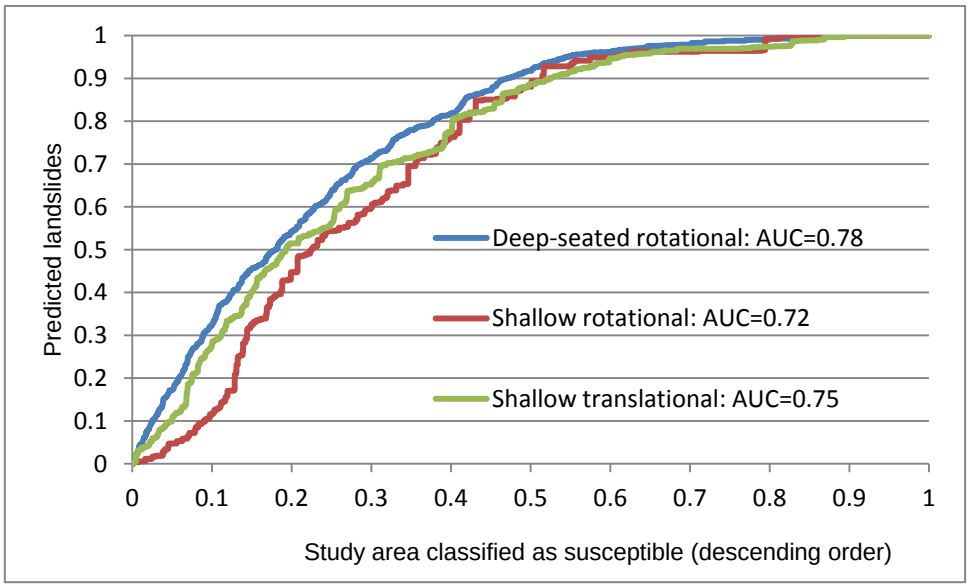

Fig. 6.14 – Prediction rate curves for case B.

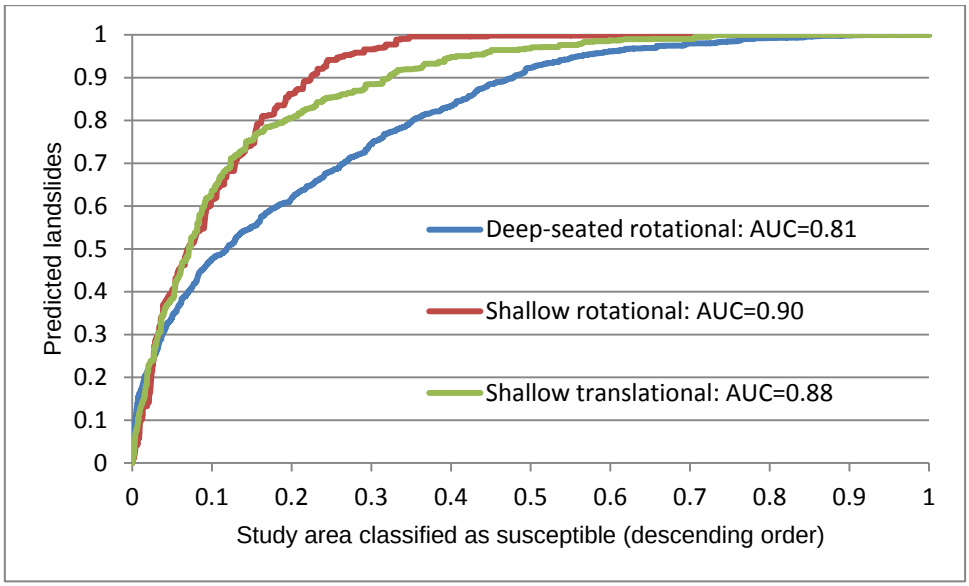

Fig. 6.15 – Success rate curves for case C.

The prediction rate curves obtained for the case A (Table 6.25 and Fig. 6.13) seem to be acceptable, (according to the values stipulated by Guzzetti (2005) with a 0.78 AUC value for the susceptible model to deep-seated rotational slides. However, for the shallow rotational and translational susceptibility models these values are lower, though, without ever decreasing below 0.70.

For the case B (Table 6.25 and Fig. 6.14) there are two types of landslides, respectively the deep-seated rotational and the shallow translational, which seem to have an acceptable performance according to the AUC values (0.78 and 0.75, respectively). The shallow rotational landslide susceptibility model has a lower value of AUC, however very close to the acceptable (0.72).

It is noteworthy that the inventories of ancient landslides were not subjected to a field validation, as the recent landslide inventory. The georeferencing and the orthorectifying processes, which were necessary steps for oldest landslide inventory recognition and drawing, could have also lead to error. Another important difficulty, that must be mentioned, was the difficulty in recognizing and differentiating into the different types of landslides, which, due to the scale of analysis, and due to a non field validation, could have also led to error and thus to lower AUC values of prediction rate curves.

The case C (Table 6.25 and Fig. 6.15) must be observed with caution since it is not validated through a prediction rate curve, but, through a success rate curve. In this case, according to the AUC values, regardless the landslide type, the models present always a good performance. The shallow rotational landslide susceptibility model can be enhanced as the best susceptibility model (with an AUC value of 0.90, which makes it an excellent model) followed by the shallow translational susceptibility model (0.88) and by deep-seated rotational susceptibility model (0.81).

The high AUC values for shallow landslides based on LI#3 may indicate that the separation of the non-pure shallow rotational slides from the pure shallow rotational slides was an asset to increase the performance of the susceptible models to shallow landslides (rotational and translational).

6.4 Comparison between the statistically-based methods and static physically-based methods

Due to many parameters involved in the landslides phenomena, no single perfect method exists to identify and map landslides, to ascertain landslide susceptibility and hazard, and to evaluate the associated risk (Guzzetti, 2005). In line with this, in this section it will be made a comparison between the results of the shallow translational landslide susceptibility obtained through two different methods for predict landslides, respectively, the static physically-based method and the statistically-based method without, however, neglecting the intrinsic advantages and disadvantages of each.

The result from the dynamic physically-based method was not considered here, for comparison, since it takes into account different kind of nature of inputs (dynamic inputs),.whereas the static physically-based method take into account static inputs such as the statistically-based methods.

Regarding the statistically-based model, the susceptible model to shallow translational slides based on LI#1+LI#2 was chosen to be compared with the susceptible model based on static physically-based model. This choice was done since the susceptible model based on LI#1+LI#2 has better performance than the susceptible model based on the LI#1 and because, like in all cases of the physically-based models, it was subjected to a prediction rate curve using the shallow translational slides from LI#3. The susceptible model derived from the static physically-based method chosen for comparison corresponded to scenario 11 (15 day of accumulated rainfall) since, according to AUC value, it is more close to the AUC value obtained for the statistically-based model and because, considering all scenarios, this is the scenario which the SF ≤1 area predicts more landslide area. It must be taken into account that, this scenario, correspond only to a possibility that could happen if the critical rainfall and return period (from Batalha county) selected for modeling, fitted the study area reality (Table 6.26).

In fact, deterministic models do not require a dependent variable (landslides) for modeling. However, for the present case, these elements were quite important for calibration and validation purposes, i.e., for parameterization of the variables, in order to fit the reality of the study area.

In order to perform the comparison a reclassification was made in both maps. Thereby, the susceptible maps were reclassified into 4 classes (quartile) by taking into account the susceptibility values (each class with 25% of the total study area), sorted in ascending order, which allowed maintaining a visual consistency in both maps (Fig 6.16 and 6.17).

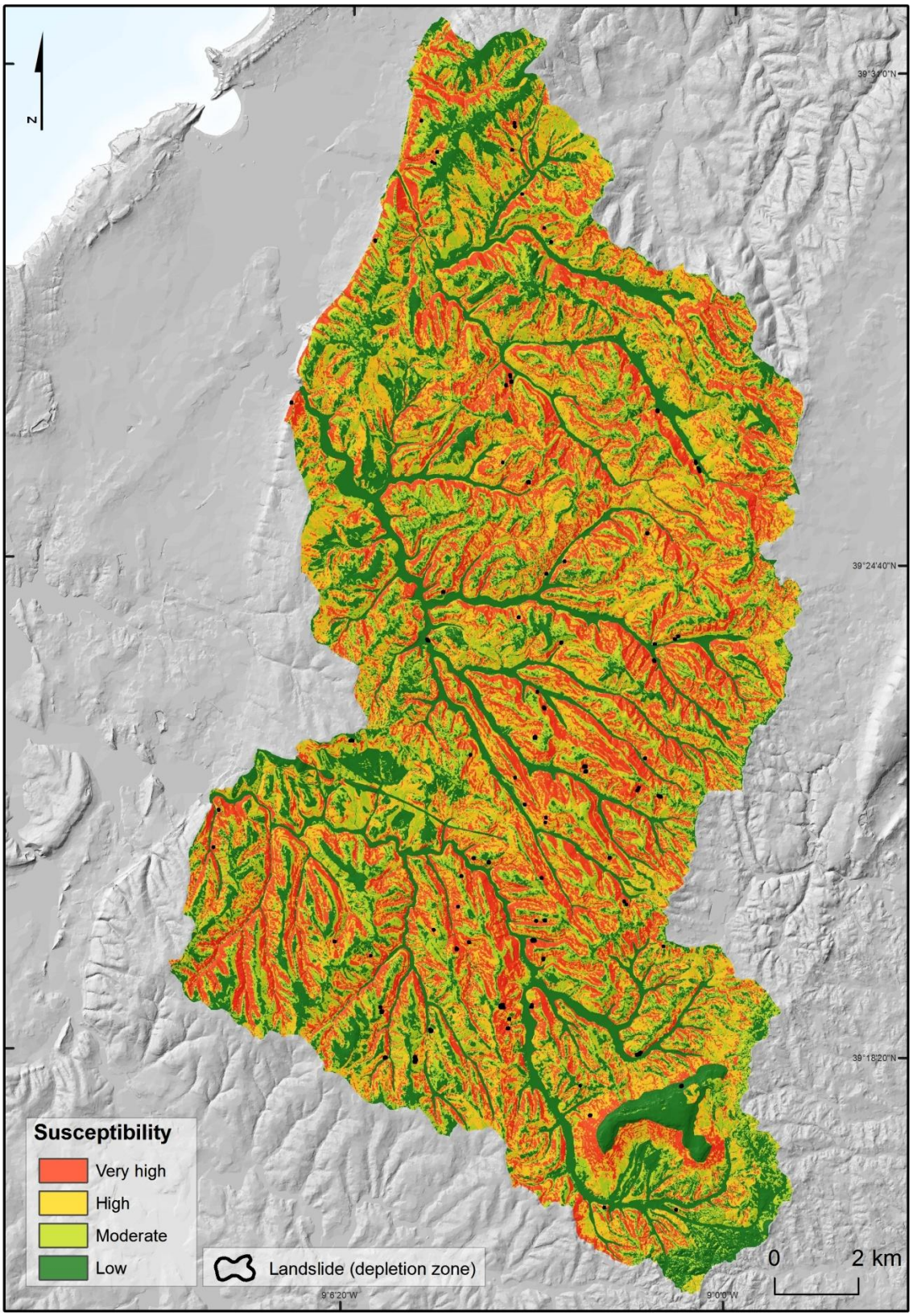

Fig. 6.16 – Shallow translational slides susceptibility assessed through the statistically-based method (SBM) classified through quartile.

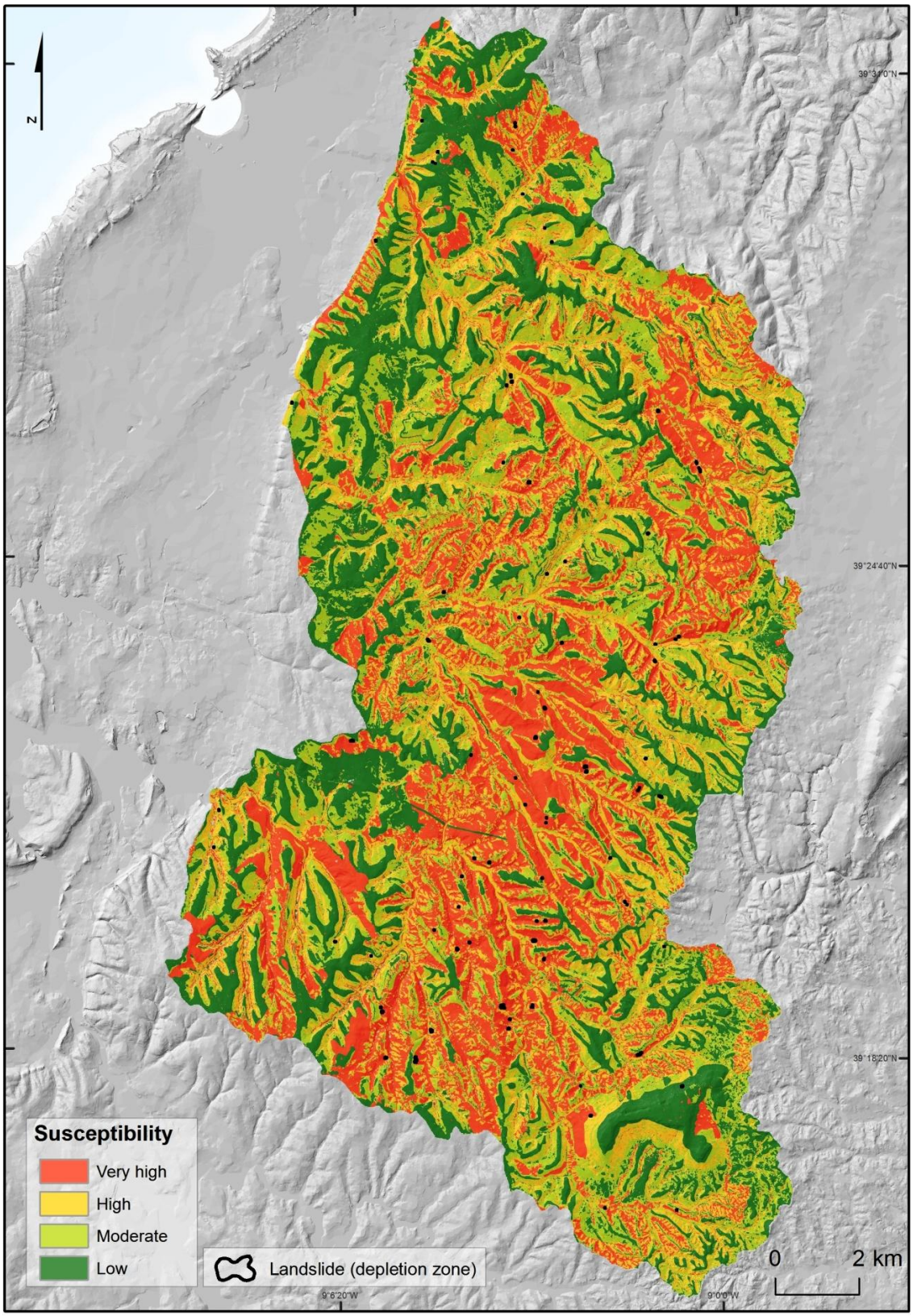

Fig. 6.17 – Shallow translational slides susceptibility assessed through the physically-based method (PBM) classified through quartile.

From Fig. 6.16 and 6.17 is possible to observe that the susceptible model based on the statistically-based method presents a more equitable trend along the study area, whereas, the susceptible model based on the physically-based method has a tendency to high susceptible values on the central part of the study area. The East part of the study area is dominated by low susceptible values. In both maps the Todo-Mundo hill is the safest place in what shallow translational slides concerns.

However, for an analytical comparison just the unstable (rupture) area corresponded to SF ≤ 1, was selected from the physically-based model (Table 6.26). The same area, corresponding to 24.7% of the total study area, classified with high susceptibility was also selected from the statistically-based model (Fig. 6.18).

Table 6.26 - Landslides susceptibility classes, for shallow translational slides obtained through the static physically-based method for the scenario 11 (see chapter 5).

Safety Factor (SF)	**Slope Stability**	**Occupancy of the study area**	
		(km^2)	**(%)**
SF ≤ 1	Unstable (rupture)	68.2	24.7
1 <SF< 1.25	Unstable (likely rupture)	15.0	5.4
1.25 <SF< 1.5	Marginally Unstable	10.1	3.7
1.5 <SF< 2	Marginally Stable	16.9	6.1
SF> 2	Stable	165.7	60.1
TOTAL		275.9	100

The unstable areas from both maps were crossed and the overlapping was assessed. This procedure allowed understanding the degree of concordance between both maps (Fig. 6.18). Then, those areas were again crossed tabulated with the shallow translational slides from LI#3 in order to quantify and validate the instability in the unstable areas modeled by the statistically-based method and by the physically-based method (Table 6.27).

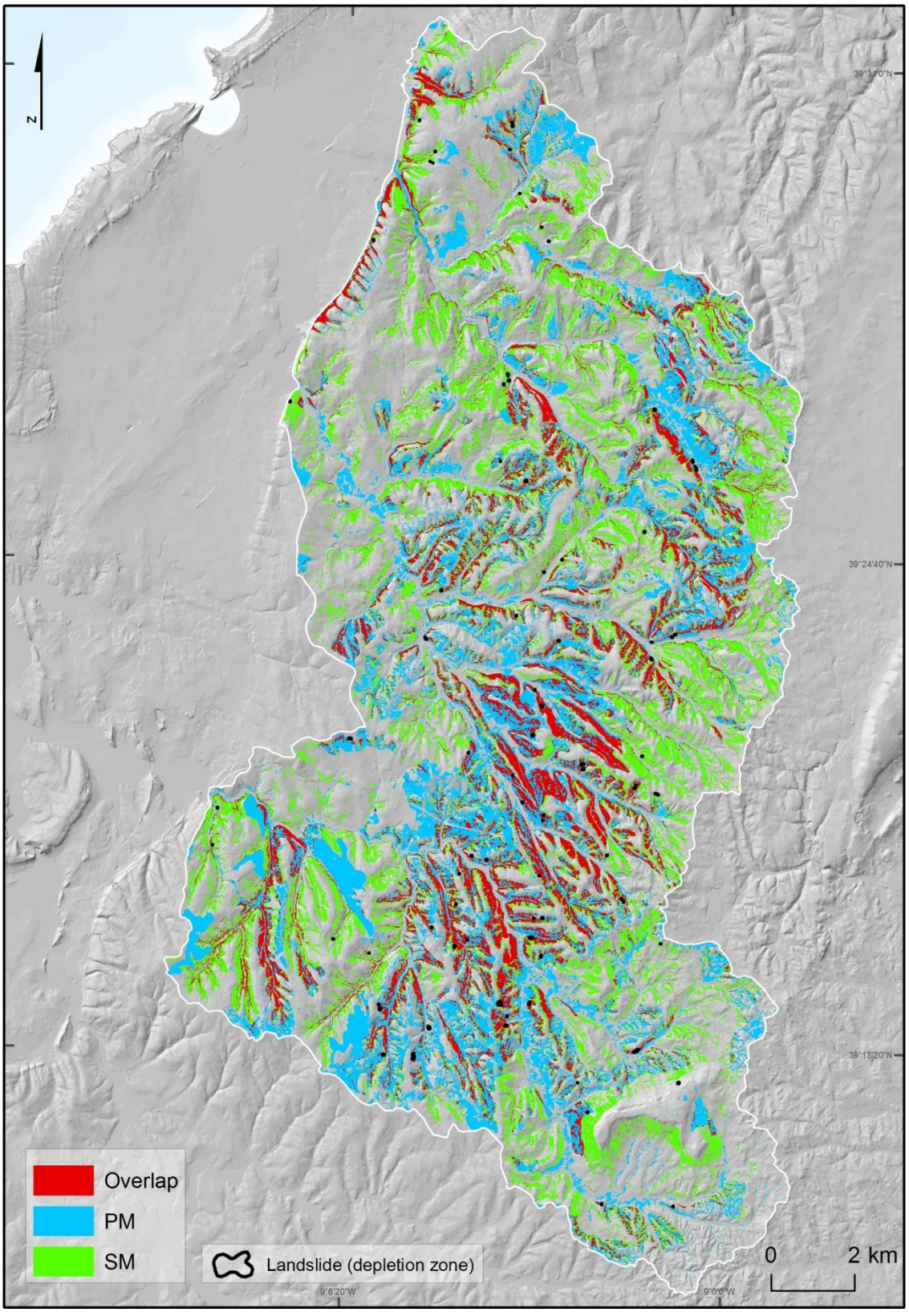

Fig. 6.18 – Shallow translational slide susceptibility represented by the 24.7% of the study area more susceptible, obtained from: 1) the statistically-based method (SBM); 2) the physically-based method (PBM); 3) and their overlapping. To facilitate visualization landslides depletion boundaries were magnified.

Table 6.27 – Comparison between the landslide susceptible maps modeled with physically (PBM) and statistically (SBM) based methods. Total 24.7% of the study area classified with high susceptibility (class below SF < 1, according to scenario 11, see chapter 5).

	Total area		**Landslide area**	
	km^2	%	m^2	%
Overlap	24.4	8.9	17218.6	40.3
PBM	43.6	15.8	13761.6	32.2
SBM	43.6	15.8	6739.234	15.8

PBM: Physically-based method
SBM: Statistically-based method

According to Table 6.27, it is possible to observe that, the results obtained through the physically-based method present better predicting skills with 24.7% of the total study area than the model obtained through the statistically-based method.

The overlapping between both susceptible models is about 36% and from this area 40.3% of the total shallow translational slides from LI#3 can be predicted. However, regarding the results obtained through physically-based method, it is important to highlight the fact that the model can actually predict 72.5% of the total shallow translational slides from LI#3 while the statistically-based model only predicts 56.1%.

From these results it can be concluded that the deterministic (physically) model presents a good performance. Hence, it can be considered that for a determinist approach, such results are indeed good, especially for a regional scale.

CONCLUDING REMARKS

CONCLUDING REMARKS

Several methods were implemented in order to explain the spatial and temporal distribution of landslides at a regional scale. The Arnoia, Tornada and Alfeizerão sub-catchments (275.9km^2) where selected due to their geologic and geomorphologic characteristics and due to the observed slope instability.

In order to assess the spatial and temporal slope instability 10 specific objectives were previously defined which intended to further answer the main goal of this work, throughout the chapters of the dissertation:

1) Multi-temporal landslide inventory and classification according to the type of movement and estimated depth in the Arnoia, Tornada and Alfeizerão sub-catchments, since 1958 to the present;

The application of different techniques and methods, of landslides inventorying, allowed identifying 1489 landslides within the Arnoia, Tornada and Alfeizerão sub-catchments. Additionally, the mapped landslides were classified according to the landslide typology and depth.

Multi-temporal landslide inventories were developed through the identification and mapping of ancient landslides from aerial photographs obtained in 1958 and 1982 and through field work identification and mapping of recent landslides. For such work it would be desirable to have the precise date of occurrence of landslides. However this task revealed to be unachievable.

From this work resulted: i) two ancient landslide inventories (LI#1 and LI#2 obtained by aerial photo-interpretation from, respectively, 1958 and 1982); ii) one inventory of landslides occurred recently (LI#3 through the previous identification on orthophotomaps

from 2004 and further field work validation performed from 2006 to 2011), at 1:10,000 scales.

Some of the shallow rotational slides indentified and mapped in LI#3 did not present a pure rotational behavior. Since these types of landslides generally affect the local agricultural activity, it was decided to keep them separately. Then, together with the pure shallow translational slides, a new set of shallow slides inventory was created in order to validate the physically-based models to assess susceptibility.

Despite not having the higher area among all the landslide types, the shallow translational slides (LI#3) happen more often throughout the study area than any other type of landslide. However, since the study area is dominated by agriculture, their evidences are much more difficult to map in the field because it is constantly removed by farming activity. Thus, it became crucial to obtain susceptibility models to shallow translational slides, either by their frequency in the study area and by its consequences on the agriculture and economics of the study area.

During the field work, in some places of the study area, it was not possible to map landslides due to the inaccessible terrain. This fact could mask some conditions where, in reality there is susceptibility but, due to the absence of past landsliding, the statistical models cannot precisely predict future instability in those areas.

2) Acquisition and production of new themes based on modeling and field observation (e.g. detailed lithological map, morpho-structural map, DEM, soil depth);

In order to obtain a correct distribution and variation of soil physical properties a detailed geological survey was carried out at 1:10,000 scale, based on interpretation of aerial photographs (1958) and field mapping focused on structural and lithological character of each geologic formation. Through the lithological improvements, it was possible to understand that landslide types and pattern are controlled by the lithological settings and, in particular, by the position of relative abundance of hard, weak or soft rocks, and

by the local hydrogeological setting and the attitude of permeable and impermeable layers. Not performing such lithological detailing layer would lead to error, since the landslide abundance and pattern vary largely within the same lithological complex, which is characterized by different geotechnical and hydrogeological properties. Thus, from the previous aggregated sandstones and claystones it was possible to observe that the detailed shale dominated complexes are more prone to landsliding than the detailed sandstones dominated complexes. Shallow landslides were identified only on shale dominated complexes which causes an increase of the importance weight of landslide susceptibility on this lithological class. However some deep-seated landslides were identified on more resistant rocks (sandstones dominated complexes).

Regarding the landslide density, two lithological classes on the previous lithological map were evidenced for having higher values such as dolerite and sandstones and claystones complexes, but, through the lithological improvements by discriminating the sandstones and claystones complexes into shale dominated complexes and sandstones dominated complexes was possible to settle that the shale dominated complexes is much more important in what landslide density concerns than the sandstone dominated complexes.
According to the global accountability and reliability scores, it is reasonable to conclude that there was a significant improvement in the lithological map. The detailed lithological map has a better discriminating power than the previous lithological map, performing better the landslide susceptibility analyses with the separation of relevant classes.

Modeling the morpho-structural settings, at a 1:10,000 scale, revealed also to be important in order to enable more detailed data versus the previous geological data already existing (at a 1:50,000 scale) which proved to be very homogeneous and constant throughout the study area producing, thus, lower quality results when assessing landslide susceptibility.

The Geobed script seems to be a reliable method for obtaining bedding attitude (BA) quantitative data. The higher uncertainty values of angular standard deviation of the dip direction are more related to sub-horizontal strata than with probable associated errors,

as also concluded by field work. There were only 19 BA points actually related to the positioning, identification and/or presence of folds errors which have been previously removed from the modeling methods.

The landslide density, which is most important for further susceptibility assessment, seemed to be higher for cataclinal overdip slopes and anaclinal steepened escarpment. The deep-seated translational slides occur on cataclinal overdip slopes and cataclinal dip slopes.

Despite the considerable morpho-structural heterogeneity, similarities between landslides types and patterns were identified specially for deep-seated landslides, namely: the presence of discontinuities dipping toward the free face of slope (cataclinal overdip slope) or into the slope (anaclinal steepened escarpment).

The distribution and the slope failure depth of landslides reflect the structural control exercised by the bedding attitude. Regarding the shallow landslides, although theoretically a more random distribution may exist in what BA classes concern it is observed that the classes with more landslide occurrence are the anaclinal normal escarpment and anaclinal steepened escarpment. This is due to the fact that those classes have the highest percentage of occupancy in the study area and therefore are more likely to contain steep slopes and thus more susceptible to landslide occurrence.

In specific cases the dynamic hydrological model (STARWARS) can incorporate also the morpho-structural data which can influence the lateral groundwater flow. However, this has not been done since the study area is dominated by lower dip angles (below 30^{o}), which, according to Philip (1990) would lead to redundancies. Whereas, when introduced as a predisposing factor in the statistical models revealed to have a relative high weight importance (according to the sensitive analysis).

The acquisition of a high resolute Digital Elevation Model (DEM) is of crucial importance for every modeling method. Thus, in order to carry out a further more detailed geomorphologic analysis a detailed DEM of the study area was carried out. Subsequently

the optimized DTM were used to derive variables such as slope angle which is one of the most important controlling variables for the occurrence of landslide in any modeling method.

The soil depth is also a very important input of the physically-based models, however, this is one of the least understood and difficult to obtain physical variable. For this reason a soil depth model was performed using a method proposed by Catani et. al (2010), which is based on DEM data, digital geological maps and general information on the land-surface units. The main characteristics and advantages of using this model is that: 1) it is performed for catchment-scale analysis; 2) it is possible to implement within a Geographic Information System; 3) it has a wide availability and low cost of the required parameters; 4) it promotes a balanced consideration of topographic attributes in conjunction with geological and/or geomorphologic factors.

In order to quantitatively define the system responses of the soil depth model, a calibration was done. This procedure was based on the lowest Root Mean Square Error (RMSE) value founded, between the modeled values and the field measured values of soil depth (using 75% of the field measured sites). Subsequently, in order to ensure the quality of the soil depth data, a validation based on the same method was performed (using the remaining 25% of the field measured sites).

The final soil depth map reflected the commitment between the four soil depth contributing factors (constant Kc, profile curvature, catenary position within the hillslope profile and slope angle). As expected, on the colluvial areas, where simultaneously the bedrock is less resistant to erosion, the soil thickness is higher. In contrast, on interfluves areas, where the bedrock is simultaneously more resistant to erosion, the soil thickness is thinner. The soil depth map achieved through the sGIST model was of crucial importance for modeling the landslide susceptibility through the physically-based methods and it was also used as a predisposing factor for the statistically-based method.

3) Acquisition of soil characteristics according to the hydrogeological and geotechnical properties of soils (through field work, laboratory measurements and back analysis);

This step was made in order to understand the role of the physical properties and the local hydrological conditions of the study area, for landslide occurrence. Initially there was no information on the geotechnical parameters for the study area and for this reason, based on the detailed lithological map six collections of soil samples were made for further laboratory analysis. This procedure was only possible to be performed on the dominant lithologies (shale dominated complexes and sandstones dominated complexes). Further, to improve the geotechnical parameters, a systematic back analysis of landslides was performed. This method was applied in order to calibrate the geotechnical parameters according to the behavior of the covering soils, present on the study area. From this procedure resulted shear strength parameters (c` and $\phi$`) coinciding with the conditions at the time when the mass movement occurred for each lithological unit containing landslides. For the remaining lithologies (less spatial dominant), the geotechnical parameters were acquired through bibliographic references.

Due to the nonexistence of previous work related to the hydrological properties of soil, carried out in the study area, and since it was not possible to perform laboratory measurements, a standard approach developed by Rawls et al. (1982) was used. Therefore the hydrogeological parameters were assigned to each soil type classified according to the United States Department of Agriculture (USDA) soil texture classes (saturated hydraulic conductivity, effective saturation, bubbling pressure (air entry), total porosity, pore size distribution index and capillary pressure) for further hydrological modeling.

4) Landslide susceptibility using the hydrological model coupled to slope stability model under static temporal conditions. Validation through the quantification of the model prediction rate;

The hydrological and slope stability behavior of the study area was calculated through the implementation of SHALSTAB method. Such method assumes that landslides occur mostly due to an intense and/or prolonged rainfall event, and reflects the effect of soil saturation and consequently loss of shear strength. To estimate the ratio between saturated and dried soil, the model takes into account the contribution of the upstream area per land unit width, the effective precipitation, the transmissivity of the soils and the slope angle.
Under static conditions, as in the SHALSTAB model, a same single value of precipitation is taken into account for all the terrain units (pixels) of the study area. Since there was no data to perform such calculations, values of critical precipitations, calculated for a neighboring area, were used in order to build hypothetic scenarios. Those scenarios are only an approximation of what could happen if the critical thresholds of the neighboring fitted the reality of the study area. Due to the adjustments of K_{sat} data and to critical rainfall scenarios it was possible to obtain 11 different scenarios.

The scenarios obtained with the previous standard values of K_{sat} were overestimated and, according to the Area Under Curve (AUC) of the prediction rate, not reliable for landslide forecast. This situation changes drastically when the modeling is based on the calibrated values of K_{sat}. The models based on the calibrated values of K_{sat} revealed a much smaller area of higher susceptibility classes when compared to the maps based on the initial values of K_{sat}.

According to the calibrated values of Ksat and considering only one day of effective precipitation the model can be assumed as having a good performance (with an AUC of 0.81), however, when analyzing the SF≤1 area the model with best predictive ability is the one corresponding to scenario 11 (15 days of accumulated rainfall).

The adjustment of the K_{sat} values turns out to be critical for improving the results. The improvement of the geotechnical data through back analysis also increases the robustness of the models, although in a softer manner.

5) Acquisition, processing and modeling of long term climatic data;

The long term climatic data were acquired and modeled in order to enter the dynamic physically-based model. The temporal dynamic climatic data acquired were, respectively: 1) daily precipitation; 2) daily radiation; 3) daily temperature; 4) daily evapotranspiration. According to several authors, precipitation is the main factor triggering landslides, however, it must not be neglected the evapotranspiration which, globally reduces the water rainfall in about 62%, reducing, thus, the water available for infiltration and for percolation. In this sense, the input of net precipitation has to be balanced against the loss of the soil moisture by evapotranspiration.

Precipitation data was available as 24 hour totals from the Sistema Nacional de Informação de Recursos Hídricos (SNIRH) for eleven meteorological stations located within or near the study area, namely: Alfeizerão; Cela; Salir de Matos; Óbidos; Asseiceira; Alcoentre; Alvorninha; Santa Catarina; Vermelha; Vimeiro; Turquel.

A considerable time length, from 1975/1976 to 2011/2012, was choose in order to evaluate the behavior on the field throughout these hydrological years and also due to the available real discharge data (from 1977/1978 to 1989/1990), which were used for calibrating the spatial-temporal hydrological model (STARWARS). The length of the record was thus 37 years, which is close to the conventional 30 years used in climatic research. The missing values were calculated through regression. To produce the continuous spatial daily rainfall maps (daily total and duration) the Inverse Distance weight (IDW) interpolator was used.

The large differences between the individual hydrological years are reflected by the seasonal variability. The average daily precipitation (calculated from the daily totals over

the period 1975/1976 to 2011/2012) exhibits a large range over the period of 37 years in every meteorological station.

The solar radiation was also daily calculated since it is an important input parameter to assess evapotranspiration. For calculating such data an approach, given by Dingman (2002) was performed. This methodology includes the solar constant, the latitude of the study area, the angular velocity and several previous calculations such as extraterrestrial radiation, day angle, eccentricity correction, declination, solar sunrise and solar sunset. This data was achieved as a map series, for each Julian day (with the same spatial value but different temporal value).

The effective evapotranspiration was obtained by multiplying the reference potential evapotranspiration (1) with the crop factor (2):

1) The reference potential evapotranspiration was calculated through the Hargreaves equation, which takes into account temperature and incident radiation. The temperature data were obtained as daily records for four meteorological stations, namely: Cela; Óbidos; Asseiceira and Alcoentre. Then, for daily continuous map acquisition, the *IDW* interpolating method was performed by incorporating also the Lapse rate, i.e., the rate of decrease with height for temperature;

2) The crop factor was achieved through the sum between the crop transpiration, and soil evaporation. To obtain the parameters needed for calculating the transpiration component (K_{cb}), the Land use, derived from *Direcção Geral do Teritório* (DGT) at a 1:25,000 scale, was used. Such kind of data discriminates the types of vegetation, which is crucial for converting into the global ecosystem types for subsequently estimate specific parameters for calculating the crop transpiration, such as the leaf area index, ground covering and plant height and the growth of the vegetation (which is mainly limited by temperature). The potential rate of soil evaporation (EOS) is then calculated using the leaf area index.

A major number of land use maps with different dates would be important for modeling the variations of the crop coefficient (Kc) parameter, over certain years (in this case, from 2002 to 2011). However, only the land use map (named COS 90) from 1990 was possible to obtain. There are more land use maps for the study area for different years, although, only the map from 1990 has all the detailing needed for subsequent acquisition of the Kc parameter.

This fact is here reported as an additional limitation on the landslide assessment based on the dynamic approach. A way of overcoming this problem could be achieved by working on satellite images, in order to detail the land use information and get it for several years. However, this work requires new methodologies care and time and thus, unfortunately it was not possible to carry out for the present study.

6) Landslide susceptibility using the hydrological model coupled to slope stability model under dynamic temporal conditions. Validation through the quantification of the model prediction rate;

The dynamic hydrological model allowed the incorporation of daily climatic data, which helps to simulate, in a more realistic and parameterized manner, the spatial and temporal occurrence of critical pore pressures including the delay and loss of percolation in the unsaturated zone. The hydrological model (STARWARS) described, thus, the saturated and the unsaturated transient flow in the vertical and lateral directions.

By using a dynamic approach, it was possible to simulate the hydrology over time (2002 to 2011) and evaluate the effects on the slope stability. Another great advantage, when compared to the static approach, was the possibility to calibrate the model not only spatially but also temporally by using the actual discharge data.

An analysis of each landslide was preceded independently in order to understand which could have been the years or, more precisely, the exact days or periods more prone to the occurrence of such phenomena. This statistical analysis was performed based on the

location of the centroid of each depletion zone of each shallow translational slide. According to the modeled areas where SF ≤ 1 and to the to the total rain duration and period, some landslides could have occurred in almost every year, while some have an occasional or seasonal trend.

There are some landslides lying in a permanent area of SF≤1. This is not a realistic situation which is not possible to calibrate due to a lack of data. However, there are other realistic cases where landslides lying in an occasional or seasonal area of SF≤1. There are also some landslides, generally located on the south part of the study area, that are not explained by this model.

A more profound analysis was performed to the single dated landslide. Thereby, it was possible to observe that the date of occurrence matches with the SF≤1 modeled by the model for that day, and it was also possible to reconstitute all the conditions registered on that day.

There was a greatly reduced amount of precipitation on that day. However, that occurrence can be explained by the groundwater table which had acquired a very high level. According to the model results the trigger of the landslide is due to a rise in groundwater table which has begun 14 days before, due to a maximum daily precipitation.

The year more susceptible to landslides, according to the safety factor, modeled for the period 2002-2011 was 2006. The mean annual precipitation and also the daily maximum precipitation (among all the other years) were very high. At the same time, 2006 was the year with best predictive performance, having the higher AUC value (0.85) among all the modeled years.

Moreover, the year less susceptible to landslide occurrence was 2008, although not being the year with the lowest annual precipitation, or with the lowest maximum daily

precipitation. By comparing the AUC values with other years it is possible to note that the year 2008 is the year with the lowest predictive ability.

7) Comparisons between physically base models: static and dynamic approach;

The static physically approach turns out to be very difficult to reconstitute the previous conditions of precipitation and/or water storage that triggered landslides. This simplest approach does not address influences of temporally varying precipitation, vegetation dynamics, uncertainty associated with input parameters, as well as various scenarios that may be implemented through an extended monitoring period.

The static model with the best performance corresponded to a one day of critical precipitation. However, being a hypothetical scenario such situation could never happen in the study area. Obviously, this problem could be partly overcome if the return period and critical precipitation could have been calculated for the study area, however, due to a lack of dated landslide such calculations could not be performed.

The dynamic physically-based coupled model of slope hydrology and stability (STARWARS + PROBSTAB) seemed to overcome partially the limitations of the simplest static model. In fact, the rainfall and evapotranspiration time series modeling, involves an important temporal dimension.

Besides all the advantages already described, the dynamic model has also the ability to assess the key dates, which could have lead to landsliding. For assessing the key dates a spatial comparison between landslides (already occurred) and the modeled safety factor was performed. This is also considered an important contribution to the evaluation of past landslides on which it was not possible to obtain the date of occurrence.
However, such model are not free from limitations and it can actually be enumerated some of them: 1) It is very time computing consuming; 2) it is necessary to learn Python and PCRaster programming, at least, to a level that allows handling the program, the models and its inputs; 3) Many times it is difficult and very time consuming to obtained all

the parameters needed for modeling. Despite these limitations implementing such dynamic and complex model allows the acquisition of much more realistic and consistent results which justify its use in preference to static and simplest models.

8) Sensitivity analysis of the predisposing factors: morphometric data (i.e., elevation, slope, curvature, profile curvature) and nonmorphometric data (i.e., soils, lithology, soil depth);

The predisposing factors are those that, due to their static characteristics and terrain representativeness, are more often used for landslide susceptibility, assessed through statistically-based models. Such factors are described as a set of layers that are expected to have an effect on the occurrence of landslides, and can be used as causal factors in the prediction of future landslides. The static data sets used as predisposing factors was the slope angle, slope aspect, curvature profile, inverse of the wetness index, lithology; morpho-structure, soil depth and soils type. These themes were classified into categorical variables.

A data-driven landslide susceptibility zonation map depicts division of the land surface into zones of varying degrees of stability based on estimated significance of the predisposing factors. The sensitivity analysis of the variables was performed in order to assess the relative weight importance and hierarchy of predisposing factor according to the landslides distribution. From the results, it was possible to conclude that all variables can be included in the statistically-based method without reducing the model ability to predict landslides. Later, by using the percent contribution, the accountability and reliability it was also possible to establish a hierarchy between the predisposing factors for each landslide type belonging to each Landslide Inventory. Thereby, apart from landslide period or type, the detailed lithology seemed to be always the best predictive factor followed by slope angle and morpho-structure.

9) Landslide susceptibility using the statistically-based method (Information Value Method). Validation through the quantification of the degree of prediction rate;

There are different methods of landslide susceptibility zonation. However, for the present study, and in order to understand the possible advantages and disadvantages of using statistically and physically-based methods, a simple and robust statistical bivariated method, named Information Value, was selected for landslide susceptibility assessment. The prediction rate curves obtained for the LI#1 seem to be acceptable, (according to the values stipulated by Guzzetti (2005) with a 0.78 AUC value for the susceptible model to deep-seated rotational slides. However, for the shallow rotational and translational susceptibility models these values are lower, though, without ever decreasing below 0.70. For the LI#1+LI#2 the susceptibility models for the deep-seated rotational slides and the shallow translational slides have acceptable performance according to the AUC values (0.78 and 0.75). The shallow rotational slide susceptibility model has a lower AUC, however very close to the acceptable (0.72). The reason why this susceptible models do never exceed 0.8 can derive from three situations: 1) The inventories of ancient landslides (LI#1 and LI#2) were not subjected to a field validation; 2) errors derived from the georeferencing and the orthorectifying processes, which were necessary for interpretation of ancient landslides; 3) Difficulties in the recognition of the landslides types through the aerial photographs due to the scale of analysis.

The validation results obtained for the susceptible models based on the LI#3 must be observed with caution since it were not validated through a prediction rate curve, but, through a success rate curve. In this case, according to the AUC values, regardless the landslide type, the models have always a good performance because the model is validated with the same set of landslides that were used for modeling. The shallow rotational slide susceptibility model can be enhanced as the best predictive model (with an AUC value of 0.90, which makes it an excellent model) followed by susceptibility models obtained for shallow translational slides (0.88) and deep-seated rotational slides (0.81).

10) Comparisons between statistically and physically static based models.

The physically-based methods allow the quantification of instability through the explanation of the physical mechanisms and responses to the influential factors that lead to the occurrence of slope instability which can numerically integrate other models of hydrological and geotechnical nature, whose main objective is mathematically approach the reality in order to improve the ability to forecast where and when new landslides will be triggered. Such methods are favoured by the capability of predicting alterations in the hydrological behaviour by means of the constituent equations (Grayson et al., 1992). The physical method here implemented is specific to model only shallow translational landslides, whereas the statistical method fit any type of landsliding process.

Through an objective comparison between the obtained results through the statistically (SBM) and physically-based methods (PBM) it is possible to conclude that, according to the AUC values and to the physically modeled unstable area (SF≤1 area), the PBM present higher skills for predicting the spatial occurrence of shallow translational slides (0.79) than the SBM (0.75).

Spatial differences can be observed when both maps are reclassified into quartiles (25% of the total study area each class). Thereby, the SBM model provides a more diffuse distribution of the susceptibility classes, while the PBM model makes a more refined separation between the classes of highest susceptibility and lowest susceptibility, being the first more concentrated in the central part of the study area and the second located in the western and NW part of the study area.

Regarding the area corresponding to SF≤1 obtained through the PBM (24.7% of the total study area), it is important to highlight the fact that 72.5% of the total shallow translational slides from LI#3 are included inside the this unstable class while the same portion of the territory, with 24.7% of highest instability, only includes 56.1% in the SBM model. Hence, it can be considered that for a determinist approach, such results are indeed very good, especially for a regional scale.

Considering only the area of SF≤1 the overlapping between both susceptible models is about 36%. From this area 40.3% of the total shallow translational slides from LI#3 can be predicted which shows an agreement between the two models.

Based on the results obtained in this work, it is possible to assert that no method is better than another but they can, however become complementary in the shallow translational landslide susceptibility assessment. Preferably, crossing both methods for obtaining high landslide susceptibility zones would be adequate for future works.

REFERENCES

REFERENCES

ABELLA, E.A.C. (2008) - *Multi-scale landslide risk assessment in Cuba*. International Institute for Geo-information Science and Earth Observation, Utrecht, Utrecht University. ITC Dissertation 154, 273 p. ISBN: 978-90-6164-268-8

AGUILO, M.; *et al*. (2004) - *Guía para la elaboración de estudios del medio físico: contenido y metodología*. Serie Monografías. Ministerio de medio ambiente, pp. 187-196.

ALLEN, R.G. (2003) - Crop Coefficients. *In*: Stewart, B.A.; Howell, T. (Eds.), *Encyclopedia of Water Science*. Marcel Dekker Inc., New York.

ALLEN, R.G.; PEREIRA, L.S.; RAES, D.; SMITH, M. (1998) - *Crop evapotranspiration: Guidelines for computing crop requirements*. FAO Irrigation and Drainage Paper No. 56, FAO, Rome, Italy.

ALEOTTI, P.; CHOWDHURY, R. (1999) - Landslide hazard assessment: summary review and new perspectives. *Bulletin of Engineering Geology and the Environment*, 58: 21-44.

AMARAL, P. (2011) - *Monitorização multidisciplinar de vertentes instáveis em terrenos vulcânicos no arquipélago dos Açores. Modelação do comportamento hidromecânico do solo com vista à predição e mitigação da instabilidade geomorfológica*. PhD thesis in Vulcanology and Geologic Risks Evaluation. Azores University.

ANBALAGAN, D. (1992) - Landslide hazard evaluation and zonation mapping in mountainous terrain. *Engineering Geology,* 32(4): 269-277.

ARDIZZONE, F.; CARDINALI, M.; GALLI, M.; GUZZETTI, F.; REICHENBACH, P. (2007) - Identification and mapping of recent rainfall-induced landslides using elevation data collected by airborne Lidar. *Natural Hazards and Earth System Sciences*, 7: 637-650.

ASCENSO, V. (2011) - *Análise da ocorrência de cheias e deslizamentos de vertente no Concelho da Batalha*. Master thesis in Physical Geography, Institute of Geography and Spatial Planning, University of Lisbon.

BAEZA, C.; COROMINAS, J. (2001) - Assessment of shallow landslide susceptibility by means of multivariate statistical techniques. *Earth Surface Processes and Landforms.* 26: 1251-1263.

BAUM, R.L.; SAVAGE, W.Z.; GODT, J.W. (2002) - *TRIGRS: A Fortran program for transient rainfall infiltration and grid-based regional slope-stability analysis*. US Geological Survey Open-File Report 02-0424, 35pp.

BAUM, R.L.; SAVAGE, W.Z.; GODT, J.W. (2008) - *TRIGRS: A Fortran program for transient rainfall infiltration and grid-based regional slope stability analysis*, version 2.0, US Geological Survey Open-File Report 2008-1159, 75 pp.

BEEK, L.P.H. VAN (2002) – Assessment of the influence of changes in land use and climate on landslide activity in a Mediterranean environment. Dissertation, Utrecht University.

BERG, M.; CHEONG, O.; VAN KREVELD, O.; OVERMARS, O. (2008) - Computational Geometry. Chapter 9. Algorithms and application. Third edition. Springer-Verlag.

BEVEN, K.; BINLEY, A. (1992) – The future of distributed models - Model calibration and uncertainty in predictions. *Hydrological processes,* 6(3): 279-298.

BEVEN, K.; KIRKBY, M. (1993) - *Channel Network Hydrology*. John Wiley & Sons, Chichester.

BIERMAN, P.; STEIG, E.J. (1996) – Estimating rates of denudation using cosmogenic isotope abundances in sediment, *Earth Surface Processes and Landforms*, 21, 125-139.

BLAHUT, J.; VAN WESTEN, C.J.; STERLACCHINI, S. (2010) - Analysis of landslide inventories for accurate prediction of debris-flow source areas. *Geomorphology*, 119: 36-51.

BLASIO, F.V. (2011) - *Introduction to the Physics of Landslide. Lecture notes on the dynamics of mass wasting*. Springer Dordrecht Heidelberg London New York.

BOER, M.; DEL BARRIO, G.; PUIGDEFABREGAS, J. (1996) - Mapping soil depth classes in dry Mediterranean areas using terrain attributes derived from a digital elevation model. *Geoderma*, 7: 99-118.

BOLTZMANN, L. (1877) – Ueber die Beziehung eines allgemeine mechanischen Satzes zum zweiten Hauptsatzes der Warmetheorie *Sitzungsber. Akad. Wiss. Wien, Math.-Naturwiss. Kl.* 75, pp. 67-73

BONHAM-CARTER, G.F. (1994) - *Geographic Information Systems for Geoscientists: Modelling with GIS*. Pergamon, Oxford, 398 pp.

BOURENNANE, H.; KING, D.; COUTURIER, A. (2000) - Comparison of kriging with external drift and simple linear regression for predicting soil horizon thickness with different sample densities. *Geoderma,* 97(3-4): 255-271.

BRABB, E.E.; HARROD, B.L. (1989) - Landslides: extent and economic significance. *Proceedings of the 28th International Geological Congress: Symposium on Landslides*. Washington DC, 17 July, 385 pp.

BRAUN, J.; HEIMSATH, A.M.; CHAPPELL, J. (2001) - Sediment transport mechanisms on soil-mantled hillslopes. *Geology*, 29(8): 683-686.

BRUNSDEN, D.; IBSEN, M.L. (1996) - Mudslide (translational) *In:* Dikau, R.; Brunsden, D.; Schrott, L.; Ibsen, M.-L. (Eds.), *Landslide Recognition. Identification, Movement and Causes*. John Wiley & Sons, Chichester, pp. 103-119.

BRUTSAERT, W. (1982) - *Evaporation into the atmosphere: Theory, History and applications*. Kluwer Academics, Dordrecht, 299 pp.

BUMA, J.; VAN ASCH, T. (1996) - Slide (rotational). *In:* R. DIKAU, D. BRUNSDEN, L. SCHROTT; M.-L. IBSEN (Eds.), *Landslide recognition. Identification, movement and causes*. Wiley & Sons, Chichester, 43-61.

BURROUGH, P.A. (1986) - *Principles of Geographical Information Systems for Land Resources Assessment*. Oxford University Press, Oxford, 193 pp.

BURROUGH, P.A.; MCDONNELL, R.A. (1998) - *Principles of Geographical Information* Systems. Oxford University Press, Oxford, 333 pp.

BUTLER, R.F. (1992) - *Paleomagnetism: Magnetic Domains to Geologic Terranes*. Blackwell Scientific Publications, Boston, 319 pp.

CABRAL, J. (1993) - *Neotectónica de Portugal Continental*. PhD thesis. Faculty of Sciences, Lisbon University, 435 pp.

CABRAL, J. (2012) Neotectonics of mainland Portugal: state of the art and future perspectives. Journal of Iberian Geology 38 (1): 71-84.

CÂMARA MUNICIPAL DAS CALDAS DA RAINHA (2002) - *Plano Director Municipal das Caldas da Rainha*. Câmara Municipal Caldas das Rainha.

CÂMARA MUNICIPAL DE CALDAS DA RAINHA (2008) - Caracterização - Diagnóstico da Estrutura biofísica. *Estudos especializados sobre a Estrutura Ambiental: Revisão do Plano Director Municipal de Caldas da Rainha*. Relatório 1.

CARDINALI, M.; ANTONINI, G.; REICHENBACH, P.; GUZZETTI, F. (2001) - Photo geological and landslide inventory map for the Upper Tiber River basin. Pubblication CNR GNDCI n. 2116, Scale 1:1,200,000.

CARRARA, A. (1993) - Uncertainty in evaluating landslide hazard and risk. *In*: Nemec, J.; Nigg, J.M.; Siccardi, F. (Eds.), *Predictions and Perception of Natural Hazards*. Proceedings Symposium, 22-26 October 1990, Perugia, Italy. Advances in natural and Technological hazards Research, Kluwer Academic Publishers, Dordrecht, pp. 101-109.

CARRARA, A.; CARDINALI, M.; GUZZETTI, F.; REICHENBACH, P. (1995) – GIS technology in mapping landslide hazard. Carrara A., Guzetti F (ed.). Geographical Information Systems in Assessing Natural Hazards: 135-176..

CARRARA, A.; CARDINALI, M.; DETTI, R.; GUZZETTI, F.; PASQUI, V.; REICHENBACH, P. (1991) - GIS Techniques and Statistical Models in Evaluating Landslide Hazard. *Earth Surface Processes and Landforms*, 16: 427-445.

CARVALHO, S.C.P.; de LIMA, M.I.P.; de LIMA, J.L.M.P.; COELHO, M.F.E.S. (2010) - The effect of rainfall trends in the estimation of intensity-duration-frequency curves. *Geophysical Research Abstracts*, Vol. 12, EGU2010-814, EGU General Assembly 2010.

CATANI, F.; SEGONI, S.; FALORNI, G. (2010) - An empirical geomorphology-based approach to the spatial prediction of soil thickness at catchment scale. *Water Resources Research*, 46: W05508.

CENCETTI, C.; DE ROSA, P.; FREDDUZZI, A.; MINELLI, A.; MARCHESINI, I. (2009) – Un contributo allo studio del problema relativo all'interpolazione di dati giaciturali. *IV Convegno Nazionale del Gruppo GIT*. Cagli 15-17 June, 2009.

CHACÓN, J.; IRIGARAY, C.; FERNÁNDEZ, T.; EL HAMDOUNI, R. (2006) – Engineering geology maps: landslides and geographical information systems. *Bullettin of Engineering Geology and the Environment,* 65: 341-411.

CHOROWICZ, J.; BRÉARD, J.Y.; GUILLANDE, R.; MORASSE, C.R.; PRUDON, D.; RUDANT, J.P. (1991) - Dip and strike measured systematically on digitized three-dimensional geological maps. *Photogrammetric Engineering and Remote Sensing*, 57(4): 431-436.

CHOROWICZ, J.; PARROT, J. F.; TAUD, H.; HAKDAOUI, H.; RUDANT, J. P.; ROUIS, T. (1995) - Automated pattern-recognition of geomorphic features from DEMs and satellite images. *Zeitschrift fur Geomorphologie*, 101: 69-84.

CHUNG, C-J.F.; FABBRI, A.G. (2003) - Validation of spatial prediction models for landslide hazard mapping. *Natural Hazards*, 30(3): 451-472.

CLERICI, A.; PEREGO, S.; TELLINI, C.; VESCOVI, P. (2002) - A procedure for landslide susceptibility zonation by the conditional analysis method. *Geomorphology*, 48(4): 349-364.

CLERICI, A.; PEREGO, S.; TELLINI, C.; VESCOVI, P. (2006) - A GIS-based automated procedure for landslide susceptibility mapping by the Conditional Analysis method: the Baganza valley case study (Italian Northern Apennines). *Environmental Geology*, 50(7): 941-961.

CLERICI, A.; PEREGO, S.; TELLINI, C.; VESCOVI, P. (2010) - Landslide failure and runout susceptibility in the upper T. Ceno valley (Northern Apennines, Italy). *Natural Hazards*. 52: 1-29.

CLOETINGH, S.; BUROV, E.; BEEKMAN, F.; ANDEWEG, B.; ANDRIESSEN, P.A.M.; GARCIA-CASTELLANOS, D.; VICENTE, G. DE; VEGAS, R. (2002) - Lithospheric folding in Iberia. *Tectonics*, 21(5): 1041.

CONACHER, A.J.; DALRYMPLE, J.B. (1977) - The nine unit land surface model: An approach to pedogeomorphic research. *Geoderma*, 18: 1-154.

COROMINAS, J. (1996) - *Debris slide. In*: DIKAU, R.; BRUNSDEN, D.; SCHROTT, L.; IBSEN, M.- L. (Eds.), *Landslide Recognition. Identification, Movement and Causes*. John Wiley & Sons, Chichester, pp. 97-102.

CROSTA, G.B.; AGLIARDI, F.; FRATTINI, P.; SOSIO, R. (2012) - *SafeLand Living with landslide risk in Europe: Assessment, effects of global change, and risk management strategies*. Grant Agreement No.: 226479. 7 th Framework Programme Cooperation Theme 6 Environment (including climate change) Sub-Activity 6.1.3 Natural Hazards.

CROSTA, G.B.; FRATTINI, P. (2003) - Distributed modelling of shallow landslides triggered by intense rainfall. *Natural Hazards and Earth System Sciences*, 3: 81-93.

CROZIER, M. (1973) - Techniques for the morphometric analysis of landslips. *Zeitschrift fur Geomorphologie*, 17: 78-101.

CROZIER, M. (1984) - *Field assessment of slope instability. In:* D. Brusden and D.B. Prior (eds.), Slope Instability, Wiley Press, Chichester, p. 103-142.

CROZIER, M. (1986) - Landslides: causes, consequences and environment, Croom Helm, London, 252 pp.

CROZIER, M. (1989) - Landslides: Causes, consequences and environment, Routledge.

CROZIER, M.; GLADE, T. (2005) - Landslide hazard and risk: issues, concepts and approach. *In:* Glade, T., Anderson, M.G. and Crozier, M.J. (eds.), Landslide hazard and risk, John Wiley & Sons, Chichester, pp. 1-40.

CRUDEN, D.M. (1988) - Thresholds for catastrophic instabilities in sedimentary rock slopes. *Zeitschrift fur. Geomorphologie*, 67: 67-76.

CRUDEN, D.M. (1989) - Limits to common toppling. *Canadian Geotechnical Journal*, 26: 737-742.

CRUDEN, D.M. (1991) - A simple definition of a landslide. *Bulletin of the International Association of Engineering Geology*, 43: 27-29.

CRUDEN, D.M. (2000) - Some forms of mountain peaks in the Canadian Rockies controlled by their rock structure. *Quaternary International,* 68-71: 59-65.

CRUDEN, D.M.; HU, X.Q. (1996) - Hazardous modes of rock slope movement in the Canadian Rockies. *Environmental and Engineering Geoscience*, 2(4): 507-516.

CRUDEN, D.M.; VARNES, D.J. (1996) - Landslide Types and Processes. *In*: Turner, A.K.; Schuster, R.L. (Eds.), *Landslides. Investigation and Mitigation*. Transportation Research Board. National Academy Press, Washington D.C.. Special Report 247, pp. 36-75.

CUSTODIO, E.; LLAMAS, M.R. (1976) - *Hidrologia Subterrânea*. Ediciones Omega S.A., Barcelona.

DAI, F.C.; LEE, C.F. (2001) – Frequency - volume relation and prediction of rainfall -induced landslides. *Engineering Geology*, 59(3-4): 253-266.

DAVIS, J.C. (1973) - *Statistics and data analysis in geology* (second edition). John Wiley & Sons, New York.

DE KEMP, E.A. (1998) - Three-dimensional projection of curvilinear geological features through direction cosine interpolation of structural field observations. *Computers & Geosciences*, 24 (3): 269-284.

DIAS, M.H. (2007) - *Cartografia Temática: programa*. Área de Investigação de Geo-Ecologia. Centro de Estudos Geográficos da Universidade de Lisboa. Relatório nº 6, 146 pp.

DIETRICH, W.E.; MONTGOMERY, D.R. (1998) - *SHALSTAB: A Digital Terrain Model for Mapping Shallow Landslide Potential*. National Council of the Paper Industry for Air and Stream Improvement. Technical Report, 29 pp.

DIETRICH, W.E.; REISS, R.; HSU, M.-L.; MONTGOMERY, D.R. (1995) - A process-based model for colluvial soil depth and shallow landsliding using digital elevation data. *Hydrological Processes*, 9: 383-400.

DIKAU, R.; BRUNSDEN, D.; SCHROTT, L.; IBSEN, M.-L. (1996) – *Landslide Recognition*. *Identification, Movement and Causes*. John Wiley & Sons, Chichester.

DIMITRIOU, P.A. (2005) - *Georeferencing Raster Images; Registering an Image for the Purpose of Data Creation*. Pennsylvania State University World Campus Geography 484 Lesson 3 Concept Gallery.

DINGMAN, S. L. (2002) - *Physical hydrology* (second edition). New York: McMillan.

DINIS, J.; BERNARDES, C. (2004) The upper jurassic outcrops along the Caldas da Rainha diapir, Portugal: a regional geoheritage overview. *Rivista Italiana di Paleontologia i Stratigrafia*, 10 (110): 407-415.

DOORENBOS, J.; PRUITT, W.O. (1977) - *Guidelines for predicting crop water requirements*. Irrigation and Drainage, Paper No.24., FAO, Rome.

DUMAN, T.Y.; CAN, T.; GOKCEOGLU, C.; NEFESLIOGLU, H.A.; SONMEZ, H. (2006) - Application of logistic regression for landslide susceptibility zoning of Cekmece Area, Istanbul, Turkey. *Environmental Geology*, 51(2): 241-256.

DUNCAN, C.W.; CHRISTOPHER, W.M. (2004) - *Rock Slope Engineering: Civil and Mining*. CRC Press; 4 edition, 456 pp. ISBN-13: 978-0415280006.

EATON, T.M. (1986) - *Reconnaissance of rockslide hazards in Kananaski Country*. Master thesis, University of Alberta, Edmonton.

ERDAS (2009) - *Image Analysis for ArcGIS*™. Geographic Imaging by ERDAS.

ERISMANN, T.H.; ABELE, G. (2001) - Dynamics of Rockslides and Rockfalls. New York, Springer-Verlag, 316 pp.

ERSKINE, C. F. (1973) - *Landslides in the vicinity of the Fort Randall Reservoir South Dakota*. Geological Survey Professional Paper, 675, Washington.

ESRI (2008) - ArcGis Desktop 9.3 Help. [Accessed in 27th November 2012] http://webhelp.esri.com/arcgisdesktop/9.3/index.cfm?TopicName=Redistribution_rights

ESRI (2008) – ArcGis Desktop 9.3 Help. [Accessed in 25th October 2012]. http://webhelp.esri.com/arcgisdesktop/9.3/index.cfm?TopicName=Redistribution_rights

ESRI (2012a) – ArcGis Desktop 10.0 Help. [Accessed in 12th November 2012. http://help.arcgis.com/en/arcgisdesktop/10.0/help/index.html#/Welcome_to_the_ArcGIS_Help_Library/00r90000001n000000/

ESRI (2012b) – GIS Dictionary. [Accessed in 15th November 2012]. http://support.esri.com/en/knowledgebase/GISDictionary/term/kriging

FABBRI, A.G.; CHUNG, C.F. (2008) - On blind tests and spatial predictions models. *Natural Resources Research*. 17(2): 107-118.

FABBRI, A.G.; CHUNG, C.F.; NAPOLITANO, P.; REMONDO, J.; ZÊZERE, J.L. (2003) - Prediction rate functions of landslide susceptibility applied in the Iberian Peninsula. *In*: Brebbia, C.A. (Ed.), *Risk Analysis III*, Series: Management Information Systems, vol. 5, WIT Press, Southampton, Boston, pp. 703-718.

FARREL, D.; LARSON, W. (1972) - Modeling the pore structure of porous media. *Water Resources Research,* 8(3): 699-706.

FRANÇA, J.C.; ZBYSZEWSKI, G. (1963) - *Notícia explicativa da folha 26-B de Alcobaça*. Serviços Geológicos de Portugal, Lisboa.

FREDLUND, D.G. (1987) - Slope stability analysis incorporating the effect of soil suction. *In:* Anderson, M.G.; Richards, K.S. (Eds.), *Slope Stability*. John Wiley & Sons, pp. 113-144.

FREEZE, R.A.; CHERRY, J.A. (1979) - *Groundwater*. Prentice-Hall, Inc. Englewood Cliffs, NJ. 604 p.

GANAS. A.; PAVLIDES, S.; KARASTATHIS, V. (2005) - DEM-based morphometry of range-front escarpments in Attica, central Greece, and its relation to fault slip rates. *Geomorphology*, 65: 301–319.

GAO, J. (2009) - *Digital analysis of remotely sensed imagery*. School of Geography, Geology and Environmental Science The University of Auckland Auckland, McGraw-Hill, New Zealand.

GARCIA, R.A.C. (2002) - *Avaliação do Risco de Movimentos de Vertente na Depressão da Abadia (Torres Vedras)*. Master thesis in Physical Geography. Faculty of Letters, University of Lisbon.

GARCIA, R.A.C. (2012) - *Metodologias de Avaliação da Perigosidade e Risco associado a movimentos de vertente. Aplicação na bacia do rio Alenquer*. PhD thesis in Physical Geography, Institute of Geography and Spatial Planning, University of Lisbon.

GARCIA, R.A.C.; ZÊZERE, J.L. (2003) - Avaliação de Riscos Geomorfológicos: Conceitos, Terminologia e Métodos de Análise. *III Seminário Recursos Geológicos, Ambiente e Ordenamento do Território*, Livro de Actas, Vila Real, pp. 299-308.

GARCIA, R.A.C.; ZÊZERE, J.L.; OLIVEIRA, S.C. (2007) - A importância do processo de classificação de dados na cartografia: um exemplo na cartografia de susceptibilidade a movimentos de vertente. *Dinâmicas geomorfológicas. Metodologias. Aplicação*. Publicações da Associação Portuguesa de Geomorfólogos. Vol. V. Lisboa: 265-279.

GEORGIADOU, P.Y.; KNIPPERS, R.A.; KRAAK, M. J.; SUN, Y.; WEIR, M.J. C.; VAN WESTEN, C.J. (2001) - *Principles of geographic information systems* (Chapter 4.2 on spatial referencing), 2nd edition, ITC Educational Textbook, ITC, Enschede.

GHOSH, S.; GÜNTHER, A.; CARRANZA, E.J.M.; VAN WESTEN C.J.; JETTEN, V.G. (2010) - Rock slope instability assessment using spatially distributed structural orientation data in Darjeeling Himalaya (India). *Earth Surface Processes and Landforms*, 35: 1773-1792.

GLADE, T.; CROZIER, M. J. (2005) - A review of scale dependency in landslide hazard and risk analysis. *In*: Glade, T.; Anderson, M.; Crozier, M.J. (Eds.), *Landslide Hazard and Risk*. Jonh Wiley & Sons, Ltd. Chichester, pp. 75-138.

GORSEVSKI, P.V., GESSLER, P.E., JANKOWSKI, P. (2003) - Integrating a fuzzy k-means classification and a Bayesian approach for spatial prediction of landslide hazard. *Journal of Geographical Systems*, 5(3): 223-251.

GORSEVSKI, P.V., GESSLER, P.E., BOLL, J., ELLIOT, W.J., FOLTZ, R.B. (2006) - Spatially and temporally distributed modeling of landslide susceptibility. *Geomorphology*, 80(3-4): 178-198.

GORUM T. (2009) - *Towards an Improved Method for Earthquake Induced Landslide Susceptibility and Hazard*. PhD thesis. Department of Earth Systems Analysis International Institute for Geoinformation Science and Earth Observation, Enschede, The Netherlands.

GRASS Development Team (2010) - *Geographic Resources Analysis Support System (GRASS) Software*, Version 6.4.0. Open Source Geospatial Foundation. http://grass.osgeo.org.

GRAYSON, R.B.; MOORE, I.D.; MCMAHON, T.A. (1992) - Physically based modeling: 2. Is concept realistic? *Water Resources Research*, 26(10): 2659-2666.

GREENBAUM, D.; BOWKER, M.R.; DAU, I.; DROPSY, H.; GREALLY, K.B.; MCDONALD, A.J.W.; MARSH, S.H.; NORTHMORE, K.J.; O'CONNOR, E.A.; PRASAD, S.; TRAGHEIM, D.G. (1995a) - *Rapid methods of landslide hazard mapping: Fiji case study*. Technical Report WC/95/28. British Geological Survey (BGS), Natural Enviromental Research Council, Keyworth, Nottingham.

GREENBAUM, D.; TUTTON, M.; BOWKER, M.R.; BROWNE, T.J.; BULEKA, J.; GREALLY, K.B.; KUNA, G.; MCDONALD, A.J.W.; MARSH, S.H.; O'CONNOR, E.A.; TRAGHEIM, D.G. (1995b) - *Rapid methods of landslide hazard mapping: Papua New Guinea case study*. Technical Report WC/95/27, British Geological Survey (BGS), Natural Enviromental Research Council, Keyworth, Nottingham.

GRELLE, G.; REVELLINO, P.; DONNARUMMA, A.; GUADAGNO, F.M. (2011) - Bedding control on landslides: a methodological approach for computer-aided mapping analysis. *Natural Hazards and Earth System Sciences*, 11: 13951409.

GRIFFITHS, J. S. (1999) – Proving the occurrence and cause of landslide in a legal context. *Bulletin of Engineering Geology and Environment*, 58, 75-85.

GUILLARD, C. (2009) - *Evaluation et cartographie du risque glissement de terrain d'une zone située au nord de Lisbonne*. Master thesis. Ecole Nationale Supérieure des Mines. Saint-Etienne.

GÜNTHER, A. (2003) - SLOPEMAP: programs for automated mapping of geometrical and kinematical properties of hard rock hill slopes. *Computers & Geosciences*. 29(7): 865-875.

GÜNTHER, A.; CARSTENSEN, A.; POHL, W. (2004) - Automated sliding susceptibility mapping of rock slopes. *Natural Hazards and Earth System Sciences,* 4: 95-102.

GUZZETTI, F. (2005) - *Landslide hazard and risk assessment: concepts, methods and tools for the detection and mapping of landslides, for landslide susceptibility zonation and hazard assessment, and for landslide risk evaluation*. PhD thesis.

Mathematchinaturwissenschaftlichen Fakultät da Rheinischen Friedrich-Wilhelms, Bona University.

GUZZETTI, F.; CARDINALI, M.; REICHENBACH, P. (1996) - The influence of structural setting and lithology on landslide type and pattern. *Envirenmental & Engineering Geoscience*, 2: 531-555.

GUZZETTI, F.; CARRARA, A.; CARDINALI, M.; REICHENBACH, P. (1999) - Landslide hazard evaluation: an aid to a sustainable development. Geomorphology, 31: 181-216.

GUZZETTI, F.; GALLI, M.; REICHENBACH, P.; ARDIZZONE, F.; CARDINALI, M. (2006) - Landslide hazard assessment in the Collazzone area, Umbria, Central Italy. *Natural Hazards and Earth System Sciences*. 6: 115-131.

GUZZETTI, F.; MANUNTA M.; ARDIZZONE, F.; PEPE, A.; CARDINALI, M.; ZENI, G.; REICHENBACH, P.; LANARI, R. (2009) - Analysis of ground deformation detected using the SBAS-DInSAR technique in Umbria, Central Italy. *Pure and Applied Geophysics*, 166(8-9): 1425-1459.

GUZZETTI, F.; REICHENBACH, P.; ARDIZZONE, F.; CARDINALI, M.; GALLI, M. (2006) - Estimating the quality of landslide susceptibility models. *Geomorphology*, 81: 166-184.

GUZZETTI, F.; REICHENBACH, P.; CARDINALI, M.; GALLI, M.; ARDIZZONE, F. (2005) - Probabilistic landslide hazard assessment at the basin scale. *Geomorphology*. 72: 272-299.

HAGEMANN, S. (2002) - *An improved land surface parameter dataset for global and regional climate models*. Max-Planck-Institute for Meteorology, Report 336, Hamburg

HARGREAVES, G.H.; SAMANI. Z.A. (1985) - Reference crop evapotranspiration from temperature. Applied Engineering in Agriculture, 1(2): 96-99.

HEIMSATH, A.M.; DIETRICH, W.E.; NISHIIZUMI, K.; FINKEL, R.C. (1997) - The soil production function and landscape equilibrium. *Nature*, 388, 358-361.

HEIMSATH, A.M.; CHAPPELL, J.; DIETRICH, W.E.; NISHIIZUMI, K.; FINKEL, R.C. (2000) - Soil production on a retreating escarpment in southeastern Australia. *Geology*, 28(9): 787-790.

HEIMSATH, A.M.; CHAPPELL, J.; DIETRICH, W.E.; NISHIIZUMI, K.; FINKEL, R.C. (2001a) - Late Quaternary erosion in southeastern Australia: A field example using cosmogenic nuclides. *Quaternary International*, 83-85: 169-185.

HEIMSATH, A.M.; DIETRICH, W.E.; NISHIIZUMI, K.; FINKEL, R.C. (2001b) - Stochastic processes of soil production and transport: Erosion rates, topographic variation and cosmogenic nuclides in the Oregon coast range. *Earth Surface Processes and Landforms*, 26: 531-552.

HEIMSATH, A.M.; DIETRICH, W.E.; NISHIIZUMI, K.; FINKEL, R.C. (1999) - Cosmogenic nuclides, topography, and the spatial variation of soil depth. *Geomorphology*, 27(1-2): 151-172.

HEINE, G.W. (1986) - A Controlled Study of Some Two-Dimensional Interpolation Methods. *COGS Computer Contributions,* 3(2): 60-72.

HENRIQUES, C.S. (2009) - *Dinâmica de Vertentes no contexto da Reserva Ecológica Nacional: o caso de estudo do concelho de Caldas da Rainha*. Master thesis in Geographic Information Systems. Institute of Geography and Spatial Planning, University of Lisbon.

HENRIQUES, M.V. (1996) - *A faixa litoral entre Nazaré e Peniche: Unidades geomorfológicas e dinâmica actual dos sistemas litorais*. PhD thesis. University of Évora.

HENRIQUES, M. V.; FREITAS, M. C.; ANDRADE, C.; CRUCES, A. (2002) – Alterações morfológicas em ambientes litorais desde o último máximo transgressivo – exemplos da

Estremadura e do Alentejo, Contribuições para a dinâmica geomorfológica , Assoc. Port. Geomorf., Vol. 1, Lisboa, p.99-109.

HUTCHINSON, J.N. (1988) - Morphological and geotechnical parameters of landslides in relation to geology and hydrogeology. General report. *In*: Bonnard, C. (Ed.), *Landslides, Proceedings of the Fifth International Symposium on Landslides*, Lausanne, 1988, Vol. 1, Balkema, Rotterdam, p. 3-35.

HUTCHINSON, J.N. (1995) - Landslide hazard assessment. In: Proc VI Int Symp on Landslides, Christchurch, 1: p. 1805–1842.

HUTCHINSON, J.N.; CHANDLER, M. P. (1991) - A preliminary landslide hazard zonation of the Undercliff of the Isle of Wight. In Slope Stability Engineering : Development and Applications (ed. R. J. Chandler). Thomas Telford, London, p. 197-205.

IBSEN, M.-L.; BRUNSDEN, D.; BROMHEAD, E.; COLLISON, A. (1996) – Block slide. *In*: DIKAU, R.; BRUNSDEN, D.; SCHROTT, L.; IBSEN, M.-L. (Eds.), Landslide Recognition. *Identification, Movement and Causes*. John Wiley & Sons, Chichester, p. 64-77.

IBSEN, M-L.; BRUSDEN, D. (1996) - The nature, use and problems of historical archives for the temporal occurence of landslides, with specific reference to the south coast of Britain, Ventnor, Isle of Wight. *Geomorphology*, 15: 241-258.

ICHOKU, C.; CHOROWICZ, J.; PARROT, J.-F. (1994) – Computerized construction of geological cross sections from digital maps. *Computers & Geosciences,* 20(9), 1321-1327.

IGME (1987) - *Manual de Taludes*. Serie Geotecnia, Instituto Geológico y Minero de España, Madrid, 456 pp.

ISAAKS, E.H.; SRIVASTAVA, R.M. (1989) - *An Introduction to Applied Geostatistics*. Oxford University Press, Oxford, 561 pp.

ITC (2001) - *ILWIS 3.0 User's Guide*. Faculty of Geo-Information Science and Earth Observation of the University of Twente.

ITC (2007) - *ILWIS 3.3 Download page*. Faculty of Geo-Information Science and Earth Observation of the University of Twente.

IVERSON, R.M. (2000) - Landslide triggering by rain infiltration. *Water Resources Research*, 36(7): 1897-1910.

JACKSON, C.R. (1992) - Hillslope infiltration and lateral downslope unsaturated flow. *Water Resources Research*, 28(9): 2533-2539.

JACKSON, J.; LEEDER, M. (1994) - Drainage systems and the development of normal faults: an example from Pleasant Valley, Nevada. *Journal of Structural Geology,* 16(8): 1041-1959.

JAYNES, E. T. (1957) – Information Theory and Statistical Mechanics. In Physical Review, Vol. 106, #4 (pp 620-630).

JENNESS, J; BROST, B.; BEIER, P. (2011) - Land Facet Corridor Designer: Extension for ArcGIS. Jenness Enterprises.
Available from: http://www. jennessent.com/arcgis/land_facets.htm.

KONIKOW, L.F.; BREDEHOEFT, J.D. (1992) – Ground-water models cannot be validate. *Advances in Water Resources,* 15(1): 75-83.

KOSA, P. (2011) - The Effect of Temperature on Actual Evapotranspiration based on Landsat 5 TM Satellite Imagery, Evapotranspiration, Prof. Leszek Labedzki (Ed.), ISBN: 978-953-307-251-7, InTech.

KUTÍLEK, M.; NIELSEN D. R. (1994) - *Soil Hydrology*. Cremlingen, Catena.

LACHENBRUCH, P.A. (1967) - An Almost Unbiased Method of Otaining Confidence Intervals for the Probability of Misclassification in Discriminant Analysis. *Biometrics*, 23(4): 639-645.

LEE, I.K.; WHITE, W.; INGLES, O.G. (1983) - *Geotechnical engineering*. Boston: Pitman.

LEEDER, M.R.; JACKSON, J.A.; (1993) - The interaction between normal faulting and drainage in active extensional basins, with examples from western United States and central Greece. *Basin Research,* 5(2): 79-102.

LENCASTRE, A.; FRANCO, F. (2006) - *Lições de Hidrologia*. Fundação FCT, Lisboa, 451 pp.

LOPES, P.S.P. (2008) - Avaliação Regional da Susceptibilidade Geomorfológica no Concelho de Santarém. Master thesis in Physical Geography. Faculty of Letters, University of Lisbon.

LUZI, L.; PERGALANI, F. (1999) - Slope instability in static and dynamic conditions for urban planning: the "Oltre Po Pavese" case history (Regione Lombardia-Italy). Natural Hazard, 20(1): 57-82.

MARCHESINI, I.; SANTANGELO, M.; FIORUCCI, F.; CARDINALI, M.; ROSSI, M.; GUZZETTI, F. (2011) - A GIS method for obtaining geologic bedding attitude. *Proceedings of the Second World Landslide Forum* - 3-7 October 2011, Rome.

MARQUES, F. (2003) - Landslide activity in upper Paleozoic shale sea cliffs: a case study along the western coast of the Algarve (Portugal). *Bulletin of Engineering Geology and the Environment*, 62(4): 299-313.

MARTIN, Y. (2000) - Modelling hillslope evolution: Linear and nonlinear transport relations. *Geomorphology*, 34(1-2): 1-21.

MATULA, M. (1981) - Rock and soil description and classification for engineering geological mapping. *Bullettin of Engineering Geology and the Environment*, 24: 235-274.

MCBRATNEY, A.B.; WEBSTER, R. (1986) - Choosing Functions for Semi-variograms of Soil Properties and Fitting Them to Sampling Estimates. *Journal of Soil Science,* 37(4): 617-639.

MEENTEMEYER, R.K.; MOODY, A. (2000) - Automated mapping of conformity between topographic and geological surfaces. *Computers & Geosciences*, 26(7): 815-829.

MEJIA-NAVARRO, M.; GARCIA, L.A. (1996) - Natural Hazard and Risk Assessment Using Decision Support Systems, Application; Glenwood Springs, Colorado. *Environmental and Engineering Geoscience*, 2(3): 299-324.

MEJIA-NAVARRO, M.; WOHL, E. E. (1994) - Geological hazard and risk evaluation using GIS: Methodology and model applied to Medellin, Colombia. *Bulletin of the Association of Engineering Geologists*, 31: 459-481.

MENGES, C.M.; (1990) - Late Quaternary fault scarps, mountain-front landforms, and Pliocene–Quaternary segmentation on the range-bounding fault zone, Sangre de Cristo Mountains, New Mexico. *In*: Krinitzsky, E.L., Slemmons, D.B (Eds.), *Neotectonics in Earthquake Evaluation*, Geological Society of America Reviews in Engineering Geology, Boulder, Colorado, p. 131-156.

MERRIAM, R. (1960) - A note on the interception loss equation. *Journal of Geophysical Research,* 65(11): 3850-3851.

MILLINGTON, R. J.; QUIRK, J. P. (1959) - Permeability of porous media. *Nature*, 183: 387-388.

MILLINGTON, R. J.; QUIRK, J. P. (1961) - Permeability of porous media. *Transactions of the Faraday Society*, 57: 1200-1207.

MINASNY, B.; MCBRATNEY, A.B. (1999) - A rudimentary mechanistic model for soil production and landscape development. *Geoderma*, 90(1-2): 3-21.

MINASNY, B.; MCBRATNEY, A.B. (2001) - A rudimentary mechanistic model for soil production and landscape development: Part II. A twodimensional model incorporating chemical weathering. *Geoderma*, 103(1-2): 161-179.

MONTGOMERY, D.R.; DIETRICH, W.E. (1994) - A physically based model for the topographic control on shallow landsliding. *Water Resources Research*, 30(4): 1153-1171.

MONTGOMERY, D.R.; BRANDON, M.T. (2002) - Topographic controls on erosion rates in tectonically active mountain ranges. *Earth and Planetary Science Letters*, 201: 481-489.

MORGAN, R.P.C. (2005) - *Soil erosion and conservation*. Third edition, Blackwell publishing, Oxford, UK. 303 p.

MORRIS, K. (1991) - Using knowledge-based rules to map the three-dimensional nature of geological features. *Photogrammetric Engineering and Remote Sensing*, 57(9): 1209-1216.

MUDD, S.M.; FURBISH, D.J. (2004) - Influence of chemical denudation on hillslope morphology. *Journal of Geophysical Research*, 109: F02001.

MUDD, S.M.; FURBISH, D.J. (2006) – Using chemical tracers in hillslope soils to estimate the importance of chemical denudation under conditions of downslope sediment transport. *Journal of Geophysical Research*, Earth surface, 111: F02021.

NANDAKUMAR, N.; MEIN, R.G. (1997) - Uncertainty in rainfall-runoff model simulations and the implication for predicting the hydrologic effects of land use change. *Journal of Hydrology*, 192(1-4): 211-232.

NASH, D. (1987) - A comparative review of limit equilibrium methods of stability analysis. *In:* Anderson, M.G.; Richards, K.S. (Eds.), *Slope Stability*. John Wiley & Sons, New York, p. 11-75.

NEOPHYTOU, E.; CHARITOU, A.; CHARALAMBOUS, C. (2000) - *Predicting corporate failure: empirical evidence for the UK.* University of Southampton, Sep. 2000, Working Paper.

NICHOLS, G. (2009) - *Sedimentology and stratigraphy*. Wiley, Blackwell, ChiChester, UK.

NICO, G.; OLIVEIRA, S.; CATALÃO, J.; ZÊZERE, J.L. (2010) - *On the Statistical Properties of Persistent Scatterers Location to Discriminate Landslide Predisposing Factors.* FRINGE 2009, ESA - European Space Agency.

NIELSEN, D.R.; VAN GENUCHTEN, M.Th.; BIGGAR, J.W. (1986) - Water flow and solute transport processes in the unsaturated zone, Water Resources Research, 22(9): 89-108.

OLIVEIRA, S.C. (2012) - *Incidência espacial e temporal da instabilidade geomorfológica na bacia do Rio Grande da Pipa (Arruda dos Vinhos)*. PhD thesis in Physical Geography, Institute of Geography and Spatial Planning, University of Lisbon.

OLIVER, M.A. (1990) - Kriging: A Method of Interpolation for Geographical Information Systems. *International Journal of Geographic Information Systems,* 4(3): 313-332.

OLSON, J. (1994a) - Global ecosystem framework-definitions. USGS EROS Data Center Internal Report, Sioux Falls, South Dakota, USA.

OLSON, J. (1994b) - Global ecosystem framework-translation strategy. USGS EROS Data Center Internal Report, Sioux Falls, South Dakota, USA.

PACHAURI, A.K.; GUPTA, P.V.; CHANDER, R. (1998) - Landslide zoning in a part of the Garhwal Himalayas. *Environmental Geology*, 36(3-4): 325-334.

PACHAURI, A.K.; PANT, M. (1992) - Landslide hazard mapping based on geological attributes. *Engineering Geology*, 32(1-2): 81-100.

PARK, S.J.; MCSWEENEY, K.; LOWERY, B. (2001) - Identification of the spatial distribution of soils using a process-based terrain characterization. *Geoderma*, 103(3-4): 249 272.

PASUTO, A.; SOLDATI, M. (1996) - Rock spreading. *In:* Dikau, R.; Brunsden, D.; Schrott, L.; Ibsen, M.-L. (Eds.), *Landslide Recognition. Identification, Movement and Causes*. John Wiley & Sons, Chichester, p. 103-119.

PENMAN, H.L. (1948) - Natural evaporation from open water, bare soil and grass. *Proceedings of the Royal Society A*, 193(1032): 120-145.

PENNOCK, D.J.; ZEBARTH, B.J.; DE JONG, E. (1987) - Landform classification and soil distribution in hummocky terrain. *Geoderma*, 40(3-4): 297-315.

PEREIRA, S. (2010) – *Perigosidade a Movimentos de Vertente na região Norte de Portugal*. PhD thesis. Faculty of Letters, University of Oporto.

PHILLIPS, S.J., DUDÍK, M.E; SCHAPIRE, R.E. (2004) - A maximum entropy approach to species distribution modeling. *Proceedings of the Twenty-First International Conference on Machine Learning*, pp 655-662.

PIEDADE, A. (2009) - *Modelação espacial em Sistemas de Informação Geográfica da susceptibilidade a deslizamentos na área de Lousa - Loures*. Master thesis in Territorial Management, specialization in Geographic Information Systems (GIS) and Remote Sensing, New University of Lisbon.

PIMENTA, R.S.G.G. (2011) - Avaliação da susceptibilidade à ocorrência de movimentos de vertente com métodos de base física. Master thesis. Faculty of Sciences, Lisbon University.

PHILIP, J.R. (1990) - Hillslope infiltration: planar slopes. *Water Resources Research,* 27(1): 109-117.

POPESCU, M.E. (2002) - Keynote Lecture. *Proceedings 3rd International Conference on Landslides, Slope Stability and Safety of Infra-Structures*, Singapore, p 61-81.

POPESCU, M. (1994) - A suggested method for reporting landslide causes. *Bulletin of the International Association of Engineering Geology*, 50: 71-74.

POWELL, J.W. (1875) - *Exploration of the Colorado River of the West and its Tributaries*. Government Printing Office, Washington, DC, 291 pp.

PRESS, W.H.; TEUKOLSKY, S.A.; VETTERLING, W.T.; FLANNERY, B.P. (1988) - *Numerical Recipes in C, The Art of Scientific Computing*. New York: Cambridge University Press.

PRIGOGINE, I. AND STENGERS, I. (1984) – *Order out of Chaos*, New York, Bantam.

RAIA, S.; ALVIOLI, M.; ROSSI, M.; BAUM, R.L.; GODT, J. W.; GUZZETTI, F. (2013) - Improving predictive power of physically based rainfall-induced shallow landslide models: a probabilistic approach. *Geoscientific Model Development Discussions*, 6: 1367-1426.

RAWLS, W.J.; BRAKENSIEK, D.L.; SAXTON, K.E. (1982) - Estimation of soil water properties. *Transaction of the ASAE*, 25(5): 1316-1320.

REGINATTO G.M.P.; MACCARINI, M.; KOBIYAMA, M.; HIGASHI, R.A.R.; GRANDO, A.; CORSEUIL, C.W.; CARAMEZ, M.L. (2012) - Shalstab Application to identify the susceptible areas of shallow landslide in Cunha River watersheb, Rio dos Cedros city, SC, Brazil. *Proceedings of the 4th GEOBIA*, May 7-9, 2012. Rio de Janeiro, Brazil. p. 108-113.

REICHENBACH, P.; CARDINALI, M.; DE VITA, P.; GUZZETTI, F. (1998) - Regional hydrological thresholds for landslides and floods in the Tiber River Basin (central Italy). *Environmental Geology*, 35(2-3): 146-159.

REIS, E.; ZÊZERE, J.L.; VIEIRA, G.T.; RODRIGUES, M.L. (2003) - Integração de dados espaciais em SIG para avaliação da susceptibilidade à ocorrência de deslizamentos. *Finisterra*, 38(76): 3- 34.

RIBEIRO, A. (1984) - *Néotectonique du Portugal*, *Livro de Homenagem a Orlando Ribeiro*. Vol. 1, Centro de Estudos Geográficos, Lisboa, p.173-182.

RIBEIRO, O.; LAUTENSACH, H.; DAVEAU, S. (1988) - *Geografia de Portugal.* Vol. 2
O Ritmo Climático e a Paisagem. Ed. João Sá da Costa, Lisboa, p. 337-623.

RITCHIE, J.T. (1998) - Soil Water Balance and Plant Water Stress. *In:* Tsuji, G.Y.; Hoogenboom, G.; Thornton, F.K. (Eds.), *Understanding Options for Agricultural Production*. Vol. 7, Kluwer Academic Publishers, Dordrecht, p. 45-58.

ROCHA, F.F.J (2012) - *Sistemas complexos, modelação e geosimulação da evolução de padrões de uso e ocupação do solo*. PhD thesis in Geographic Information Science Institute of Geography and Spatial Planning, University of Lisbon.

ROERING, J.J.; KIRCHNER, J.W.; SKLAR, L.S.; DIETRICH, W.E. (2001) - Hillslope evolution by nonlinear creep and landsliding: An experimental study. *Geology*, 29(2): 143-146.

ROSENBERG, R.; ARNTZ, W.E.; DE FLORES, E.C.; FLORES, L.A.; CARBAJAL, G.; FINGER, I.; TARAZONA, J. (1983) - Benthos biomass and oxygen deficiency in the upwelling system off Peru. *Journal of Marine Research,* 41(2): 263-279.

ROWLAND, S.M.; DUEBENDORFER, E.M. (1994) - *Structural analysis and synthesis: a laboratory course in structural geology*. Blackwell Publishing, Malden USA.

ROYLE, A.G.; CLAUSEN, F.L.; FREDERIKSEN, P. (1981) - Practical Universal Kriging and Automatic Contouring. *Geoprocessing*, 1: 377-394.

SACO, P.M.; WILLGOOSE, G.R.; HANCOCK, G.R. (2006) - Spatial organization of soil depths using a landform evolution model. *Journal of Geophysical Research*, 111: F02016.

SANDER, B. (1970) - *An Introduction to the Study of Fabric of Geological Bodies*. Pergamon, Oxford, 641 pp.

SANTANGELO, M.; BUCCI, F.; CARDINALI, M.; MARCHESINI, I.; ROSSI, M.; GUZZETTI, F. (2012) - Morpho-structural influences on landslide pattern and distribution: GRASS GIS tool application. *Geophysical Research Abstracts*, Vol. 14, EGU2012-12457, EGU General Assembly 2012.

SARKAR, S.; KANUNGO, D.P.; MEHROTRA, G.S. (1995) - Landslide hazard zonation: A case study in Garhwal Himalaya, India. *Mountain Research and Development,* 15(4): 301-309.

SAULNIER, G.-M.; BEVEN, K.; OBLED, C. (1997) - Including spatially variable effective soil depths in TOPMODEL. *Journal of Hydrology*, 202(1-4): 158-172.

SCHUSTER, R.L. (1978) - Introduction. *In:* SCHUSTER, R.L.; KRIZEK, R.J. (Eds.), *Landslides: analysis and control*. Nacional Reseach Council. Transportation Research Board, Special Report 176, p. 1-10.

SELBY, M.J. (1993) - *Hillslope Materials and Processes*. Oxford University Press, Oxford, 451 pp.

SHANNON, C.E. (1948) – A mathematical theory of communication, *Bell System Technical Journal* 27, 379-423 pp.and 623-656 pp.

SHARMA, S. (2002) - Slope Stability Concepts. *In*: ABRAMSON, L.W.; LEE, T.S.; SHARMA, S.; BOYCE, G.M. (Eds.), *Slope Stability and Stabilization Methods*. John Wiley & Sons, Inc., New York, p. 329-461.

SIDLE, R.C.; PEARCE, A.J.; O`LOUGHLIN, C.L. (1985) - *Hillslope stability and land use. Water Resources Monograph,* Vol. 11, American Geophysical Union. Washington, D.C., 140 pp.

SOETERS, R.; VAN WESTEN, C.J. (1996) - Slope instability recognition, analysis, and zonation. *In*: TURNER, A.K.; SCHUSTER, R.L. (Eds.), *Landslides: investigation and mitigation*. Special Report 247. Transportation Research Board. National Academic Press, Washington D. C., p. 129-177.

SØRENSEN, R.; ZINKO, U.; SEIBERT, J. (2006) - On the calculation of the topographic wetness index: evaluation of different methods based on field observations. *Hydrology and Earth System Sciences*, 10: 101-112.

SORRISO-VALVO, M.; GULLA, G. (1996) - Rockslide. *In*: DIKAU, R.; BRUNSDEN, D.; SCHROTT, L.; IBSEN, M.L. (Eds.), Landslide Recognition, John Wiley & Sons, Ltd. Chichester, pp. 85-96.

STAMATOPOULOS, C.; FRASER, C. (2011) - An orthogonal projection model for photogrammetric orientation of long focal length imagery. *AfricaGeo 2011 conference*, 31st May-2nd June 2011, Cape Town, South.

STERLACCHINI, S.; BALLABIO, C.; BLAHUT, J.; MASETTI, M.; SORICHETTA, A. (2011) - Spatial agreement of predicted patterns in landslide susceptibility maps. *Geomorphology*, 125(1): 51-61.

SÜZEN, M.L.; DOYURAN, V. (2004) - A comparison of the GIS based landslide susceptibility assessment methods*:* multivariate versus bivariate. *Environmental Geology*, 45 (5): p.665-679.

TAYLOR, D.W. (1948) - *Fundamentals of Soil Mechanics*. John Wiley & Sons, New York, 700 pp.

TEERARUNGSIGUL, S.; CHONGLAKMANI, C.; KUEHU, F. (2007) - Landslide prediction model using remote sensing, GIS and field geology: a case study of wang chin district, Phrae province, Northern Thailand. *GeoThai'07 International Conference on Geology of Thailand: Towards Sustainable Development and Sufficiency Economy*. Department of Mineral resources, Bangkok, Thailand, p. 156-168.

TEJERO, R.; GARZÓN HEYDT, G.; BABÍN VICH, R.; FERNÁNDEZ GARCÍA, P. (2010) - Long-Term evolving ''Tectonic'' landscapes within intra-plate domains: The Iberian Peninsula. *In:* VERESS, B.; SZIGETHY, J (Eds.), *Horizons in Earth Science Research*, Nova Science Publishers Inc, USA, Vol. 2. Cap 4. P. 103-124.

TERZAGHI, K. (1950) - Mechanism of landslides. *In*: Paige, S. (Ed.), *Application of Geology to Engineering Practice, Berkey Vol*ume, Geological Society of America, New York, p. 83-123.

TERZAGHI, K. (1951) - *Mechanism of Landslides*. Department of Engineering. Harvard University, 41 pp.

TERZAGHI, K. (1953) - *Mecanismo dos escorregamentos de terra.* Instituto de Pesquisas Tecnológicas de São Paulo, separata nº467, São Paulo.

THEIL, H. (1972) – *Statistical Decomposition Analysis,*Amsterdam, North-Holland.

TSAI, C.C.; CHEN, Z.S.; DUH C.T.; HORNG, F.V. (2001) - Prediction of soil depth using a soil-landscape regression model: A case study on forest soils in southern Taiwan. *Proceedings of the National Science Council Republic of China*, 25(1): 34-49.

TUCKER, G.E.; CATANI, F.; RINALDO, A.; BRAS, R.L. (2001) - Statistical analysis of drainage density from digital terrain data. *Geomorphology*, 36(3-4): 187-202.

TURNER, A. K.; SCHUSTER, R. L. (1996) – Landslides Investigation and Mitigation, Transportation Research Board, TRB Special Report 247, National Academy Press, Washington, DC, 673 pp.

VALLEJO, L.G.; FERRER, M.; ORTUÑO, L.; OTEO, C. (2002) - *Ingeniería Geológica*. Pearson Educación, Madrid, 744 pp.

VAN ASCH, TH.W.J. (1980) - *Water erosion on slopes and landsliding in a Mediterranean landscape.* University of Utrecht, Department of Geography, Utrecht Geographical Studies 20. 240 pp.

VAN ASCH, TH.W.J.; MALET, J.-P.; BEEK, L.P.H VAN.; AMITRANO, D. (2007) - Techniques, advances, problems and issues in numerical modelling of landslide hazard. *Bulletin de la Société Géologique de France*, 178(2): 6-35.

VAN ASCH, TH.W.J.; VAN DIJCK, S.J.E.; HENDRIKS, M.R. (2001) - The role of the overland flow and subsurface flow on the spatial distribution of soil moisture in the topsoil. *Hydrological processes*, 15(12): 2325-2340.

VAN WESTEN C.J. (1994) - GIS in landslide hazard zonation: A review with examples from the Colombian Andes. In: Price M.F. & Heywood D.I. (eds.), Taylor and Francis, London: 135-165.

VAN WESTEN C.J.; CASTELLANOS, E.; KURIAKOSE, S.L. (2008) - Spatial data for landslide susceptibility, hazards, and vulnerability assessment: An overview. *Engineering geology*, 102(3-4): 112-131.

VARNES, D.J. (1984) - *Landslide hazard zonation: a review of principles and practice.* Volume 3, Natural Hazards. UNESCO, Paris, 63 pp.

VARNES, D.J. (1978) - Slope Movement Types and Processes. *In*: Schuster, R.L.; Krizek, R.J. (Eds.), *Landslides, Analysis and Control*. Special Report, 176. Transportation and Road Research Board, National Academy of Science, Washington D.C., p.11-33.

WESTERBERG, I.K.; GUERRERO, J.-L.; YOUNGER, P.M.; BEVEN, K.J.; SEIBERT, J.; HALLDIN, S.; FREER, J.E.; XU, C.-Y. (2011) - Calibration of hydrological models using flow-duration curves. *Hydrology and Earth System Sciences*, 15: 2205-2227.

WOLMAN, M.G.; MILLER, J.P. (1960) - Magnitude and Frequency of forces in geomorphic processes. *Journal of Geology*, 68(1): 54-74.

WORBOYS, M.; DUCKHAM, M. (2004) - GIS: A Computing Perspective, 2nd Edition, CRC Press, Inc.

WU, C.; QIAO, J. (2009) - Relationship between landslides and lithology in the Three Gorges Reservoir area based on GIS and information value model. *Frontiers of Forestry in China*, 4(2): 165-170.

WU, I-P. (1997) - *A Simple Evapotranspiration Model for Hawaii*: The Hargreaves Model. CTAHR Fact Sheet. Engeineer's Notebook no. 106.

WU, W.; SIDLE, R.C. (1995) - A distributed slope stability model for steep forested Basins. *Water Resources Research*, 31(8), pp. 2097-2110.

YALCIN, A. (2008) - GIS based landslide susceptibility mapping using analytical hierarchy process and bivariate statistics in Ardesen (Turkey): comparision of results and confirmations. *Catena, 72*, 1-12.

YAN, T.Z. (1988) - Recent advances of quantitative prognoses of landslides in China. *In:* Bonnard, C. (Ed.) *Landslides*. Proceedings of the 5th ISL, Lausanne. Vol. 2. Balkema, Rotterdam, p. 1263-1268.

YIN, K.L.; YAN, T.Z. (1988) - Statistical prediction models for slope instability of metamorphosed rocks *in* Bonnard, C. (Ed.) *Landslides*. Proceedings of the 5th ISL, Lausanne. Vol. 2. Balkema, Rotterdam, p. 1269-1272.

ZBYSZEWSKI, G.; ALMEIDA, F.M. (1960) - *Notícia explicativa da folha 26-D de Caldas da Rainha*. Lisboa: Serviços Geológicos de Portugal.

ZBYSZEWSKI, G.; FERREIRA, O.V.; MANUPELLA, G.; ASSUNÇÃO, C.T. (1966) - *Notícia explicativa da folha 30-B de Bombarral*. Lisboa: Serviços Geológicos de Portugal.

ZÊZERE, J.L. (2000) - *A classificação dos movimentos de vertente.* Tipologia, actividade e morfologia. Apontamentos de Geografia, série investigação, nº6, CEG, Lisboa.

ZÊZERE, J.L. (2002) - Landslide susceptibility assessment considering landslide typology. A case study in the area north of Lisbon (Portugal). *Natural Hazards and Earth System Sciences,* 2: 73-82.

ZÊZERE, J.L. (2005a) - A geomorfologia da região das Caldas da Rainha. *In:* COSTA, C.M.M. et al. (Eds.), Caldas da Rainha: património das águas. *A legacy of waters*. Câmara Municipal das Caldas da Rainha, p. 57-65.

ZÊZERE, J.L. (2005b) - *Dinâmica de Vertentes e Riscos Geomorfológicos*. Centro de Estudos Geográficos, Relatório nº. 41, Lisboa.

ZÊZERE, J.L. (2007) - Riscos e Ordenamento do Território. Inforgeo, 20/21, Ordenamento Territorial, Associação Portuguesa de Geógrafos: pp. 59-63.

ZÊZERE, J.L. (2010) - *Relatório do programa de Perigosidade, Vulnerabilidade e Riscos no Território: aplicação aos movimentos de vertente*. Provas de Agregação. Universidade de Lisboa.

ZÊZERE, J.L.; GARCIA, R.A.C.; OLIVEIRA, S.C.; REIS, E. (2008) - Probabilistic landslide risk analysis considering direct costs in the area north of Lisbon (Portugal). *Geomorphology*, 94: 467-495.

ZÊZERE, J.L.; REIS, R.; GARCIA, R.A.C.; OLIVEIRA, S.C.; RODRIGUES, M.L.; FERREIRA, A. B. (2004) - Integration of spatial and temporal data for the definition of different landslide hazard scenarios in the area north of Lisbon (Portugal). *Natural Hazards and Earth System Sciences,* 4(1): 133-146.

ZÊZERE, J.L.; RODRIGUES, M.L. (2002) - Rainfall thresholds for landsliding in Lisbon Area (Portugal). *In:* Rybar, J.; Stemberk, J., Wagner, P. (Eds.), *Landslides.* A.A. Balkema, Lisse, p. 333-338.

ZÊZERE, J.L.; TRIGO, R. (2011) - Impacts of the North Atlantic Oscillation on Landslides. *In:* Vicente-Serrano, S.M.; Trigo, R. (Eds.), *Hydrological, Socioeconomic and Ecological Impacts of the North Atlantic Oscillation in the Mediterranean Region*. Advances in Global Change Research, Vol. 46, Springer, p.199-212.

ZÊZERE, J.L.; TRIGO, R.; TRIGO, I. (2005) - Shallow and deep landslides induced by rainfall in the Lisbon region (Portugal): assessment of relationships with the North Atlantic Oscillation. *Natural Hazards and Earth System Sciences,* 5: 331-344.

APPENDICES

APPENDIX 1: CALCULATION FORM OF ACCOUNTABILITY AND RELIABILITY INDEXES FOR EACH LANDSLIDE TYPE OF EACH LANDSLIDE INVENTORY.

Table A1.1 – Calculation form of Accountability and Reliability indexes: Deep seated landslides for LI#2 for the previous lithological map.

	A	B	C	D	E	F	G
1	Previous Lithology classes	Area (m^2)	Deep seated landslides area (m^2)	"C"/"D"	"C" values to be used	ACC	RLB
2	Aluvium and sand dunes (Holocene)	19376170	11825	0.001			
3	Sands (Pliocene)	1832444	3925	0.002			
4	Sandstones, claystones and limestones (Miocene)	43777	0	0.000			
5	Sandstones and claystones (lower and middle Miocene)	1353234	625	0.000			
6	Sandstones and claystones (Cretaceous)	4906542	4000	0.001			
7	Sandstones and claystones (upper Jurassic)	242466538	847325	0.003*	847325		
8	Marls, sandstones and claystones (upper Jurassic)	122573	0	0.000			
9	Limestones and claystones (upper Jurassic)	1142319	0	0.000			
10	Limestones and marls (middle and upper Jurassic)	1467536	3000	0.002			
11	Dolerite	3181253	42150	0.013*	42150		
12	**SUM**	275892387	912850		889475		
13				"C12"/"B12"= **0.003**		"E12"/"C12" *100= 97.44	"E12"/("B7" +"B11") *100= 0.36

* Green values are the values that are greater or equal than the value on E13 cell. Those values indicate whose values on C and B column will be inserted for Accountability and Reliability scores.

Table A1.2 – Calculation form of Accountability and Reliability indexes: Deep seated landslides for LI#3 for the previous lithological map.

	A	B	C	D	E	F	G
1	Previous Lithology classes	Area (m^2)	Deep seated landslides area (m^2)	"C"/"D"	"C" values to be used	ACC	RLB
2	Aluvium and sand dunes (Holocene)	19376170	2500	0.000			
3	Sands (Pliocene)	1832444	0	0.000			
4	Sandstones, claystones and limestones (Miocene)	43777	0	0.000			
5	Sandstones and claystones (lower and middle Miocene)	1353234	250	0.000			
6	Sandstones and claystones (Cretaceous)	4906542	900	0.000			
7	Sandstones and claystones (upper Jurassic)	242466538	248525	0.000			
8	Marls, sandstones and claystones (upper Jurassic)	122573	0	0.000			
9	Limestones and claystones (upper Jurassic)	1142319	0	0.000			
10	Limestones and marls (middle and upper Jurassic)	1467536	0	0.000			
11	Dolerite	3181253	36500	0.011*	36500		
12	**SUM**	275892387	288675		36500		
13				"C12"/"B12"= **0.001**		"E12"/"C12" *100= 12.64	"E12"/ ("B11") *100= 1.15

* Green values are the values that are greater or equal than the value on E13 cell. Those values indicate whose values on C and B column will be inserted for Account ability and Reliability scores.

Table A1.3 – Calculation form of Accountability and Reliability indexes: Deep seated landslides for Sum Iv for the previous lithological map.

	A	B	C	D	E	F	G
1	Previous Lithology classes	Area (m^2)	Deep seated landslides area (m^2)	"C"/"D"	"C" values to be used	ACC	RLB
2	Aluvium and sand dunes (Holocene)	19376170	19875	0.001			
3	Sands (Pliocene)	1832444	5175	0.003			
4	Sandstones, claystones and limestones (Miocene)	43777	0	0.000			
5	Sandstones and claystones (lower and middle Miocene)	1353234	1775	0.001			
6	Sandstones and claystones (Cretaceous)	4906542	10900	0.002			
7	Sandstones and claystones (upper Jurassic)	242466538	3253150	0.013*	3253150		
8	Marls, sandstones and claystones (upper Jurassic)	122573	0	0.000			
9	Limestones and claystones (upper Jurassic)	1142319	0	0.000			
10	Limestones and marls (middle and upper Jurassic)	1467536	8050	0.005			
11	Dolerite	3181253	198125	0.062*	198125		
12	**SUM**	275892387	3497050		3451275		
13				"C12"/"B12"= **0.013**		"E12"/"C12" *100= 98.69	"E12"/ ("B11") *100= 1.41

* Green values are the values that are greater or equal than the value on E13 cell. Those values indicate whose values on C and B column will be inserted for Accountability and Reliability scores.

Table A1.4 – Calculation form of Accountability and Reliability indexes: Deep seated landslides for LI#2 for the detailed lithological map.

	A	B	C	D	E	F	G
1	Detailed Lithology classes	Area (m^2)	Deep seated landslides area (m^2)	"C"/"D"	"C" values to be used	ACC	RLB
2	Alluvium and sand dunes (Holocene)	18786916	0	0.000			
3	Sands (Pliocene)	1960624	3925	0.002			
4	Sandstones, claystones and limestones (Miocene)	43777	0	0.000			
5	Sandstone dominated complexes (lower and middle Miocene)	683297	0	0.000			
6	Shale dominated complexes (lower and middle Miocene)	669937	625	0.001			
7	Sandstone dominated complexes (Cretaceous)	1465099	150	0.000			
8	Shale dominated complexes (Cretaceous)	3441443	3850	0.001			
9	Sandstone dominated complexes (upper Jurassic)	79310723	59150	0.001			
10	Shale dominated complexes (upper Jurassic)	163608615	800000	0.005*	800000		
11	Marls, sandstones and claystones (upper Jurassic)	122573	0	0.000			
12	Limestones and claystones (upper Jurassic)	1142319	0	0.000			
13	Limestones and marls (middle and upper Jurassic)	1467536	3000	0.002			
14	Dolerite	3189527	42150	0.013*	42150		
15	**SUM**	275892387	912850		842150		
16				C12/B12= **0.003**		"E15"/"C15" *100= 92.26	"E15"/ ("B10"+"B14") *100= 0.51

* Green values are the values that are greater or equal than the value on E16 cell. Those values indicate whose values on C and B column will be inserted for Accountability and Reliability scores.

Table A1.5 – Calculation form of Accountability and Reliability indexes: Deep seated landslides for LI#3 for the detailed lithological map.

	A	B	C	D	E	F	G
1	Detailed Lithology classes	Area (m^2)	Deep seated landslides area (m^2)	"C"/"D"	"C" values to be used	ACC	RLB
2	Alluvium and sand dunes (Holocene)	18786916	0	0.000			
3	Sands (Pliocene)	1960624	0	0.000			
4	Sandstones, claystones and limestones (Miocene)	43777	0	0.000			
5	Sandstone dominated complexes (lower and middle Miocene)	683297	0	0.000			
6	Shale dominated complexes (lower and middle Miocene)	669937	250	0.000			
7	Sandstone dominated complexes (Cretaceous)	1465099	0	0.000			
8	Shale dominated complexes (Cretaceous)	3441443	900	0.000			
9	Sandstone dominated complexes (upper Jurassic)	79310723	17950	0.000			
10	Shale dominated complexes (upper Jurassic)	163608615	233075	0.001*	233075		
11	Marls, sandstones and claystones (upper Jurassic)	122573	0	0.000			
12	Limestones and claystones (upper Jurassic)	1142319	0	0.000			
13	Limestones and marls (middle and upper Jurassic)	1467536	0	0.000			
14	Dolerite	3189527	36500	0.011*	36500		
15	**SUM**	275892387	288675		269575		
16				C12/B12= **0.001**		"E15"/"C15" *100= 93.38	"E15"/ ("B10"+"B14") *100= 0.16

* Green values are the values that are greater or equal than the value on E16 cell. Those values indicate whose values on C and B column will be inserted for Accountability and Reliability scores.

Table A1.6 – Calculation form of Accountability and Reliability indexes: Deep seated landslides for Sum Iv for the detailed lithological map.

	A	B	C	D	E	F	G
1	Detailed Lithology classes	Area (m^2)	Deep seated landslides area (m^2)	"C"/"D"	"C" values to be used	ACC	RLB
2	Alluvium and sand dunes (Holocene)	18786916	0	0.000			
3	Sands (Pliocene)	1960624	5175	0.003			
4	Sandstones, claystones and limestones (Miocene)	43777	0	0.000			
5	Sandstone dominated complexes (lower and middle Miocene)	683297	0	0.000			
6	Shale dominated complexes (lower and middle Miocene)	669937	1775	0.003			
7	Sandstone dominated complexes (Cretaceous)	1465099	875	0.001			
8	Shale dominated complexes (Cretaceous)	3441443	10025	0.003			
9	Sandstone dominated complexes (upper Jurassic)	79310723	147325	0.002			
10	Shale dominated complexes (upper Jurassic)	163608615	3125700	0.019*	3125700		
11	Marls, sandstones and claystones (upper Jurassic)	122573	0	0.000			
12	Limestones and claystones (upper Jurassic)	1142319	0	0.000			
13	Limestones and marls (middle and upper Jurassic)	1467536	8050	0.005			
14	Dolerite	3189527	198125	0.062*	198125		
15	**SUM**	275892387	3497050		3323825		
16				C12/B12= **0.013**		"E15"/"C15" *100= 95.05	"E15"/ ("B10"+"B14") *100= 1.99

* Green values are the values that are greater or equal than the value on E16 cell. Those values indicate whose values on C and B column will be inserted for Accountability and Reliability scores.

Table A1.7 – Calculation form of Accountability and Reliability indexes: Shallow landslides for LI#1 for the previous lithological map.

	A	B	C	D	E	F	G
1	Previous Lithology classes	Area (m^2)	Deep seated landslides area (m^2)	"C"/"D"	"C" values to be used	ACC	RLB
2	Aluvium and sand dunes (Holocene)	19376170	3575	0.0000			
3	Sands (Pliocene)	1832444	1525	0.0001			
4	Sandstones, claystones and limestones (Miocene)	43777	0	0.0000			
5	Sandstones and claystones (lower and middle Miocene)	1353234	0	0.0000			
6	Sandstones and claystones (Cretaceous)	4906542	0	0.0000			
7	Sandstones and claystones (upper Jurassic)	242466538	133975	0.0006*	133975		
8	Marls, sandstones and claystones (upper Jurassic)	122573	0	0.0000			
9	Limestones and claystones (upper Jurassic)	1142319	0	0.0000			
10	Limestones and marls (middle and upper Jurassic)	1467536	3025	0.0021*	3025		
11	Dolerite	3181253	0	0.000			
12	**SUM**	275892387	284200		137000		
13				C12/B12= **0.0005**		"E12"/"C12" *100= 96.41	"E12"/ ("B7"+"B10") *100= 0.06

* Green values are the values that are greater or equal than the value on E13 cell. Those values indicate whose values on C and B column will be inserted for Accountability and Reliability scores.

Table A1.8 – Calculation form of Accountability and Reliability indexes: Shallow landslides for LI#2 for the previous lithological map.

	A	B	C	D	E	F	G
1	Previous Lithology classes	Area (m^2)	Deep seated landslides area (m^2)	"C"/"D"	"C" values to be used	ACC	RLB
2	Aluvium and sand dunes (Holocene)	19376170	150	0.0000			
3	Sands (Pliocene)	1832444	800	0.0004*	800		
4	Sandstones, claystones and limestones (Miocene)	43777	0	0.0000			
5	Sandstones and claystones (lower and middle Miocene)	1353234	0	0.0000			
6	Sandstones and claystones (Cretaceous)	4906542	525	0.0001			
7	Sandstones and claystones (upper Jurassic)	242466538	67575	0.0003*	67575		
8	Marls, sandstones and claystones (upper Jurassic)	122573	0	0.0000			
9	Limestones and claystones (upper Jurassic)	1142319	0	0.0000			
10	Limestones and marls (middle and upper Jurassic)	1467536	150	0.0001			
11	Dolerite	3181253	400	0.0001			
12	**SUM**	275892387	69600		68375		
13				C12/B12= **0.0003**		"E12"/"C12" *100= 98.24	"E12"/ ("B3"+"B7") *100= 0.03

* Green values are the values that are greater or equal than the value on E13 cell. Those values indicate whose values on C and B column will be inserted for Accountability and Reliability scores.

Table A1.9 – Calculation form of Accountability and Reliability indexes: Shallow landslides for LI#3 for the previous lithological map.

	A	B	C	D	E	F	G
1	Previous Lithology classes	Area (m^2)	Deep seated landslides area (m^2)	"C"/"D"	"C" values to be used	ACC	RLB
2	Aluvium and sand dunes (Holocene)	19376170	3375	0.0002			
3	Sands (Pliocene)	1832444	0	0.0000			
4	Sandstones, claystones and limestones (Miocene)	43777	0	0.0000			
5	Sandstones and claystones (lower and middle Miocene)	1353234	0	0.0000			
6	Sandstones and claystones (Cretaceous)	4906542	175	0.0000			
7	Sandstones and claystones (upper Jurassic)	242466538	50825	0.0002*	50825		
8	Marls, sandstones and claystones (upper Jurassic)	122573	0	0.0000			
9	Limestones and claystones (upper Jurassic)	1142319	0	0.0000			
10	Limestones and marls (middle and upper Jurassic)	1467536	375	0.0003*	375		
11	Dolerite	3181253	1250	0.0004*	1250		
12	**SUM**	275892387	56000		52450		
13				C12/B12= **0.0002**		"E12"/"C12" *100= **93.66**	E12"/ ("B7"+"B10*+ "B11")*100= **0.02**

* Green values are the values that are greater or equal than the value on E13 cell. Those values indicate whose values on C and B column will be inserted for Accountability and Reliability scores.

Table A1.10 – Calculation form of Accountability and Reliability indexes: Shallow landslides for Sum Iv for the previous lithological map.

	A	B	C	D	E	F	G
1	Previous Lithology classes	Area (m^2)	Deep seated landslides area (m^2)	"C"/"D"	"C" values to be used	ACC	RLB
2	Aluvium and sand dunes (Holocene)	19376170	6850	0.00035			
3	Sands (Pliocene)	1832444	2275	0.00124*	2275		
4	Sandstones, claystones and limestones (Miocene)	43777	0	0.00000			
5	Sandstones and claystones (lower and middle Miocene)	1353234	0	0.00000			
6	Sandstones and claystones (Cretaceous)	4906542	675	0.00014			
7	Sandstones and claystones (upper Jurassic)	242466538	252450	0.00104*	252450		
8	Marls, sandstones and claystones (upper Jurassic)	122573	0	0.00000			
9	Limestones and claystones (upper Jurassic)	1142319	0	0.00000			
10	Limestones and marls (middle and upper Jurassic)	1467536	3475	0.00237*	3475		
11	Dolerite	3181253	1625	0.00051			
12	**SUM**	275892387	267350		258200		
13				C12/B12= **0.00097**		"E12"/"C12" *100= 96.58	E12"/ ("B3"+"B7*+ "B10")*100= **0.11**

* Green values are the values that are greater or equal than the value on E13 cell. Those values indicate whose values on C and B column will be inserted for Accountability and Reliability scores.

Table A1.11 – Calculation form of Accountability and Reliability indexes: Shallow landslides for LI#1 for the detailed lithological map.

	A	B	C	D	E	F	G
1	Detailed Lithology classes	Area (m^2)	Deep seated landslides area (m^2)	"C"/"D"	"C" values to be used	ACC	RLB
2	Alluvium and sand dunes (Holocene)	18786916	0	0.0000			
3	Sands (Pliocene)	1960624	1675	0.0009*	1675		
4	Sandstones, claystones and limestones (Miocene)	43777	0	0.0000			
5	Sandstone dominated complexes (lower and middle Miocene)	683297	0	0.0000			
6	Shale dominated complexes (lower and middle Miocene)	669937	0	0.0000			
7	Sandstone dominated complexes (Cretaceous)	1465099	0	0.0000			
8	Shale dominated complexes (Cretaceous)	3441443	0	0.0000			
9	Sandstone dominated complexes (upper Jurassic)	79310723	0	0.0000			
10	Shale dominated complexes (upper Jurassic)	163608615	137400	0.0008*	137400		
11	Marls, sandstones and claystones (upper Jurassic)	122573	0	0.0000			
12	Limestones and claystones (upper Jurassic)	1142319	0	0.0000			
13	Limestones and marls (middle and upper Jurassic)	1467536	3025	0.0021*	3025		
14	Dolerite	3189527	0	0.0000			
15	**SUM**	275892387	142100		142100		
16				C12/B12= **0.0005**		"E15"/"C15" *100= 100	"E15"/ ("B3"+"B10" +"B13")*100= 0.09

* Green values are the values that are greater or equal than the value on E16 cell. Those values indicate whose values on C and B column will be inserted for Accountability and Reliability scores.

Table A1.12 – Calculation form of Accountability and Reliability indexes: Shallow landslides for LI#2 for the detailed lithological map.

	A	B	C	D	E	F	G
1	Detailed Lithology classes	Area (m^2)	Deep seated landslides area (m^2)	"C"/"D"	"C" values to be used	ACC	RLB
2	Alluvium and sand dunes (Holocene)	18786916	0	0.0000			
3	Sands (Pliocene)	1960624	800	0.0004*	800		
4	Sandstones, claystones and limestones (Miocene)	43777	0	0.0000			
5	Sandstone dominated complexes (lower and middle Miocene)	683297	0	0.0000			
6	Shale dominated complexes (lower and middle Miocene)	669937	0	0.0000			
7	Sandstone dominated complexes (Cretaceous)	1465099	0	0.0000			
8	Shale dominated complexes (Cretaceous)	3441443	525	0.0002			
9	Sandstone dominated complexes (upper Jurassic)	79310723	0	0.0000			
10	Shale dominated complexes (upper Jurassic)	163608615	67725	0.0004*	67725		
11	Marls, sandstones and claystones (upper Jurassic)	122573	0	0.0000			
12	Limestones and claystones (upper Jurassic)	1142319	0	0.0000			
13	Limestones and marls (middle and upper Jurassic)	1467536	150	0.0001			
14	Dolerite	3189527	400	0.0001			
15	**SUM**	275892387	69600		68525		
16				C12/B12= **0.0003**		"E15"/"C15" *100= 98.46	"E15"/ ("B3"+"B10") *100= 0.04

* Green values are the values that are greater or equal than the value on E16 cell. Those values indicate whose values on C and B column will be inserted for Accountability and Reliability scores

Table A1.13 – Calculation form of Accountability and Reliability indexes: Shallow landslides for LI#3 for the detailed lithological map.

	A	B	C	D	E	F	G
1	Detailed Lithology classes	Area (m^2)	Deep seated landslides area (m^2)	"C"/"D"	"C" values to be used	ACC	RLB
2	Alluvium and sand dunes (Holocene)	18786916	0	0.0000			
3	Sands (Pliocene)	1960624	0	0.0000			
4	Sandstones, claystones and limestones (Miocene)	43777	0	0.0000			
5	Sandstone dominated complexes (lower and middle Miocene)	683297	0	0.0000			
6	Shale dominated complexes (lower and middle Miocene)	669937	0	0.0000			
7	Sandstone dominated complexes (Cretaceous)	1465099	0	0.0000			
8	Shale dominated complexes (Cretaceous)	3441443	175	0.0001			
9	Sandstone dominated complexes (upper Jurassic)	79310723	0	0.0000			
10	Shale dominated complexes (upper Jurassic)	163608615	54200	0.0003*	54200		
11	Marls, sandstones and claystones (upper Jurassic)	122573	0	0.0000			
12	Limestones and claystones (upper Jurassic)	1142319	0	0.0000			
13	Limestones and marls (middle and upper Jurassic)	1467536	375	0.0003*	375		
14	Dolerite	3189527	1250	0.0004*	1250		
15	**SUM**	275892387	56000		55825		
16				C12/B12= **0.0002**		"E15"/"C15" *100= 99.69	"E15"/ ("B10"+"B13" +"B14")*100= 0.03

* Green values are the values that are greater or equal than the value on E16 cell. Those values indicate whose values on C and B column will be inserted for Accountability and Reliability scores.

Table A1.14 – Calculation form of Accountability and Reliability indexes: Shallow landslides for Sum Iv for the detailed lithological map.

	A	B	C	D	E	F	G
1	Detailed Lithology classes	Area (m^2)	Deep seated landslides area (m^2)	"C"/"D"	"C" values to be used	ACC	RLB
2	Alluvium and sand dunes (Holocene)	18786916	0	0.0000			
3	Sands (Pliocene)	1960624	2450	0.0012*	2450		
4	Sandstones, claystones and limestones (Miocene)	43777	0	0.0000			
5	Sandstone dominated complexes (lower and middle Miocene)	683297	0	0.0000			
6	Shale dominated complexes (lower and middle Miocene)	669937	0	0.0000			
7	Sandstone dominated complexes (Cretaceous)	1465099	0	0.0000			
8	Shale dominated complexes (Cretaceous)	3441443	675	0.0002			
9	Sandstone dominated complexes (upper Jurassic)	79310723	0	0.0000			
10	Shale dominated complexes (upper Jurassic)	163608615	259125	0.0016*	259125		
11	Marls, sandstones and claystones (upper Jurassic)	122573	0	0.0000			
12	Limestones and claystones (upper Jurassic)	1142319	0	0.0000			
13	Limestones and marls (middle and upper Jurassic)	1467536	3475	0.0024*	3475		
14	Dolerite	3189527	1625	0.0005			
15	**SUM**	275892387	267350		265050		
16				C12/B12= **0.0010**		"E15"/"C15" *100= 99.14	"E15"/ ("B3"+"B10" +"B13")*100= 0.16

* Green values are the values that are greater or equal than the value on E16 cell. Those values indicate whose values on C and B column will be inserted for Accountability and Reliability scores.

Table A1.15 – Calculation form of Accountability and Reliability indexes: Shallow and Deep seated landslides for LI#1 for the previous lithological map.

	A	B	C	D	E	F	G
1	Previous Lithology classes	Area (m^2)	Deep seated landslides area (m^2)	"C"/"D"	"C" values to be used	ACC	RLB
2	Aluvium and sand dunes (Holocene)	19376170	9275	0.0005			
3	Sands (Pliocene)	1832444	2750	0.0015			
4	Sandstones, claystones and limestones (Miocene)	43777	0	0.0000			
5	Sandstones and claystones (lower and middle Miocene)	1353234	825	0.0006			
6	Sandstones and claystones (Cretaceous)	4906542	5950	0.0012			
7	Sandstones and claystones (upper Jurassic)	242466538	2332950	0.0096*	2332950		
8	Marls, sandstones and claystones (upper Jurassic)	122573	0	0.0000			
9	Limestones and claystones (upper Jurassic)	1142319	0	0.0000			
10	Limestones and marls (middle and upper Jurassic)	1467536	8000	0.0055			
11	Dolerite	3181253	136050	0.0428*	136050		
12	**SUM**	275892387	2495800		2469000		
13				"C12"/"B12"= **0.009**		"E12"/"C12" *100= 98.93	"E12"/ ("B7"+"B11") *100= 1.01

* Green values are the values that are greater or equal than the value on E13 cell. Those values indicate whose values on C and B column will be inserted for Accountability and Reliability scores.

Table A1.16 – Calculation form of Accountability and Reliability indexes: Shallow and Deep seated landslides for LI#2 for the previous lithological map.

	A	B	C	D	E	F	G
1	Previous Lithology classes	Area (m^2)	Deep seated landslides area (m^2)	"C"/"D"	"C" values to be used	ACC	RLB
2	Aluvium and sand dunes (Holocene)	19376170	11925	0.001			
3	Sands (Pliocene)	1832444	4675	0.003			
4	Sandstones, claystones and limestones (Miocene)	43777	0	0.000			
5	Sandstones and claystones (lower and middle Miocene)	1353234	675	0.000			
6	Sandstones and claystones (Cretaceous)	4906542	4550	0.001			
7	Sandstones and claystones (upper Jurassic)	242466538	915275	0.004*	915275		
8	Marls, sandstones and claystones (upper Jurassic)	122573	0	0.000			
9	Limestones and claystones (upper Jurassic)	1142319	0	0.000			
10	Limestones and marls (middle and upper Jurassic)	1467536	3125	0.002			
11	Dolerite	3181253	42725	0.013*	42725		
12	**SUM**	275892387	982950		958000		
13				"C12"/"B12"= **0.004**		"E12"/"C12" *100= 97.46	"E12"/ ("B7"+"B11") *100= 0.39

* Green values are the values that are greater or equal than the value on E13 cell. Those values indicate whose values on C and B column will be inserted for Accountability and Reliability scores.

Table A1.17 – Calculation form of Accountability and Reliability indexes: Shallow and Deep seated landslides for LI#3 for the previous lithological map.

	A	B	C	D	E	F	G
1	Previous Lithology classes	Area (m^2)	Deep seated landslides area (m^2)	"C"/"D"	"C" values to be used	ACC	RLB
2	Aluvium and sand dunes (Holocene)	19376170	5825	0.0003			
3	Sands (Pliocene)	1832444	0	0.0000			
4	Sandstones, claystones and limestones (Miocene)	43777	0	0.0000			
5	Sandstones and claystones (lower and middle Miocene)	1353234	275	0.0002			
6	Sandstones and claystones (Cretaceous)	4906542	1150	0.0002			
7	Sandstones and claystones (upper Jurassic)	242466538	299500	0.0012			
8	Marls, sandstones and claystones (upper Jurassic)	122573	0	0.0000			
9	Limestones and claystones (upper Jurassic)	1142319	0	0.0000			
10	Limestones and marls (middle and upper Jurassic)	1467536	375	0.0003			
11	Dolerite	3181253	37975	0.0119*	37975		
12	**SUM**	275892387	345100		37975		
13				"C12"/"B12"= **0.0013**		"E12"/"C12" *100= 11.00	"E12"/ ("B11") *100= 1.19

* Green values are the values that are greater or equal than the value on E13 cell. Those values indicate whose values on C and B column will be inserted for Accountability and Reliability scores.

Table A1.18 – Calculation form of Accountability and Reliability indexes: Shallow and Deep seated landslides for Sum Iv for the previous lithological map.

	A	B	C	D	E	F	G
1	Previous Lithology classes	Area (m^2)	Deep seated landslides area (m^2)	"C"/"D"	"C" values to be used	ACC	RLB
2	Aluvium and sand dunes (Holocene)	19376170	27025	0.0014			
3	Sands (Pliocene)	1832444	7425	0.0041			
4	Sandstones, claystones and limestones (Miocene)	43777	0	0.0000			
5	Sandstones and claystones (lower and middle Miocene)	1353234	1775	0.0013			
6	Sandstones and claystones (Cretaceous)	4906542	11650	0.0024			
7	Sandstones and claystones (upper Jurassic)	242466538	3547725	0.0146*	3547725		
8	Marls, sandstones and claystones (upper Jurassic)	122573	0	0.0000			
9	Limestones and claystones (upper Jurassic)	1142319	0	0.0000			
10	Limestones and marls (middle and upper Jurassic)	1467536	11500	0.0078			
11	Dolerite	3181253	216750	0.0681*	216750		
12	**SUM**	275892387	3823850		3764475		
13				"C12"/"B12"= **0.0139**		"E12"/"C12" *100= 98.45	"E12"/ ("B7"+"B11") *100= 1.53

* Green values are the values that are greater or equal than the value on E13 cell. Those values indicate whose values on C and B column will be inserted for Accountability and Reliability scores.

Table A1.19 – Calculation form of Accountability and Reliability indexes: Shallow and Deep seated landslides for LI#1 for the detailed lithological map.

	A	B	C	D	E	F	G
1	Detailed Lithology classes	Area (m^2)	Deep seated landslides area (m^2)	"C"/"D"	"C" values to be used	ACC	RLB
2	Alluvium and sand dunes (Holocene)	18786916	0	0.0000			
3	Sands (Pliocene)	1960624	2900	0.0015			
4	Sandstones, claystones and limestones (Miocene)	43777	0	0.0000			
5	Sandstone dominated complexes (lower and middle Miocene)	683297	0	0.0000			
6	Shale dominated complexes (lower and middle Miocene)	669937	825	0.0012			
7	Sandstone dominated complexes (Cretaceous)	1465099	750	0.0005			
8	Shale dominated complexes (Cretaceous)	3441443	5200	0.0015			
9	Sandstone dominated complexes (upper Jurassic)	79310723	71525	0.0009			
10	Shale dominated complexes (upper Jurassic)	163608615	2270550	0.0139*	2270550		
11	Marls, sandstones and claystones (upper Jurassic)	122573	0	0.0000			
12	Limestones and claystones (upper Jurassic)	1142319	0	0.0000			
13	Limestones and marls (middle and upper Jurassic)	1467536	8000	0.0055			
14	Dolerite	3189527	136050	0.0427*	136050		
15	**SUM**	275892387	2495800		2406600		
16				C12/B12= **0.0090**		"E15"/"C15" *100= 96.43	"E15"/ ("B10"+"B14") *100= 1.44

* Green values are the values that are greater or equal than the value on E16 cell. Those values indicate whose values on C and B column will be inserted for Accountability and Reliability scores.

Table A1.20 – Calculation form of Accountability and Reliability indexes: Shallow and Deep seated for LI#2 for the detailed lithological map.

	A	B	C	D	E	F	G
1	Detailed Lithology classes	Area (m^2)	Deep seated landslides area (m^2)	"C"/"D"	"C" values to be used	ACC	RLB
2	Alluvium and sand dunes (Holocene)	18786916	0	0.0000			
3	Sands (Pliocene)	1960624	4675	0.0024			
4	Sandstones, claystones and limestones (Miocene)	43777	0	0.0000			
5	Sandstone dominated complexes (lower and middle Miocene)	683297	0	0.0000			
6	Shale dominated complexes (lower and middle Miocene)	669937	675	0.0010			
7	Sandstone dominated complexes (Cretaceous)	1465099	150	0.0001			
8	Shale dominated complexes (Cretaceous)	3441443	4400	0.0013			
9	Sandstone dominated complexes (upper Jurassic)	79310723	58675	0.0007			
10	Shale dominated complexes (upper Jurassic)	163608615	868525	0.0053*	868525		
11	Marls, sandstones and claystones (upper Jurassic)	122573	0	0.0000			
12	Limestones and claystones (upper Jurassic)	1142319	0	0.0000			
13	Limestones and marls (middle and upper Jurassic)	1467536	3125	0.0021			
14	Dolerite	3189527	42725	0.0134*	42725		
15	**SUM**	275892387	982950		911250		
16				C12/B12= **0.0036**		"E15"/"C15"*100= 92.71	"E15"/("B10"+"B14")*100= 0.55

* Green values are the values that are greater or equal than the value on E16 cell. Those values indicate whose values on C and B column will be inserted for Accountability and Reliability scores.

Table A1.21 – Calculation form of Accountability and Reliability indexes: Shallow and Deep seated for LI#3 for the detailed lithological map.

	A	B	C	D	E	F	G
1	Detailed Lithology classes	Area (m^2)	Deep seated landslides area (m^2)	"C"/"D"	"C" values to be used	ACC	RLB
2	Alluvium and sand dunes (Holocene)	18786916	0	0.0000			
3	Sands (Pliocene)	1960624	0	0.0000			
4	Sandstones, claystones and limestones (Miocene)	43777	0	0.0000			
5	Sandstone dominated complexes (lower and middle Miocene)	683297	0	0.0000			
6	Shale dominated complexes (lower and middle Miocene)	669937	275	0.0004			
7	Sandstone dominated complexes (Cretaceous)	1465099	0	0.0000			
8	Shale dominated complexes (Cretaceous)	3441443	1150	0.0003			
9	Sandstone dominated complexes (upper Jurassic)	79310723	17675	0.0002			
10	Shale dominated complexes (upper Jurassic)	163608615	287650	0.0018*	287650		
11	Marls, sandstones and claystones (upper Jurassic)	122573	0	0.0000			
12	Limestones and claystones (upper Jurassic)	1142319	0	0.0000			
13	Limestones and marls (middle and upper Jurassic)	1467536	375	0.0003			
14	Dolerite	3189527	37975	0.0119*	37975		
15	**SUM**	275892387	345100		325625		
16				C12/B12= **0.0013**		"E15"/"C15" *100= 94.36	"E15"/ ("B10"+"B14") *100= 0.20

* Green values are the values that are greater or equal than the value on E16 cell. Those values indicate whose values on C and B column will be inserted for Accountability and Reliability scores.

Table A1.22 – Calculation form of Accountability and Reliability indexes: Shallow and Deep seated for Sum Iv for the detailed lithological map.

	A	B	C	D	E	F	G
1	Detailed Lithology classes	Area (m^2)	Deep seated landslides area (m^2)	"C"/"D"	"C" values to be used	ACC	RLB
2	Alluvium and sand dunes (Holocene)	18786916	0	0.0000			
3	Sands (Pliocene)	1960624	7575	0.0039			
4	Sandstones, claystones and limestones (Miocene)	43777	0	0.0000			
5	Sandstone dominated complexes (lower and middle Miocene)	683297	0	0.0000			
6	Shale dominated complexes (lower and middle Miocene)	669937	1775	0.0026			
7	Sandstone dominated complexes (Cretaceous)	1465099	900	0.0006			
8	Shale dominated complexes (Cretaceous)	3441443	10750	0.0031			
9	Sandstone dominated complexes (upper Jurassic)	79310723	147875	0.0019			
10	Shale dominated complexes (upper Jurassic)	163608615	3426725	0.0209*	3426725		
11	Marls, sandstones and claystones (upper Jurassic)	122573	0	0.0000			
12	Limestones and claystones (upper Jurassic)	1142319	0	0.0000			
13	Limestones and marls (middle and upper Jurassic)	1467536	11500	0.0078			
14	Dolerite	3189527	216750	0.0680*	216750		
15	**SUM**	275892387	3823850		3643475		
16				C12/B12= **0.0139**		"E15"/"C15" *100= 95.28	"E15"/ ("B10"+"B14") *100= 2.18

* Green values are the values that are greater or equal than the value on E16 cell. Those values indicate whose values on C and B column will be inserted for Accountability and Reliability scores.

APPENDIX 2: GEOBED GIS SCRIPT.

Script A2.1 – Geobed GIS script. By Ivan Marchesini. The script is available (v. 0.1 alpha), under the terms of the GPL license.

```
#!/bin/sh

############################################################################

#

# MODULE:       v.geobed 0.1 (alpha)

# AUTHOR(S):    Ivan Marchesini <ivan.marchesini AT irpi.cnr.it>

# PURPOSE:      Calculates geologic bedding attitudes starting from bedding traces and DEM

# COPYRIGHT:    (C) 2011 Ivan Marchesini

#

#           This program is free software under the GNU General Public

#           License (>=v2). Read the file COPYING that comes with GRASS

#           for details.

#

############################################################################

#attenzione in input devono essere date le tracce dei markers (m) geologici 3d (anche se forse non serve che siano 3d) ed i punti 3d da queste estratti


START=$(date +%s)


bed_trc=$1

dtm=$2

sinuos=$3

output=$4

contour=$5
```

```
#faccio partire il monitor

d.mon start=x0



#aggiungo il valore di sinuosità bidimensionale

echo "I select only sinuous lines ........"

v.db.addcol map=$bed_trc layer=1 'columns=sinuos double precision'

v.to.db map=$bed_trc type=line layer=1 qlayer=1 option=sinuous units=meters
columns=sinuos

eval `v.info -t map=$bed_trc layer=1`

linee_iniziali=$lines



#drappeggio le linee sul DEM

echo "I drape the beddings on the dtm ........."

eval `r.info -s map=$dtm`

region_inc=`echo "$nsres*2" | bc -l | cut -f1 -d'.'`

g.region vect=$bed_trc res=$nsres e=e+$region_inc w=w-$region_inc s=s-$region_inc
n=n+$region_inc

v.drape input=$bed_trc type=line rast=$dtm output=bedd_3d method=nearest scale=1.0
layer=1 --o



#estraggo le sole linee che hanno sinuosità sopra il valore fornito o che hanno sinuosità nulla
(linee chiuse)

v.extract input=bedd_3d output=bed_trc_3d_sinuos type=line layer=1 where="sinuos>$sinuos
or sinuos is null" new=-1 --o

eval `v.info -t map=bed_trc_3d_sinuos layer=1`

echo "

-----------------------------------------------------------------

---------- SELEZIONATE $lines linee di $linee_iniziali iniziali --

-----------------------------------------------------------------
```

```
"

sleep 3


#setto la variabile risoluzione di lavoro alla risoluzione del dem

res_dem=$nsres


#inizializzo un contatore

k=1

for i in `v.category -g input=bed_trc_3d_sinuos option=print type=line`

        do

                #estraggo la prima linea

                v.extract input=bedd_3d output=m_bacino_$i list=$i --o


                #calcolo le coordinate iniziali e finali di questa linea

                g.region vect=m_bacino_$i res=$res_dem -a e=e+20 w=w-20 s=s-20 n=n+20

                startx=`v.to.db -p map=m_bacino_$i type=line layer=1 qlayer=1 option=start
units=meters | sed 1d | cut -f2 -d'|'`

                starty=`v.to.db -p map=m_bacino_$i type=line layer=1 qlayer=1 option=start
units=meters | sed 1d | cut -f3 -d'|'`

                startz=`v.to.db -p map=m_bacino_$i type=line layer=1 qlayer=1 option=start
units=meters | sed 1d | cut -f4 -d'|'`

                endx=`v.to.db -p map=m_bacino_$i type=line layer=1 qlayer=1 option=end
units=meters | sed 1d | cut -f2 -d'|'`

                endy=`v.to.db -p map=m_bacino_$i type=line layer=1 qlayer=1 option=end
units=meters | sed 1d | cut -f3 -d'|'`

                endz=`v.to.db -p map=m_bacino_$i type=line layer=1 qlayer=1 option=end
units=meters | sed 1d | cut -f4 -d'|'`


                #creo un area chiusa costituita dal marker più la linea che unisce gli estremi
```

```
                echo "L 2 1

                $startx $starty $startz

                $endx $endy $endz

                1 $i" | v.edit -n tool=add map=m_bacino_$i snap=node thresh=1

                v.to.points -v -i input=m_bacino_$i output=m_bacino_pnt_$i type=line
llayer=1 dmax=$res_dem --o

                #calcolo "l'ampiezza media" dell'area definita dal marker più la linea che
unisce gli estremi

                echo "L 2 1

                $startx $starty $startz

                $endx $endy $endz

                1 $i" | v.in.ascii -nz out=connect format=standard --overwrite

                v.type input=m_bacino_$i output=m_bacino_bound_$i type=line,boundary --o

                v.to.3d -r input=m_bacino_bound_$i output=m_bacino_bound_2d_$i
type=boundary layer=1 --o

                v.clean input=m_bacino_bound_2d_$i output=m_bacino_bound_2d_break_$i
type=boundary tool=break --overwrite

                v.centroids input=m_bacino_bound_2d_break_$i
output=m_bacino_bound_cent_$i option=add layer=1 cat=1 step=1 --o

                area=`v.to.db -p -c map=m_bacino_bound_cent_$i type=centroid layer=1
qlayer=1 option=area units=meters columns=m | cut -f2 -d':' | tr -d ' ' | cut -f1 -d'.'`

                base=`v.to.db -p map=connect type=line layer=1 qlayer=1 option=length
units=meters columns=p | sed 1d | cut -f2 -d'|' | cut -f1 -d'.'`

                heigh=`echo "$area/($base+1)" | bc -l | cut -f1 -d'.'`



                #verifico se l'altezza media è molto bassa (cioè ho un marker molto allungato)
o se l'altezza media è molto alta (cioè ho un marker che si piega su se stesso in modo molto
stretto)

                #e nel caso cambio la risoluzione in modo tale che il calcolo del piano inclinato
avvenga anche per linee molto diritte

                heigh_min=`echo "3*$res_dem" | bc -l`
```

```
heigh_max=`echo "$area/(3*$res_dem)" | bc -l | cut -f1 -d'.'`
if [ $heigh -lt $heigh_min ]
then
	res=`echo "$heigh/5" | bc -l`
	g.region res=$res
	echo "la risoluzione è $res"
elif [ $heigh -gt $heigh_max ] && [$heigh -ne $area ]
then
	res=`echo "$base/5" | bc -l | cut -f1 -d'.'`
	g.region res=$res
	echo "la risoluzione è $res"
else
	echo "la risoluzione è $res_dem"
fi

#Produco la mappa del "piano" passante per il marker e le sue mappe derivate di slope ed aspect
v.extract input=m_bacino_pnt_$i output=m_pt_3dim_$i layer=2 where="lcat=$i" --o
v.to.rast input=m_pt_3dim_$i output=m_pt_3dim_$i use=z type=point layer=2 value=1 rows=4096 --overwrite
#read
NOW=$(date +%s)
DIFF=$(( $NOW - $START ))
echo "
------------------------------------------------------------------
--------- Sto analizzando la linea $k di $lines linee totali ------
--------- Sto lavorando da $DIFF secondi -------------------------
```

```
                --------- Categoria della linea: $i ------------------------------

                ------------------------------------------------------------------

                "

                r.surf.nnbathy input=m_pt_3dim_$i output=m_pt_3dim_nn alg=l --overwrite

                v.to.rast input=m_bacino_bound_cent_$i output=MASK use=val type=area
layer=1 value=1 rows=4096 --o

                r.mapcalc "m_pt_3dim_nn_$i=m_pt_3dim_nn"

                g.remove rast=MASK

                d.erase

                d.rast m_pt_3dim_nn_$i -o

                d.vect $contour color=red

                d.vect m_bacino_bound_cent_$i fcolor=none width=2

                r.slope.aspect elevation=m_pt_3dim_nn_$i slope=slope_$i aspect=aspect_$i
format=degrees prec=float zfactor=1.0 min_slp_allowed=0.0 --overwrite

                r.mapcalc "m_pt_3dim_1_nn_poly=m_pt_3dim_nn_$i/m_pt_3dim_nn_$i"

                r.to.vect input=m_pt_3dim_1_nn_poly output=m_pt_3dim_1_nn_poly_$i
feature=area --overwrite

                thresh=`echo "$res_dem*$res_dem*2" | bc -l`

                v.clean input=m_pt_3dim_1_nn_poly_$i
output=m_pt_3dim_1_nn_poly_clean_$i type=area tool=rmarea thresh=$thresh --o



                #assegno le variabili slope ed azimuth al poligono che rappresenta il marker

                g.copy rast=m_pt_3dim_1_nn_poly,MASK

                        #assegno slope

                eval `r.univar -eg map=slope_$i`

                slope50=$median

                echo "

                ------------------------------------------------------------------

                --------- Sto analizzando la linea $k di $lines linee totali ------
```

```
--------- Sto lavorando da $DIFF secondi -------------------------

--------- Categoria della linea: $i ------------------------------

-------------------------------------------------------------------

"

g.remove rast=MASK

v.db.addcol map=m_pt_3dim_1_nn_poly_clean_$i columns="slopestdev
double precision, slope50 double precision, invslope50 double precision, aspect double
precision, azimuth double precision, circvar double precision, angstddev double precision"

slopestdev=`echo $stddev | cut -f1 -d'.'`

slope50=`echo $slope50 | cut -f1 -d'.'`

inv_slope50=`echo "90-$slope50" | bc -l`

v.db.update map=m_pt_3dim_1_nn_poly_clean_$i layer=1
column=slopestdev value=$slopestdev

v.db.update map=m_pt_3dim_1_nn_poly_clean_$i layer=1 column=slope50
value=$slope50

v.db.update map=m_pt_3dim_1_nn_poly_clean_$i layer=1
column=invslope50 value=$inv_slope50

#read

        #assegno azimuth

r.mapcalc "sen_aspect_$i=sin(aspect_$i)"

r.mapcalc "cos_aspect_$i=cos(aspect_$i)"

eval `r.univar -eg map=sen_aspect_$i`

mean_sen=$mean

eval `r.univar -eg map=cos_aspect_$i`

mean_cos=$mean

echo $mean_sen

echo $mean_cos

mean_sen_int=`echo "$mean_sen*1000000000" | bc -l | cut -f1 -d'.' `

mean_cos_int=`echo "$mean_cos*1000000000" | bc -l | cut -f1 -d'.' `
```

```
                echo $mean_sen_int
                echo $mean_cos_int
                if [ "$mean_sen_int" -gt "0" ] && [ "$mean_cos_int" -gt "0" ]
                then
                        aspect_avg=`echo "a($mean_sen/$mean_cos)*360/6.28" | bc -l`
                        azimuth=`echo "90-$aspect_avg" | bc -l`
                elif [ "$mean_sen_int" -gt "0" ] && [ "$mean_cos_int" -lt "0" ]
                then
                        aspect_avg=`echo "a($mean_sen/$mean_cos)*360/6.28+180" | bc -l`
                        azimuth=`echo "360-$aspect_avg+90" | bc -l`
                elif [ "$mean_sen_int" -lt "0" ] && [ "$mean_cos_int" -lt "0" ]
                then
                        aspect_avg=`echo "a($mean_sen/$mean_cos)*360/6.28+180" | bc -l`
                        echo "l'aspect medio è: $aspect_avg"
                        azimuth=`echo "360-$aspect_avg+90" | bc -l`
                        echo "l'azimuth è: $azimuth"
                elif [ "$mean_sen_int" -lt "0" ] && [ "$mean_cos_int" -gt "0" ]
                then
                        aspect_avg=`echo "a($mean_sen/$mean_cos)*360/6.28+360" | bc -l`
                        azimuth=`echo "-($aspect_avg-360)+90" | bc -l`
                fi
                azimuth=`echo $azimuth | cut -f1 -d'.'`
                #~ echo $aspect_avg
                #~ echo $azimuth
                v.db.update map=m_pt_3dim_1_nn_poly_clean_$i layer=1 column=aspect
value=$aspect_avg
                v.db.update map=m_pt_3dim_1_nn_poly_clean_$i layer=1 column=azimuth
value=$azimuth
```

```
		#assegno variabilità aspect
	eval `r.univar -g map=sen_aspect_$i`
	sen_sum=$sum
	eval `r.univar -g map=cos_aspect_$i`
	cos_sum=$sum
	n_cells=$n
	circvar=`echo "1-sqrt($sen_sum^2+$cos_sum^2)/$n" | bc -l`
	v.db.update map=m_pt_3dim_1_nn_poly_clean_$i layer=1 column=circvar
value=$circvar
		#assegno variabilità aspect, altro metodo
	r.mapcalc "asp_semi_$i=if(aspect_$i<=180,aspect_$i,aspect_$i-360)"
	aspect_avg_int=`echo "$aspect_avg" | cut -f1 -d'.'`
	if [ $aspect_avg_int -le 180 ]
	then
		aspect_avg_new=$aspect_avg_int
	elif [ $aspect_avg_int -gt 180 ]
	then
		aspect_avg_new=`echo "$aspect_avg_int-360" | bc -l`
	fi
	r.mapcalc "diff_angoli_$i=asp_semi_$i-$aspect_avg_new"
	r.mapcalc
"diff_angoli_semi_$i=if(abs(diff_angoli_$i)<=180,diff_angoli_$i,(360-abs(diff_angoli_$i)))"
	r.univar asp_semi_$i
	r.univar diff_angoli_semi_$i
	r.mapcalc "diff_angoli_semi_squared_$i=diff_angoli_semi_$i^2"
	r.univar diff_angoli_semi_squared_$i
	eval `r.univar -g diff_angoli_semi_squared_$i`
```

```
angstddev=`echo "sqrt($sum/$n)" | bc -l`

v.db.update map=m_pt_3dim_1_nn_poly_clean_$i layer=1 column=angstddev value=$angstddev

#trasformo i centroidi delle aree dei markers in punti, li sposto al centro della region e poi, laddove ne esista più di uno, prendo solo il primo

v.type input=m_pt_3dim_1_nn_poly_clean_$i output=ptbound_$i type=centroid,point  --o

eval `g.region -c -g vect=m_pt_3dim_1_nn_poly_clean_$i`

first_pt_cat=`v.category input=ptbound_$i option=print type=point layer=1 | tail -1`

v.extract input=ptbound_$i output=pt_$i type=point list=$first_pt_cat --o


d.vect pt_$i

point_cat=`v.to.db -p map="pt_$i" type=point layer=1 qlayer=1 option=cat columns=cat | sed 1d | sed 2,100d`

point_easting=`v.to.db -p map=pt_$i type=point layer=1 qlayer=1 option=coor columns=x,y | cut -f2 -d'|' | sed 1d | sed 2,100d`

point_northing=`v.to.db -p map=pt_$i type=point layer=1 qlayer=1 option=coor columns=x,y | cut -f3 -d'|'  | sed 1d | sed 2,100d`

x_move=`echo "$center_easting-$point_easting" | bc -l`

y_move=`echo "$center_northing-$point_northing" | bc -l`

v.edit tool=move map=pt_$i coords="$point_easting,$point_northing" move="$x_move,$y_move"

d.vect pt_$i icon="geology/strike_circle" size=8


#creo una mappa che contiene solo le giaciture medie per la zona di interesse

if [ "$k" -eq "1" ]

then

        eval `g.region vect=pt_$i -p -g`

        g.remove vect=giaciture_mediate

        g.copy vect=pt_$i,giaciture_mediate
```

```
                        v.edit tool=catdel map=giaciture_mediate ids="1-99999" cats="1-
99999" layer=1

                        v.edit tool=catadd map=giaciture_mediate bbox="$w,$s,$e,$n"
layer=1 cat=$i

                        v.db.update map=giaciture_mediate layer=1 column=cat value=$i

                        echo "creo la mappa delle giaciture mediate"

                        #read

                else

                        eval `g.region vect=pt_$i -p -g`

                        v.patch -a -e input=pt_$i output=giaciture_mediate --o

                        last_cat=`v.category input=giaciture_mediate option=print type=point
layer=1 | tail -1`

                        v.edit tool=catdel map=giaciture_mediate ids="1-99999"
cats="$last_cat" layer=1

                        v.edit tool=catadd map=giaciture_mediate bbox="$w,$s,$e,$n"
layer=1 cat=$i

                        v.db.update map=giaciture_mediate layer=1 column=cat value=$i
where="cat=$last_cat"

                        echo "patcho le mappe delle giaciture mediate"

                fi


                #rimuovo mappe temporanee

                g.remove vect=m_bacino_bound_$i

                g.remove vect=m_bacino_bound_2d_$i

                g.remove vect=m_bacino_bound_2d_break_$i

                g.remove vect=m_bacino_bound_cent_$i

                g.remove vect=m_bacino_pnt_$i

                g.remove vect=m_pt_3dim_1_nn_poly_$i

                g.remove vect=m_pt_3dim_1_nn_poly_clean_$i
```

```
                #g.rename vect=giac_temp_$i,giaciture

                g.remove vect=m_pt_3d_delaunay_point_$i

                g.remove vect=m_pt_3d_delaunay_$i

                g.remove vect=m_bacino_$i

                g.remove vect=m_pt_3dim_$i

                g.remove vect=area_$i

                g.remove vect=ptbound_$i

                g.remove vect=pt_$i

                g.remove vect=pti_3d_$i

                g.remove vect=pti_3d_bis_$i

                g.remove vect=giac_temp_$i

                g.remove rast=cos_aspect_$i,sen_aspect_$i,m_pt_3dim_$i

                g.remove rast=aspect_$i

                g.remove rast=area_$i

                g.remove rast=slope_$i

                g.remove rast=m_pt_3dim_nn_$i


                #incremento il contatore

                k=`echo "$k+1" | bc -l`


        done

        #stranamente qgis non vede il layer della mappa giaciture_mediate, quindi creo un
anuova mappa in output e gli cambio nome

        v.category input=giaciture_mediate output=$output option=chlayer type=point
layer=1,1 cat=1 step=1 --o
```

APPENDIX 3: CONSOLIDATED UNDRAINED DIRECT SIMPLE SHEAR TEST OF COHESIVE SOILS AND SOIL WATER CONTENT DETERMINATION TESTS.

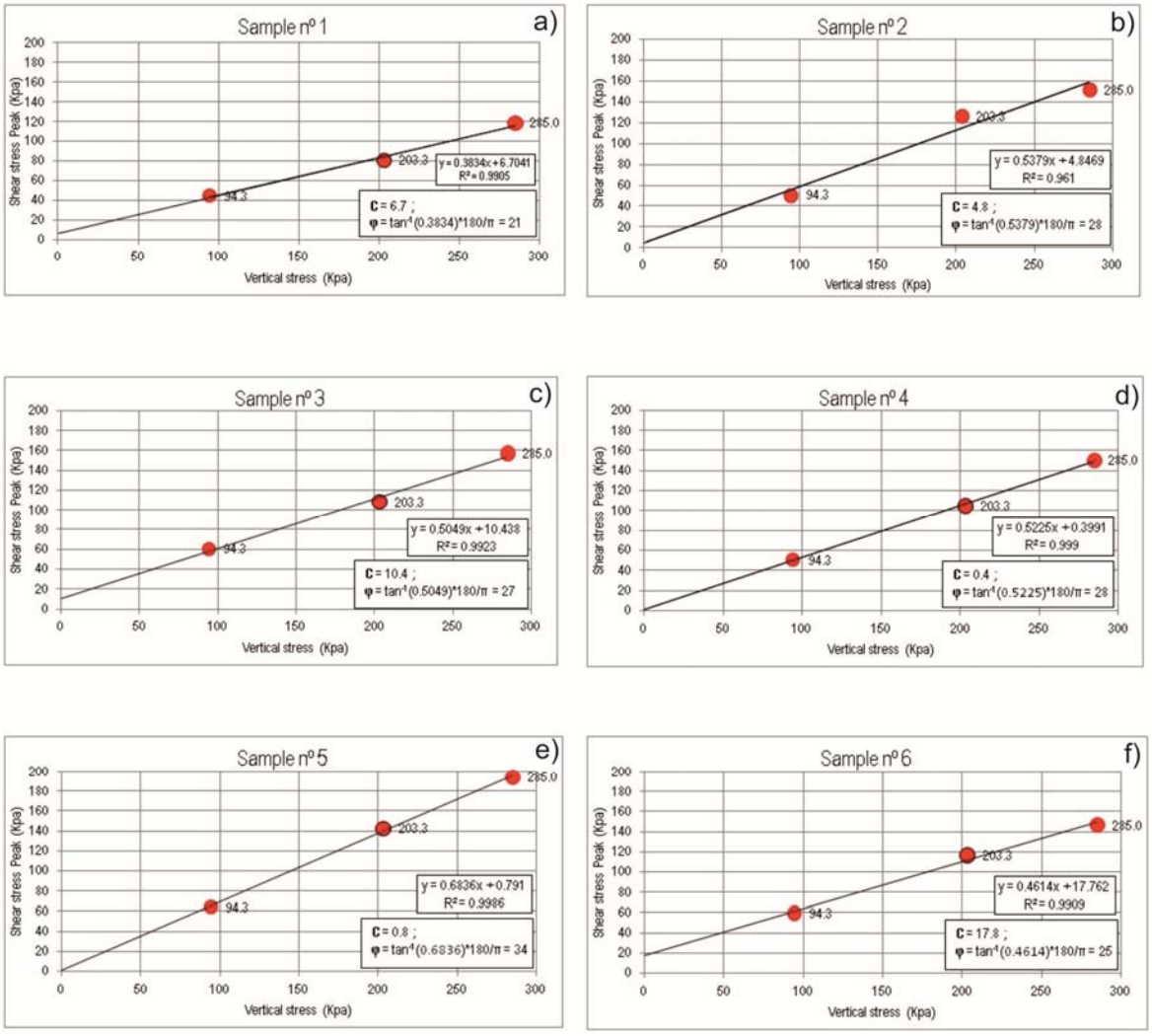

Fig. A3.1 – Shear stress peak as a function of vertical stress applied in direct shear tests under consolidated and undrained soil samples: a) for sample nº1; b) for sample nº2; c) for sample nº3; d) for sample nº4; e) for sample nº5; f) for sample nº6.

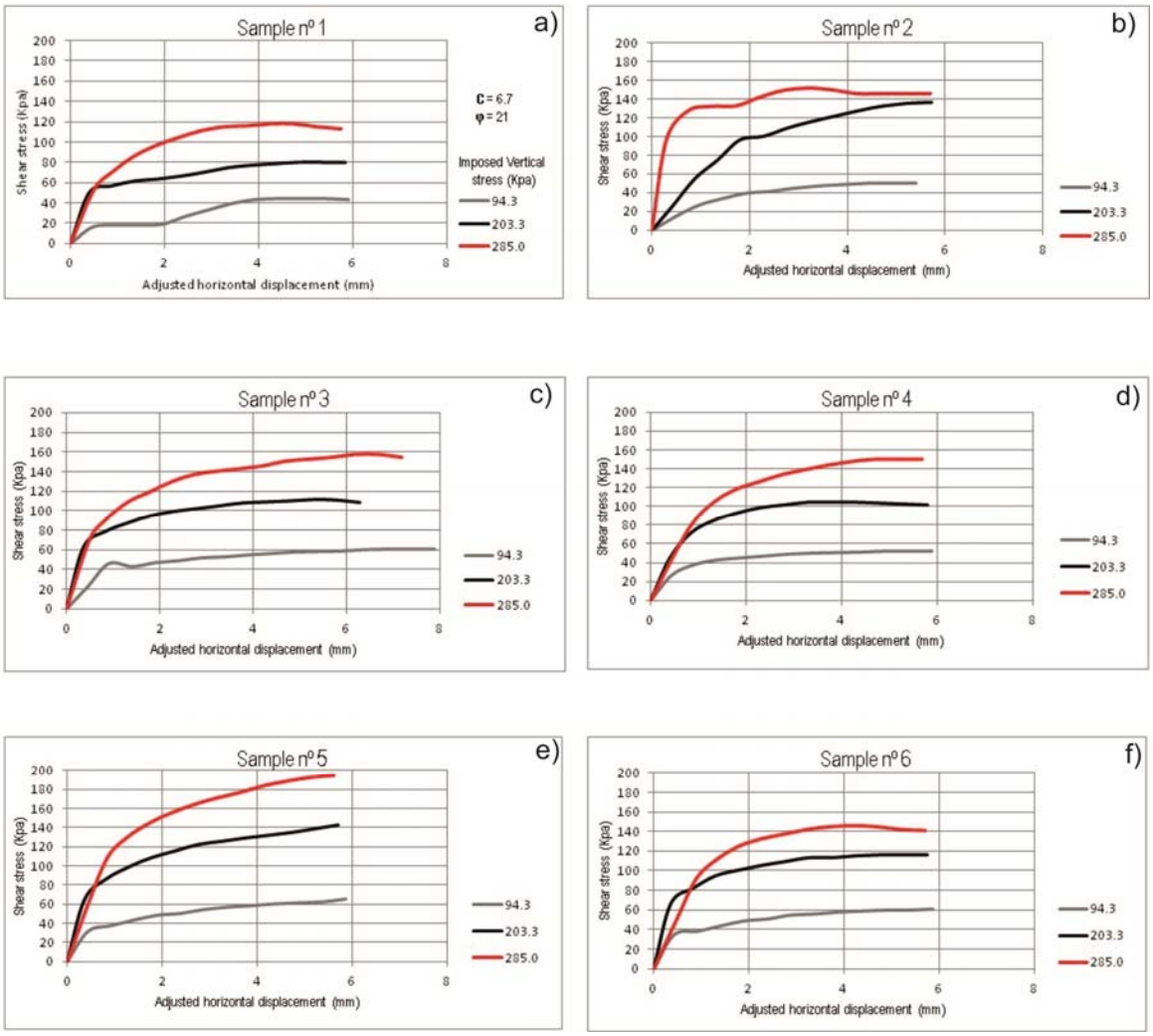

Fig. A3.2 – Shear stress peak as a function of vertical stress applied in direct shear tests under consolidated and undrained soil samples: a) for sample nº1; b) for sample nº2; c) for sample nº3; d) for sample nº4; e) for sample nº5; f) for sample nº6.

Table A3.1 – Soil water content test for Shale dominated complexes.

	Shale dominated complexes											
	Sample nº 1			Sample nº 2			Sample nº 3			Sample nº 4		
Imposed Vertical Stres (Kpa) / Weight (g)	94.3	203.3	285.0	94.3	203.3	285.0	94.3	203.3	285.0	94.3	203.3	285.0
Metal capsule	22.195	22.195	22.124	22.195	22.195	22.195	22.195	22.195	22.195	22.195	22.195	22.195
Saturated sample + Metal capsule	61.015	63.044	63.022	62.588	61.059	64.86	64.102	63.546	65.6	61.164	64.66	66.889
Saturated sample - Metal capsule (Wt)	38.82	40.849	40.896	40.393	38.864	42.665	41.907	41.351	43.405	38.969	42.465	44.694
Dry sample (Ws)	27.61	31.406	35.229	31.969	28.972	34.984	33.597	33.561	36.125	31.676	35.1	37.858
Wt – Ws = Ww	11.21	9.443	5.667	8.424	9.892	7.681	8.31	7.79	7.28	7.293	7.365	6.836
Natural moist sample (from field) - Metal capsule	37.433	37.433	37.433	37.51	37.51	37.51	38.242	38.242	38.242	38.157	38.157	38.157

Table A3.2 – Soil water content test for Sandstone dominated complexes.

	Sandstones dominated complexes					
	Sample nº 5			Sample nº6		
Imposed Vertical Stress (Kpa) / Weight (g)	94.3	203.3	285.0	94.3	203.3	285.0
Metal capsule	22.195	22.195	22.195	22.195	22.195	22.195
Saturated sample + Metal capsule	67.631	65.713	66.308	64.16	64.831	63.545
Saturated sample - Metal capsule (Wt)	45.436	43.518	44.113	41.965	42.636	41.35
Dry sample (Ws)	38.169	37.358	39.155	35.429	35.251	34.25
Wt – Ws = Ww	7.267	6.16	4.958	6.536	7.385	7.1
Natural moist sample (from field) - Metal capsule	39.199	39.199	39.199	35.869	35.869	35.869

Table A3.3 – Soil water content test for Shale dominated complexes: Bulk densities and volumes.

	Shale dominated complexes											
	Sample nº 1			Sample nº 2			Sample nº 3			Sample nº 4		
Imposed Vertical Stress (Kpa)	94.3	203.3	285.0	94.3	203.3	285.0	94.3	203.3	285.0	94.3	203.3	285.0
Sample: displaced volume (using mercury) (cm^3)	196.837	217.370	229.500	239.813	227.700	248.494	223.099	226.457	237.480	217.829	237.532	255.623
Tota Volume: metal capsule: Vt (cm^3)	19.809	19.809	19.809	19.809	19.809	19.809	19.809	19.809	19.809	19.809	19.809	19.809
Dry sample Volume: Vd (cm^3)	14.527	16.042	16.937	17.698	16.804	18.339	16.465	16.713	17.526	16.076	17.530	18.865
Void Volume: Vv = Vt – Vd (cm^3)	5.282	3.767	2.872	2.111	3.005	1.470	3.344	3.096	2.283	3.733	2.279	0.944
γ_w (g/cm^3)	1.000	1.000	1.000	1.000	1.000	1.000	1.000	1.000	1.000	1.000	1.000	1.000
γ_w (KN/m^3)	9.810	9.810	9.810	9.810	9.810	9.810	9.810	9.810	9.810	9.810	9.810	9.810
γ_d (g/cm^3)	1.394	1.585	1.778	1.614	1.463	1.766	1.696	1.694	1.824	1.599	1.772	1.911
γ_d (KN/m^3)	13.673	15.553	17.446	15.832	14.348	17.325	16.638	16.620	17.890	15.687	17.383	18.748
γ (g/cm^3)	1.890	1.890	1.890	1.894	1.894	1.894	1.931	1.931	1.931	1.926	1.926	1.926
γ (KN/m^3)	18.538	18.538	18.538	18.576	18.576	18.576	18.939	18.939	18.939	18.896	18.896	18.896
γ_s (g/cm^3)	1.960	2.062	2.065	2.039	1.962	2.154	2.116	2.087	2.191	1.967	2.144	2.256
γ_s (KN/m^3)	19.225	20.230	20.253	20.004	19.247	21.129	20.754	20.478	21.495	19.299	21.030	22.134
γ' (KN/m^3)	9.415	10.420	10.443	10.194	9.437	11.319	10.944	10.668	11.685	9.489	11.220	12.324
Void ratio (e) (KN/m^3)	0.364	0.235	0.170	0.119	0.179	0.080	0.203	0.185	0.130	0.232	0.130	0.050
Porosity (n) (%)	26.666	19.017	14.497	10.655	15.168	7.421	16.882	15.631	11.524	18.846	11.505	4.765

Table A3.4 – Soil water content test for Sandstone dominated complexes: Bulk densities and volumes.

	Sandstones dominated complexes					
	Sample nº5			Sample nº6		
Imposed Vertical Stress (Kpa)	**94.3**	**203.3**	**285.0**	**94.3**	**203.3**	**285.0**
Sample: displaced volume (using mercury) (cm^3)	267.537	265.540	267.594	241.355	237.713	225.599
Tota Volume: metal capsule: Vt (cm^3)	19.809	19.809	19.809	19.809	19.809	19.809
Dry sample Volume: Vd (cm^3)	19.744	19.597	19.749	17.812	17.543	16.549
Void Volume: Vv = Vt – Vd (cm^3)	0.065	0.212	0.060	1.997	2.266	3.160
γ_w (g/cm^3)	1.000	1.000	1.000	1.000	1.000	1.000
γ_w (KN/m^3)	9.810	9.810	9.810	9.810	9.810	9.810
γ_d (g/cm^3)	1.927	1.886	1.977	1.789	1.780	1.729
γ_d (KN/m^3)	18.902	18.501	19.391	17.545	17.457	16.962
γ (g/cm^3)	1.979	1.979	1.979	1.811	1.811	1.811
γ (KN/m^3)	19.412	19.412	19.412	17.763	17.763	17.763
γ_s (g/cm^3)	2.294	2.197	2.227	2.118	2.152	2.087
γ_s (KN/m^3)	22.501	21.551	21.846	20.782	21.115	20.478
γ' (KN/m^3)	12.691	11.741	12.036	10.972	11.305	10.568
Void ratio (e) (KN/m^3)	0.003	0.011	0.003	0.112	0.129	0.190
Porosity (n) (%)	0.326	1.070	0.305	10.081	11.438	15.951

APPENDIX 4: COEFFICIENT OF DETERMINATION (r^2) AND SLOPE OF THE REGRESSION LINE, OF EACH MONTH AND FOR EACH METEOROLOGICAL STATION AND INTERPOLATION OF METEOROLOGICAL DATA (PRECIPITATION, TEMPERATURE, EVAPOTRANSPIRATION).

Table A4.1 – Misclassification table: coefficient of determination (r^2) of the regression line for January (for the period between 1975/1976 to 2011/2012).

	Alfeizerão	Cela	Salir de Matos	Óbidos	Asseiceira	Alcoentre	Alvorninha	Santa Catarina	Vermelha	Vimeiro	Turquel
Alfeizerão	1	0.91	0.89	0.31	0.83	0.83	0.87	0.67	0.87	0.77	0.71
Cela	0.91	1	0.84	0.30	0.79	0.79	0.86	0.75	0.72	0.78	0.73
Salir de Matos	0.89	0.84	1	0.24	0.81	0.82	0.89	0.82	0.73	0.77	0.70
Óbidos	0.31	0.30	0.24	1	0.29	0.23	0.27	0.32	0.25	0.36	0.39
Asseiceira	0.83	0.79	0.81	0.29	1	0.90	0.88	0.77	0.81	0.73	0.69
Alcoentre	0.83	0.79	0.82	0.23	0.90	1	0.86	0.75	0.80	0.72	0.67
Alvorninha	0.87	0.86	0.89	0.27	0.88	0.86	1	0.82	0.84	0.77	0.76
Santa Catarina	0.67	0.75	0.82	0.32	0.77	0.75	0.82	1	0.73	0.76	0.72
Vermelha	0.87	0.72	0.73	0.25	0.81	0.80	0.84	0.73	1	0.66	0.62
Vimeiro	0.77	0.78	0.77	0.36	0.73	0.72	0.77	0.76	0.66	1	0.67
Turquel	0.71	0.73	0.70	0.39	0.69	0.67	0.76	0.72	0.62	0.67	1

Table A4.2 – Misclassification table: slope (b) of the regression line for January (for the period between 1975/1976 to 2011/2012).

	Alfeizerão	Cela	Salir de Matos	Óbidos	Asseiceira	Alcoentre	Alvorninha	Santa Catarina	Vermelha	Vimeiro	Turquel
Alfeizerão	1	1.25	1.09	0.63	0.94	1.12	1.12	0.65	0.78	0.85	0.67
Cela	1.25	1	0.82	0.48	0.71	0.83	0.85	0.62	0.97	1.11	0.87
Salir de Matos	1.09	0.82	1	0.51	0.79	0.94	0.96	0.71	0.86	0.99	0.78
Óbidos	0.63	0.48	0.51	1	0.50	0.47	0.56	0.42	0.53	0.70	0.57
Asseiceira	0.94	0.71	0.79	0.50	1	1.12	1.09	0.78	0.80	0.85	0.72
Alcoentre	1.12	0.83	0.94	0.47	1.12	1	0.92	0.67	0.94	0.98	0.83
Alvorninha	1.12	0.85	0.96	0.56	1.09	0.92	1	0.71	0.93	1.01	0.86
Santa Catarina	0.65	0.62	0.71	0.42	0.78	0.67	0.71	1	0.68	0.78	0.65
Vermelha	0.78	0.97	0.86	0.53	0.80	0.94	0.93	0.68	1	0.93	0.72
Vimeiro	0.85	1.11	0.99	0.70	0.85	0.98	1.01	0.78	0.93	1	0.62
Turquel	0.67	0.87	0.78	0.57	0.72	0.83	0.86	0.65	0.72	0.62	1

Table A4.3 – Misclassification table: coefficient of determination (r^2) of the regression line for February (for the period between 1975/1976 to 2011/2012).

	Alfeizerão	Cela	Salir de Matos	Óbidos	Asseiceira	Alcoentre	Alvorninha	Santa Catarina	Vermelha	Vimeiro	Turquel
Alfeizerão	1	0.92	0.90	0.23	0.72	0.67	0.87	0.71	0.87	0.78	0.66
Cela	0.92	1	0.84	0.25	0.69	0.64	0.85	0.74	0.80	0.79	0.61
Salir de Matos	0.90	0.84	1	0.19	0.71	0.62	0.86	0.74	0.81	0.79	0.62
Óbidos	0.23	0.25	0.19	1	0.25	0.20	0.24	0.27	0.26	0.28	0.24
Asseiceira	0.72	0.69	0.71	0.25	1	0.79	0.79	0.54	0.79	0.60	0.54
Alcoentre	0.67	0.64	0.62	0.20	0.79	1	0.75	0.60	0.83	0.61	0.51
Alvorninha	0.87	0.85	0.86	0.24	0.79	0.75	1	0.69	0.86	0.72	0.68
Santa Catarina	0.71	0.74	0.74	0.27	0.54	0.60	0.69	1	0.64	0.79	0.50
Vermelha	0.87	0.80	0.81	0.26	0.79	0.83	0.86	0.64	1	0.69	0.58
Vimeiro	0.78	0.79	0.79	0.28	0.60	0.61	0.72	0.79	0.69	1	0.70
Turquel	0.66	0.61	0.62	0.24	0.54	0.51	0.68	0.50	0.58	0.70	1

Table A4.4 – Misclassification table: slope (b) of the regression line for February (for the period between 1975/1976 to 2011/2012).

	Alfeizerão	Cela	Salir de Matos	Óbidos	Asseiceira	Alcoentre	Alvorninha	Santa Catarina	Vermelha	Vimeiro	Turquel
Alfeizerão	1	1.29	1.13	0.56	0.93	1.09	1.03	0.72	0.85	0.84	0.53
Cela	1.29	1	0.83	0.42	0.67	0.78	0.79	0.62	1.07	1.10	0.70
Salir de Matos	1.13	0.83	1	0.40	0.76	0.86	0.85	0.67	0.99	1.00	0.63
Óbidos	0.56	0.42	0.40	1	0.47	0.49	0.43	0.41	0.55	0.55	0.35
Asseiceira	0.93	0.67	0.76	0.47	1	1.08	0.89	0.63	0.87	0.78	0.53
Alcoentre	1.09	0.78	0.86	0.49	1.08	1	0.70	0.60	0.98	0.97	0.62
Alvorninha	1.03	0.79	0.85	0.43	0.89	0.70	1	0.71	0.94	0.86	0.62
Santa Catarina	0.72	0.62	0.67	0.41	0.63	0.60	0.71	1	0.68	0.78	0.48
Vermelha	0.85	1.07	0.99	0.55	0.87	0.98	0.94	0.68	1	0.85	0.52
Vimeiro	0.84	1.10	1.00	0.55	0.78	0.97	0.86	0.78	0.85	1	0.73
Turquel	0.53	0.70	0.63	0.35	0.53	0.62	0.62	0.48	0.52	0.73	1

Table A4.5 – Misclassification table: coefficient of determination (r^2) of the regression line for March (for the period between 1975/1976 to 2011/2012).

	Alfeizerão	Cela	Salir de Matos	Óbidos	Asseiceira	Alcoentre	Alvorninha	Santa Catarina	Vermelha	Vimeiro	Turquel
Alfeizerão	1	0.89	0.85	0.35	0.75	0.69	0.79	0.79	0.79	0.80	0.73
Cela	0.89	1	0.81	0.30	0.73	0.64	0.78	0.74	0.76	0.76	0.74
Salir de Matos	0.85	0.81	1	0.36	0.74	0.65	0.84	0.75	0.77	0.80	0.76
Óbidos	0.35	0.30	0.36	1	0.33	0.24	0.31	0.51	0.43	0.36	0.33
Asseiceira	0.75	0.73	0.74	0.33	1	0.83	0.75	0.70	0.77	0.72	0.75
Alcoentre	0.69	0.64	0.65	0.24	0.83	1	0.74	0.61	0.74	0.69	0.67
Alvorninha	0.79	0.78	0.84	0.31	0.75	0.74	1	0.76	0.83	0.80	0.83
Santa Catarina	0.79	0.74	0.75	0.51	0.70	0.61	0.76	1	0.75	0.75	0.80
Vermelha	0.79	0.76	0.77	0.43	0.77	0.74	0.83	0.75	1	0.75	0.70
Vimeiro	0.80	0.76	0.80	0.36	0.72	0.69	0.80	0.75	0.75	1	0.75
Turquel	0.73	0.74	0.76	0.33	0.75	0.67	0.83	0.80	0.70	0.75	1

Table A4.6 – Misclassification table: slope (b) of the regression line for March (for the period between 1975/1976 to 2011/2012).

	Alfeizerão	Cela	Salir de Matos	Óbidos	Asseiceira	Alcoentre	Alvorninha	Santa Catarina	Vermelha	Vimeiro	Turquel
Alfeizerão	1	1.38	1.08	0.67	1.01	1.12	1.01	0.72	0.79	0.82	0.61
Cela	1.38	1	0.72	0.44	0.70	0.78	0.68	0.55	1.12	1.12	0.92
Salir de Matos	1.08	0.72	1	0.59	0.89	0.96	0.89	0.69	0.92	0.94	0.82
Óbidos	0.67	0.44	0.59	1	0.56	0.50	0.53	0.61	0.66	0.64	0.62
Asseiceira	1.01	0.70	0.89	0.56	1	1.05	0.77	0.62	0.95	0.91	0.84
Alcoentre	1.12	0.78	0.96	0.50	1.05	1	0.71	0.53	1.04	1.03	0.93
Alvorninha	1.01	0.68	0.89	0.53	0.77	0.71	1	0.72	0.91	0.91	0.77
Santa Catarina	0.72	0.55	0.69	0.61	0.62	0.53	0.72	1	0.71	0.71	0.66
Vermelha	0.79	1.12	0.92	0.66	0.95	1.04	0.91	0.71	1	0.87	0.71
Vimeiro	0.82	1.12	0.94	0.64	0.91	1.03	0.91	0.71	0.87	1	0.73
Turquel	0.61	0.92	0.82	0.62	0.84	0.93	0.77	0.66	0.71	0.73	1

Table A4.7 – Misclassification table: coefficient of determination (r^2) of the regression line for April (for the period between 1975/1976 to 2011/2012).

	Alfeizerão	Cela	Salir de Matos	Óbidos	Asseiceira	Alcoentre	Alvorninha	Santa Catarina	Vermelha	Vimeiro	Turquel
Alfeizerão	1	0.85	0.77	0.25	0.59	0.54	0.75	0.73	0.75	0.72	0.78
Cela	0.85	1	0.69	0.30	0.68	0.54	0.80	0.71	0.76	0.74	0.76
Salir de Matos	0.77	0.69	1	0.26	0.65	0.63	0.75	0.65	0.70	0.73	0.64
Óbidos	0.25	0.30	0.26	1	0.27	0.18	0.24	0.48	0.37	0.29	0.30
Asseiceira	0.59	0.68	0.65	0.27	1	0.82	0.77	0.71	0.78	0.70	0.79
Alcoentre	0.54	0.54	0.63	0.18	0.82	1	0.70	0.65	0.78	0.67	0.56
Alvorninha	0.75	0.80	0.75	0.24	0.77	0.70	1	0.74	0.82	0.81	0.84
Santa Catarina	0.73	0.71	0.65	0.48	0.71	0.65	0.74	1	0.70	0.81	0.75
Vermelha	0.75	0.76	0.70	0.37	0.78	0.78	0.82	0.70	1	0.74	0.79
Vimeiro	0.72	0.74	0.73	0.29	0.70	0.67	0.81	0.81	0.74	1	0.66
Turquel	0.78	0.76	0.64	0.30	0.79	0.56	0.84	0.75	0.79	0.66	1

Table A4.8 – Misclassification table: slope (b) of the regression line for April (for the period between 1975/1976 to 2011/2012).

	Alfeizerão	Cela	Salir de Matos	Óbidos	Asseiceira	Alcoentre	Alvorninha	Santa Catarina	Vermelha	Vimeiro	Turquel
Alfeizerão	1	1.14	0.94	0.42	0.80	0.84	0.71	0.71	1.06	0.85	0.68
Cela	1.14	1	0.77	0.40	0.65	0.68	0.58	0.56	1.09	1.10	0.88
Salir de Matos	0.94	0.77	1	0.43	0.90	0.97	0.68	0.69	0.95	0.83	0.80
Óbidos	0.42	0.40	0.43	1	0.54	0.53	0.43	0.66	0.54	0.46	0.43
Asseiceira	0.80	0.65	0.90	0.54	1	1.00	0.71	0.72	0.88	0.91	0.75
Alcoentre	0.84	0.68	0.97	0.53	1.00	1	0.60	0.66	0.94	0.98	0.77
Alvorninha	0.71	0.58	0.68	0.43	0.71	0.60	1	0.86	0.78	0.77	0.60
Santa Catarina	0.71	0.56	0.69	0.66	0.72	0.66	0.86	1	0.69	0.77	0.63
Vermelha	1.06	1.09	0.95	0.54	0.88	0.94	0.78	0.69	1	0.86	0.71
Vimeiro	0.85	1.10	0.83	0.46	0.91	0.98	0.77	0.77	0.86	1	0.60
Turquel	0.68	0.88	0.80	0.43	0.75	0.77	0.60	0.63	0.71	0.60	1

Table A4.9 – Misclassification table: coefficient of determination (r^2) of the regression line for May (for the period between 1975/1976 to 2011/2012).

	Alfeizerão	Cela	Salir de Matos	Óbidos	Asseiceira	Alcoentre	Alvorninha	Santa Catarina	Vermelha	Vimeiro	Turquel
Alfeizerão	1	0.76	0.83	0.32	0.62	0.64	0.70	0.58	0.70	0.53	0.64
Cela	0.76	1	0.73	0.31	0.62	0.65	0.62	0.62	0.60	0.48	0.66
Salir de Matos	0.83	0.73	1	0.35	0.66	0.64	0.78	0.76	0.68	0.53	0.69
Óbidos	0.32	0.31	0.35	1	0.33	0.30	0.29	0.30	0.22	0.29	0.53
Asseiceira	0.62	0.62	0.66	0.33	1	0.84	0.73	0.53	0.67	0.46	0.66
Alcoentre	0.64	0.65	0.64	0.30	0.84	1	0.71	0.68	0.71	0.48	0.71
Alvorninha	0.70	0.62	0.78	0.29	0.73	0.71	1	0.74	0.70	0.58	0.73
Santa Catarina	0.58	0.62	0.76	0.30	0.53	0.68	0.74	1	0.68	0.53	0.76
Vermelha	0.70	0.60	0.68	0.22	0.67	0.71	0.70	0.68	1	0.48	0.56
Vimeiro	0.53	0.48	0.53	0.29	0.46	0.48	0.58	0.53	0.48	1	0.75
Turquel	0.64	0.66	0.69	0.53	0.66	0.71	0.73	0.76	0.56	0.75	1

Table A4.10 – Misclassification table: slope (b) of the regression line for May (for the period between 1975/1976 to 2011/2012).

	Alfeizerão	Cela	Salir de Matos	Óbidos	Asseiceira	Alcoentre	Alvorninha	Santa Catarina	Vermelha	Vimeiro	Turquel
Alfeizerão	1	1.08	0.98	0.72	0.80	0.89	0.85	0.59	0.82	0.70	0.61
Cela	1.08	1	0.73	0.54	0.69	0.77	0.63	0.55	0.96	0.83	0.71
Salir de Matos	0.98	0.73	1	0.69	0.80	0.84	0.84	0.72	0.93	0.69	0.69
Óbidos	0.72	0.54	0.69	1	0.53	0.52	0.42	0.36	0.55	0.69	0.55
Asseiceira	0.80	0.69	0.80	0.53	1	0.97	0.82	0.61	0.86	0.69	0.62
Alcoentre	0.89	0.77	0.84	0.52	0.97	1	0.74	0.60	0.95	0.73	0.77
Alvorninha	0.85	0.63	0.84	0.42	0.82	0.74	1	0.80	0.84	0.69	0.66
Santa Catarina	0.59	0.55	0.72	0.36	0.61	0.60	0.80	1	0.73	0.60	0.60
Vermelha	0.82	0.96	0.93	0.55	0.86	0.95	0.84	0.73	1	0.65	0.53
Vimeiro	0.70	0.83	0.69	0.69	0.69	0.73	0.69	0.60	0.65	1	0.58
Turquel	0.61	0.71	0.69	0.55	0.62	0.77	0.66	0.60	0.53	0.58	1

Table A4.11 – Misclassification table: coefficient of determination (r^2) of the regression line for June (for the period between 1975/1976 to 2011/2012).

	Alfeizerão	Cela	Salir de Matos	Óbidos	Asseiceira	Alcoentre	Alvorninha	Santa Catarina	Vermelha	Vimeiro	Turquel
Alfeizerão	1	0.83	0.84	0.15	0.53	0.56	0.73	0.66	0.73	0.77	0.82
Cela	0.83	1	0.74	0.22	0.65	0.60	0.76	0.62	0.72	0.68	0.72
Salir de Matos	0.84	0.74	1	0.21	0.70	0.69	0.68	0.76	0.72	0.80	0.75
Óbidos	0.15	0.22	0.21	1	0.22	0.16	0.26	0.46	0.29	0.32	0.48
Asseiceira	0.53	0.65	0.70	0.22	1	0.86	0.76	0.60	0.76	0.54	0.64
Alcoentre	0.56	0.60	0.69	0.16	0.86	1	0.79	0.60	0.80	0.50	0.66
Alvorninha	0.73	0.76	0.68	0.26	0.76	0.79	1	0.69	0.82	0.72	0.78
Santa Catarina	0.66	0.62	0.76	0.46	0.60	0.60	0.69	1	0.64	0.69	0.89
Vermelha	0.73	0.72	0.72	0.29	0.76	0.80	0.82	0.64	1	0.65	0.79
Vimeiro	0.77	0.68	0.80	0.32	0.54	0.50	0.72	0.69	0.65	1	0.77
Turquel	0.82	0.72	0.75	0.48	0.64	0.66	0.78	0.89	0.79	0.77	1

Table A4.12 – Misclassification table: slope (b) of the regression line for June (for the period between 1975/1976 to 2011/2012).

	Alfeizerão	Cela	Salir de Matos	Óbidos	Asseiceira	Alcoentre	Alvorninha	Santa Catarina	Vermelha	Vimeiro	Turquel
Alfeizerão	1	1.36	1.17	0.45	0.89	0.98	1.20	0.66	0.61	0.91	0.49
Cela	1.36	1	0.74	0.37	0.66	0.75	0.86	0.44	1.12	1.23	0.66
Salir de Matos	1.17	0.74	1	0.44	0.72	0.83	0.80	0.60	1.02	1.16	0.74
Óbidos	0.45	0.37	0.44	1	0.37	0.37	0.63	0.59	0.58	0.57	0.85
Asseiceira	0.89	0.66	0.72	0.37	1	1.05	1.06	0.59	0.91	0.83	0.57
Alcoentre	0.98	0.75	0.83	0.37	1.05	1	0.96	0.49	1.10	0.90	0.70
Alvorninha	1.20	0.86	0.80	0.63	1.06	0.96	1	0.50	1.21	1.19	0.68
Santa Catarina	0.66	0.44	0.60	0.59	0.59	0.49	0.50	1	0.65	0.72	0.47
Vermelha	0.61	1.12	1.02	0.58	0.91	1.10	1.21	0.65	1	0.85	0.49
Vimeiro	0.91	1.23	1.16	0.57	0.83	0.90	1.19	0.72	0.85	1	0.61
Turquel	0.49	0.66	0.74	0.85	0.57	0.70	0.68	0.47	0.49	0.61	1

Table A4.13 – Misclassification table: coefficient of determination (r^2) of the regression line for July (for the period between 1975/1976 to 2011/2012).

	Alfeizerão	Cela	Salir de Matos	Óbidos	Asseiceira	Alcoentre	Alvorninha	Santa Catarina	Vermelha	Vimeiro	Turquel
Alfeizerão	1	0.79	0.80	0.28	0.64	0.68	0.40	0.62	0.40	0.65	0.48
Cela	0.79	1	0.86	0.20	0.48	0.48	0.41	0.62	0.41	0.53	0.70
Salir de Matos	0.80	0.86	1	0.17	0.48	0.54	0.35	0.53	0.36	0.58	0.77
Óbidos	0.28	0.20	0.17	1	0.32	0.32	0.28	0.21	0.34	0.17	0.23
Asseiceira	0.64	0.48	0.48	0.32	1	0.92	0.78	0.45	0.83	0.40	0.38
Alcoentre	0.68	0.48	0.54	0.32	0.92	1	0.87	0.53	0.93	0.51	0.44
Alvorninha	0.40	0.41	0.35	0.28	0.78	0.87	1	0.71	0.89	0.58	0.60
Santa Catarina	0.62	0.62	0.53	0.21	0.45	0.53	0.71	1	0.64	0.81	0.81
Vermelha	0.40	0.41	0.36	0.34	0.83	0.93	0.89	0.64	1	0.48	0.53
Vimeiro	0.65	0.53	0.58	0.17	0.40	0.51	0.58	0.81	0.48	1	0.88
Turquel	0.48	0.70	0.77	0.23	0.38	0.44	0.60	0.81	0.53	0.88	1

Table A4.14 – Misclassification table: slope (b) of the regression line for July (for the period between 1975/1976 to 2011/2012).

	Alfeizerão	Cela	Salir de Matos	Óbidos	Asseiceira	Alcoentre	Alvorninha	Santa Catarina	Vermelha	Vimeiro	Turquel
Alfeizerão	1	0.86	0.94	0.49	0.85	0.61	0.52	0.33	0.76	1.30	0.57
Cela	0.86	1	1.01	0.38	0.73	0.43	0.53	0.31	1.16	1.17	0.60
Salir de Matos	0.94	1.01	1	0.32	0.68	0.50	0.48	0.28	1.03	1.32	0.58
Óbidos	0.49	0.38	0.32	1	0.82	0.51	0.84	0.25	0.53	0.43	0.22
Asseiceira	0.85	0.73	0.68	0.82	1	0.64	1.13	0.37	1.00	0.79	0.47
Alcoentre	0.61	0.43	0.50	0.51	0.64	1	1.81	0.61	0.69	0.58	0.32
Alvorninha	0.52	0.53	0.48	0.84	1.13	1.81	1	0.41	1.30	1.07	0.65
Santa Catarina	0.33	0.31	0.28	0.25	0.37	0.61	0.41	1	0.50	0.61	0.40
Vermelha	0.76	1.16	1.03	0.53	1.00	0.69	1.30	0.50	1	0.77	0.43
Vimeiro	1.30	1.17	1.32	0.43	0.79	0.58	1.07	0.61	0.77	1	0.68
Turquel	0.57	0.60	0.58	0.22	0.47	0.32	0.65	0.40	0.43	0.68	1

Table A4.15 – Misclassification table: coefficient of determination (r^2) of the regression line for August (for the period between 1975/1976 to 2011/2012).

	Alfeizerão	Cela	Salir de Matos	Óbidos	Asseiceira	Alcoentre	Alvorninha	Santa Catarina	Vermelha	Vimeiro	Turquel
Alfeizerão	1	0.72	0.62	0.12	0.39	0.30	0.56	0.52	0.56	0.78	0.70
Cela	0.72	1	0.38	0.06	0.28	0.26	0.31	0.43	0.49	0.66	0.54
Salir de Matos	0.62	0.38	1	0.08	0.31	0.38	0.54	0.41	0.35	0.63	0.59
Óbidos	0.12	0.06	0.08	1	0.02	0.14	0.13	0.27	0.12	0.18	0.14
Asseiceira	0.39	0.28	0.31	0.02	1	0.36	0.68	0.30	0.48	0.37	0.42
Alcoentre	0.30	0.26	0.38	0.14	0.36	1	0.73	0.41	0.50	0.28	0.53
Alvorninha	0.56	0.31	0.54	0.13	0.68	0.73	1	0.50	0.57	0.51	0.63
Santa Catarina	0.52	0.43	0.41	0.27	0.30	0.41	0.50	1	0.62	0.70	0.72
Vermelha	0.56	0.49	0.35	0.12	0.48	0.50	0.57	0.62	1	0.52	0.67
Vimeiro	0.78	0.66	0.63	0.18	0.37	0.28	0.51	0.70	0.52	1	0.65
Turquel	0.70	0.54	0.59	0.14	0.42	0.53	0.63	0.72	0.67	0.65	1

Table A4.16 – Misclassification table: slope (b) of the regression line for August (for the period between 1975/1976 to 2011/2012).

	Alfeizerão	Cela	Salir de Matos	Óbidos	Asseiceira	Alcoentre	Alvorninha	Santa Catarina	Vermelha	Vimeiro	Turquel
Alfeizerão	1	1.16	0.79	0.35	0.37	0.38	0.45	0.49	1.26	1.26	0.73
Cela	1.16	1	0.44	0.28	0.25	0.30	0.25	0.26	1.07	1.62	1.00
Salir de Matos	0.79	0.44	1	0.24	0.34	0.43	0.43	0.53	0.74	1.16	0.61
Óbidos	0.35	0.28	0.24	1	0.13	0.13	0.16	0.23	0.74	0.40	0.36
Asseiceira	0.37	0.25	0.34	0.13	1	0.48	0.84	0.63	0.59	0.49	0.36
Alcoentre	0.38	0.30	0.43	0.13	0.48	1	0.75	0.48	0.69	0.57	0.46
Alvorninha	0.45	0.25	0.43	0.16	0.84	0.75	1	0.72	0.76	0.56	0.42
Santa Catarina	0.49	0.26	0.53	0.23	0.63	0.48	0.72	1	0.60	0.76	0.47
Vermelha	1.26	1.07	0.74	0.74	0.59	0.69	0.76	0.60	1	0.76	0.50
Vimeiro	1.26	1.62	1.16	0.40	0.49	0.57	0.56	0.76	0.76	1	0.97
Turquel	0.73	1.00	0.61	0.36	0.36	0.46	0.42	0.47	0.50	0.97	1.00

Table A4.17 – Misclassification table: coefficient of determination (r^2) of the regression line for September (for the period between 1975/1976 to 2011/2012).

	Alfeizerão	Cela	Salir de Matos	Óbidos	Asseiceira	Alcoentre	Alvorninha	Santa Catarina	Vermelha	Vimeiro	Turquel
Alfeizerão	1	0.82	0.79	0.37	0.52	0.46	0.73	0.64	0.73	0.77	0.63
Cela	0.82	1	0.68	0.34	0.40	0.34	0.60	0.53	0.62	0.65	0.46
Salir de Matos	0.79	0.68	1	0.26	0.57	0.46	0.85	0.78	0.69	0.86	0.81
Óbidos	0.37	0.34	0.26	1	0.33	0.26	0.27	0.32	0.20	0.30	0.22
Asseiceira	0.52	0.40	0.57	0.33	1	0.78	0.60	0.57	0.58	0.53	0.46
Alcoentre	0.46	0.34	0.46	0.26	0.78	1	0.49	0.54	0.61	0.48	0.36
Alvorninha	0.73	0.60	0.85	0.27	0.60	0.49	1	0.80	0.75	0.83	0.77
Santa Catarina	0.64	0.53	0.78	0.32	0.57	0.54	0.80	1	0.58	0.80	0.76
Vermelha	0.73	0.62	0.69	0.20	0.58	0.61	0.75	0.58	1	0.63	0.60
Vimeiro	0.77	0.65	0.86	0.30	0.53	0.48	0.83	0.80	0.63	1	0.50
Turquel	0.63	0.46	0.81	0.22	0.46	0.36	0.77	0.76	0.60	0.50	1

Table A4.18 – Misclassification table: slope (b) of the regression line for September (for the period between 1975/1976 to 2011/2012).

	Alfeizerão	Cela	Salir de Matos	Óbidos	Asseiceira	Alcoentre	Alvorninha	Santa Catarina	Vermelha	Vimeiro	Turquel
Alfeizerão	1	1.25	1.04	0.54	0.79	0.76	0.77	0.59	0.95	0.92	0.55
Cela	1.25	1	0.70	0.45	0.52	0.49	0.50	0.44	1.15	1.24	0.65
Salir de Matos	1.04	0.70	1	0.49	0.72	0.66	0.73	0.65	1.05	1.15	0.75
Óbidos	0.54	0.45	0.49	1	0.59	0.59	0.43	0.41	0.42	0.60	0.51
Asseiceira	0.79	0.52	0.72	0.59	1	0.91	0.64	0.67	0.78	0.82	0.59
Alcoentre	0.76	0.49	0.66	0.59	0.91	1	0.56	0.75	0.76	0.78	0.56
Alvorninha	0.77	0.50	0.73	0.43	0.64	0.56	1	0.86	0.81	0.90	0.53
Santa Catarina	0.59	0.44	0.65	0.41	0.67	0.75	0.86	1	0.73	0.85	0.54
Vermelha	0.95	1.15	1.05	0.42	0.78	0.76	0.81	0.73	1	0.83	0.53
Vimeiro	0.92	1.24	1.15	0.60	0.82	0.78	0.90	0.85	0.83	1	0.57
Turquel	0.55	0.65	0.75	0.51	0.59	0.56	0.53	0.54	0.53	0.57	1

Table A4.19 – Misclassification table: coefficient of determination (r^2) of the regression line for October (for the period between 1975/1976 to 2011/2012).

	Alfeizerão	Cela	Salir de Matos	Óbidos	Asseiceira	Alcoentre	Alvorninha	Santa Catarina	Vermelha	Vimeiro	Turquel
Alfeizerão	1	0.87	0.89	0.16	0.76	0.68	0.78	0.67	0.78	0.79	0.63
Cela	0.87	1	0.86	0.15	0.75	0.65	0.76	0.69	0.75	0.82	0.65
Salir de Matos	0.89	0.86	1	0.17	0.81	0.68	0.80	0.74	0.80	0.84	0.70
Óbidos	0.16	0.15	0.17	1	0.18	0.12	0.18	0.19	0.15	0.21	0.32
Asseiceira	0.76	0.75	0.81	0.18	1	0.82	0.82	0.70	0.84	0.75	0.62
Alcoentre	0.68	0.65	0.68	0.12	0.82	1	0.68	0.64	0.72	0.66	0.56
Alvorninha	0.78	0.76	0.80	0.18	0.82	0.68	1	0.68	0.81	0.78	0.65
Santa Catarina	0.67	0.69	0.74	0.19	0.70	0.64	0.68	1	0.78	0.74	0.57
Vermelha	0.78	0.75	0.80	0.15	0.84	0.72	0.81	0.78	1	0.77	0.63
Vimeiro	0.79	0.82	0.84	0.21	0.75	0.66	0.78	0.74	0.77	1	0.74
Turquel	0.63	0.65	0.70	0.32	0.62	0.56	0.65	0.57	0.63	0.74	1

Table A4.20 – Misclassification table: slope (b) of the regression line for October (for the period between 1975/1976 to 2011/2012).

	Alfeizerão	Cela	Salir de Matos	Óbidos	Asseiceira	Alcoentre	Alvorninha	Santa Catarina	Vermelha	Vimeiro	Turquel
Alfeizerão	1	1.08	0.92	0.39	0.83	0.87	0.80	0.78	0.98	0.96	0.68
Cela	1.08	1	0.79	0.33	0.69	0.71	0.68	0.61	0.98	1.19	0.78
Salir de Matos	0.92	0.79	1	0.44	0.89	0.91	0.82	0.82	0.86	0.97	0.72
Óbidos	0.39	0.33	0.44	1	0.38	0.35	0.34	0.34	0.41	0.48	0.53
Asseiceira	0.83	0.69	0.89	0.38	1	1.01	0.86	0.75	0.87	0.90	0.65
Alcoentre	0.87	0.71	0.91	0.35	1.01	1	0.71	0.67	0.86	0.93	0.70
Alvorninha	0.80	0.68	0.82	0.34	0.86	0.71	1	0.86	0.80	0.86	0.65
Santa Catarina	0.78	0.61	0.82	0.34	0.75	0.67	0.86	1	0.79	0.86	0.63
Vermelha	0.98	0.98	0.86	0.41	0.87	0.86	0.80	0.79	1	1.02	0.69
Vimeiro	0.96	1.19	0.97	0.48	0.90	0.93	0.86	0.86	1.02	1	0.74
Turquel	0.68	0.78	0.72	0.53	0.65	0.70	0.65	0.63	0.69	0.74	1

Table A4.21 – Misclassification table: coefficient of determination (r^2) of the regression line for November (for the period between 1975/1976 to 2011/2012).

	Alfeizerão	Cela	Salir de Matos	Óbidos	Asseiceira	Alcoentre	Alvorninha	Santa Catarina	Vermelha	Vimeiro	Turquel
Alfeizerão	1	0.88	0.89	0.32	0.70	0.63	0.82	0.77	0.82	0.79	0.79
Cela	0.88	1	0.82	0.28	0.69	0.66	0.74	0.66	0.77	0.74	0.74
Salir de Matos	0.89	0.82	1	0.30	0.75	0.66	0.80	0.77	0.80	0.83	0.81
Óbidos	0.32	0.28	0.30	1	0.29	0.26	0.33	0.39	0.32	0.29	0.41
Asseiceira	0.70	0.69	0.75	0.29	1	0.87	0.83	0.66	0.88	0.71	0.63
Alcoentre	0.63	0.66	0.66	0.26	0.87	1	0.75	0.60	0.83	0.64	0.61
Alvorninha	0.82	0.74	0.80	0.33	0.83	0.75	1	0.73	0.87	0.79	0.73
Santa Catarina	0.77	0.66	0.77	0.39	0.66	0.60	0.73	1	0.69	0.77	0.74
Vermelha	0.82	0.77	0.80	0.32	0.88	0.83	0.87	0.69	1	0.76	0.73
Vimeiro	0.79	0.74	0.83	0.29	0.71	0.64	0.79	0.77	0.76	1	0.73
Turquel	0.79	0.74	0.81	0.41	0.63	0.61	0.73	0.74	0.73	0.73	1

Table A4.22 – Misclassification table: slope (b) of the regression line for November (for the period between 1975/1976 to 2011/2012).

	Alfeizerão	Cela	Salir de Matos	Óbidos	Asseiceira	Alcoentre	Alvorninha	Santa Catarina	Vermelha	Vimeiro	Turquel
Alfeizerão	1	1.06	0.92	0.53	0.83	0.91	0.79	0.79	1.04	0.93	0.79
Cela	1.06	1	0.79	0.43	0.67	0.72	0.66	0.60	1.03	1.09	0.82
Salir de Matos	0.92	0.79	1	0.54	0.87	0.95	0.78	0.79	0.88	0.94	0.79
Óbidos	0.53	0.43	0.54	1	0.58	0.63	0.47	0.58	0.52	0.55	0.45
Asseiceira	0.83	0.67	0.87	0.58	1	1.08	0.78	0.70	0.93	0.88	0.65
Alcoentre	0.91	0.72	0.95	0.63	1.08	1	0.63	0.59	1.02	0.98	0.70
Alvorninha	0.79	0.66	0.78	0.47	0.78	0.63	1	0.91	0.81	0.80	0.62
Santa Catarina	0.79	0.60	0.79	0.58	0.70	0.59	0.91	1	0.71	0.84	0.66
Vermelha	1.04	1.03	0.88	0.52	0.93	1.02	0.81	0.71	1	0.95	0.68
Vimeiro	0.93	1.09	0.94	0.55	0.88	0.98	0.80	0.84	0.95	1	0.70
Turquel	0.79	0.82	0.79	0.45	0.65	0.70	0.62	0.66	0.68	0.70	1

Table A4.23 – Misclassification table: coefficient of determination (r^2) of the regression line for December (for the period between 1975/1976 to 2011/2012).

	Alfeizerão	Cela	Salir de Matos	Óbidos	Asseiceira	Alcoentre	Alvorninha	Santa Catarina	Vermelha	Vimeiro	Turquel
Alfeizerão	1	0.91	0.88	0.37	0.76	0.75	0.83	0.67	0.83	0.73	0.73
Cela	0.91	1	0.84	0.29	0.73	0.74	0.79	0.67	0.74	0.74	0.70
Salir de Matos	0.88	0.84	1	0.38	0.79	0.77	0.83	0.75	0.83	0.81	0.72
Óbidos	0.37	0.29	0.38	1	0.38	0.35	0.35	0.46	0.41	0.42	0.44
Asseiceira	0.76	0.73	0.79	0.38	1	0.90	0.83	0.71	0.87	0.71	0.77
Alcoentre	0.75	0.74	0.77	0.35	0.90	1	0.81	0.69	0.88	0.73	0.72
Alvorninha	0.83	0.79	0.83	0.35	0.83	0.81	1	0.75	0.86	0.77	0.80
Santa Catarina	0.67	0.67	0.75	0.46	0.71	0.69	0.75	1	0.71	0.70	0.74
Vermelha	0.83	0.74	0.83	0.41	0.87	0.88	0.86	0.71	1	0.78	0.79
Vimeiro	0.73	0.74	0.81	0.42	0.71	0.73	0.77	0.70	0.78	1	0.78
Turquel	0.73	0.70	0.72	0.44	0.77	0.72	0.80	0.74	0.79	0.78	1

Table A4.24 – Misclassification table: slope (b) of the regression line for December (for the period between 1975/1976 to 2011/2012).

	Alfeizerão	Cela	Salir de Matos	Óbidos	Asseiceira	Alcoentre	Alvorninha	Santa Catarina	Vermelha	Vimeiro	Turquel
Alfeizerão	1	1.33	0.96	0.66	0.95	1.04	0.88	0.71	0.94	0.91	0.68
Cela	1.33	1	0.72	0.38	0.69	0.75	0.63	0.55	1.11	1.30	0.89
Salir de Matos	0.96	0.72	1	0.60	0.91	1.00	0.81	0.77	0.86	1.01	0.75
Óbidos	0.66	0.38	0.60	1	0.61	0.68	0.53	0.52	0.60	0.75	0.58
Asseiceira	0.95	0.69	0.91	0.61	1	1.05	0.81	0.68	0.95	0.98	0.84
Alcoentre	1.04	0.75	1.00	0.68	1.05	1	0.72	0.64	1.03	1.11	0.83
Alvorninha	0.88	0.63	0.81	0.53	0.81	0.72	1	0.84	0.82	0.90	0.71
Santa Catarina	0.71	0.55	0.77	0.52	0.68	0.64	0.84	1	0.71	0.85	0.70
Vermelha	0.94	1.11	0.86	0.60	0.95	1.03	0.82	0.71	1	1.04	0.72
Vimeiro	0.91	1.30	1.01	0.75	0.98	1.11	0.90	0.85	1.04	1	1.04
Turquel	0.68	0.89	0.75	0.58	0.84	0.83	0.71	0.70	0.72	1.04	1

Script A4.1 – Python script for interpolating missing daily Rainfall according to the r^2 and slope.

```
#-reads in partial rainfall records and fills in missing
# values on the basis of the similarity with adjacent stations

import os,datetime
import numpy as np

def retrieveDate(dateStr,sep= '-'):
   #-retrieves the serial date number from a string composed of day,month,year separated
by hyphens
   dateList= dateStr.split(sep)
   day= int(dateList[0])
   month= int(dateList[1])
   year= int(dateList[2])
   if year < 100:
      if year > 70:
         year= year+1900
      else:
         year= year+2000
   return datetime.datetime(year,month,day)

#-main
print 'Processing precipitation data'
#-initialization of variables: stations and file names
meteoStations= ['Alfeizerao','Cela','Salir de Matos','Obidos',\
   'Asseiceira','Alcoentre','Alvorninha','Santa Catarina',\
   'Vermelha','Vimeiro','Turquel']
monthNames= ['january','february','march','april','may','june','july',\
         'august','september','october','november','december']
numberStations= len(meteoStations)
numberMonths= len(monthNames)
originalPrecipFileName= 'precorg_%s.txt'
updatedPrecipFileName=  'precupd_%s.txt'
statFileName= 'stats_%s.txt'
#-boolean variable to create new files once first called
createFile= True
#-dates: start and end year
startYear= 1977
endYear= 2012
#-default MV
MV= -999.
#-reading statistics
print '*\treading statistics:'
slopeArray= np.ones((numberMonths,numberStations,numberStations),\
   dtype= 'float')*MV
rsqArray=  np.ones((numberMonths,numberStations,numberStations),\
   dtype= 'float')*MV
monthCnt= 0
for month in monthNames:
   #-read in values per month: count months, valid lines read and
```

```
    # total number of entries
    try:
       datFile= open(statFileName % month.lower())
       lineCnt= 0
       try:
          for line in datFile:
             rawList= line.split()
             testList= [0.]*numberStations
             entryCnt= 0
             for entry in rawList:
                try:
                   testList[entryCnt]= float(entry)
                   entryCnt+= 1
                except:
                   pass
             if entryCnt == numberStations:
                if lineCnt < numberStations:
                   rowCnt= lineCnt
                   for colCnt in range(entryCnt):
                      slopeArray[monthCnt,rowCnt,colCnt]= testList[colCnt]
                else:
                   rowCnt= lineCnt-numberStations
                   for colCnt in range(entryCnt):
                      rsqArray[monthCnt,rowCnt,colCnt]= testList[colCnt]
                lineCnt+= 1
       finally:
          datFile.close()
    except:
       pass
    print '\t%s read' % month
    monthCnt+= 1
#-step through time and retrieve data
# data are stored in a 3-dimensional array holding on the rows the
# day and on the symmetrical columns the station information,
# these entries are subsequently updated and the best entry returned
print '*\tprocessing station information per year:'
for year in range(startYear,endYear):
    print'\t%d' % year
    for month in range(1,numberMonths+1):
       monthCnt= month-1
       startDate= datetime.datetime(year,month,1)
       if month < 12:
          lastDate= datetime.datetime(year,month+1,1)
       else:
          lastDate= datetime.datetime(year+1,1,1)
       #-retrieve number of days in current month and initialize array
       numberDays= lastDate.toordinal()-startDate.toordinal()
       precipArray= np.ones((numberDays,numberStations,numberStations),\
          dtype= 'float')*MV
       #-read in files and process using column counter, adding homogeneous rainfall
       # data to the first column dimension
       colCnt= 0
```

```
    for station in meteoStations:
      try:
        datFile= open(originalPrecipFileName % station.replace(' ','_').lower())
        try:
          for line in datFile:
            rawList= line.split()
            if len(rawList) == 2:
              currentDate= retrieveDate(rawList[0])
              if (currentDate.toordinal() >= startDate.toordinal()) & \
                  (currentDate.toordinal() < lastDate.toordinal()):
                rowCnt= currentDate.toordinal()-startDate.toordinal()
                precipArray[rowCnt,colCnt,:]= float(rawList[1])
        finally:
          datFile.close()
      except:
        pass
      #-increment column counter
      colCnt+= 1
    #-array filled with data, process column wise by multiplying all entries with the slope
    for colCnt in range(numberStations):
      for rowCnt in range(numberDays):
        if precipArray[rowCnt,colCnt,colCnt] <> MV:
          precipArray[rowCnt,colCnt,:]= precipArray[rowCnt,colCnt,:]*\
            slopeArray[monthCnt,colCnt,:]
    #-array updated, retrieve best fit for station per day
    #-open file per station
    for colCnt in range(numberStations):
      #-station name
      station= meteoStations[colCnt]
      #-write new file or append to existing
      if createFile:
        datFile= open(updatedPrecipFileName % station.replace(' ','_').lower(),'w')
      else:
        datFile= open(updatedPrecipFileName % station.replace(' ','_').lower(),'a')
      #-retrieve data from array
      for rowCnt in range(numberDays):
        #-date and retrieving match, using station counter as default
        currentDate= startDate+datetime.timedelta(rowCnt)
        matchCnt= colCnt
        mask= precipArray[rowCnt,:,colCnt] <> MV
        if any(mask):
          rsq= rsqArray[monthCnt,:,colCnt][mask].max()
          if rsq > 0.:
            matchCnt= np.arange(numberStations)[rsqArray[monthCnt,:,colCnt] == rsq][0]
        else:
            matchCnt= colCnt
##          print month,station,rsq,matchCnt,\
##            rsqArray[monthCnt,:,colCnt],[rsqArray[monthCnt,:,colCnt] == rsq]
        line= '%s\t%.2f\t%s\n' % \

(currentDate.date(),precipArray[rowCnt,matchCnt,colCnt],meteoStations[matchCnt])
```

```
            datFile.write(line)
          #-close file
          datFile.close()
       #-reset file creation to false
       createFile= False
#-all done
print 'all done!'
```

Script A4.2 – Python Script for interpolating daily radiation; daily precipitation; daily precipitation duration; daily temperature; daily potential evapotranspiration; daily actual evapotranspiration; and fi, continuously in space and time.

```
#!/usr/bin/env python

#-modules

import os, sys, shutil, calendar, zlib, zipfile

import numpy as np

import matplotlib.pyplot as plt

from scipy import interpolate

import PCRaster as pcr

from PCRaster.Framework import generateNameT



#-initialization

#-area

domainName= 'portugal'

#-constants: missing value identifier and power

# to interpolate inverse distance weight fields (positive, reverts to average when set to zero)

MV= -999.9

idwPower= 2.0

reportWeights= True

#-years to be processed

years= range(1975,2012)

nrMonths= 12

nrDays= 365

julianDay= [1,32,60,91,121,152,182,213,244,274,305,335,366]

addDay= [0,0,1,1,1,1,1,1,1,1,1,1,1]

#-dataPath

dataPath= 'G:\\Modelo_utrecht\\Model\\MODEL_final\\Input\\'
```

```
mapPath= os.path.join(dataPath,'maps')

meteoData= os.path.join(dataPath,'TSS')

#-DEM

DEMFileName= os.path.join(meteoData,'dem_full.map')

#-meteo constants and files

meteoResults= 'G:\\Modelo_utrecht\\Model\\MODEL_final\\Portugal\\meteo'

meteoArchives= 'G:\\Modelo_utrecht\\Model\\MODEL_final\\Portugal\\meteoarchives'

meteoVariables= {}

#-main variables: mean daily temperature [degC] and daily precipitation sum [m]

meteoVariables['precipitation']= {}

meteoVariables['temperature']= {}

meteoVariables['precipitation']['stations']= os.path.join(meteoData,'est_11.map')

meteoVariables['temperature']['stations']= os.path.join(meteoData,'est_4.map')

meteoVariables['precipitation']['fileroot']=
os.path.join(meteoData,'stations_precipitation_%04d.tss')

meteoVariables['temperature']['fileroot']=
os.path.join(meteoData,'station_temperature_%04d.tss')

meteoVariables['temperature']['alternative']=
os.path.join(meteoData,'station_temperature_until_1980.tss')

meteoVariables['precipitation']['varname']= 'prec'

meteoVariables['temperature']['varname']= 'temp'

meteoVariables['precipitation']['reportFactor']= 0.001

meteoVariables['temperature']['reportFactor']= 1.00

#-these entries are filled in; stations is replaced by map and a interpolated zonal coverage

meteoVariables['precipitation']['climatology']= np.array([])

meteoVariables['temperature']['climatology']= np.array([])

meteoVariables['precipitation']['lapserate']= np.array([])

meteoVariables['temperature']['lapserate']= np.array([])
```

```
meteoVariables['precipitation']['nrstations']= 0

meteoVariables['temperature']['nrstations']= 0

meteoVariables['precipitation']['elevation']= []

meteoVariables['temperature']['elevation']= []

#-derived variables: precipitation duration [day], daily potential reference evapotranspiration
[m]

# and BATS-based temperature function to derive LAI

derivedVariables= ['duration','evapotranspiration','fbats']

for derivedVariable in derivedVariables:

  meteoVariables[derivedVariable]= {}

meteoVariables['duration']['varname']= 'pdur'

meteoVariables['evapotranspiration']['varname']= 'epot'

meteoVariables['fbats']['varname']= 'ftmp'

meteoVariables['duration']['reportFactor']= 1.00

meteoVariables['evapotranspiration']['reportFactor']= 0.001

meteoVariables['fbats']['reportFactor']= 1.00

#-timeseries holding incoming shortwave radiation in W/m2

swRadiationTSS= os.path.join(meteoData,'rad.tss')

#-constants to convert radiation to sum in MJ over day

# and to obtain the incoming radiation under cloudy conditions

# and to derive the evapotranspiration using Hargreaves' Equation

#-Hargreaves gives mm and reduces the radiation to mm

# implicitly using the latent heat of vaporization

radConversion= 0.0864;

radConst1=  238.8;

radConst2= 595.5;

radConst3= -0.55;
```

```
harMult= 0.0135;

harConst= 17.78;

#-parameters of the duration function: the current values estimate

# the duration as D= a*Ptot^b, and the maximum intensity is 2*Ptot/D

# with Ptot in mm and D coming back in days

# for the example given, duration approaches one day if Ptot= 360 mm, with a maximum

# intensity of 30 and a mean of 15 mm/hour

precDurationConstant= 0.052704628

precDurationPower= 0.5



#-start

print 'Running the meteo pre-processor for the Starwars script for %s' % domainName

#-create paths if not existing

pathList= [meteoResults,meteoArchives]

for path in pathList:

 try:

   os.makedirs(path)

 except:

   print '\tpath %s already exists or cannot be created' % path

#-read DEM

DEM= pcr.readmap(DEMFileName)

friction= pcr.cos(pcr.atan(pcr.slope(DEM)))**-1.

#-meteo: first, read in TSS files of temperature and precipitation to create

# daily (temperature) and monthly (temperature, precipitation) to create climatology

# and lapse rates

variables= meteoVariables.keys()

for derivedVariable in derivedVariables:
```

```
  variables.remove(derivedVariable)

#-iterate over variables

for variable in variables:

  print ' * processing %s' % variable

  stations= pcr.readmap(meteoVariables[variable]['stations'])

  nrYears= 0

  nrStations= int(pcr.cellvalue(pcr.mapmaximum(pcr.scalar(stations)),1)[0])

  elevation= [0.]*nrStations

  for station in xrange(nrStations):

    elevation[station]= pcr.cellvalue(pcr.mapmaximum(pcr.ifthen(stations ==
station+1,DEM)),1)[0]

  #-iterate over years and retrieve climatology and lapse rates

  print ' - retrieving climatologies and lapse rates'

  monthlyClimatology= np.zeros((nrMonths,nrStations))

  monthlyObservations= np.zeros((nrMonths,nrStations))

  monthlyLapseRate= np.zeros((nrMonths))

  for year in years:

    if os.path.isfile(os.path.join(meteoData,meteoVariables[variable]['fileroot'] % year)):

      nrYears+= 1

      dataArray= np.loadtxt(os.path.join(meteoData,meteoVariables[variable]['fileroot'] %
year), skiprows= nrStations+3)

      for month in  xrange(nrMonths):

        startDay= julianDay[month]

        endDay= julianDay[month+1]

        if calendar.isleap(year):

          startDay+= addDay[month]

          endDay+= addDay[month+1]

        monthlyClimatology[month,:]= dataArray[startDay:endDay,1:].sum(axis= 0)
```

```
        monthlyObservations[month,:]=
np.ones(dataArray[startDay:endDay,1:].shape).sum(axis= 0)
 if variable == 'temperature':
   monthlyClimatology/= monthlyObservations
 for month in xrange(nrMonths):
   A = np.vstack([elevation, np.ones(len(elevation))]).T
   monthlyLapseRate[month], b0= np.linalg.lstsq(A,monthlyClimatology[month,:])[0]
 #-assign values to dictionaries
 meteoVariables[variable]['climatology']= monthlyClimatology.copy()
 meteoVariables[variable]['lapserate']= monthlyLapseRate.copy()
 meteoVariables[variable]['lapserate']
 meteoVariables[variable]['stations']= stations
 meteoVariables[variable]['nrstations']= nrStations
 meteoVariables[variable]['elevation']= elevation
 del monthlyClimatology
 del monthlyObservations
 del monthlyLapseRate
 del stations
 del nrStations
 del elevation
 #-create plots of lapse rates using monthly centres as dummy time
 monthlyCentre= np.ones((nrMonths))*MV
 for month in xrange(nrMonths):
   monthlyCentre[month]= 0.5*(julianDay[month]+julianDay[month+1])
 #-obtain spline with three added values on either site of the climatology
 x= np.zeros((18))
 y= np.zeros((18))
```

```
  x[3:15]= monthlyCentre[:]
  y[3:15]= meteoVariables[variable]['lapserate'][:]
  x[ 0]= monthlyCentre[ 9]-nrDays; y[ 0]= meteoVariables[variable]['lapserate'][ 9]
  x[ 1]= monthlyCentre[10]-nrDays; y[ 1]= meteoVariables[variable]['lapserate'][10]
  x[ 2]= monthlyCentre[11]-nrDays; y[ 2]= meteoVariables[variable]['lapserate'][11]
  x[15]= monthlyCentre[ 0]+nrDays; y[15]= meteoVariables[variable]['lapserate'][ 0]
  x[16]= monthlyCentre[ 1]+nrDays; y[16]= meteoVariables[variable]['lapserate'][ 1]
  x[17]= monthlyCentre[ 2]+nrDays; y[17]= meteoVariables[variable]['lapserate'][ 2]
  fspline= interpolate.InterpolatedUnivariateSpline(x,y)
  #-plot and save figure
  plt.figure()
  plt.plot(monthlyCentre,meteoVariables[variable]['lapserate'],'o')
  if variable == 'temperature':
    plt.plot(np.arange(1,365),fspline(np.arange(1,365)))
  else:
    plt.plot(monthlyCentre,fspline(monthlyCentre))
  plt.legend(['Monthly observations','Interpolated spline', 'True'])
  plt.title('Lapse rate for %s based on %d stations\nover %d years over the period %d-%d' %\
    (variable,meteoVariables[variable]['nrstations'],nrYears,min(years),max(years)))
  plt.savefig('lapserate_%s.png' % variable)
  plt.close()


#-creating yearly zip files
print ' * creating yearly meteo input'
#-first, remove any existing zip files
for year in years:
  try:
```

```
    os.remove(os.path.join(meteoArchives,'meteo_%s_%04d.zip' %\
      (domainName,year)))
  except:
    pass
try:
  os.remove(os.path.join(meteoArchives,'fbats_%s.zip' %\
    domainName))
except:
  pass
#-iterate over variables
for variable in variables:
  print ' - processing variable %s' % variable
  #-create weights as dictionary of PCRaster maps
  # weights are multiplicative and represent the influence of a station at any point
  weights= {}
  totalWeights= pcr.scalar(0.)
  for station in xrange(1,meteoVariables[variable]['nrstations']+1):
    weights[station]= pcr.spread(meteoVariables[variable]['stations'] == station,\
      0.5*pcr.celllength(),friction)**-idwPower
    totalWeights+= weights[station]
  for station in xrange(1,meteoVariables[variable]['nrstations']+1):
    weights[station]/= totalWeights
    if reportWeights:
      pcr.report(weights[station],'weight_%s_%d.map' % (variable,station))
  #-delete total
  del totalWeights
  #-set minimum and maximum for temperature
```

```
  if variable == 'temperature':
   meteoVariables[variable]['min']= pcr.scalar(pcr.abs(MV**2))
   meteoVariables[variable]['max']= pcr.scalar(-pcr.abs(MV**2))
   #-create empty LAI files
   derivedVariable= 'fbats'
   for day in xrange(1,julianDay[12]):
    derivedField= pcr.scalar(0.)
    pcr.report(derivedField,os.path.join(meteoResults,\
     generateNameT(meteoVariables[derivedVariable]['varname'],day)))
  #-iterate over years
  print ' - ',
  for year in years:
   print year,
   #-check for the length of each record
   nrDays= 365
   if calendar.isleap(year):
    nrDays= 366
   #-read in and complement data array if number of days is not met
   if os.path.isfile(os.path.join(meteoData,meteoVariables[variable]['fileroot'] % year)):
    dataArray= np.loadtxt(os.path.join(meteoData,meteoVariables[variable]['fileroot'] %
year),\
      skiprows= meteoVariables[variable]['nrstations']+3)
   else:
    dataArray= np.loadtxt(os.path.join(meteoData,meteoVariables[variable]['alternative']),\
      skiprows= meteoVariables[variable]['nrstations']+3)
   if dataArray.shape[0] <> nrDays:
    if dataArray.shape[0] < nrDays:
```

```
      x= dataArray[julianDay[3]-1:julianDay[3],:].mean(axis= 0)
      if variable == 'precipitation':
        x*= 0.
      dataArray= np.insert(dataArray,julianDay[3],x,axis= 0)
      dataArray[julianDay[3]:,0]= np.arange(julianDay[3],nrDays)
    elif dataArray.shape[0] > nrDays:
      dataArray= np.delete(dataArray,julianDay[3],axis= 0)
      dataArray[julianDay[3]:,0]= np.arange(julianDay[3],nrDays+1)
    else:
      sys.exit('not defined!')
  #-obtain elevation corrected values for temperature and precipitation
  # use daily correction in case of temperature to scale temperature to sea level
  #-also read timeseries with incoming shortwave radiation and complement time series
when needed
  if variable == 'temperature':
    #-lapse rates etc.
    monthlyCentre= np.zeros(nrMonths)
    for month in xrange(nrMonths):
      startDay= julianDay[month]
      endDay= julianDay[month+1]
      if calendar.isleap(year):
        startDay+= addDay[month]
        endDay+= addDay[month+1]
      monthlyCentre[month]= 0.5*(startDay+endDay)
    #-daily lapse rates from monthly values
    x= np.zeros((18))
    y= np.zeros((18))
```

```
x[3:15]= monthlyCentre[:]
y[3:15]= meteoVariables[variable]['lapserate'][:]
x[ 0]= monthlyCentre[ 9]-nrDays; y[ 0]= meteoVariables[variable]['lapserate'][ 9]
x[ 1]= monthlyCentre[10]-nrDays; y[ 1]= meteoVariables[variable]['lapserate'][10]
x[ 2]= monthlyCentre[11]-nrDays; y[ 2]= meteoVariables[variable]['lapserate'][11]
x[15]= monthlyCentre[ 0]+nrDays; y[15]= meteoVariables[variable]['lapserate'][ 0]
x[16]= monthlyCentre[ 1]+nrDays; y[16]= meteoVariables[variable]['lapserate'][ 1]
x[17]= monthlyCentre[ 2]+nrDays; y[17]= meteoVariables[variable]['lapserate'][ 2]
fspline= interpolate.InterpolatedUnivariateSpline(x,y)
b0= fspline(np.arange(1,nrDays+1))
deltaVariable= b0.copy()
for iCnt in xrange(meteoVariables[variable]['nrstations']-1):
  deltaVariable= np.c_[deltaVariable,b0]
for day in xrange(nrDays):
  dataArray[day,1:]-=deltaVariable[day,:]*meteoVariables[variable]['elevation']
#-radiation
radiationArray= np.loadtxt(swRadiationTSS, skiprows= 4)
if radiationArray.shape[0] <> nrDays:
  if radiationArray.shape[0] < nrDays:
    x= radiationArray[julianDay[3]-1:julianDay[3],:].mean(axis= 0)
    radiationArray= np.insert(radiationArray,julianDay[3],x,axis= 0)
    radiationArray[julianDay[3]:,0]= np.arange(julianDay[3],nrDays)
  elif radiationArray.shape[0] > nrDays:
    radiationArray= np.delete(radiationArray,julianDay[3],axis= 0)
    radiationArray[julianDay[3]:,0]= np.arange(julianDay[3],nrDays+1)
  else:
    sys.exit('not defined!')
```

```
#-iterate over months and days to create maps from inverse distance interpolation
# process precipitation on a monthly basis first
for month in xrange(nrMonths):
 #set start and end date
 startDay= julianDay[month]
 endDay= julianDay[month+1]
 if calendar.isleap(year):
  startDay+= addDay[month]
  endDay+= addDay[month+1]
 #-update to indices of array
 startDay-= 1
 endDay-= 1
 #-process preciptation to derive corrected rainfall amounts
 if variable == 'precipitation':
  #-obtain first the monthly sum and the change due to the lapse rate
  # and compute the multiplicative anomaly, scaling rainfall to sea level
  monthlyObservations= dataArray[startDay:endDay,1:].sum(axis= 0)
  #-change in rainfall due to elevation
  deltaVariable= np.array([meteoVariables[variable]['lapserate'][month]])*\
   meteoVariables[variable]['elevation']
  #-multiplicative anomaly; if no rainfall is present, this factor is set to zero
  # in order to avoid any missing  values, or to 1 if the anomaly becomes negative but
  # rainfall is present (sparse raindays)
  deltaVariable[monthlyObservations > 0.]= (monthlyObservations[monthlyObservations >
0.]\
   -deltaVariable[monthlyObservations > 0.])/monthlyObservations[monthlyObservations
> 0.]
  deltaVariable[monthlyObservations <= 0.]= 0.
```

```
  deltaVariable[(monthlyObservations > 0.) & (deltaVariable < 0.)]= 1.
  #-update variable
  dataArray[startDay:endDay,1:]*= deltaVariable
#-obtain anomaly for current month; additive value is used directly
# in the case of temperature, it is applied to the monthly sum in case
# of precipitation
if variable == 'precipitation':
  #-monthly value
  anomaly= meteoVariables[variable]['lapserate'][month]*DEM
  field= pcr.scalar(0.)
  for station in xrange(1,meteoVariables[variable]['nrstations']+1):
    field+= weights[station]*dataArray[startDay:endDay,station].sum()
  #-anomaly
  anomaly= pcr.ifthenelse(field > 1.e-4,\
    (field+anomaly)/field,1.0)
  anomaly= pcr.ifthenelse(anomaly < 0.,1.0,anomaly)
#iterate over days: this pertains to temperature and precipitation alike
for day in xrange(startDay,endDay):
  field= pcr.scalar(0.)
  for station in xrange(1,meteoVariables[variable]['nrstations']+1):
    field+= weights[station]*dataArray[day,station]
  #-apply anomaly
  if variable == 'temperature':
    field+= deltaVariable[day,0]*DEM
  elif variable == 'precipitation':
    field*= anomaly
  #-round off to nearest decimal
```

```
      field= 0.1*pcr.roundoff(field*10.)
      pcr.report(meteoVariables[variable]['reportFactor']*\
       field,os.path.join(meteoResults,\
        generateNameT(meteoVariables[variable]['varname'],day+1)))
      #-statistics and derived variables
      if variable == 'temperature':
       #-update minimum and maximum temperature to obtain the BATS temperature
       # function, update the LAI and compute the potential evapotranspiration
       #-long-term statistics
       meteoVariables[variable]['min']= pcr.min(field,\
        meteoVariables[variable]['min'])
       meteoVariables[variable]['max']= pcr.max(field,\
        meteoVariables[variable]['max'])
       #-update temperature function as long-term daily sum
       derivedVariable= 'fbats'
       index= range(startDay,endDay).index(day)
       if index < len(range(julianDay[month],julianDay[month+1])):
        fileName= os.path.join(meteoResults,\
         generateNameT(meteoVariables[derivedVariable]['varname'],
          range(julianDay[month],julianDay[month+1])[index]))
        derivedField=
pcr.readmap(fileName)/meteoVariables[derivedVariable]['reportFactor']+field
        pcr.report(meteoVariables[derivedVariable]['reportFactor']*derivedField,fileName)
       #-reference potential evapotranspiration
       derivedVariable= 'evapotranspiration'
       fileName= os.path.join(meteoResults,\
        generateNameT(meteoVariables[derivedVariable]['varname'],day+1))
```

```
        derivedField= radConversion*radiationArray[day,1]
        derivedField= harMult*(field+harConst)*derivedField*\
          (radConst1/(radConst2+radConst3*field))
        pcr.report(meteoVariables[derivedVariable]['reportFactor']*derivedField,fileName)
      elif variable == 'precipitation':
        #-obtain duration
        derivedVariable= 'duration'
        derivedField= pcr.min(1.0,precDurationConstant*field**precDurationPower)
        pcr.report(meteoVariables[derivedVariable]['reportFactor']*\
          derivedField,os.path.join(meteoResults,\
            generateNameT(meteoVariables[derivedVariable]['varname'],day+1)))
    #-add fields to zip file and delete data
    if os.path.exists(os.path.join(meteoArchives,'meteo_%s_%04d.zip' %
(domainName,year))):
      #-open archive to append
      meteoArchive= zipfile.ZipFile(os.path.join(meteoArchives,'meteo_%s_%04d.zip' %\
        (domainName,year)),'a',zipfile.ZIP_DEFLATED)
    else:
      #-else open for write
      meteoArchive= zipfile.ZipFile(os.path.join(meteoArchives,'meteo_%s_%04d.zip' %\
        (domainName,year)),'w',zipfile.ZIP_DEFLATED)
    #-write files
    derivedVariable= 'fbats'
    for fileName in os.listdir(meteoResults):
      if meteoVariables[derivedVariable]['varname'] not in fileName:
        meteoArchive.write(os.path.join(meteoResults,fileName),fileName)
        os.remove(os.path.join(meteoResults,fileName))
```

```
    meteoArchive.close()
  #-all years for present variable processed
  print


#-reprocess remaning variables to create climatology of BATS temperature function
variable= 'temperature'
derivedVariable= 'fbats'
#-open zip file
meteoArchive= zipfile.ZipFile(os.path.join(meteoArchives,'fbats_%s.zip' %\
  domainName),'w',zipfile.ZIP_DEFLATED)
#-iterate over all remaining files
for fileName in os.listdir(meteoResults):
  if meteoVariables[derivedVariable]['varname'] in fileName:
    derivedField= pcr.readmap(os.path.join(meteoResults,fileName))/len(years)
    derivedField= (derivedField-meteoVariables[variable]['min'])/\
      pcr.max(0.1,meteoVariables[variable]['max']-meteoVariables[variable]['min'])
    pcr.report(derivedField,os.path.join(meteoResults,fileName))
  #-write to zip file
  meteoArchive.write(os.path.join(meteoResults,fileName),fileName)
  os.remove(os.path.join(meteoResults,fileName))
meteoArchive.close()
#-all processed
print '-All done'
```

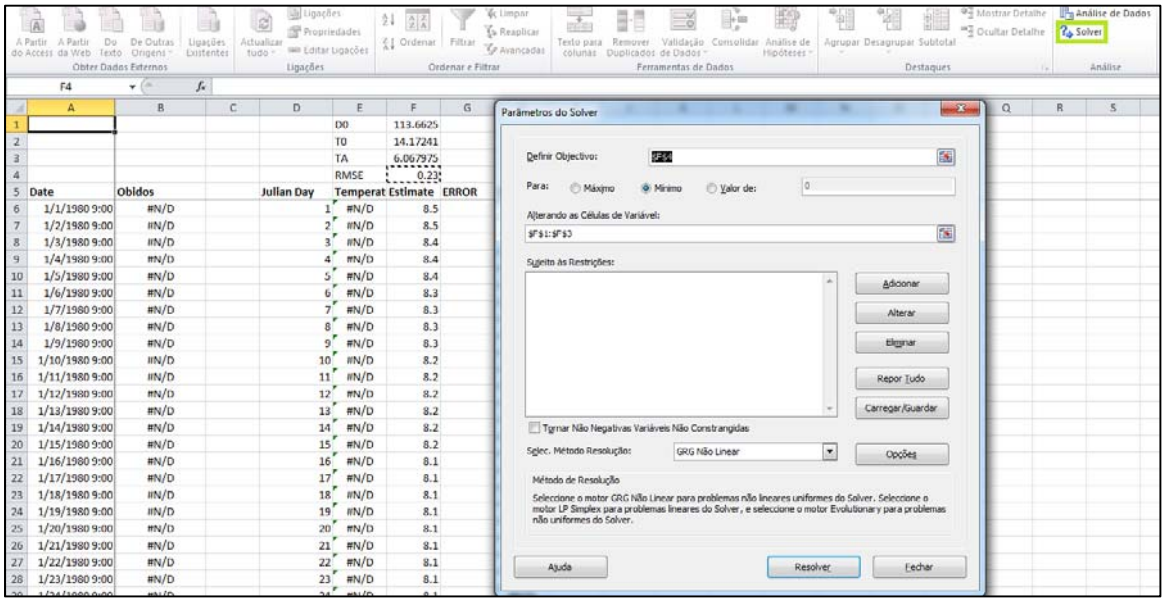

	A	B	C	D	E	F	G
1					D0	113.6625	
2					T0	14.17241	
3					TA	6.067975	
4					RMSE	0.23	
5	Date	Obidos		Julian Day	Temperat	Estimate	ERROR
6	1/1/1980 9:00	#N/D		1	#N/D	8.5	
7	1/2/1980 9:00	#N/D		2	#N/D	8.5	
8	1/3/1980 9:00	#N/D		3	#N/D	8.4	
9	1/4/1980 9:00	#N/D		4	#N/D	8.4	
10	1/5/1980 9:00	#N/D		5	#N/D	8.4	
11	1/6/1980 9:00	#N/D		6	#N/D	8.3	
12	1/7/1980 9:00	#N/D		7	#N/D	8.3	
13	1/8/1980 9:00	#N/D		8	#N/D	8.3	
14	1/9/1980 9:00	#N/D		9	#N/D	8.3	
15	1/10/1980 9:00	#N/D		10	#N/D	8.2	
16	1/11/1980 9:00	#N/D		11	#N/D	8.2	
17	1/12/1980 9:00	#N/D		12	#N/D	8.2	
18	1/13/1980 9:00	#N/D		13	#N/D	8.2	
19	1/14/1980 9:00	#N/D		14	#N/D	8.2	
20	1/15/1980 9:00	#N/D		15	#N/D	8.2	
21	1/16/1980 9:00	#N/D		16	#N/D	8.1	
22	1/17/1980 9:00	#N/D		17	#N/D	8.1	
23	1/18/1980 9:00	#N/D		18	#N/D	8.1	
24	1/19/1980 9:00	#N/D		19	#N/D	8.1	
25	1/20/1980 9:00	#N/D		20	#N/D	8.1	
26	1/21/1980 9:00	#N/D		21	#N/D	8.1	
27	1/22/1980 9:00	#N/D		22	#N/D	8.1	
28	1/23/1980 9:00	#N/D		23	#N/D	8.1	

Fig. A4.1 – Solver function from Excel software.

APPENDIX 5: CONVERTION OF THE VEGETATION TYPES INTO THE GLOBAL ECOSYSTEM TYPES.

Table A5.1 – Conversion from land use classes to Global Ecosystems types.

Land use classes	Forest Coverage*	Global Ecosystems Legend	Classes of cover properties
Industrial and commercial zones		Urban	1
Other infrastructure and equipment		Urban	1
Urban continuous zone		Urban	1
Other areas outside the urban consolidated zone		Urban	1
Quarries, gravel, open mines		Urban	1
Low Sparse Grassland		Low Sparse Grassland	2
Other degraded zones		Low Sparse Grassland	2
Pinus Pinea	below 10% covered	Coniferous Forest	3
Pinus Pinea + Pinus Pinaster	from 10% to 30% covered	Coniferous Forest	3
Pinus Pinaster + Cork-Oak	from 30% to 50% covered	Coniferous Forest	3
Pinus Pinaster + eucalyptus	from 10% to 30% covered	Coniferous Forest	3
Pinus Pinaster + Other Broadleaves	below 10% covered	Coniferous Forest	3
Pinus Pinaster + Pinus Pinea	below 10% covered	Coniferous Forest	3
Pinus Pinaster	Clearcutting or fire	Coniferous Forest	3
Chestnut + Other Broadleaves	below 10% covered	Deciduous Broadleaf Forest	4
Chestnut	>50% covered	Deciduous Broadleaf Forest	4
Chestnut + Pinus Pinaster	from 30% to 50% covered	Deciduous Broadleaf Forest	4
Oak + Other Broadleaves	from 30% to 50% covered	Deciduous Broadleaf Forest	4
Oak	>50% covered	Deciduous Broadleaf Forest	4
Oak + Pinus Pinaster	>50% covered	Deciduous Broadleaf Forest	4
Pome trees		Deciduous Broadleaf Forest	4
Pome trees (without Almond trees)		Deciduous Broadleaf Forest	4
Mixed Orchards		Deciduous Broadleaf Forest	4
Orchard + Annual crop		Deciduous Broadleaf Forest	4
Orchard + Olive		Deciduous Broadleaf Forest	4
Orchard + vineyard		Deciduous Broadleaf Forest	4
citrus		Evergreen Broadleaf Forests	5
Eucalyptus + Cork-Oak	>50% covered	Evergreen Broadleaf Forests	5
Eucalyptus + Annual crop	from 30% to 50% covered	Evergreen Broadleaf Forests	5
Eucalyptus	Clearcutting or fire	Evergreen Broadleaf Forests	5
Eucalyptus + Other Broadleaves	>50% covered	Evergreen Broadleaf Forests	5
Eucalyptus + Pinus Pinea	>50% covered	Evergreen Broadleaf Forests	5
Eucalyptus + Pinus Pinaster	Clearcutting or fire	Evergreen Broadleaf Forests	5

Eucalyptus + other Resinous	>50% covered	Evergreen Broadleaf Forests	5
Semi-Natural Grasslands		Irrigated Grassland	6
Pinus Pinaster + Oak	from 30% to 50% covered	Cool Mixed Forest	7
Pinus Pinea + Cork-Oak	>50% covered	Mixed Forest	8
Pinus Pinea + Eucalyptus	from 10% to 30% covered	Mixed Forest	8
Pinus Pinea + Other Broadleaves	from 10% to 30% covered	Mixed Forest	8
Other Broadleaves + Cork-Oak	from 30% to 50% covered	Mixed Forest	8
Other Broadleaves	Urban green zone or protective	Mixed Forest	8
Other Broadleaves + Pinus Pinea	>50% covered	Mixed Forest	8
Other Broadleaves + Pinus Pinaster	>50% covered	Mixed Forest	8
Other Broadleaves+ Eucalyptus	>50% covered	Mixed Forest	8
Urban green zones (forest)		Crops and Town	9
Annual crops: Rice fields		Rice Paddy and Field	10
Annual crops: other (greenhouses, nurseries etc)		Hot Irrigated Cropland	11
Annual crops + Orchard		Cool Irrigated Cropland	12
Annual crops: Irrigated		Cool Irrigated Cropland	12
High Scrubland and degraded or transition forest + Eucalyptus		Mediterranean Scrub	13
High Scrubland and degraded or transition forest + Other Broadleaves		Mediterranean Scrub	13
Low shrubs: scrubs		Mediterranean Scrub	13
Low shrubs: scrubs + Recently burned areas		Mediterranean Scrub	13
High Scrubland and degraded or transition forest + Pinus Pinaster		Mediterranean Scrub	13
Cork-Oak	>50% covered	Dry Evergreen Woods	14
Cork-Oak + Eucalyptus	>50% covered	Dry Evergreen Woods	14
Cork-Oak + Other Broadleaves	>50% covered	Dry Evergreen Woods	14
Cork-Oak + Pinus Pinea	>50% covered	Dry Evergreen Woods	14
Cork-Oak + Oak	from 30% to 50% covered	Dry Evergreen Woods	14
Cork-Oak + Holmoak	>50% covered	Dry Evergreen Woods	14
Olive + Orchard		Dry Evergreen Woods	14
Olive		Dry Evergreen Woods	14
Olive + Vineyard		Dry Evergreen Woods	14
Beach, dunes, sands and soils without vegetation		Sand Desert	15
Mainly agricultural areas with important natural zones		Forest and Field	16
Vineyard + Orchard		Crops, Grass, Shrubs	17
Vineyard + Annual crops		Crops, Grass, Shrubs	17
Vineyard + Olive		Crops, Grass, Shrubs	17
Vineyard		Crops, Grass, Shrubs	17
Annual crops + Cork-Oak		Crops, Grass, Shrubs	17
Annual crops: nonirrigated		Crops, Grass, Shrubs	17

Annual crops + Eucalyptus		Crops, Grass, Shrubs	17
Annual crops + Other Broadleaves		Crops, Grass, Shrubs	17
Annual crops + Pinus Pinea		Crops, Grass, Shrubs	17
Annual crops + Olive		Crops, Grass, Shrubs	17
Annual crops + Pinus Pinaster		Crops, Grass, Shrubs	17
Annual crops + Vineyard		Crops, Grass, Shrubs	17
Annual crops		Crops, Grass, Shrubs	17

*Coverage for Forests: combination of two different species in which the first is the dominant (75% of surface coverage), followed by the degree of coverage of the second species.

APPENDIX 6: NATURAL LOGARITHM OF CAPILLARY PRESSURE (ψ) PLOTTED AGAINST THE 1- EFFECTIVE SATURATION.

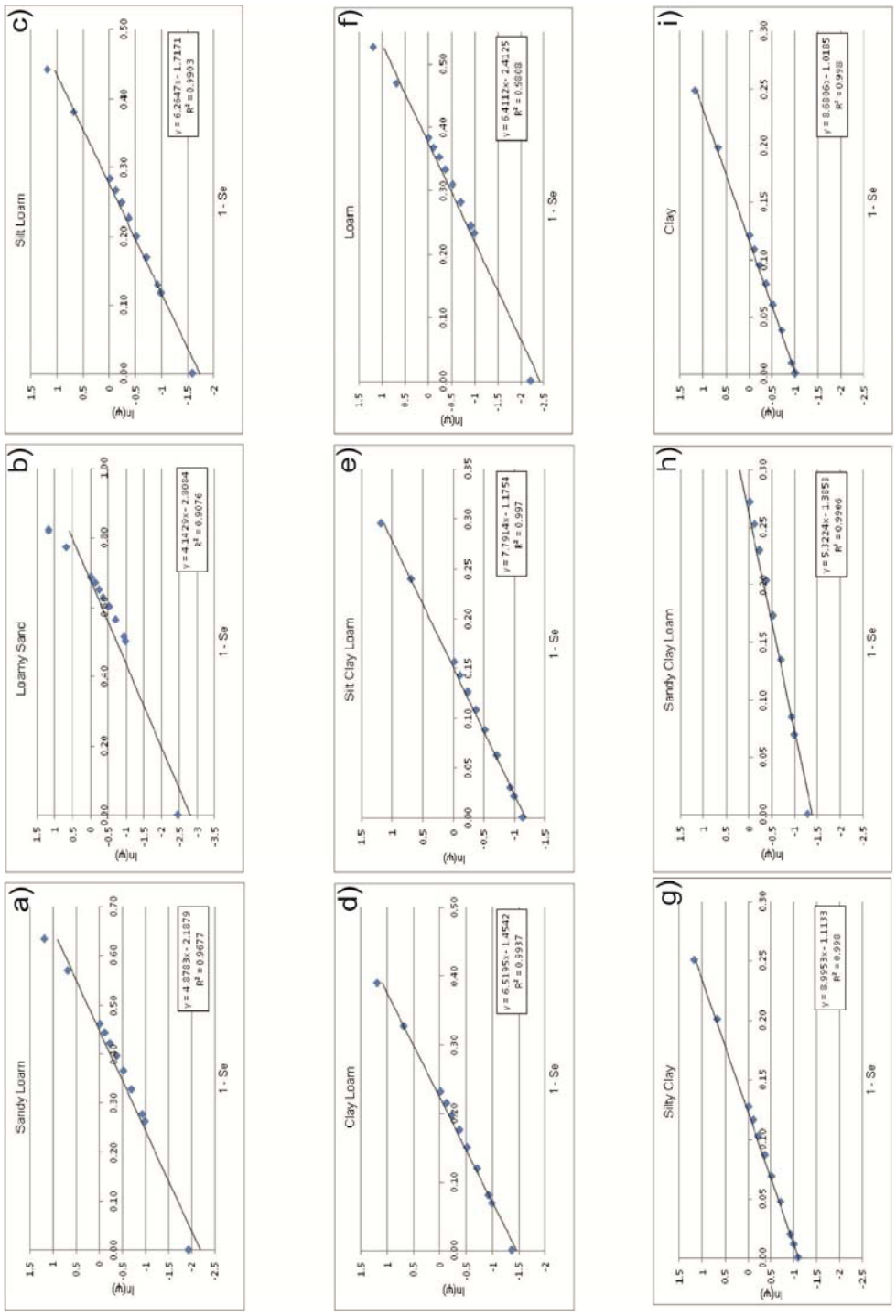

Fig. A6.1 – Natural logarithm of capillary pressure (ψ) plotted against the 1- effective saturation (Se) for: a) Sandy Loam soil; b) Loamy Sand soil; c) Silt Loam soil; d) Clay Loam soil; e) Silt Clay Loam soil; f) Loam soil; g) Silty Clay soil; h) Sandy Clay Loam soil; i) Clay soil.

APPENDIX 7: MAPS USED FOR CALIBRATION PURPOSES.

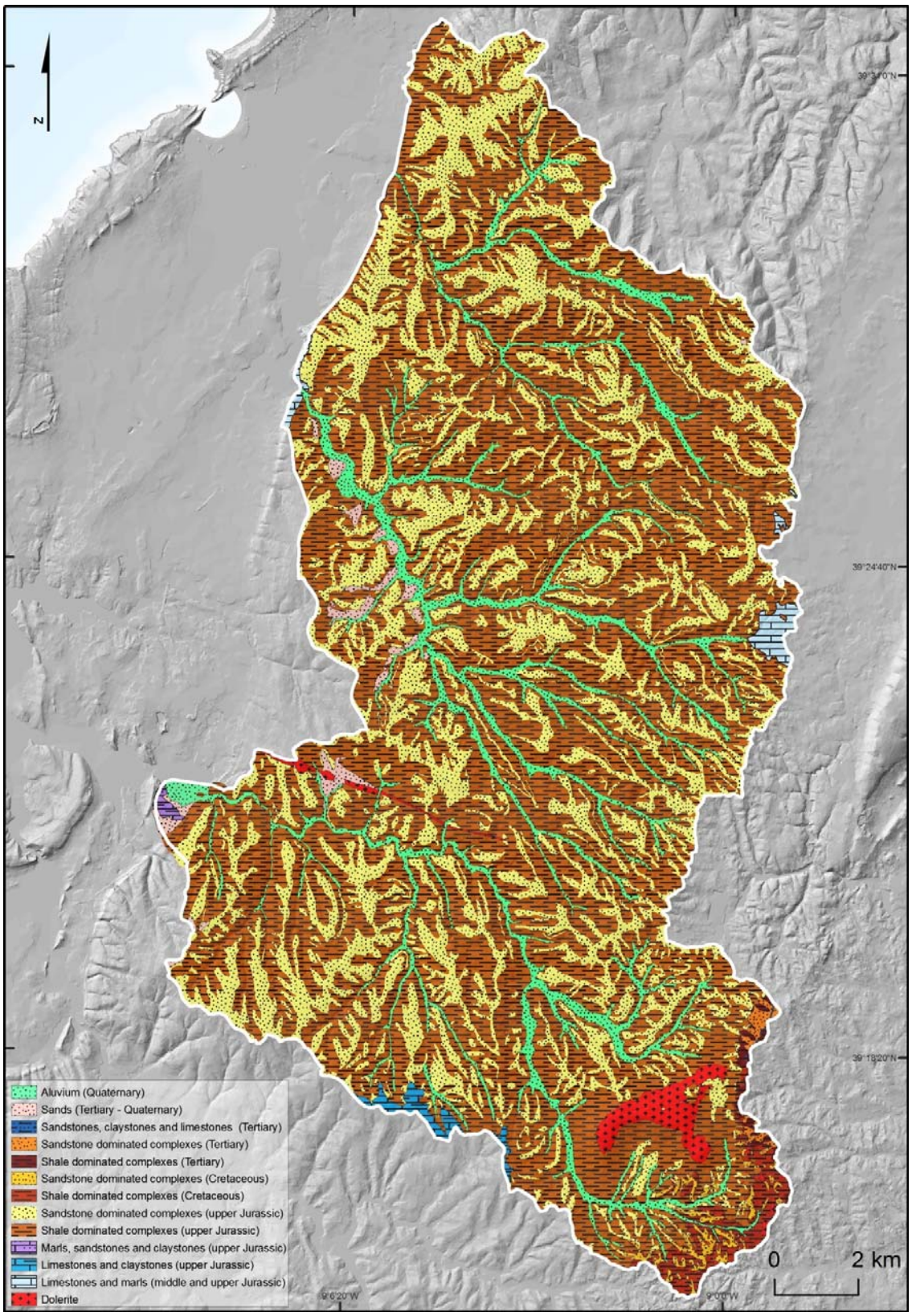

Fig. A7.1 – Lithological map incorporating part of Óbidos location used for calibration and validation purposes.

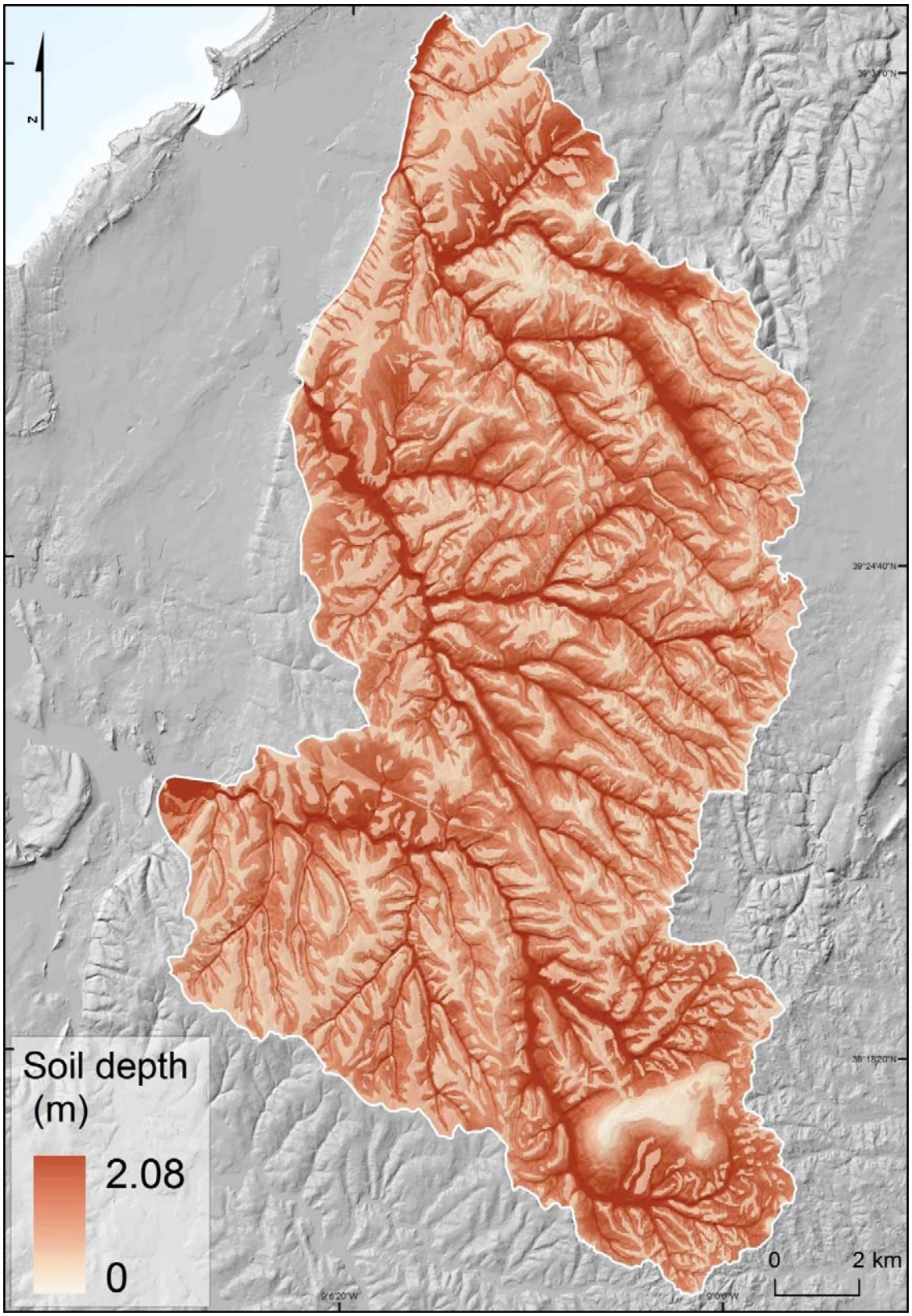

Fig. A7.2 – Soil depth map incorporating part of Óbidos location used for calibration and validation purposes.

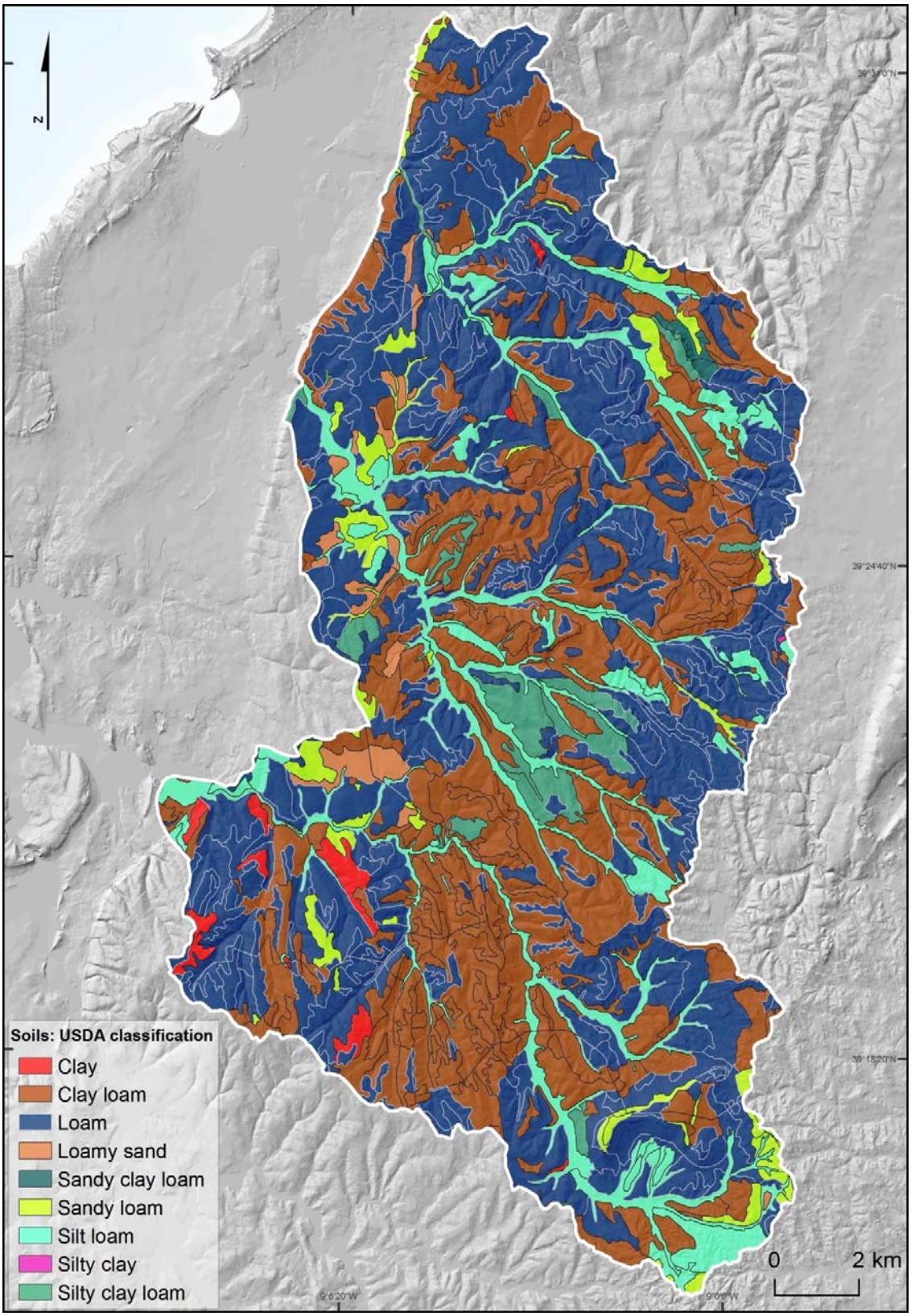

Fig. A7.3 – Soil map classified according to USDA incorporating part of Óbidos location used for calibration and validation purposes.

.

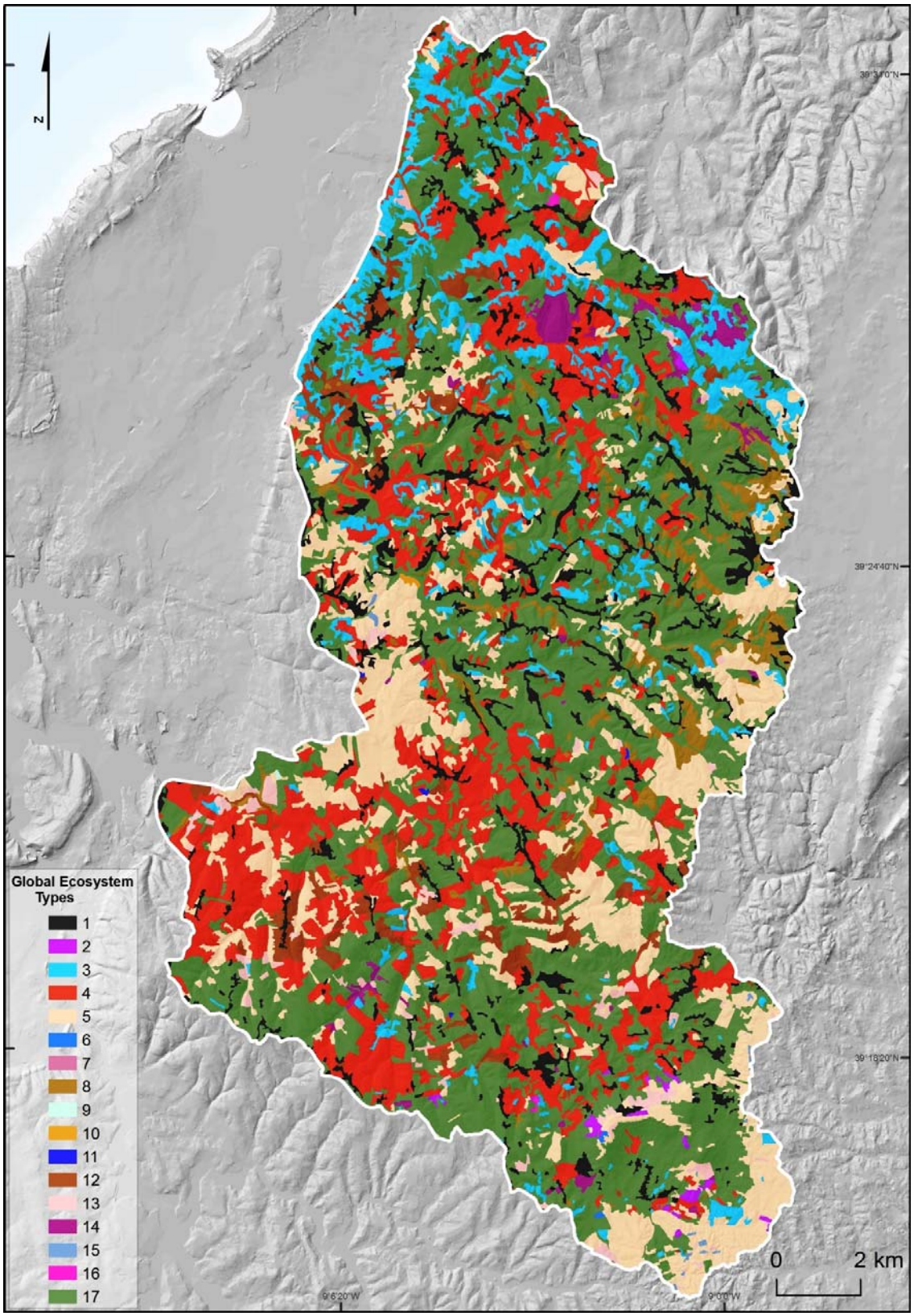

Fig. A7.4 – Global Ecosystem Types according to Olso (1994a, 1994b) incorporating part of Óbidos location used for calibration and validation purposes.

APPENDIX 8: PC RASTER SCRIPT: STARWARS + PROBSTAB.

Script A8.1 – Pc Raster Script: STARWARS + PROBSTAB (original version).

```
#!--matrixtable --lddin --radians



########## Binding: variable & constant declaration ##########

binding



 # INPUT: Maps, Timeseries and Tables

 #-General

 Duration= scalar(1.00);                    # length of timeslice in days

 AREA= DefaultParams\clone.map;                    # area of interest (boolean), should cover entire DEM or catchment(s)

 PI= scalar(3.14159265359);                    # constant pi



 #-Meteo

 #-requires stack of total precipitation and evapotranspiration in units of depth per timeslice [m/day] and

 # average air temperature [degC]

 PRECSTACK= meteo\prec;                    # precipitation input [m/day]

 PRECDURATIONSTACK= meteo\pdur;                    # duration of precipitation event, fraction of [day]

 EPOTSTACK= meteo\epot;                    # reference potential evapotranspiration [m/day]

 TEMPSTACK= meteo\temp;                    # average air temperature over time step [degC]



 #-Hydrology: constants

 MQD= scalar(4);                    # tortuosity parameter Millington & Quirk (MQD/MQN;[-])
```

```
MQN= scalar(3);

PSIFC= DefaultParams\psifc.map;                                  # matric suction at field capacity [m]

PSI50= DefaultParams\psi50.map;                                  # matric suction at which transpiration is halved [m]

PSIBC= DefaultParams\psibc.map;                                  # matric suction specifying boundary condition [m]

BYPASSFLOWFRACTION= DefaultParams\bypassflowfraction.map;        # fraction of surface detention passed on to groundwater [-]

MINRUNOFFDEPTH= scalar(0.001);                                   # minimum runoff depth [m]


#-Snow routine parameters: constants

TT= scalar(0.0);                                #threshold temperature for freezing/thawing [degC]

CFMAX=scalar(0.0055);                                            #degree-day factor [m/(degC*day]

CWH= scalar(0.10);                                  #water holding capacity snow cover [-]

CFR= scalar(0.05);                                  #refreezing coefficient [-]


#-Topography

DEM= DefaultParams\dem.map;                                      # digital elevation model of surface topography [m]

LDD= DefaultParams\ldd.map;                                      # local drainage direcion map of surface topography

OUTLETS= DefaultParams\outlets.map;                              # outlets corresponding to LDD pits

COEFVELTBL= DefaultParams\coefvelocity.tbl;                      # table with coefficients of flow velocity [m/day per (m/m slope)^0.5)]


#-Soil

#-soil geometry: layer depths [m]

D1= DefaultParams\d1.map;
```

```
D2= DefaultParams\d2.map;

D3= DefaultParams\d3.map;

#-soil properties

#-saturated hydraulic conductivity

KSAT0= DefaultParams\ksat0.map;                    # infiltration capacity [m/day]

KSAT1= DefaultParams\ksat1.map;                    # saturated hydraulic conductivity
of first layer [m/day]

KSAT2= DefaultParams\ksat2.map;                    # second layer [m/day]

KSAT3= DefaultParams\ksat3.map;                    # third layer [m/day]

KSATBC= DefaultParams\ksatbc.map;                  # lithic contact and bedrock base
[m/day]

#-volumetric moisture content: at saturation and residual moisture content

THETASAT1= DefaultParams\thetasat1.map;            # saturated volumetric moisture
content for first layer [m3/m3]

THETASAT2= DefaultParams\thetasat2.map;            # second layer [m3/m3]

THETASAT3= DefaultParams\thetasat3.map;            # third layer [m3/m3]

THETASATBC= DefaultParams\thetasatbc.map;          # bedrock base [m3/m3]

THETARES1= DefaultParams\thetares1.map;            # residual volumetric moisture
content for first layer [m3/m3]

THETARES2= DefaultParams\thetares2.map;            # second layer [m3/m3]

THETARES3= DefaultParams\thetares3.map;            # third layer [m3/m3]

THETARESBC= DefaultParams\thetaresbc.map;          # bedrock base [m3/m3]

#-SWRC: air entry value and shape factor

HA1= DefaultParams\ha1.map;                        # air entry value for first layer [m]

HA2= DefaultParams\ha2.map;                        # second layer [m]

HA3= DefaultParams\ha3.map;                        # third layer [m]

HABC= DefaultParams\habc.map;                      # lithic contact [m]

ALPHA1= DefaultParams\alpha1.map;                  # shape factor for first layer [-]

ALPHA2= DefaultParams\alpha2.map;                  # second layer [-]
```

```
ALPHA3= DefaultParams\alpha3.map;                    # third layer [-]

ALPHABC= DefaultParams\alphabc.map;                  # lithic contact [-]

#-soil mechanical properties per layer and at the slip plane

GAMMADRY1= DefaultParams\gammadry1.map;              # dry bulk weight for first
layer [kN/m3]

GAMMADRY2= DefaultParams\gammadry2.map;              # second layer [-]

GAMMADRY3= DefaultParams\gammadry3.map;              # third layer [-]

STATICSURCHARGE= DefaultParams\surcharge.map;        # surcharge -static-  in kPa

COHESION= DefaultParams\cohesion.map;                # soil cohesion [kPa] at shear
plane

ROOTCOHESION= DefaultParams\cohesion.map;            # root cohesion [kPa] at
shear plane

TANPHI= DefaultParams\tanphi.map;                    # tangent of angle of internal
friction at shear plane [-]

                                                     # at shear plane [-]

SDCOHESION= DefaultParams\cohesion_sd.map;           # for the above, the corresponding
standard deviation

SDROOTCOHESION= DefaultParams\rootcohesion_sd.map;

SDTANPHI= DefaultParams\tanphi_sd.map;



#-Land cover

#-requires stacks of land cover dependent properties

CROPFACTORSTACK= DefaultParams\kc;                   # crop factor to obtain crop-
specific potential evapotranspiration [-]

VEGETATIONCOVERSTACK= DefaultParams\cv;              # vegetation cover, used for
interception [m2/m2]

INTMAXSTACK= DefaultParams\intmax;                   # maximum canopy interception
storage [m/m2]

#-root fractions per soil layer [-]

ROOTFRAC1= DefaultParams\rootfrac1.map;
```

```
ROOTFRAC2= DefaultParams\rootfrac2.map;

ROOTFRAC3= DefaultParams\rootfrac3.map;

#-dynamic surcharge stack

DYNAMICSURCHARGESTACK= DefaultParams\vegw;          # dynamic surcharge, due to vegetation, in kPa



#-initial conditions

INTINI= DefaultParams\int00000.ini;                 # initial depth of interception storage [m]

SCINI= DefaultParams\snowcov0.ini;                  # snow cover, water equivalent [m]

SCFINI= DefaultParams\snowliq0.ini;                 # snow liquid storage, water equivalent [m]

SURFDETINI= DefaultParams\surfdet0.ini;             # amount of surface detention [m]

WATLEVELINI= DefaultParams\watlev00.ini;            # waterlevel, WL, above lithological contact [m]

THETAINI1= DefaultParams\theta1l0.ini;              # volumetric moisture content (VMC) [m3/m3], 1st layer

THETAINI2= DefaultParams\theta2l0.ini;              # VMC [m3/m3], 2nd layer

THETAINI3= DefaultParams\theta3l0.ini;              # VMC [m3/m3], 3rd layer

DEEPWATERINI= DefaultParams\deepstor.ini;           # initial storage in regional aquifer [m]



#-OUTPUT: Maps and TSS: all fluxes per time step

#-parameters

RCALPHA= results\groundwateralpha.map;              # reservoir constant [day-1]

#-states and fluxes: hydrology

INT= results\int;                                   # canopy interception [m]

SC= results\snowcov;                                # snow cover [m]

SCF= results\snowliq;                               # snow liquid storage [m]

SURFDET= results\surfdet;                           # surface detention [m]
```

```
 STREAMFLOW= results\qstr;                    # stream flow [m3]

 THETA1= results\theta1l;                     # volumetric moisture content (VMC [m3/m3]),
1st layer

 THETA2= results\theta2l;                     # VMC 2nd layer

 THETA3= results\theta3l;                     # VMC 3rd layer

 WATLEVEL= results\watlev;                    # water level [m]

 DEEPWATER= results\deepwat;                  # storage in water slice [m] of deep,
regional groundwater

 #-states: stability

 MSAFFAC= results\sf;                         # safety factor [-]

 MSAFMAR= results\sm;                         # mean expected safety margin [kPa], can
be reported with its standard

 SDSAFMAR= results\sm_sd;                     # deviation to compute more exact values of the
probability of failure

MINSAFFAC= results\sfmin.map;                 # minimum safety factor [-] over the year

TOTDURATION= results\totduration.map;         # total duration of instability (F<=1) [days]

 NUMBEREVENTS= results\numberevents.map; # number of separate instability events [-]


################ Areamap: clone-map definition #################

areamap

  AREA;


############# Timer: default time step set to days #############

timer

  1 365 1;

  rep1= endtime;

  rep2= 1+1..endtime,endtime;
```

```
######### Initial section:  definition of constants ##########

initial


#-General

#DX= DY, DX*DY

DX= celllength();                                   # cell length [m] and area [m2]

DX2= cellarea();


#-Constants: hydrology

MQ= MQD/MQN;                                        # constants of SWRC

MQALPHA1= 2*ALPHA1;

MQALPHA2= 2*ALPHA2;

MQALPHA3= 2*ALPHA3;

MQALPHABC= 2*ALPHABC;


#-Topography

#-Base level and soil depth [m]

SOILDEPTH= D1+D2+D3;

UL2= D2+D3;                                         #Surface layer 2

DEMBASE= DEM-SOILDEPTH;

#-Surface: topographical gradient [m/m] and associated flow velocity [m/s]

# and travel distance of floodwave [m] within timestep

TOPOGRADIENT= slope(DEM);

TOPOGRADIENT= max(TOPOGRADIENT,mapminimum(if(TOPOGRADIENT > 0,TOPOGRADIENT)));

COSGRAD= cos(atan(TOPOGRADIENT));

SINGRAD= sin(TOPOGRADIENT);

STREAMORDER= streamorder(LDD);
```

```
PROFCURV= profcurv(DEM);

STREAMPOINTS= PROFCURV <= mapmaximum(areaaverage(PROFCURV,if(STREAMORDER ==
mapmaximum(STREAMORDER),

  boolean(1))));

FLOWPATHS= path(LDD,STREAMPOINTS);

TRAVELDISTANCE= lookupscalar(COEFVELTBL,1,if(FLOWPATHS,nominal(1),if(STREAMORDER ==
1,3,2)))*Duration*

  (COSGRAD*SINGRAD)**0.5;

#-subcatchments and reservoir constant to determine the contribution of

# deep regional groundwater storage to stream flow

CONFLUENCE= (FLOWPATHS and upstream(LDD,DX2)/DX2 >3) or LDD == 5;

CONFLUENCE= if(CONFLUENCE,

  accuflux(LDD,DX2) == areamaximum(accuflux(LDD,DX2),clump(CONFLUENCE)),0);

STREAMID= nominal(uniqueid(CONFLUENCE));

SUBCATCHMENTID= subcatchment(LDD,STREAMID);

CATCHMENTWIDTH=
areaarea(SUBCATCHMENTID)/max(DX,areatotal(if(FLOWPATHS,DX,0),SUBCATCHMENTID));

AQUIFERTHICKNESS= max(1,areaaverage(DEMBASE,SUBCATCHMENTID)-
areaminimum(DEMBASE,SUBCATCHMENTID));

report RCALPHA= min(0.999,(PI**2*KSATBC*AQUIFERTHICKNESS)/

  (4*(THETASATBC-THETARESBC)*CATCHMENTWIDTH**2));



#-Soil and boundary conditions

#-active pore space per layer [m3/m3]

DEGSAT1= THETASAT1-THETARES1;

DEGSAT2= THETASAT2-THETARES2;

DEGSAT3= THETASAT3-THETARES3;

#-maximum available storage in the soil column [M]
```

```
STORMAX1= DEGSAT1*D1;

STORMAX2= DEGSAT2*D2;

STORMAX3= DEGSAT3*D3;

STORMAX= STORMAX1+STORMAX2+STORMAX3;

#-boundary condition [m/day]

THETAEFFBC= if(PSIBC>HABC,1-ln(PSIBC/HABC)/(0.5*MQALPHABC),1);

KUNSATBC= KSATBC*if(THETAEFFBC>0,THETAEFFBC**MQ*

  (exp(MQALPHABC*THETAEFFBC)-MQALPHABC*THETAEFFBC-1)/

  (exp(MQALPHABC)-MQALPHABC-1),0);

#-effective degree of saturation for top layer at field capacity

THETAEFFFC1= if(PSIFC>HA1,1-ln(PSIFC/HA1)/ALPHA1,0.99);

#-effective degree of saturation at which transpiration is halved

# and exponent of the power function

ROOTSTORLIM= ROOTFRAC1*STORMAX1*if(PSI50>HA1,1-ln(PSI50/HA1)/ALPHA1,0.5)+

  ROOTFRAC2*STORMAX2*if(PSI50>HA2,1-ln(PSI50/HA2)/ALPHA2,0.5)+

  ROOTFRAC3*STORMAX3*if(PSI50>HA3,1-ln(PSI50/HA3)/ALPHA3,0.5);

TRANSBETA= (ROOTFRAC1*STORMAX1*if(PSIFC>HA1,1-ln(PSIFC/HA1)/ALPHA1,0.5)+

  ROOTFRAC2*STORMAX2*if(PSIFC>HA2,1-ln(PSIFC/HA2)/ALPHA2,0.5)+

  ROOTFRAC3*STORMAX3*if(PSIFC>HA3,1-
ln(PSIFC/HA3)/ALPHA3,0.5))/max(0.001,ROOTSTORLIM);

TRANSBETA= max(0,-ln(1/0.99-1)/ln(max(0.001,TRANSBETA)));

#-relative degree of saturation in top soil under draining conditions [-]

THETAEFFDRAIN1= if(Duration>= 1,THETAEFFFC1,(1+Duration*THETAEFFFC1)/(1+Duration));

#-stability calculations

#-constants

LIMSAFFAC= scalar(9.99);                    # cut-off to report safety factor

GAMMAWATER= scalar(9.81);                   # bulk unit weight of water [kN/m3]
```

```
C1= scalar(1.2533141);                    # constants for cumulative PDF

C2= scalar(0.5792933);                    # of the Gaussian distribution

#-bulk unit weight of the soil under saturated conditions [kN/m3] and the buoyant weight

GAMMASAT1= GAMMADRY1+THETASAT1*GAMMAWATER;

GAMMASAT2= GAMMADRY2+THETASAT2*GAMMAWATER;

GAMMASAT3= GAMMADRY3+THETASAT3*GAMMAWATER;

GAMMABUO1= GAMMASAT1-GAMMAWATER;

GAMMABUO2= GAMMASAT2-GAMMAWATER;

GAMMABUO3= GAMMASAT3-GAMMAWATER;

#-variances

VARCOHESION= SDCOHESION**2;

VARCOHESIONROOT= SDROOTCOHESION**2;

VARTANPHI= SDTANPHI**2;



#-Initial values

#-hydrology

INT= INTINI;                              # initial depth of canopy storage in water slice [m]

SC= SCINI;                                # initial water equivalent depths of snow and liquid snow storage [m]

SCF= SCFINI;

SURFDET= SURFDETINI;                      # initial depth of water stored at the surface [m]

DEEPWATER= DEEPWATERINI;                  # deep, regional groundwater storage [m]

#-perched groundwater depths

WATLEVEL= WATLEVELINI;                    # perched groundwater conditions [m]

H3= min(WATLEVEL,D3);

H2= max(0,min(WATLEVEL-D3,D2));

H1= max(0,min(WATLEVEL-(D3+D2),D1));
```

```
#-effective relative degree of saturation [-]
THETAEFF1= if(WATLEVEL<SOILDEPTH,(THETAINI1-THETARES1)/DEGSAT1,scalar(0));
THETAEFF2= if(D2>0,if(WATLEVEL<UL2,(THETAINI2-THETARES2)/DEGSAT2,scalar(0)),
  (THETAINI2-THETARES2)/DEGSAT2);
THETAEFF3= if(D3>0,if(WATLEVEL<D3,(THETAINI3-THETARES3)/DEGSAT3,scalar(0)),
  THETAEFFBC);
#-stability
UNSTABLE= boolean(0);
MINSAFFAC= LIMSAFFAC;
MAXPROBFAIL= scalar(0);
TOTDURATION= scalar(0);
NUMBEREVENTS= scalar(0);


########## Dynamic section: iterated over meteo time steps ##########
dynamic


#-Storage based on state variables of previous timestep
#-bring groundwater conditions in line with relative degree of saturation and check on continuity
H1= if(THETAEFF1<1.0,H1,D1);
H2= if(THETAEFF2<1.0,H2,D2);
H3= if(THETAEFF3<1.0,H3,D3);
H2= if(D2>0,if(D3-H3>0.001,0,H2),0);
H1= if(D1>0,if(D2-H2>0.001,0,H1),0);
WATLEVEL= H1+H2+H3;
#-Unsaturated zone
#-depth of unsaturated zone (m)
DUNSAT1= max(D1-H1,0);
```

```
DUNSAT1= min(DUNSAT1,D1);

DUNSAT2= max(D2-H2,0);

DUNSAT2= min(DUNSAT2,D2);

DUNSAT3= max(D3-H3,0);

DUNSAT3= min(DUNSAT3,D3);

#-storage of pores left (-)

#  note: effective degree of saturation for overlying layer used for drainage.

#THETAEFF1= if(THETAEFF1<1,THETAEFF1,THETAEFFDRAIN1);

#THETAEFF2= if(D2>0,if(THETAEFF2<1,THETAEFF2,THETAEFF1),THETAEFF2);

#THETAEFF3= if(D3>0,if(THETAEFF3<1,THETAEFF3,THETAEFF2),THETAEFF3);

DELTATHETAEFF1= (1-THETAEFF1);

DELTATHETAEFF2= (1-THETAEFF2);

DELTATHETAEFF3= (1-THETAEFF3);

#-actual available storage in the unsaturated zone

STORCAP1= DUNSAT1*DEGSAT1;

STORCAP2= DUNSAT2*DEGSAT2;

STORCAP3= DUNSAT3*DEGSAT3;

#-unsaturated storage available for drainage (m waterslice)

STORMAT1= STORCAP1*THETAEFF1;

STORMAT2= STORCAP2*THETAEFF2;

STORMAT3= STORCAP3*THETAEFF3;

#-Saturated zone

#-saturated storage available for drainage (m waterslice)

STORSAT1= H1*DEGSAT1;

STORSAT2= H2*DEGSAT2;

STORSAT3= H3*DEGSAT3;

#-Total storage
```

```
#-pore space

STORCAP= STORCAP1+STORCAP2+STORCAP3;

#-available for drainage

STORMAT= STORMAT1+STORMAT2+STORMAT3;          #IN UNSATURATED ZONE

STORSAT= STORSAT1+STORSAT2+STORSAT3;    #IN SATURATED ZONE

STORTOT= max(0.001,STORMAT+STORSAT);     #TOTAL STORAGE IN SOIL COLUMN


#-Meteo

#-meteo input: precipitation [m], precipitation duration, fraction of [day], air temperature [degC]
and

# reference potential evapotranspiration [m]

PREC= timeinputsparse(PRECSTACK)*timeslice()*Duration;

PRECDUR= timeinputsparse(PRECDURATIONSTACK)*timeslice()*Duration;

EPOT= timeinputsparse(EPOTSTACK)*timeslice()*Duration;

TEMP= timeinputsparse(TEMPSTACK)*timeslice()*Duration;


#-Land cover

#-land cover parameterization: obtain the fraction vegetation cover [m2/m2], crop coefficient [-]
and

# interception storage [m/m2 ground surface]

CROPFACTOR= timeinputsparse(CROPFACTORSTACK);

VEGETATIONCOVER= timeinputsparse(VEGETATIONCOVERSTACK);

INTMAX= timeinputsparse(INTMAXSTACK);


#-Potential crop-specific evapotranspiration [m] and precipitation falling as snow

EPOT= CROPFACTOR*EPOT;

SNOW= if(TEMP < TT,PREC,0);
```

```
#-Canopy interception

#-computes interception and net rainfall and snow inputs to the underlying soil layer

PRECNET= (1-VEGETATIONCOVER)*PREC+max(0,VEGETATIONCOVER*PREC+INT-INTMAX);

INT= max(INT+PREC-PRECNET,0);

EVAP= min(INT,EPOT*if(INTMAX > 0,INT/INTMAX,0)**(2/3));

INT= max(0,INT-EVAP);

#-update snow depth for interception

SNOW= min(PREC,SNOW*if(PREC > 0,PRECNET/PREC,0));

PRECNET= max(0,PREC-SNOW);

#-update potential evapotranspiration

EPOT= max(0,EPOT-EVAP);


#-Snow accumulation and melt: snow cover and liquid water content, SC, SCF,  in water equivalents [m]

DSC= if(TEMP<=TT,CFR*SCF,-min(SC,max(0,TEMP-TT)*CFMAX*Duration*timeslice()));

SC= SC+DSC+SNOW;

SCF= SCF-DSC+PRECNET;

PRECNET= max(0,SCF-CWH*SC);

SCF= max(0,SCF-PRECNET);

EVAP= min(SCF,EPOT);

SCF= max(0,SCF-EVAP);

EPOT= max(0,EPOT-EVAP);


#-Surface water detention [m], bypass flow [m] and associated streamflow [m3]

BYPASSFLOW= BYPASSFLOWFRACTION*SURFDET;

SURFDET= max(0,SURFDET-BYPASSFLOW);

EVAP= min(SURFDET,EPOT);
```

```
EPOT= max(0,EPOT-EVAP);

SURFDET= max(0,SURFDET-EVAP);

#-estimate of event duration and delination of flow paths exceeding time step length

INFILDUR= if(PRECNET+SURFDET >= MINRUNOFFDEPTH,

(PRECDUR*PRECNET+Duration*SURFDET)/max(MINRUNOFFDEPTH,PRECNET+SURFDET),Duration)
;

INFILMAX= KSAT0*timeslice()*INFILDUR;

ESTH= max(0,SURFDET+PRECNET-INFILMAX);

ESTQ= accuflux(LDD,ESTH*DX2);

ESTD= ESTQ/(TRAVELDISTANCE*DX*max(MINRUNOFFDEPTH,ESTH));

FLOWPATH= path(LDD,ESTD >= timeslice()*Duration) or OUTLETS != 0;

INFILDUR= min(1,max(PRECDUR,ESTD));

INFILMAX= KSAT0*timeslice()*Duration;

#-deep drainage [m]

DEEPDRAINAGE= RCALPHA*DEEPWATER;

#-increase surface detention with rainfall

SURFDET=                    SURFDET+PRECNET+if(STREAMID                    ==
SUBCATCHMENTID,areatotal(DEEPDRAINAGE,SUBCATCHMENTID),0);

#-slope response

RUNOFF= if(FLOWPATH,0,SURFDET);

SURFDET= if(FLOWPATH,SURFDET,0);

PERC0= accuthresholdstate(LDD,RUNOFF,INFILMAX);

PERC0= if(FLOWPATH,0,PERC0);

RUNOFF= accuthresholdflux(LDD,RUNOFF,INFILMAX);

RUNOFF= if(FLOWPATH,0,RUNOFF);

#-stream response

SURFDET= SURFDET+upstream(LDD,RUNOFF);
```

```
PERC0= if(FLOWPATH,min(SURFDET,INFILMAX),PERC0);

SURFDET= if(FLOWPATH,max(0,SURFDET-PERC0),SURFDET);

STREAMFLOW= accutraveltimeflux(LDD,SURFDET,TRAVELDISTANCE);

STREAMFLOW= if(FLOWPATH,STREAMFLOW,RUNOFF)*DX2;

SURFDET= accutraveltimestate(LDD,SURFDET,TRAVELDISTANCE);



#-Soil fluxes

#-partiioning of evapotranspiration within the soil: potential evapotranspiration broken down

# into bare soil evapotranspiration and transpiration on basis of cover and ETP;

# actual bare soil evaporation is limited to k(theta)

# actual transpiration scaled to the available moisture in the root zone

TRANSPIRATION= VEGETATIONCOVER*EPOT;

ESOIL= max(0,EPOT-TRANSPIRATION);

ROOTSTOR=
ROOTFRAC1*(STORMAT1+STORSAT1)+ROOTFRAC2*(STORMAT2+STORSAT2)+ROOTFRAC3*(STOR
MAT3+STORSAT3);

REDTRANS= cover(1/(1+(ROOTSTOR/ROOTSTORLIM)**(-TRANSBETA)),0);

TRANSPIRATION= REDTRANS*TRANSPIRATION;

ESOIL= min(ESOIL,if(THETAEFF1>0,THETAEFF1**MQ*

  (exp(MQALPHA1*THETAEFF1)-MQALPHA1*THETAEFF1-1)/

  (exp(MQALPHA1)-MQALPHA1-1),0)*KSAT1);

#-scaled transpiration and bare soil evapotranspiration per layer

# from unsaturated and saturated zones

ETSAT= if(STORTOT>0,STORSAT/STORTOT*TRANSPIRATION,0);

ETMAT= max(0,TRANSPIRATION-ETSAT);

ETMAT1=
ESOIL+ETMAT*ROOTFRAC1*DUNSAT1/max(0.001,ROOTFRAC1*DUNSAT1+ROOTFRAC2*DUNSAT2
+ROOTFRAC3*DUNSAT3);

ETMAT2=
```

```
ETMAT*ROOTFRAC2*DUNSAT2/max(0.001,ROOTFRAC1*DUNSAT1+ROOTFRAC2*DUNSAT2+ROOT
FRAC3*DUNSAT3);

 ETMAT3=
ETMAT*ROOTFRAC3*DUNSAT3/max(0.001,ROOTFRAC1*DUNSAT1+ROOTFRAC2*DUNSAT2+ROOT
FRAC3*DUNSAT3);



 #-Unsaturated zone

 #-relative saturated hydraulic conductivity (-) for thetaeff(i)

 #-transmission of storage [-], drainage and average sustained percolation

 # through layer (i),

 #-balance check on fluxes, returning the actual percolation in [m] per time step

 #-Layer 1

 KR1= if(THETAEFF1>0,THETAEFF1**MQ*

  (exp(MQALPHA1*THETAEFF1)-MQALPHA1*THETAEFF1-1)/

  (exp(MQALPHA1)-MQALPHA1-1),

  0);

 PERC1= KR1*KSAT1;

 TRANS1= if(DUNSAT1>0.0,

  min(1.0,PERC1*Duration*timeslice()/DUNSAT1),0.0);

 THEFFNEW= if(DUNSAT1>0.0,max(0.0,(1-TRANS1)*STORMAT1+PERC0-ETMAT1)/STORCAP1,1.0);

 THEFFNEW= min(1.0,THEFFNEW);

 KR1= if(THEFFNEW>0,THEFFNEW**MQ*

  (exp(MQALPHA1*THEFFNEW)-MQALPHA1*THEFFNEW-1)/

  (exp(MQALPHA1)-MQALPHA1-1),

  0);

 PERC1= max(0,PERC1*KR1*KSAT1);

 PERC1= sqrt(PERC1);

 TRANS1= if(DUNSAT1>0.0,
```

```
 min(1.0,PERC1*Duration*timeslice()/DUNSAT1),0.0);

PERC1= STORMAT1*TRANS1;

MBC= ETMAT1+PERC1;

MBC= if(MBC>0,(STORMAT1+PERC0)/MBC,1.0);

MBC= min(MBC,1.0);

ETMAT1= MBC*ETMAT1;

PERC1= MBC*PERC1;

#-Layer 2

KR2= if(THETAEFF2>0,THETAEFF2**MQ*

  (exp(MQALPHA2*THETAEFF2)-MQALPHA2*THETAEFF2-1)/

  (exp(MQALPHA2)-MQALPHA2-1),

  0);

PERC2= KR2*KSAT2;

TRANS2= if(DUNSAT2>0.0,

  min(1.0,PERC2*Duration*timeslice()/DUNSAT2),0.0);

THEFFNEW= if(DUNSAT2>0.0,max(0.0,(1-TRANS2)*STORMAT2+PERC1-ETMAT2)/STORCAP2,1.0);

THEFFNEW= min(1.0,THEFFNEW);

KR2= if(THEFFNEW>0,THEFFNEW**MQ*

  (exp(MQALPHA2*THEFFNEW)-MQALPHA2*THEFFNEW-1)/

  (exp(MQALPHA2)-MQALPHA2-1),

  0);

PERC2= max(0,PERC2*KR2*KSAT2);

PERC2= sqrt(PERC2);

TRANS2= if(DUNSAT2>0.0,

  min(1.0,PERC2*Duration*timeslice()/DUNSAT2),0.0);

PERC2= STORMAT2*TRANS2;

MBC= ETMAT2+PERC2;
```

```
MBC= if(MBC>0,(STORMAT2+PERC1)/MBC,1.0);

MBC= min(MBC,1.0);

ETMAT2= MBC*ETMAT2;

PERC2= MBC*PERC2;

#-Layer 3

KR3= if(THETAEFF3>0,THETAEFF3**MQ*

 (exp(MQALPHA3*THETAEFF3)-MQALPHA3*THETAEFF3-1)/

 (exp(MQALPHA3)-MQALPHA3-1),

 0);

PERC3= KR3*KSAT3;

TRANS3= if(DUNSAT3>0.0,

 min(1.0,PERC3*Duration*timeslice()/DUNSAT3),0.0);

THEFFNEW= if(DUNSAT3>0.0,max(0.0,(1-TRANS3)*STORMAT3+PERC2-ETMAT3)/STORCAP3,1.0);

THEFFNEW= min(1.0,THEFFNEW);

KR3= if(THEFFNEW>0,THEFFNEW**MQ*

 (exp(MQALPHA3*THEFFNEW)-MQALPHA3*THEFFNEW-1)/

 (exp(MQALPHA3)-MQALPHA3-1),

 0);

PERC3= max(0,PERC3*KR3*KSAT3);

PERC3= sqrt(PERC3);

TRANS3= if(DUNSAT3>0.0,

 min(1.0,PERC3*Duration*timeslice()/DUNSAT3),0.0);

PERC3= STORMAT3*TRANS3;

MBC= ETMAT3+PERC3;

MBC= if(MBC>0,(STORMAT3+PERC2)/MBC,1.0);

MBC= min(MBC,1.0);

ETMAT3= MBC*ETMAT3;
```

```
PERC3= MBC*PERC3;

#-New state variables per layer as a result of the current matric fluxes

#-change in matrix storage and any resulting return flow working from the bottom upwards,

# leading to changes in the height of the water table

#-Layer 3

STORMAT3= if(D3>0,

  if(DUNSAT3>0,STORMAT3+PERC2-(ETMAT3+PERC3),STORMAT3),STORMAT3);

PERC2= PERC2-max(0,STORMAT3-STORCAP3);

THETAEFF3= if(D3>0,

  if(STORCAP3>0,min(1.0,STORMAT3/STORCAP3),THETAEFF3),0);

H3= if(THETAEFF3<1.0,H3,D3);

#-Layer 2

STORMAT2= if(D2>0,

  if(DUNSAT2>0,STORMAT2+PERC1-(ETMAT2+PERC2),STORMAT2),STORMAT2);

PERC1= PERC1-max(0,STORMAT2-STORCAP2);

THETAEFF2= if(D2>0,

  if(STORCAP2>0,min(1.0,STORMAT2/STORCAP2),THETAEFF2),0);

H2= if(THETAEFF2<1.0,H2,D2);

#-Layer 1

STORMAT1= if(DUNSAT1>0, STORMAT1+PERC0-(ETMAT1+PERC1),STORMAT1);

THETAEFF1= if(D1>0,if(STORCAP1>0,min(1.0,STORMAT1/STORCAP1),THETAEFF1),0);

H1= if(THETAEFF1<1.0,H1,D1);

#-exfiltration when top layer becomes saturated

MBC= max(0,STORMAT1-STORCAP1);



#-Saturated zone

#-fluxes in the saturated zone based on state variables of previous timestep
```

```
#-vertical fluxes evaluated first, ETSat already known
#-determining source of recharge
RECLAYER= if(D3>0,if(WATLEVEL<D3,3,0),-999);
RECLAYER= if(RECLAYER>0,RECLAYER,
 if(D2>0,if(WATLEVEL<UL2,2,0),-999));
RECLAYER= if(RECLAYER>0,RECLAYER,
 if(D1>0,if(WATLEVEL<SOILDEPTH,1,0),-999));
RECHARGE= if(RECLAYER==3,PERC3,
 if(RECLAYER==2,PERC2,
 if(RECLAYER==1,PERC1,0)));

#-Boundary: deep drainage and any exfiltration
#-outflow over lithic contact, vertical loss in m
BASELOSS= if(SOILDEPTH > 0,0.5*(KUNSATBC+
 max(KUNSATBC,min(1,WATLEVEL/max(0.001,SOILDEPTH))*KSATBC))*timeslice()*Duration,0);
#-actual infiltration and surface detention due to any exfiltration or infiltration
MBC= if(SOILDEPTH > 0,MBC,0);
PERC0= PERC0-MBC;
SURFDET= SURFDET+MBC;

#-Saturated zone
#-estimate of available saturated storage for the present time step and new water level, both [m]
H2= if(D2>0,if(D3-H3>0.001,0,H2),0);
H1= if(D1>0,if(D2-H2>0.001,0,H1),0);
WATLEVNEW= H1+H2+H3;
THETAEFF1= if(D1>0,if(THETAEFF1<1,THETAEFF1,THETAEFFDRAIN1),THETAEFF1);
THETAEFF2= if(D2>0,if(THETAEFF2<1,THETAEFF2,THETAEFF1),THETAEFF2);
```

```
THETAEFF3= if(D3>0,if(THETAEFF3<1,THETAEFF3,THETAEFF2),THETAEFF3);

DELTATHETAEFF1= (1-THETAEFF1);

DELTATHETAEFF2= (1-THETAEFF2);

DELTATHETAEFF3= (1-THETAEFF3);

STORSAT1= H1*DEGSAT1*DELTATHETAEFF1;

STORSAT2= H2*DEGSAT2*DELTATHETAEFF2;

STORSAT3= H3*DEGSAT3*DELTATHETAEFF3;

STORSAT=STORSAT1+STORSAT2+STORSAT3;

#-vertical fluxes

#-scale vertical fluxes to the available storage

STORSAT= STORSAT+RECHARGE+BYPASSFLOW;

MBC= BASELOSS+ETSAT;

MBC= if(MBC>0,STORSAT/MBC,1.0);

MBC= min(MBC,1.0);

ETSAT= MBC*ETSAT;

BASELOSS= MBC*BASELOSS;

STORSAT= max(STORSAT-(ETSAT+BASELOSS),0);

#-lateral fluxes

#-total head [m] and transmissivity [m2/day] based on the estimated water level over the

# current time step

TOTALHEAD= DEMBASE+0.5*(WATLEVEL+WATLEVNEW);

TSAT=
H1*KSAT1+H2*KSAT2+H3*KSAT3*min(1,0.5*(WATLEVEL+WATLEVNEW)/max(0.001,WATLEVNEW
));

#-resulting gradient and aspect with the corresponding transport fractions

GRADIENT= slope(TOTALHEAD);

ASPECT= aspect(TOTALHEAD);

NOASPECT= nodirection(directional(ASPECT));
```

```
SINASPECT= if(NOASPECT,0,sin(ASPECT));

COSASPECT= if(NOASPECT,0,cos(ASPECT));

FRACX= if(NOASPECT,0,SINASPECT/(abs(SINASPECT)+abs(COSASPECT)));

FRACY= if(NOASPECT,0,COSASPECT/(abs(SINASPECT)+abs(COSASPECT)));

#-fluxes [m] resulting from saturated lateral flow and boundary conditions

QSAT= TSAT*GRADIENT*timeslice()*Duration/DX;

QBOUNDARY= scalar(0);

QBOUNDARY= if(QBOUNDARY >= 0,QBOUNDARY,

  max(-STORSAT,QBOUNDARY));

STORSATLIM= max(0,STORSAT+QBOUNDARY);

LIMFRAC= min(1,max(0,

  if(QSAT > 1.e-3,STORSATLIM/max(1.e-6,QSAT)-0.25,0))**3);

QSAT= LIMFRAC*QSAT;

#-lateral transport

STORSAT= STORSAT-QSAT+QBOUNDARY+

  max(0,shift0(-FRACX*QSAT, 0 , 1))+

  max(0,shift0( FRACX*QSAT, 0 ,-1))+

  max(0,shift0( FRACY*QSAT, 1 , 0))+

  max(0,shift0(-FRACY*QSAT,-1 , 0));


#New state variables per layer at end of current timestep

#-Layer 3

STORSAT3= min(DELTATHETAEFF3*STORMAX3,STORSAT);

STORSAT= max(STORSAT-STORSAT3,0);

H3= STORSAT3/(DELTATHETAEFF3*DEGSAT3);

THETAEFF3= if(D3>0,

  if((D3-H3)> 0.001,THETAEFF3,1.0),0);
```

```
#-Layer 2

STORSAT2= min(DELTATHETAEFF2*STORMAX2,STORSAT);

STORSAT= max(STORSAT-STORSAT2,0);

H2= STORSAT2/(DELTATHETAEFF2*DEGSAT2);

THETAEFF2= if(D2>0,

  if((D2-H2)> 0.001,THETAEFF2,1.0),0);

#-Layer 1

STORSAT1= min(DELTATHETAEFF1*STORMAX1,STORSAT);

STORSAT= max(STORSAT-STORSAT1,0);

H1= STORSAT1/(DELTATHETAEFF1*DEGSAT1);

THETAEFF1= if(D1>0,

  if(D1-H1>0.001,THETAEFF1,1.0),0);

#Exfiltration to surface

SURFDET= SURFDET+STORSAT;


#-Regional groundwater storage, recharge, drainage and resulting surface detention along streams

DEEPRECHARGE= if(SOILDEPTH > 0,BASELOSS,PERC0);

DEEPWATER= DEEPWATER+DEEPRECHARGE-DEEPDRAINAGE;


#-calculation of VMC(i) [m3/m3]

THETA1= THETARES1+DEGSAT1*THETAEFF1;

THETA2= THETARES2+DEGSAT2*THETAEFF2;

THETA3= THETARES3+DEGSAT3*THETAEFF3;

#-total water height [m]

WATLEVEL= max(H1+H2+H3,0);
```

```
#-Stability
#-Safety factor and probability of failure computed assuming a normal distribution
#-bulk unit weight [kN/m3] per unit surface area
GAMMAMOIST1= GAMMADRY1+THETA1*GAMMAWATER;
GAMMAMOIST2= GAMMADRY2+THETA2*GAMMAWATER;
GAMMAMOIST3= GAMMADRY3+THETA3*GAMMAWATER;
#-additional strength gained from suction
SUCTION= if(D3 > 0,THETAEFF3*if(H3 > 0.001,HA3*exp(ALPHA3*(1-THETAEFF3)),0),
  if(D2 > 0,THETAEFF2*if(H2 > 0.001,HA2*exp(ALPHA2*(1-THETAEFF2)),0),
  if(D1 > 0,THETAEFF1*if(H1 > 0.001,HA1*exp(ALPHA1*(1-THETAEFF1)),0),0)));
DELTACOHESION= SUCTION*TANPHI;
#-contribution of saturated and unsaturated depths to total
# and effective weight components: computation is laborious but
# may be expanded to include other uncertainty terms
W1= max(0,D1-H1)*GAMMAMOIST1+H1*GAMMASAT1;
W2= max(0,D2-H2)*GAMMAMOIST1+H2*GAMMASAT2;
W3= max(0,D3-H3)*GAMMAMOIST1+H3*GAMMASAT3;
W= STATICSURCHARGE+timeinputsparse(DYNAMICSURCHARGESTACK)+
  W1+W2+W3;
U= GAMMAWATER*WATLEVEL*COSGRAD**2;
P= W*COSGRAD**2-U;
#-mean capacity: maximum available shear strength
MCAP= COHESION+DELTACOHESION+ROOTCOHESION+P*TANPHI;
#-mean demand: mobilized shear strength
MDEM= W*COSGRAD*SINGRAD;
#-mean safety factor
MSAFFAC= if(W > 0 and SOILDEPTH > 0,min(LIMSAFFAC,MCAP/MDEM),LIMSAFFAC);
```

```
#-mean safety margin

MSAFMAR= MCAP-MDEM;

#-components of the standard deviation and the corresponding probability of failure

VDYNTANPHI= (P*COSGRAD**2)**2*VARTANPHI;

VDYNTANPHIB= SUCTION**2*VARTANPHI;

SDSAFMAR= sqrt(VARCOHESION+VARCOHESIONROOT+VDYNTANPHI+VDYNTANPHIB);

ZSCORE= MSAFMAR/SDSAFMAR;

NORMINV= scalar(atan(abs(ZSCORE)*(C1+C2*ZSCORE**2)));

NORMINV= NORMINV/PI+0.5;

PROBFAIL= if(W > 0 and SOILDEPTH > 0,if(ZSCORE>0,1-NORMINV,NORMINV),0);

#-statistics

MAXPROBFAIL= max(MAXPROBFAIL,PROBFAIL);

MINSAFFAC= min(MINSAFFAC,MSAFFAC);

NUMBEREVENTS= NUMBEREVENTS+if(MSAFFAC <= 1 and not UNSTABLE,1,0);

UNSTABLE= MSAFFAC <= 1;

TOTDURATION= TOTDURATION+if(UNSTABLE,timeslice()*Duration,0);


#-Reporting map stacks

#-daily timestep

#-calculation of VMC(i) [m3/m3]

report (rep2) THETA1= THETARES1+DEGSAT1*THETAEFF1;

report (rep2) THETA2= THETARES2+DEGSAT2*THETAEFF2;

report (rep2) THETA3= THETARES3+DEGSAT3*THETAEFF3;

#-total water height [m]

report (rep2) WATLEVEL= max(H1+H2+H3,0);

#-streamflow [m3]

report (rep2) STREAMFLOW= STREAMFLOW;
```

```
#-initial maps

report (rep1) DEEPWATER= DEEPWATER;

report (rep1) SC= SC;

report (rep1) SCF= SCF;

report (rep1) SURFDET= SURFDET;


#-safety factor and probability of failure

report (rep2) MSAFFAC= MSAFFAC;

report (rep2) PROBFAIL= PROBFAIL;

#-statistics over time step

report (rep1) MINSAFFAC= MINSAFFAC;

report (rep1) MAXPPROBFAIL= MAXPROBFAIL;

report (rep1) TOTDURATION= TOTDURATION;

report (rep1) NUMBEREVENTS= NUMBEREVENTS;
```

APPENDIX 9: ANNUAL PRECIPITATION, MAXIMUM DAILY PRECIPITATION AND MAXIMUM DAILY GROUNDWATER LEVEL OBSERVED IN EACH YEAR.

Table A9.1 – Total anual precipitation (mm) registered for each year for each centroid of the depletion zone of the shallow translational landslides (ID1 to ID29).

ID	Years									
	2002	**2003**	**2004**	**2005**	**2006**	**2007**	**2008**	**2009**	**2010**	**2011**
1	755.8	795.3	499.2	484.9	990.0	428.8	539.1	328.4	598.8	436.1
2	739.8	676.5	456.1	408.6	754.0	367.3	506.9	568.2	573.6	419.0
3	738.9	722.2	464.6	417.9	816.7	411.5	534.4	442.8	627.1	470.9
4	738.4	709.2	458.5	408.6	802.5	410.3	530.6	440.2	628.1	475.5
5	734.5	710.2	456.4	408.2	802.3	407.7	529.7	439.4	624.3	471.7
6	729.4	716.7	451.4	404.1	809.0	399.7	523.8	438.0	617.0	461.2
7	733.1	681.5	437.9	386.1	775.0	401.3	517.1	427.3	628.2	484.0
8	736.7	742.0	475.0	435.1	846.4	412.8	541.7	448.0	621.1	458.6
9	753.6	797.3	500.1	486.8	988.3	428.0	545.2	334.6	599.6	436.2
10	761.3	804.0	500.4	490.2	1014.7	431.7	534.5	284.5	598.7	431.2
11	755.9	796.6	496.6	484.5	1002.4	427.6	531.0	291.8	595.6	429.7
12	708.1	792.2	500.6	483.3	856.0	409.8	628.7	593.5	618.7	460.1
13	693.1	794.3	498.8	481.4	810.5	397.6	646.3	691.2	613.1	470.3
14	732.9	680.0	437.3	385.0	774.3	402.2	516.6	424.9	628.5	485.3
15	732.6	691.2	448.9	398.2	779.2	403.8	525.2	446.5	628.8	477.2
16	722.4	718.7	458.1	414.9	807.6	397.0	531.4	464.5	616.5	451.1
17	736.9	735.5	471.2	429.9	839.6	411.2	539.3	444.4	621.0	460.4
18	726.8	759.4	470.5	439.3	885.1	403.1	533.1	417.0	602.2	436.7
19	728.7	749.2	476.2	443.2	865.7	404.4	540.4	442.1	610.6	440.1
20	738.7	771.9	485.8	461.7	924.2	414.7	537.9	382.2	602.8	436.0
21	732.0	770.1	486.9	463.6	908.3	411.5	550.4	424.3	606.2	437.2
22	756.5	797.2	496.7	483.7	998.2	428.0	533.0	299.2	597.2	431.3
23	753.5	794.9	496.6	482.4	992.3	426.1	535.0	310.1	597.1	431.2
24	748.5	783.7	499.1	478.6	951.1	423.8	546.2	397.7	602.1	443.7
25	736.9	789.4	498.5	480.9	930.2	418.9	570.1	439.8	605.4	444.8
26	737.2	684.7	463.4	416.6	770.1	375.4	516.1	579.0	578.4	427.2
27	703.1	774.1	490.4	467.6	822.6	393.2	607.5	649.1	605.6	463.0
28	722.2	778.8	462.0	433.1	834.3	403.3	598.0	835.2	627.1	546.4
29	742.4	717.6	452.6	397.0	801.0	409.5	519.7	408.5	622.4	470.4

Table A9.2 – Total anual precipitation (mm) registered for each year for each centroid of the depletion zone of the shallow translational landslides (ID30 to ID59).

ID	Years									
	2002	**2003**	**2004**	**2005**	**2006**	**2007**	**2008**	**2009**	**2010**	**2011**
30	760.5	739.1	462.2	389.7	779.0	415.1	513.2	389.8	627.4	467.5
31	722.2	691.1	440.4	390.4	771.4	390.5	517.9	458.8	622.6	462.4
32	734.9	669.5	438.8	387.1	764.3	404.1	519.2	431.2	632.4	489.9
33	759.4	723.0	459.0	391.2	780.3	415.0	517.5	398.9	631.8	483.7
34	718.0	717.6	457.8	415.7	804.3	393.7	531.4	472.1	615.5	445.0
35	726.2	782.5	462.8	436.6	836.0	405.3	600.1	842.9	627.2	547.3
36	721.9	778.1	461.9	432.8	834.6	403.6	597.7	835.0	627.1	546.4
37	728.0	749.4	476.5	443.9	863.1	404.8	542.4	450.8	613.1	441.0
38	741.8	718.1	454.4	397.8	800.7	410.1	520.2	409.1	623.4	471.2
39	723.9	681.3	440.6	391.1	772.4	391.5	518.2	456.1	623.7	465.1
40	738.4	717.2	452.0	398.8	805.6	406.3	520.5	413.9	620.7	467.3
41	752.1	632.8	418.4	364.4	684.9	328.2	457.5	505.5	544.9	375.9
42	732.6	721.9	449.3	394.0	804.7	404.6	513.7	394.4	612.3	448.0
43	729.6	734.2	468.6	427.4	855.0	410.7	532.6	424.1	611.5	449.1
44	717.6	784.0	496.6	476.0	865.2	411.5	605.4	553.9	618.8	454.8
45	727.3	734.1	481.7	446.5	833.7	397.1	546.8	562.8	594.6	446.9
46	730.6	781.2	498.7	476.7	889.9	414.7	583.7	519.6	610.1	456.2
47	739.2	785.5	484.9	463.9	957.5	414.8	529.9	351.3	593.7	429.5
48	704.2	799.2	502.6	481.8	810.0	401.7	634.6	734.2	619.2	490.3
49	696.4	794.5	498.3	478.7	803.8	396.7	639.4	726.6	614.6	482.1
50	727.8	756.7	470.4	437.2	884.6	406.6	530.8	408.9	602.2	440.4
51	751.9	791.8	494.0	479.0	991.5	424.3	529.5	302.6	593.3	428.4
52	704.9	799.2	503.3	482.4	809.8	402.2	635.5	731.0	619.4	489.7
53	717.4	821.1	506.1	478.0	819.3	405.1	595.4	799.8	627.0	530.7
54	723.6	796.3	479.3	454.5	827.8	406.8	603.5	824.4	627.9	540.3
55	700.2	693.7	436.6	385.4	751.5	368.5	508.1	498.0	610.7	421.4
56	641.5	620.4	398.1	326.6	590.0	292.2	437.4	588.6	599.7	308.1
57	639.5	618.6	395.3	324.1	598.7	289.8	435.1	580.6	595.6	309.4
58	750.7	762.7	412.5	399.9	850.3	402.4	599.7	913.2	621.1	570.3
59	715.2	810.4	495.9	469.5	818.4	402.6	596.2	801.2	624.0	528.7

Table A9.3 – Total anual precipitation (mm) registered for each year for each centroid of the depletion zone of the shallow translational landslides (ID60 to ID87).

ID	Years									
	2002	**2003**	**2004**	**2005**	**2006**	**2007**	**2008**	**2009**	**2010**	**2011**
60	732.3	773.9	437.8	426.5	842.5	405.4	630.4	880.1	623.3	550.9
61	749.9	762.4	409.7	397.6	849.1	400.2	597.6	910.7	617.8	566.9
62	748.2	762.4	410.4	396.9	848.2	399.6	598.0	908.2	617.5	566.4
63	711.2	695.0	445.3	397.6	767.3	384.8	521.2	483.8	619.0	442.2
64	740.2	723.4	463.3	411.5	813.5	414.5	529.2	420.7	623.4	463.7
65	712.1	694.1	444.6	396.9	765.9	386.2	522.1	483.9	617.4	441.7
66	734.5	760.7	479.1	452.1	920.0	411.5	533.1	384.5	599.5	436.0
67	743.0	777.6	489.7	467.4	934.6	418.3	542.4	382.1	605.5	437.8
68	739.0	771.6	485.4	462.2	928.2	414.8	536.2	376.5	600.7	433.5
69	731.3	740.6	471.3	433.9	851.6	407.6	537.5	438.7	613.4	449.4
70	743.1	781.8	490.4	471.6	950.3	419.1	539.9	361.4	600.9	433.3
71	730.5	773.6	496.8	473.4	880.8	413.0	577.6	527.8	608.0	455.6
72	723.2	722.0	460.4	418.2	814.5	398.0	532.3	460.9	615.2	450.3
73	746.5	779.8	496.3	476.1	945.4	421.6	545.0	404.9	600.9	442.9
74	642.0	866.6	531.4	550.5	810.4	415.8	836.9	812.6	636.9	480.0
75	726.8	738.8	469.2	432.0	862.8	405.0	533.9	432.1	609.2	445.8
76	728.4	757.5	470.5	437.7	885.1	406.9	531.2	409.0	603.1	440.8
77	728.8	756.6	470.3	436.5	883.4	407.0	531.5	410.5	603.1	441.3
78	745.1	780.4	487.5	470.4	974.4	419.0	530.7	333.2	594.3	429.8
79	745.0	780.7	488.4	471.1	975.3	419.2	530.6	331.6	593.8	429.4
80	760.9	805.6	503.4	492.1	1010.3	433.6	540.7	303.4	601.2	436.1
81	754.7	793.2	501.2	484.6	978.7	429.2	543.3	354.4	601.8	440.5
82	737.5	682.9	461.8	415.1	766.6	374.3	513.9	576.5	578.1	425.7
83	716.8	783.7	496.7	475.6	864.0	410.9	606.2	556.3	619.2	455.2
84	747.9	764.5	413.7	400.6	848.9	400.5	598.8	906.5	619.4	567.0
85	686.4	723.6	455.7	418.9	786.5	369.3	547.8	549.2	605.2	412.2
86	720.0	729.1	463.4	424.4	823.8	396.0	534.4	464.6	612.5	442.5
87	722.2	738.4	468.7	432.7	840.9	398.6	537.0	458.9	610.5	438.7
MEAN (ID1 to ID87)	729.37	749	470	437	848.7	403	550	508	611	459

Table A9.4 – First achieved maximum daily precipitation registered for each centroid of the deletion zone of the shallow translational landslide (ID1 to ID29). Year: 2002; 2003; 2004; 2005; 2006.

ID	Year									
	2002		2003		2004		2005		2006	
	(m)	(JD)	(m)	(JD)	(m)	(JD)	(m)	(JD)	(m)	(JD)
1	31.7	323	30.4	341	47.7	3	32.9	303	59.9	328
2	28.3	274	26.8	274	31.4	3	23.3	336	37.7	328
3	25.2	318	29.4	273	35.4	3	26	303	47.4	328
4	24.7	323	28.9	273	34.8	3	25.1	303	46.6	328
5	24.4	318	28.8	273	34.6	3	25.1	303	46.3	328
6	24.8	23	28.5	273	34	3	24.8	303	45.2	328
7	26.2	23	25.6	273	33.1	3	22.8	303	44.3	328
8	26.3	318	28.2	273	36.6	3	27.9	303	49.1	328
9	31.6	323	30.7	341	47.5	3	33.3	303	59.8	328
10	33.4	323	31.4	341	50	3	33.6	303	62.6	328
11	32.5	323	31.3	19	48.8	3	32.9	303	61.3	328
12	27.6	274	29.9	341	34.4	3	34.3	303	46.3	328
13	30.3	274	29.8	341	30.7	13	34.6	303	40.4	328
14	26.4	23	25.5	273	33.2	3	22.7	303	44.3	328
15	24.2	361	26.7	273	33.2	3	24.1	303	45.1	328
16	24.4	318	27.2	273	33.3	3	26.1	303	45.7	328
17	26	318	28.8	273	36.3	3	27.3	303	48.6	328
18	26.1	318	26.4	273	38.1	3	28.5	303	49.8	328
19	26.5	318	25.8	273	37.1	3	29	303	49.8	328
20	28.5	318	27.3	19	42.1	3	30.7	303	54.5	328
21	28	318	26.7	341	40.2	3	31.1	303	52.8	328
22	32.4	323	30.9	19	48.5	3	32.9	303	61	328
23	31.9	323	30.6	19	47.9	3	32.8	303	60.3	328
24	29.4	323	29.1	341	44.3	3	32	303	56	328
25	28.5	318	29.6	341	42	3	33	303	53.9	328
26	27.9	274	26.1	274	31.7	3	23.4	303	38.6	328
27	29	274	28	341	31.7	13	32.4	303	41.1	328
28	43.5	274	26.1	19	29.8	13	36.5	303	45.8	296
29	26.4	23	34.6	273	35	3	23.5	303	45.6	328

JD* Julian days

Table A9.5 – First achieved maximum daily precipitation registered for each centroid of the deletion zone of the shallow translational landslide (ID30 to ID59). Year: 2002; 2003; 2004; 2005; 2006.

ID	Year									
	2002		2003		2004		2005		2006	
	(m)	(JD)	(m)	(JD)	(m)	(JD)	(m)	(JD)	(mm)	(JD)
30	26.9	318	44.3	273	36.2	3	22.9	307	45.7	328
31	23.1	23	25.9	273	31	3	23.5	303	43.2	328
32	26.6	361	24.7	273	33	3	22.9	303	44.6	328
33	26.8	23	37.5	273	36.5	3	23.1	307	46.1	328
34	24.3	318	26.7	273	32.5	3	26.2	303	45.2	328
35	44.5	274	26.1	273	29.8	13	37	303	46.8	296
36	43.4	274	26.1	19	29.9	13	36.5	303	45.7	296
37	26.7	318	25.8	273	36.7	3	29.1	303	49.7	328
38	26.2	23	34.6	273	35.1	3	23.5	303	45.8	328
39	23.2	23	25.8	273	31.2	3	23.5	303	43.4	328
40	26.2	23	33.1	273	34.9	3	23.8	303	45.6	328
41	29.6	274	28.9	274	29.8	3	22.3	336	36.3	320
42	27	23	40.5	273	33.7	3	25.4	54	44.5	328
43	25.5	323	32	273	36.4	3	26.7	303	48	328
44	26.8	318	28.8	341	35.5	3	33.3	303	48.2	328
45	26.6	274	25.5	341	34.6	3	28	303	43.6	328
46	26.7	318	29.2	341	38.5	3	32.5	303	49.7	328
47	28.9	323	29.9	19	43.8	3	30.6	303	55.5	328
48	32.1	274	29.2	341	30.3	13	35.1	303	40.1	328
49	31.8	274	29	341	29.9	13	34.8	303	39.4	328
50	25.9	318	28.3	273	38.2	3	27.9	303	49.7	328
51	31.6	323	31.4	19	47.9	3	32.3	303	60	328
52	32.1	274	29.5	341	30.4	13	35.1	303	40.3	328
53	33.8	274	27.9	326	30	13	36.7	303	40.6	296
54	40.6	274	25.6	273	30	13	36.9	303	44.5	296
55	22	318	26.1	273	26.4	13	23.3	303	40.3	328
56	30.3	322	34.5	88	33.4	12	17.1	303	29.2	328
57	28.9	322	34.4	88	32.2	13	16.9	303	28.9	328
58	58.8	274	28.7	273	32.1	13	38.1	303	56.5	296
59	35	274	26.4	326	29.8	13	36.4	303	41.2	296

JD* Julian days

Table A9.6 – First achieved maximum daily precipitation registered for each centroid of the deletion zone of the shallow translational landslide (ID60 to ID87). Year: 2002; 2003; 2004; 2005; 2006.

	Year									
ID	2002		2003		2004		2005		2006	
	(m)	(JD)	(m)	(JD)	(m)	(JD)	(m)	(JD)	(m)	(JD)
60	52.9	274	26.9	273	29.4	13	38.5	303	53.2	296
61	58.5	274	28.8	19	33.8	13	37.8	303	56.4	296
62	58.1	274	28.8	19	33.9	13	37.7	303	56.1	296
63	23	318	26.1	273	29.6	3	24.5	303	42.8	328
64	25.7	323	35.8	273	35.3	3	25	303	46.9	328
65	27.5	1	27.7	1	41	1	29.6	1	52.8	34.7
66	27.5	323	27.7	19	41	3	29.6	303	52.8	328
67	29.2	318	27.5	341	42.8	3	31.4	303	55.5	328
68	28.5	318	27.8	19	42.4	3	30.7	303	54.7	328
69	25.9	318	27.7	273	36.7	3	27.9	303	48.8	328
70	29.6	323	28.3	19	44.1	3	31.7	303	56.6	328
71	26.7	274	28.7	341	37.9	3	31.8	303	48.8	328
72	24.5	318	27.3	273	33.8	3	26.4	303	46.1	328
73	28.8	323	28.6	341	43.6	3	31.6	303	55.2	328
74	36.1	274	40.5	341	27.8	3	43.8	303	46.7	296
75	25.6	318	27.7	273	36.7	3	27.6	303	48.6	328
76	26	323	28.3	273	38.3	3	28	303	49.8	328
77	25.9	318	28.5	273	38.2	3	27.9	303	49.7	328
78	30	323	30.4	19	45.3	3	31.3	303	57.3	328
79	30	323	30.4	19	45.5	3	31.4	303	57.4	328
80	33.4	323	31.8	341	49.5	3	33.8	303	62.3	328
81	31.2	323	30.4	341	46.7	3	32.8	303	58.8	328
82	28	274	26.3	274	31.6	3	23.2	303	38.4	328
83	26.7	318	28.7	341	35.3	3	33.3	303	47.9	328
84	57.8	274	28.5	273	32.8	13	37.8	303	55.9	296
85	23	318	24.7	273	27.3	13	27.3	303	41.1	328
86	24.9	318	26.6	273	33.9	3	27.1	303	46.5	328
87	25.5	318	26.1	273	35	3	28	303	47.7	328

JD* Julian days

Table A9.7 – First achieved maximum daily precipitation registered for each centroid of the deletion zone of the shallow translational landslide (ID1 to ID29). Year: 2007; 2008; 2009; 2010; 2011.

ID	Year									
	2007		2008		2009		2010		2011	
	(m)	(JD)	(m)	(JD)	(m)	(JD)	(m)	(JD)	(m)	(JD)
1	32.8	39	37.3	1	14.3	280	32.5	105	30.2	121
2	40	324	28.1	1	32.1	320	29.7	105	28.6	121
3	26.1	39	30.1	1	19.1	32	35	105	35.1	121
4	26	39	29.5	1	20.7	32	34.9	105	35.5	121
5	27.3	39	28.7	1	21.9	32	33.7	105	34.6	121
6	30.4	39	26.7	17	25.2	32	31	105	32.6	121
7	27.2	39	27	17	26.7	32	33.1	105	35.5	121
8	26.5	39	30.9	1	16.5	32	34.6	105	34	121
9	32.7	39	37.3	1	14.4	280	32.6	105	30.3	121
10	33.1	39	39.9	1	13.1	280	32.8	105	30.1	121
11	34.4	39	38.5	1	13.9	32	31.5	105	29.4	121
12	33.7	324	42	1	23.5	320	35	105	33.4	121
13	41.9	324	41.8	1	31.3	320	32.8	105	32.3	121
14	27.2	39	26.9	17	26.9	32	33.1	105	35.6	121
15	25.4	39	28.7	17	22.9	32	34.4	105	35.8	121
16	28.2	39	28.4	1	21.8	32	31.8	105	32.7	121
17	27.1	39	30.3	1	17.7	32	34.3	105	34	121
18	34	39	28	1	21.3	32	29.2	105	29.5	121
19	29.6	39	29.7	1	17.7	32	31.8	105	31.5	121
20	32.4	39	32.4	1	15.9	32	31.3	105	30.3	121
21	30.6	39	31.2	1	15.7	280	32.1	105	30.9	121
22	33.7	39	38.3	1	13.2	32	32	105	29.8	121
23	33.8	39	37.7	1	13.4	280	31.7	105	29.7	121
24	31.3	39	33.6	1	16.3	280	32.7	105	30.9	121
25	30.8	39	33.9	1	17.2	280	33.1	105	31.3	121
26	39.6	324	28.4	1	31.5	320	29.9	282	28.7	121
27	37.9	324	36.2	1	29.1	320	31.4	105	31.3	121
28	42.5	324	28	1	35	157	34	105	40.3	121
29	29.8	39	26.9	17	24.7	32	32.7	105	33.6	121

JD* Julian days

Table A9.8 – First achieved maximum daily precipitation registered for each centroid of the deletion zone of the shallow translational landslide (ID30 to ID59). Year: 2007; 2008; 2009; 2010; 2011.

ID	Year									
	2007		2008		2009		2010		2011	
	(m)	(JD)	(m)	(JD)	(m)	(JD)	(m)	(JD)	(m)	(JD)
30	28.4	39	27.3	1	23.4	32	34.2	105	34	121
31	26.7	39	27	17	25.5	32	31.8	105	33.9	121
32	25	39	28.1	17	25	32	34.6	105	36.9	121
33	26.7	39	28.1	17	23.3	32	35.2	105	35.8	121
34	28	39	28.3	1	21.8	32	31.4	105	32.2	121
35	43.8	324	28.2	1	36.1	157	34.7	105	40.9	121
36	42.5	324	27.9	1	34.8	157	34	105	40.3	121
37	28.1	39	30.5	1	16.5	32	32.7	105	32.1	121
38	29.3	39	27.2	17	24.1	32	33.1	105	33.9	121
39	26.4	39	27.2	17	25.3	32	32.2	105	34.3	121
40	30.4	39	26.7	17	25	32	32.1	105	33.2	121
41	37.5	324	26.4	1	33	320	28.2	105	26	121
42	34.4	39	24.6	1	27.3	32	29.7	105	30.3	121
43	32.4	39	27.5	1	21.4	32	31.1	105	31	121
44	30.7	324	39.7	1	21	157	35.7	105	33.9	121
45	32.1	324	29.3	1	25.4	320	29.9	105	29.7	121
46	28.2	39	35.4	1	19.8	280	34	105	32.4	121
47	36.7	39	33.2	1	18.9	32	28.9	105	28.2	121
48	47.3	324	39.8	1	34	320	35	105	34.8	121
49	44.9	324	39.8	1	33.4	320	33.2	105	33.3	121
50	34.8	39	27.9	1	22.1	32	29.2	105	29.4	121
51	35.7	39	37.3	1	15.7	32	30.4	105	28.7	121
52	47.7	324	40.4	1	34.1	320	35.4	105	35	121
53	48.9	324	33.2	1	35.2	320	35.6	105	37.9	121
54	46.3	324	30	1	35.1	320	35.5	105	40	121
55	27	39	25	1	26.7	32	28.2	105	30.4	121
56	24.5	324	18.3	1	27.5	32	31.7	65	25.9	121
57	22.1	324	17.1	1	30.1	32	32	65	24.9	121
58	40.8	324	24.2	1	43.7	157	33.6	105	44.9	121
59	46.4	324	32.4	1	34.7	320	34.2	105	37.3	121

JD* Julian days

Table A9.9 – First achieved maximum daily precipitation registered for each centroid of the deletion zone of the shallow translational landslide (ID60 to ID87). Year: 2007; 2008; 2009; 2010; 2011.

ID	Year									
	2007		2008		2009		2010		2011	
	(m)	(JD)	(m)	(JD)	(m)	(JD)	(m)	(JD)	(m)	(JD)
60	43.2	324	28.7	1	41.3	157	34.4	105	42.7	121
61	40.1	39	24.2	1	43.9	157	32.5	105	44.1	121
62	40.2	39	24.3	1	43.7	157	32.4	105	43.9	121
63	26.2	39	27.4	1	23.8	32	31	105	32.6	121
64	28.5	39	28.7	1	20.3	32	34	105	33.7	121
65	34.7	1	30.7	1	19.3		29.7	1	29.3	1
66	34.7	39	30.7	1	19.3	32	29.7	105	29.3	121
67	30.8	39	33.4	1	14.8	280	32.7	105	31.1	121
68	33.2	39	32.5	1	16.5	32	30.8	105	29.8	121
69	30	39	29	1	19.3	32	32	105	32	121
70	32.6	39	34.4	1	14.3	32	31.6	105	30.1	121
71	28.4	324	34.3	1	20.9	320	33.7	105	32.2	121
72	28.8	39	28.3	1	21.7	32	31.6	105	32.3	121
73	32.1	39	32.8	1	16.4	280	31.9	105	30.4	121
74	56.9	324	71.7	13	39.1	320	38.7	105	35	121
75	31.8	39	27.9	1	21	32	30.7	105	31	121
76	34.7	39	28	1	21.9	32	29.3	105	29.5	121
77	34.4	39	27.9	1	21.7	32	29.5	105	29.7	121
78	36	39	34.8	1	17.2	32	29.7	105	28.6	121
79	36	39	34.9	1	17.2	32	29.7	105	28.5	121
80	31.2	39	39.7	1	13.8	280	34.2	105	31.2	121
81	31.4	39	36.3	1	15.2	280	33.3	105	31	121
82	39.8	324	28.3	1	31.7	320	29.9	282	28.8	121
83	30.7	324	39.6	1	21.2	157	35.5	105	33.8	121
84	40.3	324	24.4	1	43.4	157	33	105	44.2	121
85	28.9	39	29.5	1	22.6	32	27.9	105	29	121
86	29.1	39	28.5	1	20.9	32	31.1	105	31.6	121
87	29.4	39	28.9	1	19.6	32	31.1	105	31.3	121

JD* Julian days

Table A9.10 – First achieved maximum daily groundwater level registered for each centroid of the deletion zone of the shallow translational landslide (ID1 to ID29). Year: 2002; 2003; 2004; 2005; 2006.

ID	Year									
	2002		2003		2004		2005		2006	
	(m)	(JD)	(m)	(JD)	(m)	(JD)	(m)	(JD)	(m)	(JD)
1	0.155	365	0.485	30	0.214	15	0.146	365	0.799	348
2	0.223	365	0.367	30	0.314	9	0.129	365	0.639	352
3	0.179	365	0.489	30	0.216	18	0.077	37	0.647	350
4	0.408	365	0.836	30	0.379	4	0.137	365	0.966	348
5	0.375	365	0.583	28	0.352	3	0.136	365	0.775	348
6	0.350	365	0.707	28	0.325	6	0.130	365	0.833	349
7	0.353	365	0.526	16	0.269	11	0.114	10	0.607	349
8	0.142	365	0.487	28	0.203	9	0.060	365	0.772	348
9	0.538	365	0.946	26	0.559	1	0.413	361	ats	349
10	0.560	365	0.995	25	0.560	1	0.547	349	ats	343
11	0.510	365	ats	26	0.506	1	0.365	360	ats	350
12	0.326	365	0.613	352	0.514	1	0.357	360	0.961	347
13	0.298	365	0.766	357	0.734	1	0.483	362	ats	350
14	0.350	365	0.598	17	0.266	11	0.114	10	0.683	350
15	0.365	365	0.546	15	0.315	7	0.118	10	0.673	348
16	0.362	365	0.696	29	0.353	3	0.152	365	0.887	353
17	0.391	365	0.694	28	0.415	1	0.193	365	0.986	347
18	0.200	365	0.597	30	0.256	10	0.114	365	0.840	347
19	0.176	365	0.546	32	0.244	13	0.109	365	0.742	348
20	0.546	365	0.930	28	0.563	1	0.422	354	ats	344
21	0.192	365	0.455	29	0.275	9	0.155	365	0.765	347
22	0.479	365	0.812	27	0.474	1	0.361	360	ats	345
23	0.602	365	ats	25	0.585	1	0.513	350	ats	343
24	0.427	365	0.799	27	0.500	1	0.349	357	ats	344
25	0.401	365	0.718	29	0.519	1	0.345	361	ats	344
26	0.099	3	0.162	37	0.116	10	0.051	54	0.364	354
27	0.102	365	0.414	38	0.382	2	0.173	365	0.718	355
28	0.129	365	0.401	32	0.248	2	0.092	365	0.522	353
29	0.529	365	0.739	27	0.469	1	0.227	365	0.843	346

ats* above topographical surface

JD* Julian days

Table A9.11 – First achieved maximum daily groundwater level registered for each centroid of the deletion zone of the shallow translational landslide (ID30 to ID59). Year: 2002; 2003; 2004; 2005; 2006.

ID	Year									
	2002		2003		2004		2005		2006	
	(m)	(JD)	(m)	(JD)	(m)	(JD)	(m)	(JD)	(m)	(JD)
30	0.240	365	0.591	26	0.230	16	0.083	30	0.583	354
31	0.136	365	0.494	33	0.160	55	0.065	37	0.504	357
32	0.148	365	0.519	32	0.150	55	0.070	37	0.514	357
33	0.190	365	0.559	26	0.159	16	0.058	19	0.526	353
34	0.339	365	0.592	29	0.365	2	0.151	365	0.827	349
35	0.126	365	0.298	27	0.251	2	0.095	365	0.410	350
36	0.128	365	0.517	38	0.358	7	0.091	365	0.675	360
37	0.379	365	0.577	29	0.426	1	0.229	365	0.946	346
38	0.927	365	ats	58	0.725	6	0.317	32	ats	346
39	0.334	365	0.593	29	0.290	9	0.110	11	0.724	351
40	0.977	365	ats	11	0.766	3	0.481	354	ats	333
41	0.332	365	0.636	30	0.368	4	0.106	365	0.762	350
42	0.018	365	0.090	27	0.017	2	0.004	1	0.082	351
43	0.150	365	0.283	28	0.168	1	0.082	358	0.343	350
44	0.185	365	0.392	357	0.359	1	0.185	352	0.606	348
45	0.122	365	0.261	31	0.195	1	0.101	363	0.363	351
46	0.111	365	0.212	354	0.171	1	0.110	355	0.326	349
47	0.178	365	0.341	29	0.189	1	0.160	357	0.472	348
48	0.036	3	0.185	364	0.187	2	0.057	365	0.252	359
49	0.061	365	0.237	357	0.200	1	0.097	360	0.226	354
50	0.171	365	0.549	28	0.201	9	0.086	365	0.877	345
51	0.171	365	0.417	30	0.184	1	0.139	360	0.620	348
52	0.120	365	0.373	354	0.328	1	0.170	360	0.382	354
53	0.101	360	0.291	360	0.280	1	0.110	353	0.429	351
54	0.072	365	0.192	362	0.186	1	0.074	365	0.282	353
55	0.035	2	0.292	43	0.129	55	0.023	38	0.135	365
56	0.022	1	0.039	85	0.018	55	0.010	38	0.011	365
57	0.021	1	0.052	43	0.026	55	0.011	38	0.013	365
58	0.194	365	0.414	33	0.146	17	0.044	365	0.504	356
59	0.039	3	0.154	362	0.151	1	0.049	365	0.223	355

ats* above topographical surface

JD* Julian days

Table A9.12 – First achieved maximum daily groundwater level registered for each centroid of the deletion zone of the shallow translational landslide (ID60 to ID87). Year: 2002; 2003; 2004; 2005; 2006.

ID	Year									
	2002		2003		2004		2005		2006	
	(m)	(JD)	(m)	(JD)	(m)	(JD)	(m)	(JD)	(m)	(JD)
60	0.064	364	0.138	32	0.096	1	0.054	360	0.199	351
61	0.086	362	0.158	31	0.083	47	0.023	365	0.198	351
62	0.090	365	0.199	33	0.091	60	0.017	365	0.236	354
63	0.198	365	0.414	30	0.210	7	0.070	36	0.413	356
64	0.342	365	0.579	27	0.317	1	0.144	365	0.788	348
65	0.000	1	0.000	1	0.000	1	0.000	1	0.000	1
66	0.200	365	0.595	30	0.251	12	0.145	365	0.893	345
67	0.397	365	0.783	26	0.444	1	0.294	361	ats	345
68	0.386	365	0.802	26	0.423	1	0.282	362	ats	345
69	0.401	365	0.692	27	0.426	1	0.260	365	0.948	346
70	0.401	365	0.808	26	0.442	1	0.311	360	ats	344
71	0.319	364	0.527	29	0.442	1	0.316	356	0.942	346
72	0.350	365	0.607	29	0.371	2	0.160	365	0.820	347
73	0.336	365	0.634	28	0.407	1	0.278	357	ats	345
74	0.000	344	0.068	345	0.000	1	0.000	345	0.012	345
75	0.447	365	0.654	27	0.464	1	0.254	365	0.887	345
76	0.170	365	0.547	28	0.202	9	0.087	365	0.807	346
77	0.373	365	0.583	27	0.397	1	0.222	365	0.822	345
78	0.400	365	0.770	27	0.411	1	0.321	362	ats	344
79	0.474	365	0.954	26	0.477	1	0.331	365	ats	345
80	0.601	365	0.997	25	0.634	1	0.586	348	ats	344
81	0.189	365	0.489	27	0.251	2	0.155	365	0.799	345
82	0.155	358	0.299	35	0.203	1	0.139	365	0.535	350
83	0.362	365	0.527	29	0.486	1	0.335	361	0.944	346
84	0.206	365	0.566	39	0.277	59	0.037	365	0.573	362
85	0.283	365	0.526	32	0.393	1	0.160	365	0.735	350
86	0.154	365	0.509	30	0.215	17	0.075	365	0.649	350
87	0.212	365	0.623	30	0.259	10	0.089	365	0.834	349

ats* above topographical surface

JD* Julian days

Table A9.13 – First achieved maximum daily groundwater level registered for each centroid of the deletion zone of the shallow translational landslide (ID1 to ID29). Year: 2007; 2008; 2009; 2010; 2011.

ID	Year									
	2007		2008		2009		2010		2011	
	(m)	(JD)	(m)	(JD)	(m)	(JD)	(m)	(JD)	(m)	(JD)
1	0.552	1	0.020	1	0.010	106	0.006	1	0.071	109
2	0.554	1	0.044	248	0.259	365	0.262	9	0.244	45
3	0.520	1	0.022	1	0.128	95	0.044	208	0.166	71
4	0.860	1	0.037	246	0.277	64	0.115	160	0.259	40
5	0.562	1	0.035	248	0.283	64	0.114	160	0.258	40
6	0.674	1	0.031	248	0.308	62	0.115	160	0.273	70
7	0.466	1	0.032	248	0.363	53	0.113	160	0.249	71
8	0.564	1	0.015	1	0.051	105	0.022	240	0.110	48
9	0.977	1	0.038	248	0.081	101	0.057	202	0.274	39
10	0.799	1	0.076	215	0.111	69	0.106	365	0.396	27
11	ats	1	0.033	250	0.075	104	0.049	365	0.259	68
12	0.689	1	0.084	209	0.165	79	0.333	33	0.284	36
13	0.993	1	0.109	194	0.474	365	0.697	22	0.463	69
14	0.527	1	0.032	248	0.375	53	0.112	160	0.250	71
15	0.468	1	0.036	247	0.309	62	0.120	160	0.242	42
16	0.731	1	0.034	248	0.246	66	0.126	157	0.244	69
17	0.734	1	0.038	248	0.206	73	0.116	160	0.266	39
18	0.721	1	0.024	1	0.086	105	0.034	160	0.194	73
19	0.543	1	0.023	1	0.073	105	0.041	160	0.165	73
20	0.786	1	0.071	214	0.186	69	0.141	152	0.384	27
21	0.484	1	0.023	1	0.048	105	0.035	218	0.164	73
22	0.762	1	0.033	248	0.076	104	0.050	365	0.256	41
23	0.983	1	0.072	217	0.123	75	0.110	160	0.391	27
24	0.913	1	0.036	248	0.103	99	0.084	160	0.286	37
25	0.842	1	0.049	246	0.112	95	0.109	160	0.280	37
26	0.310	1	0.025	1	0.100	365	0.115	11	0.114	70
27	0.670	1	0.033	230	0.138	365	0.329	33	0.209	71
28	0.434	1	0.022	79	0.339	365	0.659	11	0.170	43
29	0.663	1	0.099	195	0.502	47	0.255	132	0.431	30

ats* above topographical surface

JD* Julian days

Table A9.14 – First achieved maximum daily groundwater level registered for each centroid of the deletion zone of the shallow translational landslide (ID30 to ID59). Year: 2007; 2008; 2009; 2010; 2011.

ID	Year									
	2007		2008		2009		2010		2011	
	(m)	(JD)	(m)	(JD)	(m)	(JD)	(m)	(JD)	(m)	(JD)
30	0.531	1	0.023	1	0.194	74	0.033	230	0.199	71
31	0.480	1	0.022	1	0.171	80	0.048	160	0.152	73
32	0.487	1	0.021	1	0.196	75	0.041	214	0.151	73
33	0.451	1	0.016	1	0.133	91	0.018	267	0.115	73
34	0.636	1	0.034	248	0.240	66	0.130	154	0.239	69
35	0.284	2	0.022	79	0.309	365	0.519	8	0.163	43
36	0.640	1	0.022	79	0.455	365	0.927	20	0.173	43
37	0.621	1	0.037	248	0.158	82	0.116	160	0.252	41
38	ats	1	0.101	194	0.746	60	0.398	153	0.693	69
39	0.546	1	0.032	248	0.323	61	0.127	159	0.233	71
40	0.849	1	0.420	132	0.789	46	0.688	121	0.684	20
41	0.638	1	0.035	248	0.329	362	0.326	1	0.302	37
42	0.067	2	9.996	156	7.873	36	9.909	323	9.826	1
43	0.234	1	0.025	1	0.081	57	0.055	160	0.116	30
44	0.454	1	0.093	217	0.145	92	0.162	23	0.162	22
45	0.276	1	0.025	1	0.088	81	0.099	32	0.130	29
46	0.193	1	0.024	248	0.045	92	0.050	39	0.097	28
47	0.306	1	0.026	1	0.056	106	0.030	251	0.161	56
48	0.233	1	0.013	1	0.108	365	0.254	21	0.064	33
49	0.177	1	0.022	246	0.119	365	0.196	16	0.090	30
50	0.608	1	0.019	1	0.058	106	0.022	238	0.143	73
51	0.427	1	0.025	1	0.035	106	0.021	365	0.075	36
52	0.339	1	0.049	169	0.204	365	0.330	21	0.151	35
53	0.339	1	0.049	224	0.207	365	0.378	17	0.107	43
54	0.211	1	0.014	1	0.176	365	0.329	12	0.089	32
55	0.176	25	0.018	1	0.100	154	0.046	161	0.092	111
56	0.029	90	0.013	1	0.012	157	0.044	73	0.018	1
57	0.029	39	0.011	1	0.030	106	0.075	36	0.017	1
58	0.453	1	0.018	1	0.414	365	0.797	17	0.121	74
59	0.186	1	0.014	1	0.131	365	0.283	14	0.079	31

ats* above topographical surface

JD* Julian days

Table A9.15 – First achieved maximum daily groundwater level registered for each centroid of the deletion zone of the shallow translational landslide (ID60 to ID87). Year: 2007; 2008; 2009; 2010; 2011.

	Year									
	2007		2008		2009		2010		2011	
ID	(m)	(JD)	(m)	(JD)	(m)	(JD)	(m)	(JD)	(m)	(JD)
60	0.137	1	0.016	1	0.154	365	0.300	8	0.056	38
61	0.142	1	0.019	1	0.166	365	0.336	8	0.083	72
62	0.198	1	0.019	1	0.192	365	0.412	11	0.086	109
63	0.376	1	0.024	1	0.135	67	0.090	132	0.125	39
64	0.550	1	0.035	248	0.261	65	0.103	160	0.282	37
65	0.000	365	0.000	1	0.000	365	0.000	365	0.000	365
66	0.654	1	0.024	1	0.065	106	0.027	234	0.195	73
67	0.793	1	0.025	248	0.098	92	0.066	160	0.268	35
68	0.960	1	0.022	248	0.114	89	0.061	160	0.265	36
69	0.679	1	0.050	230	0.299	63	0.162	132	0.317	25
70	0.732	1	0.023	248	0.095	94	0.057	160	0.265	36
71	0.596	1	0.057	230	0.144	84	0.196	47	0.295	35
72	0.600	1	0.033	248	0.241	66	0.124	158	0.249	69
73	0.662	1	0.035	248	0.110	97	0.086	160	0.249	26
74	0.000	58	0.000	120	0.006	339	0.000	13	0.000	53
75	0.558	1	0.047	235	0.314	62	0.157	129	0.350	67
76	0.535	1	0.019	1	0.057	106	0.022	238	0.143	73
77	0.509	1	0.030	250	0.197	74	0.096	160	0.300	69
78	0.775	1	0.029	250	0.103	101	0.056	200	0.288	69
79	ats	1	0.029	250	0.102	102	0.056	202	0.287	69
80	ats	1	0.081	212	0.113	64	0.117	365	0.443	25
81	0.432	1	0.017	1	0.009	106	0.006	365	0.087	73
82	0.409	1	0.045	248	0.167	351	0.153	2	0.160	23
83	0.625	1	0.078	214	0.148	82	0.247	41	0.276	37
84	0.569	1	0.032	78	0.388	365	0.843	21	0.216	75
85	0.599	1	0.044	230	0.237	66	0.244	45	0.233	72
86	0.502	1	0.023	1	0.106	101	0.050	160	0.165	73
87	0.654	1	0.023	1	0.090	104	0.049	160	0.165	73

ats* above topographical surface

JD* Julian days